

---

**Self-assemblies of Sulphonamide Derived Urea, Thiourea and  
Conformational Isomers of a Mercury complex**

*A Thesis submitted to the Indian Institute of Technology  
Guwahati in fulfillment of the requirements for the Degree of*

**Doctor of Philosophy**



**Submitted by  
Jitendra Nath**

**(Roll No. 186122013)**

**Thesis Supervisor: Prof. Jubaraj B. Baruah**

**Department of Chemistry**

**Indian Institute of Technology Guwahati**

**Guwahati-781039, Assam, India**

**February 2024**

---

Dedicated to my mother



---

**Indian Institute of Technology Guwahati**  
**Department of Chemistry**



**Declaration**

I do hereby declare that this thesis entitled “*Self-assemblies of Sulphonamide Derived Urea, Thiourea and Conformational Isomers of a Mercury Complex*” is the outcome of research work carried out by me under the supervision of **Prof. Jubaraj B. Baruah**, at the Department of Chemistry, Indian Institute of Technology Guwahati, India.

In keeping with the general practice of reporting scientific observations, due acknowledgement has been made whenever the work described here has been based on the findings of other investigators.

IIT Guwahati  
February, 2024

Jitendra Nath  
Roll No.186122013



Prof. Jubaraj B. Baruah  
Department of Chemistry  
Indian Institute of Technology Guwahati  
Guwahati, 781039, Assam, India

Phone no. +91-361-258-2311(O)

Fax no. +91-361-269-0762

Email: [juba@iitg.ac.in](mailto:juba@iitg.ac.in)

### CERTIFICATE

This is to certify that the research work presented in this thesis entitled “*Self-assemblies of Sulphonamide Derived Urea, Thiourea and Conformational Isomers of a Mercury Complex*” is an authentic record of the results obtained from the research work carried out by **Mr. Jitendra Nath (Roll No. 186122013)** under my supervision in the Department of Chemistry, Indian Institute of Technology Guwahati, India. This work is original and has not been submitted elsewhere for a degree or award.

IIT Guwahati  
February, 2024

Prof. Jubaraj B. Baruah  
(Thesis Supervisor)

---

## Acknowledgements

I would like to acknowledge all the people who have contributed to this thesis in many ways.

First and foremost, I would like to express my profound appreciation to my supervisor, **Professor Jubaraj B. Baruah**, for providing me with direction during the course of my study. My understanding has been expanded as a result of his extensive knowledge and his logical manner of thinking. Without the aid that he provided, this thesis would not have been able to stand. Because of his support, I now have a great deal of self-assurance. When I was successful, he extended his heartfelt congratulations and words of support to me. Whenever I was unsuccessful, he comforted and inspired me. Because he is such a skilled educator and mentor, he is always able to assist me in finding solutions to all of my challenges. I was able to make my doctorate studies here more enjoyable because of his generosity, patience, and constructive guidance. I would want to express my gratitude to him in particular for devoting a significant amount of time to my project and for ensuring that this thesis was completed successfully.

I am highly indebted to “**Indian Institute of Technology Guwahati**” for the doctoral fellowship.

I would like to thank my doctoral committee members **Prof. Bhubaneswar Mandal** (IIT Guwahati), **Prof. Subhas Chandra Pan** (IIT Guwahati) and **Dr. Sunanda Chatterjee** (IIT Guwahati) for their valuable suggestions during progress my research work.

I am grateful to all faculty members in the Department of Chemistry, IIT Guwahati, for their help and encouragement and also to the non-teaching staff of the Department for their technical support. I am thankful to the Central Instrument Facility (CIF), IIT Guwahati for various characterization facilities.

- ❖ Thanks to, Dr. Babulal Das, Dr. Kulakamal Senapati, Mr. Aniruddha Gogoi, Mr. Basab Bhattacharjee, Mr. Imdadul Islam, Mr. Diganta Kumar Hira, Mrs. Abhilasha M. Baruah, and, Mr. Michael Deka, Mr. Tapu Ghosh for their support at instrumental laboratory during the research work.
- ❖ I express my sincere thanks to my lab mates, namely, Dr. Munendra Pal Singh, Dr. Arup Tarai, Rinki, Abhay, Jagajiban and Satyendra, for their advice, well wishes, encouragement and constant support during the research period at IIT Guwahati.

- 
- ❖ I am thankful to my friends and juniors namely, Hari, Hrushikesh, Pran, Chanreingam, Sujoy, Bapan, Pallav, Amlan, Subhrajyoti, Avi, Srijan, Monu, Saswat bhai, Praveen bhai, for their timely help, support and for the wonderful time we shared during this period.
  - ❖ This Thesis wouldn't have seen the light of this day without the care, encouragement and help of some wonderful people like Narmada Behera, Bimalkrishna Sahoo, Srikant Sahoo, Utkal Keshari Nayak, Sasadhar Nayak, Sudhakar Nayak. I would like to express my sincere gratitude to these wonderful people in my life for their constant motivation, which made me reach this point.

Finally, my Ph.D. endeavour could not be completed without the constant love, unwavering support, tolerance, and blessings bestowed upon me by my family. I would like to express my heartfelt thanks to my mother, Mrs. Yasoda Nath, my elder brothers, Amar Kumar Nath and Amulya Kumar Nath, my sisters-in-law, Rubini Nath and Bebina Nath, my sister Anita Roul, and brother-in-law, Mitu Roul, as well as my nieces, Amreeta Priyadarsenee Nath (Jhua), Liza Roul, Chinmayee Roul, and Itisree Roul. They are the main soul and inspiration for each and every step that I achieve in my life.



# ***Thesis Abstract***

The research works presented in the thesis entitled “**Self-assemblies of Sulphonamide Derived Urea, Thiourea and Conformational Isomers of a Mercury Complex**” are based on various non-covalent self-assemblies of sulphonamide derived urea, thiourea derivatives. Details studies to explore their self-assemblies as well as of their solvates, ionic-crystals, polymorphs, and isomers are presented. The content of the thesis is divided into five chapters. Each chapter other than the introduction chapter has a concise discussion, experimental and references. The first chapter provides literature examples to lay the foundation for the research; the contents of each chapter are elaborated below.

### **Chapter 1: Introduction**

Non-covalent assemblies are formed by interactions among similar or dissimilar organic, inorganic or combination from both the classes of molecules are of paramount importance in material sciences and biology. These assemblies are built by reversible weak intermolecular interactions provide flexibilities to adopt pre-organized and re-organized structures. Hence, it is a challenge to utilize non-covalent interactions such as hydrogen bond, van der Waals interaction,  $\pi$ -stacking, C-H $\cdots\pi$  interaction, ion- $\pi$  interaction, metal-ligand coordination to build new assemblies and also to analyze their presence in an identified non-covalent assembly. Concise discussion to introduce weak interactions influencing various non-covalent assemblies are provided. As the thesis has study on urea and thiourea derivatives, which themselves have widespread literature selected examples of non-covalent assemblies of these classes of compounds are deliberated. The assemblies of the parent compounds, as well as different forms such as cocrystals, polymorphs, and metal complexes are presented here. Selective examples on the utility of urea and thiourea derivatives in sensing anions, toxic cations are discussed. The significant roles of the weak interactions guiding the geometrical aspects of the host molecules are demonstrated. This chapter is ended with a section on the scopes of the research followed by the detailed list of literature references

### **Chapter 2:**

#### **Solvates and ionic cocrystals 4-[[4-(4-nitrophenyl)carbamoyl]amino]-N-(pyrimidin-2-yl)benzene-1-sulfonamide**

This chapter is on the synthesis characterization and study on various assemblies of the 4-[[4-(4-nitrophenyl)carbamoyl]amino]-N-(pyrimidin-2-yl)benzene-1-sulfonamide (**2.1**), its solvates and ionic cocrystals with tetrabutylammonium halides. The compound was synthesized by reacting 4-nitrophenylisocyanate with a drug molecule sulfadiazine and it was obtained as two different solvates which were characterized by NMR, IR, mass spectrometry

and single crystal X-ray diffraction. The self-assemblies of two (DMF) solvates (**2.1.1** and **2.1.2**), three ionic cocrystals (**2.1.3-2.1.5**), and a salt (**2.1.6**) of the sulfadiazine-derived urea were studied. Both solvates had one DMF molecule anchored by bifurcated hydrogen bonds with the urea moiety, whereas the 1:2 solvate had the second DMF in the interstitial spaces. The structural characteristics of three isostructural ionic co-crystals specifically those of tetrabutylammonium halides combined with 4-[[[(4-nitrophenyl)carbamoyl]amino]-N-(pyrimidin-2-yl)benzene-1-sulfonamide, where the halides are chloride, bromide, and iodide, were established. In contrast, when tetrabutylammonium fluoride was used, the expected ionic co-crystal did not form. Instead, the reaction yielded the salt (**2.1.6**), whose structure was also determined. In each ionic co-crystal, charge-assisted hydrogen bonds were formed between the halide ions and the N–H bonds of the urea group. The ionic co-crystals displayed homo-dimeric synthons of the parent compound, indicating that the slight adjustments in the dimer's geometrical structure, influenced by the angular variations of the host, played a crucial role in creating the necessary space to accommodate spherical halide ions of varying ionic radii. The basic nature of fluoride led to deprotonation, resulting in the formation of a salt. This chapter have showed the utilization of dimeric sub-assemblies within the assembly to have increased the solvent uptake as well as to prepared iso-structural ionic cocrystals. The potential utility of **2.1** as a substrate for fluoride detection visually is described.

### Chapter 3:

#### **Polymorphic solvates and ionic cocrystals of N-(5-methyl-1,2-oxazol-3-yl)-4-[[[(4-nitrophenyl)carbamoyl]amino] benzene-1-sulfonamide**

The structural characteristics, thermal stability, and de-solvation processes of two polymorphs of DMF solvate (**3.1.1** and **3.1.2**) of N-(5-methyl-1,2-oxazol-3-yl)-4-[[[(4-nitrophenyl)carbamoyl]amino]benzene-1-sulfonamide (**3.1**) were investigated. These polymorphs were characterized by their unique synthon assemblies and slight variations in the host molecule geometries. The compound **3.1** underwent a novel C–N bond formation reaction with tetrabutylammonium iodide (TBAI), leading to an N-butylated derivative (**3.1.4**). Similarly, DMF (**3.2.1**) and DMSO solvates (**3.2.2**) of 4-[[[(4-nitrophenyl) carbamoyl] amino]-N-(1,3-thiazol-2(3H)-ylidene)benzene-1-sulfonamide (**3.2**) exhibited analogous dimeric structures but with distinct conformations of the host molecule. De-solvation of these solvates also produced a uniform form. While TBAI generated an ionic co-crystal (**3.2.3**) with **3.2**, the formation of dimers by the host molecule created hydrophobic spaces

accommodating the cation. Both compounds were transformed into salts (**3.1.3** and **3.2.4**) via deprotonation by tetrabutylammonium fluoride, with **3.1** uniquely also undergoing deprotonation by tetrabutylammonium bromide under standard conditions. The visible spectra of the salts derived from both **3.1** and **3.2** were identical, attributed to the shared chromophore in their structures.

#### **Chapter 4:**

#### **Assemblies of Sulfathiazole and Sulfamethazine Derived Thiourea: Polymorphs, Solvates and Fluoride Detection**

The study explored the hydrogen-bonded structures of thiourea-modified sulfa-drugs, specifically 4-(3-arylthioureido)-N-(thiazol-2(3H)-ylidene)benzenesulfonamides with varying aryl groups (phenyl (**4.1**), 4-methoxyphenyl (**4.2**), and 2,3- or 2,4- or 3,4-dichlorophenyl (**4.3-4.5**), 4-nitrophenyl (**4.6** and **4.7**), along with their polymorphs and solvates. Except for a DMSO (1:2) solvate, all studied derivatives formed homo-dimeric hydrogen-bonded structures. Among these, the phenyl derivative exhibited two polymorphic forms, one with a hairpin-like configuration and another with an extended structure. The orientation of the -SO<sub>2</sub>- groups and the thiourea sections differed across the homodimers of these polymorphs. For the dichlorophenylthiourea derivatives of sulfathiazole, the nature of chlorine-chlorine interactions varied based on the chloro-groups' positions on the phenyl ring, affecting the melting points predictably across this series according to the calculated energies of the homodimers.

Additionally, the dimethylformamide hydrate and dimethylacetamide solvate of N-(4,6-dimethylpyrimidin-2(1H)-ylidene)-4-(3-(4-nitrophenyl)thioureido)benzene sulfonamide shared similar unit cell dimensions, illustrating that the water molecule in the former compensated for the space needed for an extra methyl group in dimethylacetamide compared to dimethylformamide, facilitating tight molecular packing. Furthermore, the study highlighted the ability of the 4-nitrophenylthiourea-based compounds to selectively detect fluoride ions visually, showcasing their potential application in sensing.

#### **Chapter 5:**

#### **Conformational isomers of a mercury complex of 2-(anthracen-9-ylmethylene)-N-phenylhydrazine carbothioamide.**

A study reported on an anionic mercury(II) complex with 2-(anthracen-9-ylmethylene)-N-phenylhydrazinecarbothioamide (**H5.1**) and two isomers of a neutral mercury(II) complex

involving the anion of the same ligand (**5.1**). The complex, denoted as **5.1.3**, featured a monodentate **H5.1** ligand (the neutral form of the ligand) and chloride as ligands. The neutral mercury(II) complex, exhibited two conformational isomers (**5.1.1** and **5.1.2**), arising from the E or Z geometry of the ligands across the conjugated C=N–N=C–N scaffold of the coordinated ligand. These isomers of the complex were prepared and characterized independently. The spectroscopic behaviours of the isomers in solution were examined using <sup>1</sup>HNMR and fluorescence spectroscopy. A facile transition from the E-isomer to the Z-isomer in solution was observed. The E isomer of the ligand was found to be more stable than the Z isomer by 8.37 kJ/mol. The energy barrier for the conversion of the E-isomer to the Z-isomer of the ligand was calculated to be 167.37 kJ/mol. The study also discussed the role of the mercury ion in facilitating the conversion from the E to the Z form. It was noted that the mercury complex **5.1.3** featured the E-form of the ligand. Additionally, the distinct photophysical properties of these mercury complexes were highlighted.

---

# CONTENTS

<b>Table of content:</b>	<b>Page No.</b>
<b>Chapter 1: Introduction</b>	1
1.1: Preliminary aspects of non-covalent assemblies	1
1.2: Descriptions and analysis of hydrogen-bonded assemblies	2
1.3: Varieties in hydrogen-bonded assemblies	5
1.4: Halogen bonds	11
1.5: Salient aspects of urea/thiourea derivatives for Supramolecular chemistry	13
1.6: Self-assemblies of urea and thiourea derivatives	16
1.7: Anion assisted self-assembly of urea and thiourea derivatives	22
1.8: Consequences of anion binding by urea/thiourea based receptors in detections	28
1.9: The thiourea in cation binding	31
1.10: Scope of this work	33
1.11: References	34
<b>Chapter 2: Self-assemblies of Solvates, Ionic-crystals and Salt of 4-[[4-(4-Nitrophenyl)-carbamoyl]amino}-N-(pyrimidin-2-yl)benzene-1-sulfonamide</b>	
2.1: Introduction	51
2.2: Synthesis and characterization of the DMF solvates <b>2.1.1</b> and <b>2.1.2</b>	53
2.3: Structural descriptions of the two solvates <b>2.1.1</b> and <b>2.1.2</b>	54
2.4: Synthesis and characterization of ionic-cocrystals	59
2.5: Structural descriptions of ionic cocrystals <b>2.1.3-2.1.5</b>	61
2.6: Synthesis and characterization of the TBA salt <b>2.1.6</b>	64
2.7: Structure of TBA salt <b>2.1.6</b>	65
2.8: DSC analysis of the salt ( <b>2.1.6</b> ) and the solvates ( <b>2.1.1</b> and <b>2.1.2</b> )	67
2.9: Comparisons of IR spectra of the solvates, Ionic cocrystal and salts	69
2.10: Hirshfeld surface analyses	70
2.11: Summary from the comparisons	74
2.12: Solution study of solvates and ionic co-crystal	75
2.13: <sup>1</sup> HNMR titration of <b>2.1</b> with tetrabutylammonium halides	77

---

<b>2.14:</b> UV-visible studies	80
<b>2.15:</b> Optimization of Energy by DFT calculations	81
<b>2.16:</b> Conclusion	82
<b>2.17:</b> References	83
Appendix - Chapter 2	86

### **Chapter 3: Polymorphic Solvates, Ionic-cocrystals and C-N Bond Formation to Form Ionic Cocrystal in Sulfamethoxazole and Sulfathiazole Derived Urea**

<b>3.1:</b> Introduction	94
<b>3.2:</b> Synthesis and characterization of the urea derivatives <b>3.1</b> and <b>3.2</b>	95
<b>3.3:</b> Preparation of solvates of <b>3.1</b>	95
<b>3.4:</b> Structural descriptions of the polymorphs <b>3.1.1</b> and <b>3.1.2</b>	96
<b>3.5:</b> Crystal morphologies, IR and thermal studies of the polymorphs	99
<b>3.6:</b> The Optimized energy calculation	102
<b>3.7:</b> Study on the different Supramolecular adducts of <b>3.1</b> with tetrabutylammonium halides	104
<b>3.8:</b> Structural descriptions of salt <b>3.1.3</b> and butylated- <b>3.1</b> ( <b>3.1.4</b> )	107
<b>3.9:</b> Solvates, ionic cocrystal and salt of <b>3.2</b>	108
<b>3.10:</b> Structural descriptions of solvates of <b>3.2</b>	110
<b>3.11:</b> Thermal studies of the solvates <b>3.2.1</b> and <b>3.2.2</b>	111
<b>3.12:</b> Ionic co-crystal of <b>3.2</b> with TBA iodide	112
<b>3.13:</b> Optimized energy of the solvates	114
<b>3.14:</b> Hirshfeld analysis	115
<b>3.15:</b> Solution studies on the interactions of tertbutyl ammonium halides with <b>3.1</b> and <b>3.2</b> .	116
<b>3.16:</b> UV visible studies	119
<b>3.17:</b> Conclusions	120
<b>3.18:</b> References	120
Appendix - Chapter 3	123

### **Chapter 4: Assemblies of Sulfathiazole and Sulfamethazine Derived Thiourea: Polymorphs, Solvates and Fluoride Detection**

<b>4.1:</b> Introduction	135
<b>4.2:</b> Synthesis of 4-(3-phenylthioureido)-N-(thiazol-2(3H)-ylidene)benzenesulfonamide	

---

(4.1)	136
<b>4.3:</b> Structural descriptions of the conformational polymorphs <b>4.1.1</b> and <b>4.1.2</b>	137
<b>4.4:</b> Comparison of the morphologies of the polymorphs <b>4.1.1</b> and <b>4.1.2</b>	142
<b>4.5:</b> Synthesis of thiourea derivative 4-{3-(4-methoxyphenyl)thioureido)-N-(thiazol-2(3H)-ylidene}benzenesulfonamide ( <b>4.2</b> )	143
<b>4.6:</b> Structural descriptions of the thiourea derivative <b>4.2</b>	144
<b>4.7:</b> Synthesis of 4-(3-(a,b-dichlorophenyl)thioureido)-N-(thiazol-2(3H)-ylidene)benzene sulfonamide; (a,b = 2,3 (4.3); 2,4 (4.4) or 3,4(4.5) respectively)	145
<b>4.8:</b> Structural descriptions of the thiourea derivative <b>4.3-4.5</b>	146
<b>4.9:</b> Synthesis of 4-(3-(4-nitrophenyl)thioureido)-N-(thiazol-2(3H)-ylidene)benzene sulfonamide ( <b>4.6</b> ) and its solvates ( <b>4.6.1-4.6.4</b> )	149
<b>4.10:</b> Structural descriptions of the thiourea derivative <b>4.6.1-4.6.4</b>	150
<b>4.11:</b> N-(4,6-dimethylpyrimidin-2(1H)-ylidene)-4-(3-(4-nitrophenyl)thioureido)benzenesulphon amide ( <b>4.7</b> ) and its solvates ( <b>4.7.1-4.7.4</b> ).	153
<b>4.12:</b> Structural descriptions of the thiourea derivative <b>4.7.1-4.7.4</b>	155
<b>4.13:</b> Comparison of energies of homodimers	160
<b>4.14:</b> Hirshfeld surface analysis	162
<b>4.15:</b> Trends in melting points	165
<b>4.16:</b> Solution studies on Fluoride Ions Detection	166
<b>4.17:</b> Conclusions	168
<b>4.18:</b> References	169
Appendix - Chapter 4	172

## **Chapter 5: *E* or *Z* Isomers Arising from Geometries of Ligand in Mercury Complex of 2-(Anthracen-9-ylmethylene)-N-phenylhydrazine carbothioamide**

<b>5.1:</b> Introduction	189
<b>5.2:</b> Synthesis and characterization of mercury complexes ( <b>5.1.1-5.1.3</b> )	191
<b>5.3:</b> Structural aspects of the mercury complexes ( <b>5.1.1-5.1.3</b> )	195
<b>5.4:</b> Conversion of isomers studied by <sup>1</sup> HNMR spectroscopy in solution	200
<b>5.5:</b> The implications of the orientations of the anthryl group in the emission spectra	206
<b>5.6:</b> Conclusions	211
<b>5.7:</b> References	211
Appendix - Chapter 5	216

---

<b>Thesis Conclusion</b>	226
<b>Appendices</b>	229
<b>List of Publication</b>	240



---

## ABBREVIATIONS

<b>CH<sub>3</sub>CN</b> : Acetonitrile	<b>RT</b> : Room temperature (30 °C)
<b>ACQ</b> : Aggregation Caused Quenching	<b>THF</b> : Tetrahydrofuran
<b>AIE</b> : Aggregation induced emission	<b>TGA</b> : Thermo-gravimetric analysis
<b>AIEE</b> : Aggregation Induced Enhanced Emission	<b>THB</b> : Trihydroxy benzene
<b>Å</b> : Angstrom	<b>TNP</b> : Trinitrophenol
<b>DFT</b> : Density functional theory	<b>UV-vis</b> : Ultraviolet-visible
<b>DHB</b> : Dihydroxy benzene	<b>H<sub>2</sub>O</b> : Water
<b>DNP</b> : Dinitrophenol	
<b>DMSO</b> : Dimethyl sulfoxide	
<b>DMF</b> : Dimethyl formamide	
<b>DNA</b> : Deoxyribonucleic acid	
<b>DLS</b> : Dynamic light scattering	
<b>EtOH</b> : Ethanol	
<b>ESIPT</b> : Excited state intramolecular proton transfer	
<b>FESEM</b> : Field emission scanning electron microscope	
<b>FRET</b> : Forster resonance energy transfer	
<b>HOMO</b> : Highest occupied molecular orbital	
<b>IR</b> : Infrared	
<b>ICT</b> : Internal charge transfer	
<b>ICT</b> : Isothermal calorimetric titration	
<b>LUMO</b> : Lowest unoccupied molecular orbital	
<b>MS</b> : Mass spectrometry	
<b>MeOH</b> : Methanol	
<b>μM</b> : Micromolar	
<b>nM</b> : Nanomolar	
<b>NP</b> : Nitrophenol	
<b>HNO<sub>3</sub></b> : Nitric acid	
<b>NMR</b> : Nuclear magnetic resonance	
<b>PET</b> : Photo-induced electron transfer	
<b>KBr</b> : Potassium bromide	
<b>PDC</b> : Pyridinedicarboxylate	
<b>RET</b> : Resonance energy transfer	
<b>RNA</b> : Ribonucleic acid	

# Chapter 1

## Introduction

### Introduction

#### 1.1: Preliminary aspects of non-covalent assemblies

Self-assemblies formed by non-covalent interactions among similar or dissimilar organic, inorganic or combination from both the classes of molecules or ions<sup>1</sup> are of paramount importance in material sciences<sup>2</sup> and as bio-based assemblies.<sup>3</sup> In general, the functional aspects of biological systems are guided by non-covalent interactions. For example, the self-assemblies of nucleobases<sup>4</sup> and proteins<sup>5</sup> are among the fundamental ones. These assemblies built by reversible weak intermolecular interactions provide flexibility to adopt preorganized and reorganized structures. Hence, it is a challenge to utilize non-covalent interactions such as hydrogen bond,<sup>6</sup> van der Waals interaction,<sup>7</sup>  $\pi$ -stacking,<sup>8</sup> C-H $\cdots$  $\pi$  interaction,<sup>9</sup> ion- $\pi$  interactions,<sup>10</sup> metal-ligand coordination<sup>11</sup> to build new assemblies and also to analyze their presence in an assembly. The strength of non-covalent interactions, excluding ionic interactions, is consistently weaker than that of conventional covalent bonds.<sup>12</sup>

A comparison of the energies of selected covalent bonds and non-covalent interactions is provided in Table 1.1.

**Table 1.1 Comparison of the different weak interactions with selected covalent bonds**

Non-covalent interaction (kJ/mol)		Covalent bond (kJ/mol)	
Ion-ion	200-300	C=O	690
Ion-dipole	50-200	C=C	600
Halogen bond	10-150	C-C	360
Hydrogen bond	4-120	C-S	272
Dipole-dipole	5-50	C=S	573
$\pi$ - interactions	0-50	C-X	213-485
van-der Waals interaction	< 4	X= halogen	

The non-covalent self-assemblies have diverse applications in the development of drugs<sup>13</sup> catalysis,<sup>14</sup> nano-science,<sup>15</sup> molecular machine<sup>16</sup> and as sensors.<sup>17</sup> Various topics, such as host-guest chemistry<sup>18</sup> require improvisation of weak interactions. The directional effect of weak interactions in non-covalent assemblies decides the architectures, and also provides challenges to build a desired form of an assembly from an identified set of multiple components.<sup>19</sup> The modulations of optical<sup>20</sup> and magnetic properties<sup>21</sup> of non-covalent assemblies by stimuli ions provide scopes to design advanced materials. The strength of non-covalent interactions, excluding ionic interactions, is weaker than conventional covalent

bonds.<sup>22</sup> So, for systematic research to create novel non-covalent assemblies from chemically and biologically significant species one has to analyze the weak interactions with molecular understandings.

## 1.2: Descriptions and analysis of hydrogen-bonded assemblies

A hydrogen bond is an intramolecular or intermolecular interaction between a hydrogen atom and an electronegative atom such as an X–H bond, in which X is a more electronegative atom than hydrogen.<sup>23</sup> It is represented by D-H···A, where D represents the electronegative atom (e.g., O, N, S, halogen etc.) providing the hydrogen to interact with an electronegative atom termed as an acceptor (A). An acceptor generally possesses a lone pair of electrons. A molecule may be involved in hydrogen bonds by serving as a hydrogen bond donor or acceptor or both. Intramolecular or intermolecular hydrogen bonds of the functional groups, together with other weak interactions, bring varieties to the architecture of self-assembly. The intramolecular hydrogen bonds provide stability to a particular geometry; whereas, the intermolecular hydrogen bonds among the same or different types of molecules constitute the assembly.

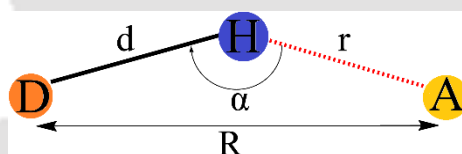


Figure 1.1: Representation of hydrogen bond

The hydrogen bonds (abbreviated as H-bonds) H-bonds are categorized into three classes: strong, moderate and weak.<sup>24</sup> A strong H-bond is formed when an acidic hydrogen interacts with a proficient hydrogen bond acceptor atom or ion. Such bonds conventionally have linear or close to geometry. When a strong hydrogen bond is between an ion and acidic hydrogen (usually found in the case when proton transfer from the acid counterpart occurs), it is known as a charge-assisted hydrogen bond.<sup>25</sup> In contrast, a moderate hydrogen bond assumes a slightly bent geometry, whereas weak hydrogen bonds are hydrogen bonds from a relatively strong bonds as hydrogen bond donors such as C-H bonds interacting with electronegative atoms such as O, N, S, halogen etc.<sup>26</sup> described as C-H···X bond or with  $\pi$ -cloud described as (C-H··· $\pi$  interaction). Table 1.2 contains a list of the bond parameters that are characteristic of strong, moderate, and weak hydrogen bonds. The bond energy of the three different types of hydrogen bonds falls within the intervals of 60 - 120 kJmol<sup>-1</sup> for strong, 16 - 60 kJmol<sup>-1</sup> for moderate, and ~12 kJmol<sup>-1</sup> for weak hydrogen bonds.



characteristics and energies of the synthons to plan for a predesigned non-covalent synthesis. Etter introduced Graph set notation to describe different hydrogen-bonded units found in non-covalent assemblies.<sup>29</sup> The graph-set notations describe hydrogen bonds as  $G_d^a(n)$  (where G as R is for ring, G as D for discrete, G as C for chain, and G as S for self- or intramolecular hydrogen-bonded systems. The total number of atoms (n) involved in hydrogen-bonded unit under description is shown within bracket, and the number of donors and acceptors in these assemblies are indicated as subscripts and superscripts after G.

The  $\pi$ -interactions among aromatic molecules play a crucial role in self-assemblies.<sup>9</sup> For simplicity, different  $\pi$ -interactions thorough face to face and edge to face arrangements between two benzene rings are shown in Fig. 1.3. In the face to face arrangements the rings are at parallel to each other, in eclipsing or translated positions. Perpendicular orientations result in C-H $\cdots\pi$  interactions as shown in the edge to face interactions. More options for stacking arrangements arise among unsymmetrically substituted rings as well as in polyaromatic systems. The X-H $\cdots\pi$  interactions (X = C, N, O etc.) contribute to stabilize conformers, guide quaternary structures and influence physiochemical properties, optical properties.

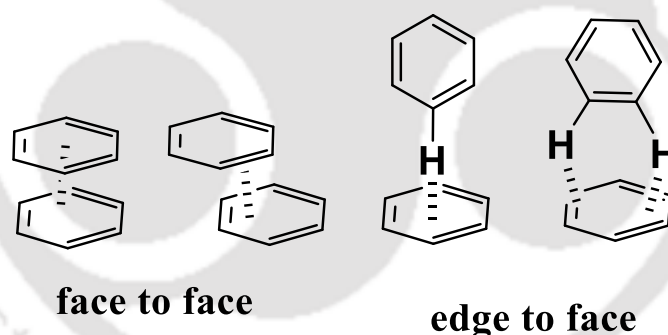


**Figure 1.3:** Different types of  $\pi$ -interactions among two benzene rings

Though weak, C-H $\cdots$ X play key roles in biology as well as guiding architectures of self-assemblies.<sup>30</sup> For example, two polymorphs of 1,3,5-trinitrobenzene has C-H $\cdots$ O and C-H $\cdots$ N interactions,<sup>31</sup> that guided it to form dimeric or trimeric assemblies in distinguishable manner in the two polymorphs (Fig. 1.4).

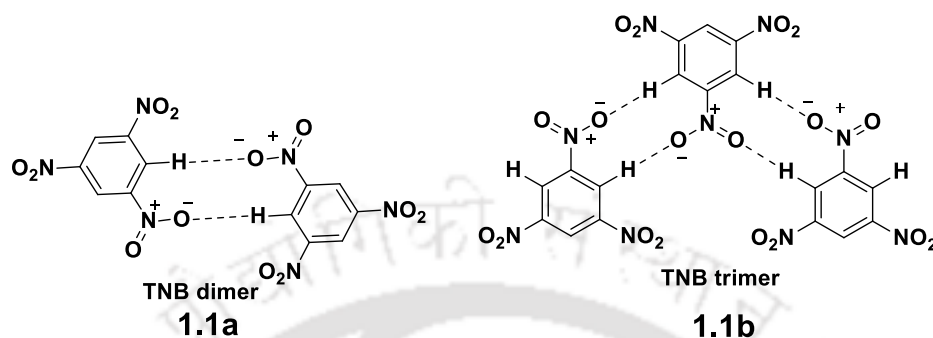


**Figure 1.4:** Two types of assemblies found in the polymorphs of 1,3,5-trinitrobenzene

These examples have clearly shown the varieties of interactions in self-assemblies. The energies being different, each has its role in an assembly. Nevertheless, the hierarchical effects of these interactions can not be ignored, so as the interplay of weak interactions.

### 1.3: Varieties in hydrogen-bonded assemblies

The functional behavior of the biological system has direct or indirect implications of hydrogen bonds, and the field is too vast and is not in the direct reach of research work carried out in this thesis; hence only the self-assembling aspects of synthetic molecules are discussed here. Most of the compounds that have both hydrogen bonding donors as well as acceptor sites form intermolecular hydrogen-bonded assemblies that are generally revealed through various spectroscopic techniques and diffraction techniques. The simplest examples of hydrogen-bonded assemblies are from hydrogen-bonded water molecules, dimers of carboxylic acids, etc. The impact of hydrogen bonds in those assemblies on the physiochemical properties is well documented in standard textbooks.

In general, the hydrogen-bonded assembly of a compound possesses different cyclic arrangements, providing dimeric or higher assemblies. Such units are referred to as homomeric synthons when the constituents of the hydrogen-bonded units are from the same functional group. Thus, utilizing them in appropriate ways provides cocrystals, multicomponent crystals or robust 1D-2D structures. For illustrations of homomeric synthons, a trimeric homo synthon and chain-arrangements through homo synthon are shown in Fig. 1.5. The first one is between two carboxylic acids through O-H $\cdots$ O hydrogen bonds

and other one is between two diamino triazine molecules through N-H $\cdots$ N bonds. Upon increasing monomeric units in an assembly, polymeric chains or cyclic assembled structures are formed.

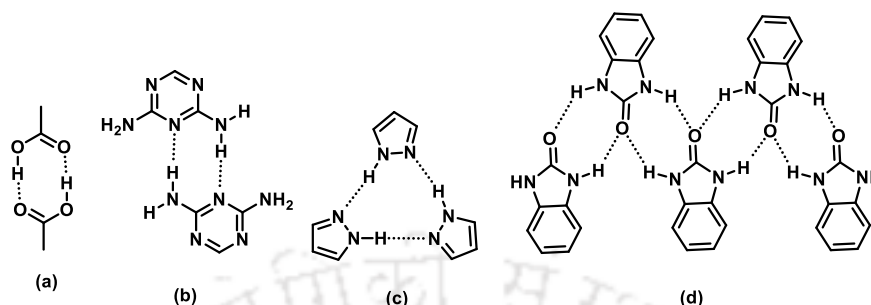


**Figure 1.5:** Examples of some homomeric synthons of (a) carboxylic acids, (b) diamino triazines, (c) pyrazole and (d) substituted urea.

Alteration arrangement of molecules in an assembly modify physical properties, which are often seen in polymorphs. The changes in the hydrogen bonds bring about differences in properties such as solubility<sup>32</sup> and thermal stability<sup>33</sup> from the original compounds. As an illustrative example, the two polymorphs of the 5,5-diethylbarbituric acid (1.3) display two types of hydrogen-bonded assemblies, namely, one having a linear chain-like structure and the other possessing square-grid structures<sup>34</sup> (Fig. 1.6). In these polymorphs the molecules are differently arranged to provide the N-H $\cdots$ O hydrogen bonds either to remain as single chain or as two assembly of two chains.

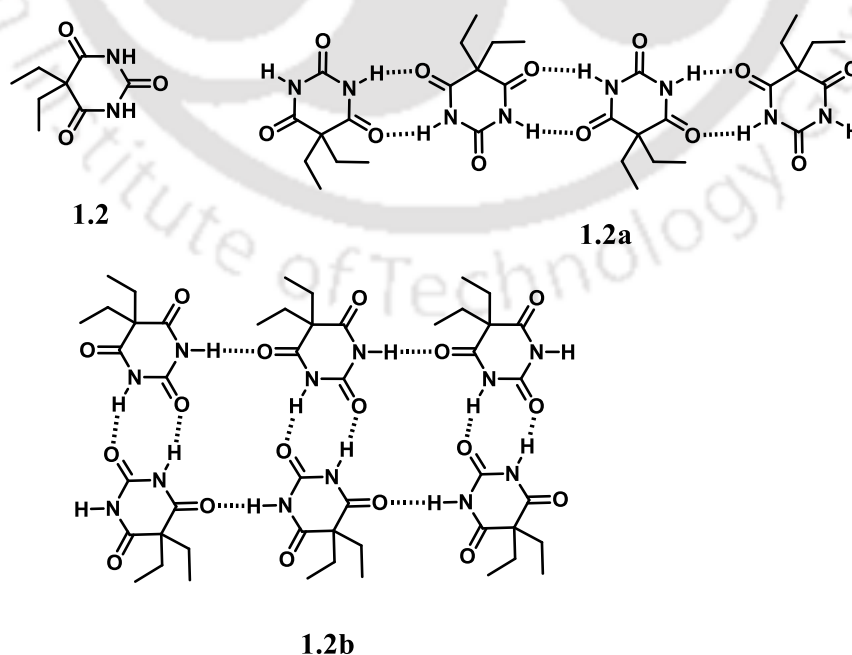


**Figure 1.6:** The structure of 5,5-diethylbarbituric acid **1.3**, **1.3a** and **1.3b** are self-assemblies of two polymorphs.

Polymorphs of cocrystals differing in synthons, such as co-crystal of 4,4'-bipyridine with 4-hydroxybenzoic acid are reported in literature.<sup>35</sup> Both the polymorphs had O-H···N and O-H···O hydrogen bonds but were with different synthons. The thermodynamically more stable polymorph referred to as **1.3a** has the self-assembly driven by carboxylic acid-carboxylic acid synthons with  $R_2^2(8)$  graph set notation. The other polymorph **1.3b** is a kinetic product and has catemers of carboxylic acid held together through linear hydrogen bonds with C(9) graph set notation.

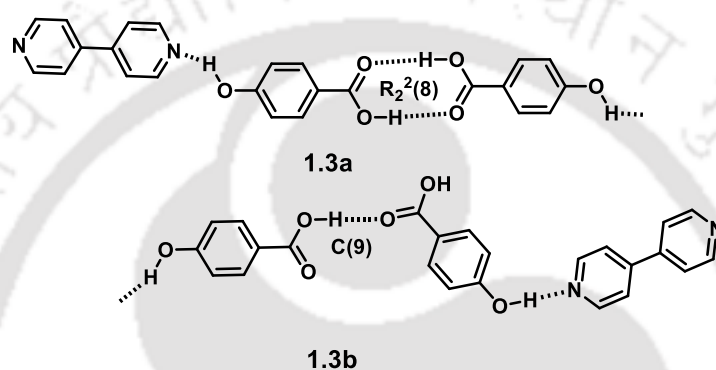
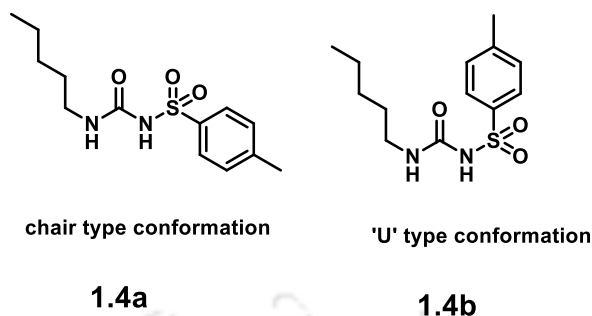


**Figure 1.7:** Synthon polymorphs of co-crystal of 4,4'-bipyridine with 4-hydroxybenzoic acid.

Multicomponent cocrystals, solvates and hydrates are cocrystals where the partner molecules are solvent molecules. They are of interest due to their availability and compositionally, form polymorphic forms with different properties. Water molecules are often observed in crystals and they are responsible to anchor multiple host units to provide multi-component assemblies. This happens as their presence in a lattice, increases the numbers of sites for the formation of hydrogen bonds or to allow the lattice water molecules to act as fillers. A large number of organic/inorganic molecules form solvates with varying amounts of solvent molecules, providing a series of solvates of the same or different solvent molecules (also called as pseudo-polymorph). It is a challenge to obtain porous structures through the de-solvation of solvates from solvated/hydrated self-assemblies of flexible molecules. But, in many rigid frameworks, the structures upon de-solvation, porous skeletons are easily obtained. Solvate formation provides scopes to stabilise different structures with different solvents, where conformational adjustments of the host occur.<sup>36</sup>

For example, tolbutamide is a urea-based drug; it shows two polymorphs (**1.4a-1.4b**),<sup>37</sup> one having chair-like and other U-like geometry. They exhibited different conformations due to

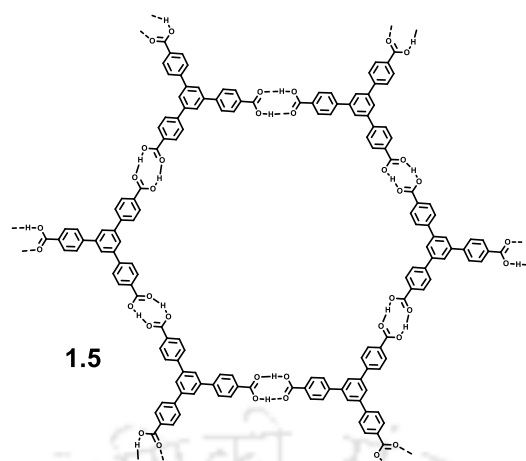
the torsional freedom of the alkyl chain. Two flexible geometries were stabilized in the solid state by the interplay of weak interactions in a different manner.



**Figure 1.8:** Two different conformations in the two polymorphs of tolbutamide

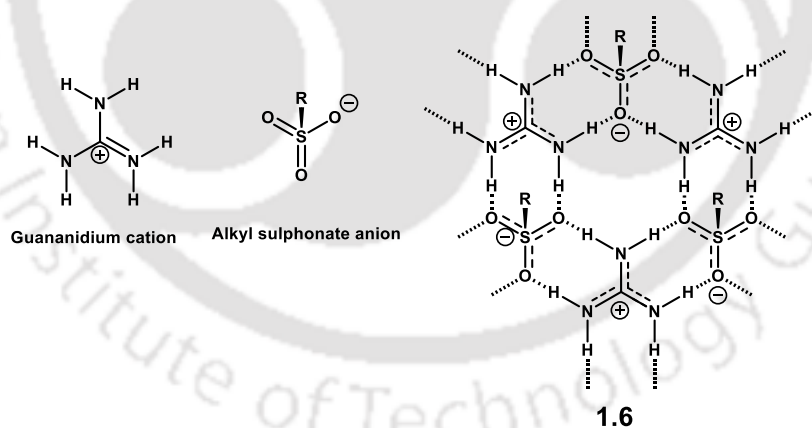
Co-crystals are among the well-studied hydrogen-bonded systems that are crystalline single-phase materials made up of two or more components.<sup>38</sup> They are composed of two or more different molecular and/or ionic compounds, generally in a stoichiometric ratio which are neither solvates nor simple salts.<sup>39</sup> Co-crystals provide a means to regulate bio-availability, solubility/dissolution and physical stability. These properties are crucial for effective drug actions, leading to enhanced therapeutic outcomes.<sup>40</sup> Furthermore, studies on pharmaceutical co-crystals offer innovative approaches to the formulation of drugs.

Hydrogen-bonded organic frameworks are prepared by utilizing the directional intermolecular hydrogen bonds of different organic functional groups in polyfunctional compounds.<sup>41</sup> Example 1.5, shown in Fig. 1.9, is a hydrogen-bonded organic framework constructed from the association of six molecules of a tricarboxylic acid 1,3,5-tris(4-carboxyphenyl)benzene as repeated units to provide robust porous architecture.<sup>42</sup> This framework has hydrogen bonds and  $\pi$ -stackings. It exhibits permanent porosity and has a BET surface area of  $1095 \text{ m}^2\text{g}^{-1}$  with ability to efficiently absorb gases such as  $\text{N}_2$ ,  $\text{H}_2$ , and  $\text{CO}_2$ .



**Figure 1.9:** Hexagonal geometry created in honeycomb assembly of 1,3,5-tris(4-carboxyphenyl)benzene.

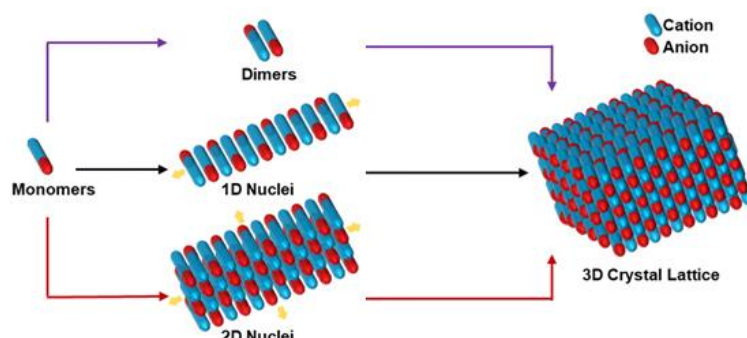
For higher stability which is obtained electrostatically, hydrogen bond guides HOFs. The HOF **1.6** is such an example, built through hydrogen bonds between guanidinium cations and arenesulfonate anions.<sup>43</sup> In this case, there are electrostatic interactions due to the counter ions, where the guanidinium cations provide six hydrogen bond donor sites, while three oxygen on the sulfonate anions serve as acceptor sites. The sulfones thus act as bridges to provide cyclic structures to form the HOF with hexagonal structural patterns.



**Figure 1.10:** The Guanidinium cation, alkyl-sulfonate anion, and hexagonal hydrogen-bonded units in the HOF **1.8**.

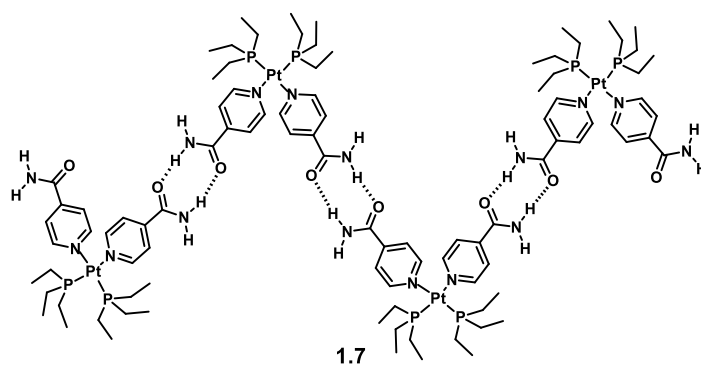
Acid-base properties controlling proton transfer remain as a limitation as there is no clear-cut conclusions to prepare an assembly with or without proton transfer when the  $Pk_a$  values of the host and guest are comparable.<sup>44</sup> The compounds having predominant electrostatically non-covalent assemblies such as cations and anions form ion-pairs;<sup>45</sup> form ladders or stacks of an infinite ionic lattice. Step-by-step assembling of organo-ammonium halide molecules

generates supramolecular clusters (Fig. 1.11).<sup>46</sup> In these examples, quaternary ammonium cations with large alkyl groups show packing similarity to that with neutral organic compounds.



**Figure 1.11:** Assembling of ion pairs of organo-ammonium cations from monomer to construct 3D structures.

The free sites outside the principal coordination sphere of a metal complex may be utilized for ions or molecules outside the central coordination sphere; these supramolecular binding sites once utilized provide the second coordination sphere of a coordination complex<sup>47a</sup> The hydrogen bond sites in second coordination sphere are utilized in various metalloenzymes.<sup>47b</sup> In synthetic complexes they are very pertinent, for example, *cis*-phosphine-based isonicotinamide platinum (II) complex **1.7** exhibited a linear chain-like arrangement due to hydrogen bonds among the free amide groups.<sup>48</sup> On the other hand, analogous phosphine-based palladium complex **1.8** with nicotinamide as co-ligand was also a *cis* complex, but with large dissimilarity in the amide-amide hydrogen bonds.<sup>49</sup> The difference was that the isonicotinamide complex had conventional homomeric amide-amide synthon, but the nicotinamide based complex had crisscross hydrogen bonded homomeric synthon as shown in Fig 1.12 These highlight the role of directional hydrogen bonds in positional isomers as ligands to modify supramolecular assemblies.



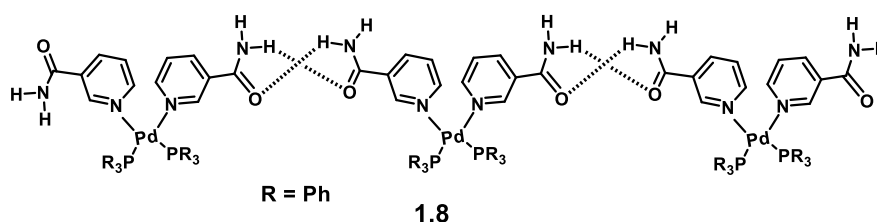


**Figure 1.12:** Zig-zag and linear hydrogen-bonded chains of **1.7** platinum (II), **1.8** palladium (II) complexes.

Self-assemblies of an inorganic complex with another complex of the same or different kinds of organic molecules undergo a modification of the intra or intermolecular interactions of the host molecules. These newly formed self-assemblies include different classes of Supramolecular systems, namely, inclusion complexes, coordination polymers and metal-organic frameworks, each exhibiting its own characteristic shape, size and dimension.<sup>50</sup> Additionally, hydrogen-bonded self-assemblies of inorganic complexes offer the possibility of generating host systems featuring different network structures with different types of pores.<sup>51</sup>

#### 1.4: Halogen bonds

Halogen bonds are another type of non-covalent interaction defined as halogen bond when there is an evidence of a net attractive interaction between an electrophilic region associated with a halogen atom in a molecular entity and a nucleophilic region in another, or the same, molecular entity.<sup>52</sup> Conventionally, a halogen bond is denoted as  $R-X\cdots Y$ , where ( $\cdots$ ) represents the halogen bond, and X and Y are halogen atoms. The  $R-X$  is a covalent bond acting as the halogen bond donor having an electrophilic region or a region with the potential for electrophilicity on its electrostatic potential surface. The Y acts as the halogen bond acceptor, encompassing anions, lone pairs, or a  $\pi$ -system. Halogen bonds exhibit energy ranging from 10 kJ/mol up to 150 kJ/mol. The halogen bond origin is due to  $\sigma$ -hole or  $\pi$ -hole interactions,<sup>53</sup> arising due to an electron deficiency located on the outer lobe of a partially filled p orbital of a halogen atom engaged in a covalent bond. This electron deficiency leads to the formation of a region characterized by an elevated positive electrostatic potential, which allows the interactions with electron-rich acceptor entities. Due to their decreased electronegativity, the halogen atom down the period of the periodic table exhibits better effects of  $\sigma$ -hole and  $\pi$ -hole; that is halogen bonds generally follows the trend  $F < Cl < Br < I$ . Desiraju and Parthasarathy categorized halogen bonds into two main types.<sup>54</sup> The first type, Type I, involves symmetrical interactions where the angles  $\theta_1$  and  $\theta_2$  are approximately

equal whereas the second type, Type II, represents bent interactions where the angles  $\theta_1 \approx 180^\circ$ , and  $\theta_2 \approx 90^\circ$ . Type II contacts are attractive halogen bonds, whereas all type I contacts are not necessarily to be considered as a true halogen bond.

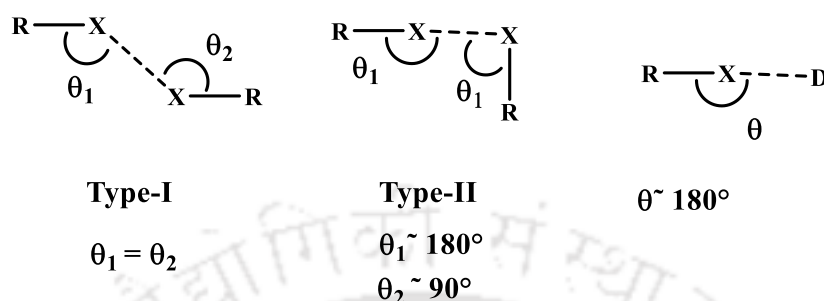


**Figure 1.13:** Commonly observed halogen-bond geometries involve halogen atoms (X) forming interactions with Lewis bases (D), where X = halogen, R = C, N, O, halogen, and D = Lewis bases that are neutral (N, O, S, Se etc.) or anionic (Cl<sup>-</sup>, Br<sup>-</sup>, I<sup>-</sup> etc.).

For example, the co-crystals of 2-aminopyrazine and 1,4-diiodo-tetrafluorobenzene,<sup>55</sup> **1.9-1.11** each have a dimensional architecture formed through hydrogen bonds and halogen bonds. In this case, the assembly has N $\cdots$ I bond, and due to the hierarchical effect as well as electronic factors, the rest of the halogen atoms are not involved in halogen bonds.

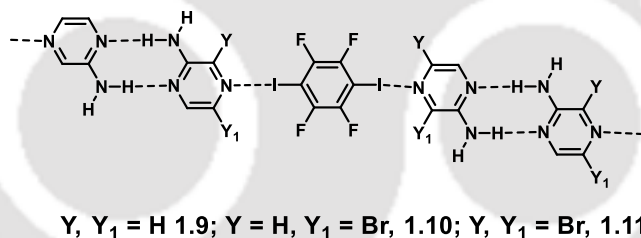


**Figure 1.14:** One-dimensional architecture of three co-crystal by halogen bonding as well as hydrogen bonding.

The differences in halogen bonds in a scheme of interactions of the packing pattern of a compound result in polymorphic structures. For example, compound **1.12** forms concurrent polymorphs that have different halogen bonds in the respective packing patterns as illustrated in Fig 1.15.56. The one having C-Br $\cdots$ O-C interactions was less stable and transformed easily upon heating to the other form, which has the assembly guided by the C-Br $\cdots$ O=C interactions.

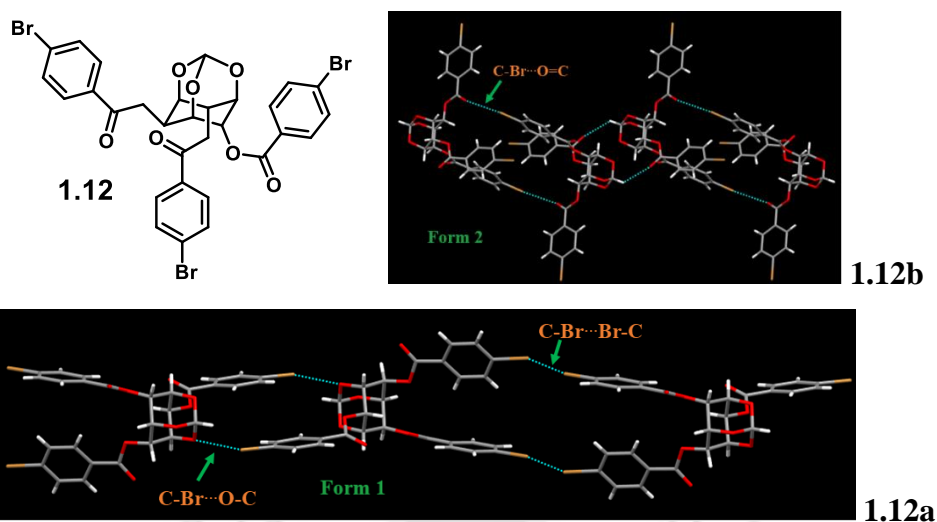
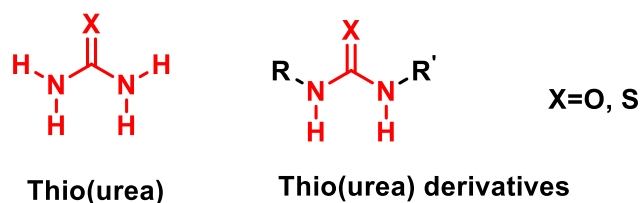


**Figure 1.15:** The line drawing of the compound **1.12** and self-assemblies of the two polymorphs having different halogen bonds

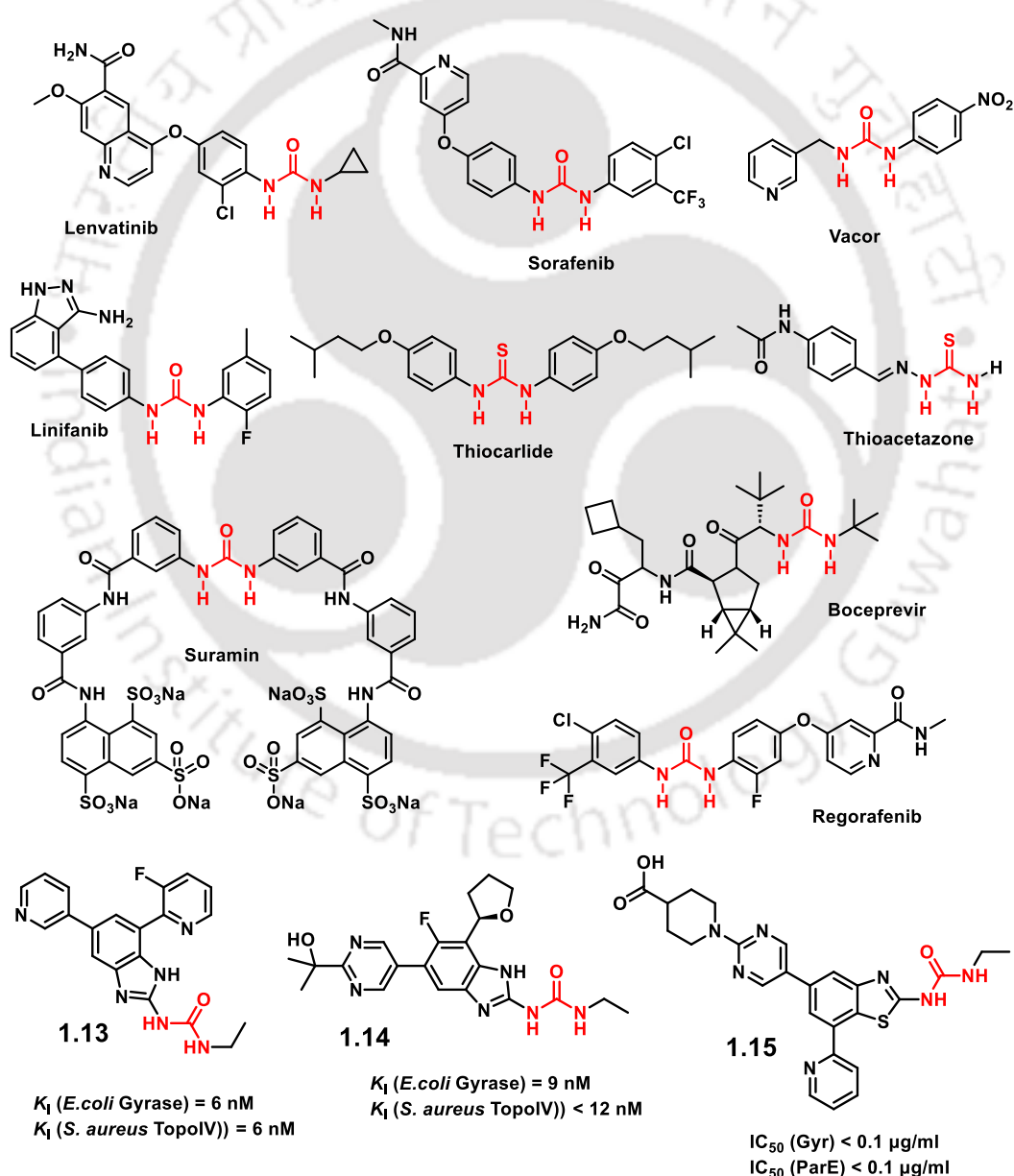
The halogen bonds have contributed to understand intrinsic structural properties and in various subject areas such as crystal engineering,<sup>57</sup> medicinal chemistry,<sup>58</sup> anion receptors,<sup>59</sup> organic catalysis,<sup>60</sup> conductive and magnetic materials,<sup>61</sup> self-healing materials,<sup>62</sup> novel optoelectronics,<sup>63</sup> porous solids,<sup>64</sup> and molecular machines,<sup>65</sup> they have shown potential roles.

### 1.5: Salient aspects of urea/thiourea derivatives for Supramolecular chemistry

The urea is the well-studied organic compound since 1828;<sup>66,67</sup> urea itself as well as their derivatives find utility in supramolecular chemistry,<sup>68</sup> agrochemicals<sup>69</sup> and materials science, where they serve as key components in drug development.<sup>70</sup> The self-assembly of urea and thiourea derivatives through non-covalent interactions is a captivating field of exploration within supramolecular chemistry and materials science.<sup>71-72</sup> Beside these, the thiourea and derivatives are the sulfur-based counterparts of urea derivatives have parallel chemistry with differences arising from the difference in having an S-atom instead of an O-atom in their structures offer a distinct chemical landscape and are also known for their strong hydrogen-bonded assemblies find applications in chemical transformations, especially in organocatalysis.<sup>73</sup> Urea and thiourea have efficacy as antibacterial,<sup>74-75</sup> antimicrobial,<sup>76</sup> antifungal,<sup>77</sup> anti-inflammatory,<sup>78-79</sup> and anti-cancer agents.<sup>80-81</sup>



Some examples of widely used urea and thiourea-based medicines are listed in Fig. 1.16. Benzimidazole urea **1.13-1.15** serve as dual-targeting drugs to block the function of gyrase and topoisomerase IV's ATPase.<sup>82-84</sup> Urea derivative **1.16-1.18** has antimalarial potency.<sup>85-87</sup> The urea derivatives **1.19-1.21**,<sup>88-90</sup> are anticancer agents.



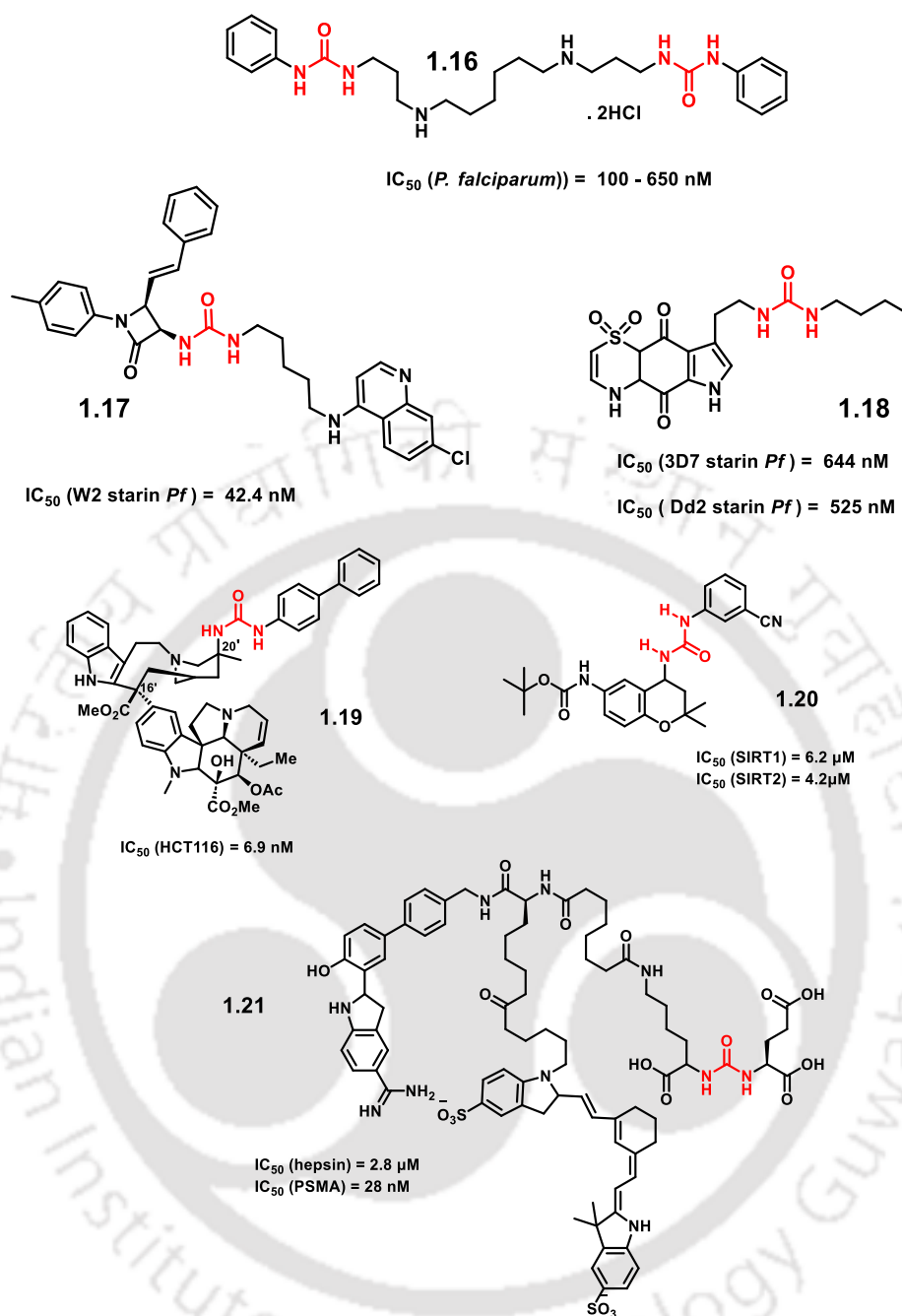


**Figure 1.16:** Chemical structures of selected urea and thiourea compounds used as chemotherapeutic agents.

This list of selective compounds makes it clear that the interactions of these in biological systems requires adequate analysis and such studies would result in new drug discovery and also the possible to make these in modulated applied pharmaceutical ingredients.<sup>91-92</sup> Accordingly, urea and thiourea are widely recognized for their ability to create numerous stable hydrogen bonds and also their interactions with biological molecules, such as with amino acid residues within the active sites of enzymes and receptors. The structural difference in functional groups and structural differences in the isomeric forms of thiourea-

based compounds make a difference in their cytotoxicity. For example, compound **1.22** shows superior anti-cancer, antimalarial, and antimicrobial activities over **1.23** (Fig 1.17).<sup>93</sup>

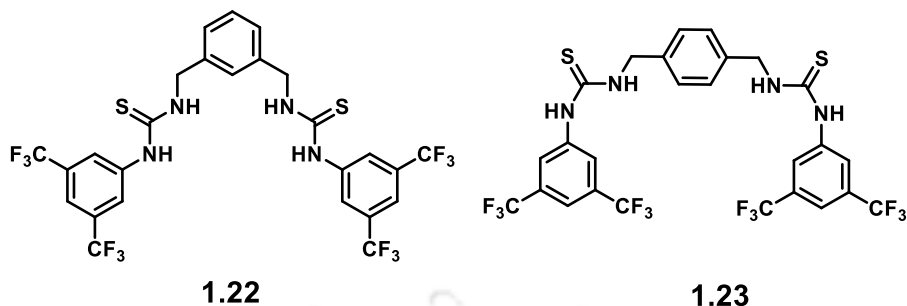


**Figure 1.17:** Two positional isomers that show anti-cancer activities.

The Ru(II)-arene complexes **1.24** and **1.25** containing acyl-thiourea coligands,<sup>94</sup> (Fig. 1.18) show cytotoxicity in human lung cell lines A549 and MRC-5. The Ru(II)-arene complexes, **1.24** having neutral acyl thiourea and chloride in coordination sphere demonstrated the higher cytotoxicity than the one having anionic acyl thiourea and without a chloride ion. Both the complex showed cytotoxicity, each having different binding behavior from the same set of ligands. It was shown that the role of the part containing Ru-Cl bonds in cytotoxicity was less prominent than the effects from the ligand part.

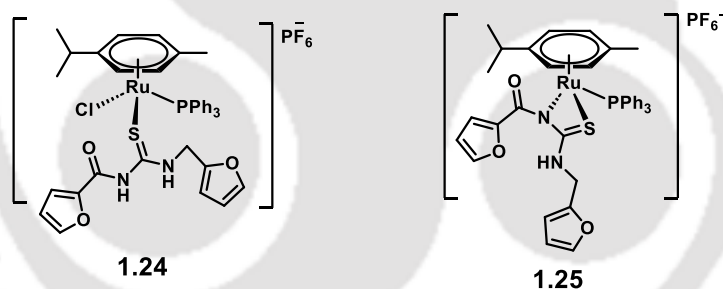
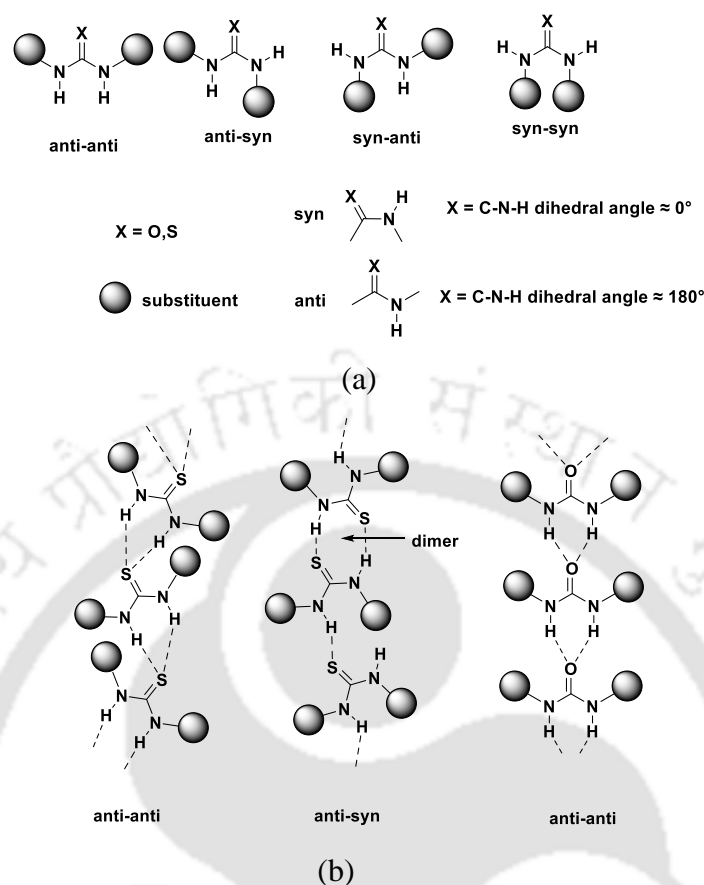


**Figure 1.18:** Ru(II)-arene complexes containing acyl thiourea ligands.

### 1.6: Self-assemblies of urea and thiourea derivatives

Urea and thiourea themselves form channel-like structures and form different clathrates.<sup>95</sup> Urea and thiourea derivatives possess hydrogen C=O/S as bond acceptor and also have two N-H as hydrogen bond donors. They may adopt any of the four distinct conformations, namely *anti/anti*, *anti/syn*, *syn/anti* and *syn/syn* conformation; these conformations play a pivotal role in guiding the formation of various self-assemblies as depicted in Scheme 1.3.<sup>96-100</sup> In *syn* conformation, S/O=C-N-H dihedral angle is close to 180° and in *anti*-conformation, S/O=C-N-H dihedral angle is close to 0°. Thus, self-assembly of urea/thiourea derivatives have far-reaching implications to organize into well-defined non-covalent assemblies.



**Scheme 1.3:** Illustration of (a) four different geometries of urea and thiourea and (b) their selected self-assemblies.

A series of meta-substituted bis-thiourea derivatives **1.26a-1.30d**<sup>101</sup> showed diverse self-assembly by adopting different conformations such as *syn-anti* and *anti-anti* arrangements, as depicted in Fig. 1.19. Three distinct types of self-assembly among these bis-thiourea compounds includes complete cyclic dimers (Figure 1.19b), incomplete cyclic dimers (Figure 1.19c), and extended hydrogen-bonded network structures (Figure 1.19-g). The compounds **1.30a-c** formed dimeric self-assemblies from the *anti-anti* conformation of thiourea moieties (Fig. 1.19b). Compound **1.30b** had dimer of dimers, and displayed incomplete dimeric self-assemblies. The compounds exhibiting incomplete cyclic self-assemblies or the absence of cyclic dimeric arrangements were specifically those containing one or two *syn/anti* conformations. The self-assemblies of compounds **1.28a-1.29a** exhibit geometries categorized as type 1, **1.26a** exhibit type 2, and 1; examples provide a glimpse on the structural diversity and self-assembly behaviors of thiourea compounds.

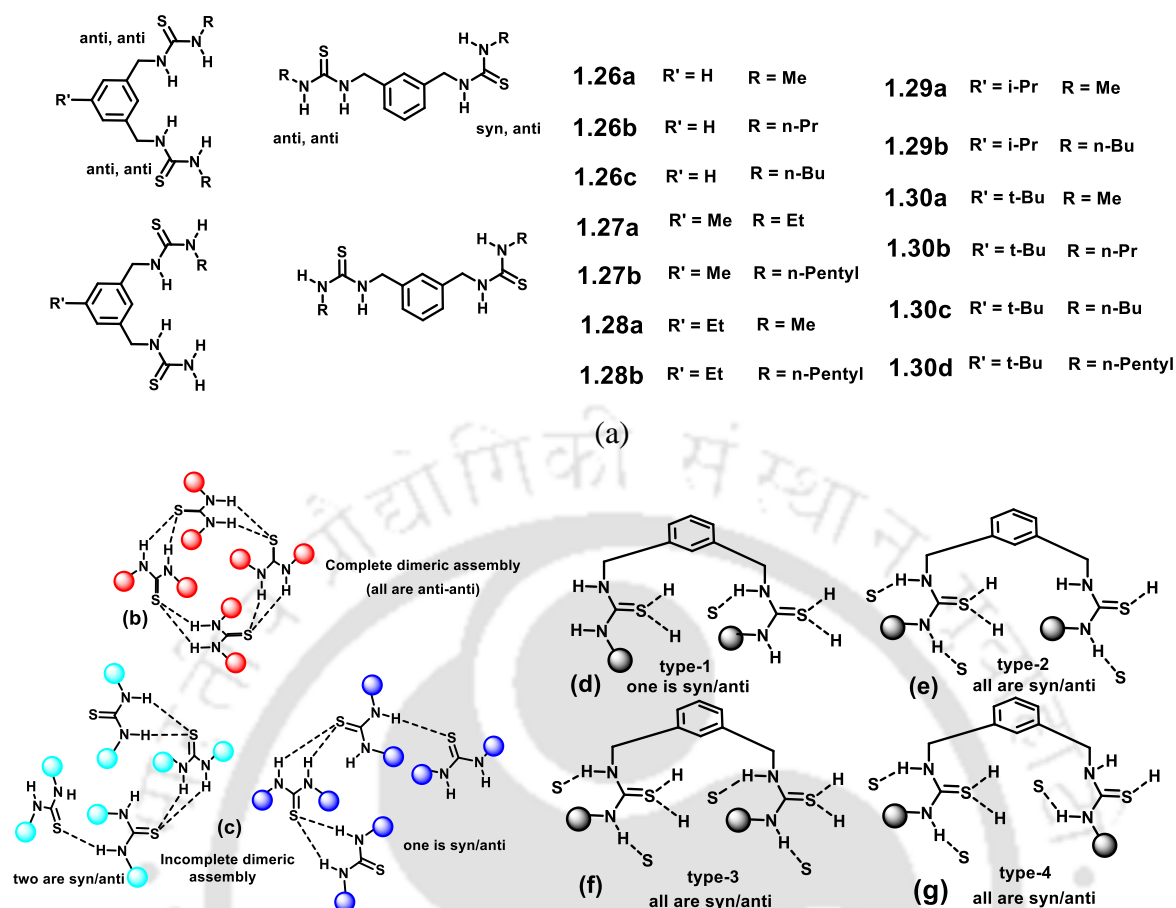


**Figure 1.19:** Different types of sub-assembled units within an assembly of urea derivatives

The carboxylic acid derived urea derivative **1.31**<sup>102</sup> ligand and also its coordination polymers **1.32** and **1.33** exhibited *anti-anti* conformation. But it adopted *syn-anti* conformation in sodium complex (**1.34**).

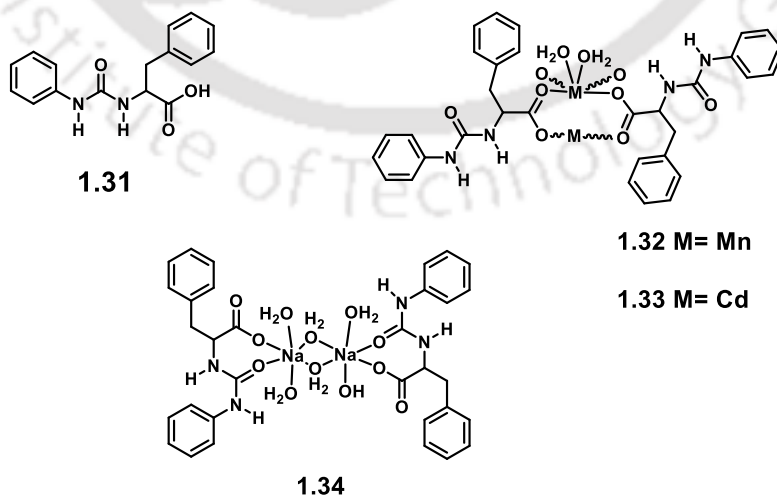


**Figure 1.20:** Stabilization of different conformers of a urea carboxylic acid

Urea tapes refers to the intermolecular bifurcated hydrogen bonded units formed between two urea units. They influence the architecture of an assembly. For example self-assembling of urea-derivatives in a head-to-tail, in oligo(*p*-phenylene vinylene) urea, provide well-defined tape-like supramolecular nanofibers and fluorescent organogels.<sup>103</sup> The cooperative hydrogen bonding,  $\pi$ -stacking and van der Waals interactions between the interactive units situated on both sides of these building blocks contributes to the overall assembly (**1.36**).

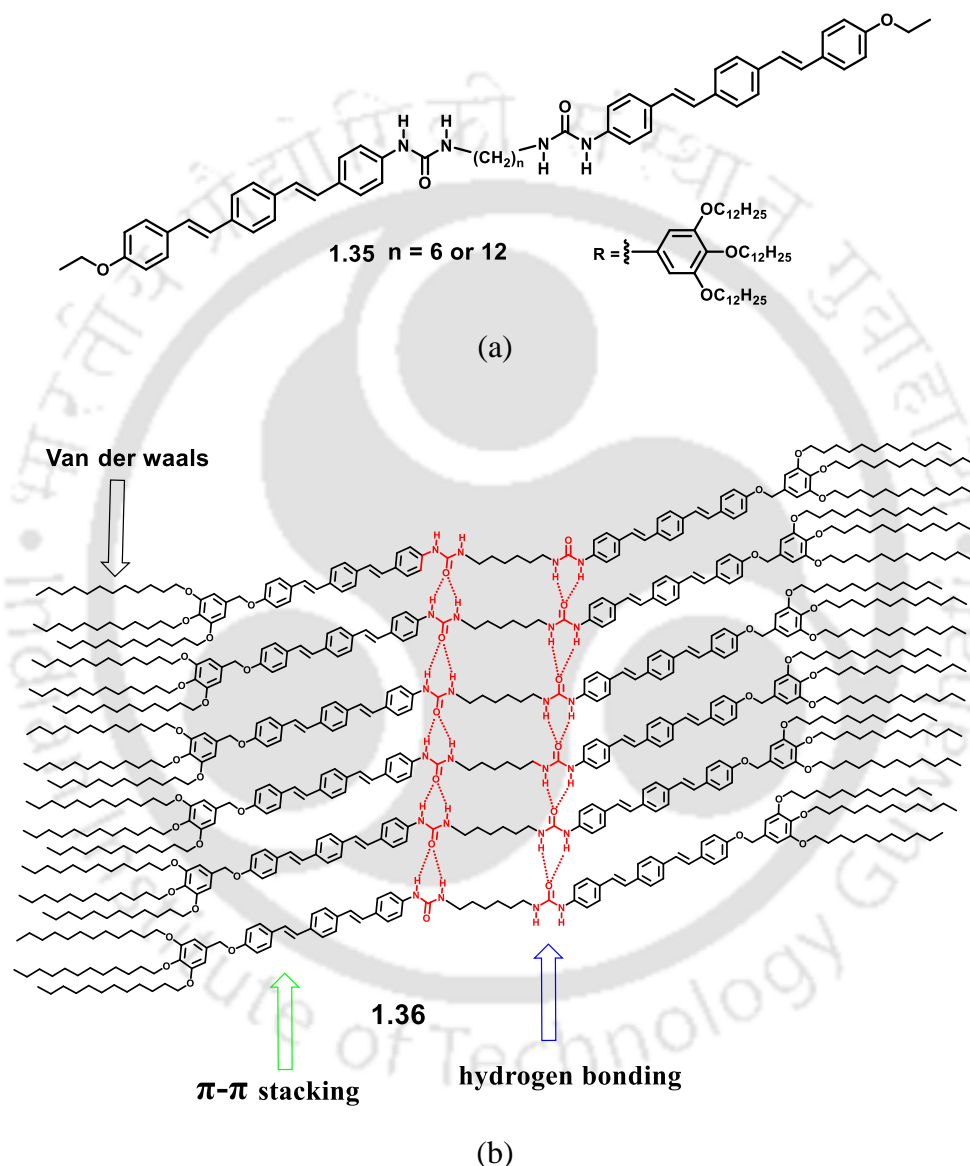


**Figure 1.21:** Structures of two bis-urea derivatives **1.35** that self-assemble through head to head arrangements of urea (**1.36**).

Non-covalently linked ureido macrocycles **1.37** nanotubes characterized by a distinctive columnar structure and a prominent central cavity as shown in Fig. 1.22.<sup>104-105</sup> This organized assembly was facilitated by intermolecular hydrogen bonds and edge-to-face  $\pi$ -stacks. Within the tubular aggregates, the ureidocarbonyl groups were aligned parallelly but in opposite

directions. The specific configuration of the ureido groups played a crucial role to provide the nanotube like structure. The assembly adsorbed a diverse range of molecules within their cavities.

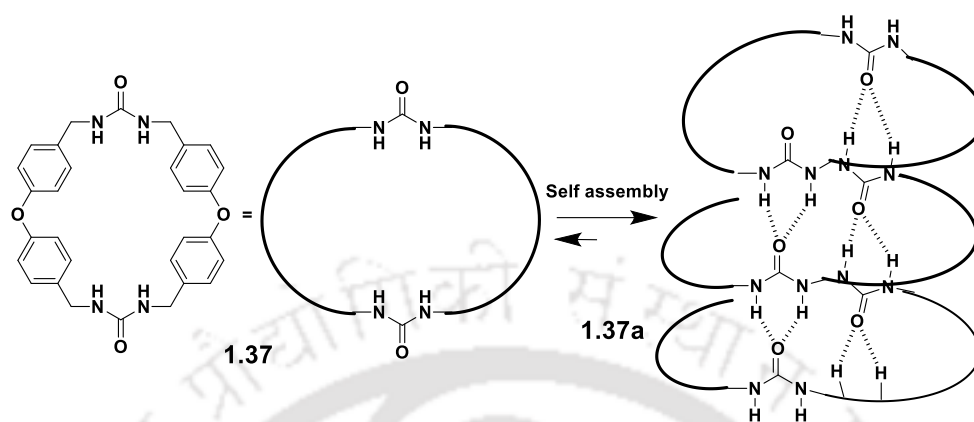


**Figure 1.22:** Self-assembly of macrocyclic ureido compound to provide nanotube like structure.

Supramolecular self-assembly formed by quadruple hydrogen bonds such as in **1.38**, results in assemblies that have higher thermal stability.<sup>106</sup> Studies carried out from solution of the compound in various solvents at various concentrations have shown its stability as supramolecular polymeric entity; for example, at higher concentrations of **1.38**, the N-H proton of the urea moiety exhibited a downfield shift in chemical shift, suggesting its hydrogen-bonded aggregate in solution. Additionally, the alkylidene protons were appeared at upfield chemical shift positions, indicating interactions with the aromatic unit.

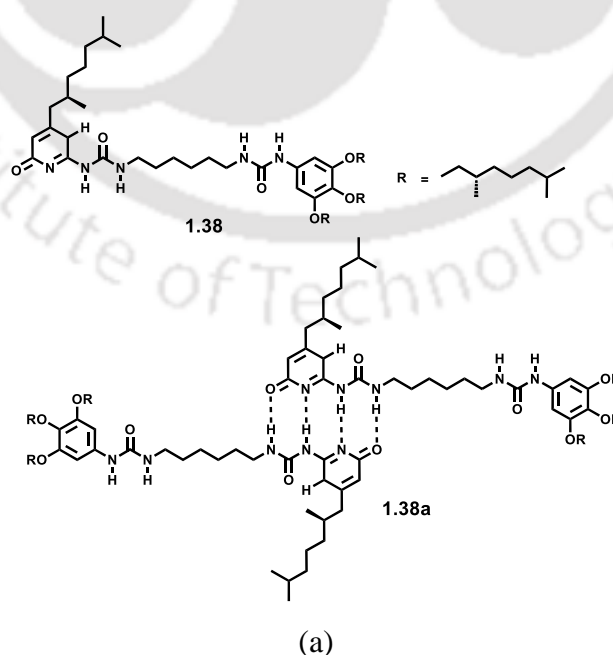


**Figure 1.23:** Example of a quadruple hydrogen bonded dimer

Meijer and coworkers reported dimers of 2-ureido-4-pyrimidinone **1.39** having quadruple hydrogen bonds as illustrated in Fig. 1.24.<sup>107-108</sup> This dimerized product formation equilibrium has high association constant ( $K_{\text{dim}} > 10^7 \text{ M}^{-1}$ ) accordingly exhibits physical properties similar to those of conventional polymers held together by covalent bond. The viscosity of this self-assembled supramolecular polymer is highly dependent on the concentration and temperature.

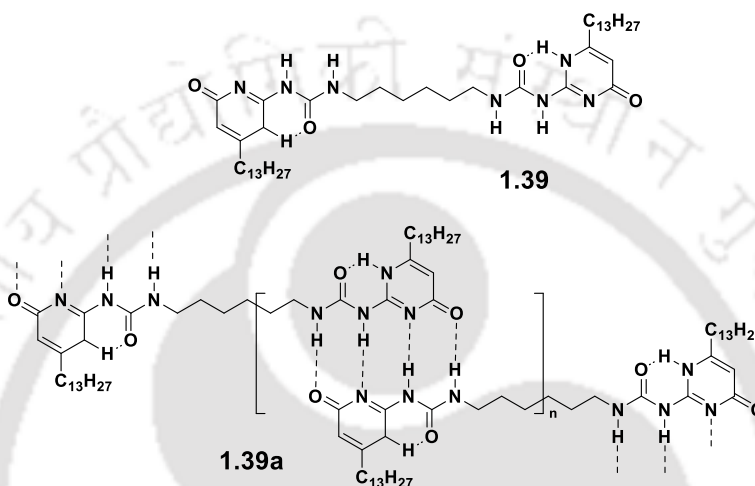


**Figure 1.24:** A Supramolecular polymer formed by quadruple hydrogen bonds

Self-assemblies of urea and related compounds have provided examples for study of conformational polymorphs, for example, a thiourea based anti-tubercular drug isoxyl has two forms, namely form 1 (**1.40**) and form 2 (**1.41**).<sup>109</sup> Polymorph **1.40**, has the thiourea part adopting a *syn-anti* orientation, while the polymorph **1.41**, assumes an *anti-anti* orientation. Polymorph **1.40** has hydrogen-bonded dimers, as illustrated in **1.40a**, while the self-assembly of polymorph **1.41** has the thiourea tape, depicted in **1.41a**. Form 1 was stable up to 91.7°C, while form 2 was stable till its melting point at 142.7°C. The form 1, upon heating beyond 91.7°C underwent a phase change, transforming into form 2. There was a residual part while preparing solution of the form 2, upon analysis of this by powder X-ray diffraction study, showed it be form 1, while the undissolved part of form 1 remained unchanged.

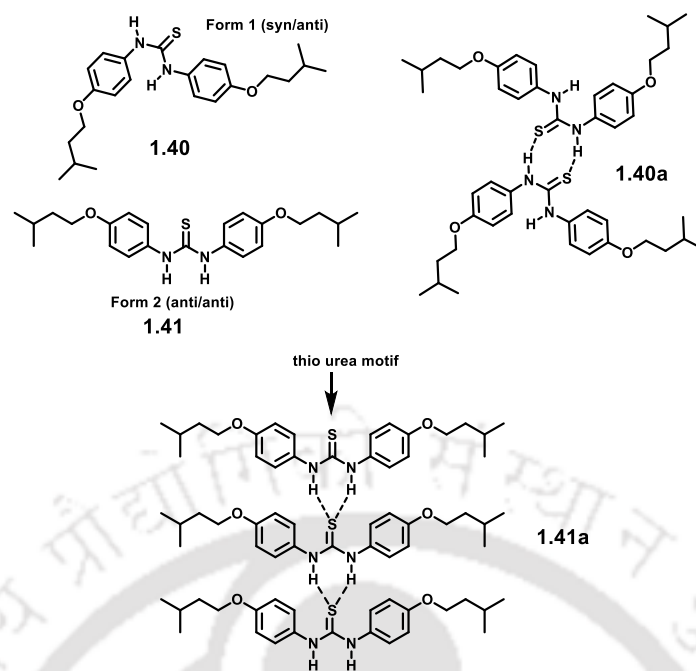


**Figure 1.25:** The structure of the two polymorphs isoxyl and their assemblies.

The formation of cocrystals of urea-based drug molecules, for example, Lenvatinib, has significantly affected the solubility of the original component.<sup>110</sup> A noteworthy improvements in solubility when compared to the parent lenvatinib was observed in the co-crystal of lenvatinib with salicylic acid. There was a 120-fold increase in solubility compared to the lenvatinib. Similarly, the co-crystal of lenvatinib with sulfamerazine exhibited a substantial 2.25-fold enhancement in solubility when compared to the pure lenvatinib drug.

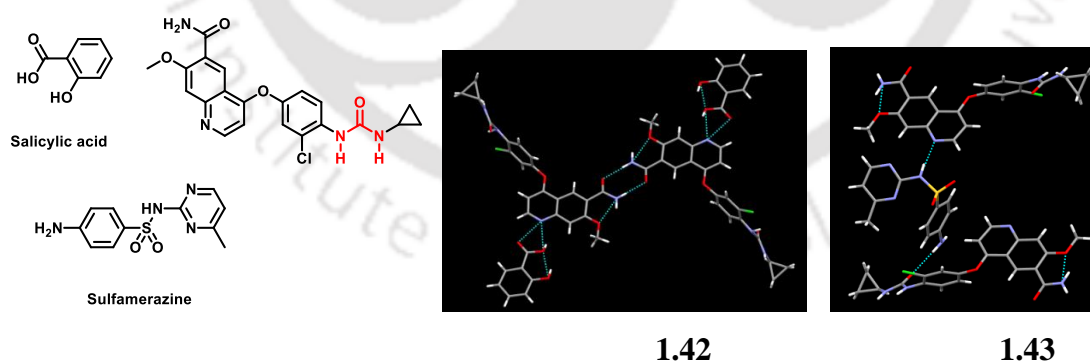
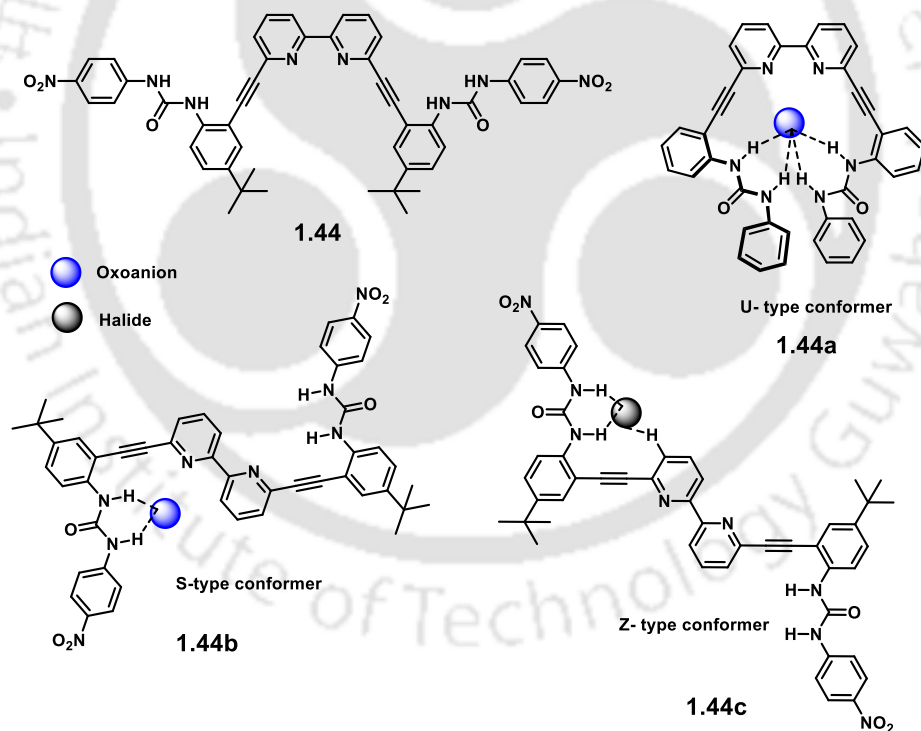


**Figure 1.26:** Co-crystal formation of lenvatinib with sulfamerazine and salicylic acid.

### 1.7: Anion assisted self-assembly of urea and thiourea derivatives

Depending on the shape and binding sites, an anion may guide the orientation of a suitably designed host urea derivative resulting molecular switches. Haley and coworkers reported a supramolecular bis-urea **1.44** featuring a bipyridine moiety.<sup>111</sup> This molecule exhibits independent binding behavior with halide and oxy-anions to provide different geometries in

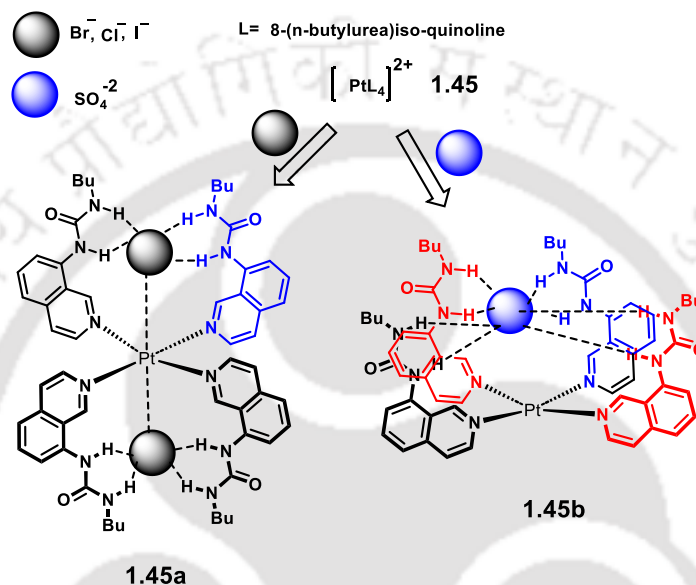
the salts. Hence had a molecular switching capability upon correct choice of the anion such as chloride, bromide, iodide, dihydrogen phosphate, and hydrogen sulfate ion to stabilize a particular form. The binding of the receptor with these anions follows the order  $\text{H}_2\text{PO}_4^- > \text{OAc}^- > \text{HSO}_4^- = \text{Cl}^- > \text{Br}^- \sim \text{NO}_3^- > \text{I}^-$ . The high affinity of the compound towards dihydrogenphosphate was attributed to the formation of a greater number of hydrogen bonds with the receptor, and a proton transfer occurring between the anion and the pyridine nitrogen of the receptor. The distinction in the conformations in presence of oxo-anions and halides, were analyzed by  $^1\text{H-NMR}$  titrations. The tetrabutylammonium halide led to a shift in the N-H of the urea and the aryl  $\text{C}_{\text{sp}^2}\text{-H}$  resonance situated on the bipyridine unit, confirming the involvement of  $\text{C}_{\text{sp}^2}\text{-H}$  in hydrogen bonding with halide guests. Conversely, with oxo-anion, the chemical shift of the  $\text{C}_{\text{sp}^2}\text{-H}$  aryl proton was not notably affected, indicating that  $\text{C}_{\text{sp}^2}\text{-H}$  did not take part in hydrogen bonding. Based on the chemical shifts of these protons and density functional theory calculations, a Z- conformer **1.44c** for halide anions, whereas, for and U (**1.44a**) or S (**1.44b**) conformer for oxo-anions were proposed.



**Figure 1.27:** Bipyridine based bis-urea receptor binding to different anions.

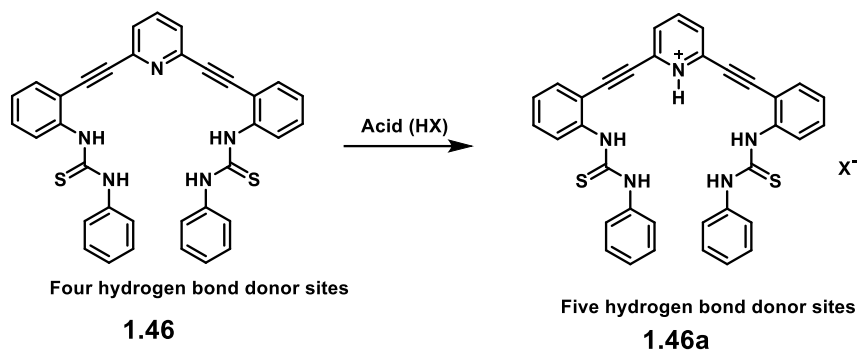
The receptor **1.45** derived is a urea functionalized iso-quinoline forms platinum complex;<sup>112</sup> the complex had showed distinct interactions with halides and oxo anions (Fig 1.28). It exhibited a 1:2 binding ratio with halides and a 1:1 binding ratio with oxo anions. The four urea groups were engaged with a single anion providing a cone-shaped arrangement (1:1

binding) with oxyanions or, with halides, the urea groups were in an alternating manner (1:2 binding). At higher concentrations of chloride, bromide or iodide, it adopted a 1:2 alternate binding of **1.45a**, while with dihydrogen phosphate and sulfate anion 1:1 cone-shaped configuration of **1.45b** was observed. The conformation of the organic part in the complexes was validated both in solution through  $^1\text{H-NMR}$  and in solid-state using X-ray crystallography. Importantly, the association constants for dihydrogen phosphate and sulfate anions were found to be higher than those for the chloride, bromide and iodide



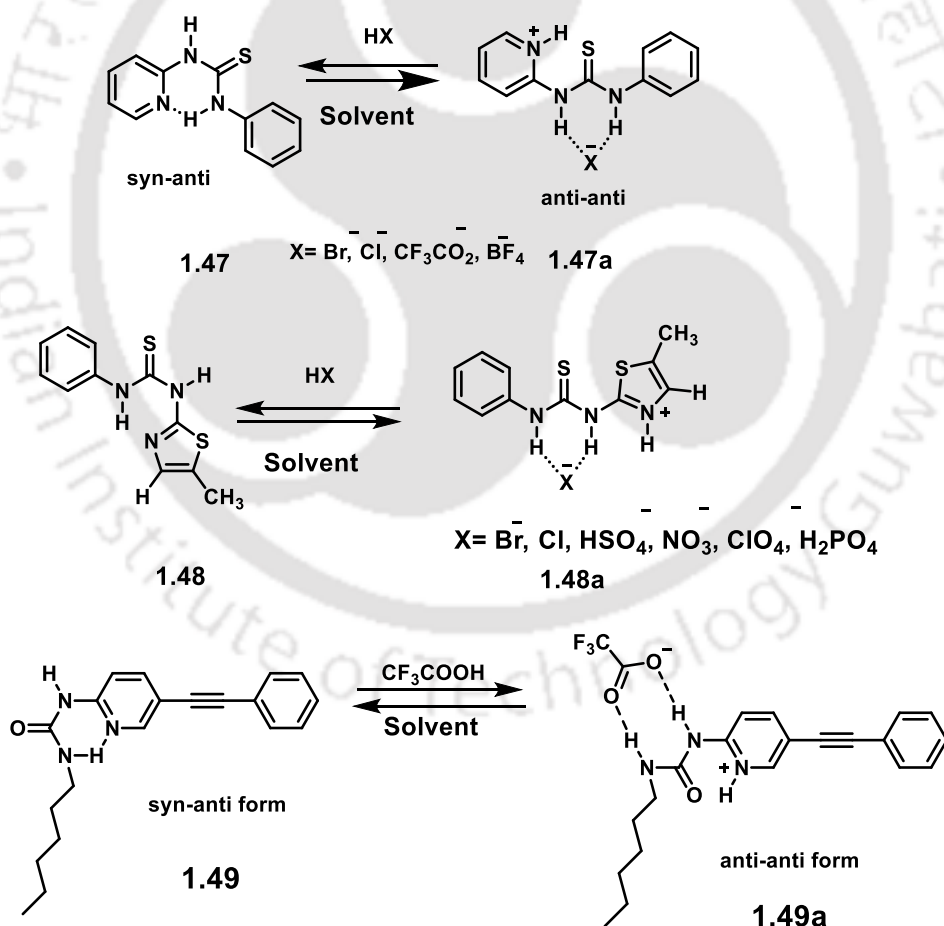
**Figure 1.28:** Iso-quinoline based urea receptor bound to halide and oxo anions.

Bis-urea **1.46**, 2,6-bis(2-anilinoethynyl)pyridine<sup>113</sup> upon protonation of pyridine group bind anions. **1.46a**, the receptor displayed a significantly enhanced anion binding affinity, substantiated by a binding constant that exceeded that of the neutral form by an order of magnitude. The salts of a series of thiourea 2-pyridyl-phenyl thiourea had intramolecular hydrogen bonds providing an *anti-anti* conformation of the N-H bond with respect to the C=S bond (**1.47a**). The protonated species of the receptor had an altogether different orientation, due to this, it had different binding selectivity toward different anions



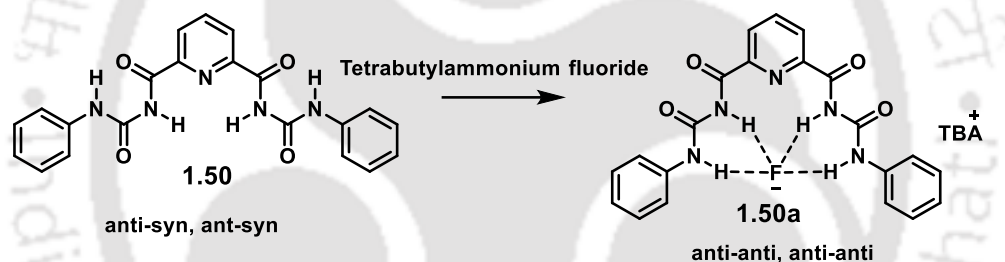
**Figure 1.29:** Pyridyl based bis-urea receptor

The neutral thiourea **1.47** was in *anti-syn* conformation, had selectivity to bind with acetate anions than bromide and chloride ions. When protonated, the compound had better affinity for bromide and chloride ions but it underwent deprotonation in the presence of acetate ions and reverting to its geometry that was associated with the neutral state.<sup>114</sup>



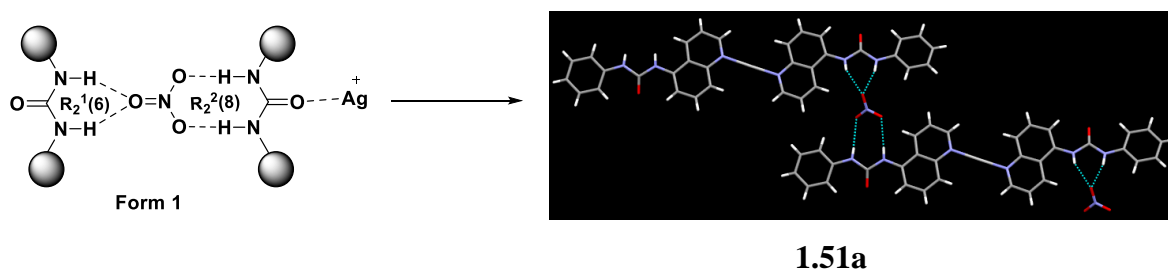
**Figure 1.30:** Triggering of intramolecular hydrogen bonded *syn-anti* conformers of thiourea and urea receptors to *anti-anti* form by anion binding.

In its neutral form, the compound **1.48**, originating from 1-(5-Methylthiazol-2-yl)-3-phenylthiourea, displays an *anti-syn* conformation.<sup>115</sup> This conformation is mainly attributed to a strong hydrogen bond formation between the N-H group of the thiourea and the N atom within the thiazole moiety (Fig. 1.31). However, this strong interaction was disrupted upon the introduction of acidic compounds such as HBr, HCl, HNO<sub>3</sub>, HClO<sub>4</sub>, and H<sub>3</sub>PO<sub>4</sub>. As a result, the *anti-syn* conformation of the neutral form transitioned into *anti-anti* conformation **1.48a**. Similar change upon anion binding properties, was observed in the intramolecular hydrogen bonded urea derivative **1.49**<sup>116</sup>. In its neutral state, this compound emitted light at a wavelength of 356 nm when excited at 321 nm and adopted an *anti-syn* conformation. However, upon protonation with a strong acid like CF<sub>3</sub>COOH, the hydrogen bond between the urea and pyridyl group was disrupted. This disruption led to a conformational change from an *anti-syn* to *anti-anti* conformation **1.49a**, resulting in a shift in the emitted light to a longer wavelength ( $\lambda_{em} = 420$  nm).



**Figure 1.31:** 2,6-pyridinedicarboxylamide based bis-urea receptor in recognition of fluoride ion.

The bis-urea derivative **1.50** has 2,6-substituted pyridinediamide moieties,<sup>117</sup> show distinct response binding to fluoride ions as compared to other halides (chloride, bromide, and iodide). In the presence of a fluoride ion it showed a notable conformational alteration from *anti-syn* geometry to *anti-anti* geometry **1.50a**. This behavior was attributed to the selective compatibility of the molecular cavity of the bis-urea receptor, to accommodate a fluoride ion to the other halides.



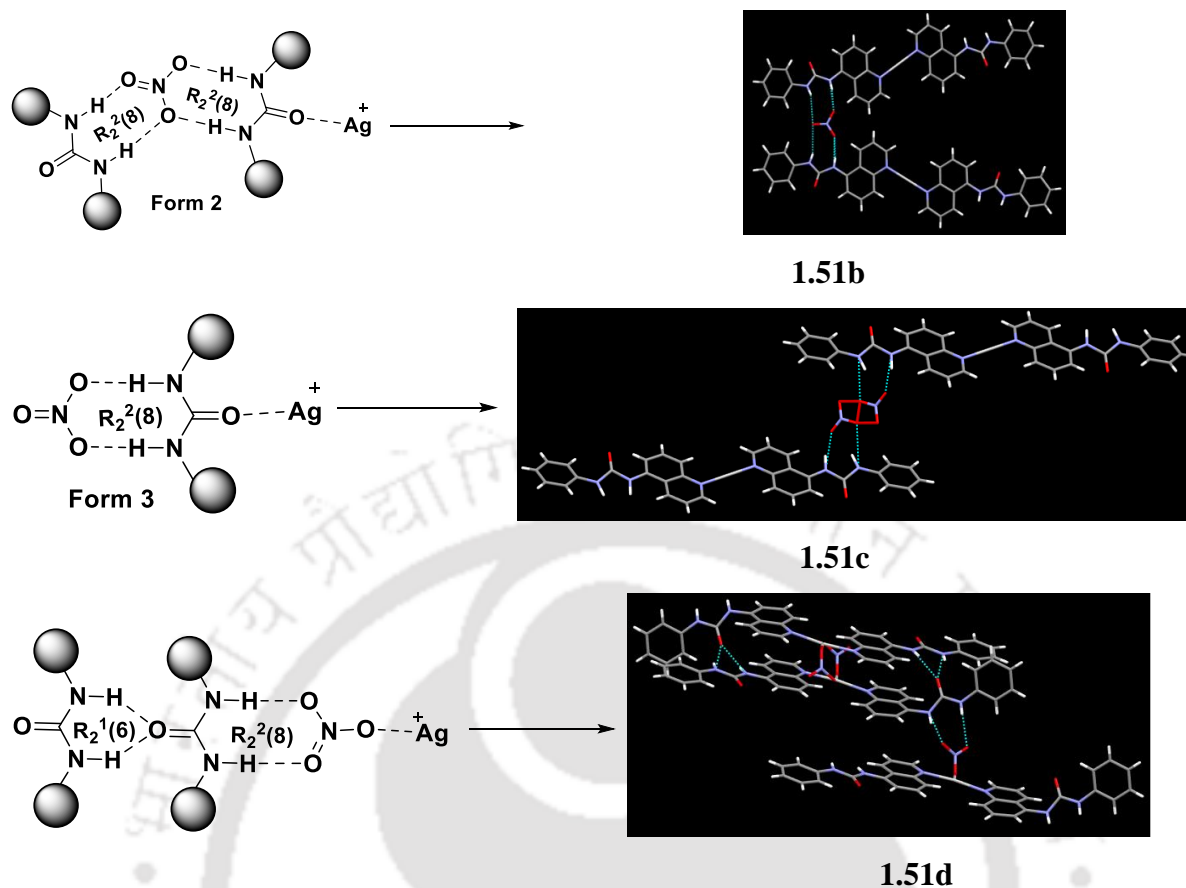


**Figure 1.32:** Formation of super gelators silver complex

Grepioni and his team conducted research on the exploration of supramolecular gels employing a silver(I) super-gelator complex that includes 1-phenyl-3-(quinolin-5-yl)urea (**1.51**) as a crucial component<sup>118</sup>. Their research reveals that these gel structures obtained in open vials display temperature-dependent transition, shifting from a gel state to a solution state. Importantly, when subjected to crystallization in sealed containers using different gelling solvents such as ethanol, methanol, and isopropanol, these gels yielded distinct crystal forms known as polymorphs. Specifically, they obtained four unique polymorphic modifications labelled as Form I to Form IV. Forms I to III share structural similarities, characterized by a lack of coordination between the nitrate anion and the silver metal. In contrast, Form IV exhibits a distinctive feature where the oxygen atom of the nitrate anion directly binds to the silver metal. This research provided insights into the effectiveness of gels as a promising method for creating new crystal structures, emphasizing the critical role of polymorphism in the field of solid-state chemistry.

### 1.8: Consequences of anion binding by urea/thiourea based receptors in detections

Membrane transport of anions is a fundamental process in biology and plays a pivotal role in various cellular functions, including osmotic regulation, signal transduction, and the movement of important molecules like chloride ions,<sup>119</sup> hence the anion detections is a very important topic.<sup>120-121</sup> Photoluminescence and colorimetry detection and identification of anions<sup>122</sup> takes advantage of specific binding of ions through supramolecular interactions. Urea and thiourea derivatives have emerged as pivotal components in the realm of anion sensing, a crucial field within analytical chemistry.<sup>123</sup> Their hydrogen bonding capabilities, have proven to be exceptional receptors for specific anions. Through hydrogen bonding interactions, they selectively and sensitively bind with anions, inducing changes in their physical and chemical properties. This ability additionally provides insight into phenomena related to anions and advances a wide range of scientific fields. The chromophoric segment of urea and thiourea receptors often serves as the signaling component. The formation of hydrogen bonding complex of receptors with anions and the process of deprotonation of these receptors is significantly affected by the basicity of anions and acidity of N-H protons.<sup>124</sup> It is important to note that the N-H bonds in thiourea are more acidic than the N-H bonds in urea. For example in the urea compound **1.52** has lower acidity than the corresponding thiourea compound **1.53**,<sup>125</sup> due to which they have different anion sensing abilities for acetate. For example, the urea derivative form hydrogen bonded species with acetate anion, whereas the thiourea gets deprotonated by acetate anion.

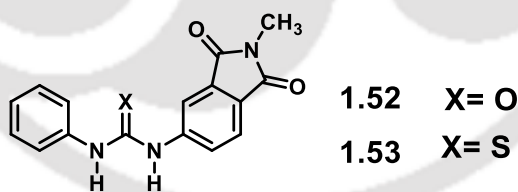


**Figure 1.33:** Urea and thiourea derivative

The urea based bis-naphthalimide receptor **1.54** upon interactions with two equivalents of fluoride or hydroxide in dimethylsulfoxide (DMSO) solution showed changes in the absorption spectra.<sup>126</sup> Specifically, the intensity of the absorption band of the parent compound at 400 nm was decreased, and a new absorption band at 540 nm emerged. These alterations likely result from the deprotonation of one of the N-H bonds within the urea group, leading to the formation of stable monoanionic species. A solution of **1.54** dimethylsulfoxide turns brown to red upon addition of limited amounts of fluoride or acetate

ions, due to deprotonation of the N-H of urea segment (due to the formation of **1.54a**), whereas, beyond a particular concentration, the same solution turns red to blue, upon addition of an excess amounts of fluoride or hydroxide ions due to formation of **1.54b** by di-deprotonation as depicted in the Fig. 1.34.

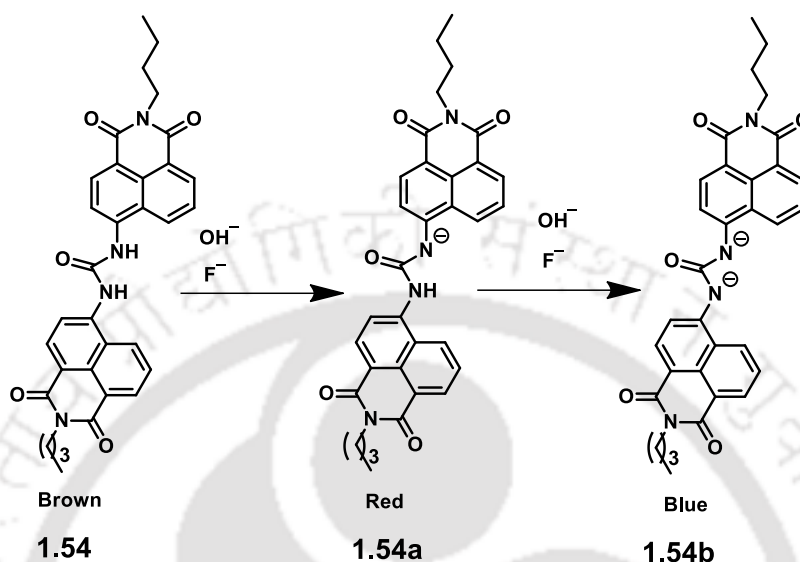


**Figure 1.34:** Stepwise binding of anions with a urea derive naphthalimide sensor.

Fluorescence quenching through the mechanism of photoinduced electron transfer (abbreviated as PET) is a common approach in optical sensing of anions. Gunnlaugsson and their team pioneered the investigation of anion sensing through PET quenching, utilizing a thiourea compound with an urea functionalized anthracene-based fluorophore **1.55**.<sup>127</sup> Various anions such as fluoride, chloride, bromide, acetate, and dihydrogen phosphate caused fluorescence quenching. Upon binding with anions, the enhancement of electron transfer from the highest occupied molecular orbital (HOMO) of the receptor-anion complex to the excited state of the fluorophore (anthracene) becomes a more competitive process. This increased competitiveness, led to the quenching or "switching off" of fluorescence emission. This quenching effect was particularly more pronounced in the presence of fluoride as compared to other anions like chloride, bromide and iodide. This was due to its smaller size and higher basicity of fluoride ion, and it has better binding with the receptor, resulting in more efficient quenching.

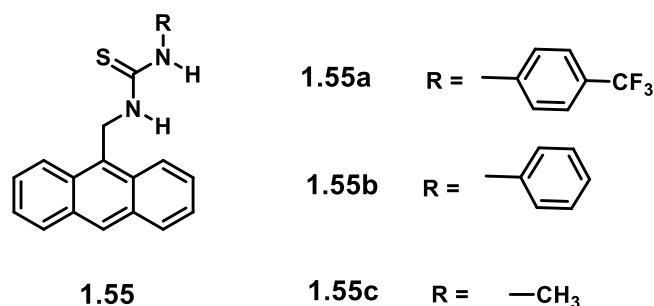


**Figure 1.35:** Thiourea derived anthracene-based fluorescence sensor.

Gunnlaugsson and coworkers also synthesized thiourea-based naphthalimide anion sensors, designated as **1.30a** and **1.30b**.<sup>128</sup> These compounds exhibit the ability to form 1:1 complex with fluoride, acetate, and dihydrogenphosphate anions. Upon the addition of specific anions, the compounds underwent a noticeable color transformation from light yellow to deep purple. On the other hand, in DMSO solvent, these compounds displayed green emission at 525 nm. However, the introduction of anions led to the quenching of this emission. Notably, fluoride exhibits a higher quenching effect compared to other anions. In contrast, chloride and bromide do not induce any observable changes upon addition to **1.56a** and **1.56b**, possibly attributable to their larger size and lower charge density. Receptor **1.57** was capable of forming a 1:1 stoichiometric salt with dihydrogen phosphate anion.<sup>129</sup> The assembly of salt was established through hydrogen bonds, with the involvement of naphthalimide N-H and thiourea N-H groups interacting with the oxygen atoms of the anion. Receptor **1.57** underwent further modification to prepare new sensors, denoted as **1.58a** and **1.58b**.<sup>130</sup> The assessment of the compound's anion-binding capabilities with dihydrogen phosphate and acetate anions involved monitoring changes in the <sup>1</sup>H-NMR and fluorescence spectra of **1.58a** and **1.58b** in the presence of these anion.

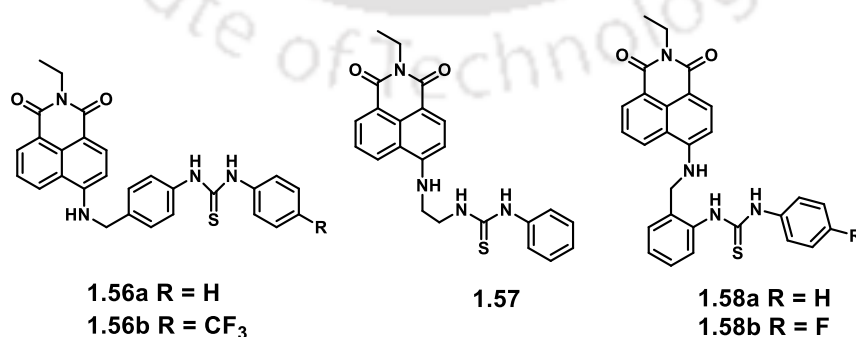


**Figure 1.36:** Thiourea based naphthalimide as fluorescent receptors

There are many examples having different chromophore/fluorophore anchored to urea/thiourea units. One such colorimetric and fluorescence chemo sensors quinine derivative **1.59** containing two anion binding sites is shown in Fig. 1.37. It showed response towards dihydrogen phosphate, acetate and fluoride ion via photoinduced electron transfer (PET) and intramolecular charge transfer (ICT) mechanisms.<sup>131</sup> The fluoride and acetate ions at low concentrations formed hydrogen bonds with the thiourea part of the receptor.

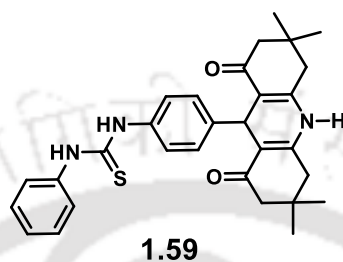


**Figure 1.37:** A chemo sensor of thiourea-derived quinone.

This led to the quenching of fluorescence due to photoinduced electron transfer. At higher concentrations of fluoride and acetate ions, deprotonation of the amino group of the acridinedione took place, but the N-H of thiourea moiety remained unchanged. Consequently, there was an increase in the charge-density on the donor group. This caused intramolecular charge-transfer, led to an increase in fluorescence intensity.

The above discussions have suggested the role of urea/thiourea part in detections of anions by (a) providing binding sites, (b) getting deprotonated, and (c) by influencing the mechanism of emission process by electronic effect. Hence the steric and electronic aspects are being studied in developing new sensors based on those principles.

### 1.9: The thiourea in cation binding

The thiophilic heavy toxic metals, such as lead, mercury, and cadmium, and other transition metal ion that contribute to toxicity in the environment,<sup>132</sup> thiourea derivatives are well known to provide binding sites to them during optical detection of those ions.<sup>133</sup> Thiourea-based compounds **1.60a** and **1.60b** are specific fluorescent chemo sensors for the detection of  $\text{Hg}^{2+}$  in aqueous solutions<sup>134</sup> The fluorescence emissions of these compounds are poor as they are in quenched state due to PET occurring from the thiourea group to the naphthalamide group. When these compounds form complexes with  $\text{Hg}^{2+}$ , the PET process gets suppressed, leading to a remarkable enhancement in their fluorescence emission (Figure 1.38).

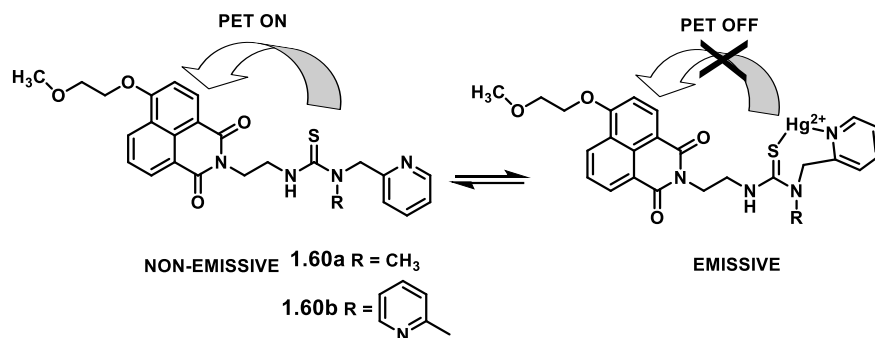


**Figure 1.38:** Fluorescence switching of **1.60a** and **1.60b** upon complexation with  $\text{Hg}^{2+}$ .

The tetra-2-pyridylthiocarbazono-based fluorescence sensor **1.61**, detects mercury ions in an aqueous medium.<sup>135</sup> Compound **1.61** exhibited an absorption peak at 345 nm, but in the presence of mercury nitrate, this peak was shifted to 395 nm. During a fluorescence titration of this compound with mercury (II) ions, weak fluorescence intensity of the compound at 530 nm was significantly increased. Furthermore, a new peak emerged at approximately 635 nm, featuring a 100-fold increase in integrated emission. Upon titration with other metal ions, the compound did not exhibit a significant absorption or emission spectral changes. The process was due to selective cyclization and desulfurization reactions caused by mercury leading to a formation of compound **1.62**, which other ions did not do, the compound **1.62** is highly emissive. Similar cyclisation reaction caused in the receptor **1.63** enables selective detection of mercury ions.<sup>136</sup> In this example also, other metal ions did not influence the fluorescence intensity.

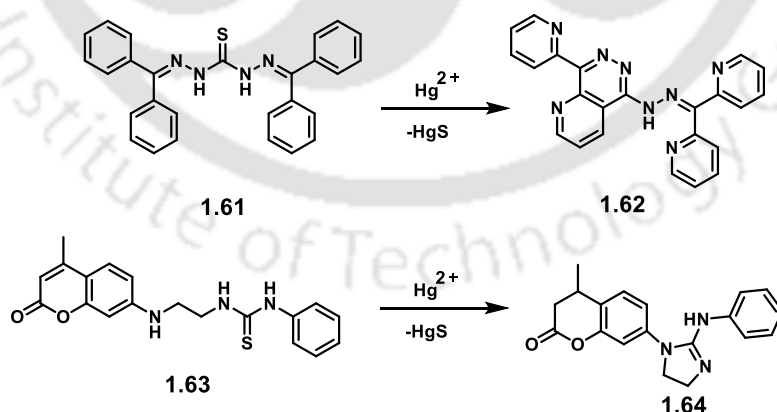


**Figure 1.39:** Cyclization and desulfurization by mercury metal ion in its detection.

The compound **1.65** has electron-rich methoxy group underwent cyclization in the presence of copper ions, in contrast to the compound **1.67** that has an electron withdrawing nitro group, latter did not undergo cyclization reaction.<sup>137</sup> The UV

absorption peaks of compound **1.65** and **1.67** were at 280 nm and 275 nm, respectively. However, upon the addition of copper nitrate salt, these peaks of the compounds underwent a significant shift to **299** nm and **345** nm, respectively. This shift in UV absorption spectra indicated the formation of new heterocyclic compound **1.66** and copper complexes **1.68** as a result of the interaction with copper ions. When other first-row transition metal ions were added, only marginal changes were observed in these absorption bands.

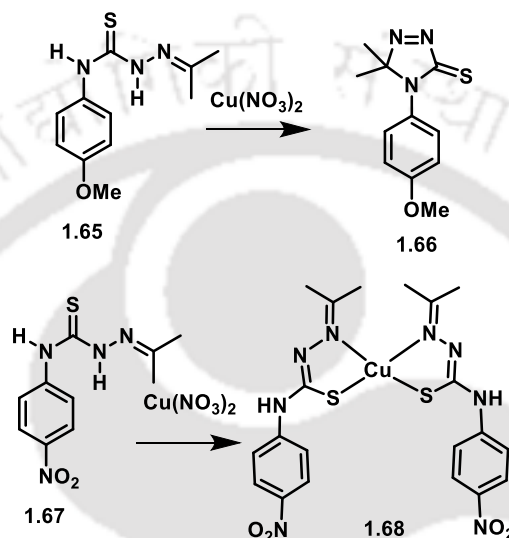


**Figure 1.40:** Cyclisation and metal complex formation by copper metal ion.

These are certain selective examples where the thiourea and related compounds binding or chemical reactivity has enabled us to serve as sensors. But there are many examples of based on similar principles and are used in metal ion sensing, primarily the urea/thiourea based receptors serves as anchoring template or undergoes changes to influence the chromophores or a fluorophore part in optical sensing.

### 1.10: Scope of this work

The emergence of new pharmaceuticals,<sup>135</sup> agrochemicals,<sup>136</sup> and pigments,<sup>137</sup> based on urea derivatives have provided wide scopes to study the various urea-based compounds. For example, in medicinal chemistry bioavailability, stability, polymorphs and cocrystals have high priority. The conformation aspects, chiral inductions guiding recognitions and enhancing active components in a drug formulation has been of great priority. Furthermore, studying of interactions of drug related molecules with solvents and toxic molecules are of importance to regulate their toxicity. Various non-covalent assemblies<sup>138</sup> including assemblies of ionic organic compounds in the form of ionic cocrystals or as salts have provided unusual packing patterns. Due to large interest in design of assemblies<sup>139</sup> related to biomolecules and wide-

spread features associated with weak interactions,<sup>140</sup> our interest has been to study the self-assembling properties of urea and thiourea derived compounds by having additional function units for hydrogen bonds. Addition of such functional units will diversify the scopes to have extended hydrogen bonds to create larger sizes of sub-assemblies, to in turn to recognize or bind guest/s in different ways. As the sulpha-drugs have large scopes to modify and diverse Supramolecular features, we have studied here sulpha-drugs derived urea to understand their assembling properties making impacts on physical and chemical properties. This would also provide an assessment on the role of sulphonamide units influencing the original assembly of the urea or thiourea without the sulphonamide part. The weak interactions of thiourea derived molecules have high impacts in specific detection of toxic ions. We have taken up a study so as to stabilize isomers across the thiolate form of urea derivative in metal complex and to stabilize conformational isomers. Conformational adjustments are routinely studied in solvates and polymorphs,<sup>36</sup> thus, more researches, to stabilize conformers in solid as well as solution from different conformations has definite interest. There are also limited studies on conformational isomers of metal complexes, hence, the present study has been able to provide examples required to clear the possibilities in such isomerism.

### 1.11: Reference

1. (a) Lehn, J.-M. Toward Complex Matter: Supramolecular Chemistry and Self-Organization. *Proc. Natl. Acad. Sci. U. S. A.* **2002**, *99* (8), 4763–4768 (b) J. M. Lehn, *Supramolecular Chemistry: Concepts and Perspectives*, VCH, Weinheim, 1995 (c) Lehn, J. *Supramolecular Chemistry-Scope and Perspectives Molecules, Supermolecules, and Molecular Devices (Nobel Lecture)*. *Angew. Chemie Int. Ed. English* **1988**, *27* (1), 89–112 (d) Chipper, M.; Meier, M. A. R.; Wouters, D.; Hoepfener, S.; Fustin, C.-A.; Gohy, J.-F.; Schubert, U. S. *Supramolecular Self-Assembled Ni (II), Fe (II), and Co (II) ABA Triblock Copolymers*. *Macromolecules* **2008**, *41* (8), 2771–2777 (e) Rowan, S. J.; Beck, J. B. *Metal-Ligand Induced Supramolecular Polymerization: A Route to Responsive Materials*. *Faraday Discuss.* **2005**, *128*, 43–53.
2. (a) Ariga, K.; Nishikawa, M.; Mori, T.; Takeya, J.; Shrestha, L. K.; Hill, J. P. *Self-Assembly as a Key Player for Materials Nanoarchitectonics*. *Sci. Technol. Adv. Mater.* **2019**, *20* (1), 51–95 (b) Stupp, S. I.; Palmer, L. C. *Supramolecular Chemistry and Self-Assembly in Organic Materials Design*. *Chem. Mater.* **2014**, *26* (1), 507–518 (c) Liu, K.; Kang, Y.; Wang, Z.; Zhang, X. *25th Anniversary Article: Reversible and Adaptive Functional Supramolecular Materials: “Noncovalent Interaction” Matters*. *Adv. Mater.*

- 2013**, 25 (39), 5530–5548 (d) Cheng, H.; Liu, R.; Zhang, R.; Huang, L.; Yuan, Q. Recent Advances in Supramolecular Self-Assembly Derived Materials for High-Performance Supercapacitors. *Nanoscale Adv.* **2023**, 5, 2394 – 2412 (e) Sun, P.; Qin, B.; Xu, J.-F.; Zhang, X. Supramonomers for Controllable Supramolecular Polymerization and Renewable Supramolecular Polymeric Materials. *Prog. Polym. Sci.* **2022**, 124, 101486 (f) Rest, C.; Kandanelli, R.; Fernández, G. Strategies to Create Hierarchical Self-Assembled Structures via Cooperative Non-Covalent Interactions. *Chem. Soc. Rev.* **2015**, 44 (8), 2543–2572 (g) Sun, J.; Decato, D. A.; Bryantsev, V. S.; John, E. A.; Berryman, O. B. The Interplay between Hydrogen and Halogen Bonding: Substituent Effects and Their Role in the Hydrogen Bond Enhanced Halogen Bond. *Chem. Sci.* **2023**, 14 (33), 8924–8935.
- (a) Stupp, S. I.; Zha, R. H.; Palmer, L. C.; Cui, H.; Bitton, R. Self-Assembly of Biomolecular Soft Matter. *Faraday Discuss.* **2013**, 166, 9–30 (b) Yin, P.; Choi, H. M. T.; Calvert, C. R.; Pierce, N. A. Programming Biomolecular Self-Assembly Pathways. *Nature* **2008**, 451 (7176), 318–322.
  - Sivakova, S.; Rowan, S. J. Nucleobases as Supramolecular Motifs. *Chem. Soc. Rev.* **2005**, 34 (1), 9–21.
  - (a) Zeng, F.; Zimmerman, S. C. Dendrimers in Supramolecular Chemistry: From Molecular Recognition to Self-Assembly. *Chem. Rev.* **1997**, 97 (5), 1681 – 1712 (b) van Dun, S.; Ottmann, C.; Milroy, L.-G.; Brunsveld, L. Supramolecular Chemistry Targeting Proteins. *J. Am. Chem. Soc.* **2017**, 139 (40), 13960 – 13968.
  - (a)Lehn, J. M. Cryptates: Inclusion Complexes of Macropolycyclic Receptor Molecules. *Pure Appl. Chem.* **1978**, 50 (9–10), 871–892 (b) Lehn, J. M. Cryptates: The Chemistry of Macropolycyclic Inclusion Complexes. *Acc. Chem. Res.* **1978**, 11 (2), 49 – 57.
  - (a)Sauvage, J.-P. Transition Metal-Containing Rotaxanes and Catenanes in Motion: Toward Molecular Machines and Motors. *Acc. Chem. Res.* **1998**, 31 (10), 611 – 619, (b) Fujita, M. Self-Assembly of [2] Catenanes Containing Metals in Their Backbones. *Acc. Chem. Res.* **1999**, 32 (1), 53 – 61 (c) Caulder, D. L.; Raymond, K. N. Supermolecules by Design. *Acc. Chem. Res.* **1999**, 32 (11), 975 – 982 (d) Leininger, S.; Olenyuk, B.; Stang, P. J. Self-Assembly of Discrete Cyclic Nanostructures Mediated by Transition Metals. *Chem. Rev.* **2000**, 100 (3), 853 – 908.
  - Burley, S. K.; Petsko, G. A. Aromatic-Aromatic Interaction: A Mechanism of Protein Structure Stabilization. *Science (80-. )*. **1985**, 229 (4708), 23 – 28.

9. Nishio, M. The CH/ $\pi$  Hydrogen Bond in Chemistry. Conformation, Supramolecules, Optical Resolution and Interactions Involving Carbohydrates. *Phys. Chem. Chem. Phys.* **2011**, *13* (31), 13873 – 13900.
10. (a) Ma, J. C.; Dougherty, D. A. The Cation– $\pi$  Interaction. *Chem. Rev.* **1997**, *97* (5), 1303–1324 (b) Crowley, P. B.; Golovin, A. Cation– $\pi$  Interactions in Protein–Protein Interfaces. *Proteins Struct. Funct. Bioinforma.* **2005**, *59* (2), 231 – 239 (c) Quiñonero, D.; Garau, C.; Rotger, C.; Frontera, A.; Ballester, P.; Costa, A.; Deyà, P. M. Anion– $\pi$  Interactions: Do They Exist? *Angew. Chemie* **2002**, *41* (18), 3389 – 3392 (d) Garau, C.; Frontera, A.; Quiñonero, D.; Ballester, P.; Costa, A.; Deyà, P. M. A Topological Analysis of the Electron Density in Anion– $\pi$  Interactions. *ChemPhysChem* **2003**, *4* (12), 1344–1348 (e) Quiñonero, D.; Frontera, A.; Garau, C.; Ballester, P.; Costa, A.; Deyà, P. M. Interplay between Cation– $\pi$ , Anion– $\pi$  and  $\pi$ – $\pi$  Interactions. *ChemPhysChem* **2006**, *7* (12), 2487–2491.
11. Beobide, G.; Castillo, O.; Luque, A.; García-Couceiro, U.; García-Terán, J. P.; Román, P. Supramolecular Architectures and Magnetic Properties of Coordination Polymers Based on Pyrazinedicarboxylato Ligands Showing Embedded Water Clusters. *Inorg. Chem.* **2006**, *45* (14), 5367–5382.
12. Gu, Y.; Kar, T.; Scheiner, S. Fundamental Properties of the CH $\cdots$ O Interaction: Is It a True Hydrogen Bond? *Journal of the American Chemical Society* **1999**, *121* (40), 9411–9422
13. (a) Webber, M. J.; Langer, R. Drug Delivery by Supramolecular Design. *Chem. Soc. Rev.* **2017**, *46* (21), 6600–6620 (b) Kawakami, K.; Ebara, M.; Izawa, H.; M Sanchez-Ballester, N.; P Hill, J.; Ariga, K. Supramolecular Approaches for Drug Development. *Curr. Med. Chem.* **2012**, *19* (15), 2388–2398 (c) Sunamoto, J. Supramolecular Assemblies for Improved Drug Delivery System. In *Advanced Biomaterials in Biomedical Engineering and Drug Delivery Systems*; Springer, 1996; 76–80 (d) Meyer, E. A.; Castellano, R. K.; Diederich, F. Interactions with Aromatic Rings in Chemical and Biological Recognition. *Angew. Chemie Int. Ed.* **2003**, *42* (11), 1210–1250 (e) Feng, Z.; Zhang, T.; Wang, H.; Xu, B. Supramolecular Catalysis and Dynamic Assemblies for Medicine. *Chem. Soc. Rev.* **2017**, *46* (21), 6470–6479 (f) Ling, X. Y.; Reinhoudt, D. N.; Huskens, J. From Supramolecular Chemistry to Nanotechnology: Assembly of 3D Nanostructures. *Pure Appl. Chem.* **2009**, *81* (12), 2225–2233 (g) Ma,

- X.; Zhao, Y. Biomedical Applications of Supramolecular Systems Based on Host–Guest Interactions. *Chem. Rev.* **2015**, *115* (15), 7794–7839.
14. Feng, Z.; Zhang, T.; Wang, H.; Xu, B. Supramolecular Catalysis and Dynamic Assemblies for Medicine. *Chem. Soc. Rev.* **2017**, *46* (21), 6470–6479.
  15. Ling, X. Y.; Reinhoudt, D. N.; Huskens, J. From Supramolecular Chemistry to Nanotechnology: Assembly of 3D Nanostructures. *Pure Appl. Chem.* **2009**, *81* (12), 2225–2233.
  16. (a) Erbas-Cakmak, S.; Leigh, D. A.; McTernan, C. T.; Nussbaumer, A. L. Artificial Molecular Machines. *Chem. Rev.* **2015**, *115* (18), 10081–10206 (b) Northrop, B. H.; Aricó, F.; Tangchiavang, N.; Badjić, J. D.; Stoddart, J. F. Template-Directed Synthesis of Mechanically Interlocked Molecular Bundles Using Dynamic Covalent Chemistry. *Org. Lett.* **2006**, *8* (18), 3899–3902 (c) Balzani, V.; Credi, A.; Raymo, F. M.; Stoddart, J. F. Artificial Molecular Machines. *Angew. Chemie Int. Ed.* **2000**, *39* (19), 3348–3391.
  17. Meyer, E. A.; Castellano, R. K.; Diederich, F. Interactions with Aromatic Rings in Chemical and Biological Recognition. *Angew. Chemie Int. Ed.* **2003**, *42* (11), 1210–1250.
  18. Roche, S.; Haslam, C.; Heath, S. L.; Thomas, J. A. Self-Assembly of a Supramolecular Cube. *Chem. Commun.* **1998**, No. 16, 1681–1682.
  19. Okesola, B. O.; Mata, A. Multicomponent Self-Assembly as a Tool to Harness New Properties from Peptides and Proteins in Material Design. *Chem. Soc. Rev.* **2018**, *47* (10), 3721–3736.
  20. Yan, Q.; Cai, K.; Zhao, D. Supramolecular Aggregates with Distinct Optical Properties from PDI Oligomers of Similar Structures. *Phys. Chem. Chem. Phys.* **2016**, *18* (3), 1905–1910.
  21. Beobide, G.; Castillo, O.; Luque, A.; García-Couceiro, U.; García-Terán, J. P.; Román, P. Supramolecular Architectures and Magnetic Properties of Coordination Polymers Based on Pyrazinedicarboxylato Ligands Showing Embedded Water Clusters. *Inorg. Chem.* **2006**, *45* (14), 5367–5382.
  22. Desiraju, G. R. The CH. Cntdot.. Cntdot.. Cntdot. O Hydrogen Bond in Crystals: What Is It? *Acc. Chem. Res.* **1991**, *24* (10), 290 – 296.
  23. Arunan, E.; Desiraju, G. R.; Klein, R. A.; Sadlej, J.; Scheiner, S.; Alkorta, I.; Clary, D. C.; Crabtree, R. H.; Dannenberg, J. J.; Hobza, P. Definition of the Hydrogen Bond (IUPAC Recommendations 2011). *Pure Appl. Chem.* **2011**, *83* (8), 1637–1641

24. Steiner, T. The Hydrogen Bond in the Solid State. *Angew. Chemie Int. Ed.* **2002**, *41* (1), 48–7.
25. Gilli, G.; Bellucci, F.; Ferretti, V.; Bertolasi, V. Evidence for Resonance-Assisted Hydrogen Bonding from Crystal-Structure Correlations on the Enol Form of the Beta.-Diketone Fragment. *J. Am. Chem. Soc.* **1989**, *111* (3), 1023–1028.
26. Desiraju, G. R. The C–H···O Hydrogen Bond: Structural Implications and Supramolecular Design. *Acc. Chem. Res.* **1996**, *29* (9), 441–449 (b) Sarma, J. A. R. P.; Desiraju, G. R. The Role of Cl···Cl and CH···O Interactions in the Crystal Engineering of 4-ANG. Short-Axis Structures. *Acc. Chem. Res.* **1986**, *19* (7), 222–228.
27. Rozas, I.; Alkorta, I.; Elguero, J. Bifurcated Hydrogen Bonds: Three-Centered Interactions. *J. Phys. Chem. A* **1998**, *102* (48), 9925–9932.
28. Desiraju, G. R. Supramolecular Synthons in Crystal Engineering—a New Organic Synthesis. *Angew. Chemie Int. Ed. English* **1995**, *34* (21), 2311–2327 (b) Desiraju, G. R. Designer Crystals: Intermolecular Interactions, Network Structures and Supramolecular Synthons. *Chem. Commun.* **1997**, No. 16, 1475–1482.
29. Etter, M. C.; MacDonald, J. C.; Bernstein, J. Graph-Set Analysis of Hydrogen-Bond Patterns in Organic Crystals. *Acta Crystallogr. Sect. B Struct. Sci.* **1990**, *46* (2), 256–262.
30. Webber, M. J.; Langer, R. Drug Delivery by Supramolecular Design. *Chem. Soc. Rev.* **2017**, *46* (21), 6600–6620.
31. Thallapally, P. K.; Jetti, R. K. R.; Katz, A. K.; Carrell, H. L.; Singh, K.; Lahiri, K.; Kotha, S.; Boese, R.; Desiraju, G. R. Polymorphism of 1, 3, 5-Trinitrobenzene Induced by a Trisindane Additive. *Angew. Chemie Int. Ed.* **2004**, *43* (9), 1149–1155.
32. Censi, R.; Di Martino, P. Polymorph Impact on the Bioavailability and Stability of Poorly Soluble Drugs. *Molecules* **2015**, *20* (10), 18759–18776.
33. Alencar, L. C. B.; Santana, C. P.; Silva, K. M. A.; Nóbrega, F. P.; Correia, L. P.; Santos, W. M.; Andrade, F. H. D.; Santos, F. S.; Macêdo, R. O.; Medeiros, A. C. D. Thermal Study of Active Pharmaceutical Ingredients Used as Analgesics by DTA and DSC Coupled to Photovisual System. *Chem. Thermodyn. Therm. Anal.* **2022**, *7*, 100072.
34. Craven, B. M.; Vizzini, E. A. t; Rodrigues, M. M. The Crystal Structure of Two Polymorphs of 5, 5'-Diethylbarbituric Acid (Barbital). *Acta Crystallogr. Sect. B Struct. Crystallogr. Cryst. Chem.* **1969**, *25* (10), 1978–1993.

35. Mukherjee, A.; Desiraju, G. R. Synthron Polymorphism and Pseudopolymorphism in Co-Crystals. The 4, 4'-Bipyridine–4-Hydroxybenzoic Acid Structural Landscape. *Chem. Commun.* **2011**, 47 (14), 4090–4092.
36. Cruz-Cabeza, A. J.; Bernstein, J. Conformational Polymorphism. *Chem. Rev.* **2014**, 114 (4), 2170–2191.
37. Thirunahari, S.; Aitipamula, S.; Chow, P. S.; Tan, R. B. H. Conformational Polymorphism of Tolbutamide: A Structural, Spectroscopic, and Thermodynamic Characterization of Burger's Forms I–IV. *J. Pharm. Sci.* **2010**, 99 (7), 2975–2990.
38. Grothe, E.; Meeke, H.; Vlieg, E.; Ter Horst, J. H.; de Gelder, R. de. Solvates, Salts, and Cocrystals: A Proposal for a Feasible Classification System. *Cryst. Growth Des.* **2016**, 16 (6), 3237–3243.
39. (a) Bis, J. A.; Vishweshwar, P.; Middleton, R. A.; Zaworotko, M. J. Concomitant and Conformational Polymorphism, Conformational Isomorphism, and Phase Relationships in 4-Cyanopyridine⊙ 4, 4'-Biphenol Cocrystals. *Cryst. Growth Des.* **2006**, 6 (4), 1048–1053  
(b) Lusi, M.; Vitorica-Yrezabal, I. J.; Zaworotko, M. J. Expanding the Scope of Molecular Mixed Crystals Enabled by Three Component Solid Solutions. *Cryst. Growth Des.* **2015**, 15 (8), 4098–4103.
40. Duggirala, N. K.; Perry, M. L.; Almarsson, Ö.; Zaworotko, M. J. Pharmaceutical Cocrystals: Along the Path to Improved Medicines. *Chem. Commun.* **2016**, 52 (4), 640–655.
41. Wang, B.; Lin, R.-B.; Zhang, Z.; Xiang, S.; Chen, B. Hydrogen-Bonded Organic Frameworks as a Tunable Platform for Functional Materials. *J. Am. Chem. Soc.* **2020**, 142 (34), 14399–14416.
42. Zentner, C. A.; Lai, H. W. H.; Greenfield, J. T.; Wiscons, R. A.; Zeller, M.; Campana, C. F.; Talu, O.; FitzGerald, S. A.; Rowsell, J. L. C. High Surface Area and Z' in a Thermally Stable 8-Fold Polycatenated Hydrogen-Bonded Framework. *Chem. Commun.* **2015**, 51 (58), 11642–11645.
43. Holman, K. T.; Pivovar, A. M.; Swift, J. A.; Ward, M. D. Metric Engineering of Soft Molecular Host Frameworks. *Acc. Chem. Res.* **2001**, 34 (2), 107–118.
44. (a) Childs, S. L.; Stahly, G. P.; Park, A. The Salt– Cocrystal Continuum: The Influence of Crystal Structure on Ionization State. *Mol. Pharm.* **2007**, 4 (3), 323–338 (b) Cruz-Cabeza, A. J. Acid–Base Crystalline Complexes and the p K a Rule. *CrystEngComm*

- 2012**, *14* (20), 6362–6365 (c) Lemmerer, A.; Admond, D. A.; Esterhuysen, C.; Bernstein, J. Polymorphic Co-Crystals from Polymorphic Co-Crystal Formers: Competition between Carboxylic Acid··· Pyridine and Phenol··· Pyridine Hydrogen Bonds. *Cryst. Growth Des.* **2013**, *13* (9), 3935–3952.
45. Sandhu, B.; McLean, A.; Sinha, A. S.; Desper, J.; Sarjeant, A. A.; Vyas, S.; Reutzel-Edens, S. M.; Aakeröy, C. B. Evaluating Competing Intermolecular Interactions through Molecular Electrostatic Potentials and Hydrogen-Bond Propensities. *Cryst. Growth Des.* **2018**, *18* (1), 466–478.
46. Weimer, G. H.; Copetti, J. P. P.; Orlando, T.; Zanatta, N.; Bonacorso, H. G.; Salbego, P. R. S.; Martins, M. A. P. The Role of Attractive and Repulsive Interactions in the Stabilization of Ammonium Salts Structures. *CrystEngComm* **2022**, *24* (40), 7039–7048.
47. (a) Herkert, L.; Sampedro, A.; Fernández, G. Cooperative Self-Assembly of Discrete Metal Complexes. *CrystEngComm* **2016**, *18* (46), 8813–8822 (b) Bäumer, N.; Matern, J.; Fernández, G. Recent Progress and Future Challenges in the Supramolecular Polymerization of Metal-Containing Monomers. *Chem. Sci.* **2021**, *12* (37), 12248–12265. (c) C. V. Stappen, Y. Deng, Y. Liu, H. Heidari, J.-X. Wang, Y. Zhou, A. P. Ledray, and Y. Lu Designing Artificial Metalloenzymes by Tuning of the Environment beyond the Primary Coordination Sphere. *Chem.Rev.* **2022** *122* (14), 11974–12045. (d) J. C. Lewis, Beyond the Second Coordination Sphere: Engineering Dirhodium Artificial Metalloenzymes To Enable Protein Control of Transition Metal Catalysis. *Acc.Chem.Res.* **2019** *52* (3), 576–584.
48. Kuehl, C. J.; Tabellion, F. M.; Arif, A. M.; Stang, P. J. Single- and Double-Stranded Chains Assembled via Concomitant Metal Coordination and Hydrogen Bonding. *Organometallics* **2001**, *20* (10), 1956–1959.
49. Qin, Z.; Jennings, M. C.; Puddephatt, R. J. Self-Assembly of Polymer and Sheet Structures from Palladium(II) Complexes by Hydrogen Bonding between Carboxamide Substituents. *Inorg. Chem.* **2001**, *40* (24), 6220–6228
50. El Bakkali, H.; Castiñeiras, A.; García-Santos, I.; González-Pérez, J. M.; Niclós-Gutiérrez, J. Metallo-Supramolecular Structures by Self-Assembly through Weak Interactions in Mixed Ligand Metal Complexes of Adenine and Malonate. *Cryst. Growth Des.* **2014**, *14* (1), 249–260.

51. Teyssandier, J.; De Feyter, S.; Mali, K. S. Host–Guest Chemistry in Two-Dimensional Supramolecular Networks. *Chem. Commun.* **2016**, 52 (77), 11465–11487.
52. Desiraju, G. R.; Ho, P. S.; Kloo, L.; Legon, A. C.; Marquardt, R.; Metrangolo, P.; Politzer, P.; Resnati, G.; Rissanen, K. Definition of the Halogen Bond (IUPAC Recommendations 2013). **2013**, 85 (8), 1711–1713.
53. Politzer, P.; Murray, J. S.; Clark, T. Halogen Bonding and Other  $\sigma$ -Hole Interactions: A Perspective. *Phys. Chem. Chem. Phys.* **2013**, 15 (27), 11178–11189.
54. Desiraju, G. R.; Parthasarathy, R. The Nature of Halogen···Halogen Interactions: Are Short Halogen Contacts Due to Specific Attractive Forces or Due to Close Packing of Nonspherical Atoms? *J. Am. Chem. Soc.* **1989**, 111 (23), 8725–8726.
55. Aakeröy, C. B.; Chopade, P. D.; Desper, J. Avoiding “Synthon Crossover” in Crystal Engineering with Halogen Bonds and Hydrogen Bonds. *Cryst. Growth Des.* **2011**, 11 (12), 5333–5336.
56. Gonnade, R. G.; Bhadbhade, M. M.; Shashidhar, M. S.; Sanki, A. K. Concomitant Dimorphs of Tri-O-[p-Halobenzoyl]-Myo-Inositol 1,3,5-Orthoformates with Different Halogen Bonding Contacts: First Order Crystal-to-Crystal Thermal Phase Transition of Kinetic Form to the Thermodynamic Form. *Chem. Commun.* **2005**, 5870 – 5872.
57. Mukherjee, A.; Tothadi, S.; Desiraju, G. R. Halogen Bonds in Crystal Engineering: Like Hydrogen Bonds yet Different. *Acc. Chem. Res.* **2014**, 47 (8), 2514–2524.
58. Wilcken, R.; Zimmermann, M. O.; Lange, A.; Joerger, A. C.; Boeckler, F. M. Principles and Applications of Halogen Bonding in Medicinal Chemistry and Chemical Biology. *J. Med. Chem.* **2013**, 56 (4), 1363–1388.
59. Brown, A.; Beer, P. D. Halogen Bonding Anion Recognition. *Chem. Commun.* **2016**, 52 (56), 8645–8658.
60. Kniep, F.; Jungbauer, S. H.; Zhang, Q.; Walter, S. M.; Schindler, S.; Schnapperelle, I.; Herdtweck, E.; Huber, S. M. Organocatalysis by Neutral Multidentate Halogen-Bond Donors. *Angew. Chemie - Int. Ed.* **2013**, 52 (27), 7028–7032.
61. Fourmigué, M. Halogen Bonding in Conducting or Magnetic Molecular Materials BT - Halogen Bonding: Fundamentals and Applications; Metrangolo, P., Resnati, G., Eds.; Springer Berlin Heidelberg: Berlin, Heidelberg, **2008**; 181–207.
62. Guo, H.; Liang, C.; Ruoko, T.-P.; Meteling, H.; Peng, B.; Zeng, H.; Priimagi, A. Programmable and Self-Healable Liquid Crystal Elastomer Actuators Based on Halogen Bonding. *Angew. Chemie Int. Ed.* **2023**, 62 (43), e202309402.

63. Yan, D.; Delori, A.; Lloyd, G. O.; Frišćić, T.; Day, G. M.; Jones, W.; Lu, J.; Wei, M.; Evans, D. G.; Duan, X. A Cocrystal Strategy to Tune the Luminescent Properties of Stilbene-Type Organic Solid-State Materials. *Angew. Chemie - Int. Ed.* **2011**, *50* (52), 12483–12486.
64. Soldatova, N. S.; Postnikov, P. S.; Ivanov, D. M.; Semyonov, O. V.; Kukurina, O. S.; Guselnikova, O.; Yamauchi, Y.; Wirth, T.; Zhdankin, V. V.; Yusubov, M. S.; Gomila, R. M.; Frontera, A.; Resnati, G.; Kukushkin, V. Y. Zwitterionic Iodonium Species Afford Halogen Bond-Based Porous Organic Frameworks. *Chem. Sci.* **2022**, *13*, 5650–5658.
65. Catalano, L.; Pérez-Estrada, S.; Terraneo, G.; Pilati, T.; Resnati, G.; Metrangolo, P.; Garcia-Garibay, M. A. Dynamic Characterization of Crystalline Supramolecular Rotors Assembled through Halogen Bonding. *J. Am. Chem. Soc.* **2015**, *137* (49), 15386–15389.
66. Wöhler, F. Ueber Künstliche Bildung Des Harnstoffs. *Ann. Phys.* **1828**, *88* (2), 253–256.
67. Ramberg, P. J. The Death of Vitalism and the Birth of Organic Chemistry: Wohler's Urea Synthesis and the Disciplinary Identity of Organic Chemistry. *Ambix* **2000**, *47* (3), 170–195.
68. Yokoya, M.; Kimura, S.; Yamanaka, M. Urea Derivatives as Functional Molecules: Supramolecular Capsules, Supramolecular Polymers, Supramolecular Gels, Artificial Hosts, and Catalysts. *Chem. - A Eur. J.* **2021**, *27* (18), 5601–5614.
69. Melnikov, N. N. Derivatives of Urea and Thiourea BT - Chemistry of Pesticides; Melnikov, N. N., Gunther, F. A., Gunther, J. D., Eds.; Springer US: New York, NY, 1971; 225–239.
70. Lombardino, J. G.; Lowe, J. A. The Role of the Medicinal Chemist in Drug Discovery — Then and Now. *Nat. Rev. Drug Discov.* **2004**, *3* (10), 853–862.
71. George, M.; Tan, G.; John, V. T.; Weiss, R. G. Urea and Thiourea Derivatives as Low Molecular-Mass Organogelators. *Chem. - A Eur. J.* **2005**, *11* (11), 3243–3254.
72. Dirany, M.; Ayzac, V.; Isare, B.; Raynal, M.; Bouteiller, L. Structural Control of Bisurea-Based Supramolecular Polymers: Influence of an Ester Moiety. *Langmuir* **2015**, *31* (42), 11443–11451.
73. Zhang, Z.; Bao, Z.; Xing, H. N,N'-Bis[3,5-Bis(Trifluoromethyl)Phenyl]Thiourea: A Privileged Motif for Catalyst Development. *Org. Biomol. Chem.* **2014**, *12* (20), 3151–3162.

74. Du, X.; Wang, M.; Hu, X.; Nie, T.; Zhu, M.; Zhang, G.; You, X.; Wang, Y. Synthesis and Biological Evaluation of Novel N, N'-Diaryurea Derivatives as Potent Antibacterial Agents against MRSA. *Bioorganic Med. Chem. Lett.* **2022**, *75* (September), 128975.
75. Hou, Y.; Zhu, S.; Chen, Y.; Yu, M.; Liu, Y.; Li, M. Evaluation of Antibacterial Activity of Thiourea Derivative TD4 against Methicillin-Resistant Staphylococcus Aureus via Destroying the NAD<sup>+</sup>/NADH Homeostasis. *Molecules*. **2023**, *28*, 3219.
76. Ommi, O.; Naiyaz Ahmad, M.; Gajula, S. N. R.; Wanjari, P.; Sau, S.; Agnivesh, P. K.; Sahoo, S. K.; Kalia, N. P.; Sonti, R.; Nanduri, S.; Dasgupta, A.; Chopra, S.; Yaddanapudi, V. M. Synthesis and Pharmacological Evaluation of 1,3-Diaryl Substituted Pyrazole Based (Thio)Urea Derivatives as Potent Antimicrobial Agents against Multi-Drug Resistant Staphylococcus Aureus and Mycobacterium Tuberculosis. *RSC Med. Chem.* **2023**, *14* (7), 1296–1308.
77. Antypenko, L.; Meyer, F.; Kholodniak, O.; Sadykova, Z.; Jirásková, T.; Troianova, A.; Buhaiova, V.; Cao, S.; Kovalenko, S.; Garbe, L.-A.; Steffens, K. G. Novel Acyl Thiourea Derivatives: Synthesis, Antifungal Activity, Gene Toxicity, Drug-like and Molecular Docking Screening. *Arch. Pharm. (Weinheim)*. **2019**, *352* (2), e1800275.
78. Maciuszek, M.; Ortega-Gomez, A.; Maas, S. L.; Perretti, M.; Merritt, A.; Soehnlein, O.; Chapman, T. M. Synthesis and Evaluation of Novel Cyclopentane Urea FPR2 Agonists and Their Potential Application in the Treatment of Cardiovascular Inflammation. *Eur. J. Med. Chem.* **2021**, *214*, 113194.
79. Nedeljković, N.; Dobričić, V.; Bošković, J.; Vesović, M.; Bradić, J.; Anđić, M.; Kočović, A.; Jeremić, N.; Novaković, J.; Jakovljević, V.; Vujić, Z.; Nikolić, M. Synthesis and Investigation of Anti-Inflammatory Activity of New Thiourea Derivatives of Naproxen. *Pharmaceuticals* **2023**, *16* (5), 666.
80. Li, H.-Q.; Lv, P.-C.; Yan, T.; Zhu, H.-L. Urea Derivatives as Anticancer Agents. *Anti-Cancer Agents in Medicinal Chemistry*. **2009**, *9*, 471–480.
81. Abbas, S. Y.; Al-Harbi, R. A. K.; Sh El-Sharief, M. A. M. Synthesis and Anticancer Activity of Thiourea Derivatives Bearing a Benzodioxole Moiety with EGFR Inhibitory Activity, Apoptosis Assay and Molecular Docking Study. *Eur. J. Med. Chem.* **2020**, *198*, 112363.
82. Charifson, P. S.; Grillot, A. L.; Grossman, T. H.; Parsons, J. D.; Badia, M.; Bellon, S.; Deininger, D. D.; Drumm, J. E.; Gross, C. H.; LeTiran, A.; Liao, Y.; Mani, N.; Nicolau, D. P.; Perola, E.; Ronkin, S.; Shannon, D.; Swenson, L. L.; Tang, Q.; Tessier, P. R.;

- Tian, S. K.; Trudeau, M.; Wang, T.; Wei, Y.; Zhang, H.; Stamos, D. Novel Dual-Targeting Benzimidazole Urea Inhibitors of DNA Gyrase and Topoisomerase IV Possessing Potent Antibacterial Activity: Intelligent Design and Evolution through the Judicious Use of Structure-Guided Design and Structure-Activity Relationships. *J. Med. Chem.* **2008**, *51* (17), 5243–5263.
83. Grillot, A. L.; Tiran, A. Le; Shannon, D.; Krueger, E.; Liao, Y.; Odowd, H.; Tang, Q.; Ronkin, S.; Wang, T.; Waal, N.; Li, P.; Lauffer, D.; Sizensky, E.; Tanoury, J.; Perola, E.; Grossman, T. H.; Doyle, T.; Hanzelka, B.; Jones, S.; Dixit, V.; Ewing, N.; Liao, S.; Boucher, B.; Jacobs, M.; Bennani, Y.; Charifson, P. S. Second-Generation Antibacterial Benzimidazole Ureas: Discovery of a Preclinical Candidate with Reduced Metabolic Liability. *J. Med. Chem.* **2014**, *57* (21), 8792–8816.
84. Stokes, N. R.; Thomaidis-Brears, H. B.; Barker, S.; Bennett, J. M.; Berry, J.; Collins, I.; Czaplewski, L. G.; Gamble, V.; Lancett, P.; Logan, A.; Lunniss, C. J.; Peasley, H.; Pommier, S.; Price, D.; Smee, C.; Haydon, D. J. Biological Evaluation of Benzothiazole Ethyl Urea Inhibitors of Bacterial Type II Topoisomerases. *Antimicrob. Agents Chemother.* **2013**, *57* (12), 5977–5986.
85. Verlinden, B. K.; Niemand, J.; Snyman, J.; Sharma, S. K.; Beattie, R. J.; Woster, P. M.; Birkholtz, L. M. Discovery of Novel Alkylated (Bis)Urea and (Bis)Thiourea Polyamine Analogues with Potent Antimalarial Activities. *J. Med. Chem.* **2011**, *54* (19), 6624–6633.
86. Singh, P.; Raj, R.; Singh, P.; Gut, J.; Rosenthal, P. J.; Kumar, V. Urea/Oxalamide Tethered  $\beta$ -Lactam-7-Chloroquinoline Conjugates: Synthesis and in Vitro Antimalarial Evaluation. *Eur. J. Med. Chem.* **2014**, *71*, 128–134.
87. Schwartz, B. D.; Skinner-Adams, T. S.; Andrews, K. T.; Coster, M. J.; Edstein, M. D.; MacKenzie, D.; Charman, S. A.; Koltun, M.; Blundell, S.; Campbell, A.; Pouwer, R. H.; Quinn, R. J.; Beattie, K. D.; Healy, P. C.; Davis, R. A. Synthesis and Antimalarial Evaluation of Amide and Urea Derivatives Based on the Thiaplakortone A Natural Product Scaffold. *Org. Biomol. Chem.* **2015**, *13* (5), 1558–1570.
88. Leggans, E. K.; Duncan, K. K.; Barker, T. J.; Schleicher, K. D.; Boger, D. L. A Remarkable Series of Vinblastine Analogues Displaying Enhanced Activity and an Unprecedented Tubulin Binding Steric Tolerance: C20' Urea Derivatives. *J. Med. Chem.* **2013**, *56* (3), 628–639.

89. Schnekenburger, M.; Goffin, E.; Lee, J. Y.; Jang, J. Y.; Mazumder, A.; Ji, S.; Rogister, B.; Bouider, N.; Lefranc, F.; Miklos, W.; Mathieu, V.; De Tullio, P.; Kim, K. W.; Dicato, M.; Berger, W.; Han, B. W.; Kiss, R.; Pirotte, B.; Diederich, M. Discovery and Characterization of R/S-N-3-Cyanophenyl-N'-(6-Tert-Butoxycarbonylamino-3,4-Dihydro-2,2-Dimethyl-2H-1-Benzopyran-4-Yl)Urea, a New Histone Deacetylase Class III Inhibitor Exerting Antiproliferative Activity against Cancer Cell Lines. *J. Med. Chem.* **2017**, *60* (11), 4714–4733.
90. Subedi, M.; Minn, I.; Chen, J.; Kim, Y. H.; Ok, K.; Jung, Y. W.; Pomper, M. G.; Byun, Y. Design, Synthesis and Biological Evaluation of PSMA/Hepsin-Targeted Heterobivalent Ligands. *Eur. J. Med. Chem.* **2016**, *118*, 208–218.
91. Ronchetti, R.; Moroni, G.; Carotti, A.; Gioiello, A.; Camaioni, E. Recent Advances in Urea- And Thiourea-Containing Compounds: Focus on Innovative Approaches in Medicinal Chemistry and Organic Synthesis. *RSC Med. Chem.* **2021**, *12* (7), 1046–1064.
92. Ghosh, A. K.; Brindisi, M. Urea Derivatives in Modern Drug Discovery and Medicinal Chemistry. *J. Med. Chem.* **2020**, *63* (6), 2751–2788.
93. Pingaew, R.; Sinthupoom, N.; Mandi, P.; Prachayasittikul, V.; Cherdtrakulkiat, R.; Prachayasittikul, S.; Ruchirawat, S.; Prachayasittikul, V. Synthesis, Biological Evaluation and in Silico Study of Bis-Thiourea Derivatives as Anticancer, Antimalarial and Antimicrobial Agents. *Med. Chem. Res.* **2017**, *26* (12), 3136–3148.
94. Cunha, B. N.; Colina-Vegas, L.; Plutín, A. M.; Silveira, R. G.; Honorato, J.; Oliveira, K. M.; Cominetti, M. R.; Ferreira, A. G.; Castellano, E. E.; Batista, A. A. Hydrolysis Reaction Promotes Changes in Coordination Mode of Ru(II)/Acylthiourea Organometallic Complexes with Cytotoxicity against Human Lung Tumor Cell Lines. *J. Inorg. Biochem.* **2018**, *186* (May), 147–156.
95. Harris, K. D. M. Meldola Lecture: Understanding the Properties of Urea and Thiourea Inclusion Compounds. *Chem. Soc. Rev.* **1997**, *26* (4), 279.
96. Matsumura, M.; Tanatani, A.; Azumaya, I.; Masu, H.; Hashizume, D.; Kagechika, H.; Muranaka, A.; Uchiyama, M. Unusual Conformational Preference of an Aromatic Secondary Urea: Solvent-Dependent Open-Closed Conformational Switching of N,N'-Bis(Porphyrinyl)Urea. *Chem. Commun.* **2013**, *49* (23), 2290–2292.

- 
97. Yamasaki, R.; Iida, M.; Ito, A.; Fukuda, K.; Tanatani, A.; Kagechika, H.; Masu, H.; Okamoto, I. Crystal Engineering of N,N'-Diphenylurea Compounds Featuring Phenyl-Perfluorophenyl Interaction. *Cryst. Growth Des.* **2017**, *17* (11), 5858–5866.
98. Bryantsev, V. S.; Firman, T. K.; Hay, B. P. Conformational Analysis and Rotational Barriers of Alkyl- And Phenyl-Substituted Urea Derivatives. *J. Phys. Chem. A* **2005**, *109* (5), 832–842.
99. Luchini, G.; Ascough, D. M. H.; Alegre-Requena, J. V.; Gouverneur, V.; Paton, R. S. Data-Mining the Diaryl(Thio)Urea Conformational Landscape: Understanding the Contrasting Behavior of Ureas and Thioureas with Quantum Chemistry. *Tetrahedron* **2019**, *75* (6), 697–702.
100. Bryantsev, V. S.; Hay, B. P. Conformational Preferences and Internal Rotation in Alkyl- and Phenyl-Substituted Thiourea Derivatives. *J. Phys. Chem. A* **2006**, *110* (14), 4678–4688.
101. Succaw, G. L.; Weakley, T. J. R.; Han, F.; Doxsee, K. M. Crystal Engineering with Bis(Thiourea) Derivatives. *Cryst. Growth Des.* **2005**, *5* (6), 2288–2298.
102. Karmakar, A.; Baruah, J. B. Metal Carboxylate Complexes of L-3-Phenyl-2-(3-Phenyl-Ureido)-Propionic Acid. *Inorg. Chem. Commun.* **2009**, *12* (2), 140–144.
103. Yagai, S.; Kubota, S.; Iwashima, T.; Kishikawa, K.; Nakanishi, T.; Karatsu, T.; Kitamura, A. Supramolecular Polymerization and Polymorphs of Oligo(p-Phenylene Vinylene)-Functionalized Bis- and Monoureas. *Chem. - A Eur. J.* **2008**, *14* (17), 5246–5257.
104. Shimizu, L. S.; Hughes, A. D.; Smith, M. D.; Davis, M. J.; Zhang, B. P.; Zur Loye, H. C.; Shimizu, K. D. Self-Assembled Nanotubes That Reversibly Bind Acetic Acid Guests. *J. Am. Chem. Soc.* **2003**, *125* (49), 14972–14973.
105. Shimizu, L. S.; Salpage, S. R.; Korous, A. A. Functional Materials from Self-Assembled Bis-Urea Macrocycles. *Acc. Chem. Res.* **2014**, *47* (7), 2116–2127.
106. Nieuwenhuizen, M. M. L.; De Greef, T. F. A.; Van Der Bruggen, R. L. J.; Paulusse, J. M. J.; Appel, W. P. J.; Smulders, M. M. J.; Sijbesma, R. P.; Meijer, E. W. Self-Assembly of Ureido-Pyrimidinone Dimers into One-Dimensional Stacks by Lateral Hydrogen Bonding. *Chem. - A Eur. J.* **2010**, *16* (5), 1601–1612.
107. Beijer, F. H.; Sijbesma, R. P.; Kooijman, H.; Spek, A. L.; Meijer, E. W. Strong Dimerization of Ureidopyrimidones via Quadruple Hydrogen Bonding. *J. Am. Chem. Soc.* **1998**, *120* (27), 6761–6769.
-

108. Sijbesma, R. P.; Beijer, F. H.; Brunsveld, L.; Folmer, B. J. B.; Hirschberg, J. H. K. K.; Lange, R. F. M.; Lowe, J. K. L.; Meijer, E. W. Reversible Polymers Formed from Self-Complementary Monomers Using Quadruple Hydrogen Bonding. *Science* (80-. ). **1997**, 278 (5343), 1601–1604.
109. Li, J.; Bourne, S. A.; De Villiers, M. M.; Crider, A. M.; Caira, M. R. Polymorphism of the Antitubercular Isoxyl. *Cryst. Growth Des.* **2011**, 11 (11), 4950–4957.
110. Hong, M.; Li, S.; Ji, W.; Qi, M. H.; Ren, G. Bin. Cocrystals of Lenvatinib with Sulfamerazine and Salicylic Acid: Crystal Structure, Equilibrium Solubility, Stability Study, and Anti-Hepatoma Activity. *Cryst. Growth Des.* **2021**, 21 (7), 3714–3727.
111. Gavette, J. V.; Mills, N. S.; Zakharov, L. N.; Johnson, C. A.; Johnson, D. W.; Haley, M. M. An Anion-Modulated Three-Way Supramolecular Switch That Selectively Binds Dihydrogen Phosphate, H<sub>2</sub>PO<sub>4</sub><sup>-</sup>. *Angew. Chemie - Int. Ed.* **2013**, 52 (39), 10270–10274.
112. Bondy, C. R.; Gale, P. A.; Loeb, S. J. Metal-Organic Anion Receptors: Arranging Urea Hydrogen-Bond Donors to Encapsulate Sulfate Ions. *J. Am. Chem. Soc.* **2004**, 126 (16), 5030–5031.
113. Carroll, C. N.; Berryman, O. B.; Johnson, C. A.; Zakharov, L. N.; Haley, M. M.; Johnson, D. W. Protonation Activates Anion Binding and Alters Binding Selectivity in New Inherently Fluorescent 2,6-Bis(2-Anilinoethynyl)Pyridine Bisureas. *Chem. Commun.* **2009**, 18, 2520–2522.
114. Rashdan, S.; Light, M. E.; Kilburn, J. D. Pyridyl Thioureas as Switchable Anion Receptors. *Chem. Commun.* **2006**, 3 (44), 4578–4580.
115. Phukan, N.; Baruah, J. B. Polymorphs of 1-(5-Methylthiazol-2-Yl)-3-Phenylthiourea and Various Anion-Assisted Assemblies of Two Positional Isomers. *Cryst. Growth Des.* **2014**, 14 (5), 2640–2653.
116. Jordan, L. M.; Boyle, P. D.; Sargent, A. L.; Allen, W. E. Binding of Carboxylic Acids by Fluorescent Pyridyl Ureas. *J. Org. Chem.* **2010**, 75 (24), 8450–8456.
117. Shu, X.; Fan, Y.; Li, S.; Jin, Y.; Xia, C.; Huang, C. Anion Binding and Fluoride Ion Induced Conformational Changes in Bisurea Receptors. *New J. Chem.* **2020**, 44 (5), 2033–2045.
118. Braga, D.; D'agostino, S.; D'amen, E.; Grepioni, F. Polymorphs from Supramolecular Gels: Four Crystal Forms of the Same Silver(I) Supergelator Crystallized Directly from Its Gels. *Chem. Commun.* **2011**, 47 (18), 5154–5156.

119. Li, C.; Liu, P.; Zhi, Y.; Zhai, Y.; Liu, Z.; Gao, L.; Jiang, L. Ultra-Mechanosensitive Chloride Ion Transport through Bioinspired High-Density Elastomeric Nanochannels. *J. Am. Chem. Soc.* **2023**, *145*, 19098–19106.
120. Davis, J. T.; Okunola, O.; Quesada, R. Recent Advances in the Transmembrane Transport of Anions. *Chem. Soc. Rev.* **2010**, *39* (10), 3843–3862.
121. Davis, J. T.; Gale, P. A.; Quesada, R. Advances in Anion Transport and Supramolecular Medicinal Chemistry. *Chem. Soc. Rev.* **2020**, *49* (16), 6056–6086.
122. Busschaert, N.; Caltagirone, C.; Van Rossom, W.; Gale, P. A. Applications of Supramolecular Anion Recognition. *Chem. Rev.* **2015**, *115* (15), 8038–8155.
123. Kundu, S.; Egboluche, T. K.; Hossain, M. A. Urea- and Thiourea-Based Receptors for Anion Binding. *Acc. Chem. Res.* **2023**, *56* (11), 1320–1329.
124. Amendola, V.; Esteban-Gómez, D.; Fabbrizzi, L.; Licchelli, M. What Anions Do to N-H-Containing Receptors. *Acc. Chem. Res.* **2006**, *39* (5), 343–353.
125. Gómez, D. E.; Fabbrizzi, L.; Licchelli, M.; Monzani, E. Urea vs. Thiourea in Anion Recognition. *Org. Biomol. Chem.* **2005**, *3* (8), 1495–1500.
126. Esteban-Gómez, D.; Fabbrizzi, L.; Licchelli, M. Why, on Interaction of Urea-Based Receptors with Fluoride, Beautiful Colors Develop. *J. Org. Chem.* **2005**, *70* (14), 5717–5720.
127. Gunnlaugsson, T.; Davis, A. P.; Glynn, M. Fluorescent Photoinduced Electron Transfer (PET) Sensing of Anions Using Charge Neutral Chemosensors. *Chem. Commun.* **2001**, *1* (24), 2556–2557.
128. Gunnlaugsson, T.; Kruger, P. E.; Lee, T. C.; Parkesh, R.; Pfeffer, F. M.; Hussey, G. M. Dual Responsive Chemosensors for Anions: The Combination of Fluorescent PET (Photoinduced Electron Transfer) and Colorimetric Chemosensors in a Single Molecule. *Tetrahedron Lett.* **2003**, *44* (35), 6575–6578.
129. Pfeffer, F. M.; Buschgens, A. M.; Barnett, N. W.; Gunnlaugsson, T.; Kruger, P. E. 4-Amino-1,8-Naphthalimide-Based Anion Receptors: Employing the Naphthalimide N-H Moiety in the Cooperative Binding of Dihydrogenphosphate. *Tetrahedron Lett.* **2005**, *46* (38), 6579–6584.
130. Pfeffer, F. M.; Seter, M.; Lewcenko, N.; Barnett, N. W. Fluorescent Anion Sensors Based on 4-Amino-1,8-Naphthalimide That Employ the 4-Amino N-H. *Tetrahedron Lett.* **2006**, *47* (30), 5241–5245.

131. Thiagarajan, V.; Ramamurthy, P.; Thirumalai, D.; Ramakrishnan, V. T. A Novel Colorimetric and Fluorescent Chemosensor for Anions Involving PET and ICT Pathways. *Org. Lett.* **2005**, *7* (4), 657–660.
132. Jaishankar, M.; Tseten, T.; Anbalagan, N.; Mathew, B. B.; Beeregowda, K. N. Toxicity, Mechanism and Health Effects of Some Heavy Metals. *Interdiscip. Toxicol.* **2014**, *7* (2), 60–72.
133. Rahman, F. U.; Bibi, M.; Khan, E.; Shah, A. B.; Muhammad, M.; Tahir, M. N.; Shahzad, A.; Ullah, F.; Zahoor, M.; Alamery, S.; Batiha, G. E. S. Thiourea Derivatives, Simple in Structure but Efficient Enzyme Inhibitors and Mercury Sensors. *Molecules* **2021**, *26* (15), 1–16.
134. Vonlanthen, M.; Connelly, C. M.; Deiters, A.; Linden, A.; Finney, N. S. Thiourea-Based Fluorescent Chemosensors for Aqueous Metal Ion Detection and Cellular Imaging. *J. Org. Chem.* **2014**, *79* (13), 6054–6060.
135. Zhao, Y.; Lin, Z.; He, C.; Wu, H.; Duan, C. A “Turn-on” Fluorescent Sensor for Selective Hg(II) Detection in Aqueous Media Based on Metal-Induced Dye Formation. *Inorg. Chem.* **2006**, *45* (25), 10013–10015.
136. Shiraishi, Y.; Sumiya, S.; Hirai, T. A Coumarin-Thiourea Conjugate as a Fluorescent Probe for Hg(Ii) in Aqueous Media with a Broad PH Range 2-12. *Org. Biomol. Chem.* **2010**, *8* (6), 1310–1314.
137. Tarai, A.; Baruah, J. B. Four-Coordinated See-Saw: N<sup>-</sup>(Aryl)-2-(Propan-2-Ylidene)Hydrazinecarbothioamide Complexes of Nickel(II), Copper(II) and Zinc(II) and Their Propensity for Catalytic Cyclisation. *Dalt. Trans.* **2018**, *47* (14), 4921–4930.
138. (a) Liu, K.; Kang, Y.; Wang, Z.; Zhang, X., 25th Anniversary article: reversible and adaptive functional supramolecular materials: “Noncovalent interaction”. *Matters. Adv. Mater.* **2013**, *25*, 5530 - 5548. (b) Cheng, H.; Liu, R.; Zhang, R.; Huang, L.; Yuan, Q., Recent advances in supramolecular self-assembly derived materials for high-performance supercapacitors. *Nanoscale Advances*, **2023**, *5*, 2394 - 2412. (c) Sun, P.; Qin, B., Xu, J. -F.; Zhang, X., Supramonomers for controllable supramolecular polymerization and renewable supramolecular polymeric materials. *Progress in Polymer Science*, **2022**, *124*, 101486. (d) Rest C.; Kandanelli, R.; Fernandez, G., Strategies to create hierarchical self-assembled structures *via* cooperative non-covalent interactions. *Chem. Soc. Rev.*, **2015**, *44*, 2543 - 2572. (e) Sun, J. ; Decato, D. A.; Bryantsev, V. S.; John, E. A.; Berryman, O. B., The interplay between hydrogen and halogen bonding:

- substituent effects and their role in the hydrogen bond enhanced halogen bond. *Chem. Sci.*, 2023, 14, 8924 - 8935.
139. (a) Stupp, S., Zha, R. H.; Palmer, L. C.; Cui, H.; Bitton, R., Self-assembly of biomolecular soft matter. *Faraday Discuss.*, 2013, 166, 9 - 30. (b) Yin, P.; Choi, H. M. T.; Calvert, C. R.; Pierce, N. A., Programming biomolecular self-assembly pathways. *Nature*, 2008, 451, 318 - 322.
140. (a) Lehn, J. -M. Toward complex matter: Supramolecular chemistry and self-Organization. *Proc. Natl. Acad. Sci. U. S. A.* **2002**, 99, 4763 - 4768. (b) Whitesides, G. M.; Boncheva, M. Beyond molecules: Self-assembly of mesoscopic and macroscopic Components. *Proc. Natl. Acad. Sci.* **2002**, 99, 4769 - 4774. (c) Nassimbeni, L. R. Physicochemical aspects of host-guest compounds. *Acc. Chem. Res.* **2003**, 36, 631 - 637. (d) Desiraju, G. R. Crystal engineering: from molecule to crystal. *J. Am. Chem. Soc.* **2013**, 135, 9952 - 9967. (e) Steiner, T. The Hydrogen Bond in the Solid State. *Angew. Chemie Int. Ed.* **2002**, 41, 48 - 76. (f) Desiraju, G. R. Hydrogen bridges in crystal engineering: interactions without borders. *Acc. Chem. Res.* **2002**, 35, 565 - 573.

## Chapter 2

### Self-assemblies of Solvates, Ionic-crystals and Salt of 4-[[4-(4-Nitrophenyl)-carbamoyl]amino]-N-(pyrimidin-2-yl)benzene-1-sulfonamide

#### 2.1: Introduction

As described in the introduction chapter, urea-derived molecules have wide ranges of applications. Realising such a necessity, a new host system having a urea part covalently linked to a drug component, namely a urea-derived sulfadiazine drug 4-[[4-(4-nitrophenyl)carbamoyl]amino]-N-(pyrimidin-2-yl)benzene-1-sulfonamide (**2.1**) has been designed, and its supramolecular aspects are presented in this chapter. This host molecule possesses multiple supramolecular binding sites based on the drug sulfadiazine and nitrophenyl urea units (Fig. 2.1). There is a vast literature on the self-assemblies where functional units, such as enamine, sulphonamide and urea contribute as key hydrogen bonding components.<sup>1, 2</sup> Hence, the host **2.1** has scopes to design different cocrystals and multicomponent assemblies by capitalizing on the hydrogen bonding abilities of the N=C–NH, nitrophenyl-urea and sulphonamide parts of its structural skeleton. To illustrate the supramolecular aspects of this selected host molecule, some of the probable hydrogen-bonded homomeric and heteromeric synthons originating from the host are illustrated in the A-F of Fig. 2.1. The hydrogen-bonded synthons of imine or amine forms or from different types of urea-O=X (X = C, S etc.) interactions differ by very small energies.<sup>3,4</sup> Notably, solvates of sulfadiazine exist in either amine or imine form, a phenomenon extensively explored in literature,<sup>5-8</sup> and their formation in a particular form was guided by environment and crystallisation conditions. Hence, the formation or availability of any of such synthons within an assembly would be controlled by subtle effects originating from electronic, steric and environmental factors. Hence, the solvent used for crystallization, crystallization conditions, nature of a guest molecule, and effect of functional groups will be reflected in non-covalent assemblies of the host. The compound **2.1** also features an intervening –SO<sub>2</sub>– group that would have a control on the overall geometry of this host molecule within a self-assembly.

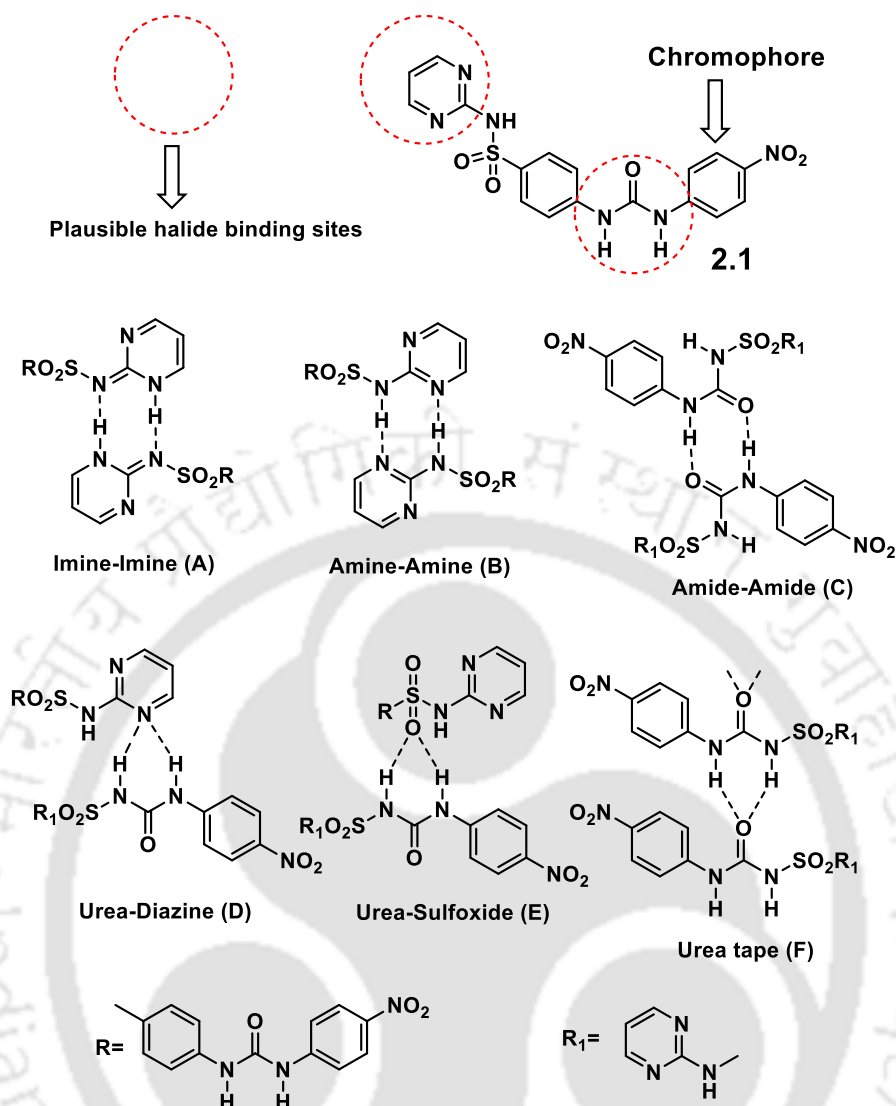


**Figure 2.1:** Structure of **2.1**, some hydrogen-bonded synthons (A-F).

Having the 4-nitrophenyl chromophore in the compound would not only influence the weak interactions but also provide a means to study the changes in absorptions resulting from a recognition of a substrate by the host. The formation of complementary hydrogen bonds or selective deprotonation of the N–H bond of the urea (E) moiety would influence the electronic levels of the 4-nitrophenyl urea group to cause a signal transduction. On the other hand, it is imperative to gain a comprehensive understanding of the several aspects stemming from the interactions between ionic organic compounds to prepare ionic cocrystals. For example, cocrystals of the host with ionic organic salt such as tetraalkylammonium halides would provide avenues to investigate: (a) ionic cocrystals, (b) systematic structural aspects on halide urea interactions, (c) assembling pattern of a series of structures of ionic cocrystals, (d) the physiochemical properties and reactivity of the ionic cocrystals, and (e) design aspects of

crystal engineering for broader ramifications in drug design. Keeping these points in mind, a systematic study on **2.1** is presented.

## 2.2: Synthesis and characterization of the DMF solvates **2.1.1** and **2.1.2**

The sulfadiazine-urea derivative **2.1** was synthesized through a condensation reaction involving 4-nitrophenyl isocyanate and sulfadiazine. The crystallization of a solution of the compound in dimethyl formamide (DMF) at room temperature resulted in the formation of the 1:1 DMF solvate, denoted as **2.1.1**. When the solution of the compound in DMF was heated at 80 °C and followed by a slow evaporation at room temperature, yielded crystals of a 1:2 solvate with DMF, it is designated as **2.1.2**. The characterization of the solvated and unsolvated forms of the compound was carried out by different spectroscopic methods, including  $^1\text{H}$ NMR, infrared spectroscopy, as well as by single-crystal X-ray structure determination and powder-X-ray diffraction technique.

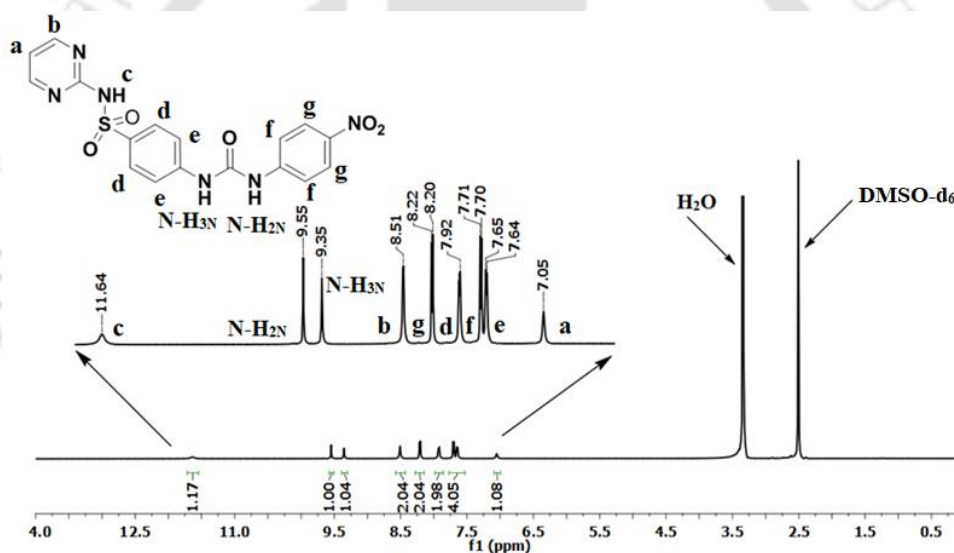


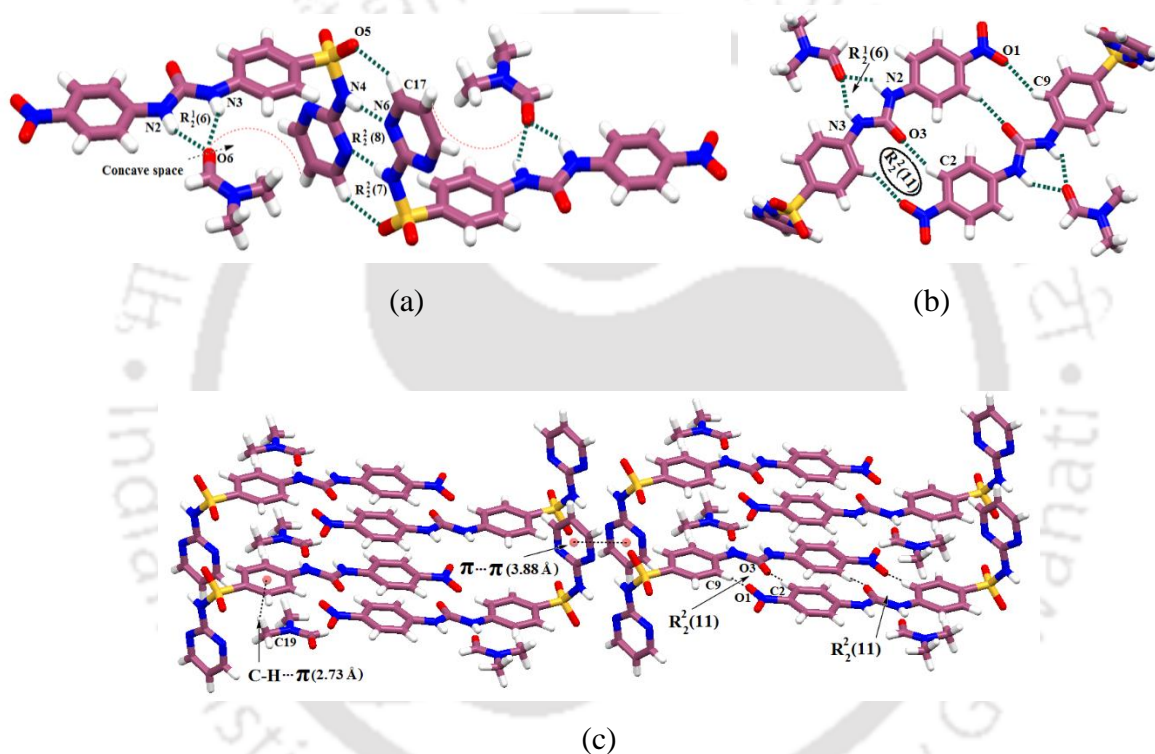
**Figure 2.2:**  $^1\text{H}$ NMR (600 MHz,  $\text{DMSO-d}_6$ ) spectra of the host **2.1**.

The  $^1\text{H}$ NMR spectra of **2.1** is shown in Fig. 2.2. The compound showed the aromatic peaks designated as *d* and *e* at 7.92 and 7.65 ppm, respectively, whereas the proton *f* and *g* appeared at 7.92 and 8.20-8.22 ppm, respectively. The peak labelled as *a* and *b* appeared at 7.05 and 8.51 ppm. The chemical shifts of the two protons of the urea portion of the **2.1** were observed at 9.55 and 9.35 ppm. The N-H of the diazine part appeared at 11.64 ppm. On the other hand, the  $^1\text{H}$ NMR spectra of the two solvates (**2.1.1** and **2.1.2**), exhibited those peaks but showed additional peaks for the DMF solvent molecules of crystallization each with appropriate integration. The integrations of the NMR signals corresponding to DMF protons indicated them to identify as the 1:1 or 1: 2 solvate of DMF (Fig A2.2 and Fig. A2.4). In the solvates

the N-methyl groups displayed signals at 2.89 and 2.73 ppm in both the solvates, while the C–H groups of the DMF molecule was observed at 7.95 ppm.

### 2.3: Structural descriptions of the two solvates 2.1.1 and 2.1.2

The structures of both the solvates were determined by single-crystal X-ray diffraction analysis. The crystals of the **2.1.1** belonged to the triclinic  $P\bar{1}$  space group with  $Z = 2$ . In the structure, it was found that each **2.1** was bound to the DMF molecule through the hydrogen bonds involving the N–H bonds of the urea portion of the molecule. The self-assembly of this solvate had hydrogen-bonded homo-dimeric amine-amine synthons of the type shown as A of Fig. 2.1a.

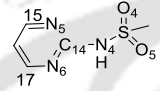


**Figure 2.3:** (a) Hydrogen bonds homodimers between the diazine rings found from the crystal structure of **2.1.1**, (b) dimers through C–H...O interactions and (c)  $\pi$ -stacking facilitating formation of layers in the self-assembly of **2.1.1**.

The hydrogen-bonded homodimers were formed by two N4–H...N6 hydrogen bonds ( $d_{D...A}$ , 2.918 Å;  $\angle D-H...A$ , 174°), represented by  $R_2^2(8)$  graph set notation<sup>9-10</sup> (Fig. 2.3a). The self-assembly of the solvate also involves intermolecular C–H...O interactions, wherein an oxygen atom of the nitro group interacted with a C–H bond of the nitrophenyl ring belonging to another host molecule (Fig. 2.3b). This interaction served as supportive hydrogen bonds to stabilise the homodimers formed by a diazine–diazine homo-synthon. It also locks the free spatial change of the rest part of the molecule. In order to ascertain imine or amine form of

the diazine-sulphonamide part present in the host molecules in the assembly of the **2.1.1**, different C-N bond parameters of the diazine part were examined and these are listed in Table 2.1. It was found that the C14-N4 bond distance in **2.1.1** was 1.375(4) Å, and this distance in **2.1.2** was 1.375(4) Å, whereas respective C14-N5 bond distances were 1.322(4) Å and 1.319(5) Å. These bond distances fit for sp<sup>2</sup>-sp<sup>2</sup> bonds and suggested a delocalised state of amine and imine forms in the ring.

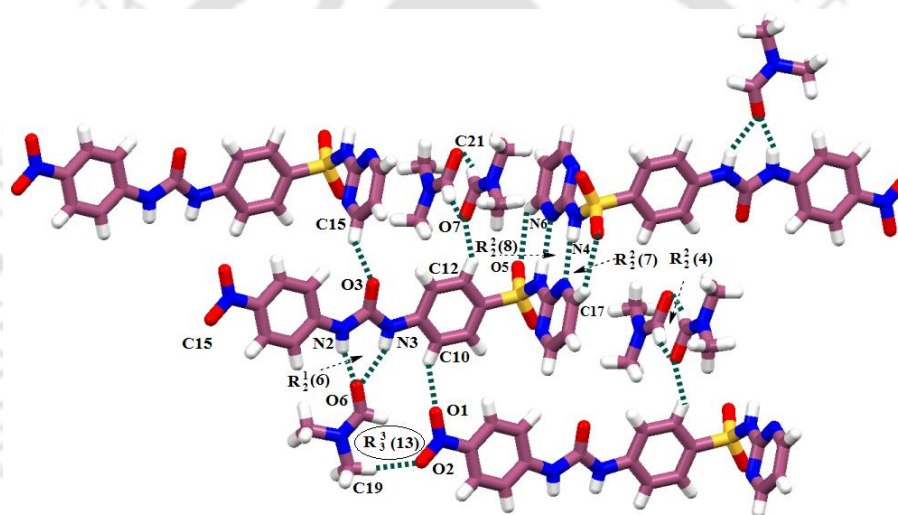
**Table 2.1:** Selected bond and contact distances involving the diazine part of the two DMF solvates of **2.1**

Bonds	Bond – distance (Å)	Bond – distance (Å)
	<b>2.1.2</b> <b>(1:2)</b>	<b>2.1.1</b> <b>(1:1)</b>
S <sub>1</sub> -O <sub>4</sub>	1.423(2)	1.424(3)
S <sub>1</sub> -O <sub>5</sub>	1.431(3)	1.439(3)
S <sub>1</sub> -N <sub>4</sub>	1.636(3)	1.644(4)
N <sub>4</sub> -C <sub>14</sub>	1.375(4)	1.383(5)
N <sub>5</sub> -C <sub>15</sub>	1.326(5)	1.333(5)
N <sub>5</sub> -C <sub>14</sub>	1.322(4)	1.319(5)
N <sub>6</sub> -C <sub>14</sub>	1.329(3)	1.347(5)
N <sub>6</sub> -C <sub>17</sub>	1.323(6)	1.335(5)
N <sub>5</sub> ...O <sub>4</sub>	3.018	3.011

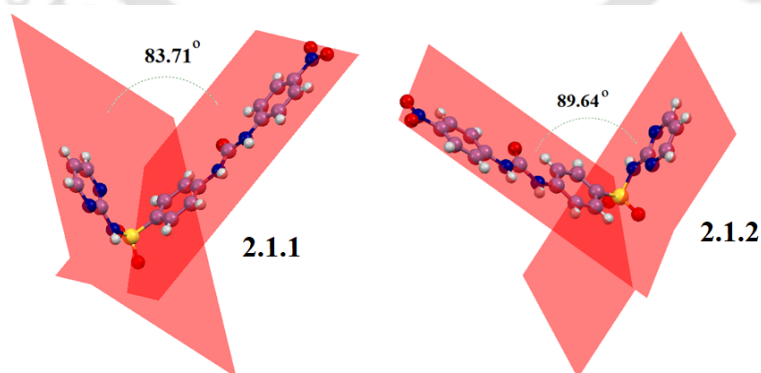
Thus, two different types of homo-dimeric synthons, as illustrated in Fig. 2.3a and 2.3b, contributed to the overall self-assembly of **2.1**. As from the free-riding model in X-ray crystallography, we could locate the hydrogen atom on the N-H next to the S atom; the amine form of the host was observed and accordingly the homo-dimeric synthon is best described as an amine-amine synthon. This synthon was strengthened by the presence of another weak but supportive C17-H...O (d<sub>D...A</sub>, 3.278 Å; ∠D-H...A, 134°) hydrogen bond involving O5 of the SO<sub>2</sub> group. Four hydrogen bonds, involving both the diazine and SO<sub>2</sub> group contributed to the homodimer. The C17-H...O5 hydrogen bond, in conjunction with the N4-H...N6 hydrogen bond, constituted another cyclic synthon characterized by a R<sub>2</sub><sup>2</sup>(7) graph set notation. As a consequence of the C17-H...O5 hydrogen bond, the locking of the orientation of the diazine moiety in a fixed direction occurred. The locked orientation provided an angular shape to the parent molecule and generated a concave hydrophobic space within the self-assembly. The dimethyl formamide molecules were accommodated in these concave spaces created as interstitial spaces.

The oxygen atom of the dimethyl formamide molecule of **2.1.1** participated in conventional bifurcated hydrogen bonds with the two N-H bonds of the 4-nitrophenylurea moiety. This hydrogen-bonded synthon was characterized as a R<sub>2</sub><sup>1</sup>(6) graph set notation. The conventional

urea tapes, arising from the hydrogen bond interaction of C=O with the N–H bonds of neighboring urea molecules, are commonly encountered in literature,<sup>11-12</sup> But in the present solvate these tapes were not evident. The formation of hydrogen bonds between the urea and DMF molecules had blocked the hydrogen-bonding sites of the urea moiety, otherwise which would have been essential to form urea tapes. The hydrogen bonds C2–H···O3 ( $d_{D...A}$ , 3.35 Å;  $\angle D-H...A$ , 151°) and C9–H···O1 ( $d_{D...A}$ , 3.31 Å;  $\angle D-H...A$ , 136°), along with weak C–H··· $\pi$  ( $d_{H...A}$ , 2.73 Å) and  $\pi... \pi$  (3.88 Å) interactions (Fig. 2.3c), played roles to control the geometry of the host and provided additional support to the primary synthon. These weak C–H···O interactions within this solvate contributed to the locking of the spatial orientation of the diazine ring, providing extra support to the diazine-diazine  $R_2^2(8)$  synthon. Furthermore, the  $\pi... \pi$  interactions contributed to the formation of a layer-like structure.



(a)



(b)

**Figure 2.4** (a) Homodimers in the self-assembly of the solvate **2.1.2**. (b) Angles between the planes containing diazines with the planes containing the rest of the host of **2.1.1** and **2.1.2**, respectively.

The crystals of the other solvate, namely **2.1.2**, belonged to the  $P\bar{1}$  space group with  $Z = 2$ . This solvate exhibited a higher unit-cell volume but lower crystal density in comparison to the 1:1 solvate. From the bond distances and bond angles among the constituent atoms of the diazine ring in the solvate, it was found that the host molecule of this solvate also had amine form. It was found that C14-N4 bond in the **2.1.2**, was 1.375(4); whereas, C14-N5 was 1.319(5) Å. The prominent hydrogen bond parameters of both solvates are listed in Table 2.2.

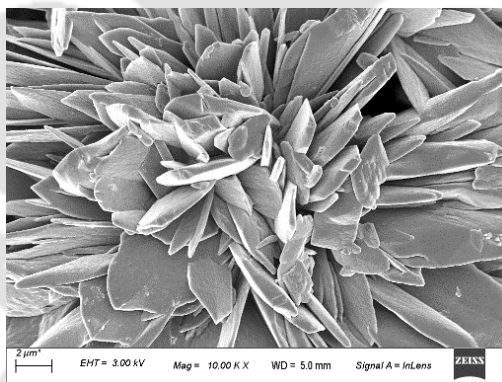
**Table 2.2:** Hydrogen bond parameters of the solvates (**2.1.1** and **2.1.2**)

Solvate	D-H...A	d <sub>D-H</sub> (Å)	d <sub>H...A</sub> (Å)	d <sub>D...A</sub> (Å)	∠D-H...A (°)
<b>2.1.1</b>	N(2)-H(2N) ...O(6) [-1+x, y, z]	1.00(5)	1.97(5)	2.857(6)	147(4)
	N(3)-H(3N) ...O(6) [-1+x, y, z]	0.84(4)	2.12(4)	2.879(5)	151(4)
	N(4)-H(4N) ...N(6) [2-x, 1-y, 1-z]	0.87(4)	2.05(4)	2.918(5)	174(5)
	C(2)-H(2) ...O(3) [2-x, 1-y, 1-z]	0.99(5)	2.46(5)	3.359(6)	151(4)
	C(17)-H(17) ...O(5) [2-x, 1-y, -z]	0.93	2.56	3.278(6)	134
	C(19)-H(19B) ...O(5) [x, 1+y, z]	0.96	2.44	3.367(5)	164
	C(20)-H(20) ...O(2) [1-x, 2-y, 1-z]	0.93	2.44	3.329(6)	159
<b>2.1.2</b>	N(2)-H(2N) ...O(6) [1-x, 1-y, 1-z]	0.83(3)	2.08(3)	2.859(4)	156(3)
	N(3)-H(3N) ...O(6) [1-x, 1-y, 1-z]	0.80(3)	2.08(3)	2.837(3)	158(3)
	N(4)-H(4N) ...N(6) [1-x, 2-y, -z]	0.83(3)	2.08(3)	2.906(4)	177.5(12)
	C(10)-H(10) ...O(1) [-1+x, 1+y, z]	0.93	2.53	3.341(4)	146
	C(12)-H(12) ...O(7) [1-x, 1-y, -z]	0.93	2.51	3.275(6)	140
	C(15)-H(15) ...O(3) [x, 1+y, z]	0.93	2.43	3.179(4)	138
	C(17)-H(17) ...O(5) [1-x, 2-y, 1-z]	0.93	2.56	3.283(4)	135
	C(19)-H(19A) ...O(2) [2-x, -y, 1-z]	0.96	2.50	3.415(5)	160

Similar to the 1:1 solvate, the **2.1.2** solvate also displayed diazine-diazine homo-dimeric synthons (Fig. 2.4a). In this solvate, a DMF molecule was anchored to the urea moiety through N-H...O bifurcated hydrogen bonds, and other DMF molecules occupied the available spaces between these dimers, as illustrated in Fig. 2.4a. The anchoring of these DMF molecules within the lattice was achieved through C-H...O interactions hence it was an interstitial DMF molecule. Notably, the interstitial DMF molecules were observed in pairs, with each pair being held together by C-H...O interactions. The geometry of the host molecules of **2.1.1** and **2.1.2** apparently look similar. However, a careful look at the geometries revealed that there was a slight difference in the orientation of the individual host molecules in the two solvates. It was evident in the interplanar angle between the plane containing the diazine and the plane containing the other part of each molecule. Specifically,

this angle was  $83.71^\circ$  in the 1:1 solvate, while it was  $89.64^\circ$  in the 1:2 solvate (Fig. 2.4b). Powder X-ray diffraction analyses of the solvates validated the purity in each case as a single phase. As the **2.1** was crystallized as DMF solvate, there was an interest to generate solvent free crystals by desolvating the solvated forms. It was not possible to obtain crystals suitable for a single-crystal structure determination of the de-solvated form of **2.1**.

From the crystallographic information file, it was determined that the unit cell volume of **2.1.2** was  $1376.67 \text{ \AA}^3$ , and the crystal density was  $1.352 \text{ g/cm}^3$ . In comparison, these values for **2.1.1** were  $1117.40 \text{ \AA}^3$  and  $1.449 \text{ g/cm}^3$ , respectively. Therefore, the solvate containing interstitial DMF of crystallization exhibited a less densely packed structure. To further analyze the samples, scanning electron microscopic images were examined, as depicted in Fig. 2.5a–25c. The de-solvated form displayed needle-shaped structures with floral arrangements, whereas the 1:1 solvate exhibited floral arrangements of plate-like structures. The 1:2 solvate displayed an agglomerated arrangement, indicating a reduction in the particle sizes. These images revealed morphological distinctions among the solvates, and the de-solvated form was there, however the de-solvated sample morphologies have some resemblances to that of the solvate that was prepared by heating solution in DMF.



(a)



**Figure 2.5:** (a) – (c) Scanning electron microscopic images of **2.1**, **2.1.1**, **2.1.2** respectively

#### 2.4: Synthesis and characterization of ionic-cocrystal

The observation of having different geometries of the host in the 1:1 solvate and the 1:2 solvate had significance, as the dimeric assemblies in both cases exhibited similarity yet showed differences in compositions. In the latter case, the stretched structure of the host provided spaces between the homomeric units to accommodate the second solvent molecules. The distinction was crucial as it helped us to design isostructural ionic cocrystals with tetrabutylammonium halides. The design is based on the fact that the urea part will have an affinity for the halide ion of an organic salt to form an ionic cocrystal. Where the cationic counterpart of the halide may be accommodated in the interstitial near the homodimers. Such inclusion of ionic salt by **2.1** will involve minimal alterations of the structural arrangements as

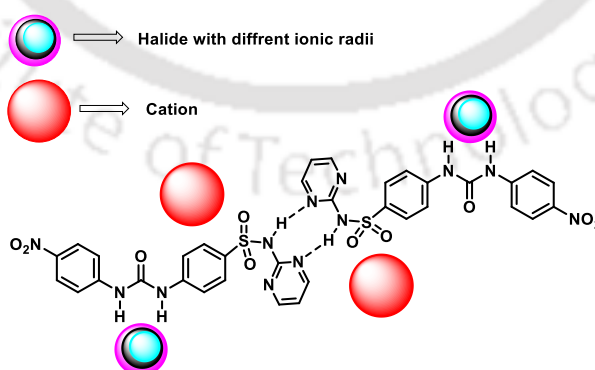
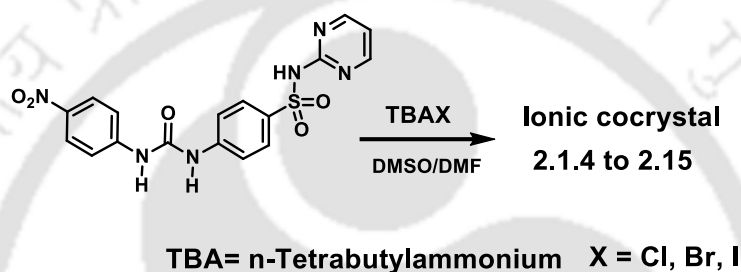


**Figure 2.6:** A schematic diagram showing predesign ionic cocrystal of **2.1** with tetra butyl ammonium halides.

as illustrated in Fig. 2.6. The halide ions being spherical are with similar supramolecular features. So, alteration of hydrogen bonds will be nominal to form the self-assemblies with salts having the same cation but the anions from a series of anions (Cl, Br, I). Based on these arguments, the three isostructural ionic cocrystals of **2.1** with tetrabutylammonium halide (halide = Chloride, bromide and iodide) denoted as **2.1.3-2.1.5** could be prepared and those were structurally characterized. The ionic cocrystals of **2.1** (**2.1.3**, **2.1.4** and **2.1.5**) were individually obtained by crystallization from respective solution of the two components in mixed solvents of DMSO/DMF. All three ionic cocrystals were obtained from crystallisation from a solution prepared by dissolving **2.1.1** together with five equivalents of the corresponding tetrabutylammonium halide.



**Scheme 2.2:** Formation of ionic co-crystals

The resulting solution in each case was stirred for 5 minutes at room temperature. Subsequently, the mixture from each case was filtered, and the filtrate was left for crystallization under undisturbed conditions in open air. After standing for 4–5 days, the crystals were collected and characterized through IR, NMR, PXRD, and single-crystal XRD analyses.

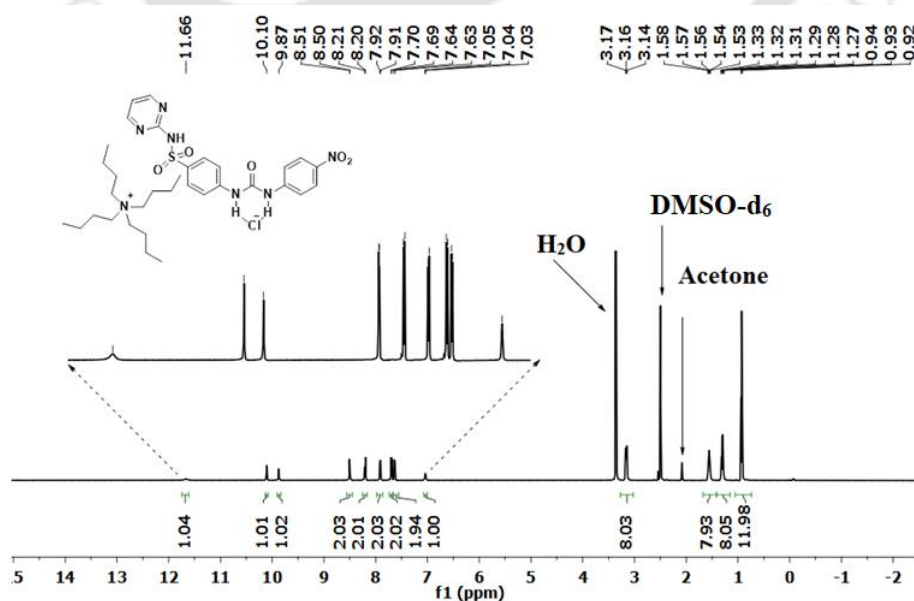


**Figure 2.7:**  $^1\text{H}$ NMR (600 MHz,  $\text{DMSO-d}_6$ ) spectra of the **2.1.3**

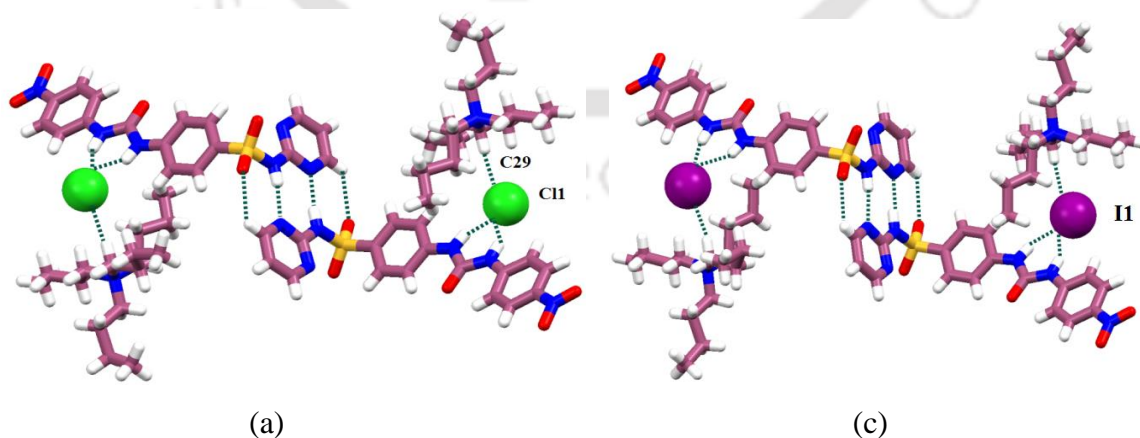
The  $^1\text{H}$ NMR spectrum of the ionic cocrystal **2.13** is presented in Fig. 2.6. The proton signal of the  $\text{CH}_3$  group of TBA group exhibited a triplet with a peak at 0.93 ppm. Among the three  $\text{CH}_2$  groups of the TBA group, one appeared as a triplet and the other two as quintet and sextet, with chemical shifts at 3.16, 1.56, and 1.31 ppm, respectively. The signal arising from the N-H of urea at 10.10 and 9.87 ppm was observed. The  $^{13}\text{C}$ -NMR spectrum of **2.13** is given in Fig A2.7. The carbonyl carbon of the urea group appeared at 152.31 ppm, and the four carbons of the TBA group appeared at 57.95, 23.51, 19.67 and 13.97 ppm, respectively.

### 2.5: Structural descriptions of ionic cocrystals 2.1.3-2.1.5

The crystal of each ionic co-crystal belonged to the  $P2_1/c$  space group. For the ionic cocrystal **2.1.3**, the crystal volume and density were  $3842.2(15) \text{ \AA}^3$  and  $1.197 \text{ g/cm}^3$ , respectively. The corresponding values for the other two ionic cocrystals were  $3872.4(5) \text{ \AA}^3$ ,  $1.264 \text{ g/cm}^3$  and  $3976.0(12) \text{ \AA}^3$ ,  $1.308 \text{ g/cm}^3$ , respectively. The similarity index ( $\pi$ ) of the unit cells is general and used to judge the isomorphous relations. It is calculated based on the formula given in Equation 1.

$$\pi = \left| \frac{a+b+c}{a'+b'+c'} - 1 \right| \dots \text{Equation 1}$$

where  $a$ ,  $b$ , and  $c$  and  $a'$ ,  $b'$ , and  $c'$  are the orthogonalized lattice parameters of the two crystals under consideration.<sup>13</sup> The calculated similarity indexes for the unit cells of chloride and bromide salts, chloride and iodide salts, and bromide and iodide salts were 0.012, 0.009, and 0.005, respectively. The value of  $\pi$  close to zero signifies the highest similarity among them. The crystal structures of **2.1.3-2.1.5** in Fig. 2.8a–2.8c.



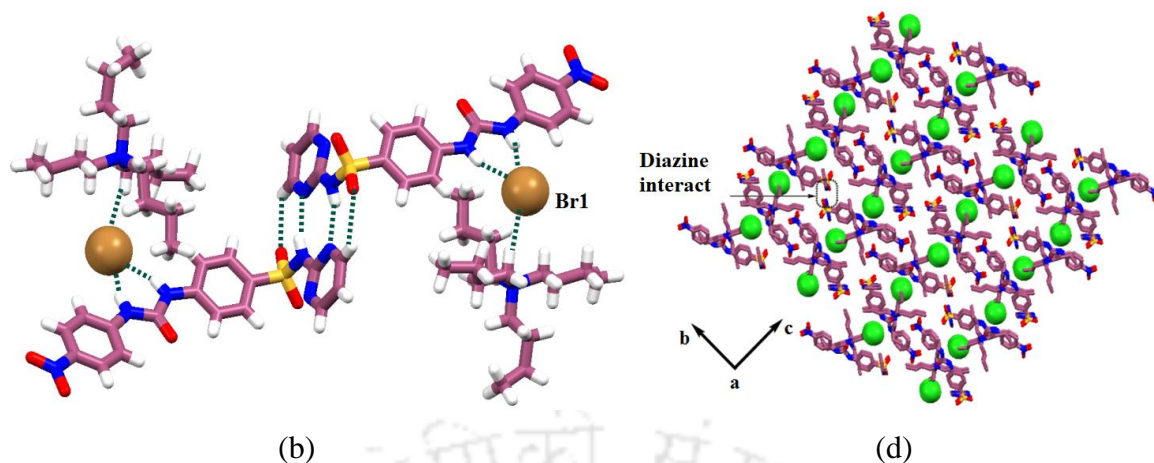


**Figure 2.8.** Hydrogen-bonded dimeric assemblies of the ionic cocrystals (a) **2.1.3**, (b) **2.1.4** and (c) **2.1.5**, and (d) packing pattern of **2.1.3**.

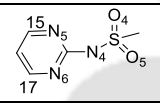
The presence of chloride, bromide, and iodide ions in these ionic cocrystals did not alter the diazine–diazine synthon of the host. In each self-assembly, homo-dimeric  $R_2^2(8)$  and  $R_2^2(7)$  synthons, similar to those observed in the DMF cocrystal of **2.1**, were retained. The urea moiety in each case formed hydrogen bonds with the respective halide ions through bifurcated hydrogen bonds. This interaction involved the two N–H bonds of the urea moiety and the halides, resulting in a  $R_2^1(6)$  synthon. Additionally, a C–H $\cdots$ X hydrogen bond was observed, involving a C–H bond of the tetrabutylammonium cation. The hydrogen-bond distances and angles within the assemblies are detailed in Table 2.3.

**Table 2.3:** Hydrogen bond parameters of ionic cocrystals (**2.1.3–2.1.5**)

Ionic cocrystal	D–H $\cdots$ A	$d_{D-H}$ (Å)	$d_{H\cdots A}$ (Å)	$d_{D\cdots A}$ (Å)	$\angle D-H\cdots A$ (°)
<b>2.1.3</b>	N(2)–H(2N) $\cdots$ Cl(1) $[-1/2+x, 1/2-y, 1/2+z]$	0.86	2.28	3.112(5)	162
	N(3)–H(3N) $\cdots$ Cl(1) $[-1/2+x, 1/2-y, 1/2+z]$	0.86	2.39	3.207(5)	159
	N(4)–H(4N) $\cdots$ N(6) $[1-x, -y, 1-z]$	0.86	2.03	2.885(7)	172
	C(17)–H(17) $\cdots$ O(5) $[1+x, y, z]$	0.93	2.56	3.417(8)	153
	C(22)–H(22A) $\cdots$ O(1) $[1-x, 1-y, 1-z]$	0.97	2.46	3.407(11)	166
	C(29)–H(29A) $\cdots$ O(3) $[x, y, z]$	0.97	2.38	3.321(8)	164
	C(29)–H(29B) $\cdots$ Cl(1) $[x, y, z]$	0.97	2.78	3.748(7)	171
<b>2.1.4</b>	N(2)–H(2N) $\cdots$ Br(1) $[1/2+x, 1/2-y, -1/2+z]$	0.86	2.43	3.267(5)	164
	N(3)–H(3N) $\cdots$ Br(1) $[1/2+x, 1/2-y, -1/2+z]$	0.86	2.56	3.374(5)	159
	N(4)–H(4N) $\cdots$ N(6) $[-x, 1-y, -z]$	0.77(5)	2.19(5)	2.900(7)	154(5)
	C(22)–H(22B) $\cdots$ O(1) $[1-x, -y, -z]$	0.97	2.45	3.392(11)	165
	C(29)–H(29A) $\cdots$ Br(1) $[1+x, y, z]$	0.97	2.86	3.813(7)	168
	C(29)–H(29B) $\cdots$ O(3) $[1+x, y, z]$	0.97	2.41	3.346(8)	161
	<b>2.1.5</b>	N(2)–H(2N) $\cdots$ I(1) $[-1/2+x, 1/2-y, 1/2+z]$	0.86	2.64	3.485(7)
N(3)–H(3N) $\cdots$ I(1) $[-1/2+x, 1/2-y, 1/2+z]$		0.86	2.81	3.633(7)	160
N(4)–H(4N) $\cdots$ N(6) $[1-x, -y, 1-z]$		0.92(5)	2.00(5)	2.910(10)	171(5)
C(22)–H(22A) $\cdots$ O(1) $[1-x, 1-y, 1-z]$		0.97	2.49	3.427(15)	162
C(29)–H(29A) $\cdots$ I(1) $[x, y, z]$		0.97	3.02	3.971(9)	167
C(29)–H(29B) $\cdots$ O(11) $[x, y, z]$		0.97	2.46	3.356(11)	154

In this investigation on the structures of the ionic co-crystal, particularly to determine the prevalence of the amine or imine form in the diazine-sulphonamide segment, a detailed analysis of the C-N bond distances in the diazine portion was conducted, as outlined in Table 2.4. The study revealed that for the ionic co-crystals labelled as **2.1.3**, **2.1.4**, and **2.1.5**, the C14-N4 bond lengths were respectively 1.391(7) Å, 1.405(6) Å, and 1.383(8) Å, while the C14-N5 bonds were 1.333(5) Å, 1.313(7) Å, and 1.320(9) Å. In the case of the TBA salt **2.1.6**, the C14-N4 and C14-N5 bonds measured 1.371(6) Å and 1.342(5) Å, respectively. Across all these structures, the C14-N4 bond consistently exhibited a longer distance than the C14-N5 bond, suggesting the dominant formation of the amine form. This contrasts with the expected shorter C14-N4 bond length in the imine form. Additionally, salt **2.1.6** displayed a unique trend where the C14-N4 bond was shorter, and the C14-N5 bond was longer compared to those in the ionic co-crystals, likely due to the introduction of a negative charge on the N4 atom.

**Table 2.4:** Selected bond and contact distances involving the diazine part of the **2.1** in the ionic cocrystals and salt.

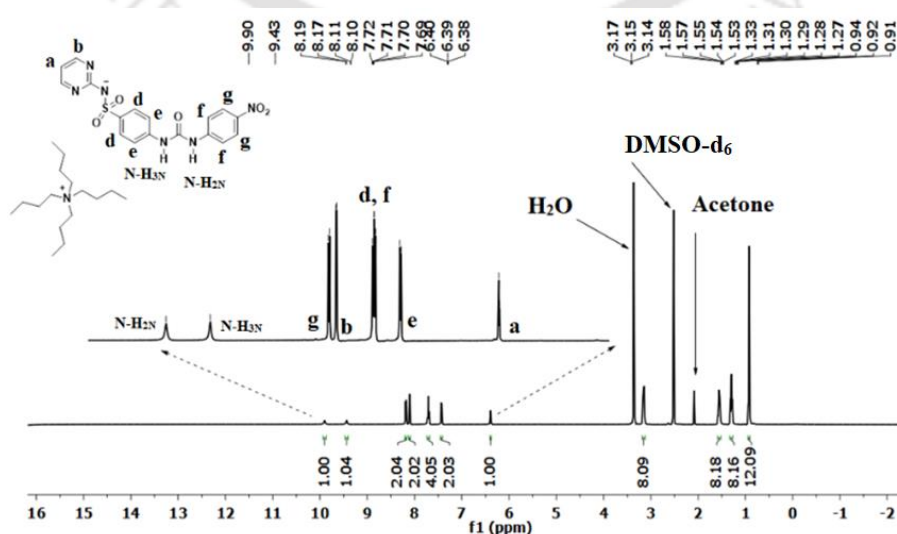
Bond	Bond – distance (Å)	Bond –distance (Å)		
		Cocrystal of <b>2.1</b> with tetrabutylammonium		
	TBA salt ( <b>2.1.6</b> )	Chloride ( <b>2.1.3</b> )	Bromide ( <b>2.1.4</b> )	Iodide ( <b>2.1.5</b> )
		S <sub>1</sub> -O <sub>4</sub>	1.439(3)	1.420(4)
S <sub>1</sub> -O <sub>5</sub>	1.453(3)	1.438(4)	1.431(4)	1.435(5)
S <sub>1</sub> -N <sub>4</sub>	1.587(4)	1.642(5)	1.631(5)	1.646(6)
N <sub>4</sub> -C <sub>14</sub>	1.371(6)	1.391(7)	1.405(6)	1.383(8)
N <sub>5</sub> -C <sub>15</sub>	1.329(7)	1.335(7)	1.339(7)	1.328(9)
N <sub>5</sub> -C <sub>14</sub>	1.342(5)	1.333(7)	1.313(7)	1.371
N <sub>6</sub> -C <sub>14</sub>	1.339(6)	1.328(7)	1.312(6)	1.341(8)
N <sub>6</sub> -C <sub>17</sub>	1.330(6)	1.339(7)	1.327(7)	1.345(9)
N <sub>5</sub> ---O <sub>4</sub>	2.962	2.916	2.925	2.917

The hydrogen bond angles, particularly those involving the halide as the central ion, exhibited a distorted Y shape. It may be noted that, depending on the hydrogen bond donors and the shapes of the receptors, a halide ion may adopt various anion coordination geometries. Among these geometries, a T shape has been commonly observed in literature.<sup>14-17</sup> The Y shape represents a deformed T-shaped geometry.<sup>18</sup> There are also examples of four coordinated hydrogen-bond environments for halide ions, characterized by the presence of four N-H···halide hydrogen bonds.<sup>19-20</sup> Certain halide-bound self-assemblies have been recognized as anion carriers.<sup>21-22</sup> In the three crystal structures of the ionic cocrystals, weak C29-H···halide interactions, along with N-H···halide hydrogen bonds, were common interactions. The hydrogen bond (N-H···X) distances  $d(D\cdots A)$ ,  $d(D-H\cdots A)$ , and bond

angles ( $\angle D-H\cdots A$ ) were observed within the ranges of 3.11–3.63 Å, 2.28–2.81 Å, and 159–167°, respectively. For a given donor, the trends in the difference in the D–H $\cdots$ X distances were 0.15 Å from chloride to bromide and 0.25 Å from bromide to iodide acceptors.<sup>15</sup> In comparing the D $\cdots$ A bonds of the two bifurcated N–H $\cdots$ X hydrogen bonds, it was observed that for chloride and bromide, the N $\cdots$ X bond differed by approximately 0.16 and 0.17 Å, respectively. On the other hand, for the bromide and iodide salts, the N $\cdots$ X bond differed by approximately 0.22 and 0.26 Å, respectively. These obvious distinctions in the bond parameters arise due to variances in the ionic radii of the three halides. In the ionic cocrystals involving tetrabutylammonium halides and urea<sup>23–25</sup> and insights from previous investigations on ionic cocrystals with oximes emphasize one of the requirements to form such cocrystals is the availability of hydrophobic space to accommodate the cation within the respective assembly.<sup>26–27</sup> In the current scenario, the hydrophobic arms of the tetrabutylammonium cation are situated within the hydrophobic concave region. This arrangement is facilitated by the geometrically adjustable angular-shaped host in the assembly, stabilized by the C29–H $\cdots$ O interactions.

## 2.6: Synthesis and characterization of the TBA salt 2.1.6

The crystalline tetrabutylammonium salt of **2.1** was synthesized by reacting **2.1** with one equivalent of tetrabutylammonium fluoride hydrate in DMF. Crystallization occurred from an undisturbed solution under ambient conditions, providing off-white crystals. These crystals were subsequently collected through decantation of the solution and subjected to comprehensive characterization using analytical methods such as <sup>1</sup>HNMR, IR, PXRD, and SC-XRD. The formation of the salt involved the deprotonation of the N–H proton adjacent to the diazine ring by tetrabutylammonium fluoride.



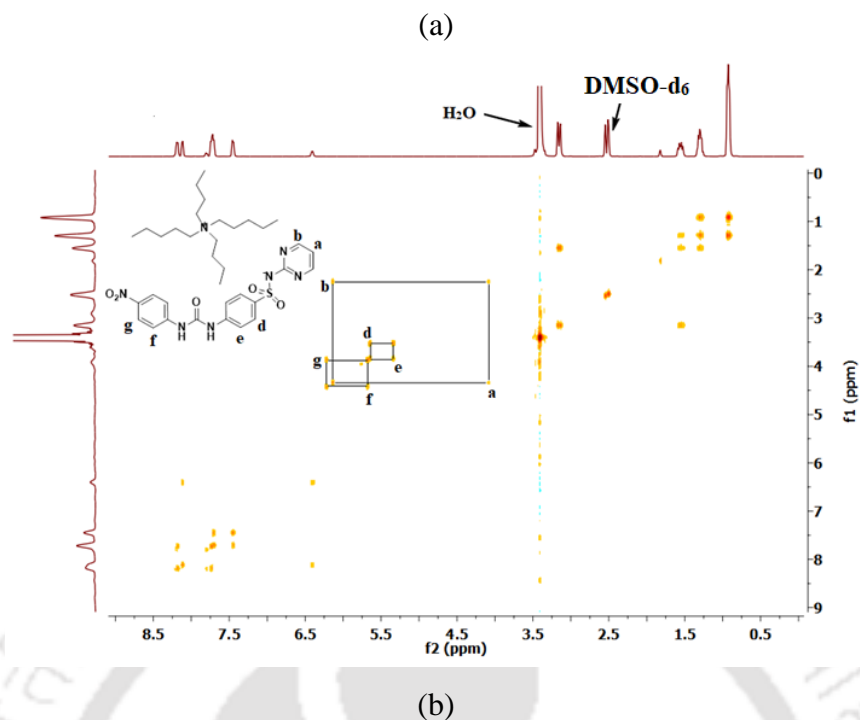


**Figure 2.9:** (a) <sup>1</sup>H NMR and (b) <sup>1</sup>H 2D-HOMOCOSY (600MHz, DMSO-d<sub>6</sub>) spectra of the TBA salt **2.1.6**

The <sup>1</sup>H NMR spectral analysis of TBA salt is showcased in Fig. 2.9a, reveals significant chemical shifts. The assignment of each peak and the coupling was confirmed through 2D-HOMOCOSY NMR spectra, as shown in Fig. 2.9b. The urea-derived N-H protons are observed at chemical shifts of 9.90 and 9.43 ppm. The spectrum lacks a peak for the N-H proton of the diazine group, signifying its deprotonation. This spectral feature confirms the development of a negative charge on the N4 nitrogen atom, resulting in pronounced shielding effects on the protons of the diazine ring relative to the original ligand. Additionally, the aromatic protons labelled as *b* and *a* exhibited more shielding in comparison to their positions in the parent ligand **2.1**, where they resonated at 8.10 ppm and 6.39 ppm, respectively, shifting to 8.51 ppm and 7.04 ppm in the TBA salt. Moreover, the aromatic protons designated as *d* and *f*, which usually appear as distinct doublets, converge into a single triplet peak with a chemical shift positioned at 7.71 ppm in the salt.

### 2.7: Structure of TBA salt 2.1.6

The crystals of the TBA salt of **2.1** were from the monoclinic  $P2_1/c$  space group ( $Z = 4$ ). The crystal volume and crystal density of **2.1.6** were 3976.0(12) Å<sup>3</sup> and 1.308 g/cm<sup>3</sup> respectively. The asymmetric unit of the compound comprises a tetrabutylammonium cation and an anion of **2.1**, depicted in Fig. 2.10a. Notably, the negatively charged N4 site of the diazine moiety

engaged in a bifurcated hydrogen-bond scheme with the urea moiety, as illustrated in Fig. 2.10b.

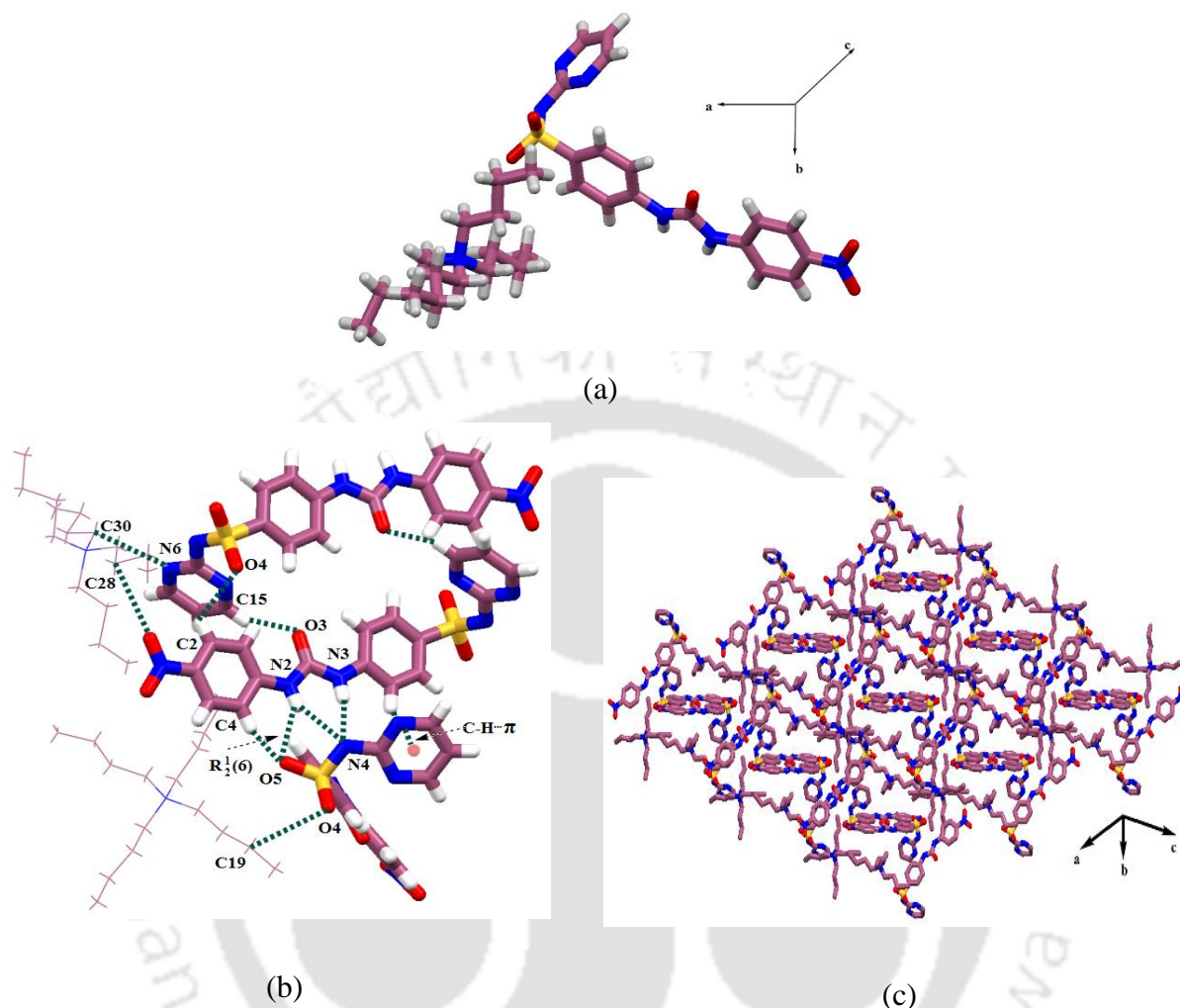


**Figure 2.10:** (a) Asymmetric unit of **2.1.6** (b) prominent hydrogen bonds and C–H $\cdots$  $\pi$  interactions in the self-assembly and (c) a packing diagram of **2.1.6**

The self-assembly exhibited bifurcated hydrogen bonds, namely N2–H $\cdots$ N4 and N3–H $\cdots$ N4, characterized by  $d_{D\cdots A}$  values of 3.275 Å and 3.059 Å, and angles  $\angle D-H\cdots A$  measuring 153° and 169°, respectively. These hydrogen bonds contributed to the formation of  $R_2^1(6)$  synthons within the self-assembly. Additionally, the O5 atom of the –SO<sub>2</sub>– group participated in N2–H $\cdots$ O5 and C4–H $\cdots$ N5 hydrogen bonds, resulting in a  $R_2^1(6)$  synthon. The adjacent urea moieties within the assembly were oriented in opposite directions within the same plane and connected through weak hydrogen bonds (C2–H $\cdots$ O4 with  $d_{D\cdots A}$  at 3.266 Å and  $\angle D-H\cdots A$  at 123°, and O3 $\cdots$ H–C15 with  $d_{D\cdots A}$  at 3.423 Å and  $\angle D-H\cdots A$  at 133°).

The tetrabutylammonium cation was incorporated into the assembly through C28–H···O1 ( $d_{D...A}$  at 3.311 Å and  $\angle D-H...A$  at 141°), C30–H···N6 ( $d_{D...A}$  at 3.506 Å and  $\angle D-H...A$  at 179°) hydrogen bonds, as well as a C–H··· $\pi$  interaction ( $d_{D...A}$  ranging from 3.68 to 3.92 Å). The diazine ring participated in a C–H··· $\pi$  interaction ( $d_{D...A}$  at 2.88 Å) as shown in Fig 2.10b. The resulting packing pattern revealed a grid-like structure with rectangular barricades formed by the self-assembled anions, effectively trapping the tetrabutylammonium cations within (Fig. 2.10c). This observation is consistent with our earlier findings regarding the encapsulation of tetrabutylammonium cations within the rectangular voids of a grid-like structure composed of hydrogen-bonded anions of oxime molecules.<sup>16-17</sup> Some important hydrogen bond parameters of salt **2.1.6** is given in Table 2.5

**Table 2.5:** Hydrogen bond parameters of salt **2.1.6**

	D-H···A	$d_{D-H}$ (Å)	$d_{H...A}$ (Å)	$d_{D...A}$ (Å)	$\angle D-H...A$ (°)
<b>2.1.6</b>	N(2) -H(2N) ...O(5) [1-x,1/2+y,1/2-z]	0.86	2.35	3.101(4)	145
	N(2) -H(2N) ...N(4) [1-x,1/2+y,1/2-z]	0.86	2.48	3.275(5)	153
	N(3) -H(3N) ...N(4) [1-x,1/2+y,1/2-z]	0.86	2.21	3.059(4)	169
	C(4) -H(4) ...O(5) [1-x,1/2+y,1/2-z]	0.93	2.32	3.131(5)	146
	C(28) -H(28B) ...O(1) [x,3/2-y,-1/2+z]	0.97	2.50	3.311(6)	141
	C(30) -H(30A) ...N(6) [1-x,1/2+y,1/2-z]	0.97	2.53	3.506(7)	179

### 2.8: TG/DSC analysis of the salt (2.1.6) and the solvates (2.1.1 and 2.1.2)

The thermogravimetry of 1:2 solvate **2.1.2** and TBA salt **2.1.6** is shown in Fig. A2.11. The differential scanning calorimetry analyses of the two solvates indicated that upon heating **2.1.2** (Fig. 2.11a), losses DMF molecules occurred in two steps at 136 °C and 156 °C. In contrast, the DMF solvents were lost from the **2.1.1** at 135 °C (Fig. A2.11a). Hence, de-solvation of **2.1.1** was performed by heating the sample at 150 °C overnight. The powder X-ray diffraction patterns of the two solvates and desolvates were compared to check whether the packing patterns of any those to be common or not. The PXRD patterns are depicted in Fig. 2.5a. These PXRD patterns suggested that the primary {hkl} reflections of **2.1.2** were retained in the de-solvated form. This was indicating the backbone observed in the 1:2 solvate was also observed in the de-solvated form. This could be due to the fact that the 1:2 de-solvate was the thermodynamic product formed in a hot solution. The host molecule of the solvate had a stretched geometry. Thus, upon heating **2.1.1** not only got de-solvated, but also the molecules slightly reorganised to adopt a similar packing as that of the host molecules in **2.1.2**.

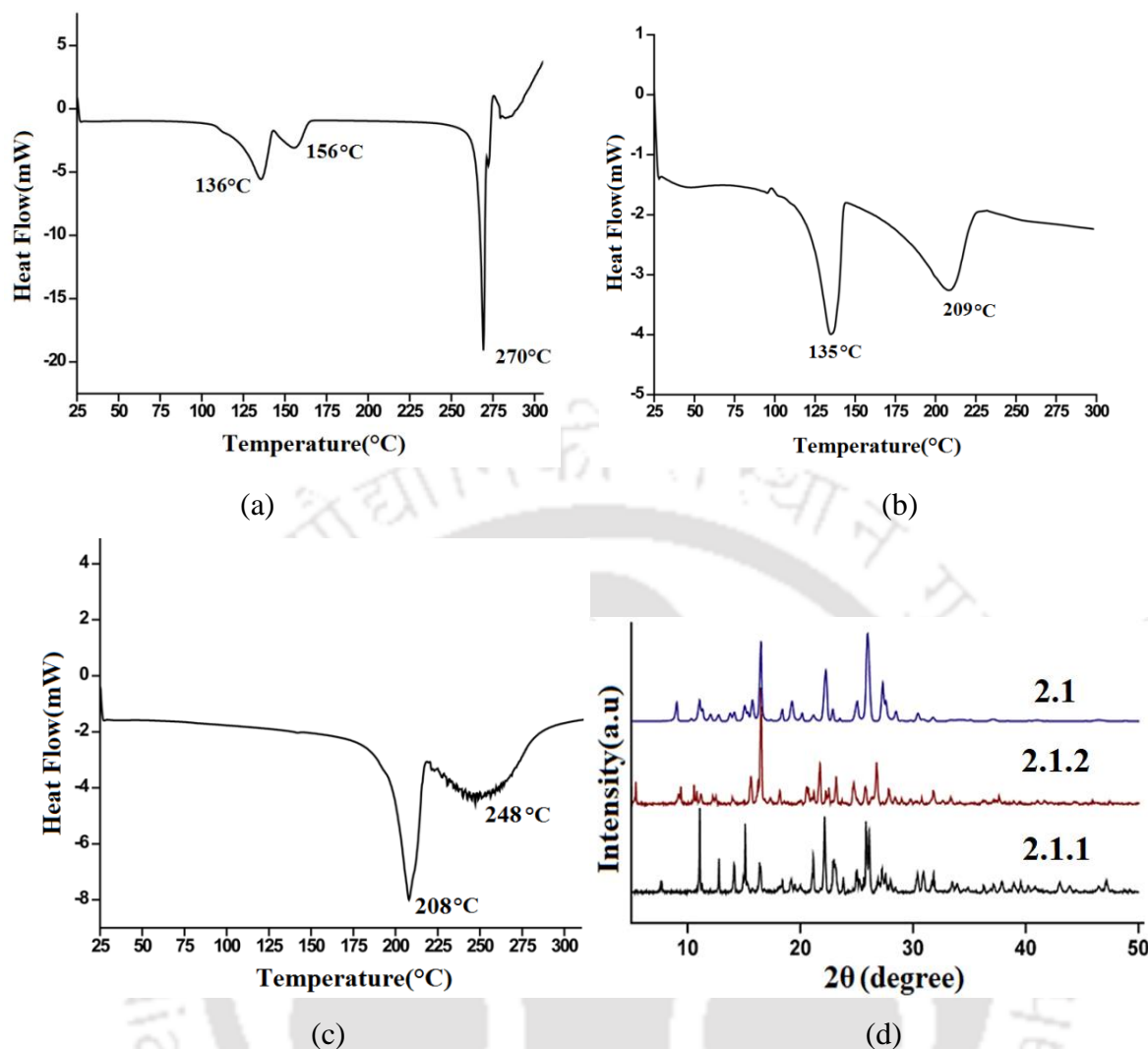


**Figure 2.11:** Differential scanning calorimetry of the (a) **2.1.2** and (b) **2.1.1** and (c) **2.1.6** (heating rate 10°C/min under nitrogen atmosphere) (d) Overlaid powder X-ray diffraction of the de-solvate and two DMF solvates of the **2.1**.

The solvate **2.1.2** underwent a stepwise weight loss due to the sequential removal of DMF molecules Fig. 2.11a. The initial loss occurred at 136°C with an enthalpy change of 38.45 kJ/mol, followed by a subsequent loss at 156°C with an enthalpy change of 13.64 kJ/mol (Fig. 2.11a). Ultimately, decomposition transpired at 270°C, accompanied by an associated enthalpy change of 68.60 kJ/mol. In contrast, **2.1.1** experienced a single event of DMF loss at 136 °C, with an enthalpy change of 19.39 kJ/mol, as shown in Fig 2.11b. Decomposition took place at 209 °C, accompanied by an enthalpy change of 11.43 kJ/mol. The decomposition temperature from TG of the solvate and the salt was similar showing that charge-assisted hydrogen bonds are effective enough to make a difference between the thermal stability of the solvates and the salt. The thermal stability of the salt **2.1.6**, in comparison to the DMF solvates, exhibited notable differences. Thermogravimetric analysis indicated decomposition

upon heating above 200 °C (Fig. A2.11b). This thermal behavior was further confirmed by differential scanning calorimetry, revealing an endothermic peak for fusion at 208°C with an enthalpy change of 49.54 kJ/mol. Subsequently, another broad endothermic peak at 248 °C, accompanied by an enthalpy change of 65.69 kJ/mol, was observed (Fig. 2.11c).

### 2.9: Comparisons of IR spectra of the solvates, Ionic cocrystals, and salt

In the overlaid diagram, as shown in Fig 2.12 for IR spectra, multiple broad stretches in the N–H and C–H regions were observed for both co-crystals and the salt, spanning the range of 2900–3500  $\text{cm}^{-1}$ . The presence and effects of weak C–H $\cdots$ O interactions of salt, cocrystal and the solvates were challenging to discern in this IR region due to overlapping signals. Each cocrystal and the salt exhibited a distinct absorption peak at 2958  $\text{cm}^{-1}$  and 2872  $\text{cm}^{-1}$  corresponding to the C–H stretching of the TBA group.

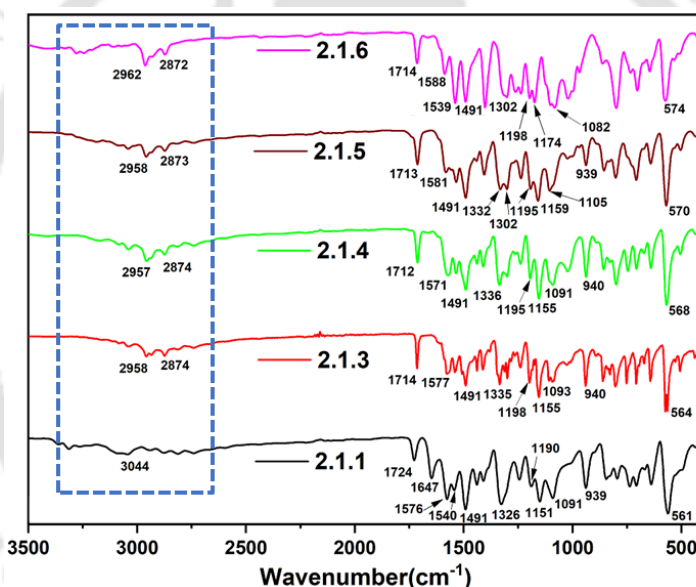


**Figure 2.12:** Overlaid diagram of IR spectra of solvate, ionic co-crystal and the TBA salt.

To assess the S–O stretching frequencies, a comparative analysis was conducted among solvates, cocrystals, and salt. In the neat sample of the parent compound **2.1.1**, an asymmetric  $\text{SO}_2$  stretch was observed at 1326  $\text{cm}^{-1}$ , and the symmetric stretches arising from the two S=O groups in slightly different environments were identified at 1190  $\text{cm}^{-1}$  and 1151  $\text{cm}^{-1}$ .<sup>27-</sup>  
<sup>28</sup> The co-crystals exhibited  $\text{SO}_2$  symmetrical stretches within the ranges of 1198–1192  $\text{cm}^{-1}$  and 1155–1159  $\text{cm}^{-1}$ , indicating a consistent environment for the  $\text{SO}_2$  group in each case. This observation aligned with the identical synthon involving C–H $\cdots$ O interactions observed in each cocrystal. In the salt, symmetrical stretches for the two S=O bonds, present in slightly

different environments, were observed at  $1198\text{ cm}^{-1}$  and  $1174\text{ cm}^{-1}$ . Notably, one of the S=O stretches in the salt was shifted by  $24\text{ cm}^{-1}$  ( $0.07\text{ kcal/mol}$ ) to higher energy compared to the parent compound. This has been attributed to the negative charge on the nitrogen atom attached to the sulfur atom. The higher  $\text{SO}_2$  symmetrical stretching frequencies observed in the three cocrystals, ranging from 5 to  $8\text{ cm}^{-1}$  above the  $\text{SO}_2$  symmetrical stretching frequency of the 1:1 DMF solvate, may suggest close similarities in the synthons involving  $\text{SO}_2$  in these ionic cocrystals. This observation suggested that the influence of C–H $\cdots$ O interactions on one of the S=O bonds played a role in shaping the overall molecular environments. The packing arrangement of **2.1.6** revealed the bifurcated C–H $\cdots$ O( $\text{SO}_2$ ) hydrogen bond. Notably, this bifurcated hydrogen bond involved urea and the nitrogen of diazine, representing a charge-assisted hydrogen bond. In aromatic nitro compounds, the asymmetrical and symmetrical N–O vibrations are typically found in the ranges of  $1550\text{--}1475\text{ cm}^{-1}$  and  $1360\text{--}1290\text{ cm}^{-1}$ , respectively. For the parent compound, these vibrations are noted at  $1539\text{ cm}^{-1}$  and  $1302\text{ cm}^{-1}$ . In both the salt and the cocrystals, these vibrations are seen at  $1535\text{ cm}^{-1}$  and between  $1335\text{--}1336\text{ cm}^{-1}$ . In each instance, the nitro group engaged in C–H $\cdots$ O hydrogen bonding, leading to similar N–O symmetrical stretches. This was also evident in the nitrophenol cocrystal, which exhibited C–H $\cdots$ O interactions. In this case, the N–O stretching was found at  $1337\text{ cm}^{-1}$ .<sup>67</sup> In **2.1.1**, the C=O stretch of the urea component was observed at  $1724\text{ cm}^{-1}$ . However, in both the ionic cocrystals and the salt, this stretching was observed in the range of  $1713\text{--}1715\text{ cm}^{-1}$ . The observed shift of approximately  $10\text{ cm}^{-1}$  (equivalent to  $0.29\text{ kcal/mol}$ ) in the ionic cocrystals and salt, compared to the neutral bifurcated hydrogen bonds, indicated a higher electrostatic character in the hydrogen bonds involving urea. This increase in electrostatic interaction led to a decrease in the C=O stretching frequency in the ionic cocrystals or in other words, weaker carbon-oxygen double bond strength of the urea group within the ionic cocrystals relative to the C=O bond was observed in the solvates.

### 2.10: Hirshfeld surface analyses

Hirshfeld surface analyses<sup>26</sup> were performed to provide supporting evidence for the hydrogen bonds in each of the solvates and the ionic cocrystal and for their comparisons. Representative examples from these analyses, focusing on the solvates and ionic cocrystals are presented in Fig. 2.13. The red spots observed at the contact points on the surfaces serve as clear indicators of the corresponding hydrogen bonds. The d-norm values for the solvate

**2.1.2** were in the range from -0.57 to 1.49, while for **2.1.1**, these values were in the range from -0.56 to 1.31. The same value for the salt (**2.1.6**) and for the ionic co-crystal (**2.1.3-2.1.5**) were -0.44 to 1.50, -0.57 to 1.98, -0.50 to 1.80 and -0.56 to 2.07 respectively. In order to retain the relatively larger size of the tetrabutylammonium cation in these self-assemblies, the host counterpart should have hydrophobic spaces. The fulfilment of this requirement was reflected in the Hirshfeld surface analyses, which are included in Fig. 2.14.

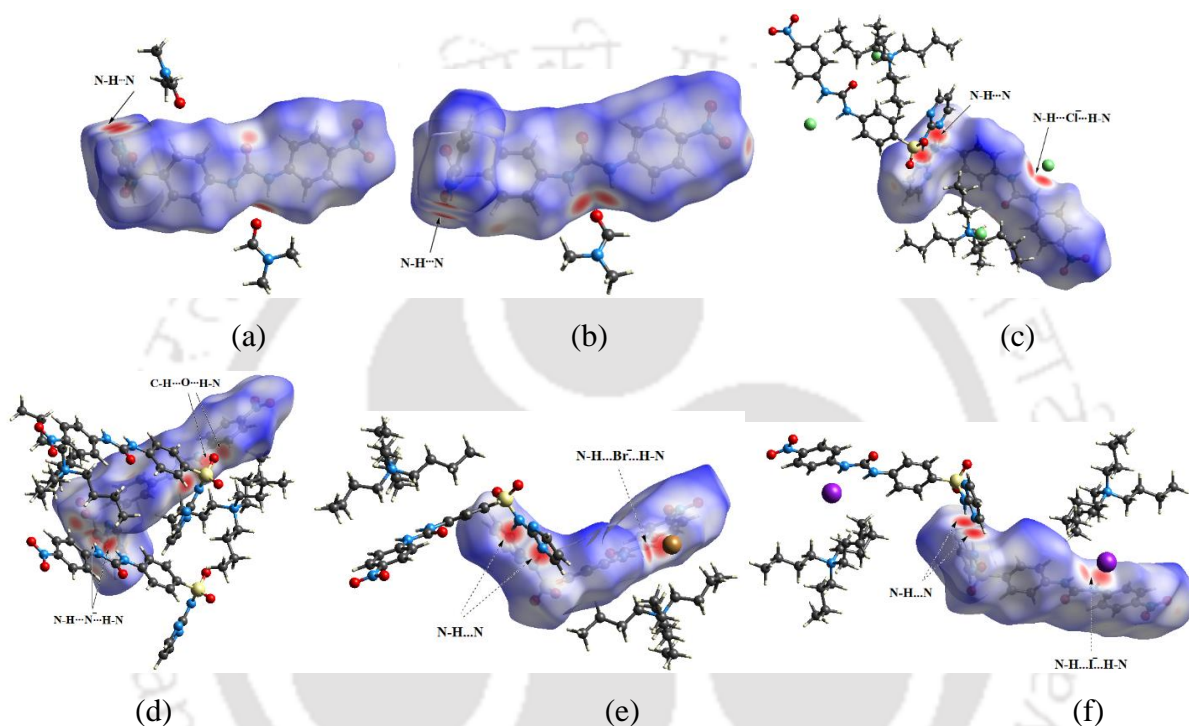


**Figure 2.13:** Hirshfeld surfaces of the (a) **2.1.1** (b) **2.1.2** (c) **2.1.3** (d) **2.1.6** (e) **2.1.4** and (f) **2.1.5**

The solvate showed a comparable percentage of hydrophobic interactions to hydrophilic interactions (Table 2.6). In contrast, the salt and the ionic cocrystals, featuring a hydrophobic tetrabutylammonium cation, exhibited higher percentages of C...H and H...H interactions compared to hydrophilic interactions involving heteroatoms (N, O, X)–H (Table 2.6). These observations suggest that both repulsive and attractive hydrophobic interactions, along with strong charge-assisted hydrogen bonds, contributed to the self-assembly of the ionic cocrystals and the salt.

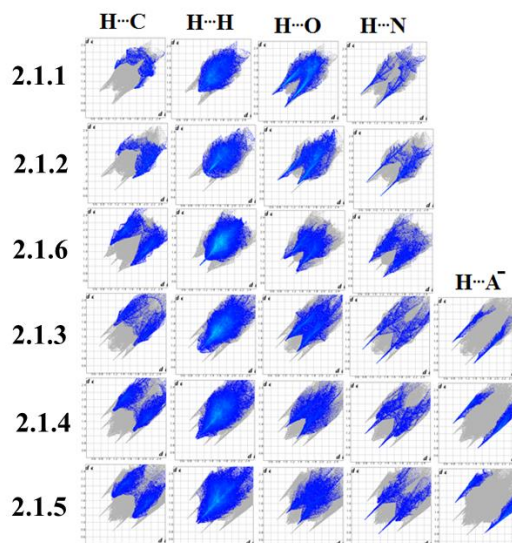


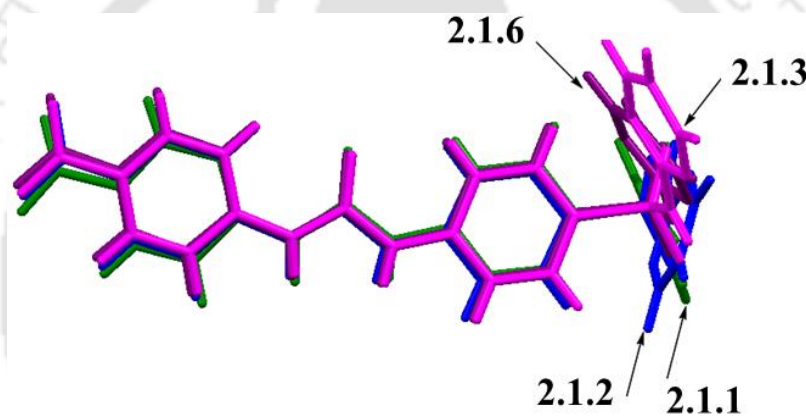
**Figure 2.14:** 2D fingerprint plots (including reciprocal contacts) of the H...C, H...H, H...O, H...N and H...anion interactions of the solvates, salt and cocrystals

**Table 2.6:** Percentages of the H...C, H...H, H...O, H...N and H...anion interaction (include reciprocal contacts) in 2D fingerprint plots.

Interactions (%)	H...C	H...H	H...O	H...N	H...anion
<b>2.1.1</b>	7.8	34.1	38.6	6.5	-
<b>2.1.2</b>	13.1	32.7	33.2	9.3	-
<b>2.1.6</b>	17.8	50.7	19.4	11.6	-
<b>2.1.3</b>	9.4	48.5	24.1	7.4	5.9
<b>2.1.4</b>	14.8	47.6	15.5	7.5	10.9
<b>2.1.5</b>	15.1	46.4	15	7.0	11.2

The orientation of the diazine moiety in each of these structures was independently analyzed by listing the key distances between atoms that could be related to explain the orientations. These distances are given in Tables 2.1 and 2.2. It was found that the S1...O4 and S1...O5 distances were comparable in each case, and these distances were in the range of 1.415(5)–1.453(5) Å. As expected, the S1–N4 distances of each ionic cocrystal and also that of the solvate were similar, which were found to be in the range between 1.646 and 1.631 Å, whereas such a distance in the salt was 1.587 Å. This suggested that considerable N=S double-bond character was present in the salt, supporting the presence of an imine form. This also suggested the presence of  $p\pi-d\pi$  interactions between the p orbital of nitrogen and the d orbital of sulfur. As a consequence of deprotonation, such a shortening of the S–N bond occurred, and a similar shortening of S–N bond was observed in the different salts of sulfadiazine.<sup>5</sup> It may be noted that the C14–N4 distance of the salt was comparable (the

difference was 0.01 Å), but in the cocrystals, the order of this bond distance was such that TBACl cocrystal > TBAI cocrystal > TBABr cocrystal. Hence, the change in C14–N4 distance in the cocrystals was not due to electronic effects but due to steric effects. This inference was also based on the fact that the S1⋯O4 and S1⋯O5 through-space distances are comparable but N5–O4 has distances that had the trend TBACl cocrystal < TBAI cocrystal ≈ TBABr cocrystal. This showed that the orientations of the diazine ring in the chloride and iodide salts were similar, whereas in the bromide salt it was slightly different. This spatial distance in the parent compound in the 1:1 DMF solvate was the highest. Further to these, the orientations of the diazine ring with respect to the urea plane in each case were nonoverlapping. An overlaid diagram drawn by keeping the urea part in one plane in the solvate, salt and an ionic cocrystal is shown in Fig 2.15.

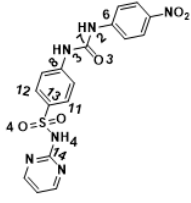


**Figure 2.15.** Overlaid diagram of **2.1.1**, **2.1.2**, **2.1.6**, and **2.1.3** (in each case the urea portion is drawn on the same plane).

The overlaid diagram distinctly illustrates variations in the orientation of the diazine moiety. The torsion angles influencing these orientation changes are outlined in Table 2.7. From the torsion angle table, it is clear that all the torsion angles in the ionic co-crystal have close similarities, while the same torsion angles were different from the solvates and the salt. In both the solvates **2.1.1** and **2.1.2**, it was found that there is some difference in the torsion angles of both the solvates. The torsion angle N4–S1–C13–C12 in the case of **2.1.1**, it is  $-123^\circ$  (4) whereas for the 1:2 solvate **2.1.2**, it is  $57.2^\circ$  (3). Similarly, the torsion angles O5–S1–C13–C12 and angles O5–S1–C13–C13 in case of **2.1.1**, it is  $128.1^\circ$  (4) and  $-51.0^\circ$  (4) respectively whereas the same torsion angles for **2.1.2**, were  $-52.4^\circ$  (3) and  $124.6^\circ$  (2) respectively. While the orientations exhibited similarities among the ionic cocrystals, a substantial difference was

evident in the salt, attributed to the formation of an imine form through deprotonation. The cations and anions were accommodated within the concave, adjustable space of an angular scaffold formed by the leaves. The flexibility of the cation, combined with the semi-rigid nature of the host, allowed for the accommodation of various spherical halide ions with different sizes.

**Table 2.7:** Torsion angles of solvates, ionic cocrystals and salts of **2.1**

Numbering of atoms in the <b>2.1</b>	Torsion angle (°)	<b>2.1.1</b>	<b>2.1.2</b>	<b>2.1.6</b>	Cocrystal with		
					TBACl (2.1.3)	TBABr (2.1.4)	TBAI (2.1.5)
	C13-S1-N4-C14	68.4(4)	67.3(3)	-67.7(4)	-75.2(5)	73.6(5)	73.1(6)
	N4-S1-C13-C12	-123.3(4)	57.2(3)	100.1(4)	95.7(5)	-95.4(5)	-94.7(6)
	C6-N2-C7-O3	-6.4(9)	6.2(5)	-3.5(7)	-6(1)	5(1)	4(1)
	C8-N3-C7-O3	-10.4(8)	6.0(5)	-1.7(7)	0(1)	-0(1)	-2(1)
	O4-S1-C13-C12	-4.5(4)	175.8(2)	-24.5(4)	-22.3(5)	22.7(5)	22.8(7)
	O4-S1-C13-C11	176.4(3)	-7.2(3)	158.4(3)	156.9(5)	-156.6(4)	-157(5)
	O5-S1-C13-C12	128.1(4)	-52.4(3)	-149(4)	-154.8(5)	154.6(4)	155.2(6)
	O5-S1-C13-C11	-51.0(4)	124.6(2)	33.8(4)	24.4(5)	-24.6(5)	-24.6(6)

### 2.11: Summary from the comparisons

From the structural examinations, several critical insights were derived. (a) In the solvates, salt, and cocrystals, the urea moiety displayed bifurcated hydrogen bonds, (b) A homodimeric synthon was consistently present in both the solvates and ionic cocrystals, suggesting a recurring structural motif. (c) The C–H···O intermolecular forces were pivotal in stabilizing a similar orientation of the diazine ring across different ionic cocrystals. (d) The structural analysis revealed a slight variation between the plane of the diazine moiety and the plane of the remaining structure of **2.1** in each case. This variation facilitated the formation of two distinct solvates with the same solvent and isostructural ionic cocrystals. (e) In the case of the salt, the orientation of the anion differed from the parent form (neutral form of host), which was attributed to the hydrogen bonding interactions of the urea with the negatively charged N4 atoms. (f) The formation of the salt involved an S=O bond character resulting from the deprotonation at the sulfonamide proton (g) To integrate the halides with minimal alterations in the molecular assemblies, there were adjustments in the geometry of the angular-shaped **2.1**. The angular discrepancies between the plane containing the diazine ring and the planes containing the remainder of **2.1**, **2.1.3**, **2.1.4**, and **2.1.5** were measured to be 70.30°, 74.12° and 78.00°, respectively. This observation implies that the varying angles were a result of the

semi-flexibility inherent in **2.1**. This flexibility facilitated the creation of additional space necessary to accommodate anions, which was directly related to the increase in their respective ionic radii.

### 2.12: Solution study of solvates and ionic co-crystal

This study has provided a scope to systematically study the interactions of various TBA halides with the host **2.1** in solution and to compare the spectral changes in solution with the data of the isolated salt and cocrystals by dissolution. In order to make adequate assignment of peaks shifting positions upon interactions with a TBAX, at first, the aromatic ring protons of **2.1.1** were assigned from the correlation observed in 2D-HOMO-COSY- $^1\text{H}$ NMR spectra shown in Fig. 2.16.

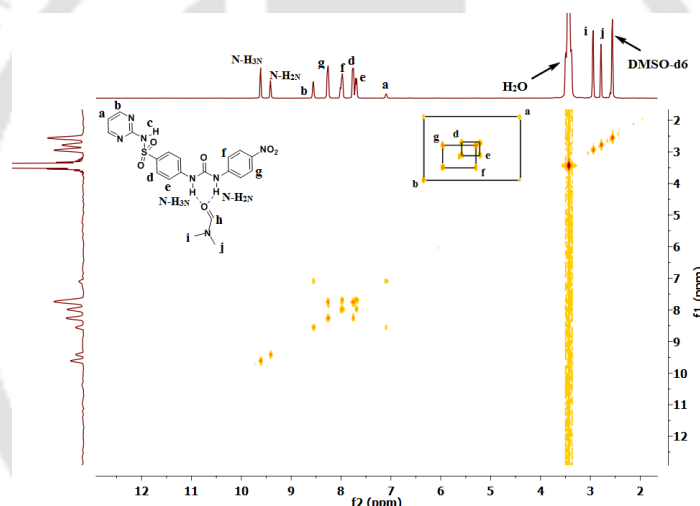


**Figure 2.16:**  $^1\text{H}$ -HOMO-COSY (600 MHz,  $\text{DMSO-d}_6$ ) spectrum of the **2.1.1**

The three hydrogen atoms of the diazine ring appeared as a triplet and doublet, whereas the nitrophenyl ring protons were observed as two doublets of doublets and the other four protons of the phenylene part on another side of urea were also identified as a doublet of doublets from the  $\text{A}_2\text{B}_2$  pattern in each case. The signals for ring protons and urea protons (N–H) of the parent host, **2.1.1**, **2.1.6** and ionic cocrystals (**2.1.3-2.1.5**) are shown in Fig. 2.17. The aromatic region of the  $^1\text{H}$  NMR spectrum of **2.1.1** was different from that of **2.1**, as the former had an extra signal at 7.95 ppm due to the aldehyde C–H of the DMF. The aliphatic region of the DMF solvate also had two singlet peaks at 2.89 and 2.73 ppm for the  $\text{CH}_3$  signal

of the DMF of the solvate (Fig. A2.2). A similar observation was made with **2.1.2**, where the integration matched with a composition as a 1:2 solvate (Fig. A2.3).

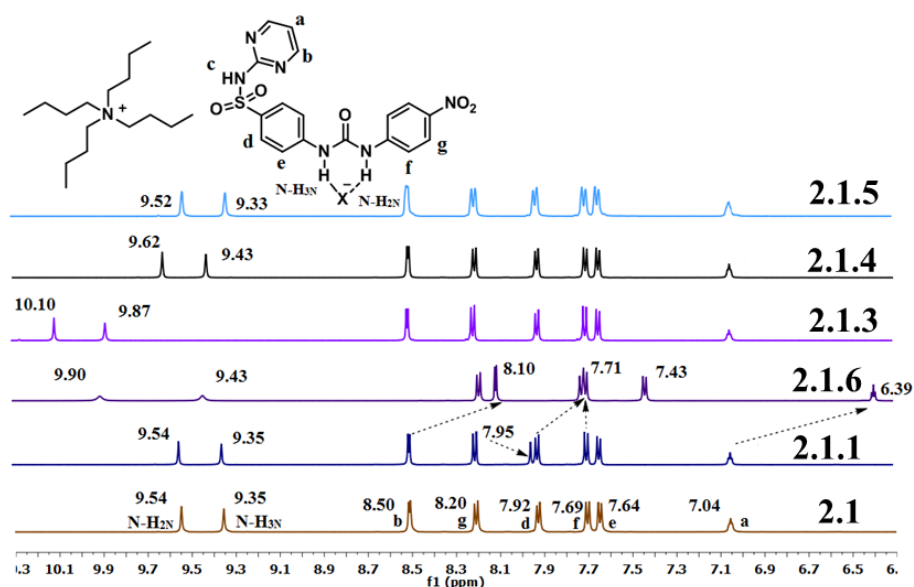
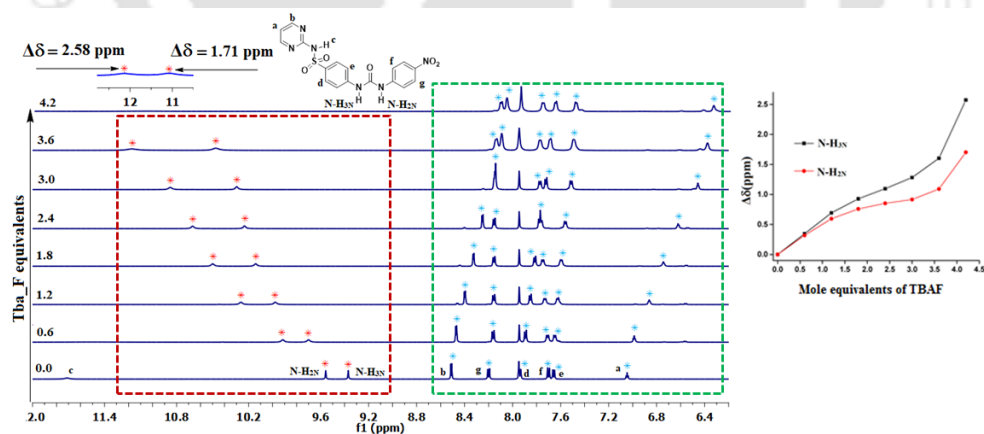


**Figure 2.17:**  $^1\text{H}$ NMR (600 MHz, DMSO- $d_6$ ) of **2.1.1**, **2.1.6** and ionic cocrystals **2.1.3-2.1.5** (aromatic region)

The  $\text{N-H}_{3\text{N}}$  proton of **2.1.6** and **2.1.4** was slightly de-shielded in comparison to **2.1.1**, whereas in the case of **2.1.3** the  $\text{N-H}_{\text{N}3}$  and  $\text{N-H}_{\text{N}2}$  protons both showed downfield shifts of 0.52 and 0.56 ppm, respectively. The  $\text{N-H}_{\text{N}2}$  proton of **2.1.6** appeared at 9.9 ppm, a shift of  $\sim 0.36$  ppm, and the cocrystal **2.1.4** showed a downfield shift. The aromatic protons of all the compounds except **2.1.6** appeared in the same region in their respective  $^1\text{H}$  NMR spectra, but in the case of **2.1.6**, the sulfadiazine ring protons were shielded and observed upfield due to the negative charge on the N4 atom. The proton next to the diazine nitrogen atom and the proton present at a meta position with reference to the  $\text{SO}_2$  group showed upfield shifts of 0.40 and 0.21 ppm, respectively. The doublet peak of the proton (ortho to the  $\text{SO}_2$  group) was shifted upfield by 0.21 ppm, and this peak merged with the doublet peak of the proton (meta to the nitro group), showing a doublet of doublet peak. The proton appearing at 7.04 ppm was shifted to 6.39 ppm. These have shown that the cocrystal or salt formation influenced the chemical shifts of host-molecule in each case. The anionic form showed large difference with respect to the cocrystals. The effect of hydrogen bonding influenced the chemical shifts of the labile N-H protons in all the ionic cocrystals.

### 2.13: $^1\text{H}$ NMR titration of **2.1** with tetrabutylammonium halides

The two NH proton signals experienced varying degrees of shift, indicating a differential impact on their electronic environments due to the addition of the tetrabutylammonium chloride. When an excess of tetrabutylammonium chloride was added to **2.1**, the N–H proton adjacent to the nitrophenyl group experienced de-shielding, resulting in a chemical shift increase of 1.32 ppm. Conversely, the N–H proton, located away from the nitrophenyl ring, was shifted by 1.23 ppm, as shown in Fig. 2.18b. The magnitude of the shifts in the chemical shifts of the N–H protons of the urea moiety varied in each case. These variations in chemical shifts are ascribed to the asymmetrical bifurcated hydrogen bonding interactions with the chloride ion. The broad singlet N–H resonance of the amino-diazine segment in **2.1**, observed at 11.67 ppm, remained unchanged even with the addition of excess amounts of TBA chloride (4.2 equivalents). It was confirmed that TBA chloride primarily interacted with the urea portion of the molecule without causing deprotonation of the diazine N–H proton. As a result, the protons on the ring of **2.1** were unaffected by the addition of TBA chloride. The observed difference in the acidity of the two N–H bonds is attributed to the distinct functional groups attached to the urea moiety. Specifically, the nitrophenyl group exerts an electron-withdrawing effect on the adjacent N–H bond, influencing its chemical environment and acidity.



(a)

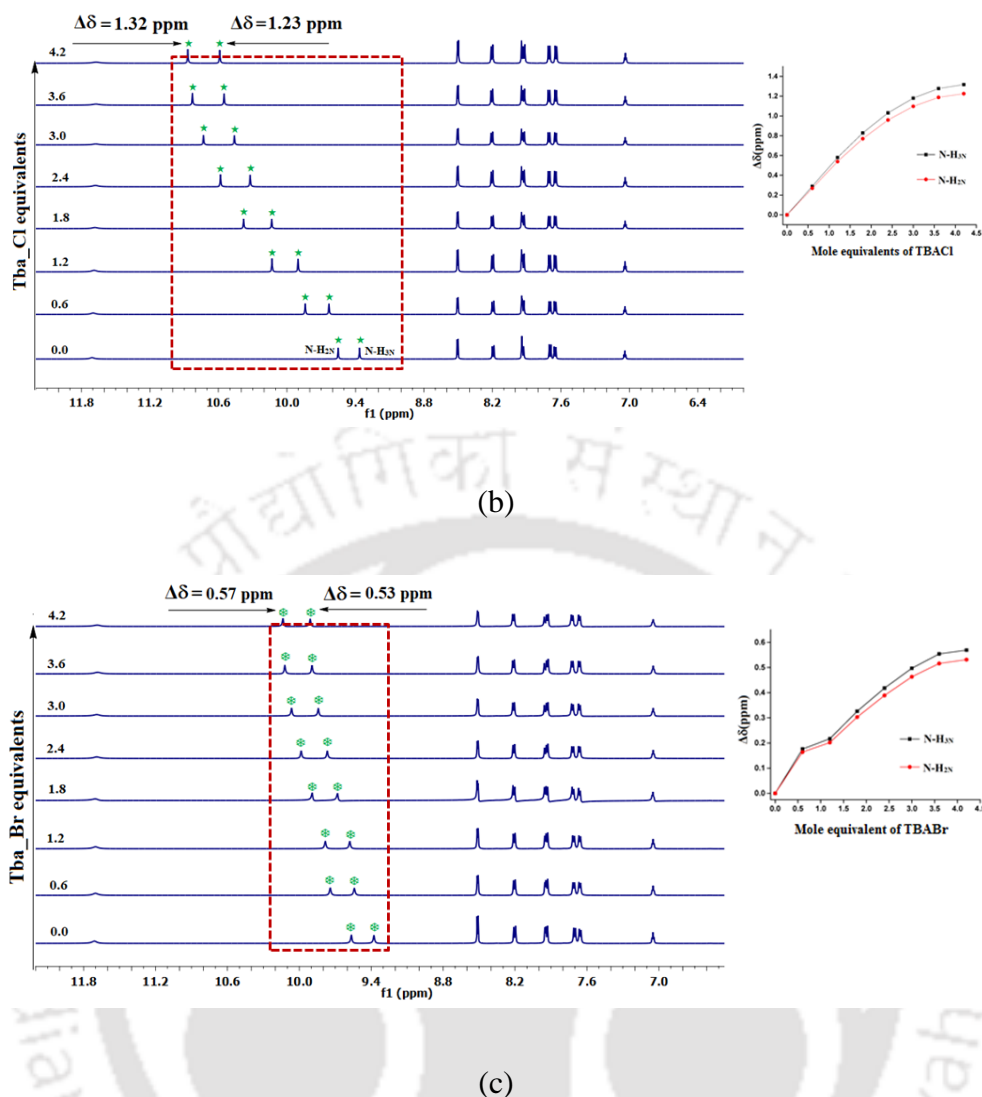


**Figure 2.18:** Changes in the chemical shifts of N-H<sub>3N</sub> and N-H<sub>2N</sub> protons in respective  $^1\text{H}$ NMR spectrum of the **2.1** upon increasing the concentrations of tetrabutylammonium a) fluoride, (b) chloride and (c) bromide.

Therefore, the deprotonation of this particular N–H bond was more favoured. Upon adding TBA chloride, distinct shifts in the chemical shifts of the two N–H bonds were observed. A  $^1\text{H}$ NMR titration using tetrabutylammonium bromide demonstrated a similar pattern of shifts, as depicted in Fig. 2.18c. However, a titration with tetrabutylammonium iodide did not result in significant alterations in the chemical shifts. This implies that the N–H protons on the urea moiety were sensitive to changes in each case. To illustrate these variations, plots of the changes in the chemical shift of the N–H versus the concentration were generated and are shown in the inset (Fig 2.18), highlighting the differential response of these protons to varying halide ions. A consistent observation across the experiments was that the difference

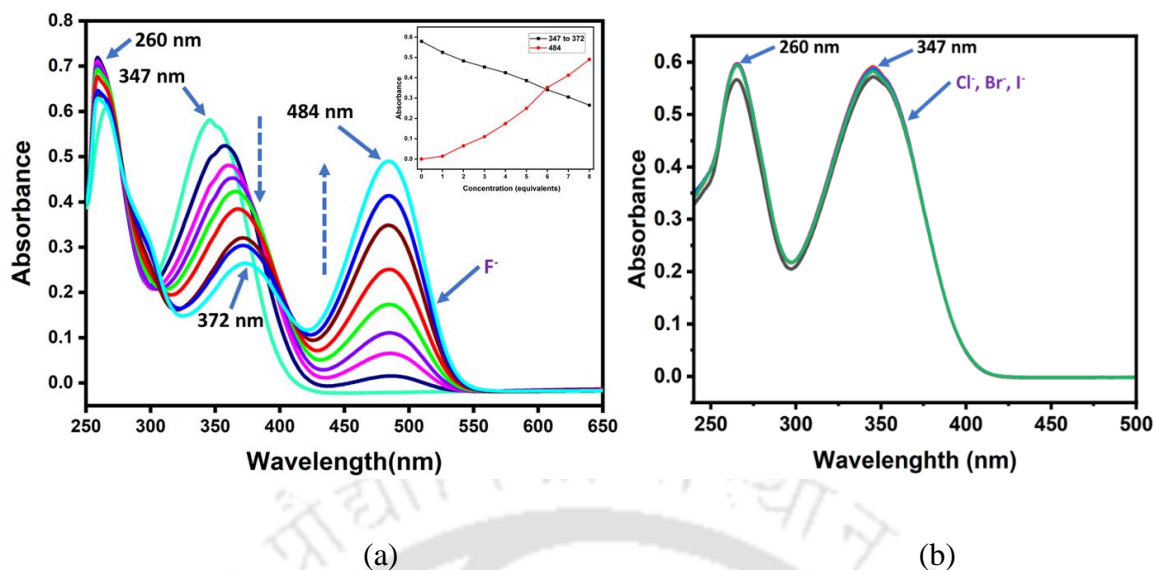
in the chemical shifts of the N–H protons increased as the concentration of TBA salts in the solution increased. However, the extent of this incremental change was varied. These variations in chemical shifts implied the formation of hydrogen bonds with anions. The differential shifts were due to the differences in electronegativity of the anions, affecting the extent of interactions and, consequently, the magnitude of the shift in the N–H proton chemical shifts.

The  $^1\text{H}$ NMR titration experiments involving **2.1** with tetrabutylammonium fluoride offered valuable insights into the deprotonation process induced by fluoride ions in **2.1**, as shown in Fig. 2.18a. These titrations indicated deprotonation of the N–H proton adjacent to the diazine part of the molecule. This phenomenon was evident from the disappearance of the peak at 11.67 ppm, originally present in the parent compound, after the addition of tetrabutylammonium fluoride. Additionally, during these titrations, the chemical shifts corresponding to the two protons of the urea moiety exhibited significant changes. The relative increments of the chemical shifts of the two N–H protons of the urea moiety by the fluoride ions were different (Fig. 2.18a). At higher fluoride ion concentrations, the  $^1\text{H}$  NMR spectra revealed a broadening of the signals corresponding to the two protons in the urea moiety. This broadening implies a proton exchange and the eventual loss of one N–H proton, a conclusion supported by the observed decrease in the overall signal integration for these two N–H protons. These observations are indicative of deprotonation occurring within the urea group, coupled with a proton transfer occurring between the two N–H protons of the urea. As the deprotonation took place, the chemical shifts of the C–H protons of the diazine ring were affected. The triplet originally observed at 7.04 ppm in the  $^1\text{H}$ NMR spectrum exhibited significant shielding, resulting in a shift to 6.34 ppm. Additionally, the resonance appearing at 8.5 ppm also showed shielding. When fluoride ions were introduced at low concentrations, the aromatic protons of the nitrophenyl and the adjacent phenylene ring to the urea moiety remained largely unaffected, particularly up to the addition of approximately 1.2 equivalents of fluoride ions. As the concentration of fluoride ions was raised, there was a noticeable effect on the chemical shifts of the protons in all the rings. This observation indicates that a second deprotonation event on the urea moiety occurred at these higher fluoride concentrations. With increased concentrations of TBAF, the protons of the nitrophenyl ring, initially resonating at 8.21–8.19 and 7.70–7.67 ppm, experienced shielding due to the negative charge developed on the urea moiety. The triplet initially observed at 7.04 ppm shifted to a higher field as a result of anion formation at the amino-diazine site. This

shift ultimately resulted in the triplet appearing at 6.4 ppm, reflecting a shift of 0.64 ppm. In the NMR titration, the formation of a dianion was further evidenced by the marked changes in chemical shifts observed beyond the addition of 1.2 molar equivalents. The association constant with TBAF as well as with TBACl were calculated by using BindFit v0.5 (<http://app.supramolecular.org/bindfit/>) and these were found to be  $37.99 (\pm 6.99) \text{ M}^{-1}$  and  $18.42 (\pm 2.12) \text{ M}^{-1}$  respectively. This was in accordance with the observation that fluoride could deprotonate the host but other halides could not.

#### 2.14: UV-visible studies

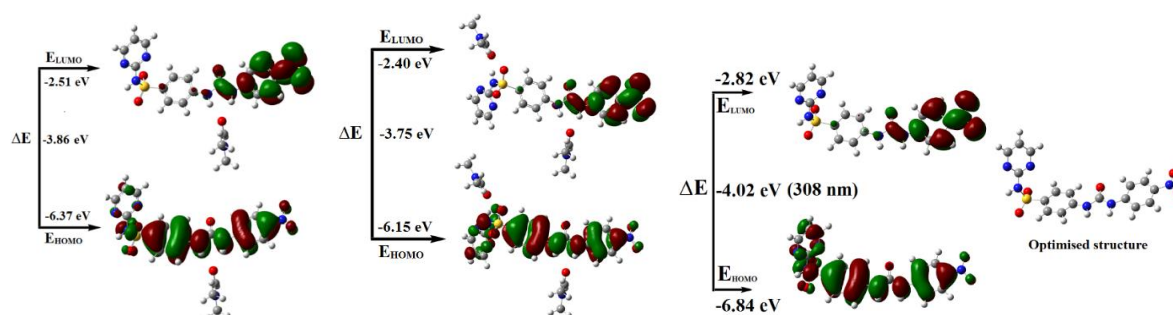
UV-visible spectroscopic spectral changes help in the understanding of molecular and on recognition by urea derivatives.<sup>29</sup> Urea-derived probes showing changes in UV-visible spectra have been used in distinguishing fluoride ions from other ions.<sup>30-32</sup> The compound **2.1** showed an absorption at 347 nm. These absorption changes change upon interaction with fluoride ions. Upon adding a solution of tetrabutylammonium fluoride t solution of 2.1, showed a noticeable change in the intensity of this  $\pi-\pi^*$  transition. The absorption intensity was diminished, and the peak was gradually shifted to 372 nm (as shown in Fig. 2.19a) with increasing fluoride concentrations. Additionally, a new absorption peak emerged at 484 nm. These specific changes were not seen with other TBA halides, as shown in Fig. 2.19b. The initial alterations in the absorption characteristics were attributed to the formation of an anion through the abstraction of the N-H proton from the amino diazine part by the fluoride ion. With the addition of increasing amounts of fluoride ions, the N-H group in the urea moiety underwent deprotonation, a phenomenon that was also evidenced by the NMR titration results. In a solution, the state of the urea moiety being mono-deprotonated was not distinguishable.



**Figure 2.19:** The changes in the UV-visible spectra of the **2.1** ( $4.3 \times 10^{-5}$ ) in dimethylsulphoxide upon addition of different aliquots (12  $\mu\text{L}$ ) of (a) tetrabutylammonium fluoride and (b) with other halides ( $10^{-2}$  M).

### 2.15: Optimization of energy by DFT calculations

To elucidate the observed absorption spectra, Density Functional Theory (DFT) calculations using the B3LYP functional with a 6-311++G (2d,2p) basis set were employed to determine the HOMO-LUMO gaps of the compounds. The calculated HOMO-LUMO gap for **2.1** was 308.4 nm, while the gap for the DMF-solvated molecule was found to be 321.2 nm. Additionally, time-dependent DFT calculations predicted two distinct electronic transitions at 348.92 nm and 315.18 nm, having oscillator strengths of 0.32 and 0.21, respectively, as shown in Fig. 2.20 and Fig. A2.12. These predicted transitions correlate well with the broad absorption peak observed for **2.1** at 347 nm. The time-dependent DFT calculations for the salt showed two closely spaced absorption peaks at 387.19 nm and 360.45 nm, each with oscillator strengths of 0.15 and 0.14, respectively (as seen in Fig 2.20 and Fig. A2.12).



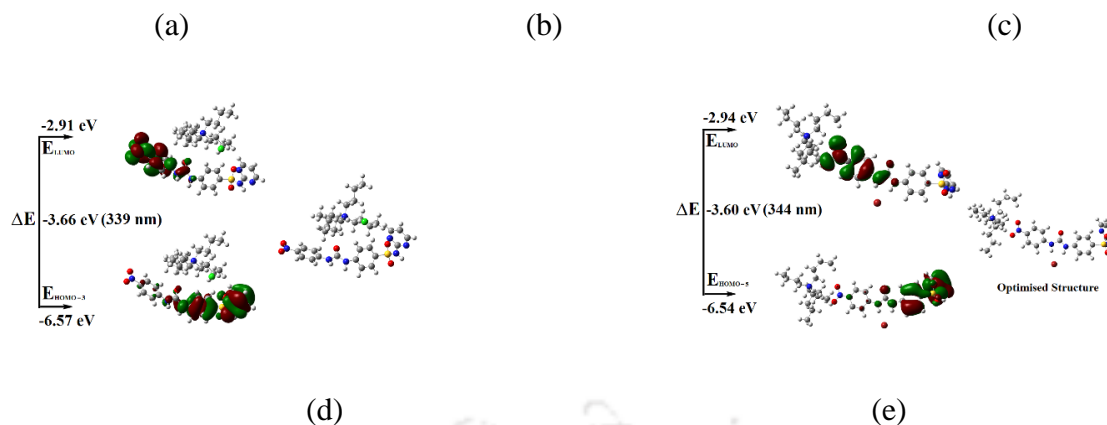


**Figure 2.20:** HOMO and LUMO gap and optimized structure of (a) **2.1.1** (b) **2.1.2** (c) **2.1** (d) **2.1.3** and (e) **2.1.4**

This data indicates an initial shift in absorption from 347 nm to 372 nm, as observed in UV-visible titration. This shift, as detailed in Fig. 2.19, is attributed to the formation of the **2.1** anion. The energy gaps between the HOMO and LUMO for both TBA chloride and TBA bromide cocrystals were found to be quite small and did not match the UV-visible spectra observed. In these instances, the HOMO was based on the anion, while the LUMO was based on the ligand. Thus, oscillator strength for the transitions between the HOMO and LUMO was investigated and found to be 0.002. The low value indicated that in these cases, the HOMO-LUMO transitions were likely forbidden. For **2.1.3** and **2.1.4**, the transitions occurred from HOMO-3 to LUMO and from HOMO-5 to LUMO, respectively, as shown in Fig. 2.20. TD-DFT calculations revealed that these transitions, occurring at 366.05 nm and 330.13 nm, had oscillator strengths of 0.15 and 0.20, respectively. The absorptions observed for the salts at 346 nm and 348 nm corresponded well with these findings, suggesting an agreement between the experimental and theoretical spectra.

## 2.16: Conclusion

In this study, we explored two distinct solvates of **2.1** with dimethylformamide. These forms exhibited a medium-strength hydrogen bond with a hydrophilic site and weak hydrogen bonds from the hydrophobic interstitial space. The homo-dimers of the semi-rigid angular shaped of **2.1** provided a required platform in synthesizing three isostructural ionic cocrystals. These isostructural cocrystals were characterized by their spherical shaped halide ions, which vary in their sizes. The structural and solution studies of the cocrystals yielded novel insights.

(a) the homo-dimeric synthons of **2.1** demonstrate showing remarkable adaptability, allowing for the formation of isostructural complexes with minimal alterations in interaction types. This adaptability is exemplified in the accommodation of various ionic salts, specifically TBA chloride, bromide, and iodide, to form structurally analogous entities. (b) in solution studies, the hydrogen bonds formed between the urea component of **2.1** and chloride or bromide ions were distinctly observed. However, these interactions did not significantly alter the absorbance characteristics of the nitrophenyl group linked to the urea segment. (c) In solution, fluoride ions caused a sequential di-deprotonation of **2.1**, a process that was evident in the changes observed in the UV-visible spectra. Interestingly, only the mono-deprotonated form of this salt could be crystalized from the solution. (d) Notably, a solution of the salt of **2.1** exhibited the same color transition mirroring the change observed when **2.1** interacted with fluoride ions. These indicated that the interaction with fluoride ions triggered the deprotonation of **2.1**, resulting in a color change and the formation of anionic species.

### 2.17: References

1. Cao, H.-L.; Zhou, J.-R.; Cai, F.-Y.; Lü, J.; Cao, R. Two-Component Pharmaceutical Cocrystals Regulated by Supramolecular Synthons Comprising Primary N $\cdots$ H $\cdots$ O Interactions. *Cryst. Growth Des.* **2018**, *19* (1), 3–16.
2. B, H.; Hasija, A.; Cruz-Cabeza, A. J.; Shruti, I.; Chopra, D. Multicomponent Crystals of Chlorpropamide: Multiple Conformers, Multiple Z', and Proton Transfer at Play. *Cryst. Growth Des.* **2021**, *21* (6), 3158–3167.
3. Léon, I.; Tasinato, N.; Spada, L.; Alonso, E. R.; Mata, S.; Balbi, A.; Puzzarini, C.; Alonso, J. L.; Barone, V. Looking for the Elusive Imine Tautomer of Creatinine: Different States of Aggregation Studied by Quantum Chemistry and Molecular Spectroscopy. *Chempluschem* **2021**, *86* (10), 1374–1386.
4. Sun, Y. P.; Ren, X. H.; Wang, H. J.; Shan, Y. Y.; Xing, L. J. Hydrogen-Bonding Interaction in a Complex of Amino Acid with Urea Studied by DFT Calculations. *Struct. Chem.* **2009**, *20* (2), 213–220.
5. Elacqua, E.; Bucar, D.-K.; Henry, R. F.; Zhang, G. G. Z.; MacGillivray, L. R. Supramolecular Complexes of Sulfadiazine and Pyridines: Reconfigurable Exteriors and Chameleon-like Behavior of Tautomers at the Co-Crystal–Salt Boundary. *Cryst. Growth Des.* **2013**, *13* (1), 393–403.

6. Singh, M. P.; Baruah, J. B. Combinations of Tautomeric Forms and Neutral-Cationic Forms in the Cocrystals of Sulfamethazine with Carboxylic Acids. *ACS Omega* **2019**, *4* (7), 11609–11620.
7. Lu, J.; Cruz-Cabeza, A. J.; Rohani, S.; Jennings, M. C. A 2: 1 Sulfamethazine–Theophylline Cocrystal Exhibiting Two Tautomers of Sulfamethazine. *Acta Crystallogr. Sect. C Cryst. Struct. Commun.* **2011**, *67* (8), o306–o309.
8. Ghosh, S.; Bag, P. P.; Reddy, C. M. Co-Crystals of Sulfamethazine with Some Carboxylic Acids and Amides: Co-Former Assisted Tautomerism in an Active Pharmaceutical Ingredient and Hydrogen Bond Competition Study. *Cryst. Growth Des.* **2011**, *11* (8), 3489–3503.
9. Bernstein, J.; Davis, R. E.; Shimoni, L.; Chang, N. Patterns in Hydrogen Bonding: Functionality and Graph Set Analysis in Crystals. *Angew. Chemie Int. Ed. English* **1995**, *34* (15), 1555–1573.
10. Etter, M. C. Encoding and Decoding Hydrogen-Bond Patterns of Organic Compounds. *Acc. Chem. Res.* **1990**, *23* (4), 120–126.
11. Turner, D. R.; Smith, B.; Goeta, A. E.; Evans, I. R.; Tocher, D. A.; Howard, J. A. K.; Steed, J. W. The R<sup>2</sup> 1 (6) Hydrogen-Bonded Synthons in Neutral Urea and Metal-Bound Halide Systems. *CrystEngComm* **2004**, *6*, 633–641.
12. Yang, Z.; Huang, X.; Zhao, Q.; Li, S.; Wu, B. Hydrogen-Bonded 1D Nanotubes and 2D Layers of Group 12 Metal Complexes with a Pyridylurea Ligand. *CrystEngComm* **2012**, *14* (17), 5446–5453.
13. Ranjan, S.; Devarapalli, R.; Kundu, S.; Saha, S.; Deolka, S.; Vangala, V. R.; Reddy, C. M. Isomorphism: Molecular Similarity to Crystal Structure Similarity in Multicomponent Forms of Analgesic Drugs Tolfenamic and Mefenamic Acid. *IUCrJ* **2020**, *7* (2), 173–183.
14. Gratzer, K.; Diemer, V.; Clayden, J. Signal Transduction in Oligoamide Foldamers by Selective Non-Covalent Binding of Chiral Phosphates at a Urea Binding Site. *Org. Biomol. Chem.* **2017**, *15* (17), 3585–3589.
15. Steiner, T. Hydrogen-Bond Distances to Halide Ions in Organic and Organometallic Crystal Structures: Up-to-Date Database Study. *Acta Crystallogr. Sect. B Struct. Sci.* **1998**, *54* (4), 456–463.
16. Tarai, A.; Baruah, J. B. Anion Assisted Conformationally Guided Self-Assemblies of Multi-Component Cocrystals of Dioxime. *CrystEngComm* **2016**, *18* (29), 5482–5491.

17. Tarai, A.; Baruah, J. B. Water-Assisted Emission Enhancement of 2-Hydroxynaphthaldoxime and Related Compounds. *ChemistrySelect* **2018**, *3* (41), 11406–11413.
18. Tamuly, C.; Sarma, R. S.; Batsanov, A. S.; Goeta, A. E.; Baruah, J. B. 4-[Bis (4-Hydroxy-3, 5-Dimethylphenyl) Methyl] Pyridinium Chloride and Bromide. *Acta Crystallogr. Sect. C Cryst. Struct. Commun.* **2005**, *61* (5), o324–o327.
19. Russell, J. M.; Parker, A. D. M.; Radosavljevic-Evans, I.; Howard, J. A. K.; Steed, J. W. Simultaneous Anion and Cation Binding by a Simple Polymer-Bound Ureidopyridyl Ligand. *Chem. Commun.* **2006**, No. 3, 269–271.
20. Hussain, S.; Brotherhood, P. R.; Judd, L. W.; Davis, A. P. Diaxial Diureido Decalins as Compact, Efficient, and Tunable Anion Transporters. *J. Am. Chem. Soc.* **2011**, *133* (6), 1614–1617.
21. Brammer, L.; Bruton, E. A.; Sherwood, P. Understanding the Behavior of Halogens as Hydrogen Bond Acceptors. *Cryst. Growth Des.* **2001**, *1* (4), 277–290.
22. Dias, C. M.; Valkenier, H.; Davis, A. P. Anthracene Bisureas as Powerful and Accessible Anion Carriers. *Chem. Eur. J.* **2018**, *24* (23), 6262–6268.
23. Manna, U.; Nayak, B.; Das, G. Dual Guest [(Chloride) 3-DMSO] Encapsulated Cation-Sealed Neutral Trimeric Capsular Assembly: Meta-Substituent Directed Halide and Oxyanion Binding Discrepancy of Isomeric Neutral Disubstituted Bis-Urea Receptors. *Cryst. Growth Des.* **2016**, *16* (12), 7163–7174.
24. Huang, C.; Wang, R.; Shu, X.; Fan, Y.; Qi, Y.; Li, S.; Xia, C. Crystal Structures of the 2: 2 Complex of 1, 1'-(1, 2-Phenylene) Bis (3-m-Tolylurea) and Tetrabutylammonium Chloride or Bromide. *Acta Crystallogr. Sect. E Crystallogr. Commun.* **2017**, *73* (9), 1316–1319.
25. Nayak, B.; Halder, S.; Das, G. Terminal Substituent Induced Differential Anion Coordination and Self-Assembly: Case Study of Flexible Linear Bis-Urea Receptors. *Cryst. Growth Des.* **2019**, *19* (4), 2298–2307.
26. Spackman, M. A.; Jayatilaka, D. Hirshfeld Surface Analysis. *CrystEngComm* **2009**, *11* (1), 19–32.
27. Qureshi, N.; Yufit, D. S.; Steed, K. M.; Howard, J. A. K.; Steed, J. W. Anion Hydrogen Bonding from a ‘Revealed’ Urea Ligand. *CrystEngComm* **2016**, *18* (28), 5333–5337.

28. Wu, B.; Huang, X.; Xia, Y.; Yang, X.-J.; Janiak, C. Oxo-Anion Binding by Protonated (Dimethylphenyl)(Pyridyl) Ureas. *CrystEngComm* **2007**, *9* (8), 676–685.
29. Amendola, V.; Fabbrizzi, L.; Mosca, L. Anion Recognition by Hydrogen Bonding: Urea-Based Receptors. *Chem. Soc. Rev.* **2010**, *39* (10), 3889–3915.
30. Evans, N. H.; Beer, P. D. Advances in Anion Supramolecular Chemistry: From Recognition to Chemical Applications. *Angew. Chemie Int. Ed.* **2014**, *53* (44), 11716–11754.
31. Braschi, I.; Paul, G.; Gatti, G.; Cossi, M.; Marchese, L. Embedding Monomers and Dimers of Sulfonamide Antibiotics into High Silica Zeolite Y: An Experimental and Computational Study of the Tautomeric Forms Involved. *RSC Adv.* **2013**, *3* (20), 7427–7437.
32. Shinde, S.; Incel, A.; Mansour, M.; Olsson, G. D.; Nicholls, I. A.; Esen, C.; Urraca, J.; Sellergren, B. Urea-Based Imprinted Polymer Hosts with Switchable Anion Preference. *J. Am. Chem. Soc.* **2020**, *142* (26), 11404–11416.

## Appendix - Chapter 2

### 2A.1: Experimental Section

**Synthesis of the N,N-dimethylformamide solvate 4-[[[(4-nitrophenyl)carbamoyl]amino]-N-(pyrimidin-2-yl)benzene-1-sulfonamide (2.1):** 4-Nitrophenyl isocyanate (328 mg, 2 mmol) was added to a well stirred solution of sulfadiazine (501 mg, 2.0 mmol) in DMF (10 ml). The resulting solution was stirred for about 8 hrs. A yellow precipitate was formed (yield 92 %), was dissolved by adding further DMF (5 ml). The solution was kept undisturbed for crystallization and crystals of the N,N-dimethylformamide solvate 4-[[[(4-nitrophenyl)carbamoyl]amino]-N-(pyrimidin-2-yl)benzene-1-sulfonamide was formed after five to six days.

#### Spectral data of solvates, ionic cocrystals and salt:

**(2.1.1):** (yield 84%). IR (neat,  $\text{cm}^{-1}$ ): 3044 (bw), 2813 (w), 1727 (s), 1647 (s), 1576 (s), 1544 (m), 1491 (s), 1439 (m), 1409 (m), 1327 (s), 1244 (s), 1190 (m), 1150 (s), 1091 (s), 939 (s), 845 (m), 795 (m), 737 (m), 706 (m), 638 (m), 561 (s).  $^1\text{H}$ NMR (600 MHz, DMSO- $d_6$ , ppm): 11.67 (bs, 1H), 9.54 (bs, N-H), 9.35 (s, N-H), 8.50- 8.49 (d, J= 5 Hz, 2H) 8.21–8.19 (d, J= 9 Hz, 2H), 7.95 (s, 1H), 7.92–7.91 (d, J=9Hz, 2H), 7.70–7.67 (d, J= 9 Hz, 2H), 7.64–7.63 (d, J=

9 Hz, 2H), 7.04 (t, 1H), 2.89 (s, 3H), 2.73 (s, 3H).  $^{13}\text{C}$  NMR (125 MHz, DMSO- $d_6$ ): 162.4, 151.8, 145.9, 143.2, 141.4, 129.0, 125.2, 117.8, 117.8, 35.8, 30.8).

**(2.1.2):** Isolated yield: 42 %. IR (Neat,  $\text{cm}^{-1}$ ): 1722 (s), 1649 (s), 1581 (s), 1546 (s), 1491 (s), 1443 (s), 1406 (s), 1333 (s), 1298 (m), 1248 (s), 1197 (s), 1149 (s), 1109 (s), 1086 (s), 945 (s), 847 (s), 799 (s), 736 (s), 708 (s), 639 (s), 561 (s).  $^1\text{H}$ NMR (600 MHz, DMSO- $d_6$ , ppm): 11.67 (s, 1H), 9.54 (s, N-H), 9.35 (s, N-H), 8.50- 8.49 (d,  $J = 5$  Hz, 2H) 8.21-8.19 (d,  $J = 9$  Hz, 2H), 7.95 (s, 1H), 7.92-7.91 (d,  $J = 9$  Hz, 2H), 7.70-7.67 (d,  $J = 9$  Hz, 2H), 7.64-7.63 (d,  $J = 9$  Hz, 2H), 7.04 (t, 1H), 2.89 (s, 6H), 2.73 (s, 6H).

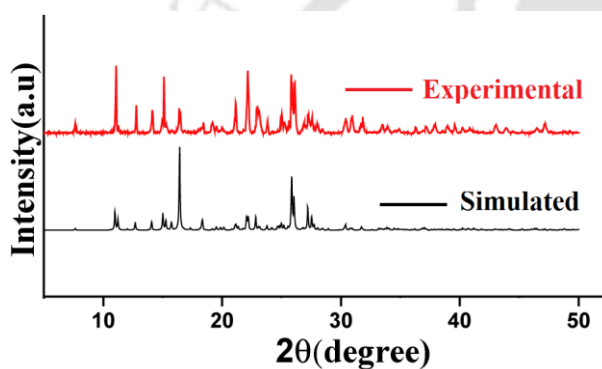
**(2.1.3):** Isolated yield: 42 %. IR (Neat,  $\text{cm}^{-1}$ ): 2958 (m), 2874 (m), 1715 (s), 1578 (s), 1541 (s), 1508 (w), 1491 (s), 1439 (s), 1412 (s), 1335 (s), 1313 (m), 1299 (s), 1283 (w), 1265 (w), 1239 (s), 1198 (s), 1174 (w), 1154 (s), 1108 (w), 1093 (s), 1026 (w), 940 (s), 860 (s), 829 (m), 804 (s), 752 (s), 708 (s), 671 (m), 643 (s).  $^1\text{H}$ NMR (600 MHz, DMSO- $d_6$ ): 11.66 (s, 1H), 10.10 (s, N-H), 9.87 (s, N-H), 8.50- 8.51 (d,  $J = 5$  Hz, 2H) 8.21-8.20 (d,  $J = 9$  Hz, 2H), 7.92-7.91 (d,  $J = 9$  Hz, 2H), 7.70-7.69 (d,  $J = 9$  Hz, 2H), 7.64-7.63 (d,  $J = 9$  Hz, 2H), 7.04 (t, 1H), 0.93 (t, 12H), 1.27-1.33 (m, 8H), 1.53-1.58 (m, 8H), 3.16 (m, 8H).  $^{13}\text{C}$ NMR (125 MHz, DMSO- $d_6$ ): 157.1, 151.9, 146.0, 143.3, 141.3, 133.2, 129.1, 125.3, 117.7, 117.6, 113.0, 57.6, 23.1, 19.3, 13.6.

**(2.1.4):** Isolated yield: 37 %. IR (Neat,  $\text{cm}^{-1}$ ): 3040 (b, w), 2957 (s), 2874 (w), 1712 (s), 1570 (s), 1535 (m), 1491 (s), 1439 (m), 1411 (s), 1336 (s), 1301 (w), 1239 (s), 1195 (s), 1155 (s), 1090 (s), 1022 (m), 938 (s), 857 (s), 800 (s), 746 (s), 707 (s), 671 (w), 640 (s).  $^1\text{H}$  NMR (600 MHz, DMSO- $d_6$ , ppm): 11.67 (s, N-H), 9.62 (s, N-H), 9.43 (s, N-H), 8.51- 8.50 (d,  $J = 5$  Hz, 2H), 8.21-8.20 (d,  $J = 9$  Hz, 2H), 7.92-7.91 (d,  $J = 9$  Hz, 2H), 7.71-7.69 (d,  $J = 10$  Hz, 2H), 7.65-7.63 (d,  $J = 8$  Hz, 2H), 7.04 (t, 1H), 3.16 (m, 8H), 1.53-1.59 (m, 8H), 1.27-1.33 (m, 8H), 0.93 (m, 12H).  $^{13}\text{C}$  NMR (125 MHz, DMSO- $d_6$ , ppm): 157.0, 151.8, 145.9, 143.2, 141.3, 129.8, 129.0, 125.2, 117.8, 117.7, 112.1.

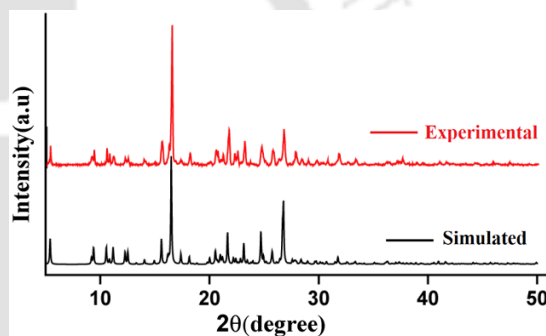
**(2.1.5):** Isolated yield: 39 %. IR Neat,  $\text{cm}^{-1}$ ): 2958 (m), 2873 (w), 1713 (s), 1406 (w), 1582 (w), 1535 (s), 1491 (s), 1406 (s), 1332 (s), 1302 (s), 1237 (s), 1193 (m), 1159 (s), 1105 (s), 1024 (w), 939 (s), 856 (s), 802 (s), 707 (s), 641 (s), 570 (s), 504 (w), 431 (w).  $^1\text{H}$ NMR (600 MHz, DMSO- $d_6$ , ppm): 11.70 (s, N-H), 9.60 (s, N-H), 9.38 (s, N-H), 8.46- 8.45 (d,  $J = 4$  Hz, 2H), 8.21-8.19 (d,  $J = 9$  Hz, 2H), 7.89-7.88 (d,  $J = 8$  Hz, 2H), 7.71-7.69 (d,  $J = 9$  Hz, 2H), 7.62-7.61 (d,  $J = 8$  Hz, 2H), 6.96 (t, 1H  $J = 8$ Hz), 3.16 (m, 8H), 1.53-1.59 (m, 8H), 1.27-1.33

(m, 8H), 0.93 (m, 12H),  $^{13}\text{C}$  NMR (125 MHz, DMSO- $d_6$ , ppm): 157.0, 151.8, 145.9, 143.2, 141.3, 133.2, 129.0, 125.2, 117.8, 117.7, 115.9, 57.6, 23.1, 19.2, 13.5.

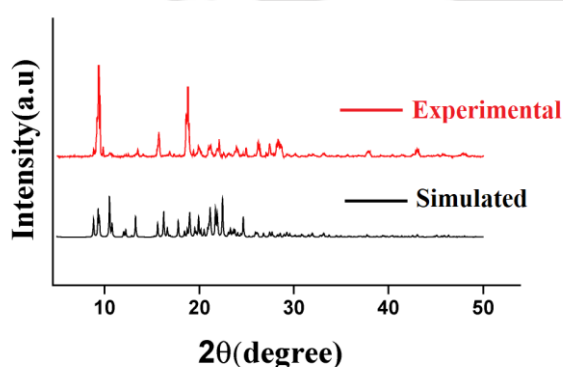
(2.1.6): The isolated yield 65 %. IR (neat,  $\text{cm}^{-1}$ ): 3279 (b, w), 2962 (m), 2872 (s), 1714 (s), 1588 (s), 1539 (s), 1492(s), 1402 (s), 1302 (s), 1262 (m), 1237 (m), 1197 (s), 1174 (s), 1082 (s), 1020 (s), 968 (w), 799 (s), 734 (w), 702 (s), 645 (m).  $^1\text{H}$ NMR (600 MHz, DMSO- $d_6$ , ppm): 9.90 (s, N-H), 9.43 (s, N-H), 8.19 - 8.17 (d,  $J = 10$  Hz, 2H), 8.11 - 8.10 (d,  $J = 5$  Hz, 2H), 7.72-7.69 (dd,  $J = 9$  Hz, 4H) 7.44-7.42 (d,  $J = 8$  Hz, 2H), 6.39 (t,  $J = 8$ Hz, 1H), 3.15 (m, 8H), 1.53 - 1.58 (m, 8H), 1.27 -1.33 (m, 8H), 0.92 (m, 12H).  $^{13}\text{C}$ NMR (125 MHz, DMSO- $d_6$ , ppm): 157.1, 152.0, 146.6, 140.95, 139.9, 127.7, 125.1, 117.6, 117.1, 109.5, 57.52, 23.1, 19.2, 13.5.



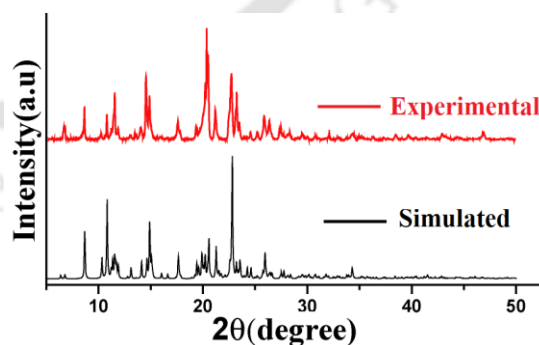
(a)



(b)



(c)



(d)

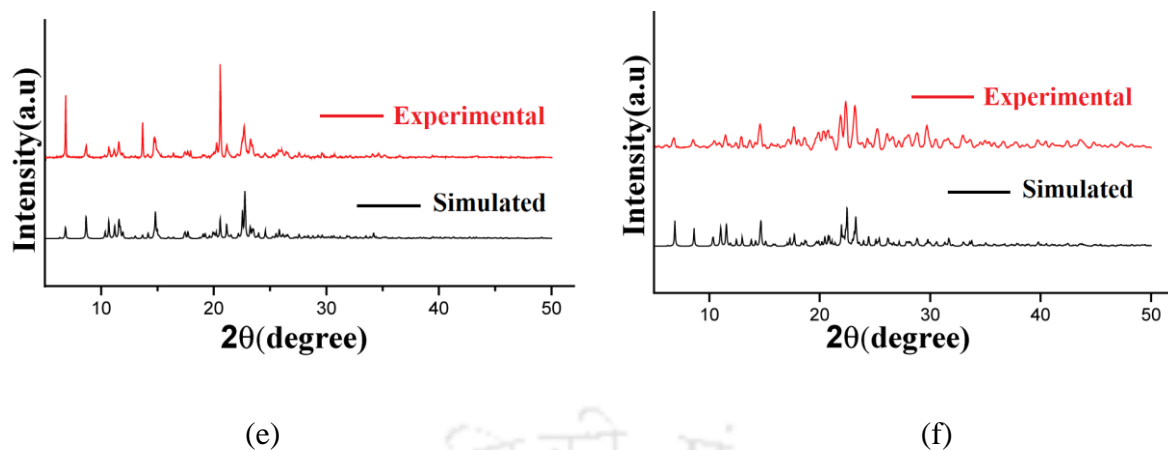


Figure A2.1: Powder X-ray diffraction patterns of the (a) 2.1.1 (b) 2.1.2 (c) 2.1.6 (d) 2.1.3 (e) 2.1.4 (f) 2.1.5

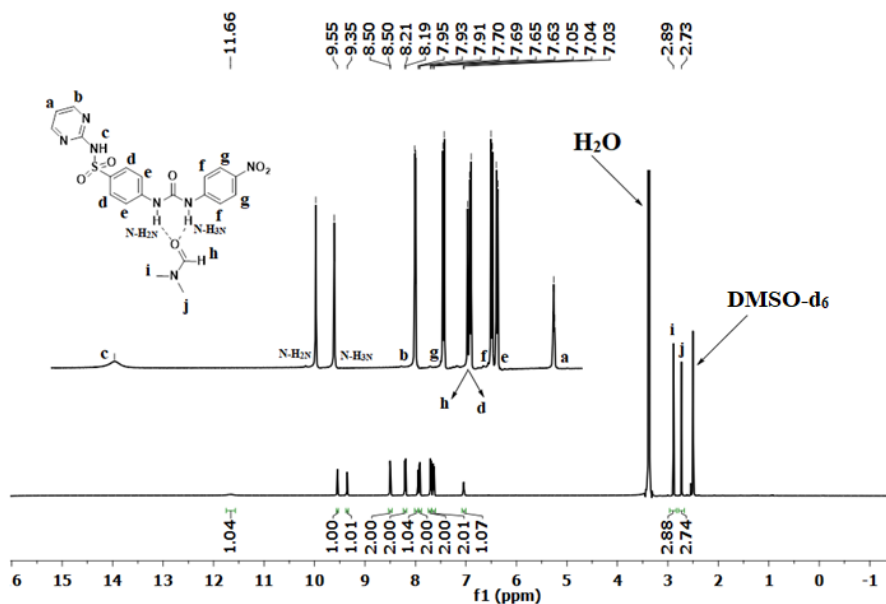


Figure A2.2:  $^1\text{H-NMR}$  (DMSO- $d_6$ , 600 MHz,) spectra of the 2.1.1

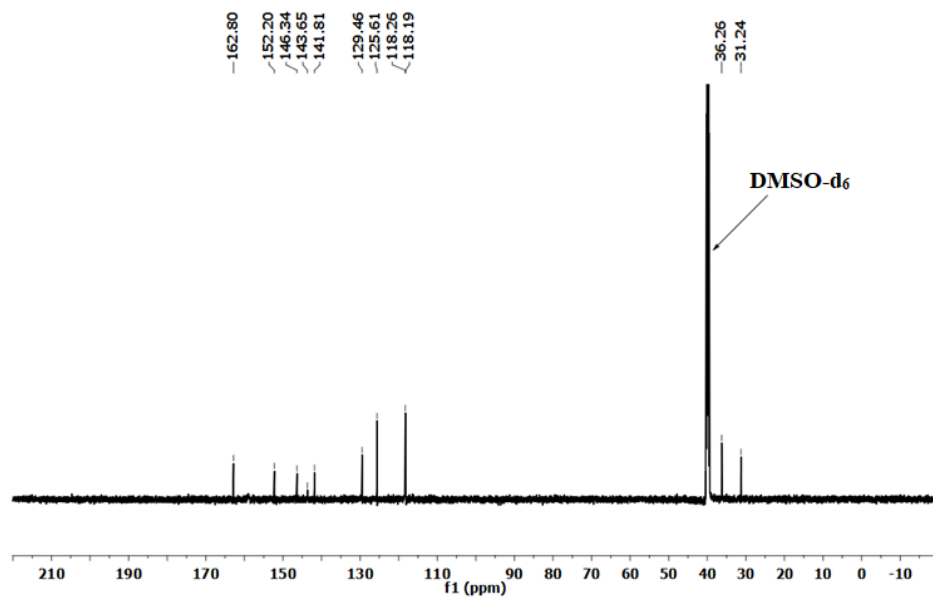


Figure A2.3:  $^{13}\text{C}$ NMR (125 MHz, DMSO- $d_6$ ) spectra of the 2.1.1

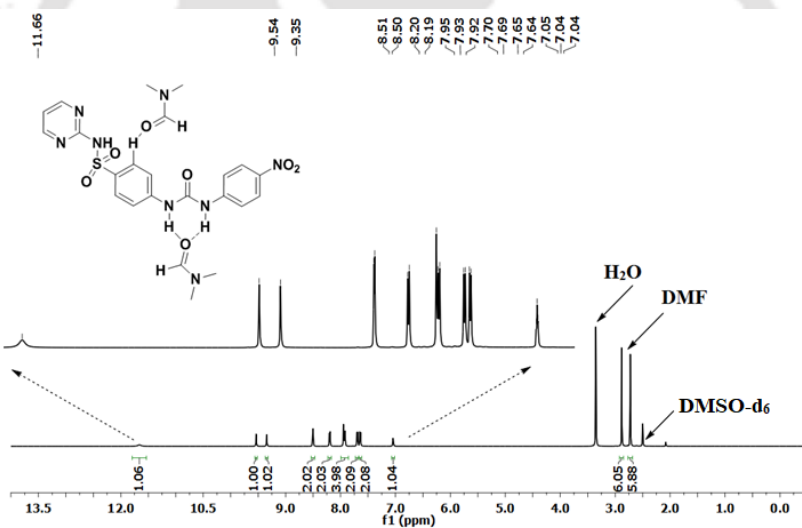


Figure A2.4:  $^1\text{H}$ NMR (600 MHz, DMSO- $d_6$ ) spectrum of the 2.1.2

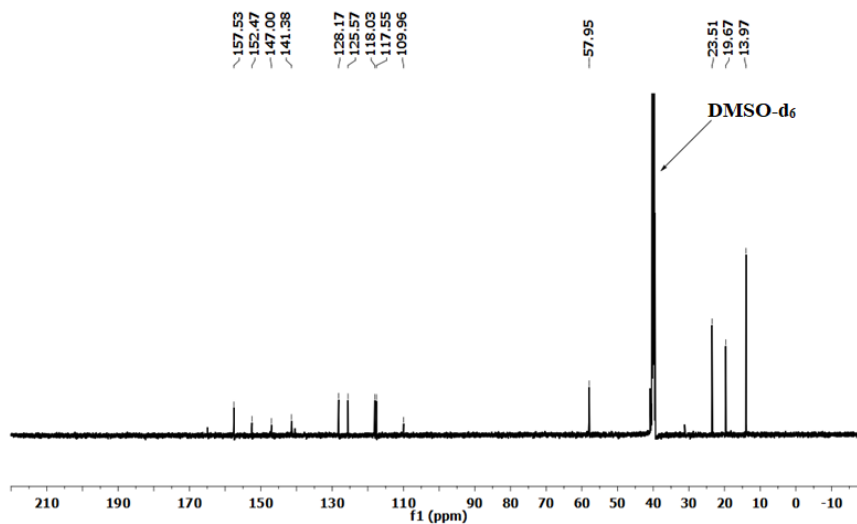


Figure A2.5:  $^{13}\text{C}$ NMR (DMSO- $d_6$ , 125 MHz) spectra of the 2.1.6

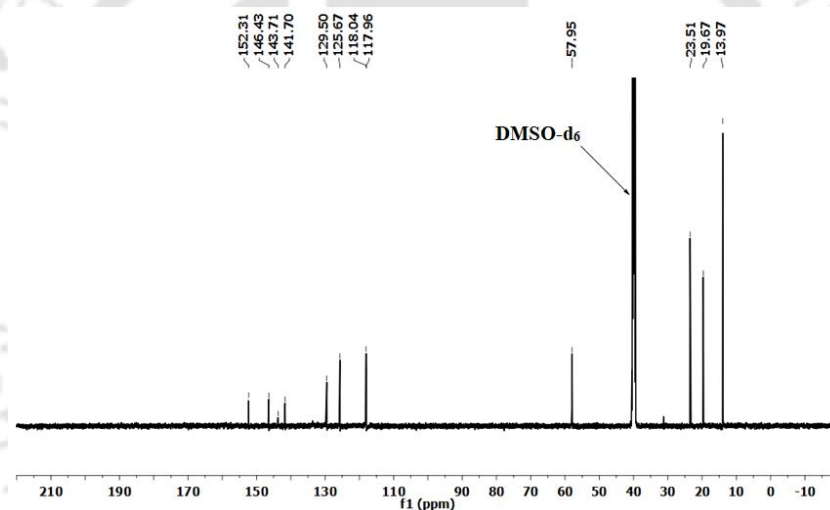
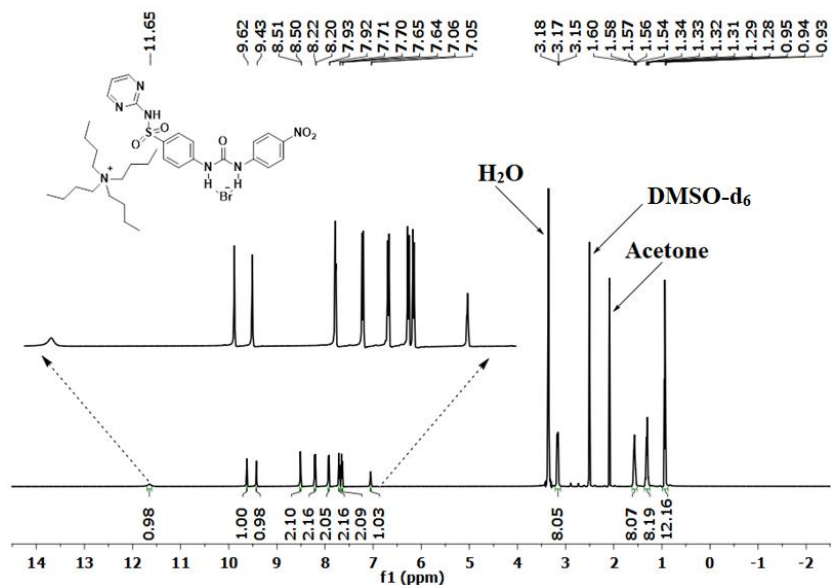
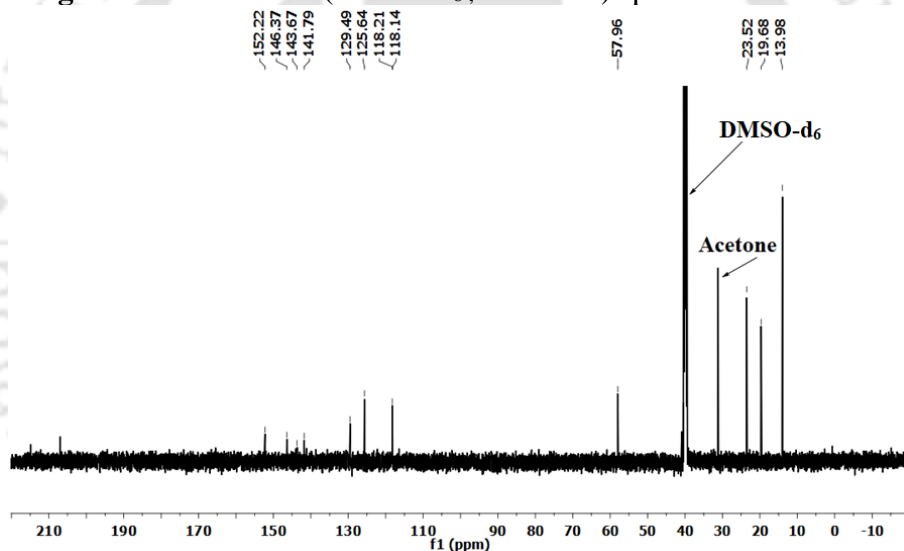


Figure A2.6:  $^{13}\text{C}$ NMR (125 MHz, DMSO- $d_6$ ) spectrum of the 2.1.3



**Figure A2.7:  $^1\text{H}$ NMR (DMSO- $d_6$ , 500 MHz) spectrum of the 2.1.4**



**Figure A2.8:  $^{13}\text{C}$ NMR (600 MHz, DMSO- $d_6$ ) spectrum of the 2.1.4**

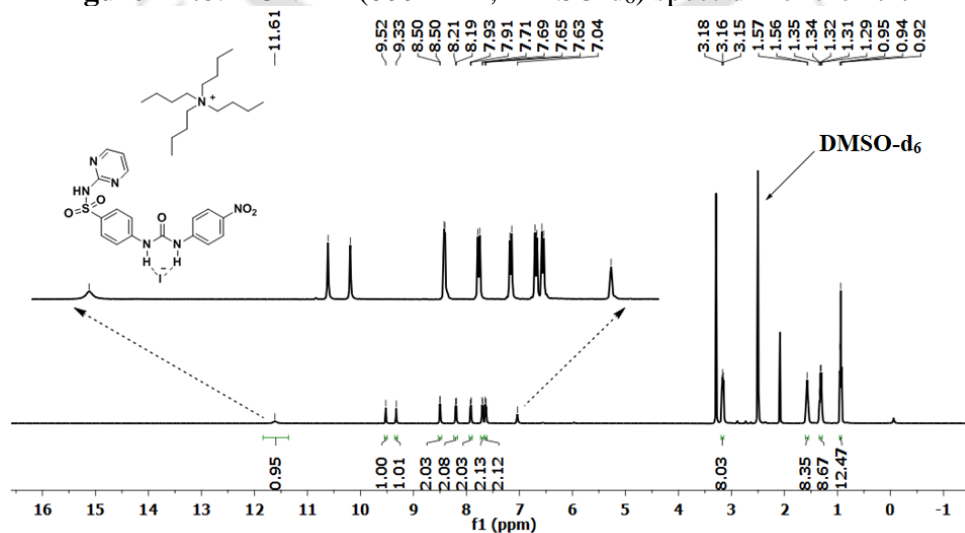
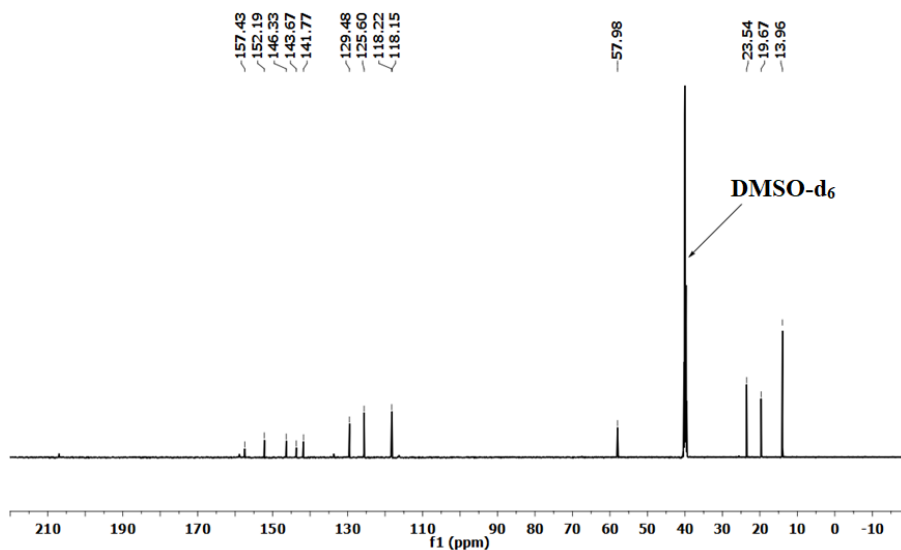
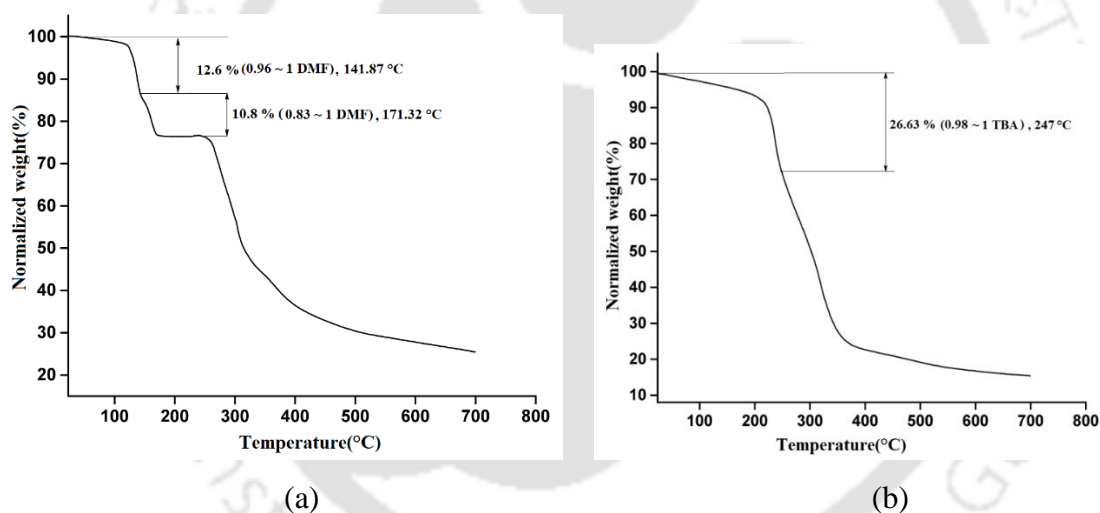
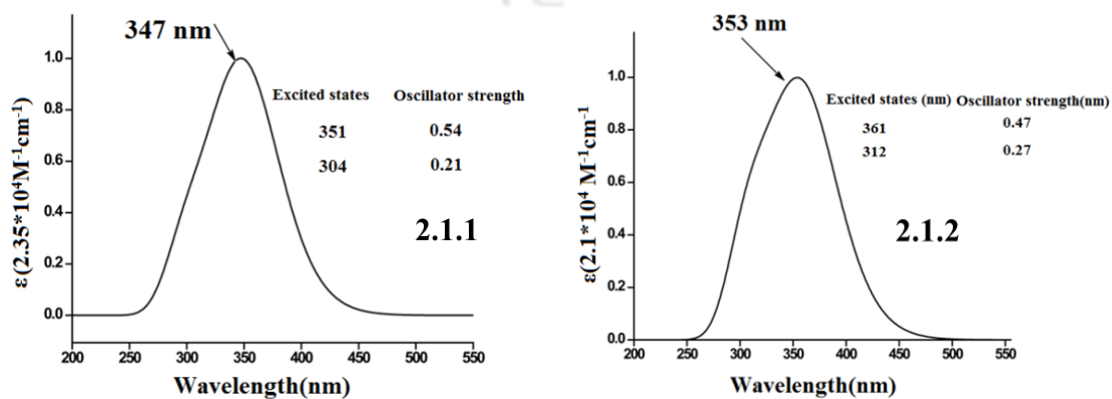
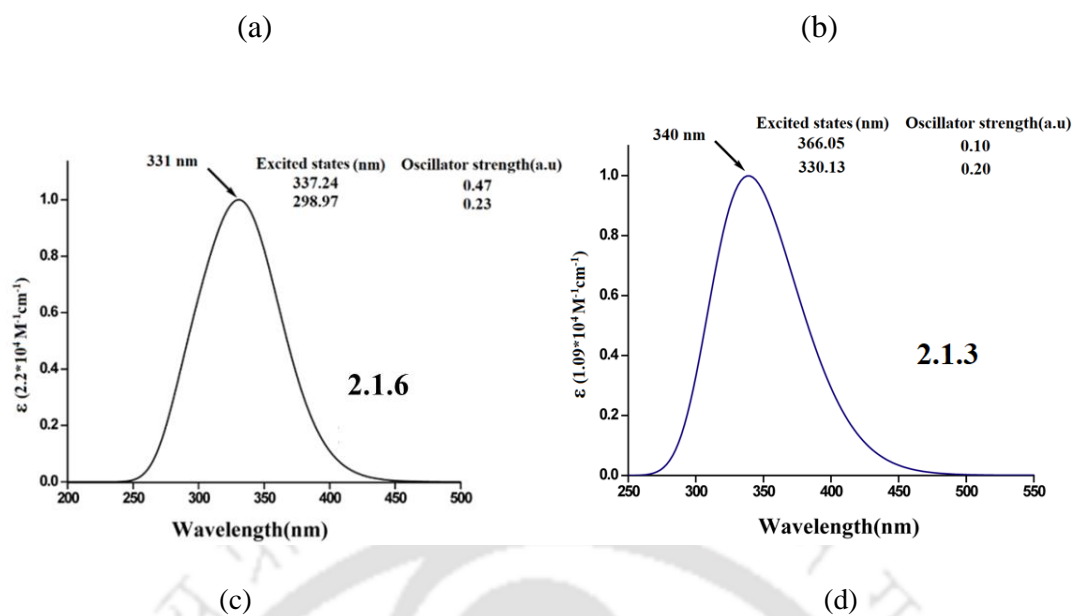


Figure A2.9:  $^1\text{H}$ NMR (500 MHz,  $\text{DMSO-d}_6$ ) spectrum of the **2.1.5**Figure A2.10:  $^{13}\text{C}$ NMR (125MHz,  $\text{DMSO-d}_6$ ) spectrum of the **2.1.5**Figure A2.11: Thermogram of (a) **2.1.2** (1:2 solvate) and (b) **2.1.6** (heating rate  $10^\circ\text{C}/\text{min}$  under nitrogen atmosphere).



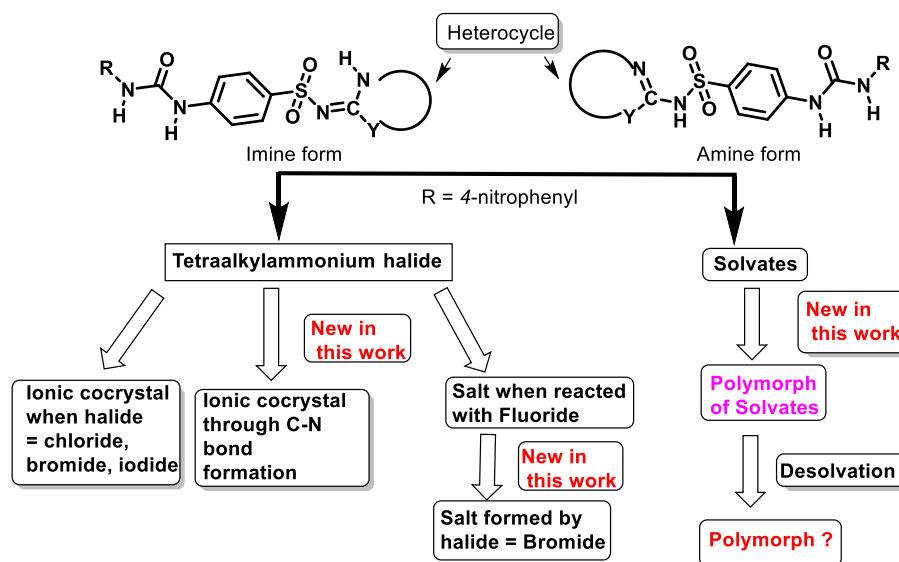
**Figure A2.12:** Molar absorptivity vs wavelength plot calculated by TD-DFT for (a) 2.1.1 (b) 2.1.2 (c) 2.1.6 and (d) 2.1.3.

## Chapter 3

### Polymorphic Solvates, Ionic-cocrystals and C-N Bond Formation to Form Ionic Cocrystal in Sulfamethoxazole and Sulfathiazole Derived Urea

#### 3.1: Introduction

In the previous chapter, we explored the synthesis and structural analyses of two solvates, salt and ionic co-crystal, from a urea molecule derived from sulfadiazine. A notable observation from that is on the presence of synthons in the self-assembly of the **2.1** molecules, which exhibited the ability to accommodate one or two DMF molecules into their interstitial spaces. Based on those observations, the homo-dimeric synthons present in the **2.1** were utilized to prepare ionic co-crystals with tetrabutylammonium halides. Building on these insights, we aimed to further explore similar self-assembly of urea derivatives derived from sulfamethoxazole and sulfathiazole. In this chapter, solvates, ionic cocrystals and anion guided reactivity of sulfa-drug modified urea derivatives, namely, nitrophenylurea N-(5-methyl-1,2-oxazol-3-yl)-4-[[[(4-nitrophenyl)carbamoyl]amino]benzene-1-sulfonamide (**3.1**) and 4-[[[(4-nitrophenyl)carbamoyl]amino]-N-(1,3-thiazol-2(3H)-ylidene)benzene-1-sulfonamide (**3.2**) are presented.



**Scheme 3.1:** A representative outline of the different crystal forms of the sulfa-drug derived urea studied in this chapter.

The two urea derivatives were chosen here has two independent heterocyclic units in their respective structure. Due to the presence of a sulfonamide unit connected to the heterocycle, the heterocyclic part may be either in imine or amine form as illustrated in Scheme 3.1.

Accordingly, this study is directed to study possible polymorphs solvates, cocrystals, in-situ chemical transformations. The compounds were utilized to prepare polymorphic solvates, series of solvates and ionic cocrystals as depicted in Scheme 3.1.

### 3.2: Synthesis and characterization of the urea derivatives 3.1 and 3.2

The nitrophenyl urea derivatives N-(5-methyl-1,2-oxazol-3-yl)-4-[[4-nitrophenyl]carbamoyl]amino}benzene-1-sulfonamide (**3.1**) and the 4-[[4-nitrophenyl]carbamoyl]amino}-N-(1,3-thiazol-2(3H)-ylidene)benzene-1-sulfonamide (**3.2**) were prepared by the reactions of the respective sulfa-drug with the 4-nitrophenylisocyanate at room temperature in dry tetrahydrofuran. Both the reactions yielded a single product, which was further purified by crystallization. The compounds were characterized by  $^1\text{H}$ NMR,  $^{13}\text{C}$ NMR, IR and mass spectroscopy. As an illustration, the  $^1\text{H}$ NMR spectra of compound **3.1** is shown in Fig 3.1.

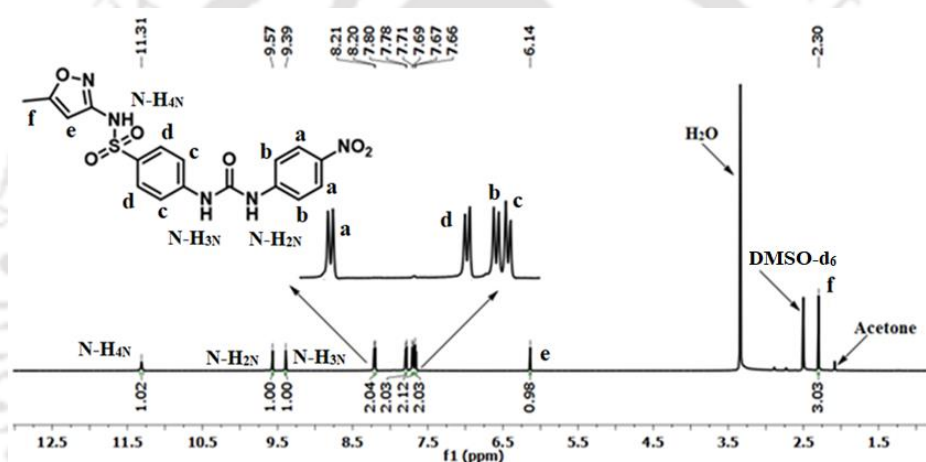


**Figure 3.1:**  $^1\text{H}$ NMR (600 MHz, DMSO- $d_6$ ) spectra of the compound **3.1**.

The compound showed the aromatic peaks designated as *a* and *b* appeared at 8.21-8.20 and 7.71-7.69 ppm, respectively, whereas the proton *c* and *d* appeared at 7.67-7.66 and 7.80-7.78 ppm, respectively. The peaks labeled as *e* and *f* appeared at 6.14 and 2.30 ppm. The chemical shifts of the two protons of the urea portion of the **3.1** were observed at 9.57 and 9.39 ppm, respectively. The N-H of the oxazole part labelled as N- $\text{H}_{4\text{N}}$  appeared at 11.31 ppm. The  $^{13}\text{C}$ NMR of this compound depicted in Fig. A3.3, showed a chemical shift at 170.47 ppm and 12.19 ppm for the carbon of carbonyl of the urea part and methyl of the oxazole part, respectively.

### 3.3: Preparation of solvates of 3.1

Two polymorphs of dimethylformamide (DMF) solvate of **3.1**, abbreviated as **3.1.1** and **3.1.2**, were obtained by crystallization from of a solution of **3.1** in DMF solvent under two different conditions. The solvate **3.1.1** was obtained from a solution of **3.1** in DMF at room

temperature. Whereas the polymorph of the solvate **3.1.2** was crystallized from a solution in DMF, that was heated at 80°C. The distinctions of the polymorphs could be made from the crystal morphologies and from the unit-cell parameters determined by indexing the Laue patterns observed from the X-ray diffraction patterns of the individual crystals. The crystals of the solvate **3.1.1** were belonged to the  $P2_1/n$  space group, and it had a unit cell volume of 2287.4(6) Å<sup>3</sup> and crystal density was 1.424 gcm<sup>-3</sup>. These crystal parameters for the **3.1.2** were  $P\bar{1}$  space group, unit-cell volume of 1135.5(5) Å<sup>3</sup> and crystal density 1.435 gcm<sup>-3</sup>, respectively. We also had limited scopes for crystallization of the **3.1** from solvents other than DMF due to limited solubility, though **3.1** was soluble in DMSO, we could not obtain crystals of solvate with this solvent.

#### 3.4: Structural descriptions of the polymorphs **3.1.1** and **3.1.2**

The asymmetric units of the two polymorphic forms of the DMF-solvate were determined by single crystal structural study is shown in Fig. 3.2. The crystal structures of the two polymorphs have suggested that the solvent DMF in the respective **3.1** in the lattice were different in environments. It was apparent from the observed N4-C14 bond distances in the respective 5-methyl-1,2-oxazole ring of polymorphs. These N4-C14 bond distances were in **3.1.1** was 1.39(6) Å, and for **3.1.2**, it was 1.39(4) Å. These distances were in accordance with the C-NH bonds in related compounds having the amine form and it may be noted that depending on the partner molecules, the imine or amine forms were observed in cocrystals of sulfonamide urea.<sup>1-2</sup> In the present case, the two polymorphs had very similar yet some differences in the conformation, due to conformational adjustments. The conformational adjustments are often observed in flexible molecules in the solid state where the geometry of the molecule is away from an expected conformer.<sup>3-6</sup> The host of the **3.1.1** was hydrogen-bonded by weak C-H...X (O, N) hydrogen bonds, as well as by moderate hydrogen N-H...O bonds (Fig 3.2a). The hydrogen bonds between these molecules along the *ac*-crystallographic plane formed R<sup>2</sup><sub>2</sub>(10) synthons by utilizing C15-H...N5 (*d*<sub>D...A</sub>, 3.198 Å; ∠D-H...A, 161°) and the N4-H...O(SO<sub>2</sub>) (*d*<sub>D...A</sub>, 3.091 Å; ∠D-H...A, 163°) hydrogen bonds as shown in the upper-left portion of the Fig. 3.2a.

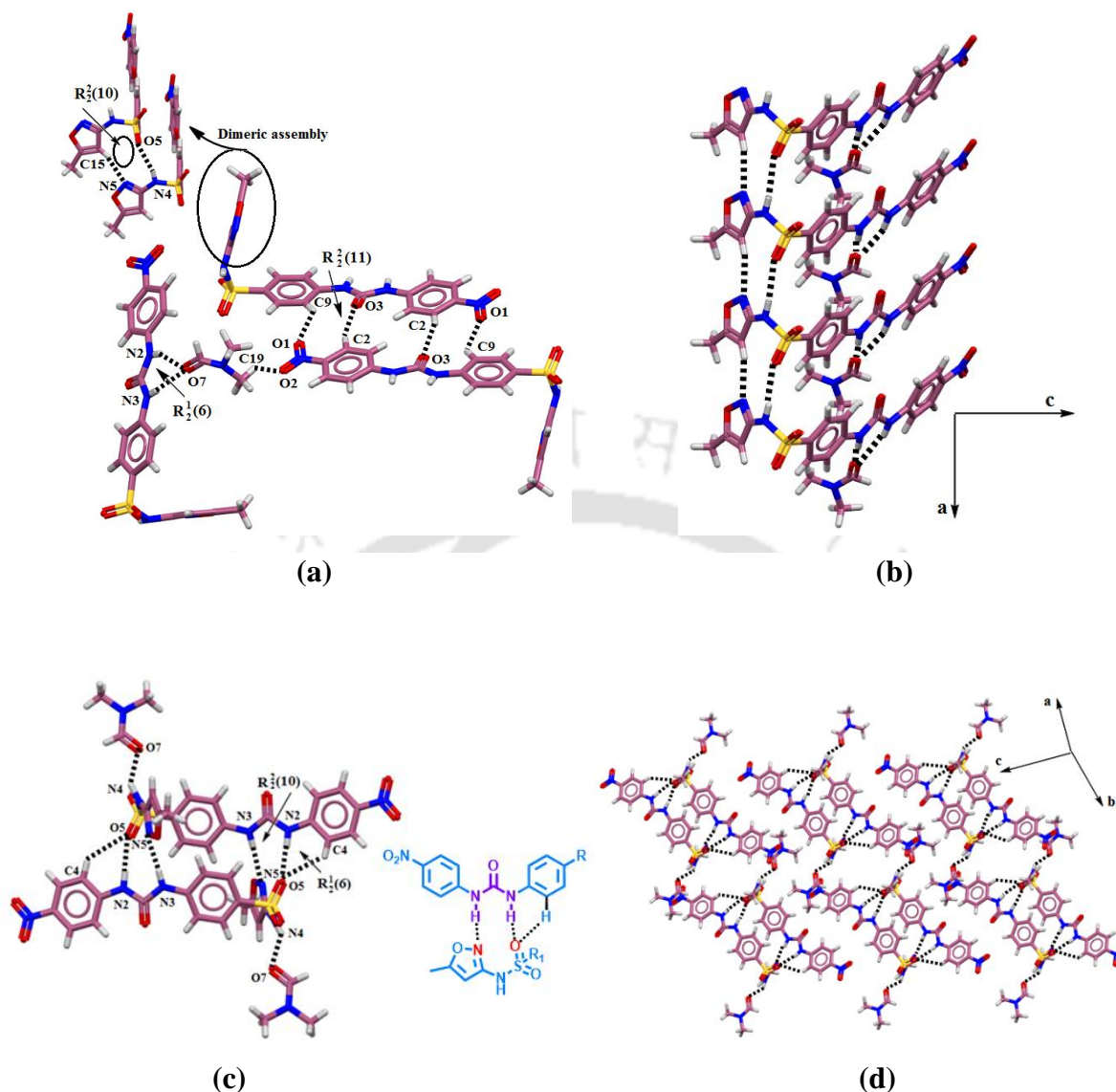


**Figure 3.2:** (a) Hydrogen-bonded assemblies of **3.1.1** (upper-left is showing a homo-dimeric synthon), (b) Assembling of the parent compounds to form chain-like structure. (c) Hydrogen bonded dimers in the assembly of **3.1.2** (drawing on the right side is the chem draw figure of hydrogen bonds of urea) and, (d) assembling of the dimers in **3.1.2**.

Each urea unit of the molecule was holding a DMF molecule by forming bifurcated N-H $\cdots$ O=C hydrogen bonds. The host molecules present in the  $ac$ -crystallographic plane were arranged as head-to-head (considering the thiazole end as the head and the nitro-phenyl end as the tail part of the molecule) arrangements to form hydrogen bonds as illustrated in Fig 3.2b. The host molecules had L-shape geometry; they formed linear chains along the  $a$ -crystallographic axis. These chains were self-assembled, and such self-assemblies were organized in such that the two 5-methyl-1,2-oxazole rings were located parallel to each other

in a stacked manner. Whereas in the case of **3.1.2**, the self-assembly was much different from **3.1.1**. In this case, there were hydrogen-bonded dimeric assemblies, which held two DMF molecules per dimer as illustrated in Fig. 3.2c. These dimers were formed by the hydrogen bonds of N-H of urea moiety with the N-atom of 5-methyl-1,2-oxazole ring of another molecule. One of the oxygen atoms of the sulfonamide group makes a hydrogen bond N2-H $\cdots$ O5<sub>(SO2)</sub> ( $d_{D\cdots A}$ , 2.975 Å;  $\angle D-H\cdots A$ , 148°) by using one of the N-H of urea moiety and formed N3-H $\cdots$ N5 ( $d_{D\cdots A}$ , 3.050 Å;  $\angle D-H\cdots A$ , 174°) hydrogen bond by using another N-H of urea moiety. The dimers had head-to-tail arrangements between two hydrogen-bonding molecules. Thus, the urea portions of the host molecules were not available to form hydrogen bonds with the carbonyl group of the DMF. Whereas, the other polymorph had interactions of the N-H bonds of the urea portion with the DMF. The self-assembly provided a geometrical arrangement to allow the N4-H bond to project away from the dimeric assembly. Hence, the DMF molecules got attached to this N-H bond by forming N4-H $\cdots$ O7 ( $d_{D\cdots A}$ , 2.704 Å;  $\angle D-H\cdots A$ , 139°) hydrogen bonds.

The dimers of both polymorphs were also connected through C-H $\cdots$ O hydrogen bonds, where the oxygen atoms of the urea and the nitro-group acted as hydrogen bond acceptors (Fig. 3.2a). Hydrogen bond parameters of both the solvates are given in Table 3.1.

**Table 3.1:** Hydrogen bond parameters of solvates (**3.1.1** and **3.1.2**)

Solvate	D-H $\cdots$ A (Symmetry)	$d_{D-H}$ (Å)	$d_{H\cdots A}$ (Å)	$d_{D\cdots A}$ (Å)	$\angle D-H\cdots A$ (°)
<b>3.1.1</b>	N(2)-H(2N) $\cdots$ O(7) [1/2-x, 1/2+y, 1/2-z]	0.80(4)	2.15(4)	2.897(6)	155(4)
	N(3)-H(3N) $\cdots$ O(7) [1/2-x, 1/2+y, 1/2-z]	0.77(4)	2.12(4)	2.839(6)	156(4)
	N(4)-H(4N) $\cdots$ O(5) [1+x, y, z]	0.85(4)	2.27(4)	3.091(4)	163(4)
	C(2)-H(2) $\cdots$ O(3) [2-x, 1-y, -z]	0.93	2.56(5)	3.455(5)	161
	C(9)-H(9) $\cdots$ O(1) [2-x, 1-y, -z]	0.93	2.53	3.234(5)	133
	C(15)-H(15) $\cdots$ N(5) [-1+x, y, z]	0.93	2.30	3.198(5)	161
	C(19)-H(19C) $\cdots$ O(2) [-x, 1-y, -z]	0.96	2.37	3.151(19)	138
<b>3.1.2</b>	N(2)-H(2N) $\cdots$ O(5) [-x, 1-y, -z]	0.86	2.21	2.975(3)	148
	N(3)-H(3N) $\cdots$ N(5) [-x, 1-y, -z]	0.86	2.19	3.050(3)	174
	N(4)-H(4N) $\cdots$ O(7) [-1+x, 1+y, z]	0.86	1.99	2.704(3)	139
	C(2)-H(2A) $\cdots$ O(3) [1-x, 1-y, 1-z]	0.93	2.57	3.424(3)	152
	C(15)-H(15) $\cdots$ O(2) [-1+x, 1+y, z]	0.93	2.54	3.331(4)	142

The angle between the planes containing the heterocycle and that of the rest of the molecule in **3.1.1** and **3.1.2** were  $71.81^\circ$  and  $57.10^\circ$ , respectively. The two polymorphs had different synthons and the packing was also different; accordingly, the two forms were synthon polymorphs. These polymorphs were formed as a consequence of synthon competition to form a dimer or monomeric form. The  $\pi$ -stacking contributing to generate synthon-polymorphs, are available in the literature.<sup>7</sup> In the present case, it is a competition of DMF molecule to form a hydrogen bond with the urea moiety and the complete ability to form hydrogen-bonded dimer, are the two apparent factors guiding the formation of the polymorphs. The difference between the assemblies of the polymorphs was that in one case, sulfonamide...5-methyl-1,2-oxazole and urea...DMF synthons were dominant, and in the other case the urea...5-methyl-1,2-oxazole and DMF...amine synthons were dominant. There are relatively lesser numbers of examples of polymorphic cocrystals in literature.<sup>8</sup> There are examples of urea-based hydrates of ionic cocrystals where the synthon polymorph was due to having and not having C-H...O interactions to be dimers or to remain as monomers.<sup>9</sup> The unit-cell volume of the former polymorph was 2.014 times higher than the latter, but the crystal densities of the crystals of the two polymorphs were comparable. Alternatively, it may be suggested that the unit-cell volume of the polymorph possessing the dimer of host in the assembly was twice that of the one with monomers of host assemblies. A recent report has revealed that hexamidine diisethionate of which two polymorphic dehydrates that may be inter-converted to each other at low temperature.<sup>10</sup> In that report, the cell axes of the unit-cell of the polymorphs were about twice as that of the others observed, and the polymorphs were interconvertible. The reversible transformation between the two forms in that example was possible as the host molecules had a nominal difference in showing just an interplanar angle difference of  $2.53(7)^\circ$ . Hence in that example, the conformational change could be easily achieved. But the situation in our present examples of the synthon polymorphs is far apart from those examples. No thermal transformation between the two forms was observed. This is attributed to the independent synthons involved in the two polymorphs. A thermal inter-conversion would require significant hydrogen-bond reorganization and orientation changes among the host molecules if they were to undergo a transition from one to another.

### **3.5: Crystal morphologies, IR and thermal studies of the polymorphs**

The crystal morphologies of the two polymorphs were clearly distinguishable as evident in their respective SEM images (Fig.3.3a, b). The **3.1.1** had flack-like morphology of  $20\mu\text{m}$  average dimensions, whereas a relatively smaller cube-like morphology of the crystals

( $\sim 2\mu\text{m}$ ) was observed in the case of the other polymorph. The Bravais, Friedel, Donnay, and Harker crystal morphology was simulated and these are shown in Fig. 3.3c and 3.3d. The simulated morphologies suggested that **3.1.1** to adopt hexagonal crystal faces, whereas a cubical growth for **3.1.2** was seen.

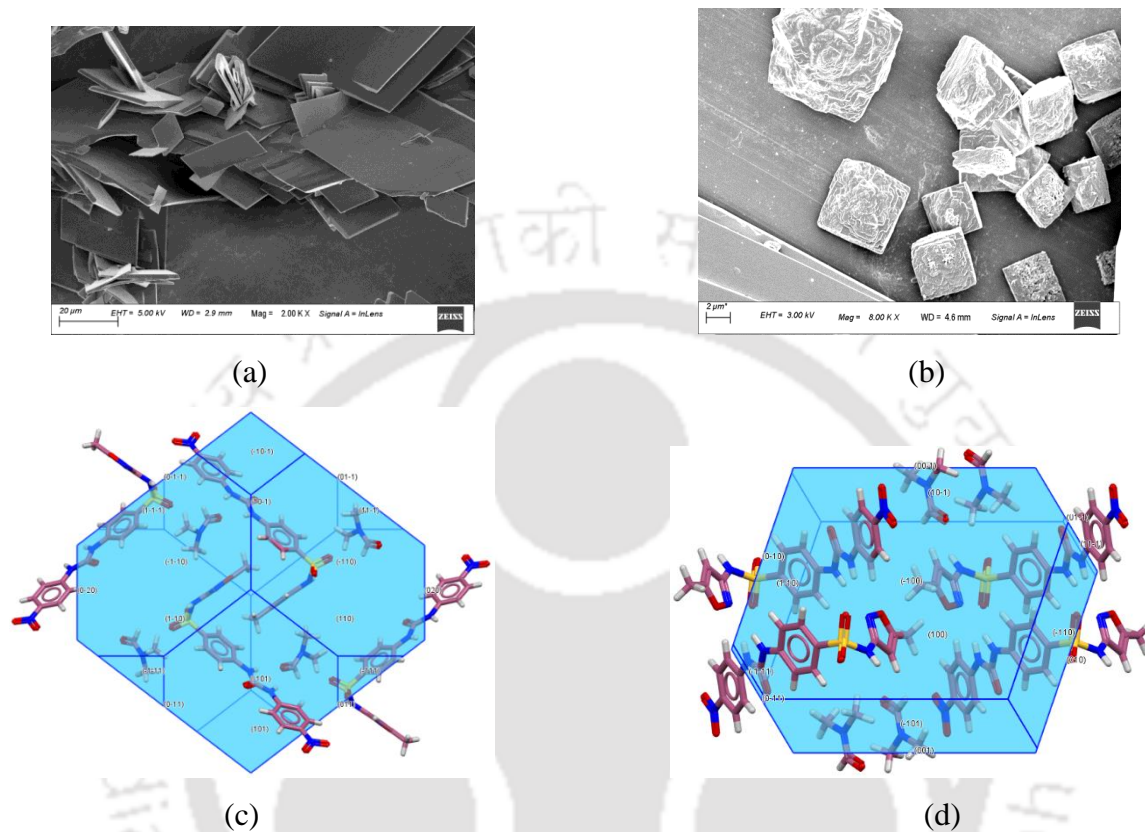


**Figure 3.3:** (a) and (b) are the scanning electron microscopic images of the solvates **3.1.1** and **3.1.2** respectively. (c) and (d) are the Bravais, Friedel, Donnay and Harker (BFDH) crystal morphologies of the **3.1.1** and **3.1.2** respectively.

We found that the host molecules in each polymorph were similar but not identical; the overlay of the two host molecules was not superimposable (Fig. 3.4a). The experimentally determined powder-XRD patterns of the two samples (Fig. 3.4b) were distinguishable but had the matching diffraction patterns as per the simulated PXRD patterns for the respective crystallographic information file. The IR spectra of the two polymorphic solvates had a close resemblance as shown in Fig 3.4c. A difference was noticed in the sharp S=O stretching appearing at  $1162\text{ cm}^{-1}$  and  $1149\text{ cm}^{-1}$  for **3.1.1** and for **3.1.2**, with a weak S=O stretch at  $1177\text{ cm}^{-1}$  and a sharp stretch at  $1163\text{ cm}^{-1}$ . The S=O stretching was split as both the S=O bonds participated in hydrogen bonds of the dimeric assembly in this case. Hirshfeld surface analyses revealed the contact points and showed the differences in the synthons (Fig. 3.18).

The DSC of the polymorphs showed that **3.1.1** lost DMF at 166°C and decomposed at 266°C whereas the **3.1.2** lost DMF at 148 °C and decomposed at 257 °C. The de-solvation temperatures, as well as the decomposition temperatures, were confirmed by recording thermogravimetry of the samples (Fig. A3.15). The thermogravimetry revealed that the individual polymorphic cocrystal lost one DMF per molecule of the solvate in the specified temperature as observed in DSC (Fig. 3.4d). We examined the de-solvated samples prepared by independently heating the respective sample of the polymorph. The powder XRD patterns of the two de-solvated samples were identical (Fig 3.4b) and indicated that they yielded a common form after the loss of solvents. In general, the de-solvation processes are known to cause conformational changes in flexible hosts,<sup>6</sup> leading to a change in the packing from the solvated form. The difference in temperature of the de-solvation of the two polymorphic solvates was 24 °C (~ 0.2 kJ/mol).

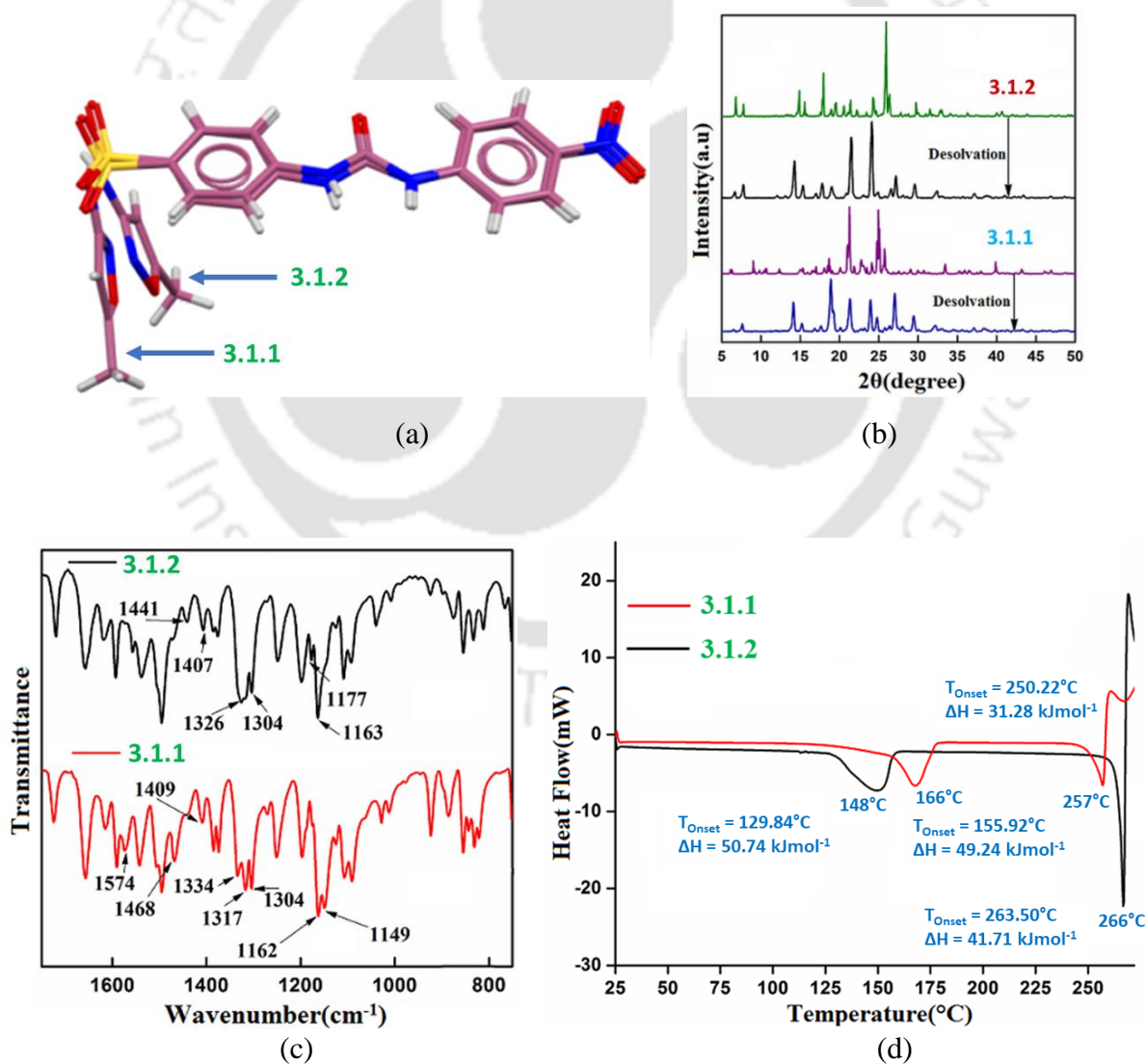


**Figure 3.4.** (a) Powder X-ray diffraction patterns, and (b) FT-IR spectrum of **3.1.1** and **3.1.2**; and (c) Differential scanning calorimetry (heating rate 10° C/min under nitrogen atmosphere) (d) The overlaid diagram of the hosts in the polymorph **3.1.1** and **3.1.2**.

The enthalpy changes for the de-solvation process of the two polymorphs **3.1.1** and **3.1.2** were 49.24 kJ/mole and 50.74 kJ per mole respectively. Though the enthalpy difference was small, de-solvation required thermal energy to release the DMF by heating the individual polymorph till the de-solvation temperatures were around 148°C and 162.59 °C respectively. The urea part of polymorph **3.1.1** had hydrogen-bonded to DMF through NHs of the urea part, whereas, in polymorph **3.1.2** the DMF molecules were in interstitial; hence, those molecules were lost on heating at a relatively lower temperature than the former polymorph. The thermal energy was provided by external heating to reach the de-solvation temperatures, disrupted the weak interactions originally present in the two polymorphs and caused the reorganization of weak interactions to form a common de-solvated form. The urea-based compounds without a solvent generally have urea-carbonyl tapes to meet the norms of Etter's rule.<sup>11</sup> In the present case, both the polymorphs were transformed to a thermodynamically favorable form of the de-solvate. In literature, the de-solvation of a series of solvates of 2,4,6-triethyl-1,3,5-tris(phenoxyethyl)-benzene showed that the solvates with a similar packing resulted in a common de-solvated polymorph. Whereas the one having a dissimilar packing yielded a different form.<sup>12</sup> In the present case, the two solvates had distinct packing patterns, yet they yielded a common form upon de-solvation, these observations pointed out that there were hydrogen bond reorganizations during the course of release of the solvent molecules from the polymorphs to provide the stable form.

### 3.6: The Optimized energy calculation

The energy of the different forms of host found in the polymorphs and the hydrogen-bonded dimers of the hosts in the two polymorphs of the DMF-solvate were calculated by DFT at B3LYP level with 6-31+G (d, p) basis set. The host molecule of the **3.1.2** had 3.68 kJ/mol less energy than the **3.1.1** (Fig. 3.5a). Analogously, the discrete solvated host of the polymorph **3.1.2** was more stable than the **3.1.1** by energy 23.05 KJ/mol (Fig. 3.5b). The energy of the H-bonded dimers comprising of the sulfonamide...5-methyl-1,2-oxazole synthon of the two polymorph **3.1.1** and urea...5-methyl-1,2-oxazole synthon present in **3.1.2** were calculated. The energy of the H-bonded dimer in **3.1.1** was lesser by 55.53 kJ/mol than the dimer in **3.1.2** (Fig. 3.5c). Hence, the relative energies were in a reverse order in the dimers than the difference between the monomers of the respective polymorphs. This

suggested that the dimeric assemblies contributed to the higher stability of **3.1.1** over the desolvated form of **3.1.2**. Furthermore, the de-solvation temperature observed in TG –DSC analysis was higher than for **3.1.2**. Hence, **3.1.1** had higher thermal stability, and theoretical analyses suggested a substantial contribution to the stability from the sulfonamide...5-methyl-1,2-oxazole synthon in the lattice.

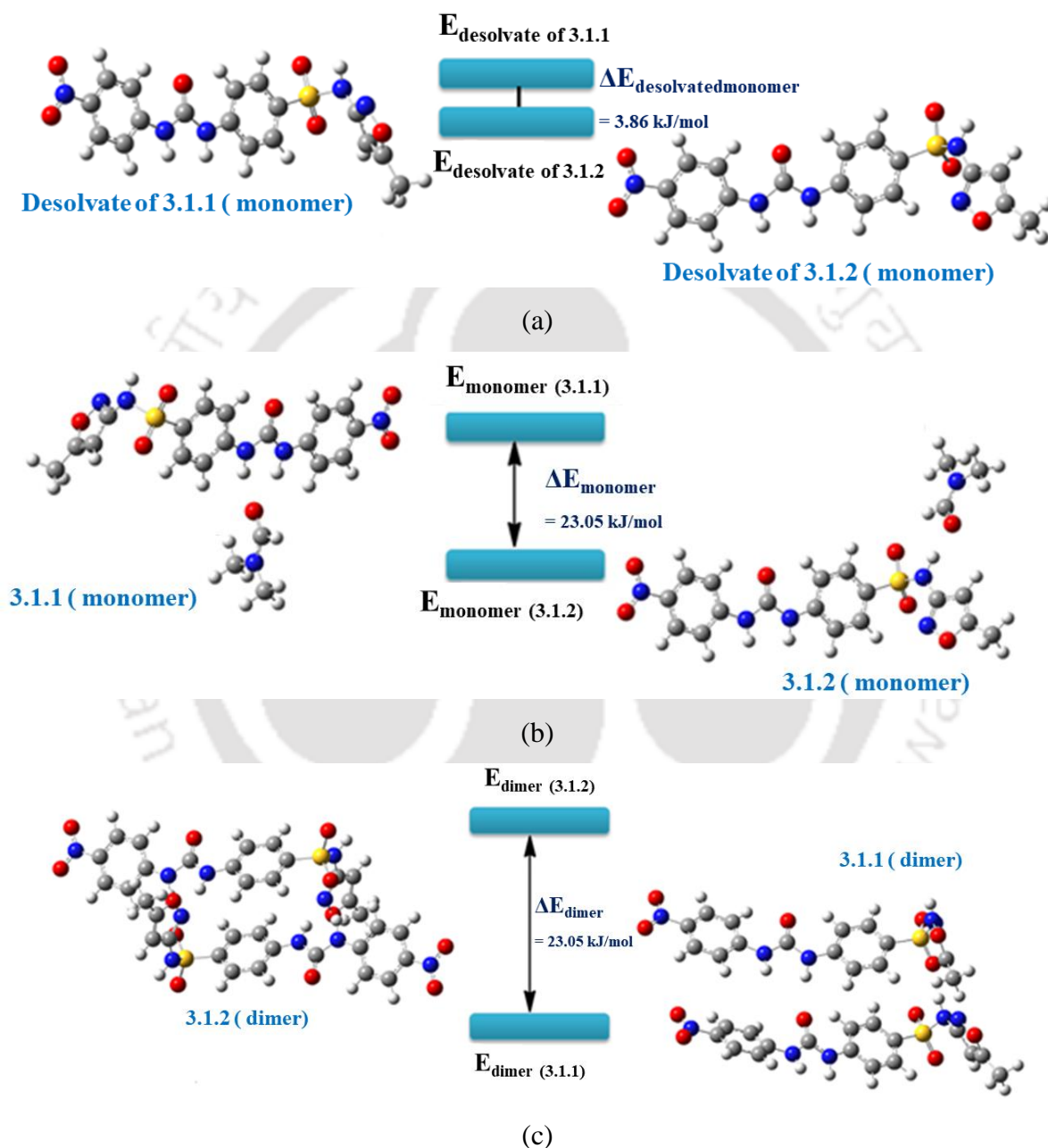


**Figure 3.5:** Energy differences between the optimized structures calculated by DFT using B3LYP level with 6-31+G (d, p) basis set by (a) the host molecules, (b) solvated host molecules and (c) dimers of the polymorphs **3.1.1** and **3.1.2**.

### 3.7: Study on the different Supramolecular adducts of 3.1 with tetrabutylammonium halides

In the last chapter, we presented ionic cocrystals with three tetrabutylammonium halides with a urea-based receptor.<sup>13</sup> The results from similar attempts to prepare the ionic cocrystals with tetrabutylammonium halides (TBAX, X = Cl, Br, I) with **3.1** were different from that study. The quaternary ammonium fluoride generally deprotonates basic N-H components of urea-derived compounds.<sup>14</sup> Hence, as expected the reaction of **3.1** with TBAF yielded the corresponding salt **3.1.3**. However, we found that the same crystalline salt was also obtained from the reaction of **3.1** with TBABr in DMF at room temperature for several days. It was an exceptional observation to have formed a salt upon treatment of the **3.1** with TBABr.

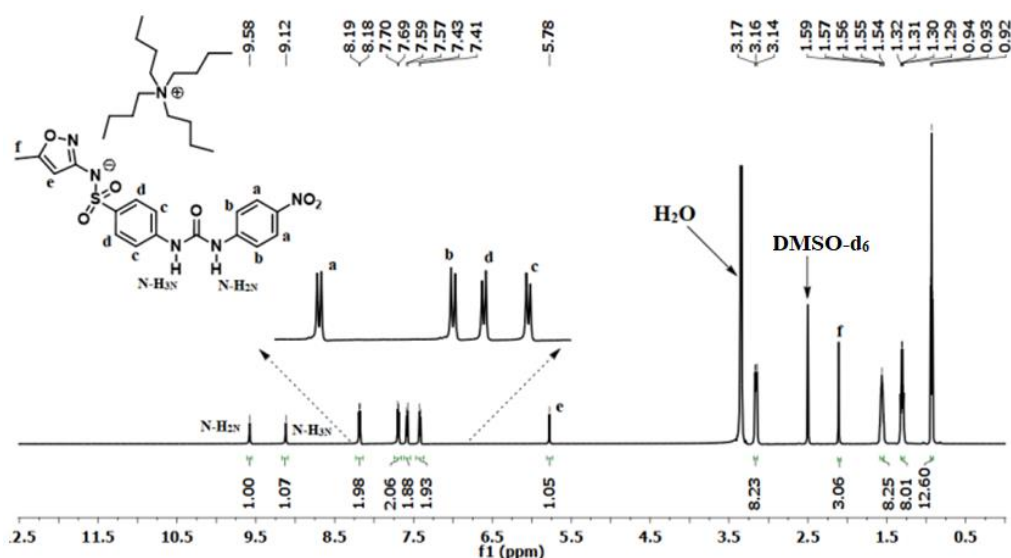
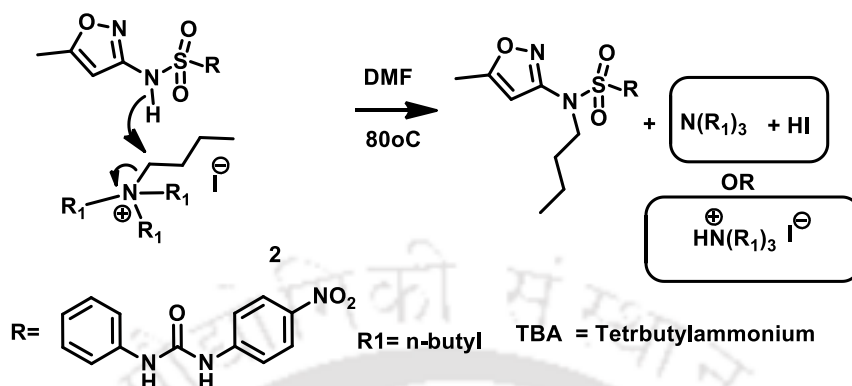


**Figure 3.6:** <sup>1</sup>H NMR (DMSO-d<sub>6</sub>, 600 MHz) spectra of the **3.1.3**.

The <sup>1</sup>H NMR spectra of the compound **3.1.3** is depicted in Fig 3.6. The compound showed the aromatic peaks designated as *a* and *b* appeared at 8.19–8.18 and 7.70–7.69 ppm respectively, whereas the proton *c* and *d* appeared at 7.43–7.41 and 7.59–7.57 ppm, respectively. The peaks labelled as *e* and *f* showed chemical shifts at 5.78 and 2.29 ppm, respectively. The chemical shifts of the two protons of the urea portion of the **3.1.3** were observed at 9.58 and 9.12 ppm respectively.

Attempted crystallization of ionic cocrystal of **3.1** with TBACl was not successful, and the host precipitated out from the solution upon concentration. But, to our surprise, a hot solution (80°C) of **3.1** with TBAI yielded an ionic cocrystal with tetrabutylammonium iodide with a chemically modified form of **3.1**. In this case, the **3.1** was N-butylated by forming a C–N bond and the **3.1.4** (butyl-**3.1**) was formed *in situ* and acted as the host. This was attributed to

TBAI formation of butyl iodide and tributylamine *in situ* leading to the formation of **3.1.4**. Such C-N bond-forming reactions do not take place under ordinary conditions, which is an unconventional observation. A Plausible mechanism is depicted in Scheme 3.2.



**Scheme 3.2:** A plausible mechanism of the C-N bond formation from reaction of **3.1** with TBAI.

The assignment of the butyl peaks of **3.1.4** is marked in Fig 3.7. The crystal was further characterized by mass spectra (Fig. A3.9), single-crystal XRD, and powder XRD (Fig. A3.1d). The  $^1\text{H-NMR}$  has established clearly the N-butylated product by showing the adequate integration for the distinguishable N-butyl group on the host from the N-butyl groups in the cation.

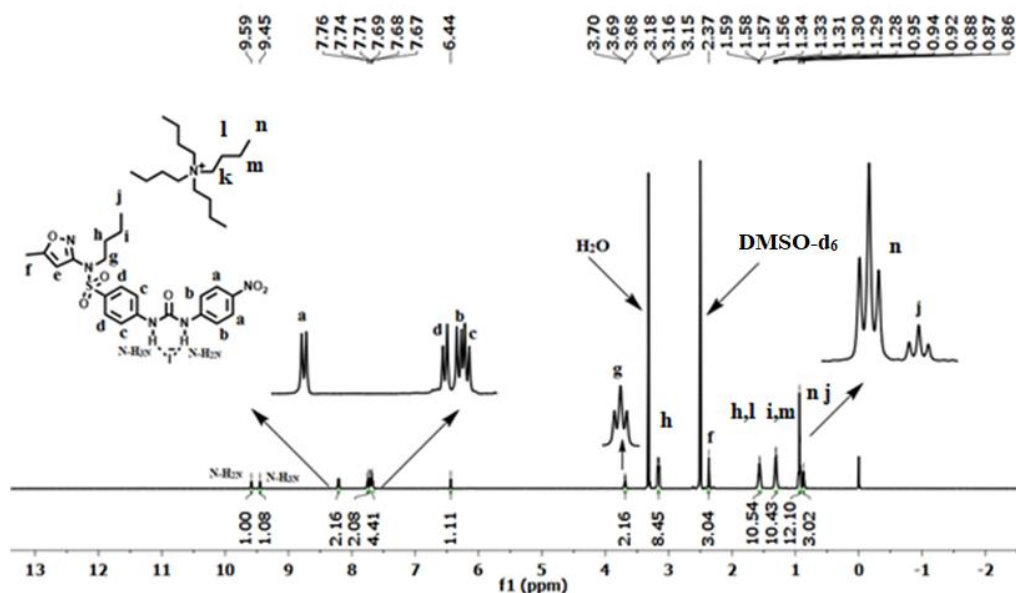


**Figure 3.7:**  $^1\text{H-NMR}$  (DMSO- $d_6$ , 600 MHz) spectra of the **3.1.4**.

The  $^1\text{H-NMR}$  spectra of the compound **3.1.4** is depicted in Fig 3.7. The proton labelled as *a* and *b* showed chemical shifts at 7.76-7.74 and 8.21-8.20 ppm, respectively, while the proton labelled as *c* and *d* appeared at 7.71-7.69 and 7.68-7.67 ppm, respectively. The proton

labelled as *e* and *f* from 5-methyl-1,2-oxazole part displayed peaks at 6.44 and 2.37 ppm respectively. The proton labelled as *g* and *j* from the butylated part appeared at 3.70-3.68 and 0.88-0.86 ppm respectively.

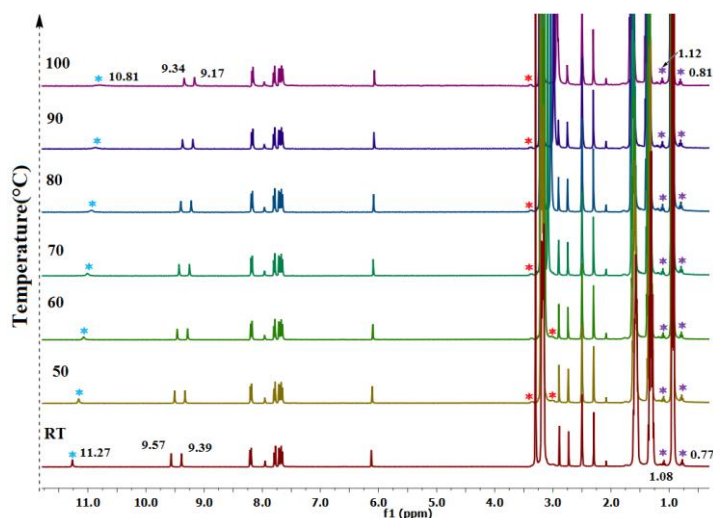


**Figure 3.8:** Variable temperature  $^1\text{H}$ NMR spectra (DMSO- $d_6$ , 600 MHz) of **3.1.1** with 10 equivalents of **TBAI** showing C-N bond formation to form the **3.1.4** (In situ in the reaction mixture)

A temperature-dependent  $^1\text{H}$ NMR study was carried out (Fig. 3.8) to check the course of the reaction. The C-N bond formation was clearly seen from such a study, carried out in the temperature varied from 25°C to 100°C, as new sets of signals for the protons  $-\text{NCH}_2-$  and  $-\text{CH}_3-$  of the *in-situ* formed N-butyl group developed as the butyl as well as for tributyl amine generated *in situ* as the temperature was increased. The integration of the proton NMR signal appearing at 11.37 ppm for the NH group of the heterocycle decreased and was shifted with the progress of the N-butylation reaction upon increasing the temperature. As per the structure of the salt shown in Scheme 3.2, there are three types of butyl environments from the three compounds in the reaction mixture which are  $\text{N}^+(\text{CH}_2^{\text{a}}\text{CH}_2^{\text{b}}\text{CH}_2^{\text{c}}\text{CH}_3^{\text{d}})_4\text{I}$ ,  $(\text{CH}_2^{\text{a}'}\text{CH}_2^{\text{b}'}\text{CH}_2^{\text{c}'}\text{CH}_3^{\text{d}'})_3\text{-3.1}$  and  $\text{N}(\text{CH}_2^{\text{a}''}\text{CH}_2^{\text{b}''}\text{CH}_2^{\text{c}''}\text{CH}_3^{\text{d}'})_3$ . The protons from the  $\text{CH}_2^{\text{b}}\text{CH}_2^{\text{c}}$ ,  $\text{CH}_2^{\text{b}'}\text{CH}_2^{\text{c}'}$ ,  $\text{CH}_2^{\text{b}''}\text{CH}_2^{\text{c}''}$  are indistinguishable as they overlap each other; the peaks with \* (red asterisk) are from  $\text{CH}_2^{\text{a}'}$  and  $\text{CH}_2^{\text{a}''}$  and with \* (violet asterisk) are from  $\text{CH}_3^{\text{d}'}$  and  $\text{CH}_3^{\text{d}''}$  respectively. The peak at 11.17, marked with \* (blue asterisk) is from the N-H next to the heterocycle. This NMR study on the kinetic of the reaction showed in intermediate formation during the C-N bond formation, and it was a process leading to the single product as depicted in Scheme 3.2.

### 3.8: Structural descriptions of salt **3.1.3** and butylated-**3.1** (**3.1.4**)

The structures of both the salt **3.1.3** and the butylated product **3.1.4** were determined by single-crystal X-ray diffraction analysis. The crystals of both **3.1.3** and **3.1.4** belonged to the  $P\bar{1}$ , space group with  $Z = 2$ . The unit cell volume of **3.1.3** was  $1751.7(7) \text{ \AA}^3$ , and the crystal density was  $1.249 \text{ g/cm}^3$  and the same values for **3.1.4** were  $2148.4(5) \text{ \AA}^3$  and  $1.303 \text{ g/cm}^3$  respectively. The self-assembly of the salt **3.1.3** included hydrogen-bonded dimers formed by two N-Hs of the urea part with the ring N-atom of the 5-methyl-1,2-oxazole part of the other participating molecule. The dimers were inter-linked by weak C-H $\cdots$ O interactions between the S=O and N=O bonds of two molecules with two independent C-H bonds of the methyl groups of the 5-methyl-1,2-oxazoles. As in the ionic cocrystal, the TBA-cations were also held in the spaces at the junction of the two dimers (Fig. 3.9a). The cations were linked to the anions by C-H $\cdots$ O hydrogen bond and C-H $\cdots$  $\pi$  interactions.

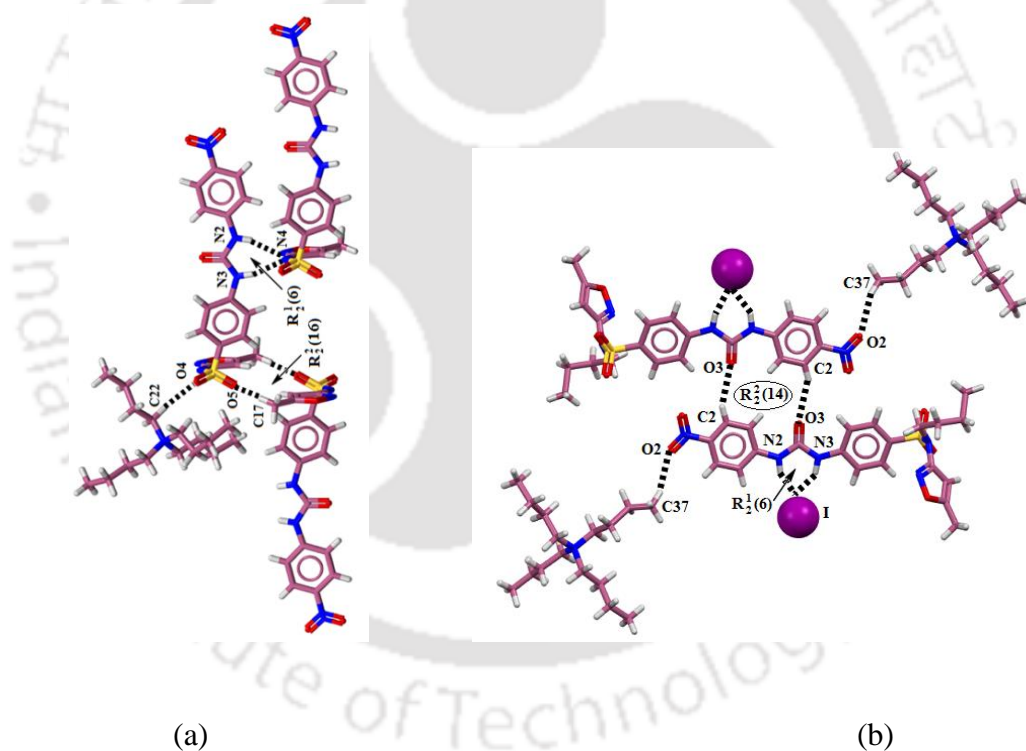
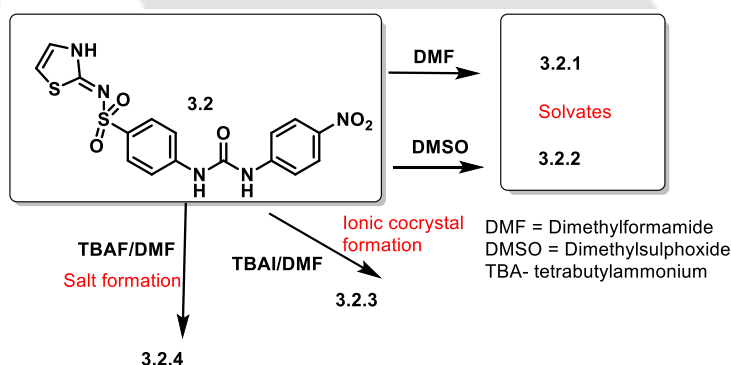


**Figure 3.9:** A portion of the hydrogen-bonded assembly of the (a) **3.1.4** and (b) **3.1.3** showing some prominent hydrogen bonds.

The host molecules accommodated the iodide anion by bifurcated hydrogen bonds of the two N-H bonds of the urea part with the iodide. Due to N-butylation, the self-assembly did not possess the dimeric synthon as seen in **3.1.2**. There were bifurcated hydrogen bonds with iodide. Instead, the two molecules of the host were present in a head-to-tail manner and assembled through C-H $\cdots$ O interactions as illustrated in Fig. 3.9b. The cations were held at

the two ends of such dimers where the hydrophobic parts were located. The inability of the **3.1** to form the ionic cocrystals with their original form as compared to the analogous 4-[[4-(4-nitrophenyl)carbamoyl]amino}-N-(pyrimidin-2-yl)benzene-1-sulfonamide (**2.1**) that was reported earlier<sup>13</sup> was attributed to the different dimeric synthon in each case. Though the compounds had an L-like shaped geometry, the dimeric synthon of **3.1** was the urea-5-methyl-1,2-oxazole based synthon, which broke down to form hydrogen bonds with a halide (the solution NMR study also supports this, which is discussed separately). In the earlier report **2.1**, the packing of dimeric synthons provided enough spaces to accommodate the ionic parts, whereas to provide space for the ions in the case of **3.1**, the host underwent modification by N-butylation to have a bigger domain of the hydrophobic part. This explanation is based on the fact that in many ionic cocrystals, to accommodate the hydrophobic part of the tetrabutylammonium cation the host adopts different spatial arrangements and self-assembles itself or with another component.<sup>15-17</sup>

### 3.9: Solvates, ionic cocrystal and salt of **3.2**



**Scheme 3.3:** The solvates, ionic cocrystal and salt of **3.2**

To delve deeper into the study of self-assemblies akin to those formed by **3.1**, our research was extended to prepare the solvates of dimethyl sulfoxide, dimethylformamide, and the ionic co-crystal with tetrabutylammonium salts of the 4-[[4-(4-nitrophenyl)carbamoyl]amino}-N-(1,3-thiazol-2(3H)-ylidene)benzene-1-sulfonamide (**3.2**). The exploration leading to the preparation of different forms of **3.2** is depicted in Scheme 3.3.

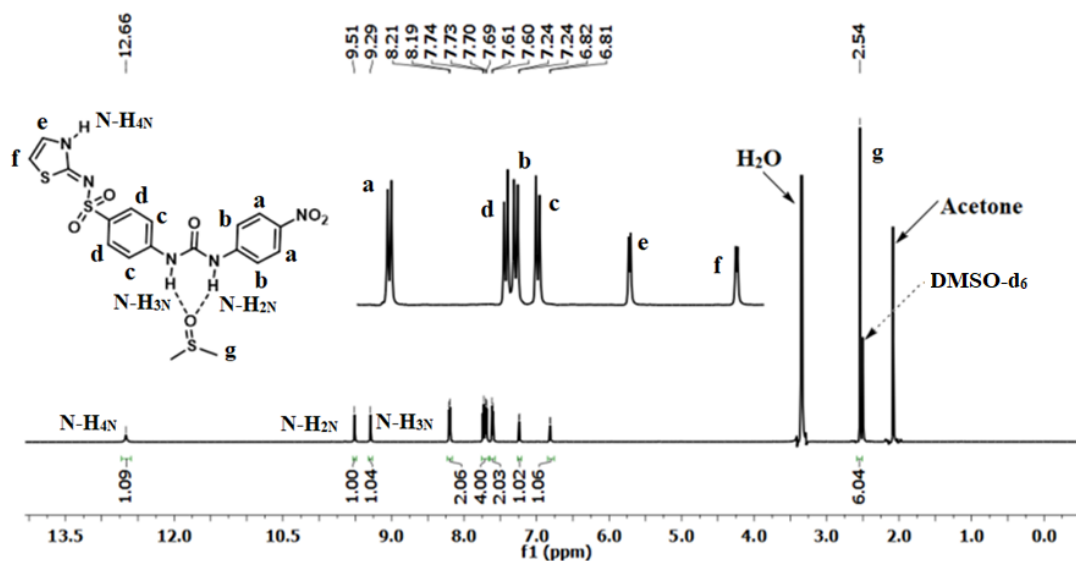


**Figure 3.10:**  $^1\text{H}$ NMR (DMSO- $d_6$ , 600 MHz,) spectra of the **3.2.2**

The  $^1\text{H}$ NMR of **3.2.2** is given in Fig. 3.10. The proton labelled as *a* and *b* appeared as 8.21-8.19 and 7.70-7.69 ppm, respectively while the proton labelled as *c* and *d* appeared at 7.61-7.60 and 7.74-7.73 ppm, respectively. The thiazole protons labelled as *e* and *f* appeared at 7.24 and 6.82-6.81 ppm respectively. The urea protons of **3.2.2** appeared at 9.51 and 9.29 ppm respectively while the N-H of thiazole showed a peak at 12.66 ppm. The assignment of all peaks was done by recording the 2D-HOMOCOSY spectrum as shown in Fig. 3.11 showed the diagonal relationship among the coupled protons. This analysis confirmed the assigned peaks in the  $^1\text{H}$ NMR spectra. The  $^1\text{H}$ NMR of the DMF solvate **3.2.1** is given in Fig. A3.10.

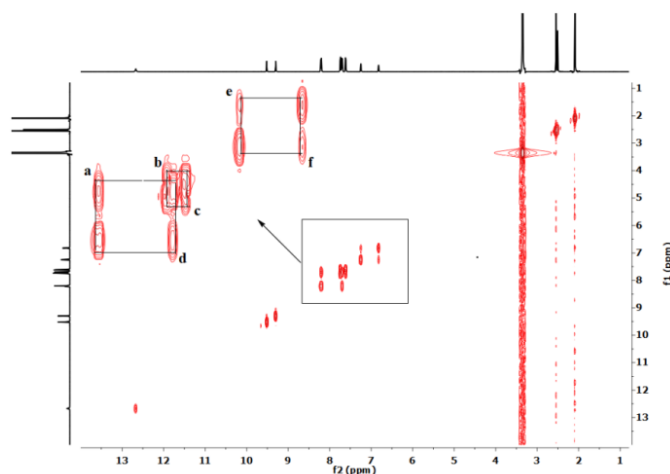


**Figure 3.11:**  $^1\text{H}$ NMR (DMSO- $d_6$ , 600 MHz,) spectra of the **3.2.2**

### 3.10: Structural descriptions of solvates of 3.2.

The crystals of DMSO solvate **3.2.1** were from the  $P2_1/n$  space group and had a unit-cell volume of  $2220.34(3) \text{ \AA}^3$  and a crystal density of  $1.473 \text{ gcm}^3$ . The crystals of DMF solvate **3.2.2**, belonged to the  $P2_1/c$  space group, with a unit cell volume of  $2183(4) \text{ \AA}^3$  and a crystal density of  $1.514 \text{ gcm}^3$ . The imine form of the host molecule was found in the DMSO and DMF solvates of the **3.2**. The heterocyclic part in the solvates had N4-C14 bond distances as  $1.33(1) \text{ \AA}$  and  $1.31(7) \text{ \AA}$  respectively, in the DMF and DMSO solvates. These distances were shorter by  $0.06 \text{ \AA}$  and  $0.09 \text{ \AA}$  than the comparable N-C bond in the heterocycle rings of the host of the solvate **3.1.1**, where amine form was observed. The host molecule in each case had different orientations of the heterocyclic units. The angle between the planes containing heterocycle and the rest of the molecule of **3.2.2** was  $87.59^\circ$ ; whereas, in **3.2.1**, it was  $78.58^\circ$ . The projections of C=O of the urea moieties were in opposite directions with respect to each other in the two solvates (Fig. 3.12a). Assemblies of the two solvates had hydrogen-bonded dimers  $\{R^2_2(8)$  synthons shown in Fig. 3.12b and c. The hydrogen-bonded dimers of hosts in the DMSO solvate were connected end-to-end by  $C3-H \cdots O2_{(\text{urea})}$  hydrogen bonds forming  $R^2_2(10)$  synthons to provide a chain-like structure; whereas, in the DMF solvate, such dimers were located at translated positions providing zig-zag arrangements.

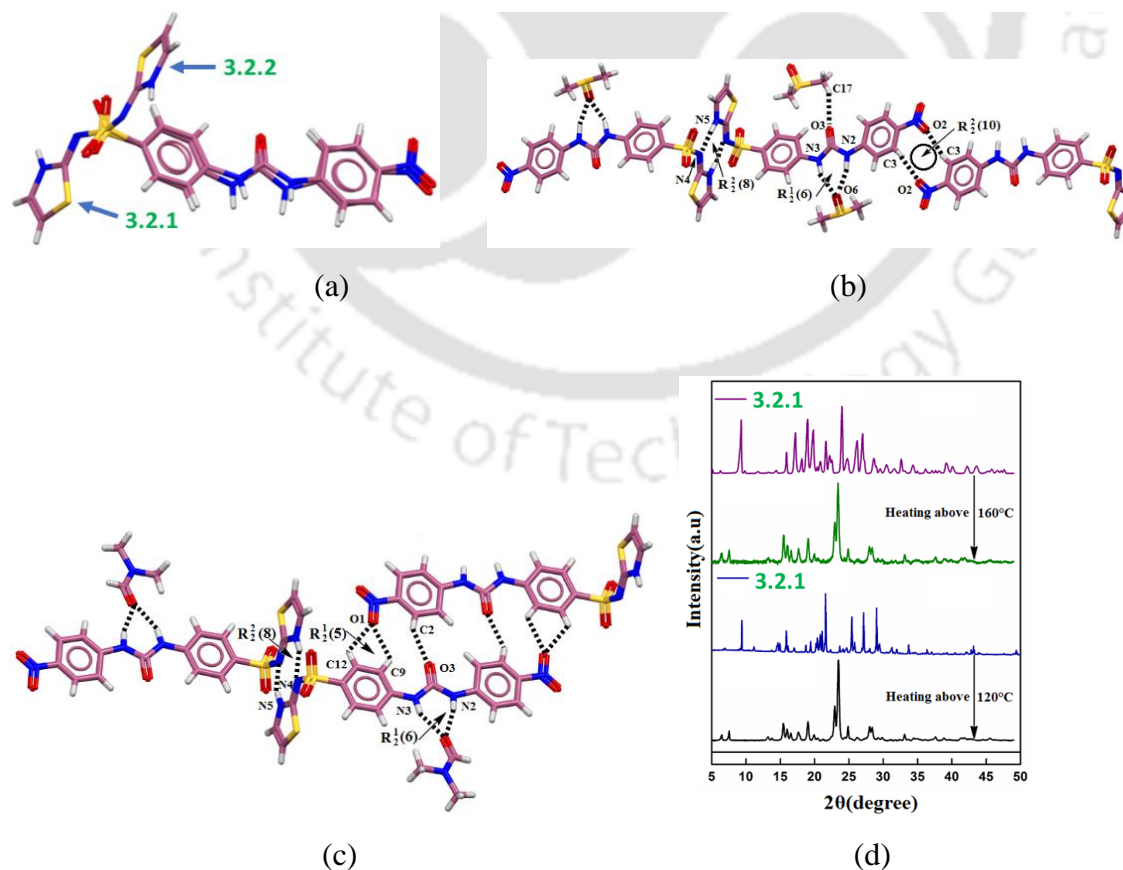


**Figure 3.12:** (a) Overlaid diagram of the hosts in 3.2.2 and 3.2.1. Assembling of the hydrogen-bonded dimers of (b) 3.2.2, (c) 3.2.1 (d) Powder XRD patterns of the 3.2.2 and 3.2.1 and after de-solvation.

### 3.11: Thermal studies of the solvates 3.2.1 and 3.2.2

Thermal gravimetric analyses of the 3.2.1 showed that the DMF molecule of the solvate was lost at 124 °C, and the host got decomposed at 277 °C; whereas the DMSO solvate lost the DMSO molecule at 163°C and in this case, the host decomposed at 263 °C as illustrated in Fig. 3.13. The enthalpy of de-solvation from DSC for the DMSO and DMF solvates of the host were 54.41 kJ/mole and 45.14 kJ per mole respectively. The difference in the two de-solvation temperatures was 39 °C ( $\sim 0.32$  kJmol<sup>-1</sup>). We de-solvated the 3.2.1 and 3.2.2 by heating the samples above the de-solvation temperature which was observed in thermogravimetry (Fig. A3.15). The PXRD patterns of the samples before and after de-solvation are shown in Fig. 3.12d. The PXRD patterns of the de-solvated samples were identical. Hence, the de-solvation yielded a common de-solvated form. This was an interesting point to us, as many solvates such as in the case of several solvates of furosemide, have different conformational adjusted structures.<sup>18</sup> The literature suggests that the phase transition during heating causes de-solvation of isostructural solvates to transform them into a common polymorph,<sup>19</sup> that was possible due to phase transitions during heating.

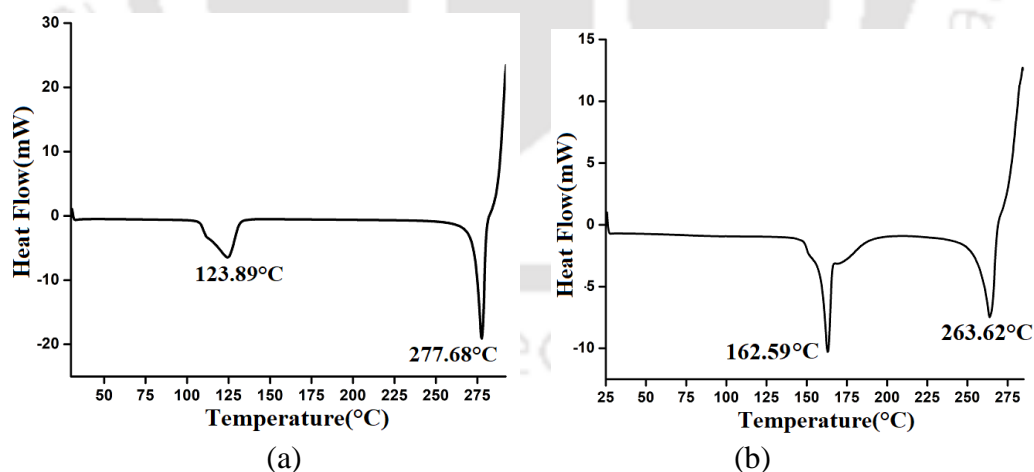


**Figure 3.13:** Differential scanning calorimetry of (a) 3.2.1 (b) 3.2.2 (heating rate 10°C/min under nitrogen atmosphere).

Thermal stability,<sup>20</sup> phase-transition<sup>21</sup> and formation of hydrates<sup>22</sup> are also key issues that complicate the de-solvation of solvates/ cocrystals. The issue on thermal stability during de-

solvation was not a concern in our samples as there were no decompositions below the de-solvation temperature (vide thermogravimetry). The DMSO and DMF solvates in the present case were not isostructural, but their respective lattice had identical H-bonded dimers, holding the solvent molecules in different manners. Once solvent molecules were removed from those dimers, the thermal energy converted them into a common de-solvated form. In addition to these, de-solvation of solvates generating polymorphs has also been reported earlier.<sup>60-63</sup> However, in those examples, relatively higher activation energies were required to remove partner molecules. Hence such studies generate interest in search for a new polymorph and also to develop porous structures. Our observations on the de-solvation as compared to literature on the de-solvation of solvates, suggested a substrate dependency in the de-solvation rather than packing similarities. Though we do not have a generalized inference to make, this may suggest that the external heat required to be applied to expel the solvent molecules, but it is evident that the domain of the self-assembly is the key factor in transforming to the common form of the host in the given example.

### 3.12: Ionic co-crystal of **3.2** with TBA iodide

Attempts to prepare the cocrystal of **3.2** with TBACl or TBABr, from the respective solution in DMSO or DMF were not successful. However, we could obtain a cocrystal of the **3.2** with TBAI. In this case, the quality of the structure was not good, but we could obtain the arrangements of the molecules in the cocrystal. <sup>1</sup>HNMR spectra of the ionic co-crystal **3.2.3** is depicted in Fig 3.14. The ionic cocrystal showed N-H proton of the urea group in <sup>1</sup>HNMR at 9.57 and 9.29 ppm respectively. The N-H of the thiazole part appeared at 12.67 ppm while the protons of the TBA group appeared in the range 3.17-0.92 ppm. The <sup>13</sup>CNMR of **3.2.3** is given in Fig. A3.13. The carbon of the carbonyl group appeared at 168.73 ppm, whereas the four carbon peaks of the TBA group appeared at 57.53, 23.08, 19.23 and 13.52 ppm respectively.

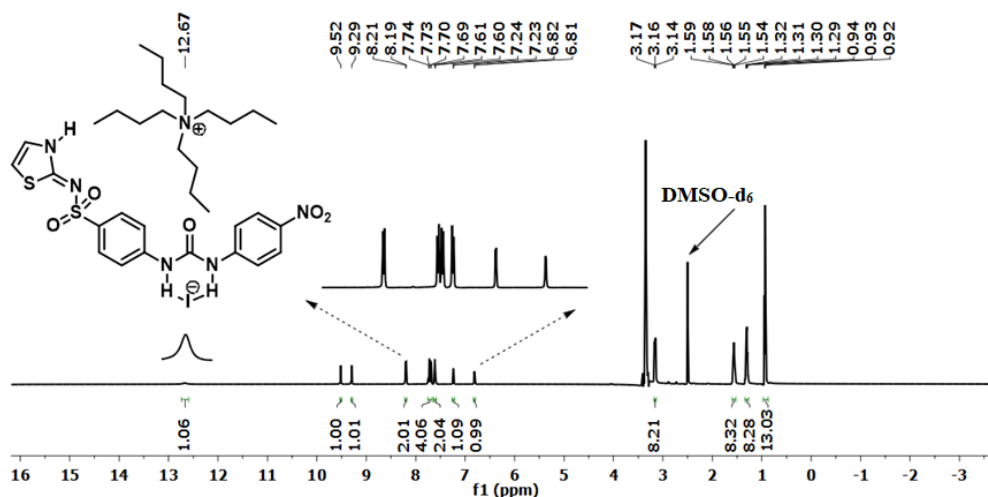


**Figure 3.14:**  $^1\text{H}$ NMR (DMSO- $d_6$ , 600 MHz) spectra of the **3.2.3**

The ionic co-crystal, **3.2.3**, was from the  $P \bar{1}$  space group, exhibiting a crystal volume of 1985.5(2)  $\text{\AA}^3$  and a crystal density of 1.319  $\text{g cm}^3$ . This ionic cocrystal had dimeric assemblies of **3.2**, similar to the DMF cocrystal (Fig. 3.15). The H-bonded dimers were positioned on top of each other in a slightly displaced position. The dimers were connected to each other by C2-H $\cdots$ O3 interactions providing an  $R_2^2(14)$  synthons. The iodide had a tetrahedral hydrogen bonding environment.

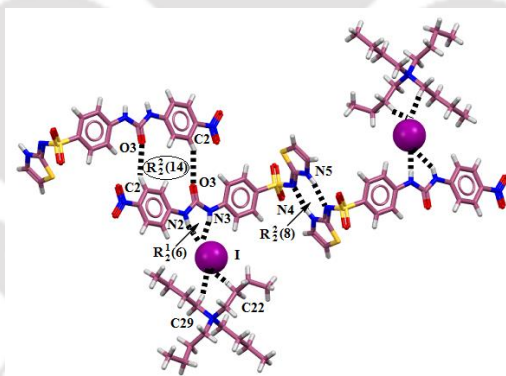


**Figure 3.15:** A part of the self-assembly of the **3.2.3** showing the H-bonded  $R_2^2(8)$  dimer.

We also obtained a tetrabutylammonium salt of **3.2** from a spontaneous reaction between **3.2** with TBAF. The salt was obtained as a semi-solid, hence it was characterized in the solution state by recording  $^1\text{H}$ NMR, IR, and UV-visible spectra. The  $^1\text{H}$ NMR of the compound **3.2.4** is depicted in Fig. 3.16. The protons labelled as *a* and *b* showed chemical shifts at 8.19–8.17 ppm and 7.70–7.68 ppm, respectively while the aromatic protons labelled as *c* and *d* appeared at 7.43–7.41 and 7.64–7.63, respectively. The thiazole proton got de-shielded due to the formation of a negative charge on the nitrogen atom and displayed chemical shift at 6.92–6.91

and 6.43 respectively. One of the urea protons was de-shielded in comparison to the parent host and appeared at 9.61 and 9.16 ppm, respectively.

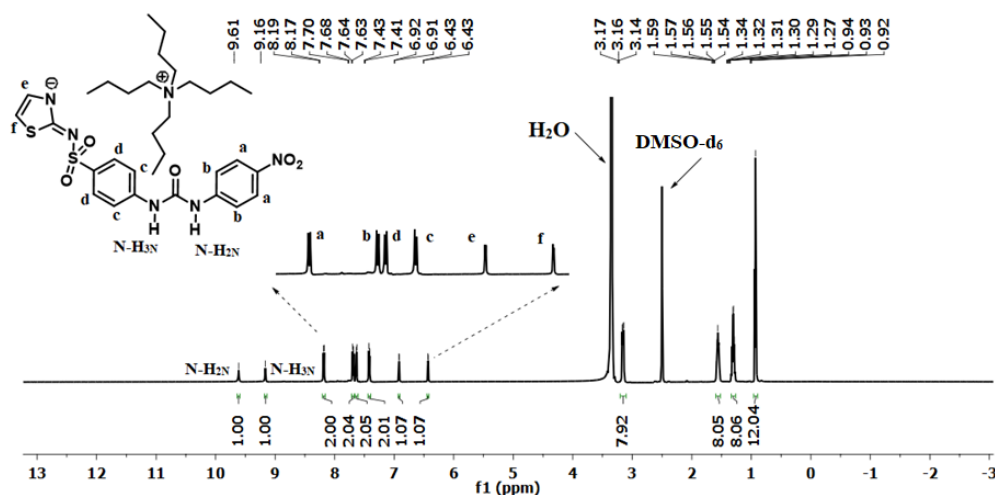
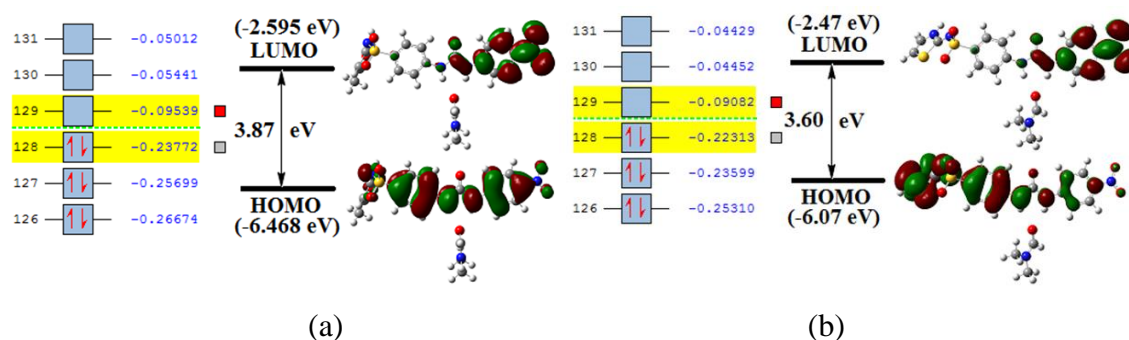


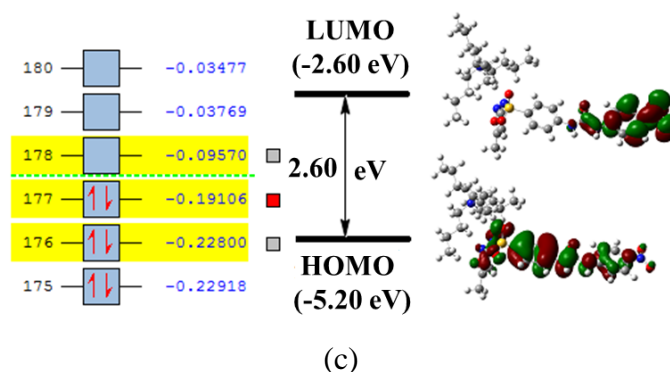
**Figure 3.16:**  $^1\text{H}$ NMR (DMSO- $d_6$ , 600 MHz) spectra of the **3.2.4**

From the structural study on the different solvates and cocrystals, we found that in the case of **3.1** the heterocyclic unit had an amine form; but the salt of the **3.1** had the imine form. Whereas, in the case of **3.2** the hetero-cyclic part had imine form consistently in all the forms.

### 3.13: Optimized energy of the solvates

The absorptions due to the  $S_0-S_1$  of the two solvates **3.2.1** and **3.1.1** were found to be at 352 and 353 nm. Whereas the peak  $S_0-S_1$  transition of the anion was at 484 nm. The HOMO–LUMO gaps of the solvates and salt were calculated by DFT (Fig. 3.17). The energy difference between the HOMO and the LUMO for DMF solvates, labelled as **3.1.1** and **3.2.1**, was found to be 3.87 eV (320.37 nm) and 3.60 eV (344.4 nm), respectively. In contrast, for the salt **3.1.3**, this gap was significantly lower at 2.60 eV, which corresponds to a wavelength of 477 nm. This theoretical transition peak at 477 nm aligns closely with the experimentally observed peak at 484 nm.

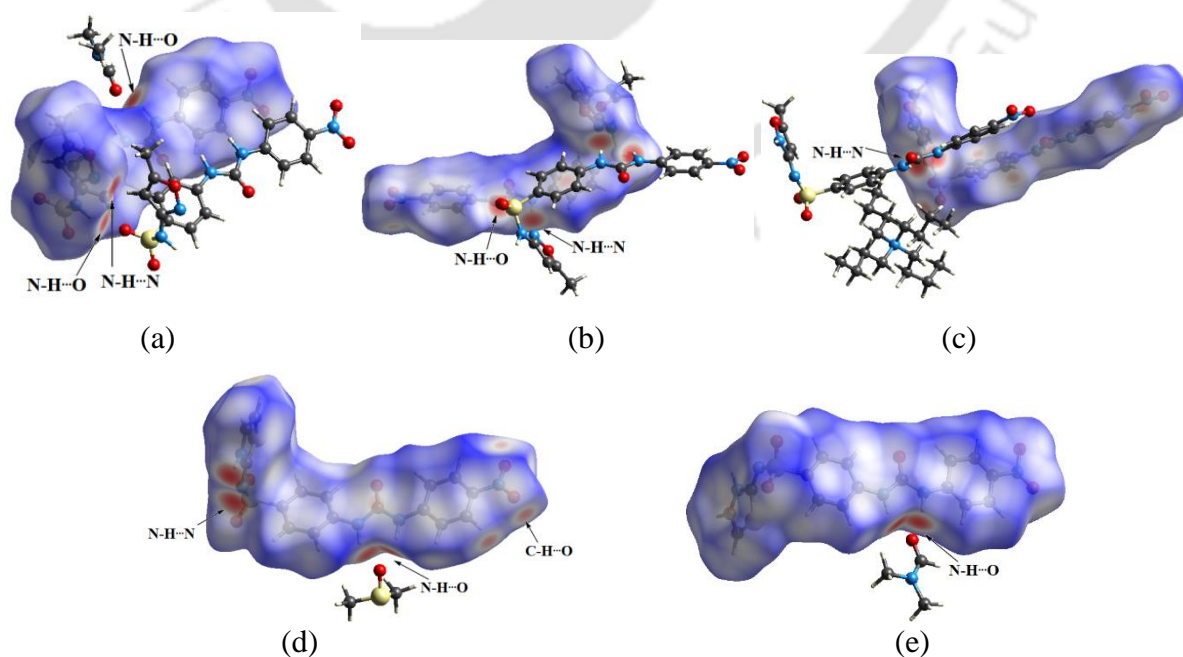




**Figure 3.17:** HOMO and LUMO gap (a) **3.1.1** (b) **3.2.2** (c) **3.1.3**, (calculated by DFT using B3LYP/6-31+G (d, p) as basis set.

### 3.14: Hirshfeld analysis

Hirshfeld analysis is an excellent method for quantifying the nature of the intermolecular interaction. As predicted, Hirshfeld surface analysis revealed hydrogen bond contact sites of each form of the hosts. Figure 3.18 shows the Hirshfeld plotted over  $d_{\text{norm}}$ . The colour coding was used to demonstrate intermolecular interactions. Red, white, and blue dots indicate intermolecular interactions with distances less than, equal to, and greater than van der Waal radii, respectively. The negative value of the  $d_{\text{norm}}$  represents the red spot area, whereas the positive value represents the blue zone. The  $d_{\text{norm}}$  value for polymorphic solvate **3.1.1** was -0.54 to 1.40 Å, but for **3.1.2** it was -0.56 to 1.29 Å. The  $d_{\text{norm}}$  value for TBA salt **3.1.3** ranged from -0.53 to 1.59 Å. The  $d_{\text{norm}}$  values for solvates **3.2.1**, **3.2.2**, and ionic co-crystal **3.2.3** were -0.58 to 1.23, -0.62 Å to 1.19, and -0.59 to 1.68 Å, respectively.



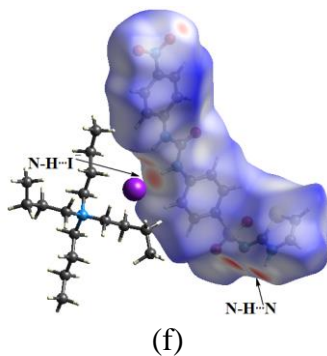
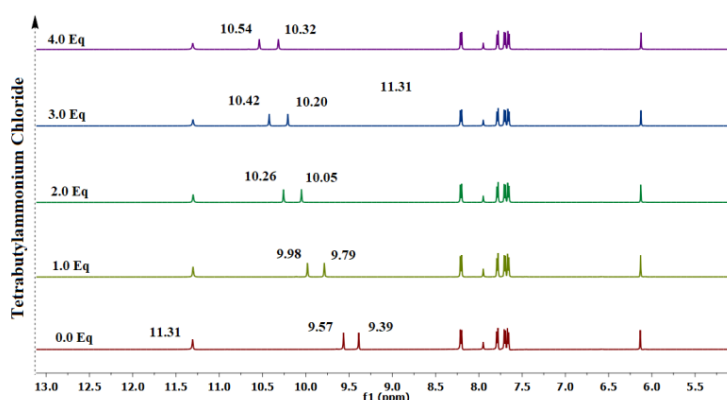


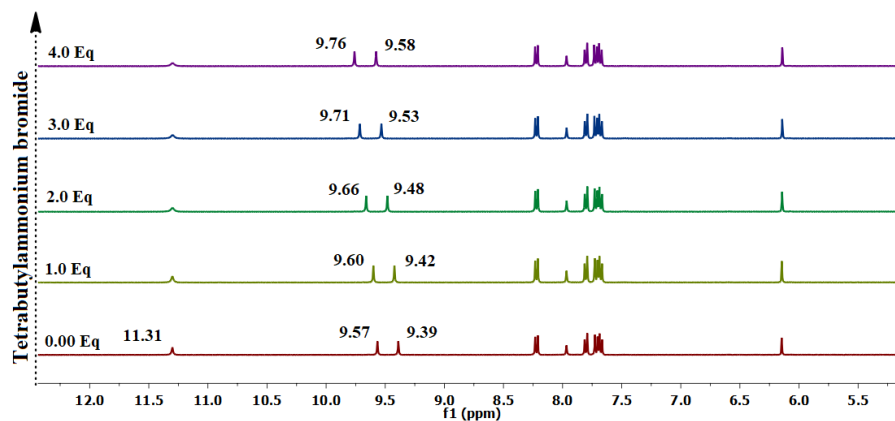
**Figure 3.18:** Hirshfeld surfaces of (a) **3.1.1**(b) **3.1.2**, (c) **3.1.3** (d) **3.2.1** (e) **3.2.2** (f) **3.2.3**

### 3.15: Solution studies on the interactions of tertbutyl ammonium halides with **3.1** and **3.2**

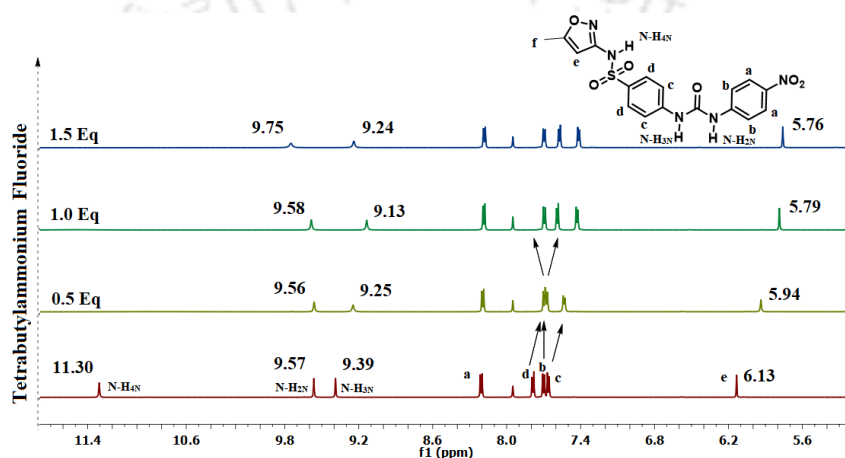
The  $^1\text{H}$ NMR spectrum of the **3.1.1** was recorded by adding different amounts of tetrabutylammonium chloride, bromide, and fluoride in independent experiments as shown in Fig. 3.19. The **3.1** had three labile protons from the urea part and the heterocyclic part which appeared at 9.37 ppm, 9.57 ppm, and 11.31 ppm. These signals were significantly affected by the hydrogen bond formation or deprotonation. In the case of TBACl and TBABr (Fig. 3.19a and b), there was an insignificant effect on the signal of the N-H of the heterocycle, whereas, the two peaks of urea were de-shielded. These were de-shielded to an extent ( $\Delta\delta$ ) of 0.97 ppm and 0.93 ppm, respectively by TBACl, whereas with TBABr, these were shifted to higher side  $\delta$  by 0.21 ppm and 0.18 ppm, respectively. This indicated that **3.1** primarily interacted with chloride and bromide by hydrogen bonds with the N-H bonds of urea. The same compound when treated with TBAI, formed the N-butylated product **3.1.4** as discussed earlier.



(a)



(b)

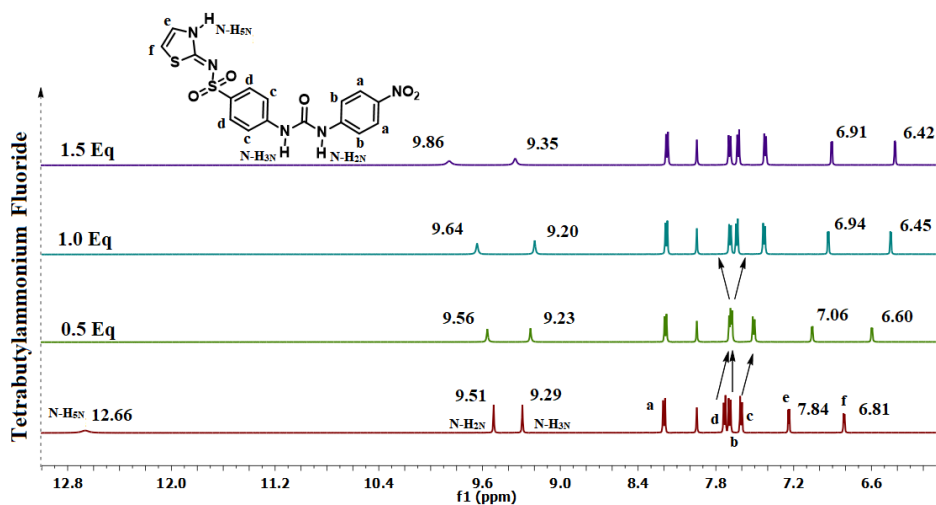


(c)

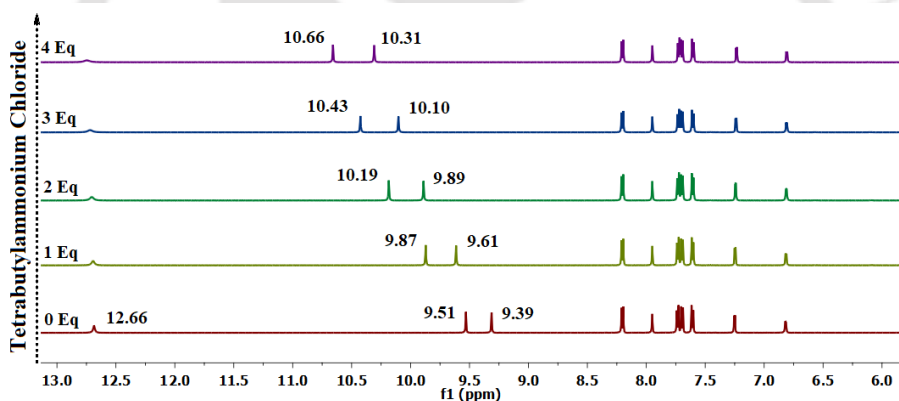
**Figure 3.19:** The aromatic region of the  $^1\text{H}$  NMR (600 MHz,  $\text{DMSO-d}_6$ ) titration showing the aromatic protons of **3.1.1** was recorded by adding different amounts of tetrabutylammonium (a) chloride and (b) bromide (up to 4 equivalents) (c) fluoride (up to 1.5 equivalents) (Only the range of 6.4 ppm to 13 ppm are shown for clarity).

The  $^1\text{H}$ NMR titrations of **3.1.1** with TBAF are shown in Fig. 3.19c. It could be clearly seen that a significant change in the  $\text{HC=}$  proton of the ring appeared at 6.13 ppm. This was shielded to an extent of 0.37 ppm, due to the anion formation by proton abstraction of the amine, resulting in a change in the conjugation of the ring to transform into the imine form. In this case, the two  $\text{N-H}$  of the rings get shifted in different manners. The  $\text{N-H}_{3\text{N}}$  got shielded and the  $\text{N-H}_{2\text{N}}$  was de-shielded with the increase in fluoride concentration. Fluoride, having the ability to form charge-assisted hydrogen bonds, formed hydrogen bonds in an unsymmetrical manner with  $\text{N-H}_{2\text{N}}$  and  $\text{N-H}_{3\text{N}}$ . The enhanced acidity of such H-atoms is due to H-bonds with the electronegative counterpart which caused the de-shielding ( $\Delta\delta = 0.18$  ppm) of  $\text{N-H}_{2\text{N}}$ , whereas the  $\text{N-H}_{3\text{N}}$  was shielded due to the partial negative charge created at

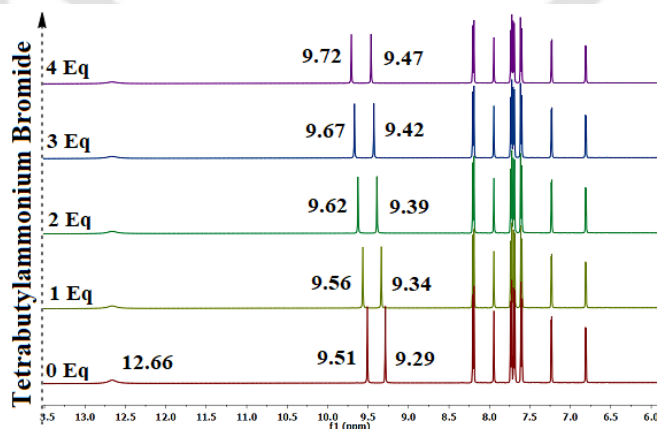
the nitrogen site and the diamagnetic effect of fluoride in its vicinity (Fig. 3.19c). The deprotonation had also caused shifts in the proton resonances of the aromatic protons connected to the urea moiety, thereby affecting the chemical shift positions.



(a)



(b)



(c)

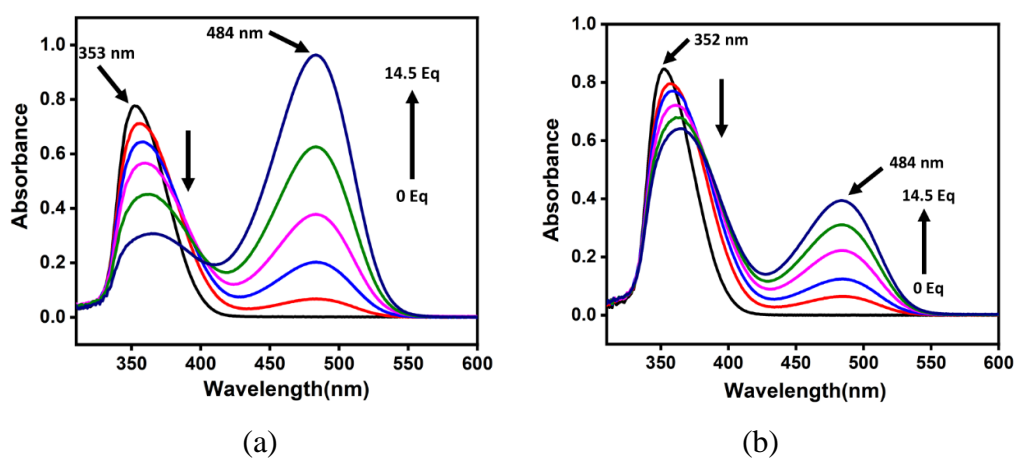
**Figure 3.20:** The aromatic region of  $^1\text{H}$  NMR (600 MHz,  $\text{DMSO-d}_6$ ) during the titration of the **3.2.1** performed by adding different amounts of tetrabutylammonium (a) fluoride (up to

1.5 equivalents) (b) chloride and (c) bromide (up to 4 equivalents) (Only the range of 6.4 ppm to 13 ppm are shown for clarity).

A similar deprotonation of **3.2** was also observed from its titration with TBAF (Fig. 3.20a). In this case, the N–H of the ring was lost, and as a consequence, the peak at 11.30 ppm disappeared. The two olefin peaks of the thiazole ring at 6.81 and 6.74 ppm were shielded by 0.93 and 0.39 ppm, respectively. The urea NH were de-shielded and shielded as explained for the other salt. In this case, these signals appeared at 9.86 and 9.35 ppm, whence the former proton signal was de-shielded to an extent of 0.35 ppm and the latter one was shielded by 0.06 ppm. The titration of **3.2** with TBACl and TBABr (Fig. 3.20b and c) (up to four equivalent of corresponding salt) showed that there was only de-shielding of N-H proton of the urea part, while other protons remained unaffected as the respective anions only formed the hydrogen bonding with the urea group. These solution-state studies added an incremental understanding of the fact that halides are substrate-selective for the two hosts.<sup>14</sup> The chemical shift changes upon the interactions of **3.1** with fluoride ions affected significant changes in the CHC = proton of the heterocycle as it was transformed from the amine to imine form.

### 3.16: UV visible studies

The anion binding and deprotonation in sulfonamide-derived urea decide the color changes for specific detection processes.<sup>23</sup> Both compounds had nitro-phenyl as the common chromophore and showed identical color changes due to the formation of new absorption at 484 nm as depicted in Fig. 3.21a and b. The changes caused by fluoride and bromide salts could be observed by visual changes, as depicted in Fig. 3.21b and 3.21c.



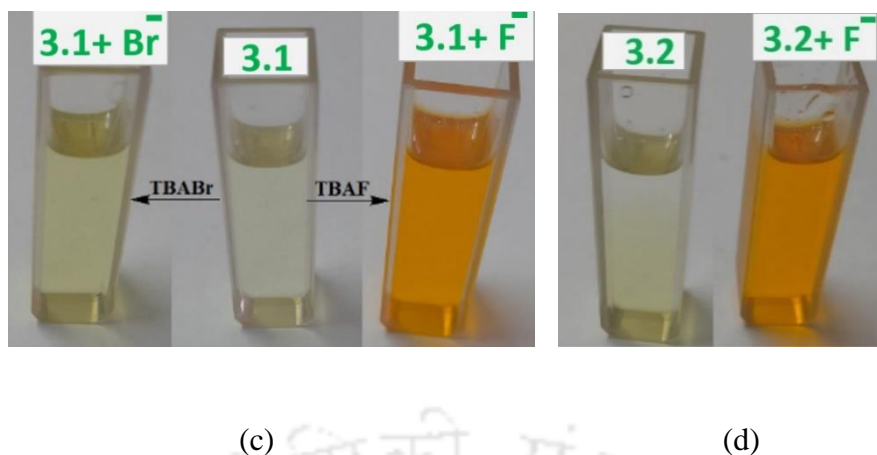


**Figure 3.21:** Changes in the UV-visible spectra of (a) **3.2** and (b) **3.1** ( $3.3 \times 10^{-5}$  M, 2mL in each case) in dimethylsulfoxide by aliquots ( $30 \mu\text{L}$ ) of tetrabutylammonium fluoride ( $10^{-2}$  M) and visual color change of (c) **3.1** (d) **3.2** after addition of TBAF and TBABr respectively.

### 3.17: Conclusions

The polymorphs of a DMF solvate of **3.1** were prepared by crystallization from a solution at room temperature and from a solution heated to  $80^\circ\text{C}$ . The two polymorphs had different synthons: in one polymorph, there were direct hydrogen bonds between DMF, with the urea part being more stable. DFT calculations of the H-bonded dimers of the polymorphs provided support for such stability. On the other hand, the self-assemblies of the DMSO and DMF solvate of **3.2** showed similar hydrogen-bonded dimers of the host molecules, but the conformers of the host in these solvates were completely different. Despite the dissimilarities in geometrical features, the de-solvation of the two solvates yielded a common form. There was in situ C–N bond formation on **3.1** forming an N-butylated host and leading to the formation of an ionic cocrystal with TBAI. The two sulfonamide urea derivatives, **3.1** as well as **3.2** formed respective salts by proton abstraction in the presence of TBAF, and both showed identical color changes due to the changes in the conjugation of the common nitrophenyl unit within their structures.

### 3.18: References

1. Ghosh, S.; Bag, P. P.; Reddy, C. M. Co-Crystals of Sulfamethazine with Some Carboxylic Acids and Amides: Co-Former Assisted Tautomerism in an Active Pharmaceutical Ingredient and Hydrogen Bond Competition Study. *Cryst. Growth Des.* **2011**, *11* (8), 3489–3503

2. Singh, M. P.; Baruah, J. B. Combinations of Tautomeric Forms and Neutral-Cationic Forms in the Cocrystals of Sulfamethazine with Carboxylic Acids. *ACS Omega* **2019**, *4* (7), 11609–11620.
3. Nangia, A. Conformational Polymorphism in Organic Crystals. *Acc. Chem. Res.* **2008**, *41* (5), 595–604.
4. Braun, D. E.; Gelbrich, T.; Kahlenberg, V.; Tessadri, R.; Wieser, J.; Griesser, U. J. Stability of Solvates and Packing Systematics of Nine Crystal Forms of the Antipsychotic Drug Aripiprazole. *Cryst. Growth Des.* **2009**, *9* (2), 1054–1065
5. Kons, A.; Mishnev, A.; Mukhametzyanov, T. A.; Buzyurov, A. V.; Lapuk, S. E.; Berzins, A. Hexamorphism of Dantrolene: Insight into the Crystal Structures, Stability, and Phase Transformations. *Cryst. Growth Des.* **2021**, *21* (2), 1190–1201.
6. Basford, P. A.; Cameron, C. A.; Cruz-Cabeza, A. J. Conformational Change Initiates Dehydration in Fluconazole Monohydrate. *Cryst. Growth Des.* **2020**, *20* (9), 6044–6056.
7. Zhoujin, Y.; Yang, X.; Zhang, M.; Guo, J.; Parkin, S.; Li, T.; Yu, F.; Long, S. Synthron Polymorphism and  $\pi$ - $\pi$  Stacking in N -Phenyl-2-Hydroxynicotinanilides . *Cryst. Growth Des.* **2021**, *21* (11), 6155–6165.
8. Caira, M. R. Sulfa Drugs as Model Cocrystal Formers. *Mol. Pharm.* **2007**, *4* (3), 310–316.
9. Phukan, N.; Baruah, J. B. Conformational Adjustments over Synthons of Urea and Thiourea Based Assemblies. *CrystEngComm* **2016**, *18* (40), 7753–7763.
10. Edkins, K.; McIntyre, G. J.; Wilkinson, C.; Kahlenberg, V.; Töbrens, D.; Griesser, U. J.; Brüning, J.; Schmidt, M. U.; Steed, J. W. Extensive Sequential Polymorphic Interconversion in the Solid State: Two Hydrates and Ten Anhydrous Phases of Hexamidine Diisethionate. *Cryst. Growth Des.* **2019**, *19* (12), 7280–7289.
11. Bernstein, J.; Davis, R. E.; Shimon, L.; Chang, N. Patterns in Hydrogen Bonding: Functionality and Graph Set Analysis in Crystals. *Angew. Chemie Int. Ed. English* **1995**, *34* (15), 1555–1573.
12. Bhattacharya, S.; Saha, B. K. Polymorphism through Desolvation of the Solvates of a van Der Waals Host. *Cryst. Growth Des.* **2013**, *13* (2), 606–613.
13. Nath, J.; Baruah, J. B. Self-Assemblies of Solvates, Ionic Cocrystals, and a Salt Based on 4-[[[4-Nitrophenyl)Carbamoyl]Amino]- N-(Pyrimidin-2-Yl)Benzene-1-

- Sulfonamide: Study in the Solid and Solution States. *Cryst. Growth Des.* **2021**, *21* (9), 5325–5341.
14. Cametti, M.; Rissanen, K. Recognition and Sensing of Fluoride Anion. *Chem. Commun.* **2009**, No. 20, 2809–2829.
  15. Tarai, A.; Baruah, J. B. Conformation and Visual Distinction between Urea and Thiourea Derivatives by an Acetate Ion and a Hexafluorosilicate Cocrystal of the Urea Derivative in the Detection of Water in Dimethylsulfoxide. *ACS Omega* **2017**, *2* (10), 6991–7001.
  16. Tarai, A.; Baruah, J. B. Anion Assisted Conformationally Guided Self-Assemblies of Multi-Component Cocrystals of Dioxime. *CrystEngComm* **2016**, *18* (29), 5482–5491.
  17. Leclercq, L.; Suisse, I.; Roussel, P.; Agbossou-Niedercorn, F. Inclusion of Tetrabutylammonium Cations in a Chiral Thiazolium/Triflate Network: Solid State and Solution Structural Investigation. *J. Mol. Struct.* **2012**, *1010*, 152–157.
  18. Minkov, V. S.; Beloborodova, A. A.; Drebuschak, V. A.; Boldyreva, E. V. Furosemide Solvates: Can They Serve as Precursors to Different Polymorphs of Furosemide? *Cryst. Growth Des.* **2014**, *14* (2), 513–522.
  19. Yang, P.; Qin, C.; Du, S.; Jia, L.; Qin, Y.; Gong, J.; Wu, S. Crystal Structure, Stability and Desolvation of the Solvates of Sorafenib Tosylate. *Crystals* **2019**, *9* (7), 367.
  20. Svard, M.; Ahuja, D.; Rasmuson, Å. C. Calorimetric Determination of Cocrystal Thermodynamic Stability: Sulfamethazine–Salicylic Acid Case Study. *Cryst. Growth Des.* **2020**, *20* (7), 4243–4251.
  21. Aitipamula, S.; Chow, P. S.; Tan, R. B. H. Solvates and Polymorphic Phase Transformations of 2-Chloro-4-Nitrobenzoic Acid. *CrystEngComm* **2011**, *13* (3), 1037–1045.
  22. Dai, J.; Yang, W.; Zhang, S.; Jia, L.; Niu, Y.; Cui, P.; Li, Q.; Zhou, L.; Yin, Q. Phase Transformation among Multiple Hydrates of Creatine Phosphate Sodium in Solution and in the Vapor: A Distinction between Solution- and Solvent-Mediated Transformation. *J. Mol. Liq.* **2021**, *334*, 116507.
  23. Caltagirone, C.; Bates, G. W.; Gale, P. A.; Light, M. E. Anion Binding vs. Sulfonamide Deprotonation in Functionalised Ureas. *Chem. Commun.* **2008**, No. 1, 61–63.

## Appendix - Chapter 3

### A3.1: Experimental section

#### Synthesis and characterization of the hosts, solvates, cocrystals and salts:

**(3.1.1):** A solution of 4-nitrophenylisocyanate (328 mg, 2 mmol) and sulfamethoxazole (507 mg, 2 mmol) in acetonitrile (30 ml) was refluxed for 2 hrs. after which the reaction mixture was stirred at room temperature for about 6 hrs. This had resulted in the formation of a yellow precipitate. This precipitate was filtered and it was dissolved in 3 ml DMF. The solution thus prepared was kept undisturbed, which provided the crystals of **3.1.1** yield = 76 %. IR (Neat,  $\text{cm}^{-1}$ ): 3272 (w), 3135 (w) 1724 (s), 1657 (s), 1615 (s), 1590 (s), 1574 (s), 1542 (s), 1495 (s), 1468 (s), 1409 (s), 1374 (s), 1384 (s), 1333 (m), 1317(s), 1251 (s), 1197 (s), 1162 (s), 1106 (s), 1091 (s), 1028 (m), 928 (s), 885 (s), 854 (s), 843 (m), 831 (s), 751 (s), 715 (s), 667 (s), 645 (s), 579 (s), 556 (s).  $^1\text{H}$ NMR (600 MHz,  $\text{DMSO-d}_6$ , ppm): 11.31 (s, 1H), 9.57 (s, N-H), 9.39 (s, N-H), 8.21- 8.20 (d,  $J = 10$  Hz, 2H ), 7.95 (s, 1H ), 7.79 (d,  $J = 8$  Hz), 7.70 (d,  $J = 9$  Hz ), 7.67 (d,  $J = 8$  Hz ), 6.13 (s, 1H), 2.89 (s, 3H), 2.73 (s, 3H), 2.29 (s, 3H).  $^{13}\text{C}$  NMR (125 MHz,  $\text{DMSO-d}_6$ ): 170.3, 162.3, 157.6, 151.8, 145.9, 143.6, 141.4, 132.3, 128.2, 125.2, 118.2, 117.8, 95.4, 35.8, 30.7, 12.1.

**(3.1.2):** A solution of the crude yellow precipitate of **3.1** (103 mg, 0.25 mmol) was dissolved in DMF (10 ml) was stirred at  $80^\circ\text{C}$  for about 1 h. The solution was filtered to discard suspended material (if any) and it was kept undisturbed for crystallization. Upon standing for 8-10 days red block crystals of the **3.1.2** were obtained (yield 82 %). IR (Neat,  $\text{cm}^{-1}$ ): 3358 (s), 1719 (s), 1657 (s), 1618 (s), 1593 (s), 1557 (w), 1572 (s), 1538 (s), 1495 (s), 1441 (m), 1406 (s), 1376 (s), 1326 (s), 1304 (w), 1249 (s), 1198 (s), 1177 (m), 1163 (s), 1108 (s), 1092 (m), 1040 (s), 924 (m), 875 (s), 854 (s), 833 (s), 812 (s), 752 (s), 702 (s), 666 (s), 643 (s), 574 (s), 556 (s).

**(3.1.3):** The crude **3.1** (42 mg, 0.1 mmol) was dissolved in DMF (5 ml). To this solution TBAF trihydrate (63 mg, 0.2 mmol) was added and stirred for 30 mins. The solution was filtered and kept for crystallization, which yielded crystalline **3.1.3**. The crystals were decanted and characterized (yield 85 %). IR (Neat  $\text{cm}^{-1}$ ): 2959 (s), 2874 (s), 1719 (s), 1609 (s), 1592 (s), 1543 (s), 1494 (s), 1456 (s), 1404 (s), 1334 (s), 1314 (s), 1302(s), 1273 (s), 1246 (s), 1195 (s), 1175 (s), 1141(s), 1109(s), 1094(s), 1045(s), 1007(m), 931(s), 883(s), 851(s), 802(s), 750(s), 704(s), 645(s), 587(s), 566(s).  $^1\text{H}$ NMR (600 MHz,  $\text{DMSO-d}_6$ , ppm): 9.58(s, N-H), 9.12(s, N-H), 8.19 (d,  $J = 9$  Hz, 2H), 7.70 (d,  $J = 9$  Hz, 2H), 7.58 (d,  $J = 8$  Hz, 2H),

7.42 (d, J = 9 Hz, 2H), 5.78 (s, 1H), 3.16 (t, J = 8 Hz, 8H), 1.59- 1.54 (m, 8H), 1.34- 1.27 (m, 8H), 0.93(t, J = 7 Hz, 12H). Same reaction with excess amounts of TBABr (5 mmol) instead of TBAF yielded the same salt.

**(3.1.4):** A solution of tetrabutylammonium iodide (185 mg, 0.5 mmol) and **3.1** (42 mg, 0.1 mmol) in DMF (10 ml) was stirred at 80 °C for 6 hs and the resulting solution left undisturbed for 8 days yielded crystals of the salt. The supernatant liquid was decanted and the crystals were dried by pressing filter paper (yield 49 %). IR (Neat, cm<sup>-1</sup>): 2958 (s), 2934 (w), 2873(m), 1713 (s), 1611 (m), 1590 (s), 1560 (s), 1539 (s), 1508(s), 1493 (s), 1448 (s), 1405(m), 1374(m), 1341 (s), 1314 (m), 1304 (s), 1247 (s), 1198 (s), 1162 (s), 1113 (s), 1092 (s), 1027 (s), 925 (w), 882 (s), 856 (s), 827 (m), 804 (m), 749 (s), 712 (s), 678 (s), 645 (s), 594 (s), 569 (s), 556 (s). <sup>1</sup>HNMR (600 MHz, DMSO-d<sub>6</sub>, ppm): 9.59 (s, N-H), 9.45 (s, N-H), 8.21 (d, J = 9 Hz, 2H), 7.77 (d, J = 8 Hz, 2H), 7.70 (d, J = 10 Hz, 2H), 7.68 (d, J = 9 Hz, 2H), 6.44 (s, 1H), 3.69 (t, J = 7 Hz, 3H), 3.18-3.15 (t, J = 8 Hz, 8H), 2.37 (s, 3H), 1.59-1.54 (m, 10H), 1.34-1.28 (m, 10H), 0.94(t, J = 7Hz, 12H), 0.87 (t, J = 7 Hz, 3H). <sup>13</sup>C NMR (125 MHz, DMSO-d<sub>6</sub>): 170.8, 159.2, 151.7, 145.8, 144.1, 141.4, 130.4, 128.4, 125.2, 118.3, 117.9, 97.8, 57.5, 48.1, 29.8, 23.1, 19.2, 13.5, 12.2.

**(3.2.1):** A solution of 4-nitrophenylisocyanate (328 mg, 2 mmol) (20 ml), sulfathiazole (511 mg, 2 mmol) in dry acetonitrile (20 ml) was stirred for 8 h. This yielded yellow precipitate, which was filtered. It was dissolved in DMF (3 ml) and kept undisturbed condition for crystallization. Needle shaped crystals of **3.2.1** were formed after 2-3 days (yield, 81 %). IR (Neat cm<sup>-1</sup>) : 3093 (bs), 1725 (s), 1651 (s), 1588 (s), 1567 (s), 1526 (s), 1492 (s), 1414 (s), 1331 (s), 1301 (s), 1249 (s), 1190 (s), 1173 (s), 1145 (s), 1102 (s), 1087 (s), 927 (s), 851 (s), 828 (s), 733 (s), 711 (s), 690 (s), 669 (s), 649 (s), 631 (s), 602 (s), 575 (s), 559 (s). <sup>1</sup>HNMR (600 MHz, DMSO-d<sub>6</sub>, ppm): 12.70 (s, 1H), 9.53 (s, N-H), 9.31 (s, N-H), 8.21 (d, J = 9 Hz, 2H ), 7.94 (s, 1H), 7.74 (d, J = Hz, 2H ), 7.70 (d, J = 9 Hz, 2H ), 7.61 (d, J = 9 Hz, 2H ), 7.24 (d, J = 5 Hz, 1H ), 6.82 (d, J = 4 Hz, 1H ), 2.88 (s, 3H ), 2.72 (s, 3H ). <sup>13</sup>CNMR (125 MHz, DMSO-d<sub>6</sub>): 168.8, 162.5, 151.9, 146.1, 142.5, 141.4, 135.6, 127.2, 125.3, 118.1, 117.9, 108.2, 35.9, 30.9.

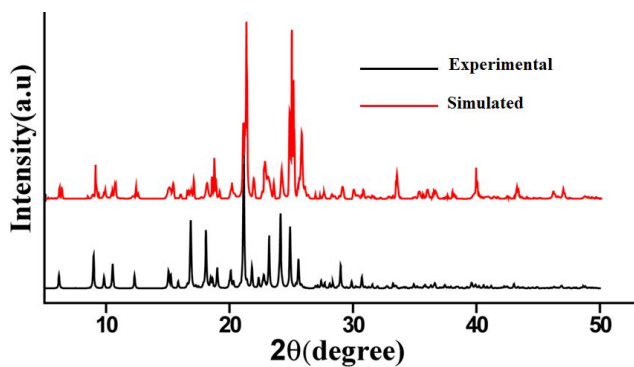
**(3.2.2):** The **3.2** (42 mg, 0.1 mmol) was dissolved in DMSO (0.5 ml) in a plastic vial (1ml capacity) and left undisturbed for crystallization. Block type of crystals of **3.2.2** were formed in a week. The crystals were collected by decanting the supernatant liquid. IR (Neat, cm<sup>-1</sup>) : 3101 (bs), 1716 (s), 1595 (s), 1538 (s), 1489 (s), 1435 (s), 1332 (s), 1299 (s), 1246 (s), 1195 (s), 1174 (s), 1143 (s), 1113 (s), 1088 (s), 1011 (s), 939 (s), 849 (s), 733 (s), 709 (s), 652 (s),

631 (s), 576 (s), 552 (s).  $^1\text{H}$ NMR (600 MHz, DMSO- $d_6$ , ppm): 12.67 (s, 1H), 9.51(s, N-H), 9.29 (s, N-H), 8.21 (d, J = 9 Hz, 2H), 7.74 (d, J = 8 Hz, 2H), 7.70 (d, J = 9 Hz, 2H), 7.60 (d, J = 9 Hz), 7.24 (d, J = 4 Hz, 1H), 6.82 (d, J = 4 Hz, 1H), 2.54 (s, 6H).  $^{13}\text{C}$  NMR (125 MHz, DMSO- $d_6$ ): 168.7, 151.8, 145.9, 142.4, 141.3, 135.6, 127.1, 125.2, 124.4, 118.0, 117.8, 108.1.

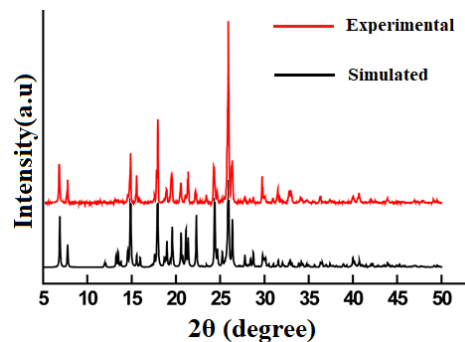
**(3.2.3):** Cocrystal of **3.2** with tetrabutylammonium iodide was prepared by stirring a mixture of **3.2** (42 mg, 0.1 mmol) with ten equivalents amounts of TBAI (369 mg, 1 mmol) in DMF (10ml) for 5 mins at room temperature. The mixture was filtered and filtrate was kept in open air for slow evaporation to obtain the crystals of **3.2.3** after 12 days (yield 53 %). IR (Neat,  $\text{cm}^{-1}$ ): 2958 (m), 2870 (m), 1713 (s), 1590 (s), 1560 (s), 1536 (s), 1493 (s), 1411 (s), 1302 (s), 1245 (s), 1196 (s), 1146 (s), 1112 (s), 1087 (s), 934 (s), 854 (s), 740 (s), 702 (s), 650 (s), 634 (s), 574 (s), 558 (s).  $^1\text{H}$ NMR (600 MHz, DMSO- $d_6$ , ppm): 12.67 (s, 1H), 9.52 (s, N-H), 9.29 (s, N-H), 8.20 (d, J = 9 Hz, 2H), 7.73 (d, J = 8 Hz, 2H), 7.69 (d, J = 9 Hz, 2H), 7.60 (d, J = 8 Hz, 2H), 7.24 (d, J = 5 Hz, 1H), 6.81 (d, J = 4 Hz, 1H), 3.15 (t, 8H), 1.59- 1.54 (m, 8H), 1.34- 1.28 (m, 8H), 0.93 (t, 12H).  $^{13}\text{C}$  NMR (125 MHz, DMSO- $d_6$ ): 168.7, 151.8, 145.9, 142.4, 141.3, 135.6, 127.1, 125.2, 124.4, 117.9, 117.8, 108.1, 57.5, 23.1, 19.2, 13.5.

**(3.2.4):** A solution of tetrabutylammonium fluoride trihydrate (63 mg, 0.2 mmol) **3.2** (42 mg, 0.1 mmol) in DMF (5 ml) was stirred for 1 h to obtain **3.2.4** as a white precipitate. IR (Neat  $\text{cm}^{-1}$ ): 2959 (m), 2872 (m), 1709 (s), 1657 (s), 1592 (s), 1539 (s), 1495 (s), 1433 (s), 1304 (s), 1266 (m), 1233 (s), 1201 (s), 1178 (s), 1164 (m), 1141 (s), 1091 (s), 948 (s), 856 (s), 842 (s), 752 (s), 736 (s), 697 (s), 655 (s), 644 (s), 618 (s), 576 (s), 560 (s).  $^1\text{H}$ NMR (600 MHz, DMSO- $d_6$ , ppm): 9.61 (s, N-H), 9.17 (s, N-H), 8.18 (d, J = 9 Hz, 2H), 7.69 (d, J = 9 Hz, 2H), 7.63 (d, J = 8 Hz, 2H), 7.42 (d, J = 9 Hz, 2H), 6.920 (d, J = 4 Hz, 1H), 6.43 (d, J = 4 Hz, 1H), 3.16 (t, 8H), 1.59- 1.54 (m, 8H), 1.33- 1.27 (m, 8H), 0.93 (t, 12H).  $^{13}\text{C}$  NMR (125 MHz, DMSO- $d_6$ ): 169.6, 151.8, 146.3, 141.1, 140.4, 139.7, 136.9, 126.9, 125.1, 117.6, 117.4, 107.1, 57.5, 23.1, 19.2, 13.5.

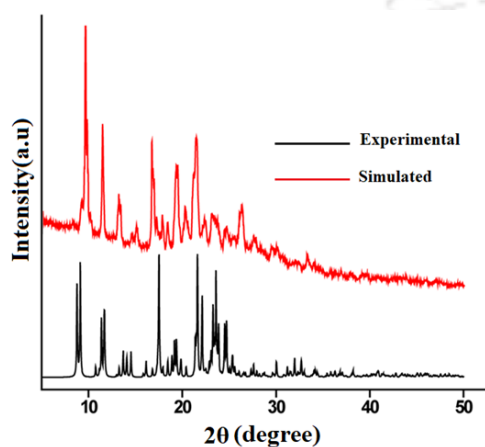
All the solvates and cocrystals were stable at room temperature under ambient conditions at least for a week.



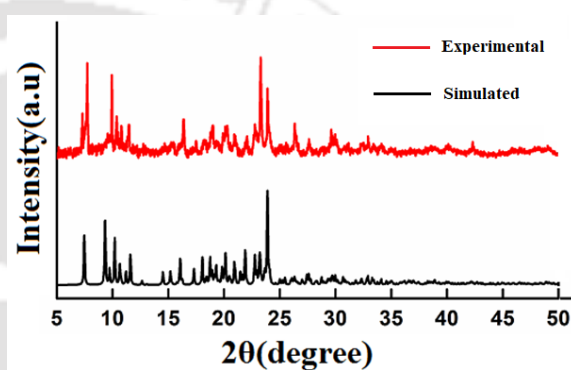
(a)



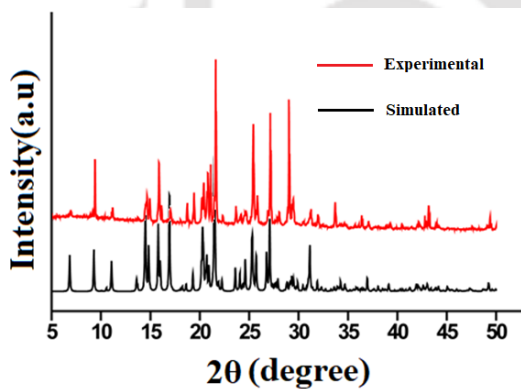
(b)



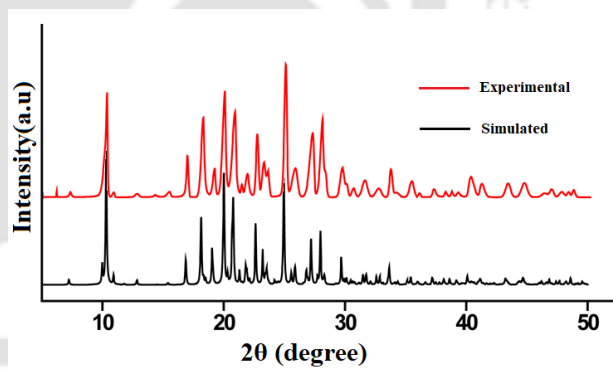
(c)



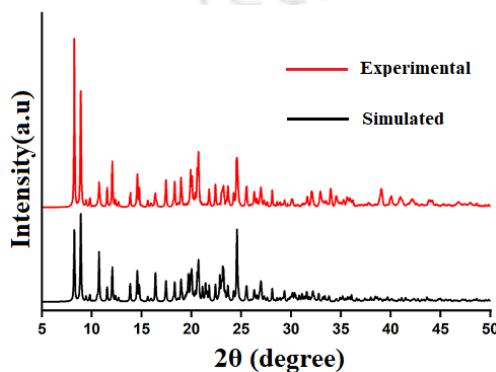
(d)



(e)

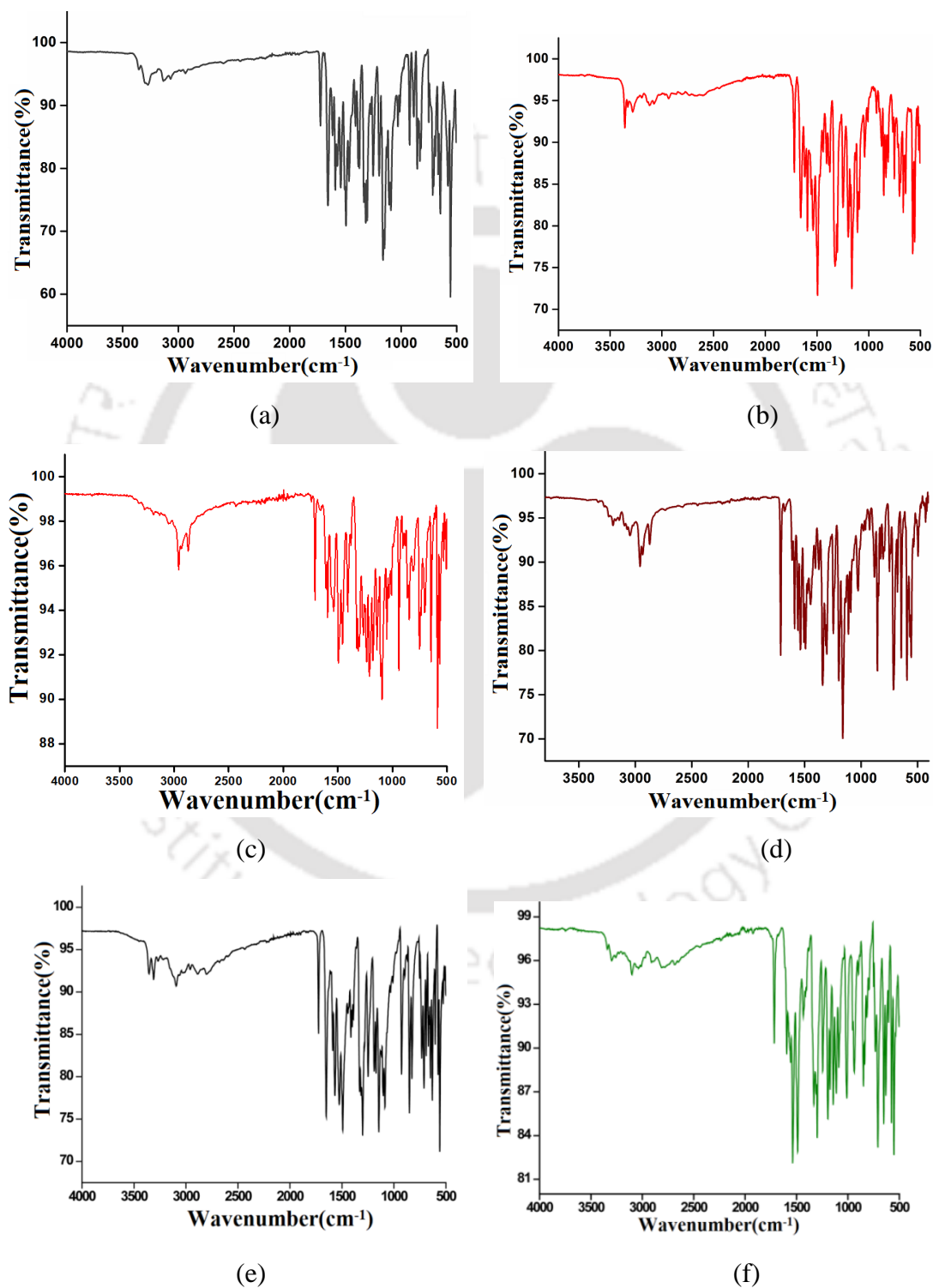


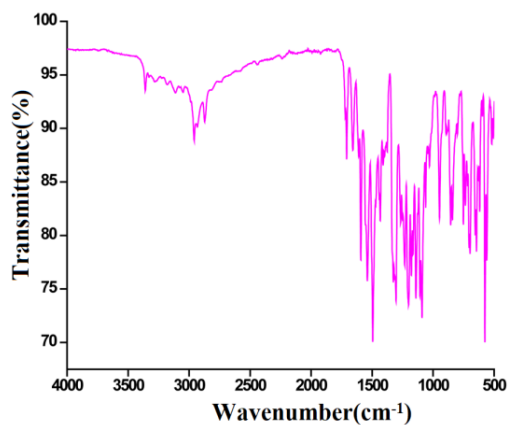
(f)



(g)

**Figure A3.1:** PXRD pattern of complexes (a) 3.1.1, (b) 3.1.2, (c) 3.1.3, (d) 3.1.4 and (e) 3.2.1 (f) 3.2.2 (g) 3.2.3 (Red = Experimental, Black = Simulated). Simulated pattern generated from CIF file.





(g)

Figure A3.2: FT-IR spectrum (neat) of the (a) 3.1.1 (b) 3.1.2 (c) 3.1.3 (d) 3.1.4 (e) 3.2.1 (f) 3.2.2 and (g) 3.2.4

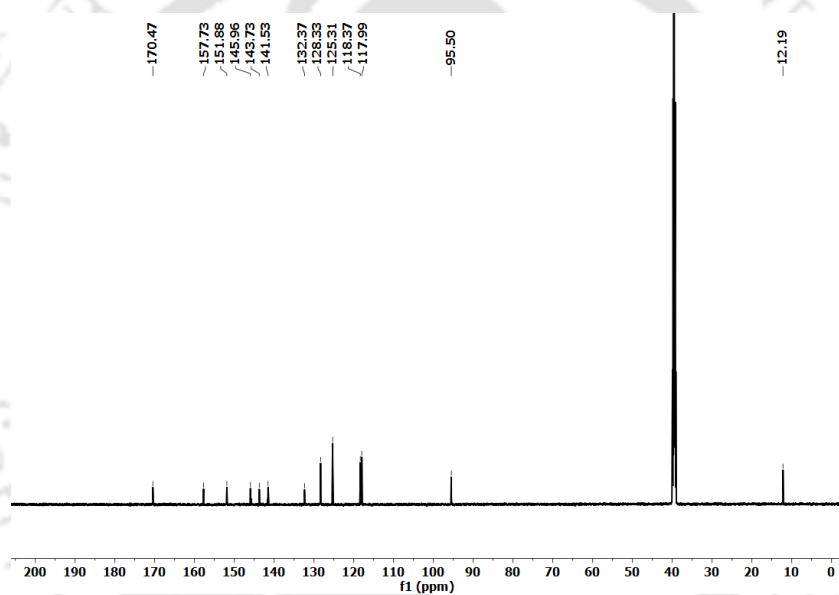
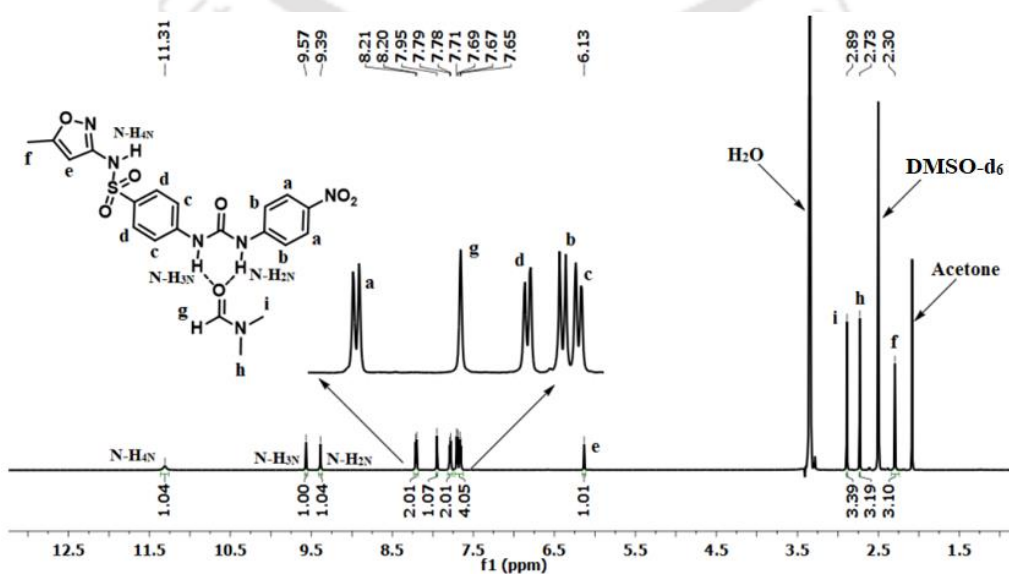
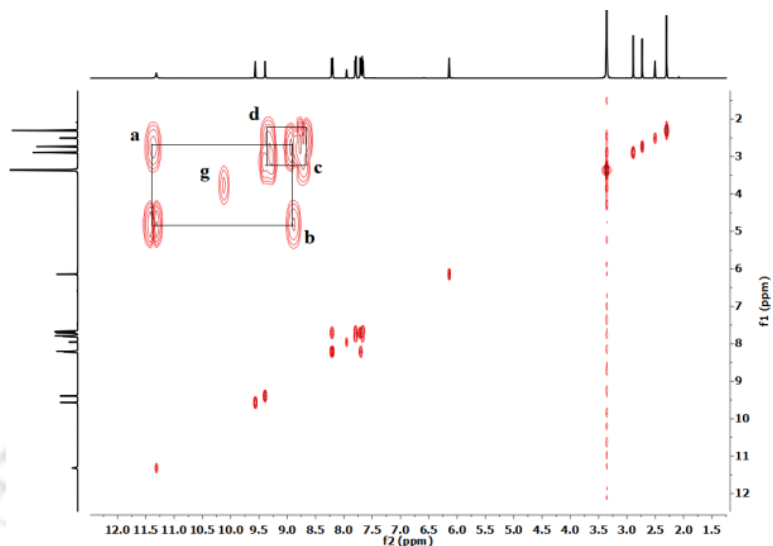
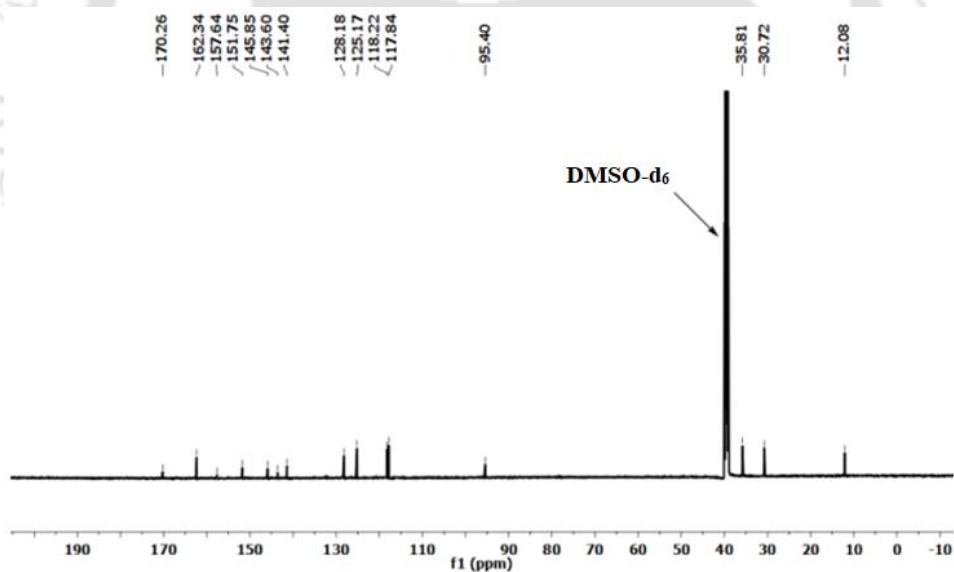


Figure A3.3:  $^{13}\text{C}$  NMR (125 MHz, DMSO- $\text{d}_6$ ) spectra of the 3.1



**Figure A3.4:**  $^1\text{H}$ NMR (DMSO- $d_6$ , 600 MHz) spectra of the **3.1.1**.**Figure A3.5:**  $^1\text{H}$ -2D-HOMOCOSY (600 MHz, DMSO- $d_6$ ) spectrum of the **3.1.1**.**Figure A3.6:**  $^{13}\text{C}$ NMR (125 MHz, DMSO- $d_6$ ) spectra of the **3.1.1**

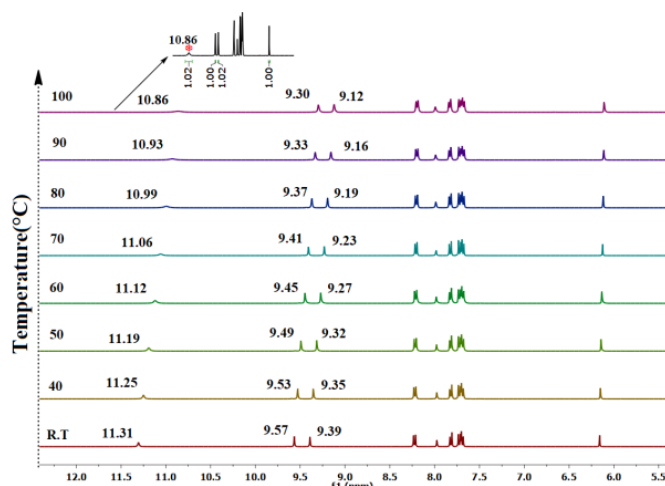


Figure A3.7:  $^1\text{H}$ NMR (DMSO- $d_6$ , 600 MHz) spectra of the **3.1.1** at variable temperatures.

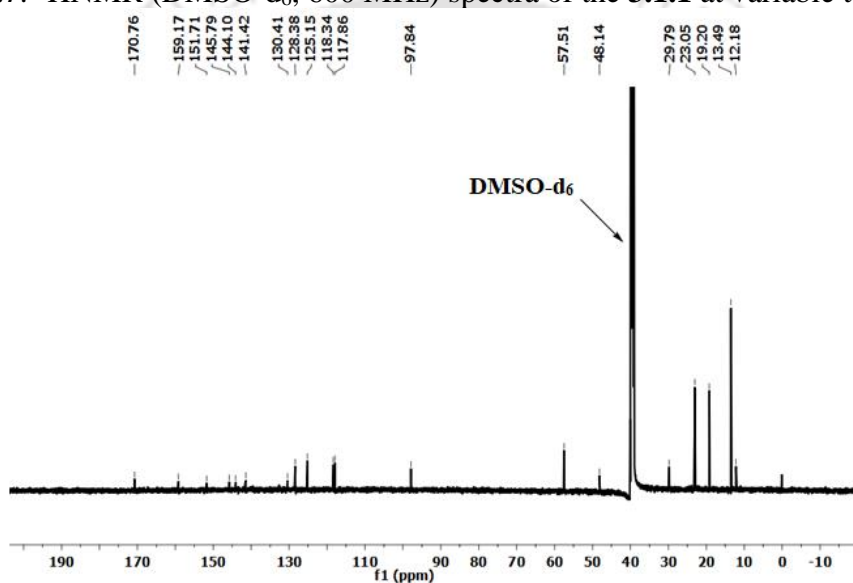


Figure A3.8:  $^{13}\text{C}$ NMR (125 MHz, DMSO- $d_6$ ) spectra of the **3.1.4**.

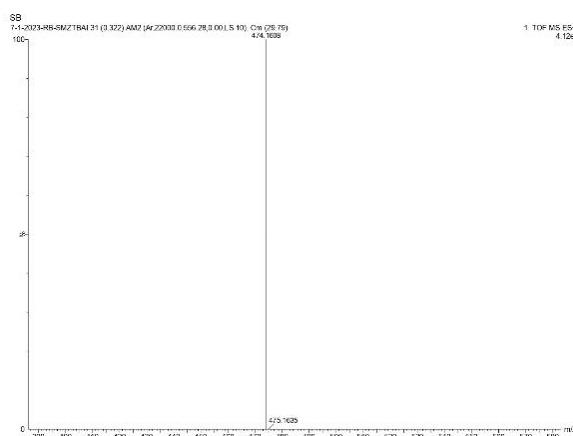


Figure A3.9: ESI mass spectrum of the **3.1.4**

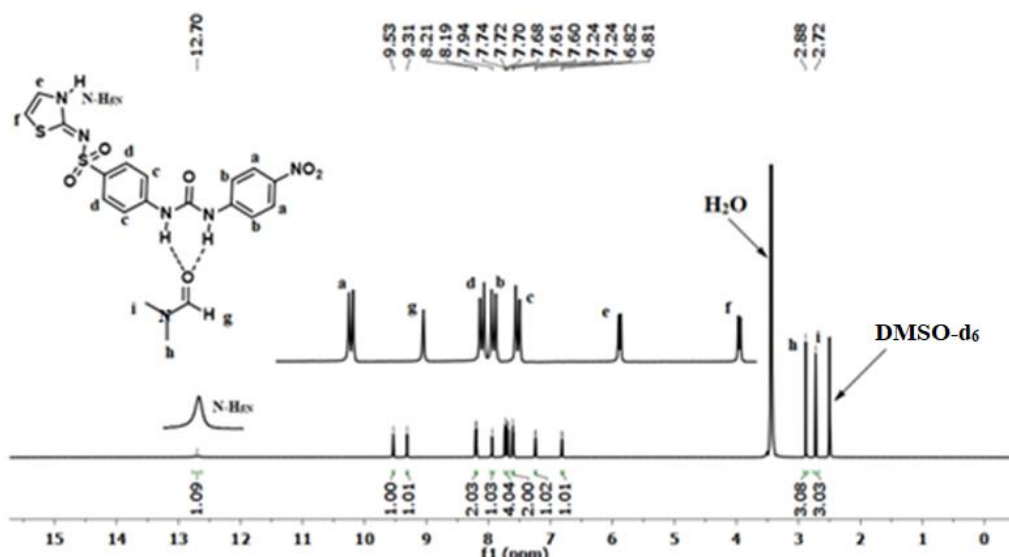


Figure A3.10: <sup>1</sup>H NMR (DMSO-d<sub>6</sub>, 600 MHz,) spectra of the 3.2.1.

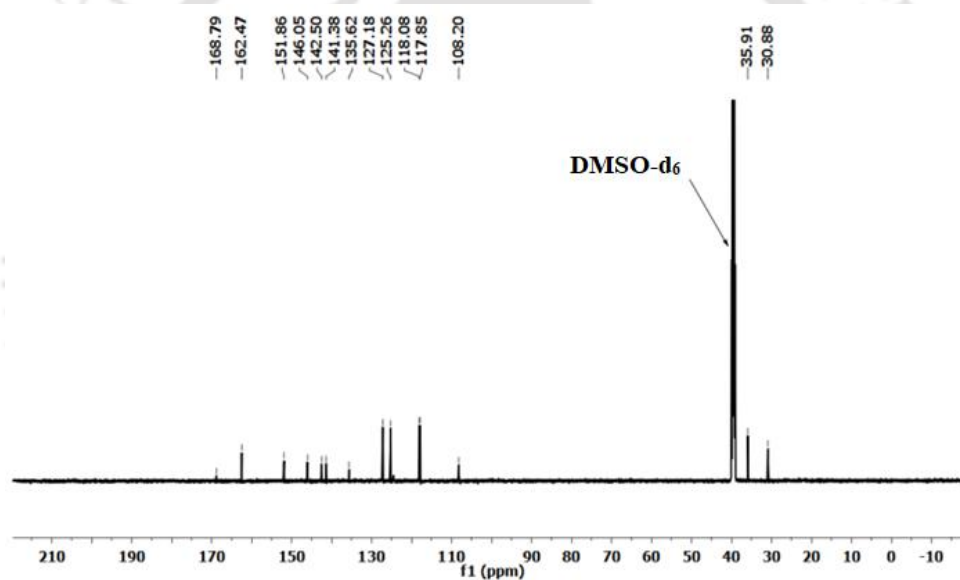


Figure A3.11: <sup>13</sup>C NMR (125 MHz, DMSO-d<sub>6</sub>) spectra of the 3.2.1

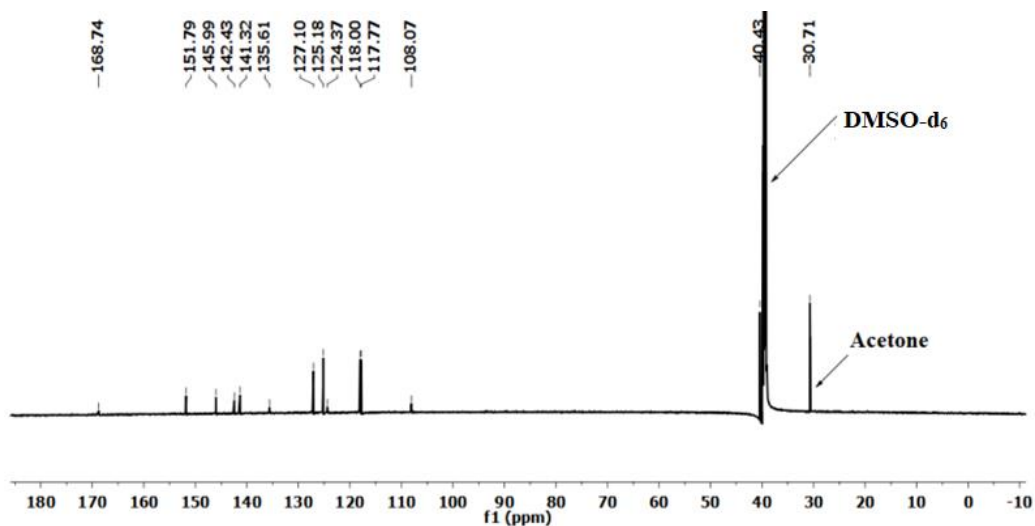


Figure A3.12:  $^{13}\text{C}$ NMR (125 MHz,  $\text{DMSO-d}_6$ ) spectra of the 3.2.2

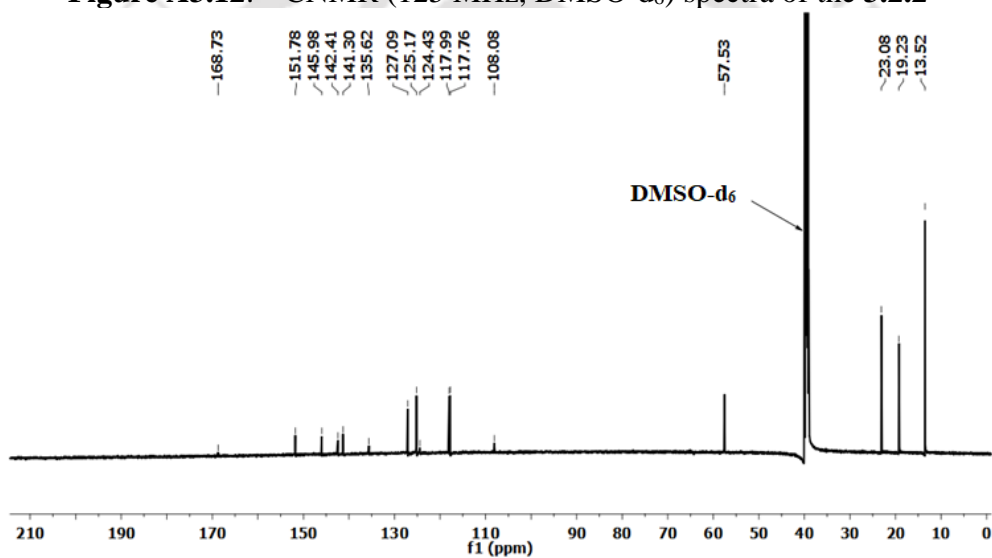


Figure A3.13:  $^{13}\text{C}$ NMR (125 MHz,  $\text{DMSO-d}_6$ ) spectra of the 3.2.3

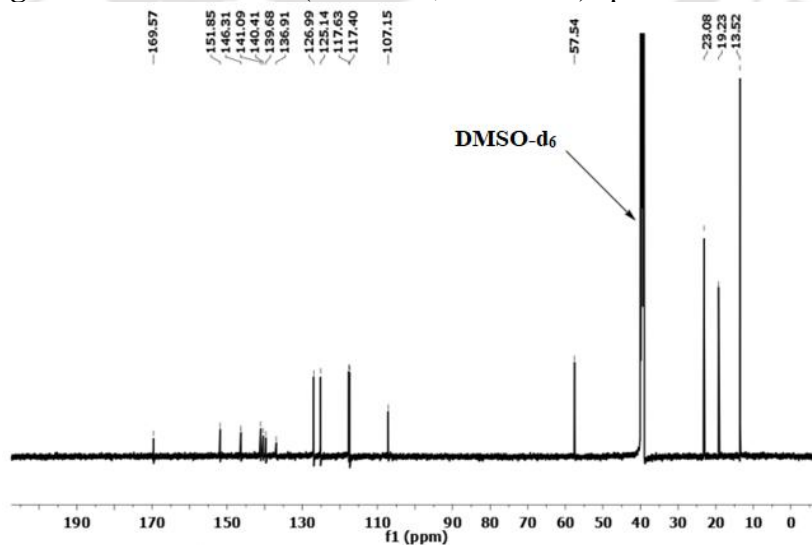


Figure A3.14:  $^{13}\text{C}$ NMR (125 MHz,  $\text{DMSO-d}_6$ ) spectra of the 3.2.4

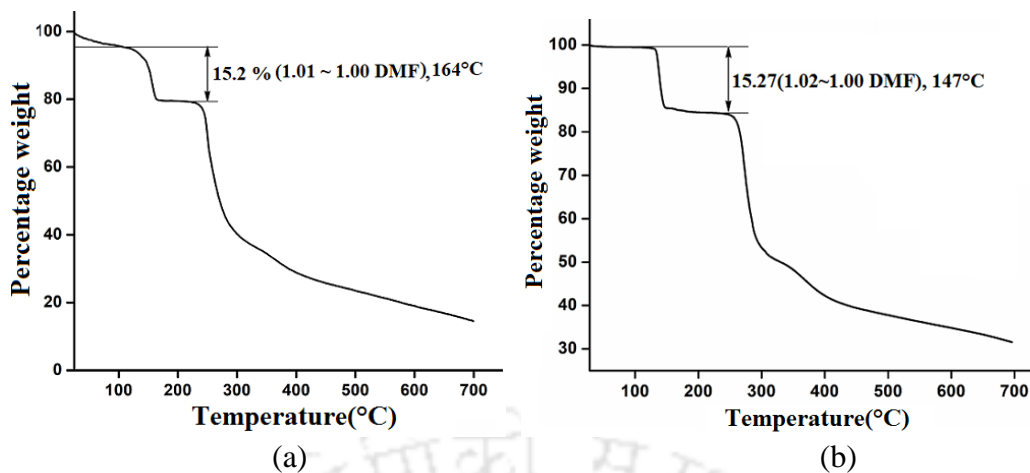


Figure A3.15: Thermogram of the polymorph (a) 3.1.1 (b) 3.1.2.

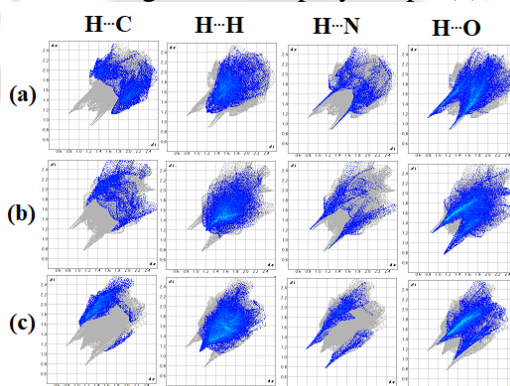


Figure A3.16: 2D fingerprint plots (including reciprocal contacts) of the H···C, H···H, H···O, H···N and H···anion interactions of (a) 3.1.1 (b) 3.1.2 (c) 3.1.3.

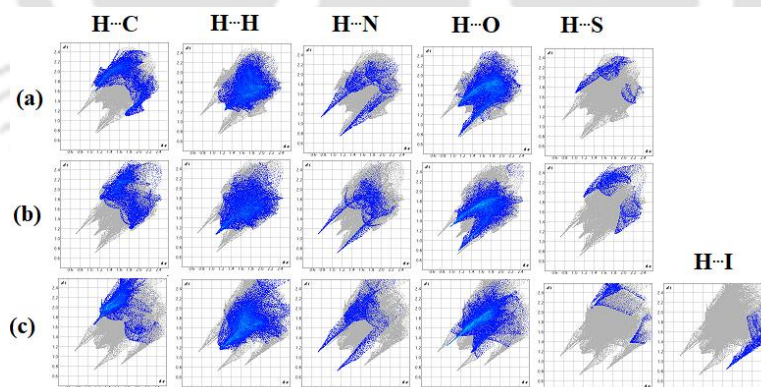
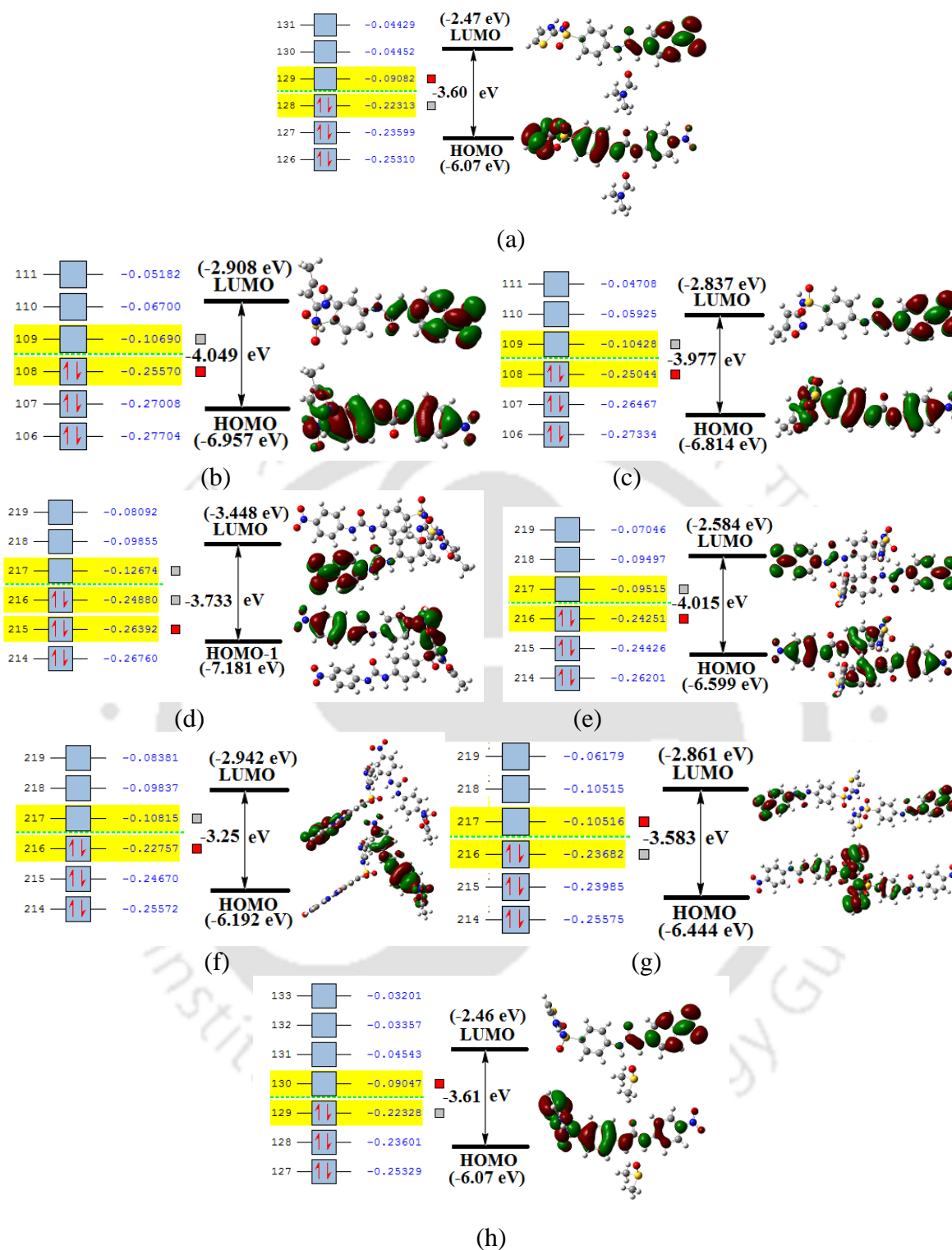


Figure A3.17: 2D fingerprint plots (including reciprocal contacts) of the H···C, H···H, H···O, H···N and H···anion interactions of (a) 3.2.1 (b) 3.2.2 (c) 3.2.3



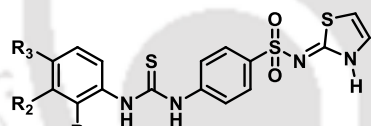
**Figure A3.18:** HOMO and LUMO gap (a) **3.2.1** (b) de-solvate of **3.1.1** (c) de-solvate of **3.1.2** (d) dimer of **3.1.1** (e) dimer of **3.1.2** (f) dimer of **3.1.3** (g) dimer of **3.2.1** (h) **3.2.2** calculated by DFT using B3LYP/6-31+G (d, p) as basis set.

## Chapter 4

### Assemblies of Sulfathiazole and Sulfamethazine Derived Thiourea: Polymorphs, Solvates and Fluoride Detection

#### 4.1: Introduction

In the last two chapters, the role of homo-dimers in the self-assemblies of urea derivatives derived from various sulpha drugs was presented. Thus, it was essential to study analogous thiourea-derived sulfa-drugs to explore the role of thiourea units in generating polymorphic and ionic cocrystals. In this chapter, a study of the role of the sub-assemblies within the self-assemblies of six sulfathiazole thiourea derivatives and a sulfamethazine-based thiourea derivative listed in Fig. 4.1 is presented. The study was carried out primarily to find out the common build-up units from a series of closely related members of compounds with differences in the substitution or positional isomers in their respective assemblies. It was with an expectation that the sub-assemblies formed within the assemblies would be guided by steric as well as electronic and organized through packing requirements. Systematic analysis of the crystal structures of a series of closely related compounds would help to establish the characteristic signature of those assemblies.



- 4.1 :  $R_1, R_2, R_3 = H$   
 4.2 :  $R_1, R_2 = H, R_3 = OCH_3$   
 4.3 :  $R_1, R_2 = Cl, R_3 = H$   
 4.4 :  $R_1, R_3 = Cl, R_2 = H$   
 4.5 :  $R_2, R_3 = Cl, R_1 = H$   
 4.6 :  $R_1, R_2 = H, R_3 = NO_2$

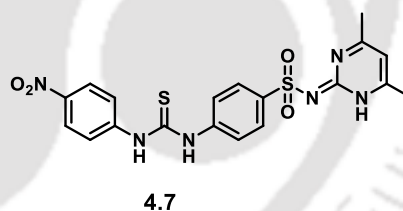


**Figure 4.1:** Different sulfathiazole and sulfamethazine derivatives studied in this work.

The energy associated with those sub-assembling units will impact physical properties. Accordingly, the energy of the series of principal sub-assemblies is theoretically evaluated. Namely, there will be many possibilities, such as the  $-SO_2-$  units of sub-assemblies may have different projections, or the arylthiourea portion may adopt *syn-syn* or *syn-anti* or *anti-anti* orientations to provide differences to generate polymorphs. Furthermore, a study on the assembling of the positional isomers of the dichloro-phenyl thiourea derivatives (**4.3**, **4.4** and **4.5**) listed in Fig. 4.1 would provide scopes to understand the role of halogen-bond interactions in providing the directionality to those assemblies. Thus, to identify the core

repeat units on which the self-assemblies of each form would be built, the compounds listed in Fig. 4.1 were studied.

#### 4.2: Synthesis of 4-(3-phenylthioureido)-N-(thiazol-2(3H)-ylidene)benzenesulfonamide (4.1)

The thiourea derivative **4.1** was prepared by condensation of sulfa drug sulfathiazole and phenyl isothiocyanate. The crude product **4.1** was characterized by the ESI-mass spectrum ( $[M+1]^+ = 391.0351$ ). The crude product **4.1** was dissolved separately in dimethylformamide (DMF) and acetone to produce two conformational polymorphs, **4.1.1** and **4.1.2**, respectively. The two conformational polymorphs were characterized by SC-XRD, PXRD,  $^1\text{H}$ NMR and  $^{13}\text{C}$ NMR.

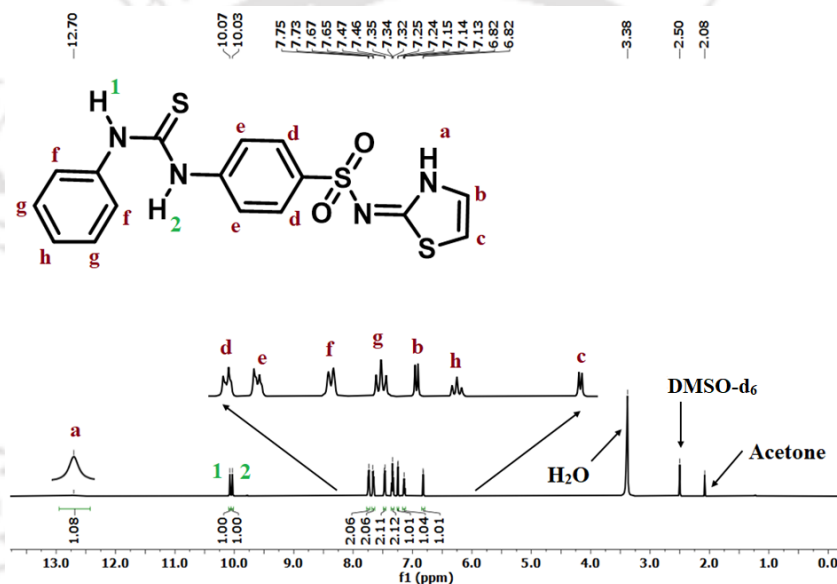


**Figure 4.2:**  $^1\text{H}$ -NMR (DMSO- $d_6$ , 600 MHz) spectra of the **4.1.2**

The  $^1\text{H}$ NMR spectrum of the polymorph is depicted in Fig. 4.2. The thiazole protons labelled as *b* and *c* appeared at 7.25-7.24 ppm and 6.82 ppm respectively, while the N-H proton on the heterocyclic ring labelled as *a* was observed at 12.70 ppm. The phenyl protons labelled as *d* and *e* were appeared at 7.75-7.73 ppm and 7.67-7.65 ppm, respectively. The aromatic protons labelled as *f*, *g* and *h* were observed at 7.47-4.46 ppm, 7.35-7.32 ppm and 7.15-7.13 ppm, respectively. The thiourea N-H protons labelled as 1 and 2 of the thiourea part appeared as 10.07 ppm and 10.03 ppm, respectively. The  $^{13}\text{C}$ NMR of **4.1.1** is shown in Fig A4.4b. The carbon atom of the thiocarbonyl of the thiourea part in the  $^{13}\text{C}$  NMR spectra appeared at 179.53 ppm. The geometry difference of the molecule in the polymorphs **4.1.1** and **4.1.2** influenced the C=S stretch appearing in the  $800\text{ cm}^{-1}$  to  $860\text{ cm}^{-1}$  regions of the respective IR

spectra. The *syn-anti* form had C=S stretch at  $822\text{ cm}^{-1}$  and  $851\text{ cm}^{-1}$ , and the *anti-anti* form had at  $835\text{ cm}^{-1}$  and  $858\text{ cm}^{-1}$  (Fig. 4.3).

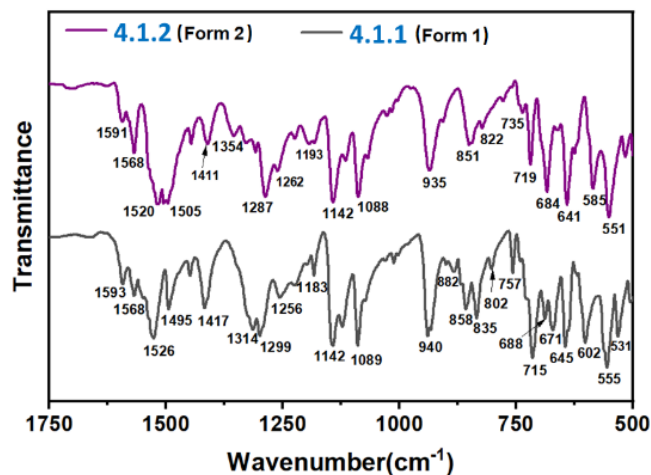


**Figure 4.3:** (a) Overlaid FT-IR spectra in region of  $1750\text{ cm}^{-1}$  to  $500\text{ cm}^{-1}$  of the two polymorphs **4.1.1** and **4.1.2**.

#### 4.3: Structural descriptions of the conformational polymorphs **4.1.1** and **4.1.2**

The two polymorphs of **4.1** could be prepared by crystallization from solution in a specific solvent. For this purpose, crystallization from different solvents was undertaken, and it was found that crystallization from DMF provided one polymorph, and a mixed solvent of methanol and acetone provided another polymorph. The one polymorphic form obtained from a solution in dimethylformamide (DMF) (crystals belong to  $P 2_1/c$ ) is referred to here as **4.1.1** had unit cell volume and crystal density  $3445.9(7)\text{ \AA}^3$ ,  $1.505\text{ g cm}^{-3}$ , respectively. On the other hand, the other polymorph was obtained from the crystallization from a solution in a mixed solvent of methanol and acetone ( $P \bar{1}$ , space group) is referred to as **4.1.2** had unit cell volume and crystal density  $878.1(4)\text{ \AA}^3$ ,  $1.477\text{ g cm}^{-3}$ , respectively. Though the crystallization of any of the two polymorphs was solvent-specific, each polymorph could be transformed into one another by re-crystallizing from the specific solvent that provided the particular polymorph. A report in the literature showed that the polymorphs of sulfamerazine were inter-convertible upon crystallization from different mixed solvents.<sup>1</sup> Hence, the solvent-induced crystallization of the polymorphs of **4.1** were not unexpected results. However, the structural aspects of this new thiourea derived from sulfathiazole provided a new outlook on the internal structures of their self-assemblies comprised of independent types of homodimers as sub-assemblies that are discussed in the following structural analysis



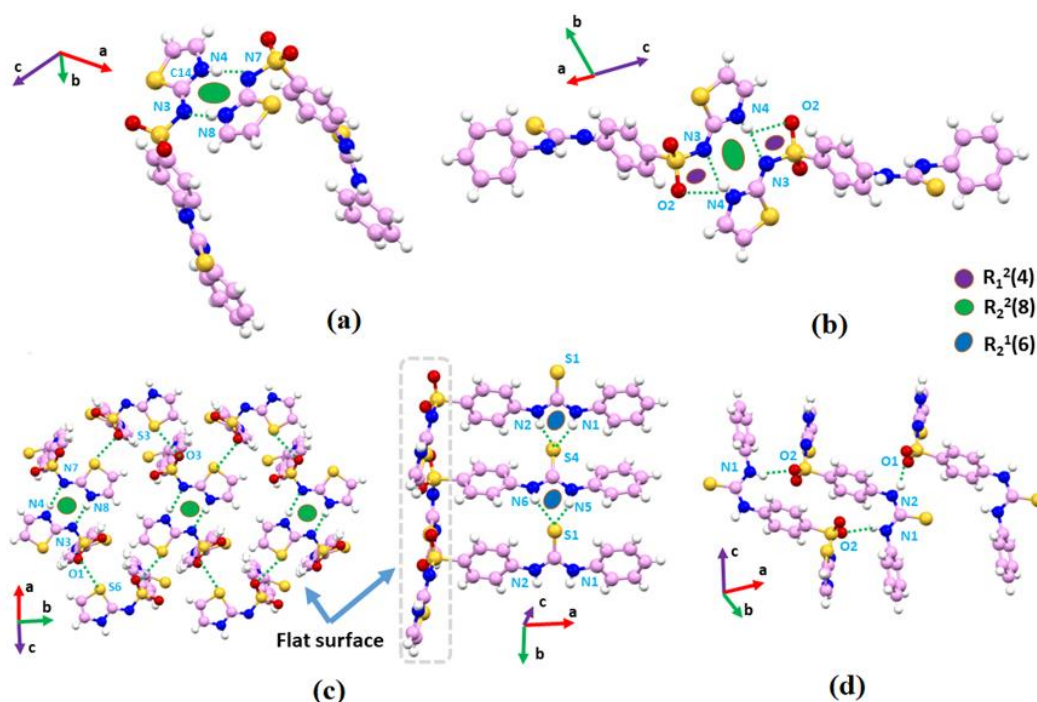


**Figure 4.5:** Hydrogen-bonded dimers of (a) **4.1.1** and (b) **4.1.2**; (c) and (d) are their respective packing diagrams. (e) The chain-like arrangements among the homodimers of **4.1.2**

The prominent hydrogen bonds are N1-H $\cdots$ S4 (2.67 Å, 151°); N2-H $\cdots$ S4 (2.56 Å, 155°) and N5-H $\cdots$ S4 (2.67 Å, 153°); N6-H $\cdots$ S4 (2.66 Å, 162°) illustrated in the Fig. 4.5c respectively. The respective hydrogen bond parameters are listed in Table 4.1. The O3 atom of the -SO<sub>2</sub>-unit had inter-molecular and intra-molecular S<sub>thiazole</sub> $\cdots$ O interactions (Fig. 4.5c; d<sub>S6 $\cdots$ O3</sub> intra-molecular 2.89 Å, and d<sub>S3 $\cdots$ O3</sub> inter-molecular 3.00 Å). On the other hand, due to the *syn-anti* orientation, the N-H of the thiourea in the polymorph **4.1.2**, formed hydrogen bond with the oxygen atom of the -SO<sub>2</sub>-unit of sulfathiazole part.

**Table 4.1:** Hydrogen bond parameters of the polymorphs (**4.1.1** and **4.1.2**)

polymorphs	D-H $\cdots$ A (Symmetry)	d <sub>D-H</sub> (Å)	d <sub>H<math>\cdots</math>A</sub> (Å)	d <sub>D<math>\cdots</math>A</sub> (Å)	$\angle$ D-H $\cdots$ A (°)
<b>4.1.1</b>	N(1)-H(1) $\cdots$ S(4) [x, 1+y, z]	0.86	2.67	3.444(7)	151
	N(2)-H(2) $\cdots$ S(4) [x, 1+y, z]	0.86	2.56	3.363(7)	155
	N(4)-H(4) $\cdots$ N(7) [x, 3/2-y, -1/2+z]	0.86	2.01	2.856(8)	170
	N(5)-H(5) $\cdots$ S(1) [x, y, z]	0.86	2.67	3.459(7)	153
	N(6)-H(6) $\cdots$ S(1) [x, y, z]	0.86	2.66	3.487(7)	162
	N(8)-H(8) $\cdots$ N(3) [x, 3/2-y, 1/2+z]	0.86	2.00	2.845(7)	168
	C(15)-H(15) $\cdots$ O(2) [x, 1+y, z]	0.93	2.59	3.349(8)	139
	C(15)-H(15) $\cdots$ O(2) [x, 1+y, z]	0.93	2.39	3.246(9)	154

<b>4.1.2</b>	N(1)-H(1) ...O(2) [2-x, 1-y, 1-z]	0.86	2.09	2.876(7)	152
	N(2)-H(2) ...O(1) [-1+x, y, z]	0.86	2.23	2.923(7)	138
	N(4)-H(4) ...O(2) [2-x, 1-y, -z]	0.86	2.59	3.263(8)	136
	N(4)-H(4) ...N(3) [2-x, 1-y, -z]	0.86	2.08	2.898(8)	159

The medium-strength hydrogen bonds N1-H...O2 (2.09 Å, 152°) and N2-H...O1 (2.23 Å, 138°) were responsible for providing a robust hydrogen-bonded cyclic structure as shown in Fig. 4.5d. The S=O(1), S=O(2) and S=O(3), S=O(4) bond-lengths in the polymorph **4.1.1** were 1.44 Å, 1.43 Å respectively; whereas, in the **4.1.2**, S=O(1) and S=O(2) bond lengths were 1.42 Å and 1.45 Å. The longer S=O(2) bond length in the **4.1.2** bond was due to its participation in the hydrogen bond by the oxygen atom with the N-H(1) of the thiourea part. In **4.1.1**, the sulphonamide group participated in weak S...O and also C15-H...O2 interactions. Whereas, in **4.1.2**, the sulphonamide group was involved in two discrete weak N-H<sub>thiourea</sub>...O=S hydrogen bonds. The clip-like arrangements were found in polymorph **4.1.1**; Each clip-like structure was located at alternate positions in upward and downward directions. This type of arrangement provided a flat outer surface of a rod-like arrangement that was extended along the *b*-crystallographic axis. In the case of **4.1.2**, the homodimers were connected by hydrogen bonds to form an extended chain-like arrangement. Stator-like structures were observed earlier in freely rotatable thiazole units linked to an imine,<sup>2</sup> and the hydrated form of such compounds also showed polymorphs.<sup>3</sup> In the present example, no solvate of **4.1** was observed during crystallization from different solvents. There was also an example in the literature on having the hairpin-like structure of a -SO<sub>2</sub>- unit containing compound, namely, di(4-bromobenzenesulfonyl)amine.<sup>4</sup> But, in the present case, the dimeric assemblies adopted a hairpin-like structure. In an earlier study, it was shown that the number of symmetry-independent molecules in a unit cell was dependent on the solvent molecules of solvates.<sup>5</sup> It was also shown that the different hydrogen-bonded homodimers<sup>6</sup> or different synthons<sup>7</sup> result in polymorphs. There are examples in which the signature of an assembly in solution gets carried to a solid-state structure.<sup>8</sup> Based on those observations, the homodimeric units in the assemblies with two different geometries were conceived during crystallization, and those were guided by the respective solvents. Our findings also complimented the occurrence of solvent-mediated conformational polymorphs in urea-derived chlorosulfanilide that was observed earlier.<sup>9</sup> In the two polymorphs, the orientations

of N-H groups of thiourea across the C=S bond had described a geometrical change rather than a conformational adjustment during crystallization from a solution.

Solvent guiding to crystallize a particular crystalline form, as well as their inter-conversion in solution, requires an understanding of the schemes of weak interactions.<sup>10</sup> In our case, the molecules of the two polymorphs had independent geometries (Fig. 4.6a). Hence, the energy of each was different. The energy of individual molecules of the two polymorphs was calculated by DFT using B3LYP hybrid functional of 6-311++G (2d, p) basis set. The molecule with *syn-anti* form (4.1.2) had energy 14 kJ/mole lower than the molecule having *anti-anti* form (4.1.1). Hence, energetically, they have a small difference. For their interconversion, the activation barrier was examined. Accordingly, the energy of the molecule with different dihedral angles was calculated using a scan-coordinate of DFT calculation. The plot of the respective energy vs the dihedral angles is plotted in Fig. 4.6b. The activation barrier for the *anti-anti* form (form 1 in Fig. 4.6a) to convert to *syn-anti* (form 2) was found from the plot to be 41 kJ/mole (Fig. 4.6b). This energy was comparable to the energy of solute-solvent hydrogen bonds. Hence, a solvent-assisted conversion between the two polymorphs was possible by changing solvents (namely, dissolving the crystalline product from DMF in methanol and vice versa). The polymorph obtained from methanol acetone mixed solvent could be converted to the polymorph that was obtained from a solution in DMF or by crystallising any of the forms from the solution in the respective solvent.

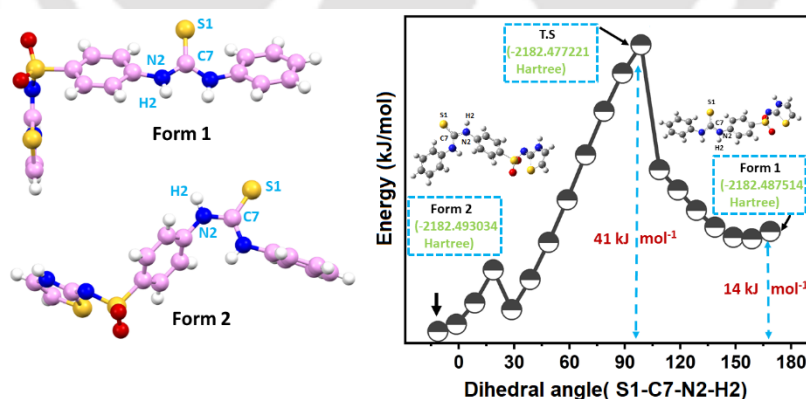


**Figure 4.6:** (a) Geometries of the 4.1 in the polymorphs; (b) Theoretically calculated change in the energy of the 4.1 with different dihedral angles S1-C7-N2-H2.

Both the polymorphs had imine forms (that is, having an exocyclic C=N on the heterocyclic part) but had slight geometrical differences. The C14=N3 and C14=N4 bonds of the thiazole part with respective carbon-nitrogen bond distances 1.33(8) Å and 1.34(7) Å (Fig. 4.5a) in

**4.1.1** were relatively longer than the corresponding counterparts in the polymorph **4.1.2** (Fig. 4.5b). In the latter case, those C=N bond distances were 1.30 (8) Å and 1.32(8) Å, respectively. This is explained by the geometrical features of the homodimers. The projection of the -SO<sub>2</sub>- unit with respect to the S-atom of the thiazole rings in the homodimers were dissimilar in the **4.1.1** (Fig. 4.5a) whereas the -SO<sub>2</sub>- units were projected in the same direction with respect to the S-atom of the thiazole (Fig 4.5b) in the homodimers of the **4.1.2**. In the latter case, the O2-atom of the S=O was involved in a hydrogen bond with N4-H<sub>(thiazole)</sub> ( $d_{D-A} = 3.263$  Å,  $\angle D-H\cdots A = 136^\circ$ ; Fig. 4.5b). However, the geometry of the homodimer of **4.1.1** did not permit such a hydrogen bond in its assembly. These differences are attributed to the nature of homodimers in the respective assemblies. The differences in the environment caused dissimilar electron conjugations in the N4H-C14=N3 part in the former case; hence, the dissimilar C=N bonds were observed due to electronic effects. Accordingly, the polymorphs are better described by the geometrical differences across the homo-dimeric units. Hence, the two polymorphs of **4.1** belong to a class of polymorphs<sup>5,11</sup> that occurred from geometrical differences among homodimers.

#### 4.4: Comparison of the morphologies of the polymorphs 4.1.1 and 4.1.2

The significant structural differences and packing differences provided avenues to explore a possible correlation to morphology from scanning electron micrographs and the arrangement patterns within unit cells.

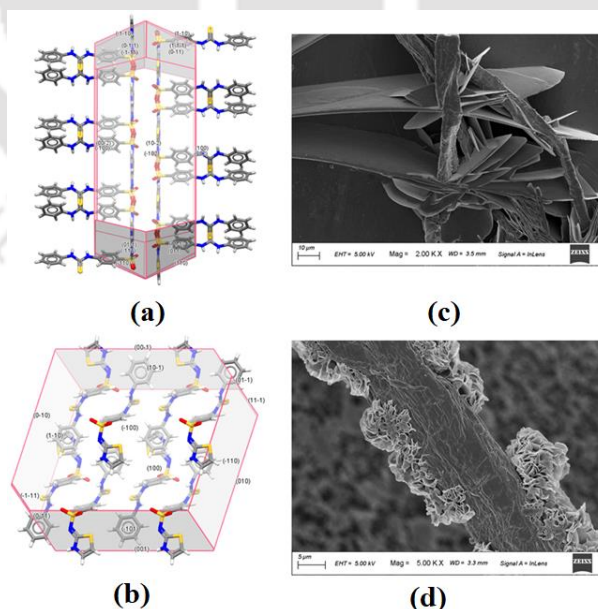


**Figure 4.7:** Bravais, Friedel, Donnay and Harker crystal morphology of (a) **4.1.1** and (b) **4.1.2**. Scanning electron microscopy images of the polymorph (c) **4.1.1** and (d) **4.1.2**

From the arrangements of molecules in the unit cell, the Bravais, Friedel, Donnay and Harker (BFDH) crystal morphologies of the two polymorphs were evaluated and are presented in Fig. 4.7a and 4.7b. The crystal morphologies of the two polymorphs under a scanning electron microscope are shown in Fig. 4.7c and 4.7d. The SEM images supported the BFDH morphologies. **4.1.1** had flat plate-type unidirectional distributions (Fig.4.7c), and **4.1.2** had aggregates of rhombus-type microcrystals (Fig. 4.7d), as expected from the arrangements of molecules in the unit cells.

#### 4.5: Synthesis of thiourea derivative 4-{3-(4-methoxyphenyl)thioureido)-N-(thiazol-2(3H)-ylidene)benzenesulfonamide (4.2)

The compound 4-{3-(4-methoxyphenyl)thioureido)-N-(thiazol-2(3H)-ylidene)benzenesulfonamide was prepared by following a procedure that was similar to the synthesis of the compound **4.1**. But in this case, 4-methoxyphenyl isothiocyanate was used as a reagent instead of the phenyl isothiocyanate. The compound was re-crystallized from methanol-acetone mixed solvent. The compound showed high-resolution ESI-mass  $[M+1]^+ = 421.0466$ , which corresponded to the structure of the compound and also confirmed the formation and purity

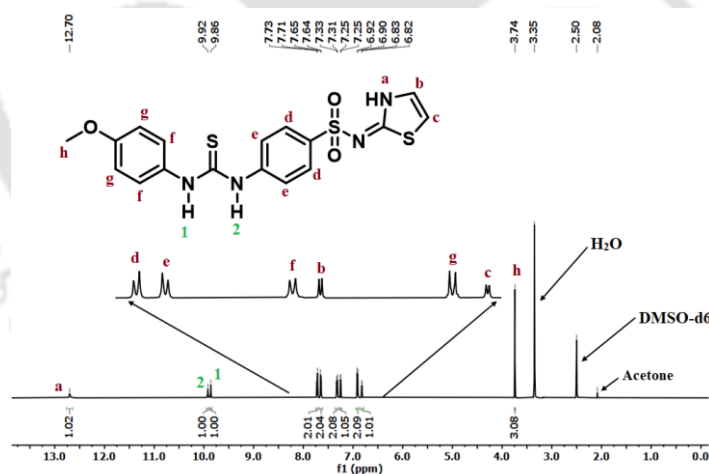


Figure 4.8:  $^1\text{H-NMR}$  ( $\text{DMSO-d}_6$ , 600 MHz) spectra of the **4.2**

The  $^1\text{H-NMR}$  spectra of compound **4.2** is depicted in Fig. 4.8. The thiazole protons labelled as *b* and *c* were observed at 7.25 ppm and 6.83-6.82 ppm, respectively. The N-H proton of the ring (*a*) appeared at 12.70 ppm. The phenyl protons (shown as *d* and *e* in the structure) appeared at 7.73-7.71 ppm and 7.65-7.64 ppm, respectively. The protons *f*, *g* and *h* appeared at 7.33-7.31 ppm, 6.92-6.90 ppm and 3.74 ppm respectively. The N-H protons of thiourea labelled as *1* and *2* appeared as 9.86 and 9.92, respectively. The  $^{13}\text{C-NMR}$  of the thiourea

derivative **4.2** is shown in Fig. A4.4c. It showed chemical shift at 179.69 ppm for the carbon of thiocarbonyl of thiourea part and a peak at 55.26 ppm for the carbon of methoxy group. The IR spectra of the compound had the C=S at  $830\text{ cm}^{-1}$  and S=O at  $1148\text{ cm}^{-1}$

#### 4.6: Structural descriptions of the thiourea derivative **4.2**

The compound **4.2** was crystallized only in one form upon independent crystallisation from solutions in different solvents. The crystal structure of the thiourea derivative **4.2** showed that its self-assembly was comprised of homo-dimeric hydrogen-bonded sub-assemblies formed by hydrogen bonds between two iminothiazole parts of two molecules (Fig. 4.9a). In these homodimers, the two S=O bonds of the -SO<sub>2</sub>- units across the dimer were projected in the same direction and had a *syn*-relationship to each other. In this regard, the structure had some structural similarities to the assembly of the polymorph **4.1.2**, whose structure was described in the previous section. The thiourea part of the molecule **4.2** had an *anti-anti* orientation. This geometry provided large differences in the packing pattern of this compound as compared to the packing pattern of the un-substituted derivative **4.1.2**, as the latter had a *syn-anti* orientation.

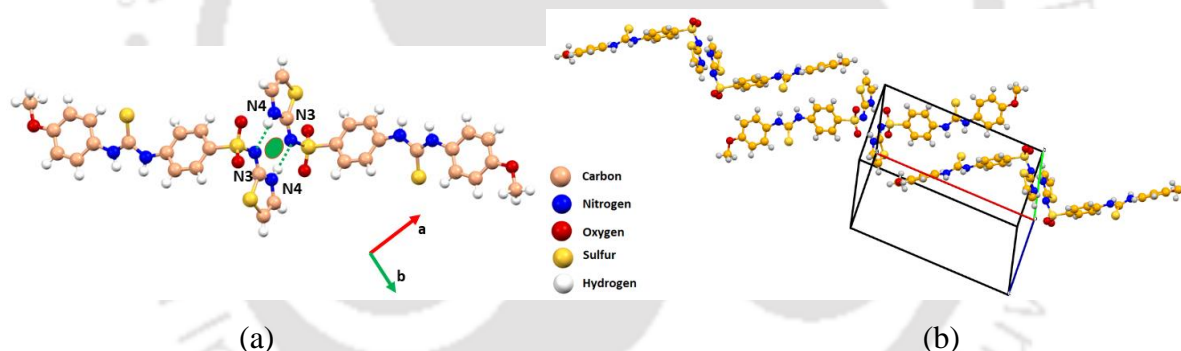


**Figure 4.9:** Homo-dimeric assembly of (a) **4.2** and (b) one-dimensional assembling of the homodimers

The self-assembly of the **4.2** had homodimers that were linked together, forming a linear chain-like arrangement (Fig. 4.9b). Whereas, the homodimers of **4.1.2** were arranged as a one-dimensional chain. It may be suggested that, due to the *anti-anti* orientation of the molecules in the dimers of **4.2**, the overall structure was observed to be a hydrogen-bonded single chain. Whereas the dimers of **4.1.2** had *syn-anti* geometry and formed double chains. The parent molecules of the **4.2** were different from **4.1.2** by having a methoxy group. The steric effect, packing requirement together with the electronic factors caused the overall differences in their assembling processes. The methoxy group did not participate in the hydrogen bonding scheme. This was an exception to Etter's rule,<sup>12</sup> but it was not surprising as there were examples where methoxy-groups remained free without participating in hydrogen

bonds in crystal lattice. Such exception is observed in assemblies where the steric effects control the weak interactions or vice-versa.<sup>13</sup> To avoid the direct repulsions between two methoxy groups in the tightly-packed structure, the molecule adopted an *anti-anti* geometry. The structural comparisons between compounds with and without the methoxy group showed that the principal homo-dimeric self-assemblies were similar in both cases.

#### 4.7: Synthesis of 4-(3-(a,b-dichlorophenyl)thioureido)-N-(thiazol-2(3H)-ylidene)benzene sulfonamide; (a,b = 2,3 (4.3); 2,4 (4.4) or 3,4 (4.5) respectively)

Three positional isomers 4-(3-(a,b-dichlorophenyl)thioureido)-N-(thiazol-2(3H)-ylidene)benzenesulfonamide (where a, b = 2,3-(4.3), 2,4-(4.4) and 3,4-(4.5)) were prepared by condensation reactions of the respective positional isomer of di-chlorophenyl isothiocyanate with sulfathiazole in acetonitrile. In each case, the crystallization of each compound was independently carried out from solvents such as a mixture of methanol and acetone, DMF and DMA. In all the solvents, only one form of individual compound was crystallized. All the positional isomeric compounds were characterized by recording the high-resolution mass, NMR and IR spectra and finally determining the crystal structures. The spectral details are listed in the experimental section, as an illustrative case some of the spectroscopic details of compound **4.3** is discussed in the text. The ESI-mass spectrum of the compound **4.3** showed the  $[M+1]^+$  (at 458.9572 which corresponded to the expected value of the same).

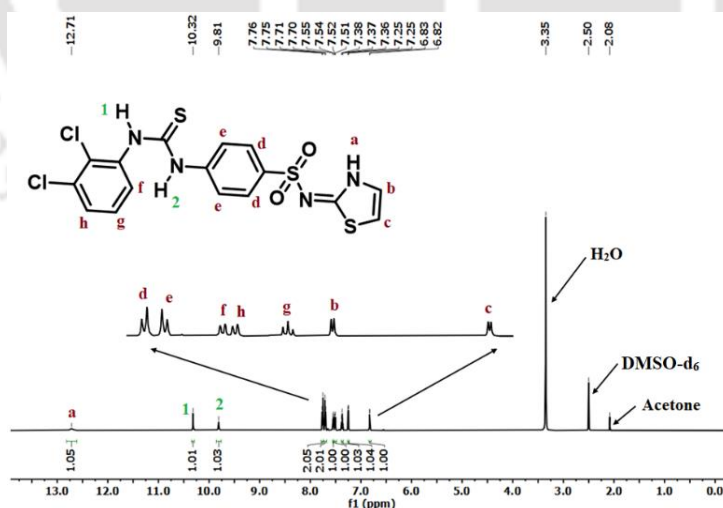


Figure 4.10:  $^1\text{H-NMR}$  (DMSO- $d_6$ , 600 MHz) spectra of the **4.3**

The  $^1\text{HNMR}$  spectra of **4.3** is depicted in Fig. 4.10. The peak appearing at 7.25 ppm and 6.83-6.82 ppm were assigned to the thiazole protons marked as *b* and *c*, respectively. The N-H proton of the thiazole (*a*) appeared at 12.71 ppm. The phenyl protons *d* and *e* appeared at

7.76-7.75 ppm and 7.71-7.70 ppm, and *f*, *g* and *h* appeared at 7.55-7.54 ppm, 6.38-6.36 ppm and 7.52-7.51 ppm, respectively. The N-H protons of thiourea **1** and **2** were observed at 10.32 ppm and 9.81 ppm respectively. The integration of each peak was in accordance with the assigned structure. The  $^{13}\text{C}$ NMR of **4.3** is given in Fig. A4.4d, showed a chemical shift at 180.41 ppm for the carbon of thiocarbonyl of thiourea part. The IR spectra of the compound had the C=S at  $834\text{ cm}^{-1}$  and S=O at  $1141\text{ cm}^{-1}$ . The  $^1\text{H}$ NMR spectrum of the other two positional isomers, **4.4** and **4.5**, are shown in Fig. A4.3b and c, respectively, while  $^{13}\text{C}$ NMR of the respective positional isomers are shown in Fig. A4.4e and f.

#### 4.8: Structural descriptions of the thiourea derivative 4.3-4.5

The crystals of **4.3** and **4.4** belong to the  $P\bar{1}$  space group, while the crystals of **4.5** belong to  $P2_1/n$  space group. The crystal volume and crystal densities of **4.3** and **4.4** are  $958.86(17)\text{ \AA}^3$ ,  $1.591\text{ g cm}^{-3}$  and  $1000.0(2)\text{ \AA}^3$ ,  $1.526\text{ g cm}^{-3}$  respectively, while for the **4.5**, these values are  $1955.52(18)\text{ \AA}^3$  and  $1.560\text{ g cm}^{-3}$ . Each of these compounds was monomorphic, and all had assemblies of homodimers similar to the ones found in the assembly of **4.1.2**. Each of them also had a *syn-anti* orientation of the thiourea portions.

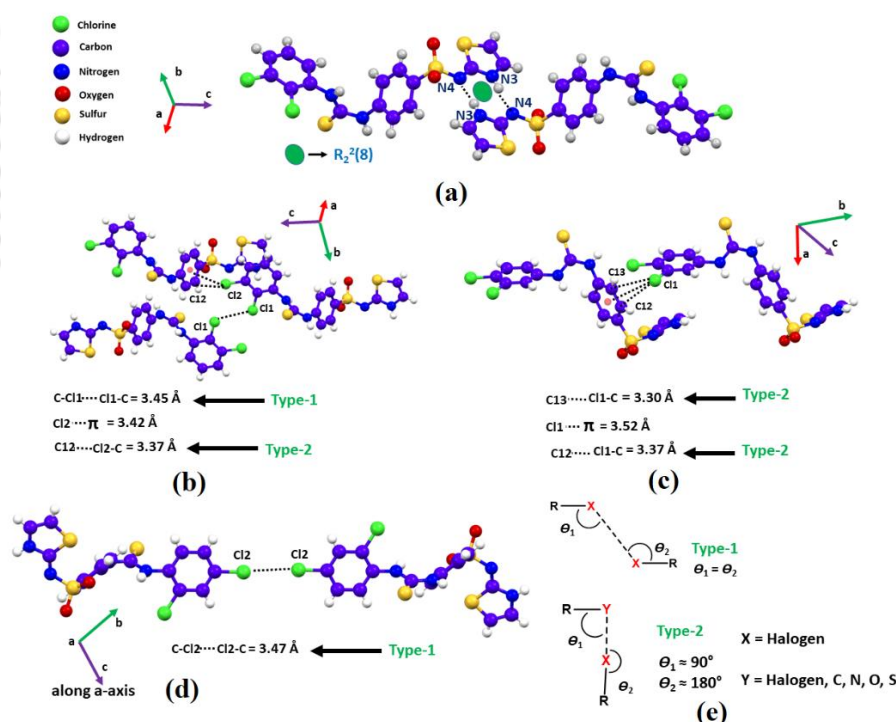


**Figure 4.11:** The packing diagrams of (a) **4.3**, (b), and (c) (d) are halogen bond interactions in **4.3**, **4.5** and **4.4**, respectively; (e) Geometries of two types of halogen bonds

To avoid a repetitive description of the packing of each positional isomer, one representative homodimer (of **4.3**) is shown in Fig. 4.11a. The assemblies of these positional isomers had inter-chlorine interactions, which are listed together with the chlorine-bond parameters in Fig.

4.11b-e. The two isomers having the chlorine at the ortho position of the phenyl rings were involved in Cl $\cdots\pi$  interactions. On the other hand, there were Cl $\cdots$ Cl interactions. The **4.3** had C-Cl $\cdots$ Cl- C (3.45 Å,  $\theta_1 = \theta_2$ , 126°) as well as C-Cl $\cdots$ C (3.37 Å,  $\theta_1 = 86.67^\circ$ ,  $\theta_2 = 153.89^\circ$ ) interactions; whereas, **4.4** and **4.5** had C-Cl $\cdots$ Cl-C (3.47 Å,  $\theta_1 = \theta_2$ , 154.69°) and C-Cl $\cdots$ C (3.30 Å,  $\theta_1 = 74.23^\circ$ ,  $\theta_2 = 147.99^\circ$ ) interactions, respectively. The **4.3** had Cl $_2\cdots\pi$ (phenylene) interactions and Cl $_1\cdots\pi$ (phenylene) interactions, which were responsible for holding the dimers together. The prominent hydrogen bond parameters of the three positional isomers are shown in Table 4.2.

**Table 4.2:** Hydrogen bond parameters of the positional isomers (**4.3-4.5**)

Positional isomers	D-H $\cdots$ A (Symmetry)	d <sub>D-H</sub> (Å)	d <sub>H<math>\cdots</math>A</sub> (Å)	d <sub>D<math>\cdots</math>A</sub> (Å)	$\angle$ D-H $\cdots$ A (°)
<b>4.3</b>	N(1)-H(1) $\cdots$ O(1) [2-x, 1-y, 1-z]	0.86	2.11	2.909(3)	154
	N(2)-H(2) $\cdots$ O(2) [-1+x, y, z]	0.86	2.10	2.904(3)	155
	N(4)-H(4) $\cdots$ N(3) [2-x, -1-y, -z]	0.86	2.02	2.870(3)	171
<b>4.4</b>	N(1)-H(1) $\cdots$ O(2) [1-x, 1-y, 1-z]	0.86	2.14	2.940(6)	155
	N(2)-H(2) $\cdots$ O(1) [1+x, y, z]	0.86	2.18	2.948(6)	148
	N(1)-H(1) $\cdots$ O(2) [1-x, 2-y, 1-z]	0.86	2.57	3.237(6)	136
	N(4)-H(4) $\cdots$ N(3) [1-x, 2-y, 1-z]	0.86	2.12	2.935(6)	158
<b>4.5</b>	N(1)-H(1) $\cdots$ O(1) [-x, -y, -z]	0.86	2.14	2.911(4)	149
	N(2)-H(2) $\cdots$ O(2) [1+x, y, z]	0.86	2.14	2.917(3)	150
	N(4)-H(4) $\cdots$ N(3) [-x, 1-y, -z]	0.86	2.03	2.884(4)	173

These interactions are based on the lengths of the distances between the interacting atoms, which were shorter than the sum of the van der Waals radii of the respective atoms involved in the interactions.<sup>14</sup> There are two types of prominent halogen-bond interactions, namely,<sup>14</sup> type 1 and type 2, as illustrated in Fig 4.11e. Both type 1 and type 2 were observed in the self-assembly of **4.3**, whereas, in the case of the compounds **4.4** and **4.5**, only the type 2 interactions were observed. In general, chlorine atoms of compounds in self-assemblies participate in weak interactions, and there were examples of compounds that adopted helical structures due to such interactions.<sup>15</sup>

The **4.3** and **4.4** belonged to the same space group; their unit-cell similarity index<sup>16</sup> [deviation of  $\{(a + b + c)/(a' + b' + c')\}$  from unity] was 0.03. But this series of positional isomers had

clear differences in their schemes of weak interactions. To illustrate the impact of homodimers contributing to packing and unit cell relationship, we have compared present findings with our earlier study on the homodimers and self-assemblies of positional isomers of the methyl esters and carboxylic acid derivatives.<sup>17</sup> The study on the assemblies of the positional isomers of the (n-methoxycarbonylmethoxy-naphthalen-1-yloxy)-acetic acid (n = 4, 5, 6, 7) showed only the positional isomers with n = 6 and n = 7 had similar space group and unit cell volume, others were not. Whereas, among the positional isomeric acids (n-methoxycarbonylmethoxy-naphthalen-1-yloxy)-acetic acid (n = 4, 6 and 7), the space group and unit cell volumes of the positional isomers n = 4 and 7 were similar. Whereas the positional isomers of the acids with n = 4 and 6 had a similar type of hydrogen-bonded homodimer in their respective assemblies but their unit cell volumes had wide differences.<sup>14</sup> Hence, the structural comparisons of structural aspects of those positional isomers with the present series, each having homodimer units in assemblies, have a similar observation on the limitation of having isomorphous structures from a series.

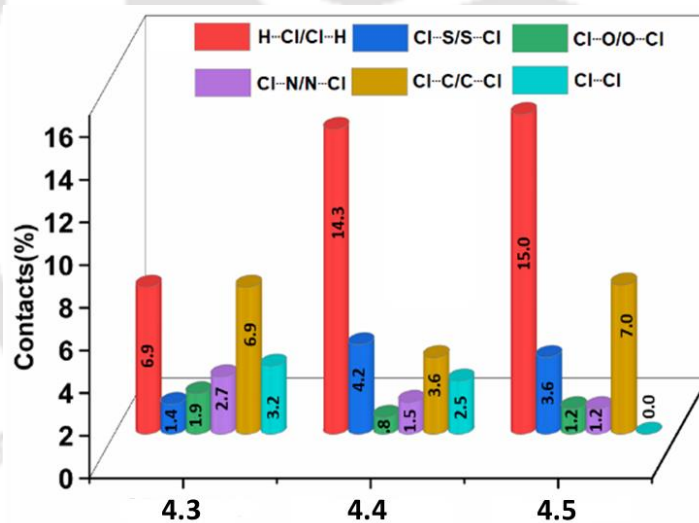


**Figure 4.12:** Bar-diagram showing the percentages of the H $\cdots$ Cl, Cl $\cdots$ S, Cl $\cdots$ O, Cl $\cdots$ N, Cl $\cdots$ C and Cl $\cdots$ Cl interactions (including reciprocal contacts) in 2D fingerprint plots.

In order to make a quantitative estimation of the various interactions in the self-assemblies of the three position isomers, the Hirshfeld analyses were carried out. It provided avenues to compare the different contacts in the three positional isomers involving the chlorine atoms. A comparative picture of percentile amounts of different contacts is shown in Fig. 4.12. From the analysis, it was clear that the hydrogen-chlorine contacts were prominent and comparable in the case of 4.4 and 4.5. It was due to the Cl being present at the para-positions; on the other

hand, the amounts of C-Cl $\cdots$ Cl-C contacts were comparable in the **4.3** and **4.5**. These percentiles of the different contacts are indicative of the fact that the contribution of the electronic factor provided by chlorine substitution was highly dependent on the position of the chlorine on the ring. The similarity in having the amounts of the Cl $\cdots$ Cl interactions played a major role in providing an isomorphous relationship between the **4.3** and **4.4** (Fig. 4.12).

These structural comparisons among the positional isomers suggested each positional isomer had different unit cell volumes despite having the same molecular formula. Each also had homodimer units in assemblies. Thus, those homodimers did not control the respective unit cell volumes. This observation is attributed to the fact that each positional isomer has different directional weak interactions of the dimeric units and requires different packing arrangements. They also need to meet the packing requirements of the unit cell to which they belong. These aspects caused the differences among the self-assemblies and resulted in observing isomorphous structures within the series of positional isomers with exceptions.

#### 4.9: Synthesis of 4-(3-(4-nitrophenyl)thioureido)-N-(thiazol-2(3H)-ylidene)benzene sulfonamide (**4.6**) and its solvates (**4.6.1-4.6.4**)

The thiourea derivative **4.6** showed  $[M+1]^+$  at 436.0203 of its ESI-mass spectrum (Fig. A4.5). The compound **4.6**, upon recrystallization from methanol and acetone, yielded an anhydrous form referred to as **4.6.1**, where crystallization of the compound from DMF, DMA, and DMSO provided crystals of three solvates, namely **4.6.2**, **4.6.3** and **4.6.4** (Fig. 4.13).

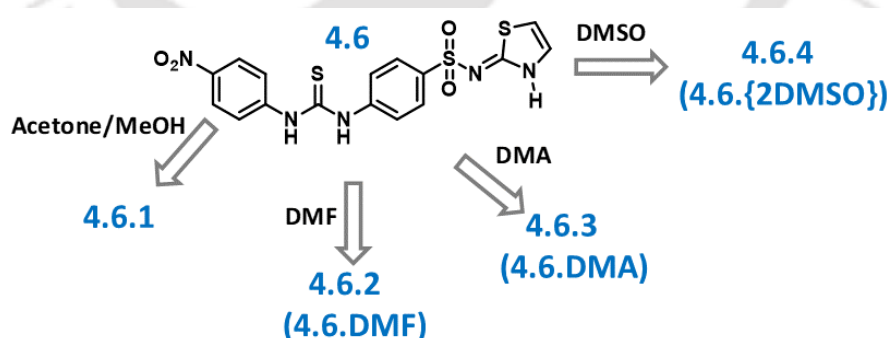


**Figure 4.13:** Different solvates of the **4.6**

The <sup>1</sup>HNMR spectra of **4.6.1** is depicted in Fig.4.14. The thiazole protons labelled as *b* and *c* exhibited chemical shifts at 7.26-7.25 ppm and 6.83 ppm, respectively. The N-H proton labelled as *a* displayed peak at 12.73 ppm. The chemical shift of the N-H protons labelled as *1* and *2* appeared at 10.57 and 10.51 ppm, respectively. The phenyl protons *d* and *e* appeared at 7.78-7.76 ppm and 7.67-7.65 ppm, respectively, and the *f* and *g* displayed chemical shifts

at 7.83-7.81 ppm and 8.22-8.20 ppm, respectively. The carbon of the C=S appeared at 179.37 ppm in the  $^{13}\text{C}$ NMR of **4.6.1**, which is given in Fig. A4.4g. The IR spectra of the compound **4.6.1** had the C=S at  $854\text{ cm}^{-1}$  and S=O at  $1142\text{ cm}^{-1}$ .

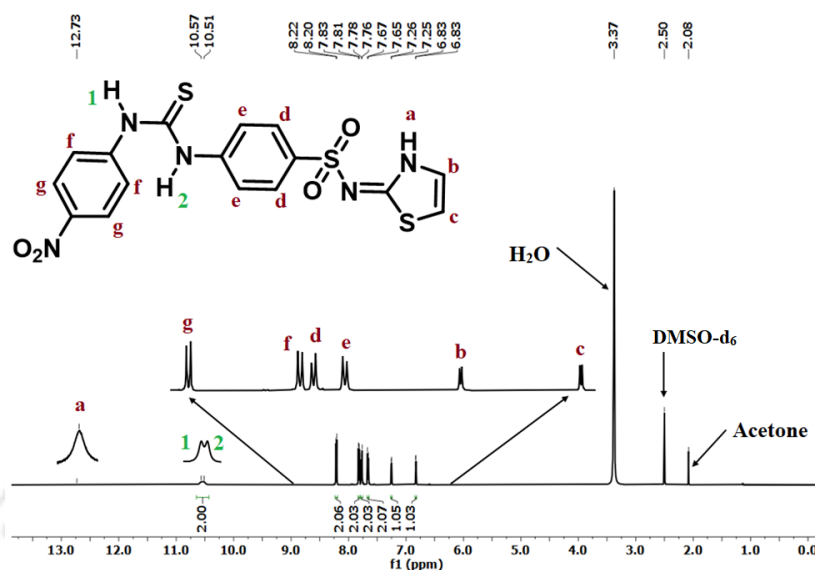


Figure 4.14:  $^1\text{H}$ -NMR (DMSO- $d_6$ , 600 MHz) spectra of the **4.6.1**

#### 4.10: Structural descriptions of the thiourea derivative 4.6.1-4.6.4

The crystals of the anhydrous form of compound **4.6** designated as **4.6.1**, belong to  $P2_1/n$  with unit cell volume  $1913.0(6)\text{ \AA}^3$  and it had a crystal density of  $1.512\text{ g cm}^{-3}$ . This form of the compound had a close structural similarity with that of the structure of the polymorph **4.1.2** described earlier. The hydrogen-bonded homo-dimers, as observed in that polymorph, were observed in the case of the self-assembly of the **4.6.1** too (Fig. 4.15a). The homodimers were stabilised by weak  $\text{N4-H}\cdots\text{O2}$  ( $d_{\text{D}\cdots\text{A}}$ ,  $2.62\text{ \AA}$ ) hydrogen bonds. It also had the *syn-anti* orientations of the thiourea parts. The molecules of the **4.6.1** were arranged in a double chain-like-arrangements by the hydrogen bonds between the hydrogen-bonded homodimers.

The self-assembly of the **4.6** solvate of DMF or DMA (1:1 solvate in each case), namely **4.6.2** and **4.6.3**, each had hydrogen-bonded homodimers similar to the anhydrous form **4.6.1**. But these solvates had *anti-anti* orientations of thiourea parts and also had the respective solvent molecules in their self-assembly (Fig. 4.15b and Fig. 4.15c). The crystals of the **4.6.2** and **4.6.3** were of  $P\bar{1}$  space group; the unit cell volume and crystal densities were  $1184.40(18)\text{ \AA}^3$ ,  $1.426\text{ g cm}^{-3}$  and  $1226.09(11)\text{ \AA}^3$ ,  $1.416\text{ g cm}^{-3}$  respectively. As the unit cell parameters are close, the unit cell similarity index<sup>16</sup> of the two solvates was calculated, and it was found as 0.012. This value was very close to zero, showing that the two solvates are isomorphous. The structural similarities were attributed to the *anti-anti* orientations of the thiourea portions in the homodimers to form complementary hydrogen bonds with solvent

molecules in a similar way. The hydrogen bonds in the solvates provided cyclic assembled units with  $R_2^1(6)$  notation in their respective assemblies. The hydrogen bonds involved in such cyclic units in **4.6.2** (DMF solvate) were (N1-H $\cdots$ O5 1.99 Å, 168°; N2-H $\cdots$ O5 2.28 Å, 144° and N1-H $\cdots$ O5 1.98 Å, 166°; N2-H $\cdots$ O5 2.22 Å, 151° in the DMA solvate (**4.6.3**) respectively. The prominent hydrogen bond parameters of the solvates of the **4.6** are shown in Table 4.3.

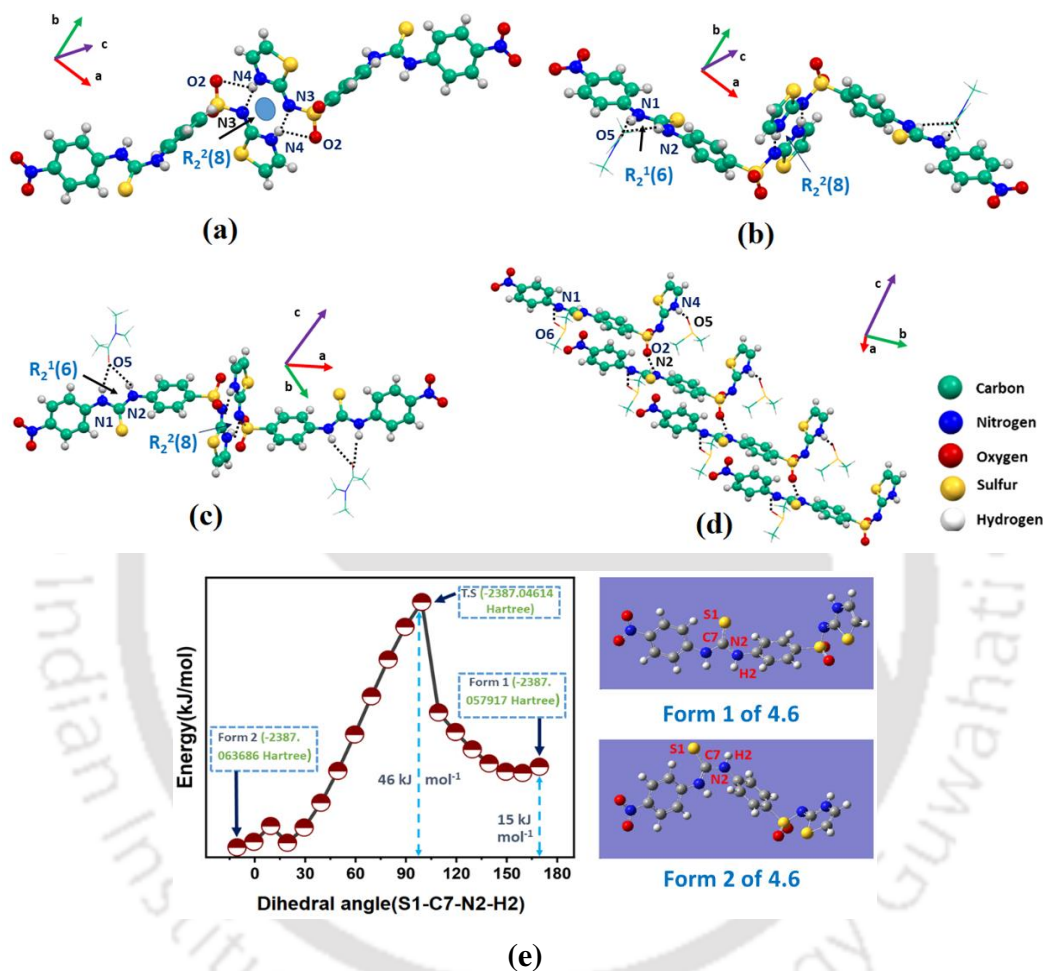


**Figure 4.15:** Homodimers of the (a) **4.6.1**, (b) **4.6.2**, (c) **4.6.3** and (d) arrangements of discrete hydrogen-bonded molecules of the **4.6.4** (e) The energy of the syn-anti to transform to the anti-anti form of **4.6**

The DMSO solvate **4.6.4** ( $P2_1/c$  space group) had unit cell volume and crystal density 2649.1(8)Å<sup>3</sup> and 1.484 gcm<sup>-3</sup>. It was found to be a 1:2 solvate, having two DMSO molecules per host. Accordingly, it had a completely different self-assembly than the other two solvates and parent form of **4.6**. In this example, the *anti-anti* orientation of the thiourea was observed and there was no homo-dimeric hydrogen-bonded assembly that was found in the other three forms. In this solvate, two independent oxygen atoms from two DMSO molecules served as

hydrogen bond acceptors. This involved N1-H $\cdots$ O6 (2.07 Å, 153° and N4-H $\cdots$ O5 1.84 Å, 166°) hydrogen bonds with the urea and thiazole N-H bonds. In the solvate, the *syn-anti* form of the thiourea part of the parent compound was changed to the *anti-anti* form. Due to these hydrogen bonds, there were no homo-dimeric sub-assemblies within the assembly. As there were two solvent molecules per host, there was an extra space requirement to accommodate the two DMSO molecules. The polarity index of DMSO and DMF are 7.2 and 6.4; hence, the DMSO, being slightly higher polar, was able to cleave the aminothiazole-aminothiazole hydrogen-bonded homodimers. Hence, the DMSO solvent could disrupt the homo-dimeric assembly if at all formed or did not allow them to form. This happened as the DMSO molecule directly hydrogen bonded to the N-H of the aminothiazole, favoured the host molecules to form hydrogen-bonded chain-like arrangements as shown in Fig. 4.15d. There were instances in literature where the space provided by dimeric sub-assemblies of bisphenol,<sup>18</sup> aminothiazole,<sup>19</sup> sulphadiazine<sup>20</sup> had scopes to form polymorphic solvates or solvates of the same solvent with different stoichiometries (pseudo polymorphs).

**Table 4.3:** Hydrogen bond parameters of the solvates of **4.6 (4.6.1-4.6.4)**

Solvates of 4.6	D-H $\cdots$ A (Symmetry)	d <sub>D-H</sub> (Å)	d <sub>H<math>\cdots</math>A</sub> (Å)	d <sub>D<math>\cdots</math>A</sub> (Å)	∠D-H $\cdots$ A (°)
<b>4.6.1</b>	N(1)-H(1) $\cdots$ O(2) [2-x, -y, -z]	0.86	2.08	2.888(7)	157
	N(2)-H(2) $\cdots$ O(1) [-1+x, y, z]	0.86	2.13	2.959(6)	161
	N(4)-H(4) $\cdots$ N(3) [2-x, -1-y, -z]	0.86	2.11	2.948(6)	164
	C(16)-H(16) $\cdots$ O(4) [3/2-x, -3/2+y, 1/2-z]	0.93	2.47	3.293(9)	147
<b>4.6.2</b>	N(1)-H(1) $\cdots$ O(5) [x, y, z]	0.87(4)	1.99(4)	2.844(6)	168(4)
	N(2)-H(2) $\cdots$ O(5) [x, y, z]	0.88(6)	2.28(6)	3.034(7)	144(4)
	N(4)-H(4) $\cdots$ N(3) [-x, -y, -z]	0.86	2.05	2.887(5)	165
<b>4.6.3</b>	N(1)-H(1) $\cdots$ O(5) [x, y, z]	0.86	1.98	2.820(5)	166
	N(2)-H(2) $\cdots$ O(5) [x, y, z]	0.86	2.22	3.000(5)	151
	N(4)-H(4) $\cdots$ N(3) [-x, -y, -z]	0.86	2.03	2.876(4)	167
<b>4.6.4</b>	N(1)-H(1) $\cdots$ O(6) [-1+x, y, z]	0.86	2.07	2.860(3)	153
	N(2)-H(2) $\cdots$ O(2) [x, 1+y, z]	0.86	2.17	2.964(3)	154
	N(4)-H(4) $\cdots$ O(5) [x, -1+y, -z]	0.86	1.84	2.683(4)	166

C(16)-H(16) ...S(1) [1-x, -1/2+y, -z]	0.93	2.75	3.557(4)	145
C(19)-H(19A) ...O(4) [2-x, 1-y, 1/2-z]	0.96	2.49	3.409(5)	161
C(19)-H(19C) ...O(6) [2-x, 1-y, 1/2-z]	0.96	2.57	3.455(5)	153
C(20)-H(20A) ...O(6) [2-x, 1-y, 1/2-z]	0.96	2.51	3.408(5)	155
C(20)-H(20C) ...O(2) [1+x, y, z]	0.96	2.51	3.331(4)	144

DFT calculation showed that the *syn-anti* form of the **4.6** was stable by 15 kJ/mol. The activation energy for converting the *syn-anti* form to the *anti-anti* form was 46 kJ/mol (Fig. 4.15e). Hence, the hydrogen bonds with different solvents were enough to cause the required geometrical changes to transform one form into another.

#### 4.11: N-(4,6-dimethylpyrimidin-2(1H)-ylidene)-4-(3-(4-nitrophenyl)thioureido)benzenesulphonamide (**4.7**) and its solvates (**4.7.1-4.7.4**)

To perform a similar study with phenylthiourea-derived sulfamethazine, its thiourea derivative, namely N-(4,6-dimethylpyrimidin-2(1H)-ylidene)-4-(3-(phenyl)thioureido)benzenesulphonamide) was prepared. However, we could not obtain crystals of this compound from attempted crystallisation from solution in different solvents. Hence, it could not take up a structural study. Due to this reason, we looked for an alternative compound that was the nitrophenyl thiourea-derived compound, namely N-(4,6-dimethylpyrimidin-2(1H)-ylidene)-4-(3-(4-nitrophenyl)thioureido)benzenesulphonamide denoted as **4.7**. This compound was prepared by the condensation reaction of 4-nitrophenyl isothiocyanate with sulfamethazine in acetonitrile. The compound showed an ESI-mass peak for  $[M+1]^+$  at 459.0902, which tallies with the calculated value for the assigned structure (Fig. A4.5g).

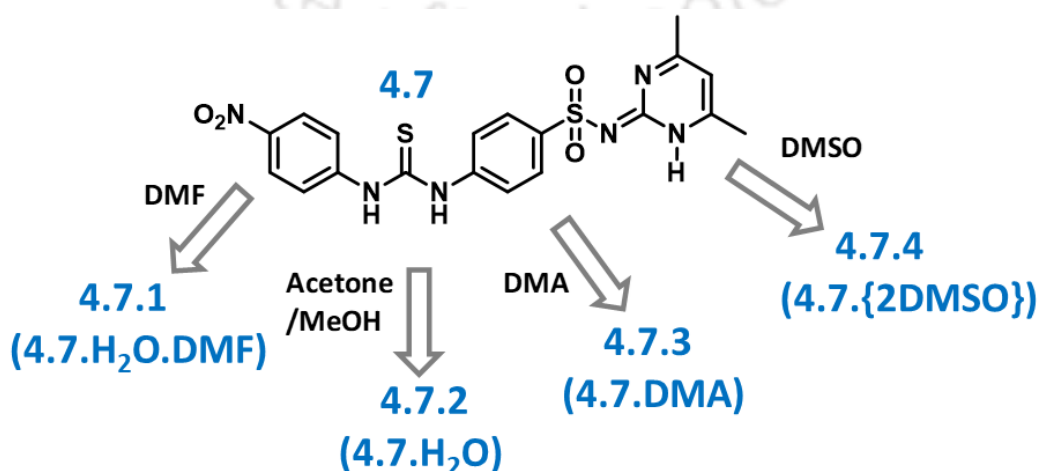
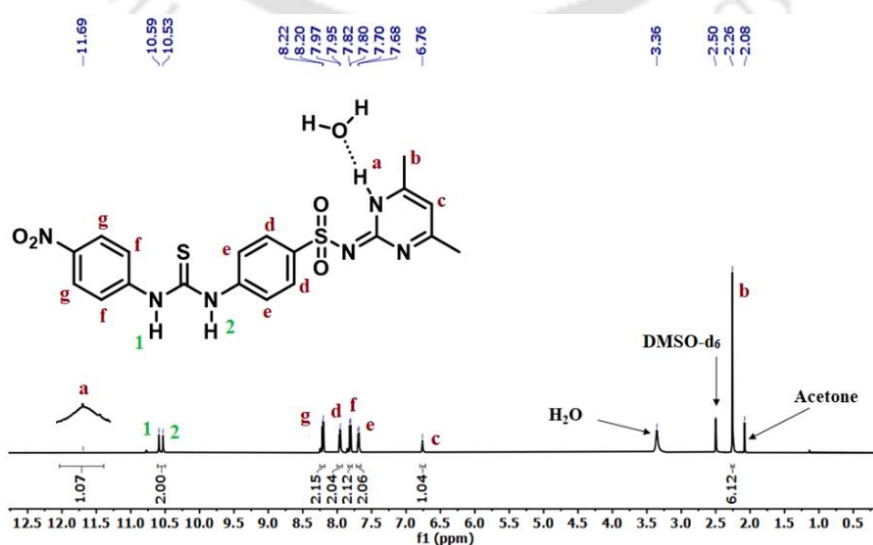


Figure 4.16: Different solvates of N-(4,6-dimethylpyrimidin-2(1H)-ylidene)-4-(3-(4-nitrophenyl)thioureido)benzene sulphonamide (**4.7**).

Four different forms of crystals were formed from this compound from crystallisation from solutions in different solvents. A DMF-hydrate solvate (**4.7.1**) was obtained from the solution of **4.7** in DMF as a solvent. Whereas, crystallisation of **4.7** from a methanol/ acetone mixed solvent solution provided crystals of the monohydrate of **4.7** (**4.7.2**). Crystallisation of the compound from solution in DMA or DMSO provided the respective solvate, namely 1:1 DMA solvate (**4.7.3**) and 1:2 DMSO solvate (**4.7.4**) (Fig. 4.16). The DMF solvate without a water molecule of crystallisation in the solvate was not formed. A cautious attempt to prepare the DMF solvate from solution in dry DMF also led to the hydrated form, and this crystallisation occurred only under humid conditions (95 % humidity in the air). Hence, the dissolved water in DMF picked from humid air or otherwise is responsible for providing the hydrated solvate. The DMSO solvate of **4.7** had similar stoichiometry to that of the DMSO solvate of **4.6**; both the DMSO solvate had host to solvent in a ratio of 1:2. The  $^1\text{H}$ NMR spectra of this solvate **4.7.2** is depicted in Fig. 4.17. The methazine protons *b* and the phenyl protons *c* showed chemical shifts at 2.26 ppm and 6.76 ppm, respectively. The N-H proton labelled as *a*, *1* and *2* appeared at 11.69 ppm, 10.59 and 10.53 ppm, respectively. The phenyl ring protons *d*, *e*, *f* and *g* exhibited chemical shifts at 7.97-7.95 ppm, 7.70-7.68 ppm, 7.82-7.80 ppm and 8.22-8.20 ppm, respectively. The  $^{13}\text{C}$ NMR of **4.7.2**, given in Fig. A4.41, showed peaks at 179.31 and 30.71 ppm for thiocarbonyl carbons of thiourea and methyl carbons of the methazine ring, respectively. The IR spectra of the compound had the C=S at  $855\text{ cm}^{-1}$  and S=O at  $1139\text{ cm}^{-1}$ .



**Figure 4.17:**  $^1\text{H-NMR}$  (DMSO- $d_6$ , 600 MHz) spectra of the **4.7.2**

#### 4.12: Structural descriptions of the thiourea derivative 4.7.1-4.7.4

The space group of the respective crystals of **4.7.1-4.7.4** were  $P \bar{1}$  whereas the crystal density and unit cell volumes were  $1.435 \text{ g cm}^{-3}$ ,  $1272.27(14) \text{ \AA}^3$ ;  $1.468 \text{ g cm}^{-3}$ ,  $1078.3(5) \text{ \AA}^3$ ,  $1.370 \text{ g cm}^{-3}$ ,  $1323.1(2) \text{ \AA}^3$ ,  $1.379 \text{ g cm}^{-3}$ ,  $1472.7(10) \text{ \AA}^3$  respectively. The sum of cell axes ( $a + b + c$ ) in the four forms were  $32.468 \text{ \AA}$ ,  $34.193 \text{ \AA}$ ,  $34.4666 \text{ \AA}$ , and  $36.671 \text{ \AA}$ , respectively. This showed that there was a lack of unit cell similarity among them except for the pair DMF hydrate and DMA solvate. A very high unit cell similarity index (0.008) was observed among the DMF hydrate and the DMA solvate. There are examples of isomorphous multicomponent crystals in the literature.<sup>21</sup>

The exciting feature of the hydrated DMF solvate (**4.7.1**) was that it had heteromeric hydrogen-bonded sub-assemblies (Fig. 4.18a). These sub-assemblies were formed by utilising the bridging water molecules. The water molecule acted as a hydrogen bond donor to create a robust hydrogen-bonded cyclic structure (extended domain).; It was constructed between two neighbouring host molecules involving a hydrogen bond between the thiourea of one molecule and  $-\text{SO}_2-$ , N-atom (methazine) of another molecule. While doing so, one oxygen atom of the  $-\text{SO}_2-$  group of one molecule form hydrogen bonds to N-H (thiourea) of another, and the water molecule formed bridges with another N-H bond of the thiourea and N-atom (methazine) of the other molecule (Fig. 4.18a). The robust sub-assembly had hydrogen bonds between the N-H of thiourea with the oxygen atom of water (N1-H1 $\cdots$ O6  $1.98 \text{ \AA}$ ,  $168^\circ$ ; N2-H2 $\cdots$ O1  $2.26 \text{ \AA}$ ,  $149^\circ$ ) and  $-\text{SO}_2-$  unit of sulfamethazine with  $R_3^2(8)$  notation as one portion and another portion with  $R_1^2(6)$  notation. In these, the water molecules acted as hydrogen bond donors forming (O6-H(6A)  $\cdots$ O1  $2.27 \text{ \AA}$ ,  $132^\circ$ ; O6-H(6A)  $\cdots$ N5  $2.38 \text{ \AA}$ ,  $143^\circ$  hydrogen bonds with the oxygen atom (O1 of  $\text{SO}_2$ ) and the nitrogen atom (N5 of methazine). Due to the steric effect of the two

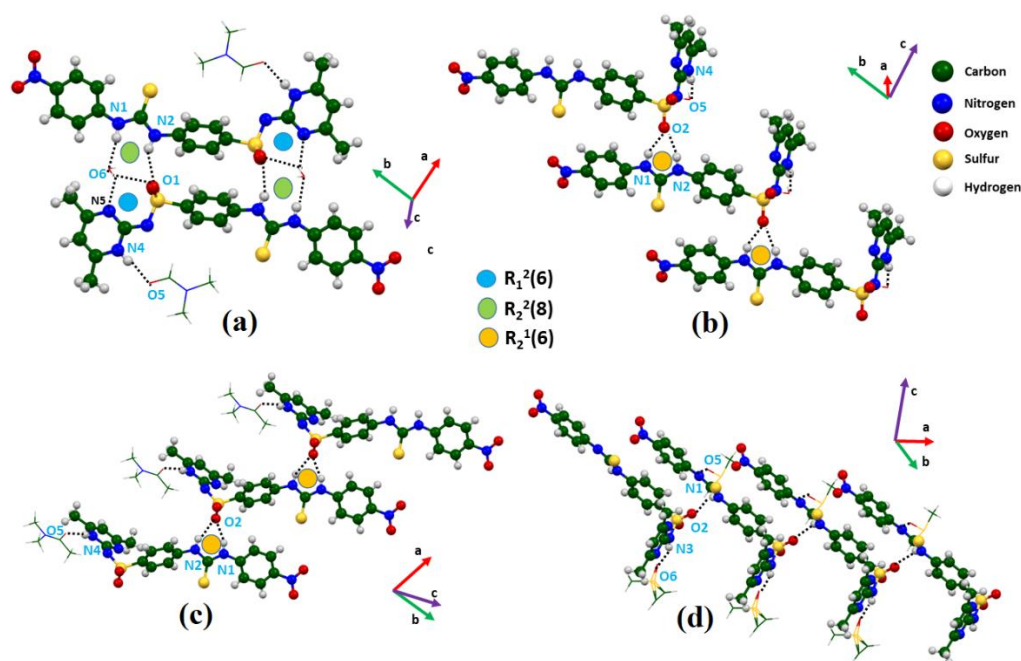


**Figure 4.18:** Crystal packing of (a) **4.7.1** (b) **4.7.2** (c) **4.7.3** and (d) **4.7.4**

methyl-groups of the methazine ring, hydrogen-bonded homodimers between two methazine units were not formed. The thiourea portion of each molecule had *anti-anti* orientation. The water molecule was accommodated in the solvate to maximise the hydrogen bonds by creating an extended domain. The carbonyl oxygen atom of the DMF molecule formed a hydrogen bond with the N-H of methazine (N4-H $\cdots$ O5 1.83 Å, 172°). Accordingly, the two DMF molecules of each dimer were located at trans-positions with respect to each other and were related by a mirror plane/ inversion centre. The hydrogen bond parameters of the solvates of **4.7** are shown in Table 4.4.

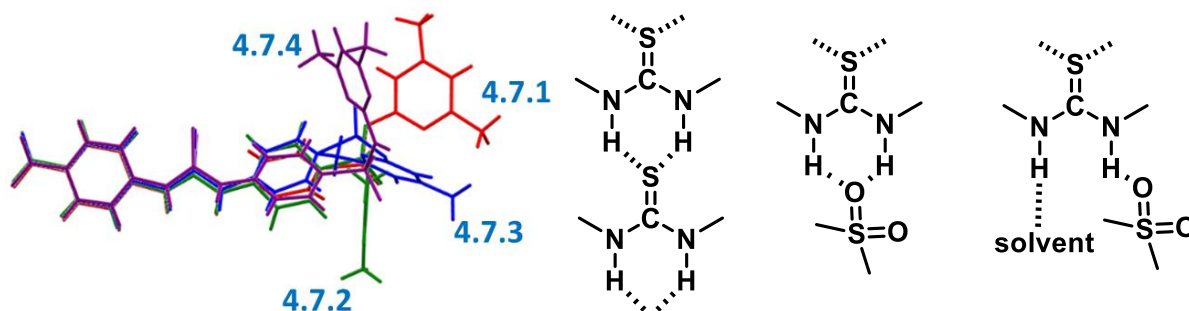
The hydrate (**4.7.2**) and the DMA solvate (**4.7.3**) had structural similarities (Fig. 4.18b and Fig. 4.18c). In both examples, the N-H of thiourea formed hydrogen bonds {N1-H $\cdots$ O2, 2.02 Å, 158°; N2-H $\cdots$ O2, 2.18 Å, 149° for **4.7.2** and N1-H $\cdots$ O2, 2.02 Å, 161°; N2-H $\cdots$ O2, 2.08 Å, 155° for **4.7.3** with oxygen atom of the SO<sub>2</sub> unit, each synthon had R<sub>2</sub><sup>1</sup>(6) notation. These hydrogen

**Table 4.4:** Hydrogen bond parameters of solvates of **4.7** (**4.7.1-4.6.3**)

Solvates of <b>4.7</b>	D-H $\cdots$ A (Symmetry)	d <sub>D-H</sub> (Å)	d <sub>H<math>\cdots</math>A</sub> (Å)	d <sub>D<math>\cdots</math>A</sub> (Å)	∠D-H $\cdots$ A (°)
------------------------	---------------------------	----------------------	--	--	---------------------

<b>4.7.1</b>	N(1) -H(1) ...O(6) [x, y, z]	0.86	1.98	2.830(3)	168
	N(2) -H(2) ...O(1) [1-x, -y, 1-z]	0.86	2.26	3.031(3)	149
	N(4) -H(4) ...O(5) [1+x, y, z]	0.86	1.83	2.685(3)	172
	O(6) -H(6A) ...O(1) [1-x, -y, 1-z]	0.81	2.27	2.874(3)	132
	O(6) -H(6A) ...N(5) [1-x, -y, 1-z]	0.81	2.38	3.064(3)	143
	O(6) -H(6B) ...S(1) [1-x, 1-y, 1-z]	0.87	2.65	3.468(2)	157
	C(12) -H(12) ...O(3) [1+x, -1+y, z]	0.93	2.59	3.456(4)	155
<b>4.7.2</b>	N(1) -H(1) ...O(2) [x, 1+y, z]	0.86	2.02	2.834(6)	158
	N(2) -H(2) ...O(2) [x, 1+y, z]	0.86	2.18	2.955(6)	149
	N(4) -H(4) ...O(5) [1-x, -y, 1-z]	0.86	2.01	2.856(6)	167
	O(5) -H(5A) ...O(1) [-x, -y, 1-z]	0.85	2.01	2.834(7)	165
	O(5) -H(5B) ...O(3) [x, -1+y, z]	0.85	2.59	3.299(7)	141
	C(2) -H(2A) ...S(1) [x, 1+y, z]	0.93	2.85	3.659(7)	146
	C(17) -H(17) ...O(4) [x, y, z]	0.93	2.53	3.390(8)	153
	C(19) -H(19C) ...O(1) [1+x, y, z]	0.96	2.37	3.257(8)	154
<b>4.7.3</b>	N(1) -H(1) ...O(2) [-1+x, y, z]	0.86	2.02	2.851(4)	161
	N(2) -H(2) ...O(2) [-1+x, y, z]	0.86	2.08	2.885(5)	155
	N(4) -H(4) ...O(5) [1-x, 1-y, 1-z]	0.86	1.84	2.694(5)	170
	C(10) -H(5) ...O(1) [1-x, -y, 1-z]	0.93	2.55	3.239(5)	131
	C(15) -H(15C) ...N(3) [1-x, -y, 1-z]	0.96	2.59	3.508(6)	161
	C(19) -H(19C) ...O(3) [1-x, 1-y, 1-z]	0.96	2.56	3.483(7)	162

bonds had resulted in linear chain-like arrangements of molecules in both these solvates. In the hydrate **4.7.2**, the water molecules acted as the intervening molecules to bridge two such chains. In the case of **4.7.3**, the DMA molecules were hydrogen bonded (N4-H...O5 1.83 Å, 172°) to the N-H of the methazine ring. The structural difference between the DMSO solvate **4.7.4** and the other solvates of **4.7** was from the composition difference where two molecules of solvents were getting accommodated with respect to a single host molecule.



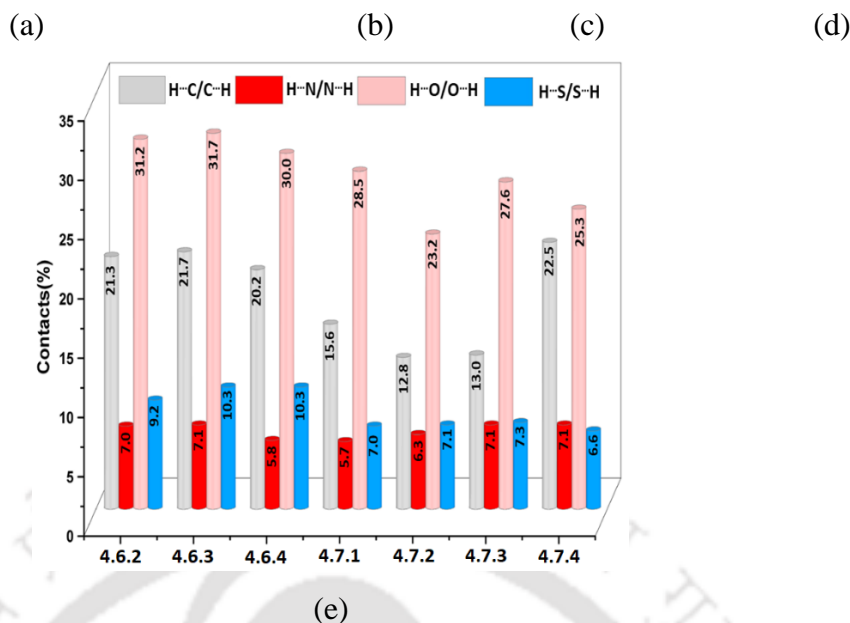
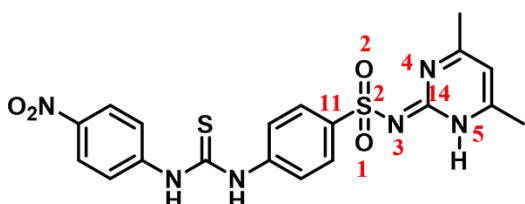


**Figure 4.19:** (a) Overlaid diagram of structures of the host in the **4.7.1**, **4.7.2**, **4.7.3** and **4.7.4** (drawn by keeping the 4-nitrophenylthiourea portion of each on a common plane). (b) Representative structure of hydrogen bonded thiourea tape; (c) and (d) Skeletal representations of two types of H-bonded chains in solvates of **4.7**. (e) Comparative percentage contacts of different types of X-H (X = C, N, O and S) bonds obtained from Hirshfeld analysis in the different forms of nitrophenyl thiourea-derived compounds/solvates.

In this case, one DMSO molecule had the crystallographic disorder, and the other was not (Fig 4.18d). The DMSO molecule without the crystallographic disorder was linked to one N-H of the thiourea located next to the nitrophenyl group by hydrogen bonds (N1-H $\cdots$ O5 1.97 Å, 168°). The other N-H bond was involved in the hydrogen bonds with an oxygen atom of -SO<sub>2</sub>- group of sulfamethazine part of a neighbouring molecule (N2-H $\cdots$ O2, 2.36 Å, 139°). This interaction provided a linear chain-like arrangement among host molecules. As the urea N-H were dissimilarly hydrogen bonded, it caused a twisting in the urea plane to adopt a puckered intermediate geometry, which was neither the *anti-anti* nor *syn-anti* form. This indeed can be projected as evidence that the water and solvent competed with differentiable capability to get anchored to the host, such as in hydrate and DMF solvate, leading to different compositions and self-assemblies. The two planes containing S1-C7-N2-H2 and S1-C7-N1-H1 of the DMSO solvate were non-overlapping, and the angle between the two planes was 7°. As the methazine portion was not forming a homodimer, the two N-H bonds of the thiourea adopted slightly different orientations to accommodate an additional DMSO molecule. As the *anti-anti* orientation of the thiourea part was observed, the projection of the

methazine portion in each case could be easily visualised by overlaying the structural skeleton of different solvates of the **4.7** by keeping the thiourea portion in the plane of the paper (Fig. 4.19a). The dihedral angles O1-S2-N3-C14 and O2-S2-N3-C14, as depicted in Table 4.5, were wide apart. This clearly depicted the independent orientation of the host in each solvate. The changes in the orientations were due to the N-H bond of the methazine portion forming hydrogen bonds with water or solvent molecules. Depending on the directional effect of those hydrogen bonds, the methazine rings got fixed in different orientations in the respective lattice.

**Table 4.5:** Torsion angles of solvates of **4.7**



Torsion angle	4.7.1	4.7.2	4.7.3	4.7.4
C11-S2-N3-C14	177.25	67.76	59.35	59.56
S2-N3-C14-N4	170.25	169.76	168.36	167.09
S2-N3-C14-N5	9.51	9.42	12.99	12.10
O2-S2-N3-C14	63.86	178.95	-57.60	57.71
O1-S2-N3-C14	68.40	-52.43	175.56	-174.19

The series of solvates from the two nitro derivatives **4.6** and **4.7** provided new information on the homodimer assembly vs. discrete assemblies of the two independent sulfa drugs. The participation of water molecules in forming a hydrated heteromeric dimer of **4.7** was clear evidence to form an extended cyclic structure to gain stability in self-assembly. As under similar conditions, an anhydrous form of **4.6** was obtained, it had homodimer units. The *syn-anti* orientation of thiourea was not observed in the solvates, this happened to make room for the solvent molecules in the solvates of **4.6**. In this case, the homomeric assembly provided the pivot, but in the case of **4.7**, the homodimer was absent due to steric reasons, but it formed cyclic hydrogen-bonded units where water was used in the DMF solvate. The hydrogen bonds were formed in the hydrate and DMA solvate involving the oxygen atom of -SO<sub>2</sub>- unit with the two N-H of thiourea, thereby providing a chain-like structure. It is worth noting that the 4-nitrophenylthiourea derived from sulfathiazole or sulfamethazine had a common structural feature; both were devoid of thiourea tapes (Fig. 4.19b). The other common feature between them was that one of the N-H thiourea had formed hydrogen bonds with DMSO, and other N-H formed hydrogen bonds with an oxygen atom to form chains of

the same kind found in both solvates (Fig. 4.19c and 4.19d). The differences arose in the space provided to the second DMSO molecules due to difference in having different heterocycle. Furthermore, a comparison on the different types of X-H (X = C, N, O, S) contacts in all the nitrophenyl thiourea-derived compounds (Fig. 4.19e) in different solvates showed dominance of the H-O/O-H contacts in each form.

#### 4.13: Comparison of energies of homodimers

The energy of compounds with the conformation that was found in the polymorphs was optimized by DFT using B3LYP hybrid functional of 6-311++G (2d, p) basis set. The optimized structures and energy differences of discrete molecule and also between the homodimers of the two polymorphs are shown in Fig.4.20. The parent conformer of the **4.1.1** was less stable than that of the **4.1.2**; the difference in energy was found to be 13.36 kJ/mol. This showed that the energy differences between the two conformers were comparable. The same trend was also observed in the stability of the hydrogen-bonded homodimers of the two polymorphs. The gain in energy by the homodimer of **4.1.2** compared to **4.1.1** was higher by 22.09 kJ/mol. Thus, the energies gained by the homodimers were also influenced by steric, electronic and conformation, as observed in isolated single hydrogen bonds due to slight changes in those parameters.<sup>22</sup>

The self-assembly of each monomorph compound presented here had two different types of homodimers that are shown in the representative case **4.4** in Table 4.6. The energy of each discrete monomer (the conformer as obtained in the crystal structure) in each case, as well as these homodimers, were optimized. The homodimer that was formed by the imine forms of two aminothiazole units of two independent compounds is represented as homodimer 1, and the one formed by hydrogen bonds between S=O and N-H (thiourea) is designated as the homodimer 2 (refer to the footnote of Table 4.6). The difference between the sum of the energies of the two molecules with respect to homodimer 1 is represented as  $\Delta E_1$  and the difference with respect to homodimer 2 is referred to as  $\Delta E_2$ . The differences in the energies clearly showed a gain in energy by forming any of the homodimers. The stability gained by forming homodimer 1 was in the range of 72 - 75 kJ/mole, whereas by forming homodimer 2, those were between 30 kJ/mol and 65 kJ/ mole (Table 4.6). The homodimer formation may be suggested to be an extended domain formation, which helps in better packing arrangements through a gain in considerable amounts of energy.

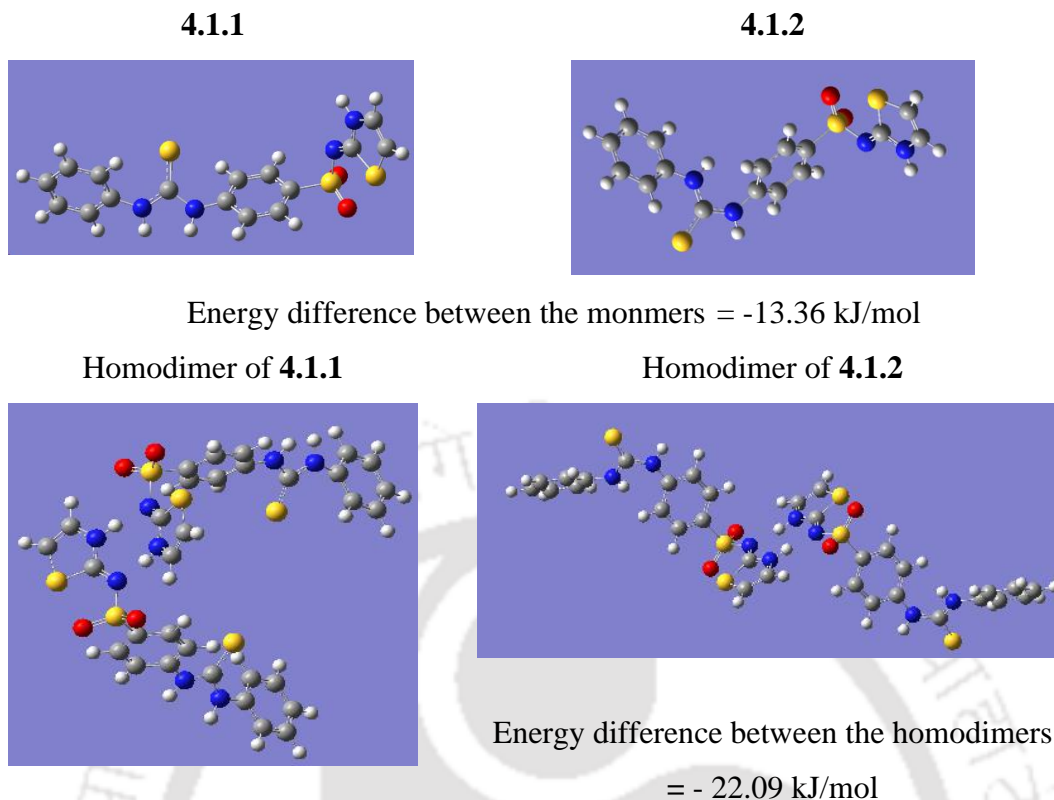
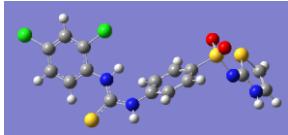


**Figure 4.20:** DFT optimized [B3LYP hybrid functional of 6-311++G (2d, p) basis set] structures of two forms of molecules and homodimers in the **4.1.1** and **4.1.2**


**Table 4.6:** Optimized structure of the conformers in the thiourea derivatives and their respective homodimers' net gain in energy by the formation of hydrogen-bonded dimers

Compound	Discrete molecule <sup>a</sup> (Hartree)	Homodimer 1 <sup>a</sup> (Hartree)	Homodimer 2 <sup>b</sup> (Hartree)	$\Delta E_1$ (kJ/mol) <sup>c</sup>	$\Delta E_2$ (kJ/mol) <sup>c</sup>
<b>4.2</b>	-2297.047071	-4594.121877	-4594.105766	-72.82	-30.52
<b>4.3</b>	-3101.736168	-6203.500783	-6203.485577	-74.68	-34.76
<b>4.4</b>	-3101.740330	-6203.508979	-6203.493315	-74.35	-33.23
<b>4.5</b>	-3101.736949	-6203.501874	-6203.497818	-73.45	-62.80
<b>4.6.1</b>	-2387.063686	-4774.154736	-4774.152157	-71.84	-65.07
<b>4.6.2</b>	-2387.058571	-4774.145336	- <sup>d</sup>	-74.69	- <sup>d</sup>

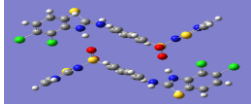
<sup>a</sup> = Representative case of a discrete molecule of **4.3**



<sup>b</sup> = Representative homodimer 1 of **4.3**



<sup>c</sup> = Representative homodimer 2 of **4.3**

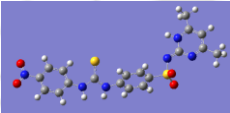
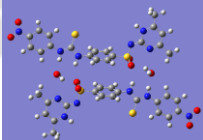
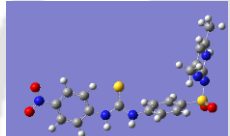
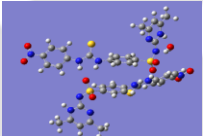
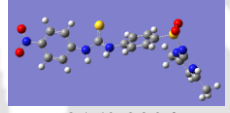
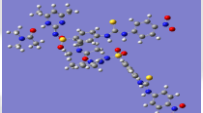


<sup>d</sup> = No homodimer 2 was observed; <sup>e</sup> = Hartree values are converted to kJ/mole from data of seven digit

In the sulfamethazine-derived thiourea, the dimers were not observed, but there were thiourea tapes formed between the N-H and C=S hydrogen bonds. As we had limitations in finding the energies of linear infinitely grown chains, the energies of homodimers, as illustrated in Table

4.7, were calculated and compared with the energy of discrete molecules. It was found that the homodimers provide extra stability ranging from 91 kJ/mol to 105 kJ/mol. In the case of the **4.7**, the steric effect of the methyl group on the heterocyclic ring hindered the formation of the hydrogen-bonded homodimers. The self-assembly of the hydrate and solvates of the **4.7** had chain-like arrangements of the self-assembled host molecules as extended domains to accommodate the water or solvent molecules.

**Table 4.7:** The DFT-optimized energy of discrete molecules and homodimers in the **4.7** solvates

Solvates	Discrete molecule of <b>4.7</b> in respective solvate (Hartree)	Dimeric units formed by thiourea tape	Difference in energy between sum of two molecules with the dimer with thiourea tape (kJ/mol)	Energy of the solvate (Hartree)
<b>4.7.1</b>	 -2160.6411	 -4474.9712	-104.17	-2486.0827
<b>4.7.2</b>	 -2160.9917	 -4398.5056	-113.22	-2237.4707
<b>4.7.3</b>	 -2160.9904	 -4897.9066	-91.22	-2448.9359

#### 4.14: Hirshfeld surface analysis

Hirshfeld surfaces<sup>23</sup> were calculated using Crystal Explorer version 17.5

$$d_{norm} = (d_i - r_i^{vdW}) / r_i^{vdW} + (d_e - r_e^{vdW}) / r_e^{vdW}$$

Where  $d_e$  and  $d_i$  are the distances from the Hirshfeld surface to the nearest atoms outside and inside the surface. Both  $d_e$  and  $d_i$  are normalised by the van der Waal radius of the atoms involved.  $r_i^{vdW}$  and  $r_e^{vdW}$  are van der Waals radii of the atoms. The value of  $d_{norm}$  = negative (red spot), where intermolecular contacts between atoms are shorter than the sum of their van der Waal radii and if the contacts are longer than van der Waal radii, then  $d_{norm}$  = positive (blue spot). Hirshfeld surface analysis of each was carried out to illustrate the contacts on the basis of their crystallographic information files. For **4.1.1**, the  $d_{norm}$  values ranged from -0.61 to 1.33, while for **4.1.2**, this range was from -0.54 to 1.22 (Fig. 4.22). For **4.1.1** and **4.1.2**, the closest contact N-H...N / N...H-N was equal to the minimal  $d_{norm}$  value (-0.61 for **4.1.1** and -0.54 for **4.1.2**). The H...N/ N...H intermolecular surface interactions were 6.8 % and 8.1 % of

the total Hirshfeld surface for **4.1.1** and **4.1.2**, respectively. The N-H of thiourea formed weak hydrogen bond with the sulphur atom forming thiourea tapes in **4.1.1**, so in this case, less bright red spots were observed, whereas both N-H of thiourea in **4.1.2** were forming strong hydrogen bond with the oxygen atom of the SO<sub>2</sub> group, so in this case intense red spot was observed. The intermolecular contacts H<sup>⋯</sup>O/ H<sup>⋯</sup>O contributed to 12.4 % and 14.1 % of the total surface for **4.1.1** and **4.1.2**, respectively. In the case of polymorph **4.1.1**, the contact S=O<sup>⋯</sup>S with a bright red spot ( $d_{\text{norm}} \sim -0.19$ ) was observed, but no such spot was observed in the case of **4.1.2**. The intermolecular contacts H<sup>⋯</sup>O/ H<sup>⋯</sup>O contributed 3.5 % in **4.1.1** and none in **4.1.2**.

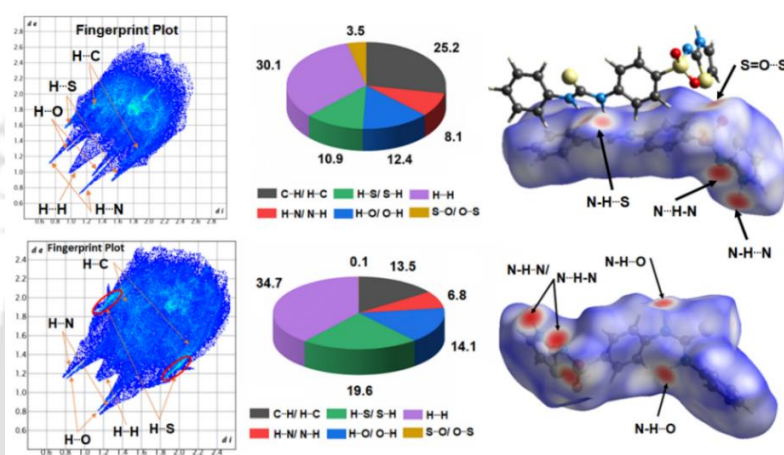


**Figure 4.22:** Fingerprint plot, percentage of interactions and Hirshfeld surfaces mapped with  $d_{\text{norm}}$  of the polymorph **4.1.1** (upper row) and **4.1.2** (lower row)

The respective range of  $d_{\text{norm}}$  values for **4.2**, **4.3**, **4.4** and **4.5** was between -0.57 to 1.44; -0.59 to 1.33, -0.5 to 2.06 and -0.58 to 1.43, respectively (Fig. 4.23a-d). All chlorine derivatives had shown strong N-H<sup>⋯</sup>O as well as N-H<sup>⋯</sup>N interactions, while **4.2** had *anti-anti* orientation of thiourea had strong N-H<sup>⋯</sup>N interaction and also had weak N-H<sup>⋯</sup>S interactions. The H<sup>⋯</sup>N, H<sup>⋯</sup>O, H<sup>⋯</sup>C and H<sup>⋯</sup>S contacts were at 7.3 %, 16.3 %, 22.9 % and 13.0 % for **4.2**, respectively. On the other hand, **4.5** had these surface contacts at 5.9 %, 13.0 %, 7.3 % and 13.1 % respectively. The **4.5** was involved in C-Cl<sup>⋯</sup>C as well as C-Cl<sup>⋯</sup>  $\pi$  contacts having  $d_{\text{norm}}$  ( $\sim -0.1324$ ). The contribution of the Cl<sup>⋯</sup>C contacts in it was 7.0 % of the total Hirshfeld surface, while the same contacts in the cases of **4.3** and **4.4** were 6.9 % and 3.6 % respectively. The **4.3** as well as **4.4** both had C-Cl<sup>⋯</sup>Cl-Cl contacts, but **4.5** had no such contacts. The two-dimensional fingerprint plots of **4.3** and **4.4** showed Cl<sup>⋯</sup>Cl contacts (3.2 % for **4.3** and 2.5 % for **4.4**)

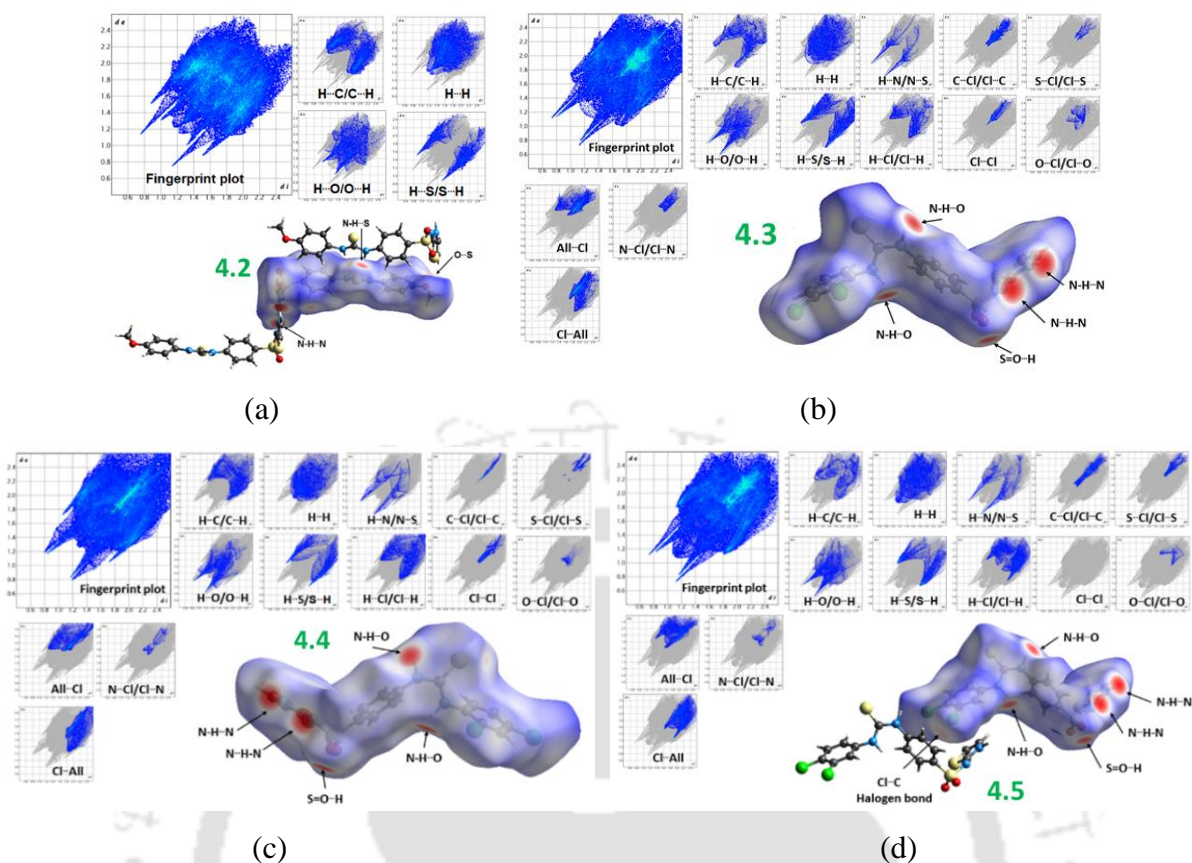


**Figure 4.23:** Fingerprint plot and Hirshfeld surfaces mapped with  $d$ -norm of (a) **4.2** (b) **4.3** (c) **4.4** (d) **4.5** (as per the designated abbreviations in each figure)

The range of  $d$ -norm values for **4.6.1**, **4.6.2**, **4.6.3** and **4.6.4** were  $-0.58$  to  $1.58$ ,  $0.51$  to  $1.42$ ,  $-0.6$  to  $1.77$  and  $-0.71$  to  $1.24$ , respectively and their minimal values of  $d_{norm}$  involved  $N-H\cdots O$  contacts (Fig. 4.24a-d). The  $H\cdots O$  and  $H\cdots N$  contacts of **4.6.1**, **4.6.2**, **4.6.3** and **4.6.4** in two-dimensional fingerprint plot contributed 21.3 %, 7.0 %; 10.3 %, 7.0 %; 21.7 %, 7.1; 20.2 %, 5.8 %, respectively. The range of  $d_{norm}$  values for **4.7.1**, **4.7.2**, **4.7.3** and **4.7.4** were  $-0.72$  to  $1.42$ ,  $-0.58$  to  $1.51$ ,  $-0.71$  to  $1.54$  and  $-0.6$  to  $1.47$ , respectively (Fig. 4.24e-h). The  $H\cdots O$  and  $H\cdots N$  contacts of **4.7.1**, **4.7.2**, **4.7.3** and **4.7.4** contributed 15.6 %, 5.7 %; 12.8 %, 6.3 %; 13.0 %, 7.1; 22.5 %, 7.1 %, respectively.

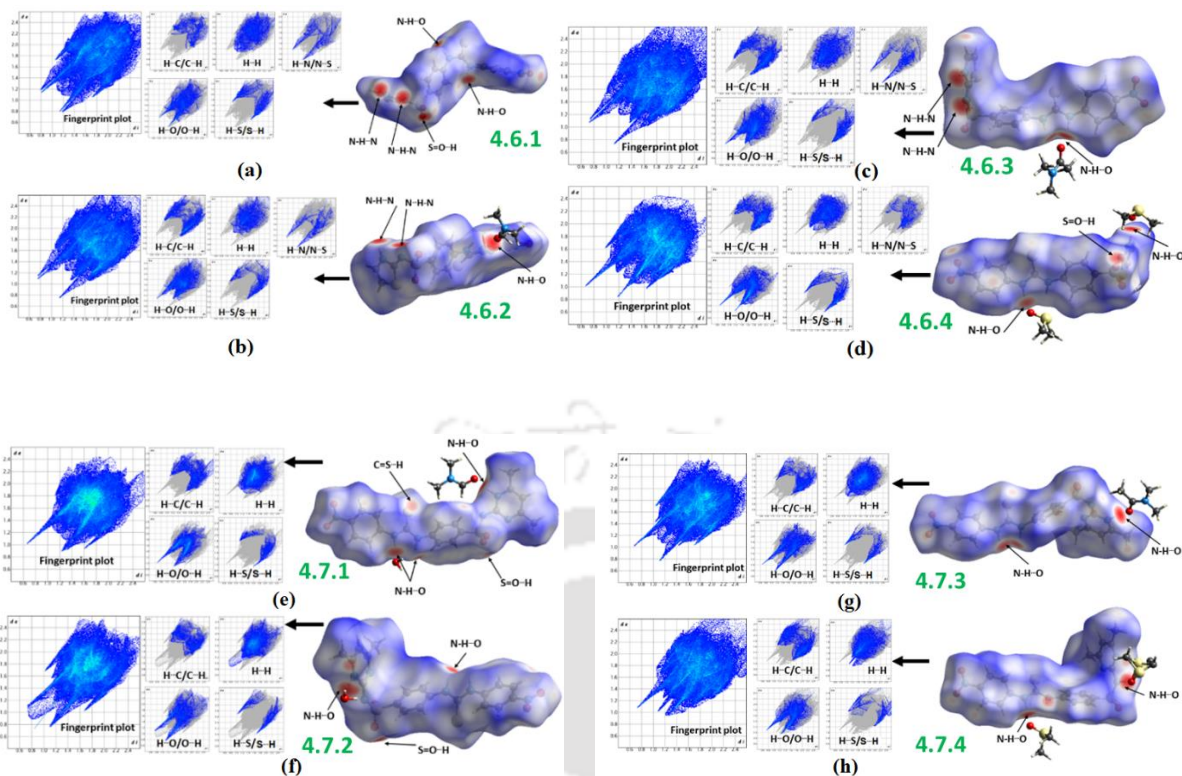


**Figure 4.24:** Fingerprint plot and Hirshfeld surfaces mapped with d-norm of the four solvates of **4.6** and **4.7** (as per the designated abbreviations in each figure)

#### 4.15: Trends in melting points

The differential scanning calorimetry studies on the two polymorphs of the **4.1** showed the respective melting point of **4.1.1** and **4.1.2** as 185 °C and 203 °C, respectively (Fig. 4.25a). It suggested better thermal stability of polymorph **4.1.2** with respect to others, as a higher amount of energy was required to melt. It is mentioned in our discussion on theoretical energy that the dimer of the **4.1.2** had higher stability by energy 22.09 kJ/mol. The enthalpy of fusion of the **4.1.1** and **4.1.2** were 71.24 kJ/mol and 55.56 kJ/mol, respectively. So, the observed hierarchy of the melting points between the two agreed with this calculation. DSC profile for a cooling cycle after heating the sample to melting temperature did not show an inter-conversion in either of the cases.

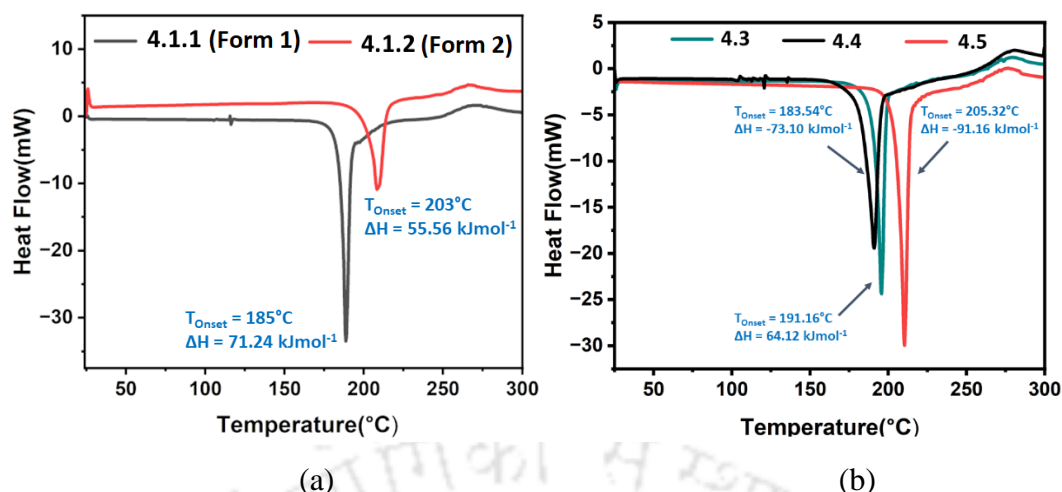


**Figure 4.25:** Differential scanning calorimetry plots of (a) of the polymorphs **4.1.1** and **4.1.2**, and (b) positional isomers (heating rate  $10^{\circ}\text{C min}^{-1}$  under a nitrogen atmosphere) **4.3**, **4.4** and **4.5**.

Similarly, the melting points of the **4.3**, **4.4** and **4.5** were determined from the respective differential scanning calorimetry, which were  $191.16^{\circ}\text{C}$ ,  $183.54^{\circ}\text{C}$  and  $205.32^{\circ}\text{C}$ , respectively (Fig. 4.25b). The respective enthalpy of fusion was  $73.20 \text{ kJ/mol}$ ,  $64.12 \text{ kJ/mol}$  and  $91.16 \text{ kJ/mol}$ , showing that the corresponding values had a trend as **4.3** ~ **4.4** < **4.5**. The isomeric compounds **4.3** and **4.4** had relatively close melting points, as compared to **4.5**, which had a higher melting point. As mentioned in an earlier section the gain in energy by both the homodimers in the case of the two isomeric cases was comparable, whereas there was a larger gain in energy by forming the homodimer in the case of the **4.5**. Thus, these supported the fact that the analysis of dimers has been able to support the trends in the melting points among these three positional isomeric compounds.

#### 4.16: Solution studies on fluoride ions detection

The  $^1\text{H}$ NMR spectra of the respective polymorphs **4.1.1** or **4.1.2** dissolved in DMSO- $d_6$  had identical chemical shifts, and the same was true with the  $^{13}\text{C}$ NMR spectra; hence, the two forms could not be distinguished by NMR. However, it is well known that discrete species of thiourea derivatives undergo deprotonation by fluoride ions in DMSO solution.<sup>24-26</sup> Hence, the consequence of deprotonation of nitrophenyl thiourea by fluoride ions of the two 4-nitrophenyl thiourea derivatives, namely **4.6** and **4.7**, were studied. In both cases, the addition of a  $0.033 \text{ mM}$  solution of tetrabutylammonium fluoride was studied by varying amounts of fluoride from  $0.033 \text{ mM}$  to  $0.166 \text{ mM}$  concentration. In the case of **4.6**, it showed a new absorption peak at  $425 \text{ nm}$  upon interaction with fluoride ions (Fig 4.26a). The visual color

change observed in **4.7** was similar to the one seen in the case of **4.6**, but there was a difference in the way the absorption change took place.

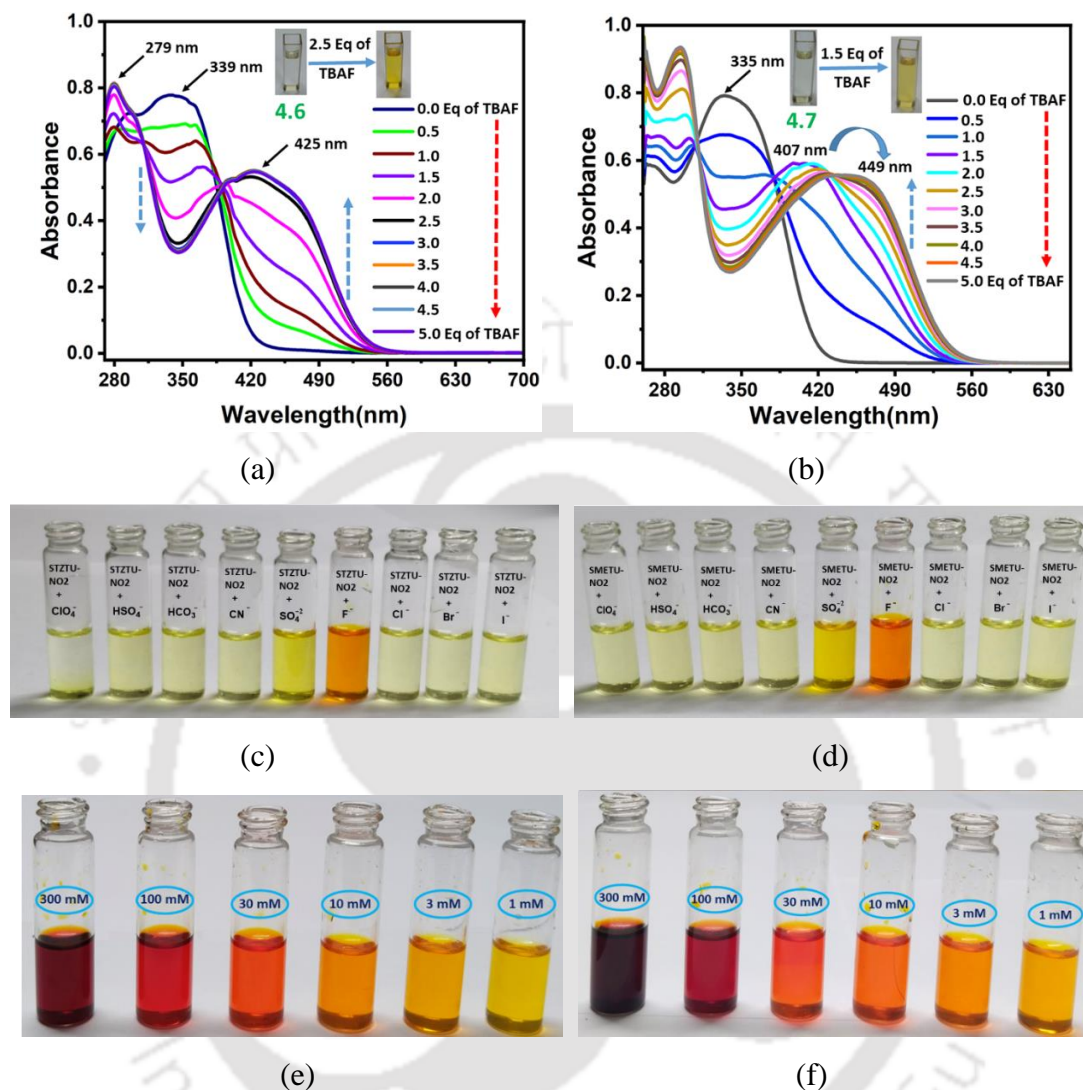


**Figure 4.26:** UV-visible titrations of (a) **4.6** and (b) **4.7** (0.033 mM) with the addition of different amounts of TBAF (insets are color changes at particular fluoride concentrations); (c) and (d) are respective visual colors with the one-mole equivalent of different anions in DMSO (4 mM in each case). The color of the solution was observed through the naked eye in the solutions of (e) **4.6** and (f) **4.7** in DMSO (10 mM in each case) with different molar concentrations of TBAF (encircled by blue ellipses on each sample tube).

In the **4.7**, stepwise absorption changes passed through a new peak at 407 nm which disappeared with additional amounts of fluoride ion to show absorption at 449 nm (Fig. 4.26b). This was due to the stepwise formation of hydrogen-bonded species, which transformed into an anionic species. This suggestion is based on the stepwise hydrogen

bonded thiourea derivatives species with fluoride ion followed by getting deprotonated, as shown earlier through solution study.<sup>24-26</sup> The color change could be visually seen at a concentration of substrate (4 mM concentration) upon the addition of an equivalent concentration of fluoride ions (Fig.4.26c and 4.26d). Whereas the addition of other salts, such as tetrabutylammonium bromide, chloride, iodide, bicarbonate, bisulphate, cyanide and perchlorate, did not cause a color change at this concentration.<sup>27</sup> The visual detection at a higher concentration of the two analytes (10 mM) with different concentrations of fluoride ions is shown in Fig. 4.26e and 4.26f. The color intensity was increased with an increase in the concentration of fluoride ions. This showed that visual detection was possible at wide ranges of concentrations of fluoride ions. The ability to detect at lower and higher concentrations suggests that discrete units of the analytes were responsible for the detection. The same experiments carried out with other thiourea derivatives did not show a visual change (Fig. A4.6); therefore, the effect of nitrophenyl thiourea part has become apparent in the visual color change. This was also reflected in the inability of the other thiourea derivatives lacking an auxo-chrome where visual detections were not observed.

#### 4.17: Conclusions

The series of thiourea-derived sulfathiazoles studied here had hydrogen-bonded homodimers as cyclic sub-assemblies. The importance of the homodimers contributing to polymorphs and related self-assemblies was established through structural analysis together with energy calculations. All these homodimers had two intermolecular N-H(thiazole)  $\cdots$ N (sulphonamide) bonds as the principal hydrogen bonds. The S=O groups provided supportive weak S=O(sulphonamide) $\cdots$ H-N(thiazole) bond to stabilize homodimer in **4.1.2** and **4.6.1**. When homodimers were not formed, the thiourea tape or bifurcated hydrogen-bonded chains involving two N-H of thiourea hydrogen bonding with O atom of -SO<sub>2</sub>- were favoured. The conformational changes across the homodimers provided different dispositions of the -SO<sub>2</sub>- groups in the polymorphs. The isomorphous **4.3** and **4.4** had similar types of chlorine-chlorine interactions. Theoretical calculations have shown that the hydrogen-bonded homodimers gain in energies than the sum of energies of the two independent components of the dimers and were dependent on the steric, conformation and electronic factors. The solvents in solvates had guided the conformation of the thiourea across the homodimers. Due to the steric effect of methyl groups, the homodimers between methazine in the solvates of **4.7** were not observed. In this case, chain-like arrangements were observed, and the conformational changes occurred across such chains. However, the methazine part also adopted hydrogen-

bonded cyclic dimeric structures to maximize hydrogen bonds. This aspect was seen in the hydrate and hydrated DMF solvate. The homodimers of sulfathiazole-derived thiourea provided a rational structural pattern in polymorphs and solvates with the exception of the DMSO solvate of **4.6**, whereas chain-like arrangements in the **4.7** were observed. The DMSO solvate (1:2 stoichiometry) of the 4-nitrophenylthiourea derivative of sulfathiazole and sulfamethazine had a similar chain-like structure, where participation of DMSO molecule in H-bonding with one N-H of thiourea had caused hindrance to form hydrogen-bonded assembly through bifurcated hydrogen bonds in the respective assembly. This study suggested that case-by-case examination is required to ascertain the extended domains (repeated sub-assemblies) contributing to their stabilities.

#### 4.18: References

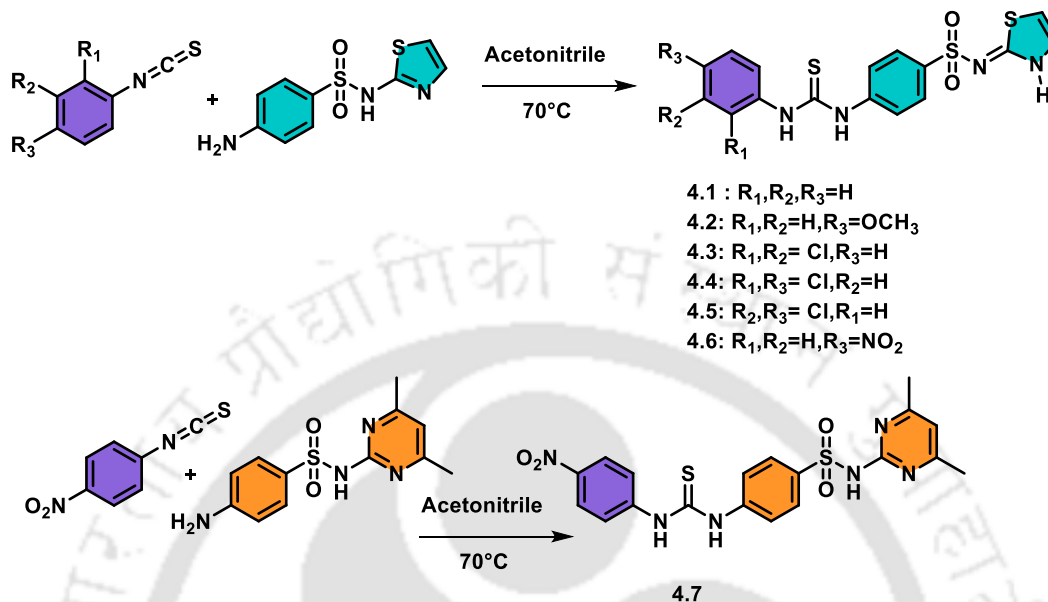
1. Liu, C.; Cao, F.; Kulkarni, S. A.; Wood, G. P. F.; Santiso, E. E. Understanding Polymorph Selection of Sulfamerazine in Solution. *Cryst. Growth Des.* **2019**, *19* (12), 6925–6934.
2. Phukan, N.; Baruah, J. B. Polymorphs of Thiazole-Derived Imines Connected to Hydroxyaromatics. *Cryst. Growth Des.* **2015**, *15* (4), 1843–1851.
3. Phukan, N.; Baruah, J. B. Conformational Adjustments over Synthons of Urea and Thiourea Based Assemblies. *CrystEngComm* **2016**, *18* (40), 7753–7763.
4. Lozano, V.; Moers, O.; Jones, P. G.; Blaschette, A. Polysulfonylamines, CLXIX. Intermolecular Interactions in Crystalline Di (Organosulfonyl) Amines. Part 1. Di (4-Bromobenzenesulfonyl) Amine: Two Conformational Polymorphs and the Structural Relationship of One Polymorph to the Corresponding 2, 4-Dimethylpyridinium Salt. *ZEITSCHRIFT FUR Naturforsch. Sect. BA J. Chem. Sci.* **2004**, *59* (6), 661–672.
5. Baruah, J. B.; Karmakar, A.; Barooah, N. Solvent Induced Symmetry Non-Equivalence in the Crystal Lattice of 7-Carboxymethyl-1, 3, 6, 8-Tetraoxo-3, 6, 7, 8-Tetrahydro-1H-Benzo [Lmn][3, 8] Phenathroline-2-Yl) Acetic Acid. *CrystEngComm* **2008**, *10* (2), 151–154.
6. Karmakar, A.; Baruah, J. B. Polymorphism and Symmetry Non-Equivalence in (3-Carboxymethoxy-Naphthalen-2-Yloxy) Acetic Acid. *J. Mol. Struct.* **2008**, *888* (1–3), 197–203.
7. Jali, B. R.; Baruah, J. B. Polymorphs and Solvates of 2-(1,4-Dihydro-1,4-Dioxonaphthalen-3-Ylthio)Benzoic Acid. *Cryst. Growth Des.* **2012**, *12* (6), 3114–3122.

8. Davey, R. J.; Dent, G.; Mughal, R. K.; Parveen, S. Concerning the Relationship between Structural and Growth Synthons in Crystal Nucleation: Solution and Crystal Chemistry of Carboxylic Acids As Revealed through IR Spectroscopy. *Cryst. Growth Des.* **2006**, *6* (8), 1788–1796.
9. Gu, C.-H.; Young, V.; Grant, D. J. W. Polymorph Screening: Influence of Solvents on the Rate of Solvent-Mediated Polymorphic Transformation. *J. Pharm. Sci.* **2001**, *90* (11), 1878–1890.
10. Drebuschak, T. N.; Chesalov, Y. A.; Boldyreva, E. V. A Conformational Polymorphic Transition in the High-Temperature  $\beta$ -Form of Chlorpropamide on Cooling: A New  $\beta'$ -Form. *Acta Crystallogr. Sect. B Struct. Sci.* **2009**, *65* (6), 770–781.
11. Sanphui, P.; Bolla, G.; Das, U.; Mukherjee, A. K.; Nangia, A. Acemetacin Polymorphs: A Rare Case of Carboxylic Acid Catemer and Dimer Synthons. *CrystEngComm* **2013**, *15* (1), 34–38.
12. Etter, M. C. Encoding and Decoding Hydrogen-Bond Patterns of Organic Compounds. *Acc. Chem. Res.* **1990**, *23* (4), 120–126.
13. Wood, P. A.; Galek, P. T. A. The Impact of Accessible Surface on Hydrogen Bond Formation. *CrystEngComm* **2010**, *12* (8), 2485–2491.
14. Cavallo, G.; Metrangolo, P.; Milani, R.; Pilati, T.; Priimagi, A.; Resnati, G.; Terraneo, G. The Halogen Bond. *Chem. Rev.* **2016**, *116* (4), 2478–2601.
15. Hou, L.; Gao, L.; Zhang, W.; Yang, X.-J.; Wu, B. Quaternary Cocrystals Based on Halide-Binding Foldamers through Both Hydrogen and Halogen Bonding. *Cryst. Growth Des.* **2021**, *21* (5), 2837–2843.
16. Kálmán, A.; Argay, G.; Scharfenberg-Pfeiffer, D.; Höhne, E.; Ribár, B. Main-Part'isostructuralism of Several Cardenolides and Bufadienolides. Structures of Three Cardenolides:(21S)-Methyldigitoxigenin, Uzarigenin and Sarmentogenin Methanol Solvate. *Acta Crystallogr. Sect. B Struct. Sci.* **1991**, *47* (1), 68–77.
17. Mondal, P.; Karmakar, A.; Singh, W. M.; Baruah, J. B. Crystal Packing in Some Flexible Carboxylic Acids and Esters Attached to a Naphthalene Ring. *CrystEngComm* **2008**, *10* (11), 1550–1559.
18. Nath, B.; Baruah, J. B. Quasi-Isostructural Solvates of Bis (4-Hydroxy-3, 5-Dimethylphenyl)(4-N, N-Dimethylaminophenyl) Methane. *Cryst. Growth Des.* **2012**, *12* (12), 6173–6180.
19. Nath, J.; Baruah, J. B. Polymorphic Solvates, Ionic Cocrystals and C-N Bond

- Formation to Form Ionic Cocrystals in Sulfamethoxazole and Sulfathiazole-Derived Urea. *CrystEngComm* **2022**, 3394–3408.
20. Nath, J.; Baruah, J. B. Self-Assemblies of Solvates, Ionic Cocrystals, and a Salt Based on 4-[[[4-Nitrophenyl]Carbamoyl]Amino]-N-(Pyrimidin-2-Yl)Benzene-1-Sulfonamide: Study in the Solid and Solution States. *Cryst. Growth Des.* **2021**, 21 (9), 5325–5341.
21. Ranjan, S.; Devarapalli, R.; Kundu, S.; Saha, S.; Deolka, S.; Vangala, V. R.; Reddy, C. M. Isomorphism: Molecular Similarity to Crystal Structure Similarity in Multicomponent Forms of Analgesic Drugs Tolfenamic and Mefenamic Acid. *IUCrJ* **2020**, 7 (2), 173–183.
22. Hao, M.-H. Theoretical Calculation of Hydrogen-Bonding Strength for Drug Molecules. *J. Chem. Theory Comput.* **2006**, 2 (3), 863–872.
23. Spackman, P. R.; Turner, M. J.; McKinnon, J. J.; Wolff, S. K.; Grimwood, D. J.; Jayatilaka, D.; Spackman, M. A. CrystalExplorer: A Program for Hirshfeld Surface Analysis, Visualization and Quantitative Analysis of Molecular Crystals. *J. Appl. Crystallogr.* **2021**, 54 (3), 1006–1011.
24. Esteban-Gómez, D.; Fabbrizzi, L.; Licchelli, M. Why, on Interaction of Urea-Based Receptors with Fluoride, Beautiful Colors Develop. *J. Org. Chem.* **2005**, 70 (14), 5717–5720.
25. Cametti, M.; Rissanen, K. Recognition and Sensing of Fluoride Anion. *Chem. Commun.* **2009**, No. 20, 2809–2829.
26. Zavala-Contreras, B.; Santacruz-Ortega, H.; Orozco-Valencia, A. U.; Inoue, M.; Ochoa Lara, K.; Navarro, R.-E. Optical Anion Receptors with Urea/Thiourea Subunits on a Tentagel Support. *ACS omega* **2021**, 6 (14), 9381–9390.
27. Ashokkumar, P.; Ramakrishnan, V. T.; Ramamurthy, P. Fluorescence Spectroscopic Evidence for Hydrogen Bonding and Deprotonation Equilibrium between Fluoride and a Thiourea Derivative. *Chem. Eur. J.* **2010**, 16 (44), 13271–13277.

## Appendix - Chapter 4

## 4A.1: Experimental



Scheme A.1: Synthesis of 4.1-4.7

**Synthesis and characterization of the polymorphs, solvates and positional isomer (4.1.1-4.7.4):**

**(4.1.1):** A solution of phenyl isothiocyanate (270.4 mg, 2 mmol) and sulfathiazole (510.6 mg, 2 mmol) was prepared in acetonitrile (30 ml), and the solution was stirred at 80°C for 8 hrs. The resulting solution was filtered, and the filtrate was evaporated using a rotary evaporator. The residue was dissolved in dimethylformamide (DMF) and kept for crystallization. After 3-4 days, the crystals of **4.1.1** were obtained. Yield = 82 %. IR (Neat,  $cm^{-1}$ ): 3266 (w), 3116 (w), 2778 (w), 1592 (m), 1568 (m), 1526 (s), 1495 (s), 1417 (s), 1314 (s), 1299 (s), 1256 (s), 1183 (m), 1142 (s), 1089 (s), 940 (s), 858 (s), 835 (s), 757 (s), 715 (s), 688 (m), 672 (s), 645 (s), 602 (s), 555 (s), 531 (s).  $^1H$ NMR (600 MHz, DMSO- $d_6$ , ppm): 12.70 (s, 1H), 10.07 {s, N-H (1)}, 10.03 {s, N-H (2)}, 7.74 (d,  $J = 9$  Hz, 2H), 7.66 (d,  $J = 8.4$  Hz, 2H), 7.47 (d,  $J = 7.8$  Hz, 2H), 7.34 (t,  $J = 7.8$  Hz, 2H), 7.25 (d,  $J = 4.2$  Hz, 1H), 7.14 (t,  $J = 7.8$  Hz, 1H), 6.82 (d,  $J = 4.8$  Hz).  $^{13}C$  NMR (125 MHz, DMSO- $d_6$ ): 179.52, 168.81, 142.95, 139.19, 137.13, 128.56, 126.41, 124.78, 123.76, 122.47, 108.18. ESI-MS. Calculated  $m/z$ - 391.0357; found: 391.0351 [(M + H)<sup>+</sup>, 100%].

**(4.1.2):** The crystals of **4.1.1** were dissolved in a methanol and acetone mixture, and the solution was heated at 80°C for 6 hrs. The resulting solution was filtered and kept for

crystallization. The crystals of **4.1.2** appeared after 2-3 days. Yield = 79 %. IR (Neat,  $\text{cm}^{-1}$ ): 3355 (w), 3255 (m), 2921 (w), 1592 (m), 1568 (s), 1520 (s), 1504 (s), 1446 (w), 1411 (s), 1354 (m), 1287 (s), 1262 (w), 1193 (s), 1142 (s), 1088 (s), 935 (s), 851 (s), 822 (w), 735 (w), 719 (s), 684 (s), 641 (s), 585 (s), 551 (s), 516 (m), 499 (m).  $^1\text{H-NMR}$  (600 MHz,  $\text{DMSO-d}_6$ , ppm): 12.70 (s, 1H), 10.07 {s, N-H (1)}, 10.03 {s, N-H (2)}, 7.74 (d,  $J = 9$  Hz, 2H), 7.66 (d,  $J = 8.4$  Hz, 2H), 7.47 (d,  $J = 7.8$  Hz, 2H), 7.34 (t,  $J = 7.8$  Hz, 2H), 7.25 (d,  $J = 4.2$  Hz, 1H), 7.14 (t,  $J = 7.8$  Hz, 1H), 6.82 (d,  $J = 4.8$  Hz).  $^{13}\text{C-NMR}$  (125 MHz,  $\text{DMSO-d}_6$ ): 179.53, 168.83, 142.97, 139.21, 137.14, 128.58, 126.43, 124.80, 123.78, 122.49, 108.21

**(4.2)**: A solution of 4-methoxyphenyl isothiocyanate (330.42 mg, 2 mmol) and sulfathiazole (510.6, 2 mmol) in acetonitrile (30 ml) was stirred at  $80^\circ\text{C}$  for 8 hrs. A yellow precipitate of **4.2** was formed, which was filtered and dissolved in DMF, the filtrate was kept undisturbed for crystallization. After 3 - 4 days, the crystals of **4.2** were formed. Yield = 71 %. IR (Neat,  $\text{cm}^{-1}$ ): 3293 (w), 3098 (w), 3037 (br), 2802 (w), 1591 (s), 1568 (s), 1526 (s), 1507 (s), 1414 (s), 1322 (s), 1297 (s), 1247 (s), 1173 (m), 1148 (s), 1115 (s), 1085 (s), 1032 (s), 931 (s), 857 (s), 830 (s), 805 (m), 770 (s), 738 (m), 717 (s), 691 (m), 674 (s), 641 (s), 589 (s), 557 (s), 514 (m).  $^1\text{H-NMR}$  (600 MHz,  $\text{DMSO-d}_6$ , ppm): 12.70 (s, 1H), 9.92 {s, N-H (1)}, 9.86 {s, N-H (2)}, 7.72 (d,  $J = 8.8$  Hz, 2H), 7.65 (d,  $J = 8.8$  Hz, 2H), 7.32 (d,  $J = 8.9$  Hz, 2H), 7.25 (d,  $J = 4.6$  Hz, 1H), 6.91 (d,  $J = 9$  Hz, 2H), 6.82 (d,  $J = 4.7$  Hz, 1H).  $^{13}\text{C}$  NMR (125 MHz,  $\text{DMSO-d}_6$ ): 179.69, 168.80, 156.73, 143.06, 136.96, 131.87, 126.34, 125.98, 124.39, 122.39, 113.76, 108.13, 55.26. ESI-MS. Calculated  $m/z$ -421.0463; found:  $m/z$  421.0466 [(M + H) $^+$ , 100%].

**(4.3)**: A solution of 2,3-dichlorophenyl isothiocyanate (408 mg, 2 mmol) and sulfathiazole (511 mg, 2 mmol) in acetonitrile (30 ml) was heated at  $80^\circ\text{C}$  for 8 hrs. The white precipitate obtained was dissolved in different solvents (a mixture of methanol and acetone, DMF and DMA). The resulting solution was filtered and kept for crystallization. After 4 days, the crystals of **4.3** were obtained. Yield = 82 %. IR (Neat,  $\text{cm}^{-1}$ ): 3318 (w), 3253 (m), 1577 (s), 1497 (s), 1454 (w), 1420 (s), 1285 (s), 1234 (w), 1141 (s), 1088 (s), 934 (s), 847 (s), 834 (s), 782 (m), 722 (s), 686 (s), 642 (s), 582 (m), 553 (s), 499(s).  $^1\text{HNMR}$  (600 MHz,  $\text{DMSO-d}_6$ , ppm): 12.71 (s, 1H), 10.32 {s, N-H (1)}, 9.81 {s, N-H (2)}, 7.76 (d,  $J = 8.8$  Hz, 2H), 7.71 (d,  $J = 8.8$  Hz, 2H), 7.55 (d,  $J = 8$  Hz, 1H), 7.52 (d,  $J = 8$  Hz, 1H), 7.37 (t,  $J = 8.1$  Hz, 1H), 7.25 (d,  $J = 4.5$  Hz, 1H), 6.83 (d,  $J = 4.7$  Hz).  $^{13}\text{CNMR}$  (125 MHz,  $\text{DMSO-d}_6$ ): 180.41, 168.83, 142.52, 138.31, 137.63, 131.85, 129.32, 128.64, 128.31, 127.83, 126.45, 124.42, 122.83, 108.19. ESI-MS. Calculated  $m/z$ - 458.9577; found:  $m/z$  458.9572 [(M + H) $^+$ , 100%].

**(4.4):** The synthesis of **4.4** was similar to the synthesis of **4.3**, the 2,4-dichlorophenyl isothiocyanate was used instead of using 2,3-dichlorophenyl isothiocyanate. Yield = 79 %. IR (Neat,  $\text{cm}^{-1}$ ): 3340 (w), 3234 (m), 3052 (w), 1585 (m), 1564 (s), 1499 (s), 1474 (w), 1410 (s), 1352 (m), 1326(m), 1306(m), 1283 (s), 1240 (m), 1195 (s), 1178 (w), 1143 (s), 1116 (m), 1091 (s), 1073 (s), 931 (s), 851 (s), 831 (s), 805 (s), 752 (m), 721 (s), 697 (s), 640 (s), 603 (m), 586 (m), 572 (s), 553 (s).  $^1\text{H}$ NMR (600 MHz,  $\text{DMSO-d}_6$ , ppm): 12.72 (s, 1H), 10.30 {s, N-H (1)}, 9.71 {s, N-H (2)}, 7.76 (d,  $J = 8.8$  Hz, 2H), 7.70 (d,  $J = 5.6$  Hz, 2H), 7.69 (s, 1H), 7.57 (d,  $J = 8.6$  Hz, 1H), 7.44 (d,  $J = 8.6$  Hz, 1H), 7.25 (d,  $J = 4.6$  Hz, 1H), 6.83 (d,  $J = 4.6$  Hz, 1H).  $^{13}\text{C}$  NMR (125 MHz,  $\text{DMSO-d}_6$ ): 180.38, 168.84, 142.50, 137.61, 135.48, 131.49, 131.25, 131.07, 129.02, 127.49, 126.45, 124.42, 122.80, 108.19. ESI-MS. Calculated  $m/z$ -458.9577; found:  $m/z$  -458.9572 [(M + H) $^+$ , 100%].

**(4.5):** The synthesis of **4.5** was similar to the synthesis of **4.3**, the 3,4-dichlorophenyl isothiocyanate was used instead of using 2,3-dichlorophenyl isothiocyanate. Yield: 86 %. IR (Neat,  $\text{cm}^{-1}$ ): 3323 (w), 3258 (m), 3096(w), 1574 (s), 1499 (s), 1411 (s), 1380 (w), 1309 (m), 1290 (s), 1246 (w), 1193 (s), 1145 (s), 1089 (s), 1066 (m), 1031 (m), 938 (s), 857 (s), 833(s), 799 (s), 737 (s), 724 (s), 713 (m), 692 (s), 642 (s), 607 (m), 591 (m), 579 (s), 551 (s), 502 (s).  $^1\text{H}$ NMR (600 MHz,  $\text{DMSO-d}_6$ , ppm): 12.72 (s, 1H), 10.29 {s, N-H (1)}, 10.18 {s, N-H (2)}, 7.87 (s, 1H), 7.76 (d,  $J = 8.7$  Hz, 2H), 7.63 (d,  $J = 8.7$  Hz, 2H), 7.59 (d,  $J = 8.7$  Hz, 1H), 7.45 (d,  $J = 8.7$  Hz, 1H), 7.26 (d,  $J = 4.7$  Hz, 1H), 6.83 (d,  $J = 4.7$  Hz.  $^{13}\text{C}$  NMR (125 MHz,  $\text{DMSO-d}_6$ ): 179.61, 168.85, 142.49, 139.50, 137.61, 130.54, 130.28, 126.50, 126.34, 124.98, 124.42, 123.75, 122.79, 108.20. ESI-MS. Calculated  $m/z$ - 458.9577; found:  $m/z$ - 458.9577 [(M + H) $^+$ , 100%].

**(4.6.1):** A solution of 4-nitrophenyl isothiocyanate (360.36 mg, 2 mmol) and sulfathiazole (510.6, 2 mmol) in acetonitrile (30 ml) was stirred at 80°C for 8 hrs. A yellow precipitate was **4.6** formed. It was dissolved in an acetone and methanol mixed solvent (1:1 v/v), and after 3 days, crystals of **4.6.1** were formed. Yield = 77 %. IR (Neat,  $\text{cm}^{-1}$ ): 3311 (w), 3244 (m), 1595 (s), 1561 (s), 1524 (s), 1503 (s), 1406 (s), 1333 (s), 1282 (s), 1260 (s), 1195 (m), 1182 (s), 1142 (s), 1109 (s), 1088 (s), 1058 (m), 941 (s), 854 (s), 804 (s), 746 (m), 736 (m), 723 (s), 716 (m), 691 (s), 641 (s), 607 (s), 585 (s), 552 (s), 505 (s).  $^1\text{H}$ -NMR (600 MHz,  $\text{DMSO-d}_6$ , ppm): 12.73 (s, 1H), 10.57 {s, N-H (1)}, 10.51 {s, N-H (2)}, 8.21 (d,  $J = 9$  Hz, 2H), 7.83 (d,  $J = 9$  Hz, 2H), 7.78 (d,  $J = 8.4$  Hz, 2H), 7.66 (d,  $J = 8.4$  Hz, 2H), 7.25 (d,  $J = 4.2$  Hz, 1H), 6.83 (d,  $J = 4.2$  Hz, 1H).  $^{13}\text{C}$  NMR (125 MHz,  $\text{DMSO-d}_6$ ): 179.37, 168.90, 145.98, 142.64,

142.38, 137.85, 126.58, 124.47, 122.82, 121.96, 108.27. ESI-MS. Calculated  $m/z$ - 436.0208; found: 436.0203 [(M + H)<sup>+</sup>, 100%].

**(4.6.2):** The yellow precipitate of crude **4.6** was dissolved in DMF. The resultant solution was left for crystallization to obtain **4.6.2** crystals after one week. Yield = 87 %. IR (Neat,  $\text{cm}^{-1}$ ): 3105 (br), 1651 (s), 1594 (s), 1565 (s), 1533 (s), 1494 (s), 1431 (w), 1387 (m), 1327 (s), 1301 (s), 1249 (s), 1180 (s), 1146 (s), 1113 (s), 1090 (s), 932 (s), 858 (m), 844 (s), 826 (m), 751 (s), 736 (s), 699 (s), 686 (s), 666 (s), 648 (s), 632 (m), 571 (s), 555 (s), 494 (s). <sup>1</sup>H-NMR (600 MHz, DMSO- $d_6$ , ppm): 12.72 (s, 1H), 10.56 {s, N-H (1)}, 10.50 {s, N-H (2)}, 8.21 (d, J = 9.6 Hz, 2H), 7.95 (s, 1H), 7.83 (d, J = 10.2 Hz, 2H), 7.78 (d, J = 7.2 Hz, 2H), 7.67 (d, J = 9 Hz, 2H), 7.25 (d, J = 4.8 Hz, 1H), 6.83 (d, J = 4.2 Hz, 1H), 2.88 (s, 3H), 2.73 (s, 3H). <sup>13</sup>C NMR (125 MHz, DMSO- $d_6$ ): 179.38, 168.90, 162.38, 145.98, 142.65, 142.39, 137.86, 126.59, 124.47, 122.84, 121.97, 108.27, 35.84, 30.83.

**(4.6.3):** The formation of **4.6.3** was similar to the formation of **4.6.2**, the solvent DMA was used instead of DMF. Yield = 79 %. IR (Neat,  $\text{cm}^{-1}$ ): 3331 (m), 3008 (w), 1613(m), 1593 (s), 1568 (s), 1537 (s), 1505 (s), 1493 (s), 1400 (s), 1302 (s), 1251 (s), 1204 (s), 1146 (s), 1114 (s), 1091 (s), 1012 (s), 930 (s), 848 (s), 839 (s), 826 (m), 735 (s), 699 (s), 663 (m), 647 (s), 634 (s), 611 (s), 592 (s), 570 (s), 553 (s), 493 (s). <sup>1</sup>H-NMR (600 MHz, DMSO- $d_6$ , ppm): 12.73 (s, 1H), 10.56 {s, N-H (1)}, 10.51 {s, N-H (2)}, 8.21 (d, J = 9 Hz, 2H), 7.83 (d, J = 9 Hz, 2H), 7.78 (d, J = 8.4 Hz, 2H), 7.67 (d, J = 9 Hz, 2H), 7.25 (d, J = 4.2 Hz, 1H), 6.83 (d, J = 4.2 Hz, 1H), 2.93 (s, 3H), 2.78 (s, 3H), 1.95 (s, 3H). <sup>13</sup>C NMR (125 MHz, DMSO- $d_6$ ): 179.36, 169.66, 168.88, 145.96, 142.63, 142.37, 137.85, 126.57, 124.44, 122.80, 121.94, 108.24

**(4.6.4):** The formation of **4.6.4** was similar to the formation of **4.6.2**, the solvent DMSO was used instead of DMF. Yield = 84 %. IR (Neat,  $\text{cm}^{-1}$ ): 3318 (m), 3094 (w), 1592 (s), 1568 (s), 1520 (s), 1505 (s), 1494 (s), 1432 (s), 1403 (s), 1323 (s), 1304 (s), 1244 (s), 1177 (m), 1134 (s), 1110 (s), 1088 (s), 1068 (m), 1014 (s), 956 (s), 936 (s), 870 (m), 850 (s), 818 (m), 737 (s), 695 (s), 668 (m), 643 (s), 632 (s), 604 (m), 567 (s), 551 (s), 484 (s). <sup>1</sup>H-NMR (600 MHz, DMSO- $d_6$ , ppm): 12.73 (s, 1H), 10.56 {s, N-H (1)}, 10.51 {s, N-H (2)}, 8.21 (d, J = 9.6 Hz, 2H), 7.83 (d, J = 9 Hz, 2H), 7.78 (d, J = 8.4 Hz, 2H), 7.67 (d, J = 9 Hz, 2H), 7.25 (d, J = 4.2 Hz, 1H), 6.83 (d, J = 4.2 Hz, 1H), 2.54 (s, 6H). <sup>13</sup>CNMR (125 MHz, DMSO- $d_6$ ): 179.40, 168.89, 145.98, 142.66, 142.40, 137.85, 126.59, 124.48, 122.86, 122.00, 108.30, 40.42.

**(4.7.1):** A solution of 4-nitrophenylisothiocyanate (328 mg, 2 mmol) and sulfamethazine (556 mg, 2 mmol) in acetonitrile (30 ml) was stirred at 80°C for 8 hrs. A yellow precipitate of **4.7**

was formed, which was filtered and dissolved in DMF, the filtrate was kept undisturbed for crystallization. After 3 - 4 days, the crystals of **4.7.1** were formed. Yield = 89 %. IR (Neat,  $\text{cm}^{-1}$ ): 3486 (w), 3251 (w), 3003 (w), 1638 (s), 1597 (s), 1582 (m), 1508 (s), 1493 (m), 1449 (m), 1408 (s), 1381 (s), 1329 (s), 1303 (s), 1245 (s), 1175 (m), 1134 (s), 1123 (s), 1075 (s), 1018 (m), 998 (s), 933 (m), 845 (s), 809 (s), 776 (m), 747 (m), 728 (s), 710 (s), 694 (m), 670 (s), 636 (s), 578 (s), 553 (m), 540 (m), 512 (s).  $^1\text{H-NMR}$  (600 MHz,  $\text{DMSO-d}_6$ , ppm): 11.56 (s, 1H), 10.59 {s, N-H (1)}, 10.53 {s, N-H (2)}, 8.21 (d,  $J = 9.1$  Hz, 2H), 7.96 (d,  $J = 8.7$  Hz, 2H), 7.95 (s, 1H), 7.81 (d,  $J = 9.2$  Hz, 2H) 7.69 (d,  $J = 8.8$  Hz, 2H), 6.77 (s, 1H).  $^{13}\text{C NMR}$  (125 MHz,  $\text{DMSO-d}_6$ ): 179.30, 162.32, 145.86, 142.62, 128.87, 124.45, 121.98, 121.90, 35.80, 30.78. ESI-MS. Calculated  $m/z$ - 459.0909; found:  $m/z$  459.0902 [(M + H)<sup>+</sup>, 100%]

**(4.7.2):** The yellow precipitate of **4.7** was dissolved in a mixture of acetone and methanol (1:1 v/v). The crystals of **4.7.2** were obtained after 2-3 days. Yield = 93 %. IR (Neat,  $\text{cm}^{-1}$ ): 3418 (w), 3323 (m), 1633 (m), 1593 (s), 1576 (m), 1538 (s), 1507 (s), 1494 (m), 1435 (s), 1383 (m), 1330 (s), 1312 (s), 1246 (s), 1180 (w), 1138 (s), 1122 (m), 1080 (s), 969 (s), 855 (s), 835 (s), 816 (m), 778 (m), 736 (s), 703 (s), 687 (s), 640 (s), 583 (s), 567 (s), 549 (s), 526 (m), 485 (s).  $^1\text{H-NMR}$  (600 MHz,  $\text{DMSO-d}_6$ , ppm): 11.69 (s, 1H), 10.59 {s, N-H (1)}, 10.53 {s, N-H (2)}, 8.21 (d,  $J = 9.2$  Hz, 2H), 7.96 (d,  $J = 8.8$  Hz, 2H), 7.81 (d,  $J = 9.3$  Hz, 2H) 7.69 (d,  $J = 8.8$  Hz, 2H), 6.76 (s, 1H).  $^{13}\text{C NMR}$  (125 MHz,  $\text{DMSO-d}_6$ ): 179.31, 156.16, 145.87, 142.63, 128.88, 124.45, 121.99, 121.91, 30.71.

**(4.7.3):** The formation of **4.7.3** was similar to that of the formation of **4.7.2**, DMA solvent was used instead of DMF. Yield = 83 %. IR (Neat,  $\text{cm}^{-1}$ ): 3310 (m), 3105 (w), 1614 (w), 1595 (s), 1577 (w), 1508 (s), 1419 (s), 1401 (s), 1334 (s), 1300 (s), 1248 (s), 1177 (m), 1131 (s), 1112 (s), 1072 (s), 1022 (s), 967 (s), 845 (s), 778 (s), 736 (s), 713 (s), 679 (s), 641 (s), 618 (m), 601 (m), 581 (s), 564 (s), 549 (m), 532 (s), 494 (s), 478 (s), 427 (s).  $^1\text{H-NMR}$  (600 MHz,  $\text{DMSO-d}_6$ , ppm): 11.69 (s, 1H), 10.58 {s, N-H (1)}, 10.52 {s, N-H (2)}, 8.21 (d,  $J = 9.6$  Hz, 2H), 7.96 (d,  $J = 9$  Hz, 2H), 7.81 (d,  $J = 9$  Hz, 2H) 7.69 (d,  $J = 9$  Hz, 2H), 6.76 (s, 1H), 2.93 (s, 3H), 2.78 (s, 3H), 2.26 (s, 6H), 1.95 (s, 3H).  $^{13}\text{C NMR}$  (125 MHz,  $\text{DMSO-d}_6$ ): 179.32, 162.63, 156.16, 145.87, 142.64, 128.87, 124.44, 122, 121.92, 37.46, 34.51, 21.41.

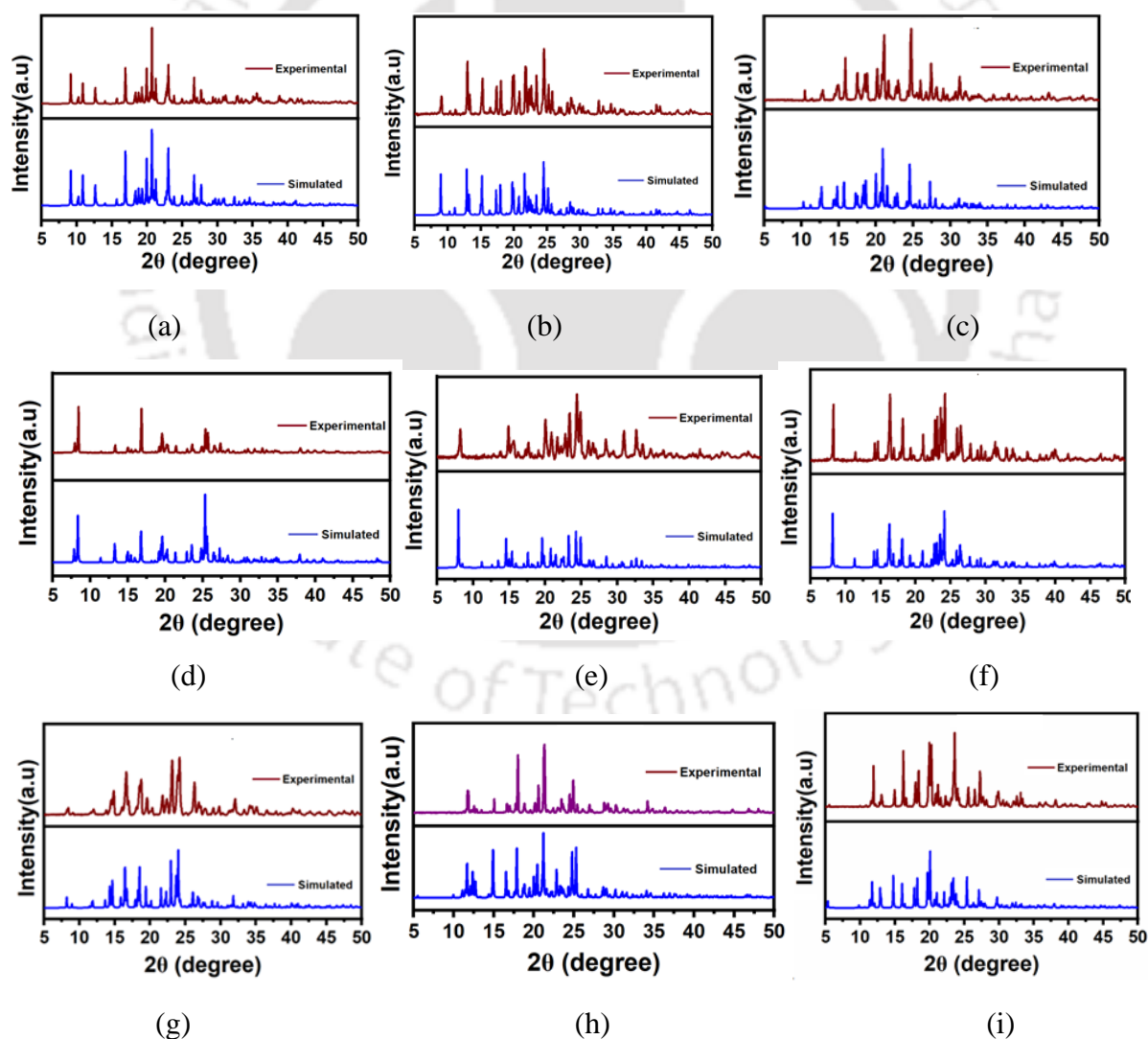
**(4.7.4):** The formation of **4.7.4** was similar to that of the formation of **4.7.2**, DMSO solvent was used instead of DMF. Yield = 68 %. IR (Neat,  $\text{cm}^{-1}$ ): 3323 (m), 2859 (w), 1635 (s), 1594 (s), 1578 (s), 1538 (s), 1506 (s), 1494 (s), 1436 (s), 1383 (s), 1329 (s), 1313 (s), 1248 (s), 1177 m), 1141 (s), 1115 (s), 1080 (s), 1032 (s), 1011 (s), 955 (s), 855 (s), 835 (s), 816 (m), 778 (m), 754 (m), 736 (s), 705 (s), 688 (s), 643 (s), 581 (s), 567 (s), 550 (s), 496 (s).  $^1\text{H-NMR}$

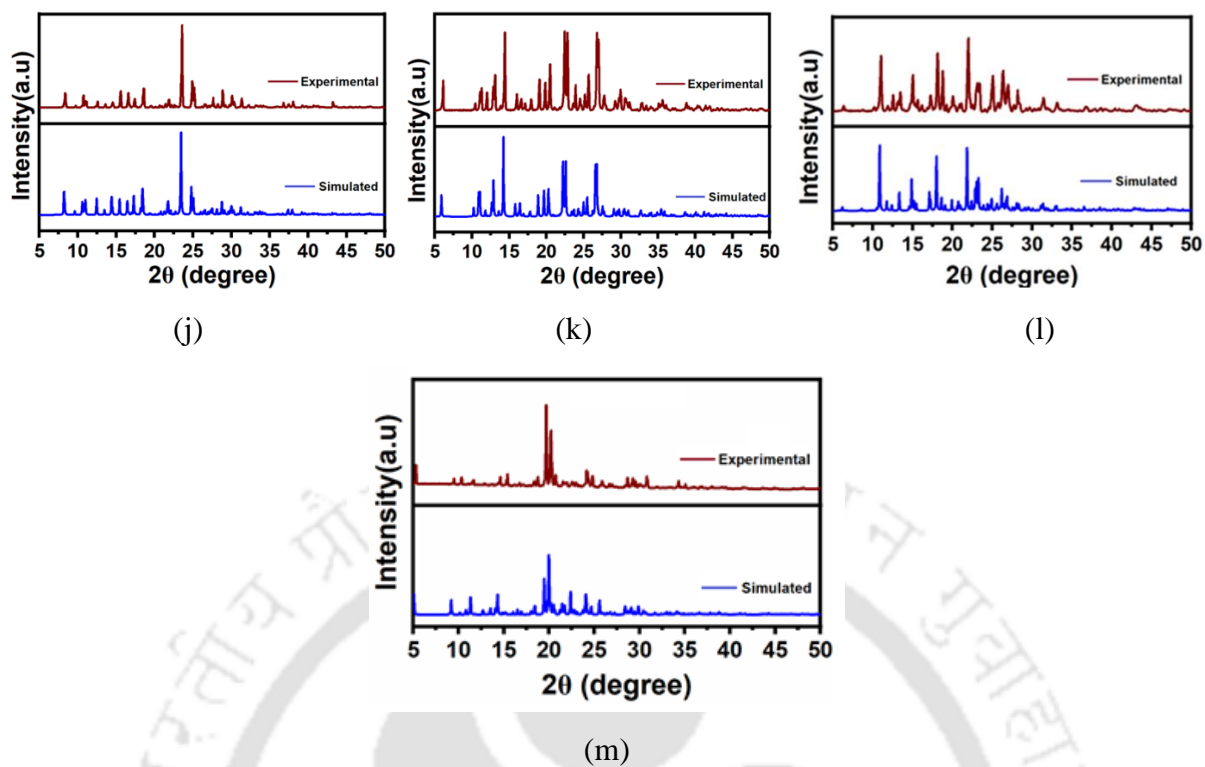
(600 MHz, DMSO- $d_6$ , ppm): 11.65 (s, 1H), 10.59 {s, N-H (1)}, 10.53 {s, N-H (2)}, 8.21 (d, J = 9 Hz, 2H), 7.96 (d, J = 8.4 Hz, 2H), 7.81 (d, J = 9.6 Hz, 2H) 7.69 (d, J = 9 Hz, 2H), 6.76 (s, 1H), 2.54 (s, 12H), 2.26 (s, 6H).  $^{13}\text{C}$  NMR (125 MHz, ppm, DMSO- $d_6$ ): 179.32, 156.17, 145.87, 142.65, 128.88, 124.46, 122.01, 121.93, 40.43.

### Typical method of crystallization:

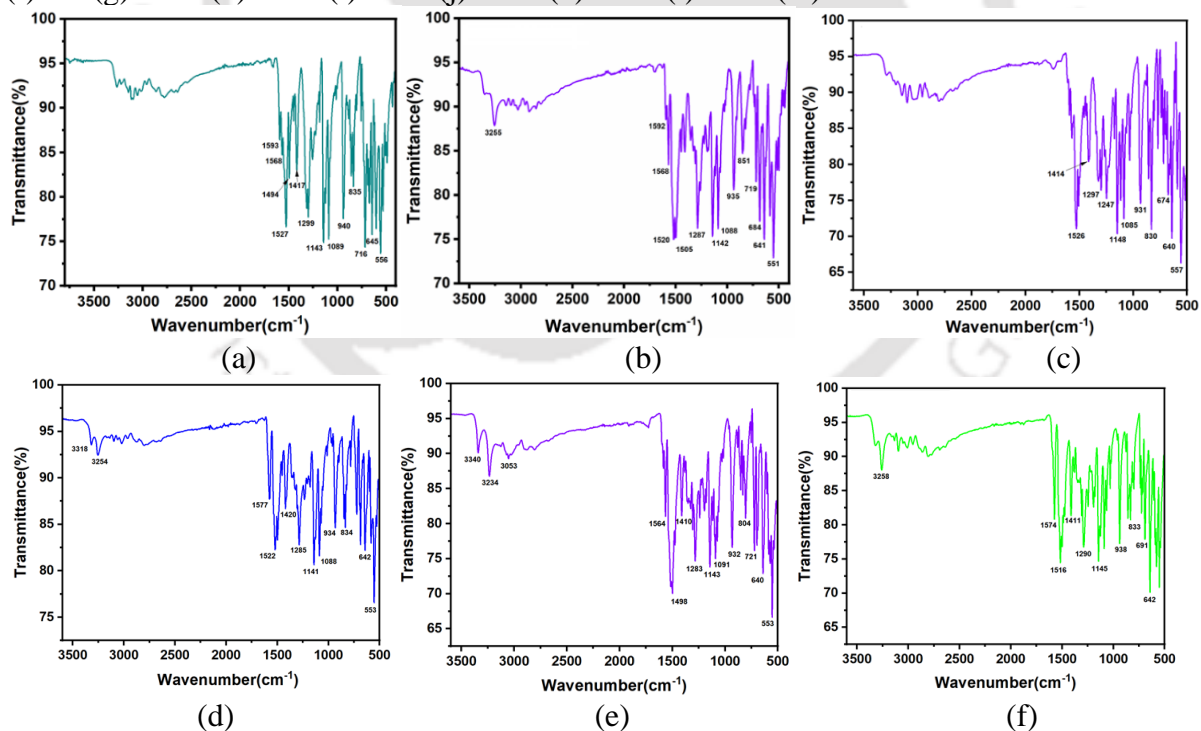
**4.1.1: 4.1** (100 mg) was dissolved in 10 ml of DMF and stirred at room temperature. The resulting solution was left for crystallization, after 6-7 days, crystals of **4.1.1** were collected by decanting the supernatant liquid, the yield of the crystals were 84% (84 mg).

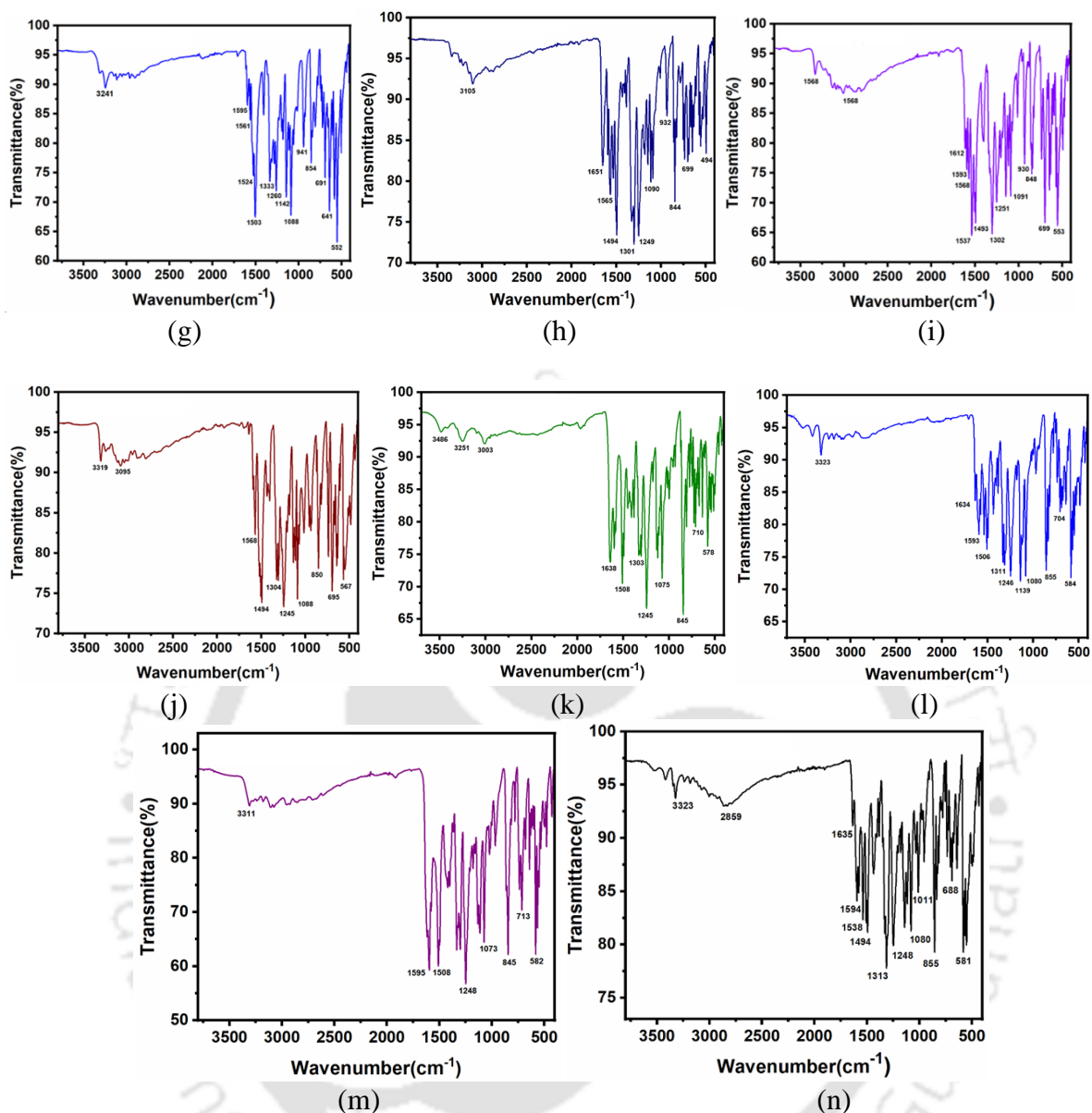
The rest of the crystals were obtained using the similar procedure and in each case the yield and purity were assessed by comparing the Powder X-ray Diffraction (PXRD) patterns with simulated spectra generated from the CIF file.





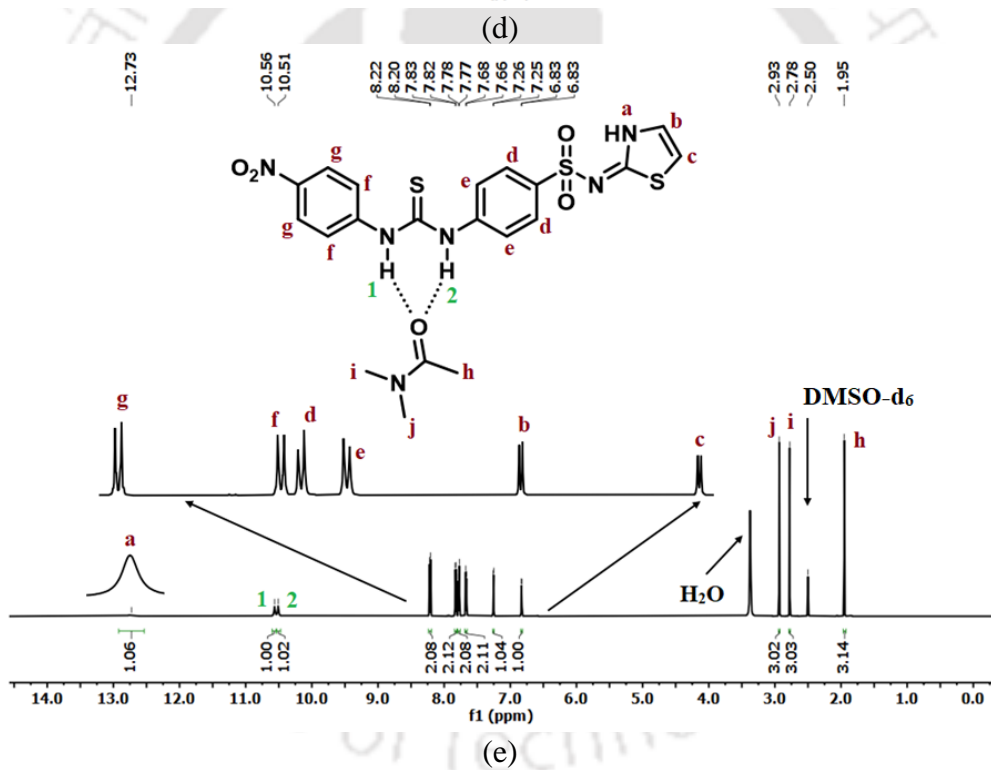
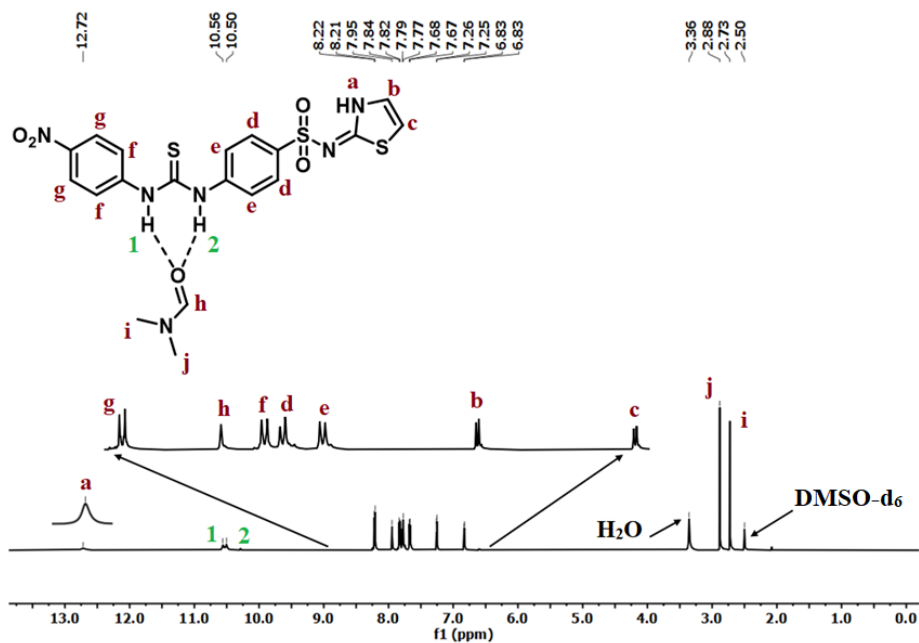
**Figure A4.1:** Powder X-ray diffraction patterns of the (a) 4.1.1 (b) 4.1.2 (c) 4.2 (d) 4.3 (e) 4.4 (f) 4.5 (g) 4.6.1 (h) 4.6.2 (i) 4.6.3 (j) 4.7.1 (k) 4.7.2 (l) 4.7.3 (m) 4.7.4

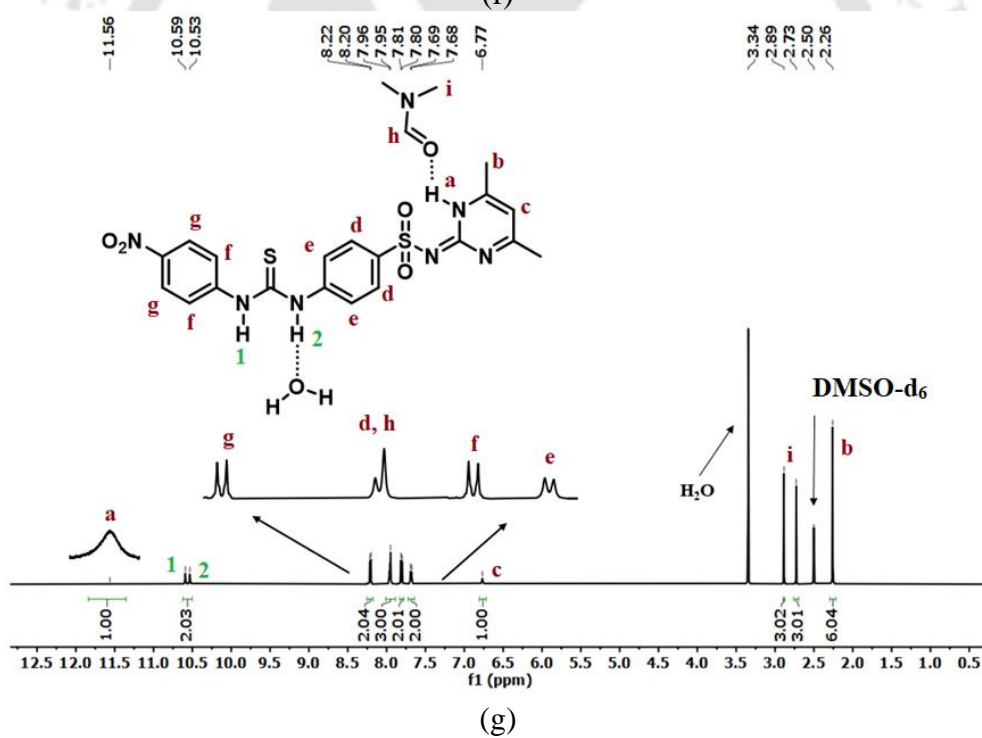
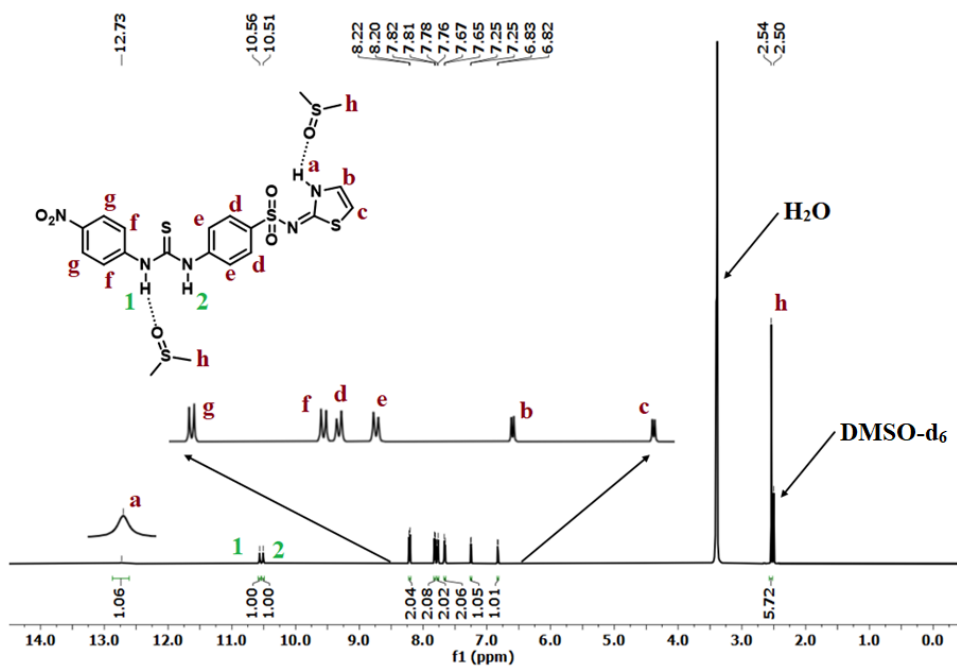


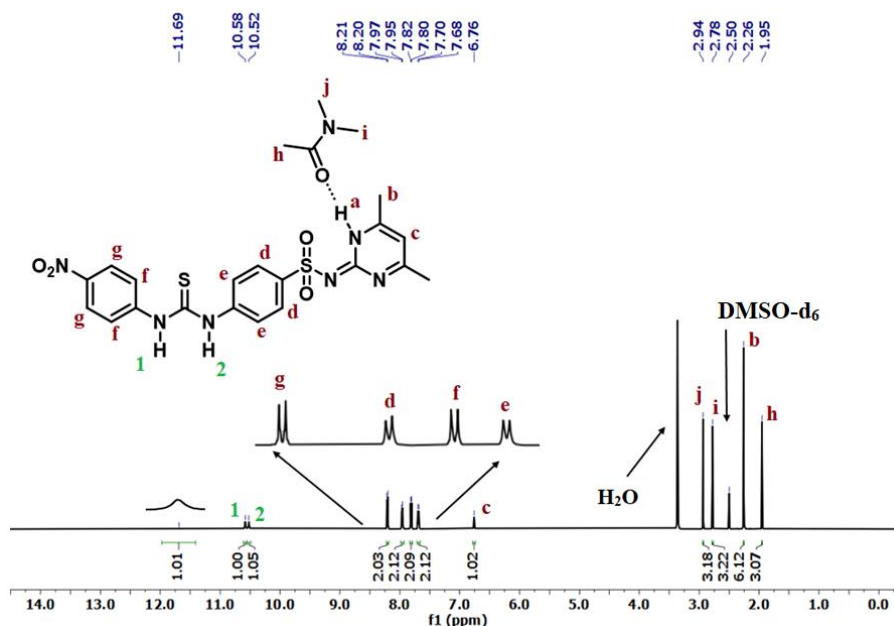


**Figure A4.2:** FT-IR spectrum (neat) of the (a) 4.1.1 (b) 4.1.2 (c) 4.2 (d) 4.3 (e) 4.4 (f) 4.5 (g) 4.6.1 (h) 4.6.2 (i) 4.6.3 (j) 4.6.4 (k) 4.7.1 (l) 4.7.2 (m) 4.7.3 (n) 4.7.4

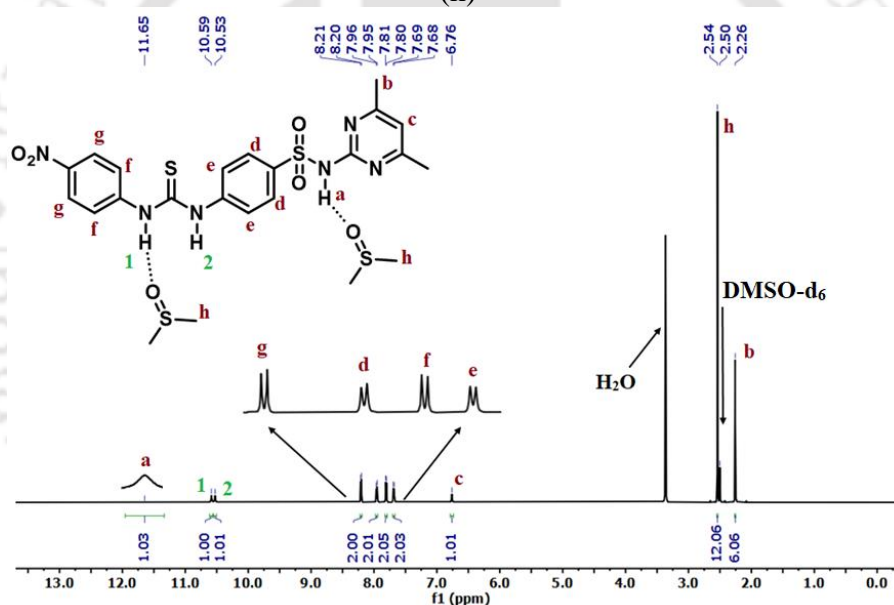






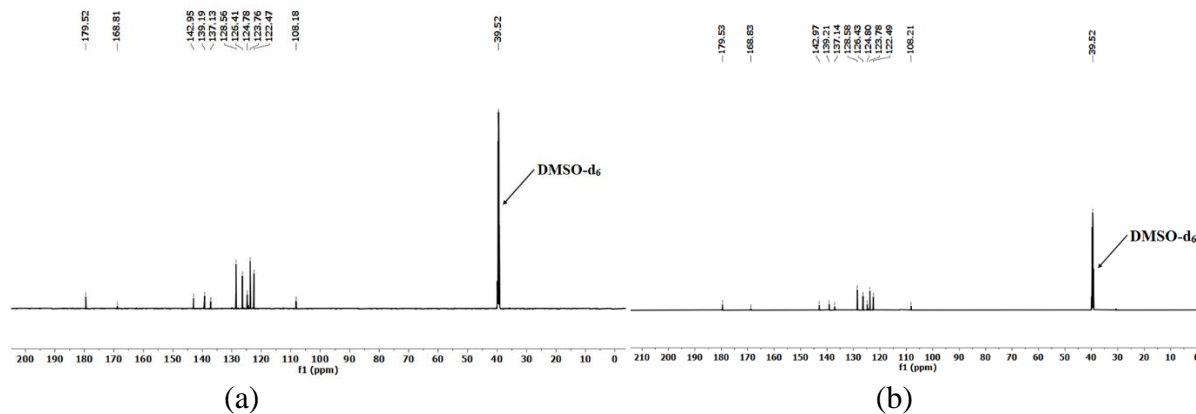


(h)



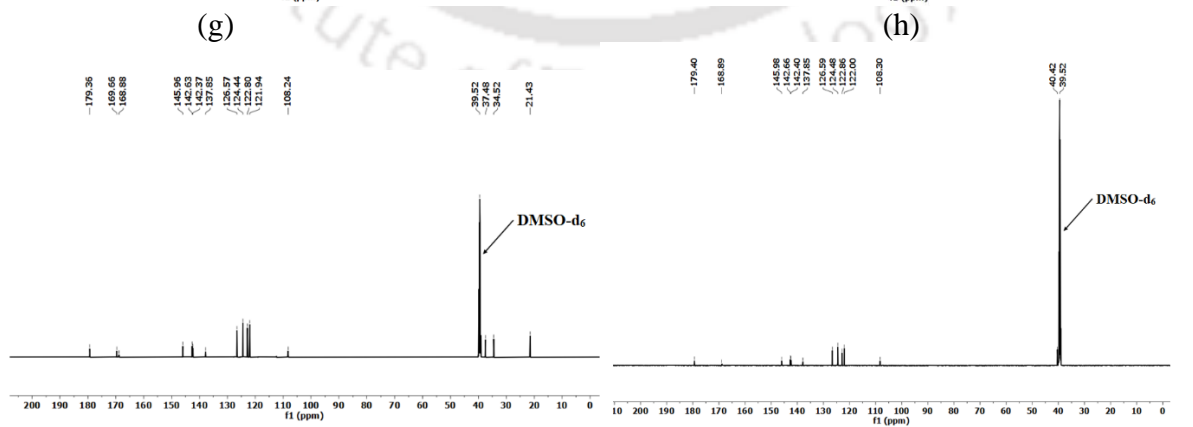
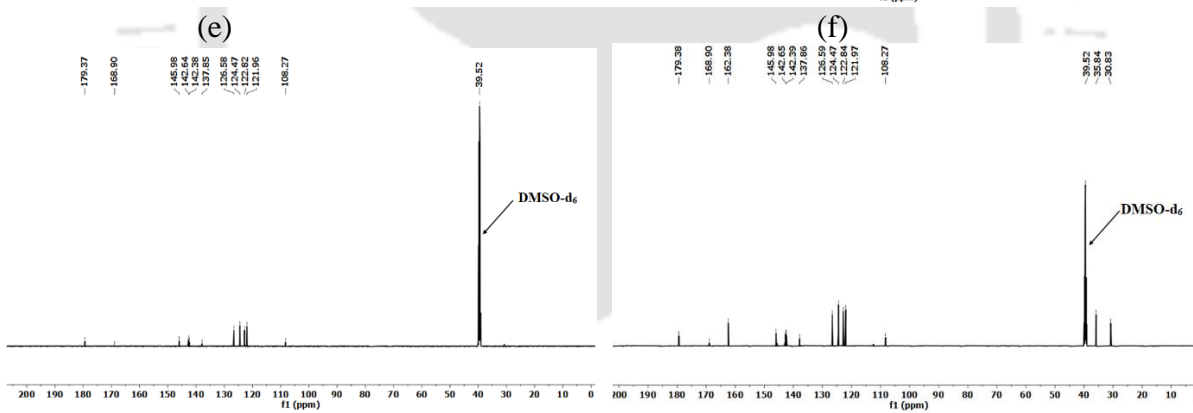
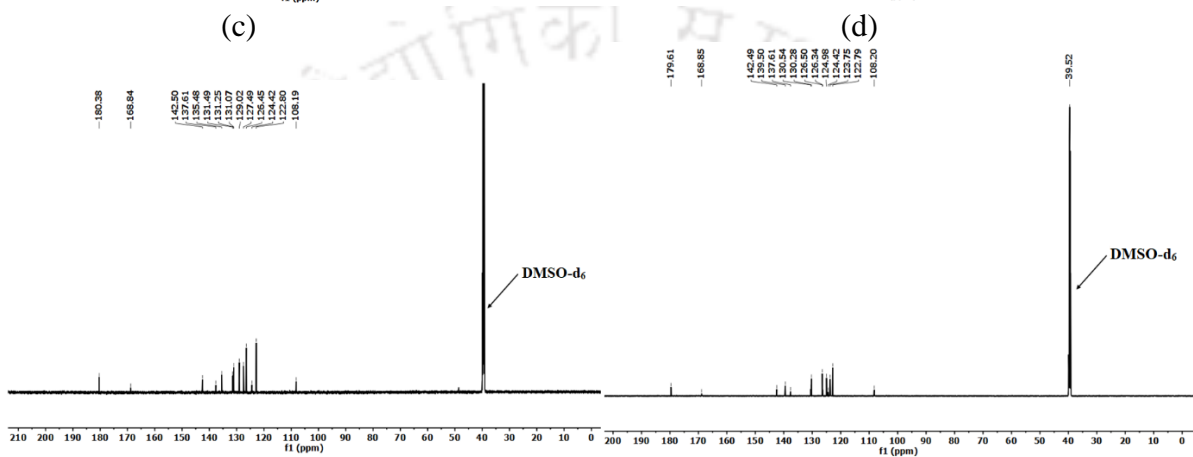
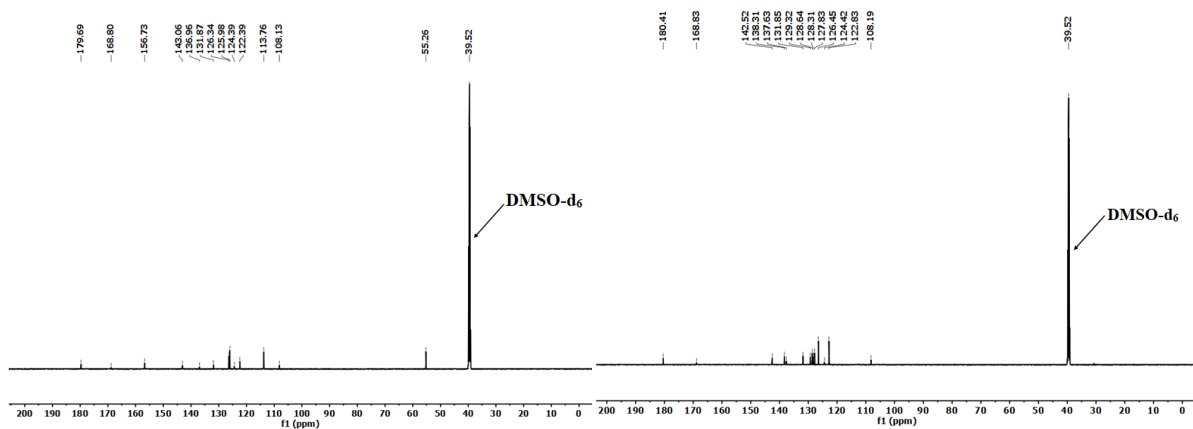
(i)

**Figure A4.3:** <sup>1</sup>H-NMR (DMSO-d<sub>6</sub>, 600 MHz) spectra of the (a) 4.1.1 (b) 4.4 (c) 4.5 (d) 4.6.2 (e) 4.6.3 (f) 4.6.4 (g) 4.7.1 (h) 4.7.3 (i) 4.7.4



(a)

(b)



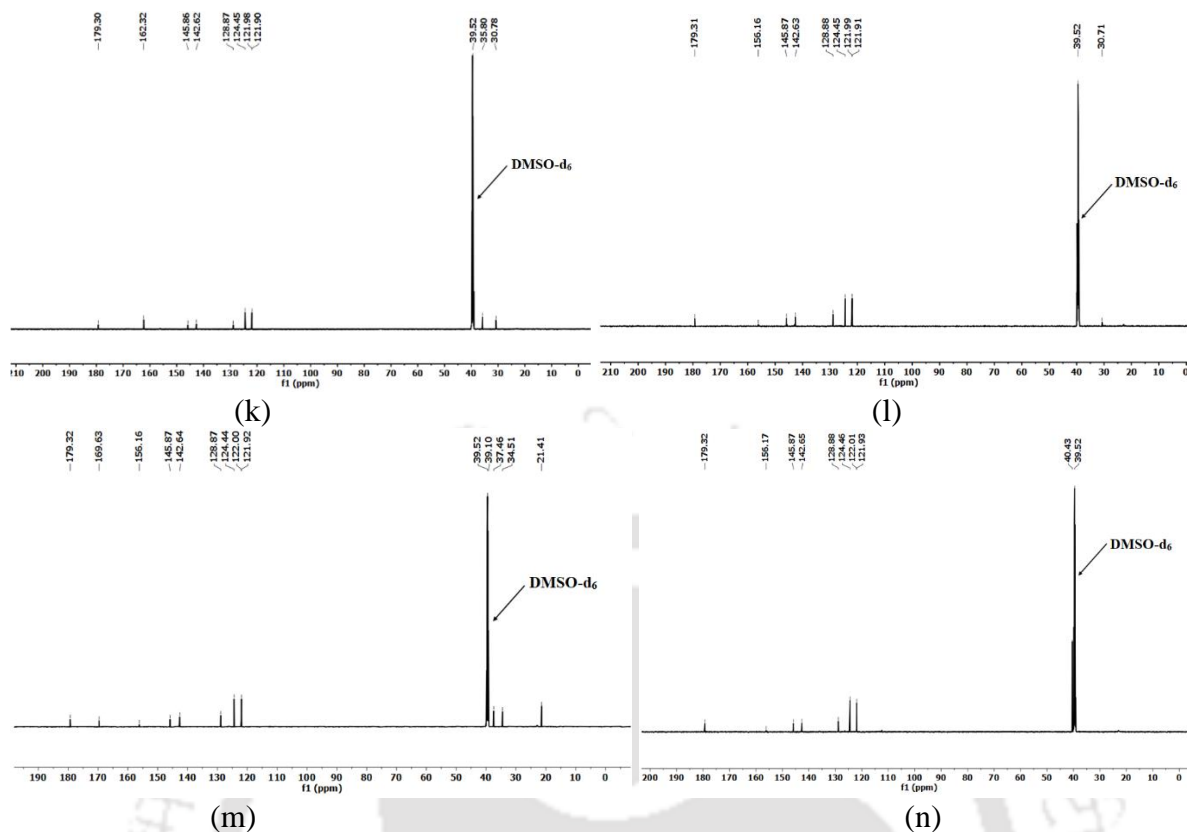
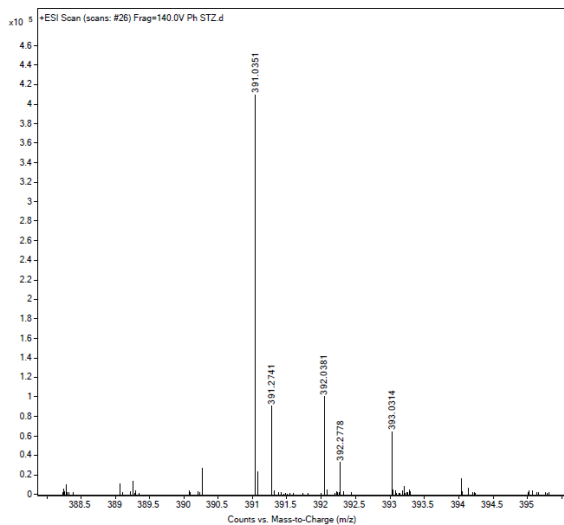
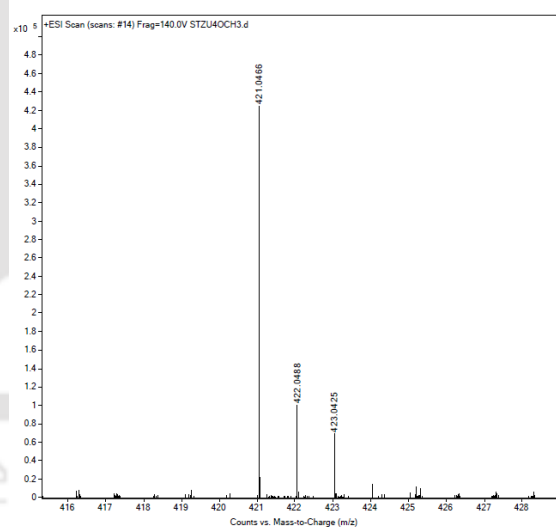


**Figure A4.4:**  $^{13}\text{C}$ -NMR (125 MHz,  $\text{DMSO-d}_6$ ) spectra of the (a) **4.1.1** (b) **4.1.2** (c) **4.2** (d) **4.3** (e) **4.4** (f) **4.5** (g) **4.6.1** (h) **4.6.2** (i) **4.6.3** (j) **4.6.4** (k) **4.7.1** (l) **4.7.2** (m) **4.7.3** (n) **4.7.4**



(a)



(b)

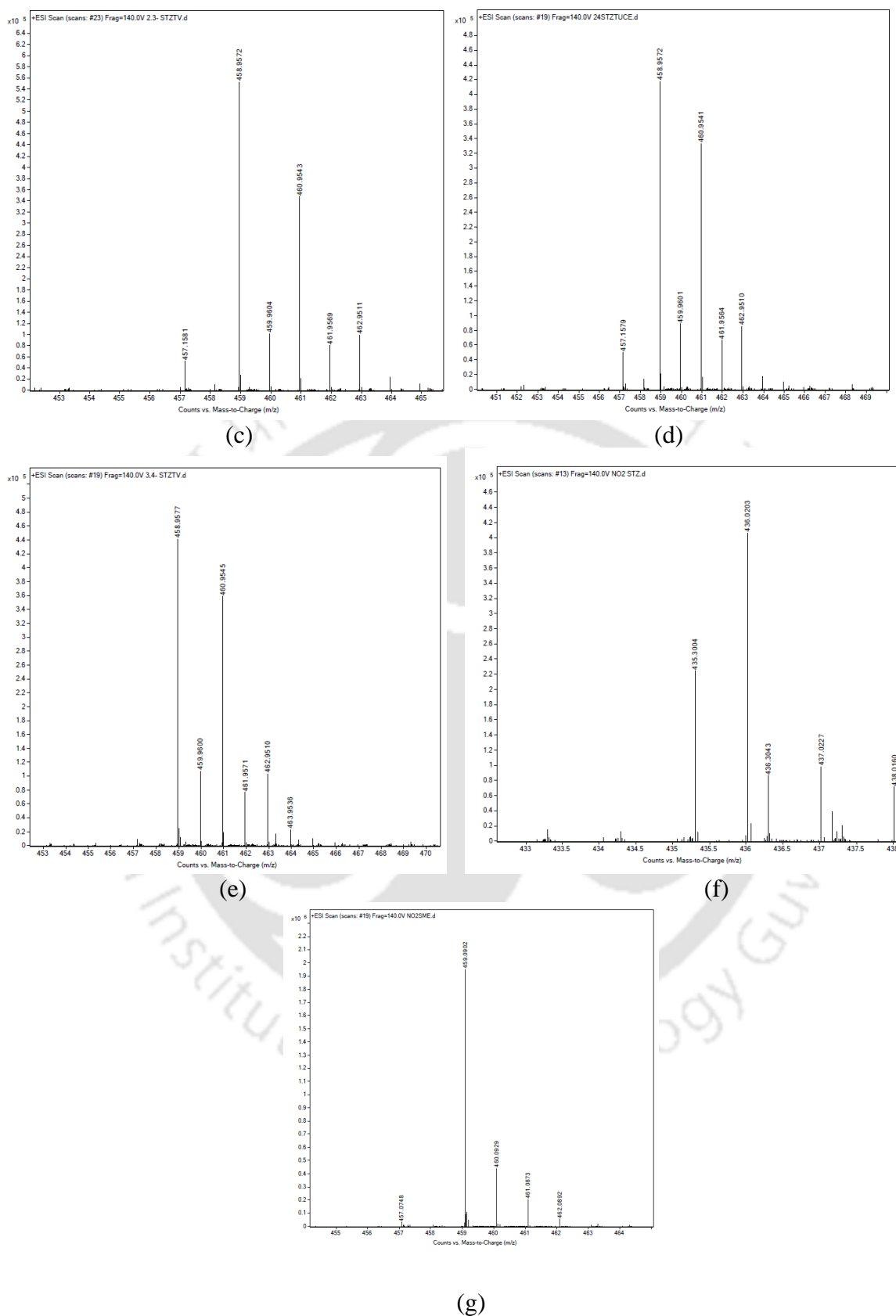
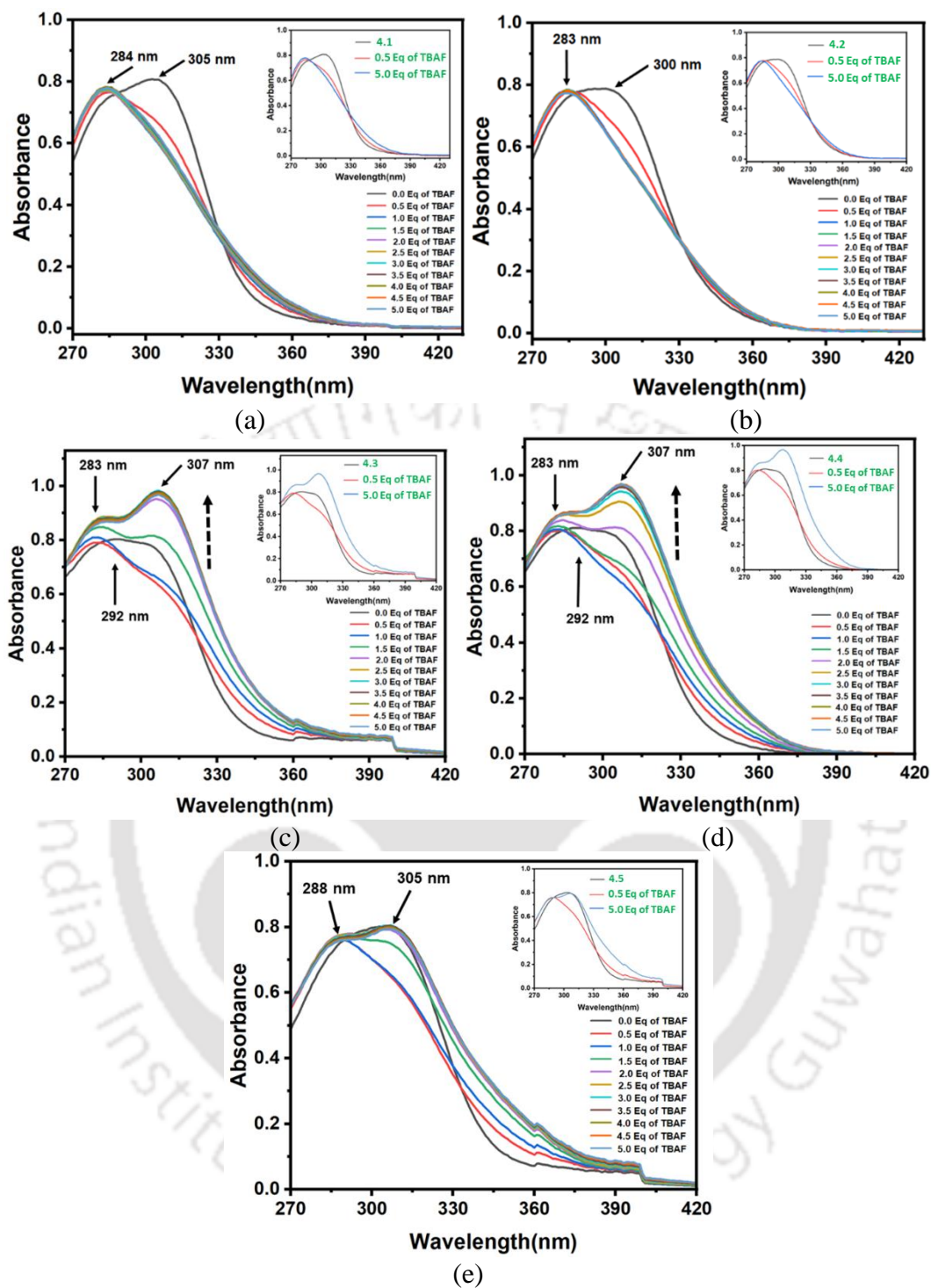
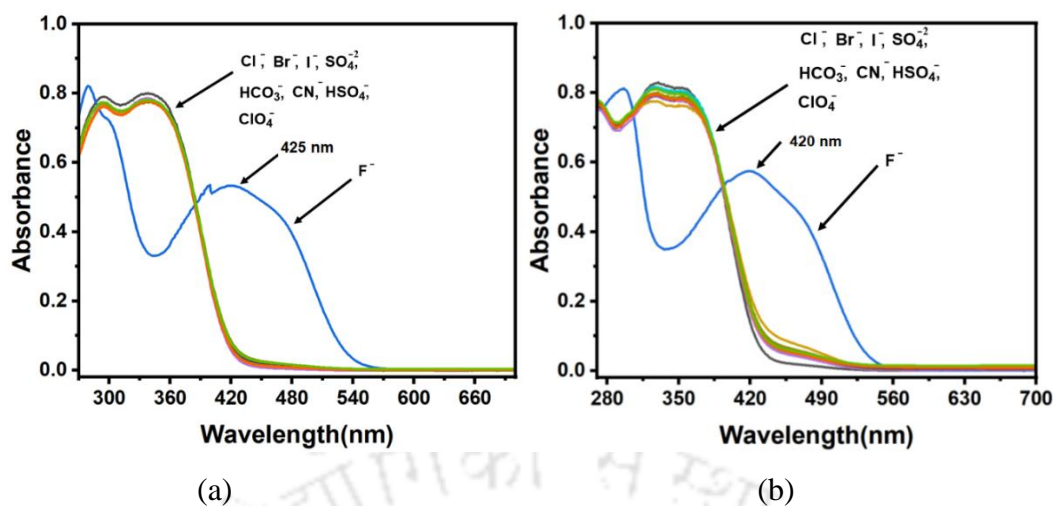


Figure A4.5: ESI-MS spectra of (a) 4.1 (b) 4.2 (c) 4.3 (d) 4.4 (e) 4.5 (f) 4.6 (g) 4.7



**Figure A4.6:** UV-visible titration of (a) **4.1** and (b) **4.2** (c) **4.3** (d) **4.4** and (e) **4.5** ( $3.34 \times 10^{-5}$  M) in dimethylsulfoxide solvent with tetra butyl ammonium fluoride (5 molar equivalents)



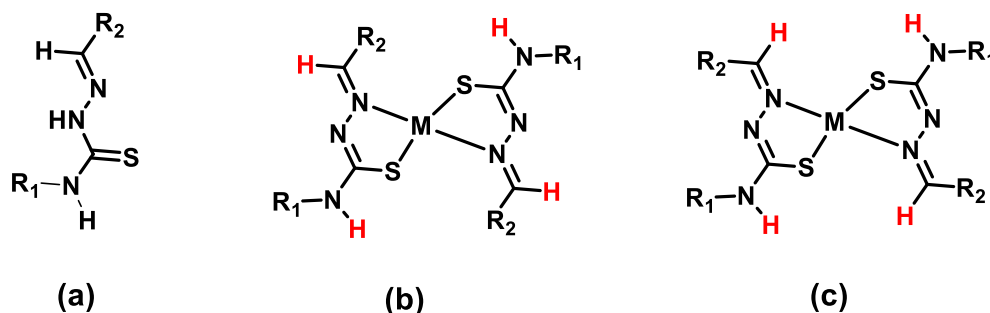
**Figure A4.7:** UV-visible titration of (a) **4.6** ( $3.34 \times 10^{-5}$  M) and (b) **4.7** ( $3.34 \times 10^{-5}$  M) in dimethylsulfoxide solvent with tetra butyl ammonium fluoride (5 molar equivalents).

## Chapter 5

### ***E or Z Isomers Arising from Geometries of Ligand in Mercury Complex of 2-(Anthracen-9-ylmethylene)-N-phenylhydrazine carbothioamide***

#### **5.1: Introduction**

From the last chapter, it is apparent that varying solvents, partner molecules and reaction conditions can prepare various crystalline forms of thiourea derivatives. We have expanded our research to hydrazine carbothioamide, a class of thiourea derivatives with structural features depicted in Fig. 5.1(a). This class of compounds find extensive use as ligands and, upon complex formation of four coordinated metal complexes, has the possibility to form two region-isomers, as illustrated in Fig. 5.1b and 1c. Hence, exploration of such isomers has an interest in understanding their individual contribution to a physical property. For example, when  $R_1$  and  $R_2$  are chosen from fluorophore units, such isomers will have characteristic emission properties. The comparative emission properties of such isomeric forms of metal complexes have not been studied, primarily because of their difficulties in synthesizing the individual isomer in pure form. Furthermore, the activation barrier among such forms is generally small; hence, from the literature, it is apparent that the energy barrier between two forms has to be above  $\sim 125$  kJ/mol to have either of the forms isolated in either of the forms or to have found in one particular form in solution. Hence, these types of conformers are categorized as conformation isomers.<sup>1-2</sup> The structural studies on such isomers have been reported since 1970,<sup>3</sup> and with the progress of time, there are more reports of conformational isomers of inorganic complexes.<sup>4-8</sup> In general, conformational polymorphs are the ones where the crystalline form of the same compound or cocrystals have different conformation in the solid state. Still, those cannot be distinguished in solution under ordinary conditions.<sup>9-10</sup> Conformation polymorphs of inorganic complexes are prepared by crystallization from different solvents.<sup>11-13</sup>



$R_1$  and  $R_2$  are different substituent or functional groups;  $M$  = metal ion

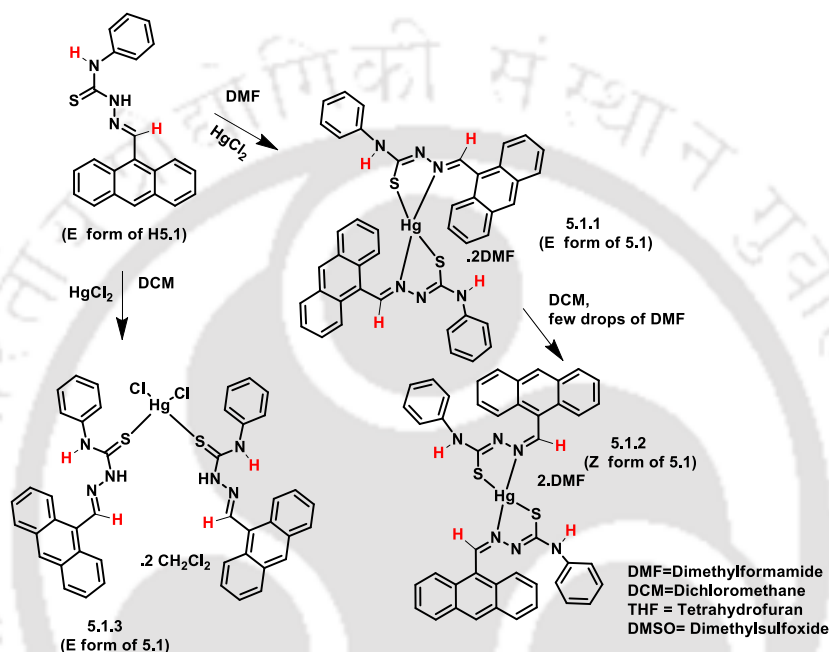
**Figure 5.1.** (a) Representation of a hydrazine carbothioamide-derived ligand and (b) E- and (c) Z-isomers of the bis-chelated of tetracoordinated metal complex (hydrogen atoms marked red are to distinguish the E and Z isomers)

In this study, we have chosen 2-(anthracen-9-ylmethylene)-N-phenylhydrazinecarbothioamide (**H5.1**; when  $R_1$  = phenyl and  $R_2$  = anthracenyl in the Scheme 5.2) as a ligand for the preparation of isomers of a mercury complex. The chosen ligand has an anthracenyl fluorescent functional group. In each of such proposed isomers, the ligands adopt  $\pi$ -conjugated structures and serve as model complexes for the study of the optical properties of such isomeric complexes. Alternatively, an ionic form (abbreviated **5.1**) of this, while serving as a ligand, adopts locked E or Z geometry through coordination to metal ions. The anthracenyl group and the phenyl ring are in *cis* or *trans* dispositions concerning each other across the C=N-N=C-N functional group, respectively. We have chosen to study the complexes of this ligand with the soft metal ion, namely, mercury complexes, due to the ability of analogous ligands to bind to Sulphur and nitrogen to provide desired chelates. Furthermore, there are also examples of isomers,<sup>14</sup> polymorphs,<sup>15</sup> and mercury complexes with different conformations of such ligands.<sup>16</sup> The choice of the ligand was also based on the extensive literature on thiosemicarbazide derivatives showing wide ranges of structures and the ability to form four coordinated complexes with structural variation.<sup>17-18</sup> Besides these, fluorescence modulation by such a ligand and the detection of mercury ions have attracted interest in environmental remediation.<sup>19-26</sup> Anthracene-based compounds show emissions that are dependent on the geometrical arrangement of the anthracenyl groups in the solid state.<sup>27-28</sup> The mercury ion is well known to either quench or enhance the fluorescence emission of a ligand.<sup>29-30</sup> The ligand **H5.1**<sup>31</sup> is a fluorescent molecule that was studied earlier as a probe for detecting mercury ions and preparing copper and zinc complexes.<sup>18</sup> So, searching for

isolating E- and Z-isomers has made it possible to obtain the two isomers in pure form with distinct characteristic signatures in solid state and solution.

### 5.2: Synthesis and characterization of mercury complexes (5.1.1-5.1.3)

The reactions of mercuric chloride with **H5.1** were dependent on the solvents and the reaction conditions. A bis-chelated neutral mercury (II) complex with **5.1** or neutral complex of mercury (II) with monodentate **H5.1** was formed under the reaction conditions as shown in Scheme 1.



**Scheme 5.1:** Preparation of the mercury complexes (5.1.1-5.1.3).

The reaction of **H5.1** with mercuric chloride in dichloromethane yielded the complex **5.1.3**. The reaction **H5.1** with mercuric chloride in methanol yielded a yellow precipitate. The precipitate upon recrystallization from a solution of the complex in dichloromethane solvent (pH of the solution = 5.3) provided the isomer **5.1.3**. The same reaction was then performed in dimethylformamide, and the pH of the solution was changed to 1.27. This reaction within 3 h yielded the E-isomer **5.1.1**. This suggested that the reaction in DMF released chloride ions from the metal salt while forming the complex by accepting the anionic form of the ligand (**5.1**), and in-situ generated hydrochloric acid made the solution acidic. When the precipitate of isomer **5.1.1** was dissolved in dichloromethane and DMF mixed solvent and crystallized, it yielded the Z-isomer **5.1.2**.

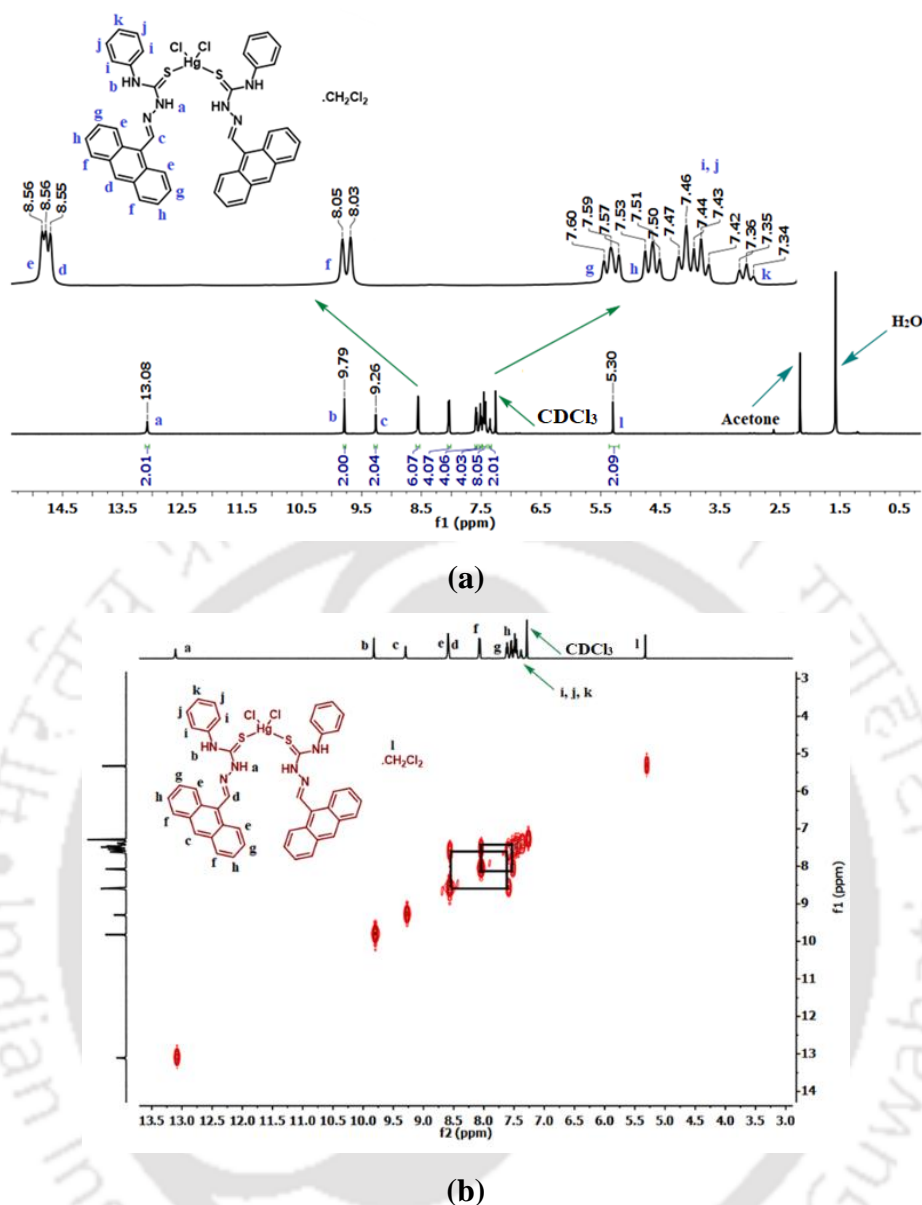


**Figure 5.2:** (a)  $^1\text{H}$ NMR and (b)  $^1\text{H}$ -2D-HOMOCOSY (600 MHz,  $\text{CDCl}_3$ ) spectra of the spectra of the **5.1.3**.

All three complexes were characterized by SC-XRD, PXRD, NMR, ESI-mass and elemental analysis. The ESI-mass spectrum is shown in Fig. A5.3 (appendix), while the PXRD of all the complexes is shown in Fig. A5.1 (appendix). The  $^1\text{H}$ NMR spectra of the mercury complex **5.1.3** was recorded in  $\text{CDCl}_3$  and is shown in Fig. 5.2. The phenyl protons labelled as *i*, *j* and *k* appeared at 7.47-7.46, 7.44-7.43 and 7.36-7.34 ppm respectively; while anthracenyl protons labelled as *d*, *e*, *f*, *g* and *h* appeared at 8.55, 8.56, 8.05-8.03, 7.60-7.57 and 7.53-7.50 ppm respectively. The thiourea N-H protons labelled as *a* and *b* appeared at 13.08 and 9.79 ppm. The proton H-C=N labelled as *c* appeared at 9.26 ppm. All these peaks were assigned by recording the  $^1\text{H}$ -2D-HOMOCOSY of the complex **5.1.3**. The spectra is

shown in Fig 5.2. The  $^1\text{H}$ NMR of two isomers of the neutral complex are discussed separately in the section dealing with the conversion of two isomers. The  $^{13}\text{C}$ NMR of all the mercury complexes is depicted in Fig. A5.2 (appendix).

The overlaid diagram of the IR spectra of the three mercury complexes is shown in Fig. 5.3. In the IR spectra, the N-H stretch of the **5.1.3** was observed at  $3250\text{ cm}^{-1}$ . There was a similar IR peak in the respective IR spectra of the isomers occurring at  $3254\text{ cm}^{-1}$ . The C=S and C=N stretches of the complex **5.1.3** were observed at  $1451\text{ cm}^{-1}$  and  $1624\text{ cm}^{-1}$ , respectively. These stretches were found at  $1430\text{ cm}^{-1}$  and  $1662\text{ cm}^{-1}$  for the two isomers (**5.1.1** and **5.1.2**). The powder XRD of each complex was determined, and phase purity was ascertained by comparing the powder X-ray diffraction (PXRD) generated from the respective crystallographic information file. For this purpose, the PXRD pattern of the recrystallized samples of **5.1.1** and **5.1.2** was recorded independently and compared with crude products obtained under different conditions (Fig. A5.1)

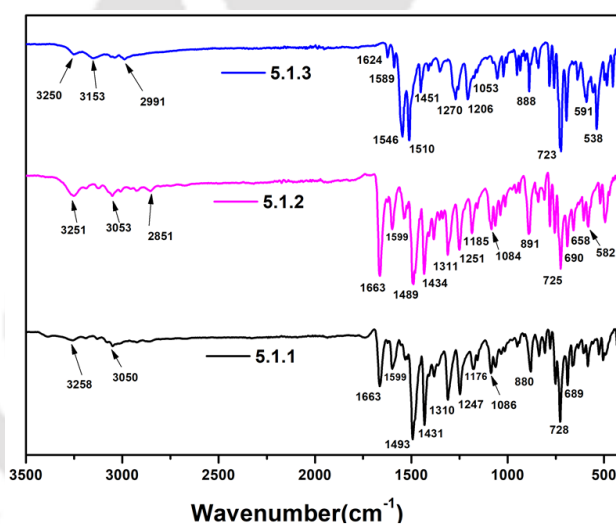
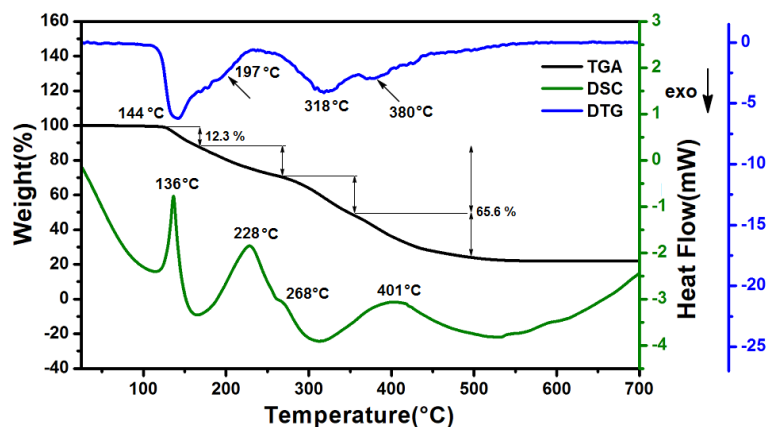
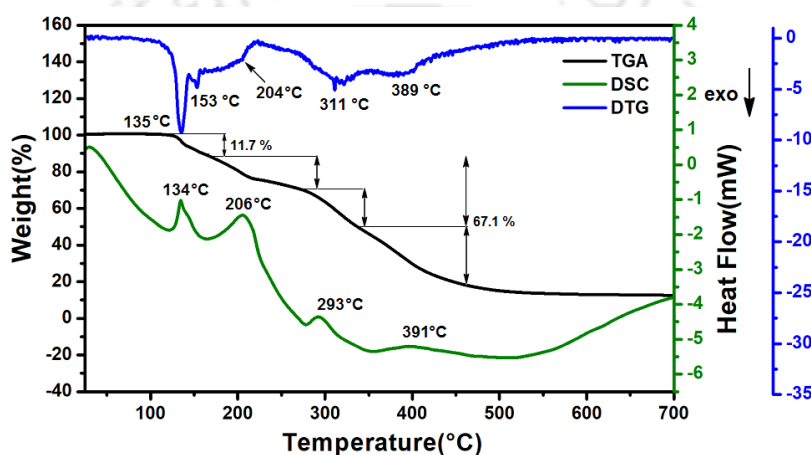


**Figure 5.3:** Overlaid FT-IR spectra of the complexes **5.1.1-5.1.3**

The thermogravimetry plots of the two isomers recorded between room temperature and  $700\text{ }^\circ\text{C}$  are shown in Fig. 5.4. Each thermogram showed four weight loss steps. In the thermogram, the first step was due to weight loss from the release of the DMF molecules, whereas the other three steps were due to weight losses by thermal degradation of the ligand **5.1** in the complex. The weight losses from **5.1.1** were observed at  $144\text{ }^\circ\text{C}$ ,  $197\text{ }^\circ\text{C}$ ,  $318\text{ }^\circ\text{C}$ , and  $380\text{ }^\circ\text{C}$ ; for **5.1.2** these weight losses were at  $135\text{ }^\circ\text{C}$ ,  $153\text{ }^\circ\text{C}$ ,  $204\text{ }^\circ\text{C}$ ,  $311\text{ }^\circ\text{C}$ , and at  $389\text{ }^\circ\text{C}$ . These weight loss processes were also reflected in the differential scanning calorimetry as there were four endothermic peaks in the DSC of both the isomers, as depicted in Fig. 5.4.



(a)



(b)

**Figure 5.4:** TG-DSC and DTG plots of the (a) **5.1.1**. (b) **5.1.2** (heating rate 10°C/min under an argon atmosphere).

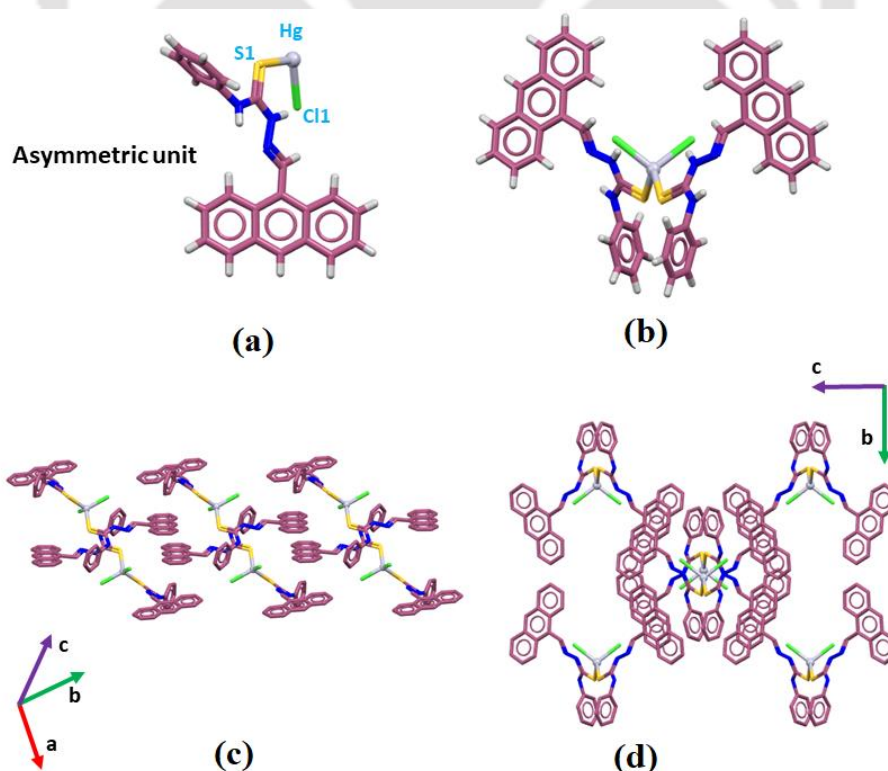
X-ray photoelectron spectroscopy (XPS) is a valuable tool to discern the oxidation state and the environment around mercury ions.<sup>32-33</sup> Accordingly, the photo-electro spectra of each complex were recorded. The ionization potentials of the complexes determined by XPS are listed in Table 5.1. The two isomers (**5.1.1** and **5.1.2**) could not be distinguished from their XPS. Both the isomers of the complex showed the  $4f$   $\text{Hg}_{7/2}$  and  $4f$   $\text{Hg}_{5/2}$  ionization as two peaks between 101.13 eV and 105.26 eV. On the other hand, complex **5.1.3** had a clear distinction in PES, showing the characteristic ionization peaks for chloride. In this complex, the  $2p\text{Cl}_{1/2}$  and  $2p\text{Cl}_{3/2}$  ionization peaks were observed at 198.18 and 199.73 eV.  $2p\text{S}_{1/2}$  and  $2p\text{S}_{3/2}$  ionizations of the complex appeared in the region of 162.7 eV to 164.2 eV.

**Table 5.1:** Binding energy from X-ray photoelectron spectroscopy of the **5.1.1**, **5.1.2**, and **5.1.3**

Mercury complexes	Binding Energy (eV)					
	C1s	N1s	O1s	S2p	Cl2p	Hg4f
<b>5.1.1</b>	284.87	398.60, 399.91	532.65	162.77, 163.97		101.23, 105.26
<b>5.1.2</b>	284.87	398.74, 400.01	532.56	162.84, 164.14		101.25, 105.28
<b>5.1.3</b>	284.80, 288.35	400.25		162.9, 164.2	198.18, 199.73	101.13, 105.17

**5.3: Structural aspects of the mercury complexes (5.1.1-5.1.3)**

The crystals of the two isomers **5.1.1** and **5.1.2** belonged to  $P 2_1/n$  and  $P \bar{1}$  space groups, respectively, and their crystal volume and crystal densities were  $4707.4(5) \text{ \AA}^3$ ,  $1.490 \text{ g cm}^{-3}$ ; and  $2354(3) \text{ \AA}^3$ ,  $1.489 \text{ g cm}^{-3}$  respectively. The crystals of **5.1.3** belonged to  $I 2/a$  space group and its crystal volume and density were  $4272.56(17) \text{ \AA}^3$  and  $1.527 \text{ g cm}^{-3}$  respectively. The crystal structure of complex **5.1.3** had dichloromethane as the solvent of crystallization. This solvent of crystallization molecule had a severe crystallographic disorder. So, the crystal structure of **5.1.3** was refined by squeezing the dichloromethane part. However, the identity of the complex was ascertained by elemental analysis and other spectral tools.

**Figure 5.5:** (a) Asymmetric unit and (b) structure of the complex **5.1.3** and (c), (d) its packing diagram.

The complex **5.1.3** was a four-coordinate complex. In the crystal structure, the asymmetric unit had a coordinated mercury ion with chloride and ligand **H5.1** (Fig. 5.5a). It had two ligands and two chlorides (Fig. 5.5b) coordinated to a mercury ion. Mercury ions formed mono-nuclear or poly-nuclear complexes with different geometries depending on the type of ligands.<sup>17,34</sup> A four-coordinate metal complex may adopt a tetrahedral and square planar structure or see-saw geometry. Thus, to clearly ascertain the geometry of the complex, the  $\tau_4$  parameter<sup>35</sup> of the complex was calculated using the formula, and it was found to be 0.967, which suggested a geometry around the mercury ion, very close to a tetrahedron. The two Hg-S distances in the complex were equal to 2.49 Å; the Hg-Cl bonds were 2.52 Å. The S-Hg-S, S-Hg-Cl, and Cl-Hg-Cl bond angles differed from the ideal tetrahedron 109.5° between - 4.1 ° to - 0.6 ° (Table 5.2).

**Table 5.2:** Metal-ligand bond distances, bond angles, and  $\tau_4$  of the complex **5.1.1**, **5.1.2**, and **5.1.3**.

Complex	Bond distance (Å)		Bond angles(°)			$\tau_4$ (Geometry)
	Hg-X	Hg-S	X-Hg-X	S-Hg-S	X-Hg-S	
<b>5.1.1</b>	2.45, 2.48 <sup>a</sup>	2.36, 2.37	91.9 <sup>a</sup>	159.2	77.2, 76.9 <sup>a</sup>	0.77 (see-saw, C <sub>2v</sub> )
<b>5.1.2</b>	2.41, 2.44 <sup>a</sup>	2.37, 2.37	106.8 <sup>a</sup>	162.9	77.5, 78.2 <sup>a</sup>	0.64 (see-saw, C <sub>2v</sub> )
<b>5.1.3</b>	2, 52, 2.52 <sup>b</sup>	2.49, 2.49	104.6 <sup>b</sup>	105.3	108.9 <sup>b</sup>	0.97 (Td)
<sup>a</sup> , X = N; <sup>b</sup> , X = Cl						

The structures of the E- and Z- isomers were comprised of two chelating **5.1** ligands bound to one four-coordinate mercury ion. The crystal structures have revealed that both the isomers had a similar coordination environment around the mercury (Fig.5.6a and 5.6b) ion. The respective Hg-N and Hg-S bond distances and the S-Hg-S, N-Hg-S, and N-Hg-N are listed in Table 5.2. The Hg-S bonds in the two cases were similar, but there were differences in the Hg-N bond distances. The Hg-N bonds of **5.1.2** were slightly shorter (0.04 Å to 0.05 Å) from the isomer **5.1.1**. There were large differences in the orientations of the anthracenyl and phenyl groups in the isomers, as depicted in the overlaid geometry of the two isomers in Fig. 5.6c.

The differences in the orientations of the aromatic groups of the two isomers were revealed by drawing two independent planes, one containing the anthracenyl group and the other containing the phenyl group of the same ligand of the two isomers.

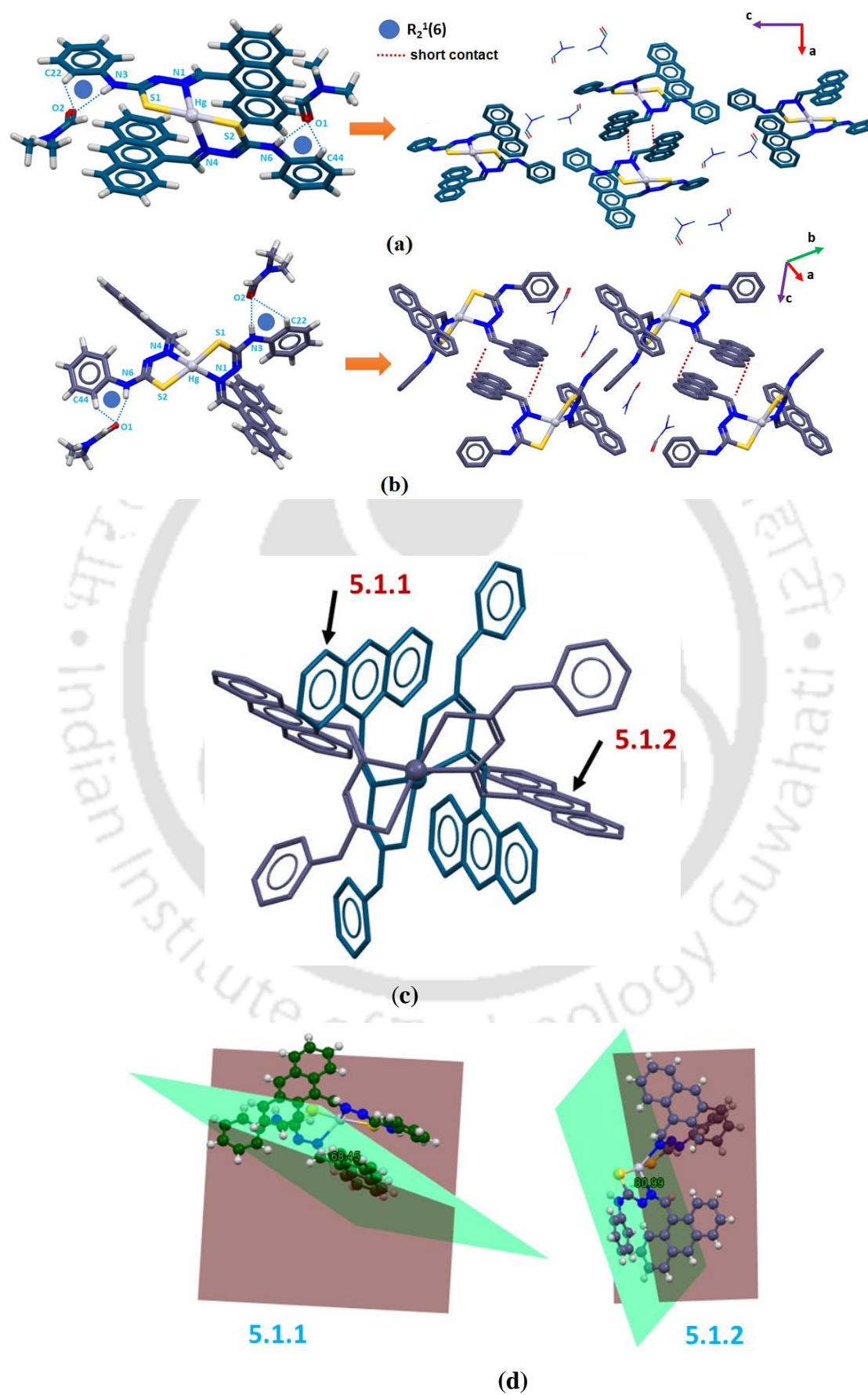


**Figure 5.6:** The structures and packing diagram of the isomers (a) **5.1.1** and (b) **5.1.2**. (c) Overlaid structures of the two isomers (hydrogen atoms are omitted for clarity). d) The angles between the planes containing the anthryl and the phenyl rings of the same ligand in the isomers **5.1.1** and **5.1.2**.

The angles between these planes are illustrated in Fig. 5.6d. The isomer **5.1.1** had a  $68.45^\circ$  angle between such planes, whereas, in **5.1.2**, it was  $80.89^\circ$ . For comparison, the angles between similar planes were evaluated for the **H5.1** and **5.1.3**, which were  $84.61^\circ$  and  $79.02^\circ$ , respectively. So, in the chloride complex, there was a change of  $5.59^\circ$  on the interplanar angle as compared to that of the ligand, whereas the change in the angle in the **5.1.2** was  $3.72^\circ$ , but the same change in the angle in the isomer **5.1.1** was  $-16.16^\circ$ . Thus, the orientations of phenyl and the anthracenyl groups of the ligand had changed drastically in the isomer **5.1.1**.

As in the solution, the E isomer was transformed to the Z isomer, and to explain this propensity for the irreversible transformation of the isomer **5.1.1**, a DFT calculation was carried out by optimising the energy of each isomer as shown in Fig. 5.7. The total optimized energy of Z and E isomers were  $-3470.925$  and  $-3470.919$  Hartrees respectively, which

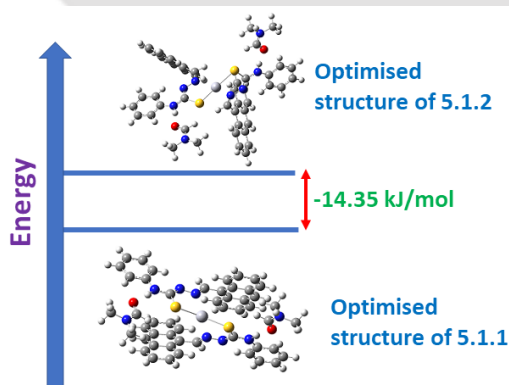


**Figure 5.7:** Energy difference of the optimised structure of **5.1.1** and **5.1.2**, calculated by B3LYP/SDD

showed **5.1.1** was more stable than **5.1.2** by  $14.35$  Kcal/mol. The difference in stability of the *cis* and *trans* isomers was attributed to the steric requirements. The electrostatic potential surfaces of the two isomers are depicted in Fig. 5.8. The decreasing orders of electrostatic potential are represented by various colours as follows: Red < Orange < Yellow < Green < Blue < Green. The colour code ranges between  $-5.044 e^{-2}$  to  $5.044 e^{-2}$  in the **5.1.1** and  $-4.936 e^{-2}$  to  $4.936 e^{-2}$  in the **5.1.2**.

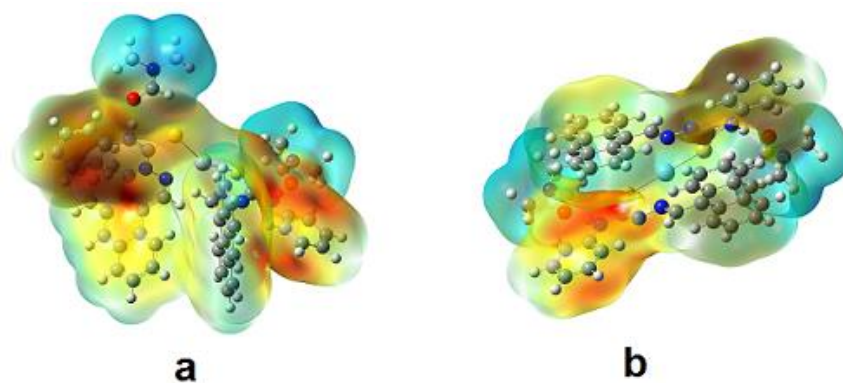


**Figure 5.8:** Electrostatic potential surfaces of (a) **5.1.1** and (b) **5.1.2**.

Hirshfeld analysis was performed for the analysis of hydrogen bonds. The  $d_{\text{norm}}$  and 2D-fingerprint plot of the two isomers (**5.1.1** and **5.1.3**) is given in Figure 5.9. The  $d_{\text{norm}}$  value of isomer **5.1.1** is in the range of -0.56 to 1.48, while for the other isomer **5.1.2**, the value is in the range of -0.57 to 1.62.

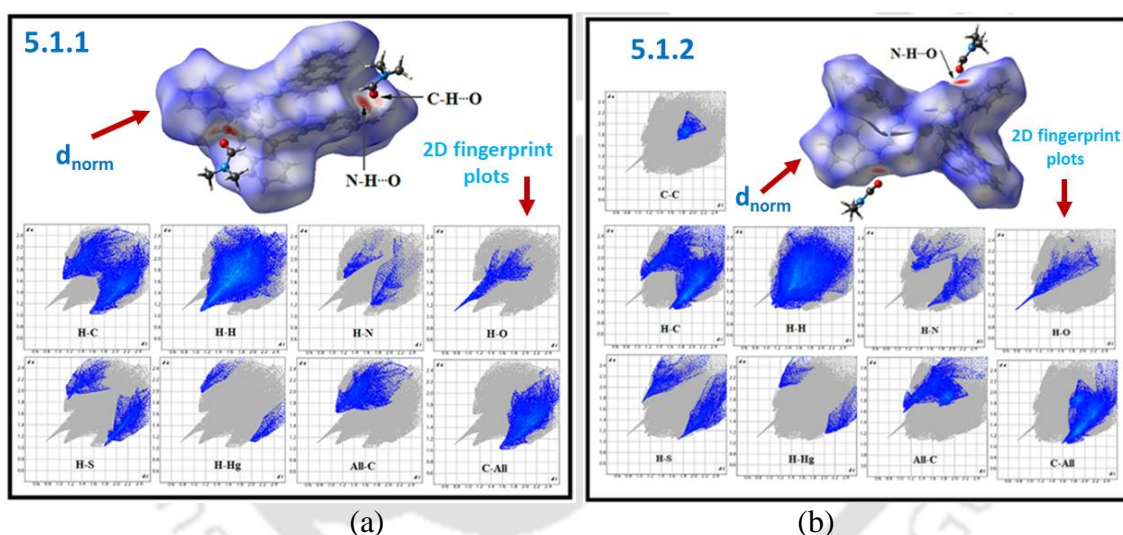


**Figure 5.9:** 2D fingerprint plots of the H...C, H...H, H...O, H...N, H...Hg, C...C, H...S (including reciprocal contacts), All...C and C...All interactions of (a) **5.1.1** and (b) **5.1.2**.

#### 5.4: Conversion of isomers studied by $^1\text{H}$ NMR spectroscopy in solution

The  $^1\text{H}$ NMR spectra of the isomers and **5.1.3** were examined under different conditions to probe the possible conversions of the complex to any of the isomers in the solution. The chemical shift of the protons in the complex was solvent-dependent, and the peaks were shifted down-field as compared to that of the free ligand. This is attributed to the diamagnetic effect of the mercury ion, contributing to the diamagnetic shielding.

The 2D- $^1\text{H}$ -HOMO-COSY NMR spectra of the isomers were also recorded to confirm the assignments of the peaks (Fig. 5.10). The assignment of each peak in the  $^1\text{H}$ NMR spectra of

the two isomers (**5.1.1** and **5.1.2**) recorded in  $\text{CDCl}_3$  are shown in the overlaid diagram (Fig. 5.11)

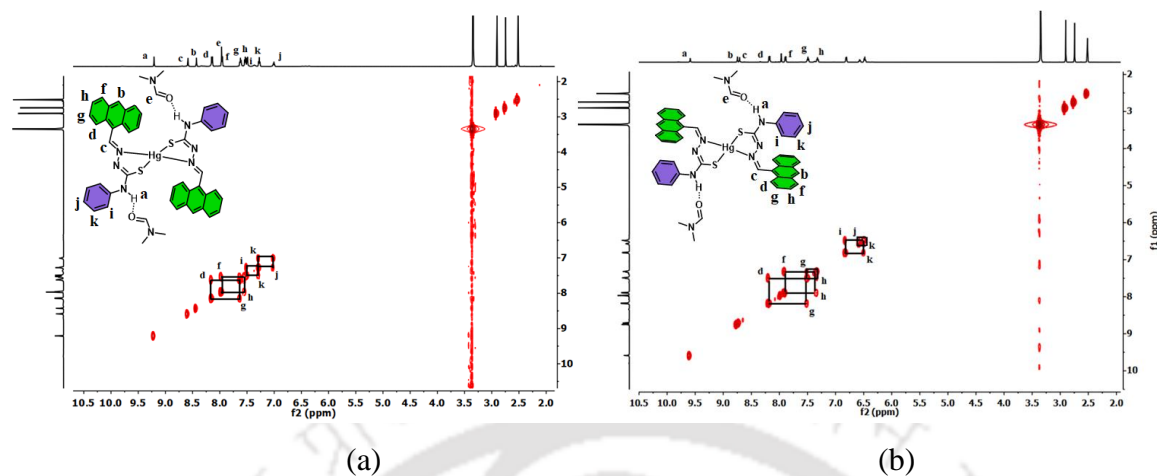


**Figure 5.10:**  $^1\text{H}$ -2D-HOMOCOSY (600 MHz,  $\text{DMSO-d}_6$ ) spectrum of the (a) **5.1.1** and (b) **5.1.2**

The two isomers' chemical shifts differed in their respective chemical shift positions, especially the  $\text{H-C=N}$  peak. This peak appeared as a singlet at 9.15 ppm and 8.68 ppm in  $\text{CDCl}_3$ , respectively, for **5.1.1** and **5.1.2** (peaks marked with blue star Fig. 5.11). The aromatic peak marked as *d* of the anthracenyl group of **5.1.1** in  $\text{CDCl}_3$  appeared at 8.22 ppm, and for **5.1.2**, it appeared at 8.52 ppm. A clear distinction between the  $\text{N-H}$  chemical shifts of the complex **5.1.3** and the isomeric complexes with the corresponding chemical shift of the free ligand **H5.1** was observed. The respective  $\text{N-H}$  protons of **5.1.1** and **5.1.2** appeared at 5.87 ppm and 6.86 ppm in  $\text{CDCl}_3$ . Thus, the chemical shift of the proton of the phenyl  $\text{N-H}$  of **5.1.1** was more magnetically shielded than the corresponding proton in **5.1.2**, which showed that the acidity of this proton was less in isomer **5.1.1**. Alternatively, a higher negative character ( $\delta^-$ ) on this nitrogen atom was observed in the isomer **5.1.2**. This was a clear difference between the *Z*-isomer and the *E*-isomer.

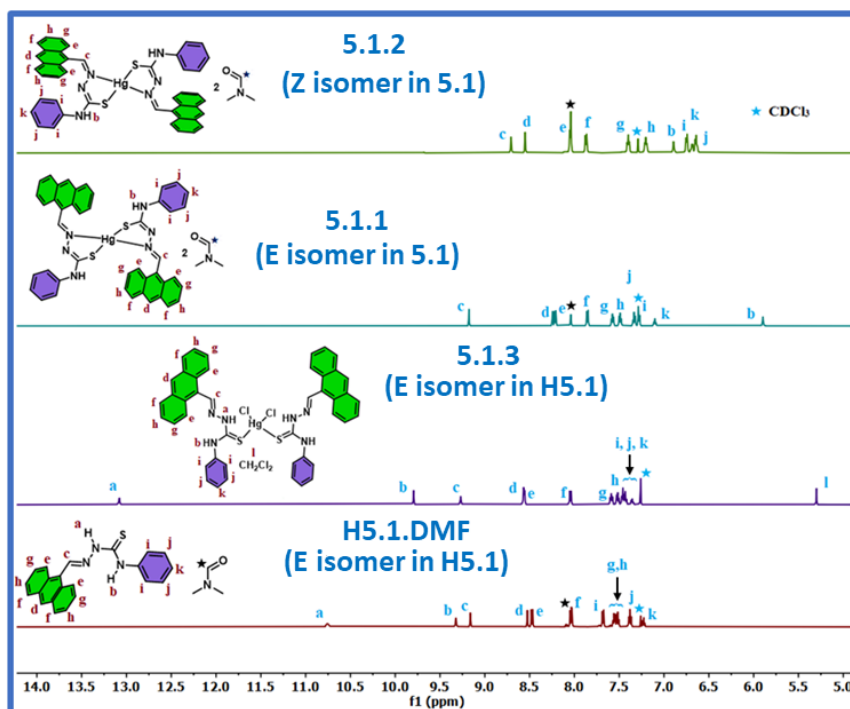


**Figure 5.11:** The  $^1\text{H}$ NMR ( $\text{CDCl}_3$ , 600 MHz) of the **H5.1.DMF**, **5.1.1**, **5.1.2** and **5.1.3**

The phenyl N–H proton of **5.1.3** was shielded from the parent ligand and showed a decrease in the acidity of this N–H upon coordination of the ligand to the mercury ion. The proton of the NH–C=S part of **5.1.3** and the parent ligand **H5.1** were also observed at distinguishable positions. For **5.1.3**, this peak appeared at 13.25 ppm while for the free ligand **H5.1**, this peak was observed at 10.75 ppm. Hence, a higher acidity of N–H in the complex than that of the ligand was observed. Accordingly, in the same solvent, the intrinsic acidity of the exchangeable protons of the complexes was different. This suggested that the geometry of the ligand and the metal ion influenced the intrinsic acidity of the N–H. The N–H proton next to the phenyl –N–H of **5.1.1** and **5.1.2** appeared at 9.19 and 9.59 ppm, respectively, in  $\text{DMSO-d}_6$  (Fig.5.12).

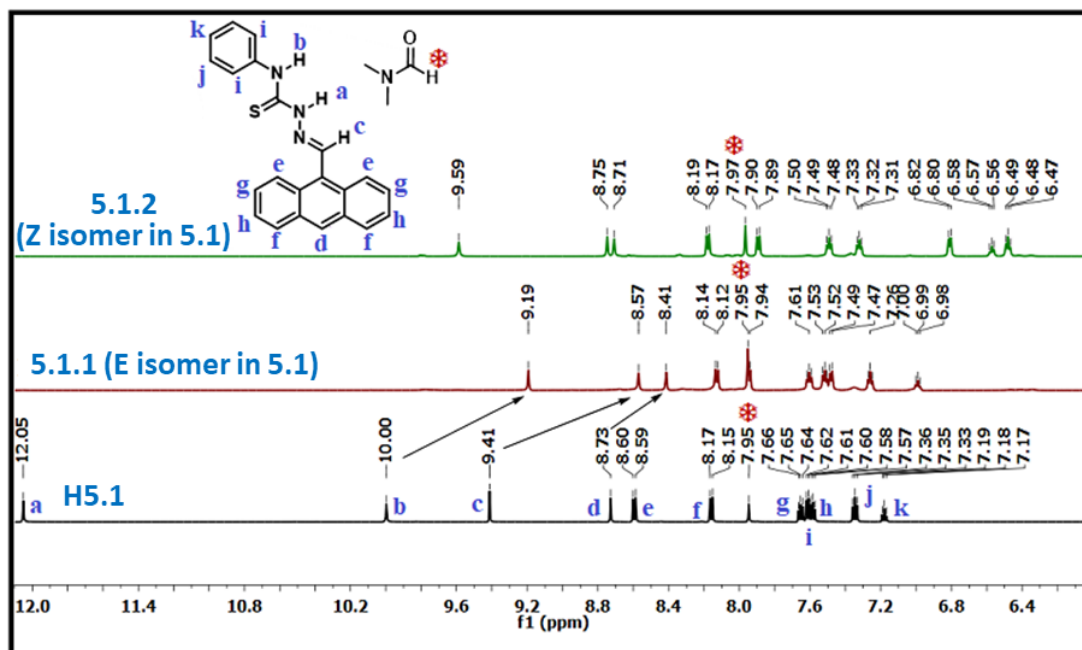
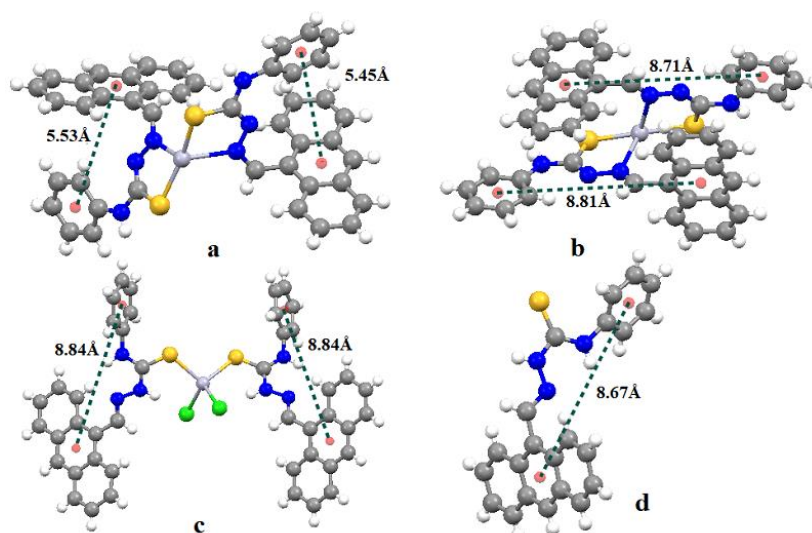


Figure 5.12:  $^1\text{H}$ NMR (DMSO- $d_6$ , 600 MHz) spectra of the 5.1.1, 5.1.2 and H5.1.DMF.

These lower values of the chemical shifts of the N–H protons in  $\text{CDCl}_3$  than that in the DMSO- $d_6$  solvent were attributed to the lower basicity of  $\text{CDCl}_3$  than that of DMSO- $d_6$ ; hence, the latter formed strong hydrogen bonds, which eventually led to deprotonation. The protons on the phenyl groups in both the isomers displayed distinct chemical shifts. The chemical shifts of the protons of the phenyl groups of 5.1.1 appeared at 7.08, 7.26, and 7.30 ppm in  $\text{CDCl}_3$ , whereas for 5.1.2, these protons appeared at 6.61, 6.66, and 6.72 ppm in  $\text{CDCl}_3$ . Thus, the phenyl peaks were de-shielded in 5.1.1 as compared to 5.1.2. This was due to the difference in the orientations of the neighbouring aromatic anthracenyl groups affecting the magnetic field. The different orientations of the phenyl group concerning the anthracenyl groups were reflected in the intramolecular centroid to the centroid of the phenyl and naphthyl rings, as shown in Fig.5.13. The proximity, as well as the angular spatial differences among the planes of the rings, had influenced the chemical shift positions.



**Figure 5.13:** The distance between the centroid of anthracene and phenyl ring of (a) **5.1.2**, (b) **5.1.1**, (c) **5.1.3**, and (d) **H5.1.DMF**

The  $^1\text{H-NMR}$  titrations in  $\text{DMSO-d}_6$  delineated the formation of the complex of  $\text{HgCl}_2$  with the ligand **H5.1**. During the titration of a solution of  $\text{HgCl}_2$  with the ligand **H5.1** in  $\text{DMSO-d}_6$ , the chemical shift of the N-H protons observed at 12.05 ppm and 10.00 ppm (Fig. 5.14) disappeared due to the formation of the **5.1.2**. The DMSO solvent has intrinsic basicity, hence causing the deprotonation<sup>36</sup> of the active N-H proton to form the corresponding anion to chelate to mercury ion, providing the **5.1.2**.

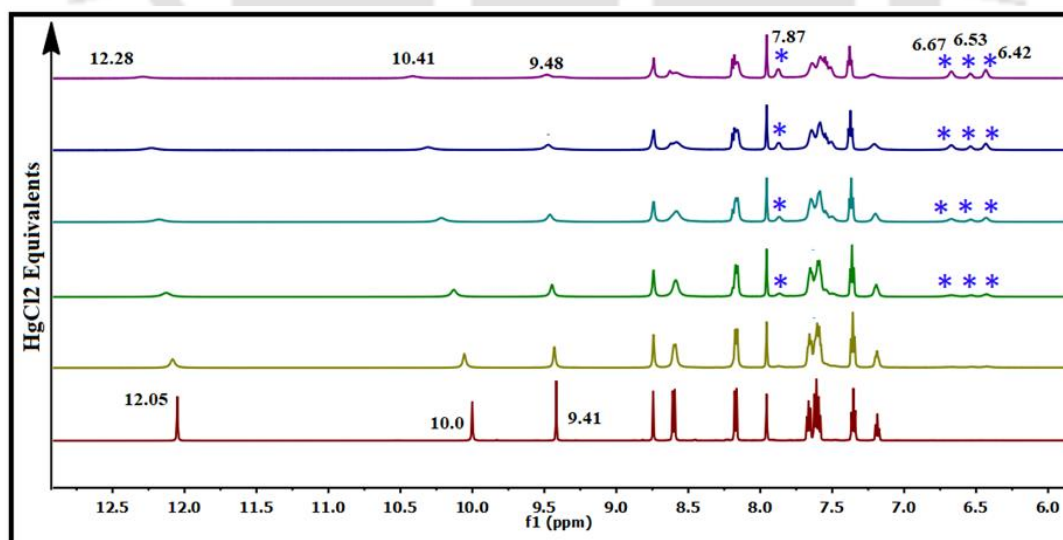


**Figure 5.14:**  $^1\text{H-NMR}$  (600 MHz,  $\text{DMSO-d}_6$ ) titration showing the aromatic protons of **H5.1.DMF** was recorded by adding different amounts of **HgCl<sub>2</sub>**.

The  $^1\text{H}$ NMR of a solution of **5.1.3** was recorded in  $\text{DMSO-d}_6$ , revealing that the complex was less stable and slowly transformed to **5.1.2**. Extra peaks (red asterisks) developed with time rather than the desired peaks for the parent complex. However, the complex was stable in  $\text{CDCl}_3$  as in this solvent; there were no extra peaks than the desired ones.

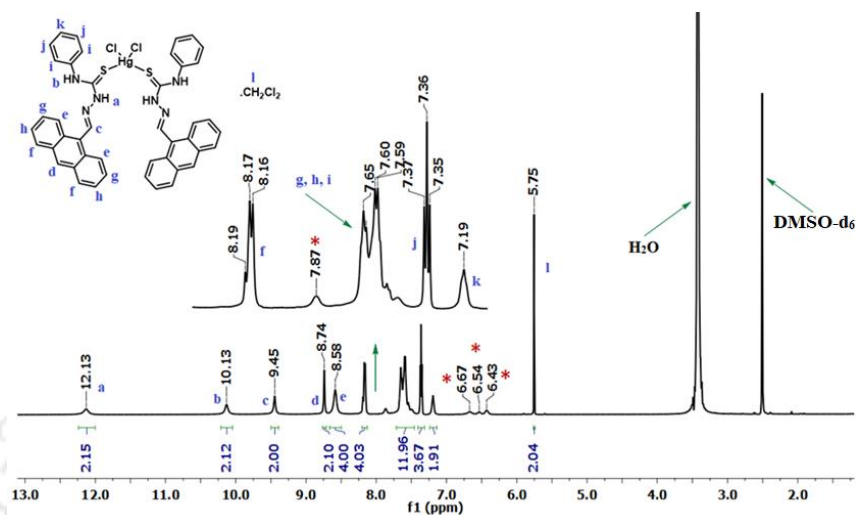


**Figure 5.15:**  $^1\text{H}$ NMR ( $\text{DMSO-d}_6$ , 600 MHz) spectra of the **5.1.3**.

It may be noted that the *E*-isomer **5.1.1** was less stable in solution and slowly transformed to **5.1.2**. The  $^1\text{H}$ NMR of the *E*-isomer **5.1.1** after 20 hours showed a new peak for phenyl proton of **5.1.2** in  $^1\text{H}$ -NMR spectra (round marked in Fig 5.16).

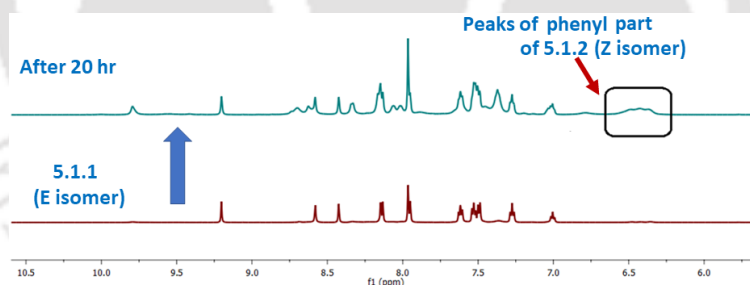


**Figure 5.16:**  $^1\text{H}$ NMR ( $\text{DMSO-d}_6$ , 600 MHz) spectra of the **5.1.1** after 20 hr.

All these transformations were examined by comparing the respective PXRD patterns of the isomers recovered in solid form from each solution by slow evaporation. These suggested that the individual signatures of the isomers in the solution were carried to the solid crystallized. From a mechanistic point of view, the *E* or *Z*, as depicted in Fig. 5.17a, was possible through a change in the  $\text{N}_2\text{-N}_1\text{-C}_{15}\text{-C}_{14}$  dihedral angle in the isomers. This involved changes in the orientations across an extended delocalized  $\text{C}=\text{N}-\text{N}=\text{C}-\text{N}$  functional group unit. The process did not require the dissociation of ligands, but it needed a resonating platform of chelating ligands to cause a free rotation to transform one form to another, as

illustrated in Fig 5.17c. It had to undergo a change by having hydrogen bonds with a solvent, which permitted the required rotation across the partial double bond.

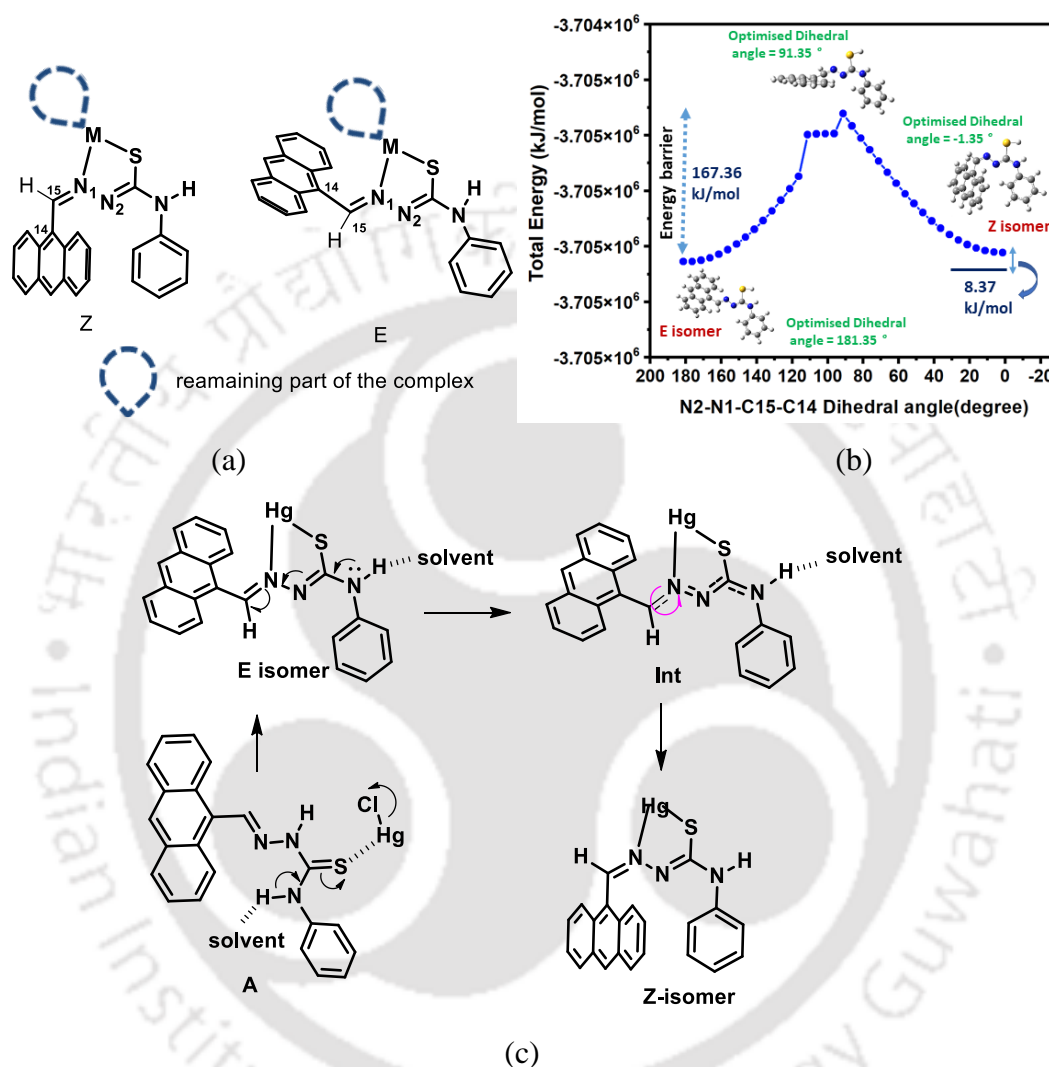


**Figure 5.17:** (a) The dihedral angle N2-N1-C25-C14 of the two isomers of the mercury complex; (b) The plot of DFT calculated energy of the different orientations of **H5.1** with respect to change of every 5° of the dihedral angle N2-N1-C25-C14; and (c) The plausible mechanism involving hydrogen bonds helping the conversion of the E form to the Z isomer and also formation of bis chelated complex from **5.1.3**.

We calculated the energy changes of the Z-form of the thiol form of **H5.1** transforming to the E-form through a DFT calculation on the energies of the ligand upon every 5° change of the N2-N1-C15-C14 dihedral angle. The energy difference between the two isomers of the free ligand **H5.1** in the neutral form was found to be 8.37 kJ/mol (Fig. 5.17b). This difference was comparable to the energy of a weak hydrogen bond or  $\pi$ -interaction. It was also found that the

activation energy required to undergo the *E* to *Z* form of the neutral ligand (**H5.1**) was 167.36 kJ/mol (Fig. 5.17b). Based on the calculated activation barrier, converting the *E* to *Z* isomer at ambient condition<sup>1</sup> would not have been possible without the assistance of hydrogen bonds with a solvent. For such a conversion, a rotation across C=N double bonds is required. This could happen if the C15=N1 bond adopts a partial double bond character to undergo the rotation.

We found that the pH of the respective solution of **H5.1** (0.5 mM) in DMF and DMSO solution were 5.32 and 4.80, respectively, and the respective pH changed to 1.02 and 2.15 respectively, upon the addition of the two-mole equivalent of mercuric chloride. Meanwhile, the pH of a solution of **H5.1** ( $10^{-3}$  M) in chloroform was 3.20, and it remained unchanged upon adding mercuric chloride in the same ratio as in the other two solvents. The decreased pH in the respective DMF and DMSO solutions upon adding mercury ions showed that complexation passed through deprotonation. A mechanistic path involving hydrogen bonds with solvent for the formation of *Z*-isomer **5.1.2** or *E*-isomer **5.1.1** is illustrated in Fig 5.17c. In this figure, the solvent molecules, such as DMF, formed hydrogen bonds with N-H, providing a partial C15=N1 character to allow the conversion of the isomers. A similar path is possible in forming isomers from complex **5.1.3**, also shown in Fig. 5.17c, where the deprotonation, rotation and chelation provided isomeric chelated complex.

### 5.5: The implications of the orientations of the anthryl group in the emission spectra

The anthracene-based mercury(II) complexes of tripodal ligands provide avenues to understand the emission mechanism.<sup>20</sup> The photo-physical properties of the *E* and *Z* isomers were examined. The UV-visible spectra of the isomers **5.1.1** and **5.1.2** in chloroform showed absorptions at 396 nm and 389 nm, respectively (inset of Fig. 5.18b). Based on these absorptions, the optical band gaps of the two isomers were ascertained by Tauc's plots<sup>37-38</sup> (Fig. 5.18b) and found to be 3.13 eV (396.1 nm) and 3.19 eV (388.7 nm) for the *E*-isomer **5.1.1** and *Z*-isomer **5.1.2** respectively. The DFT calculations by using the B3LYP/SDD basis set provided the HOMO-LUMO gaps 2.99 eV (414.7 nm) for **5.1.1** and 3.22 (385.0 nm) for **5.1.2** (Fig 5.18a). Based on the DFT calculations, the absorption peaks were attributed to the HOMO to LUMO transitions. The absorptions were from ligand-based transitions, and there was a slight difference in the absorption positions of the *Z* and *E* isomers.

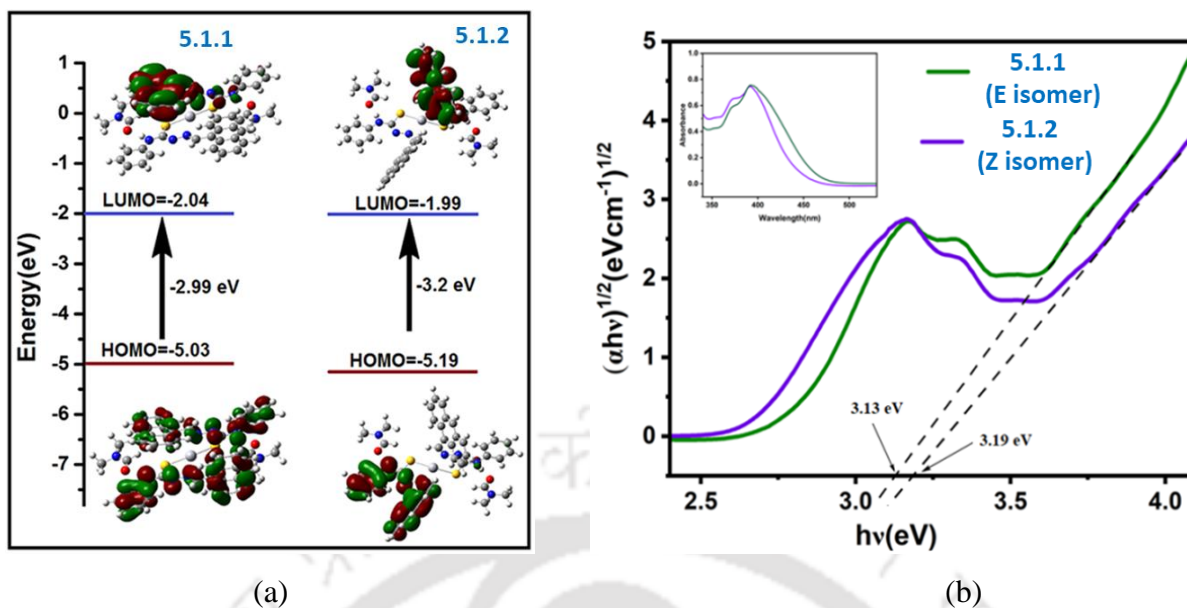


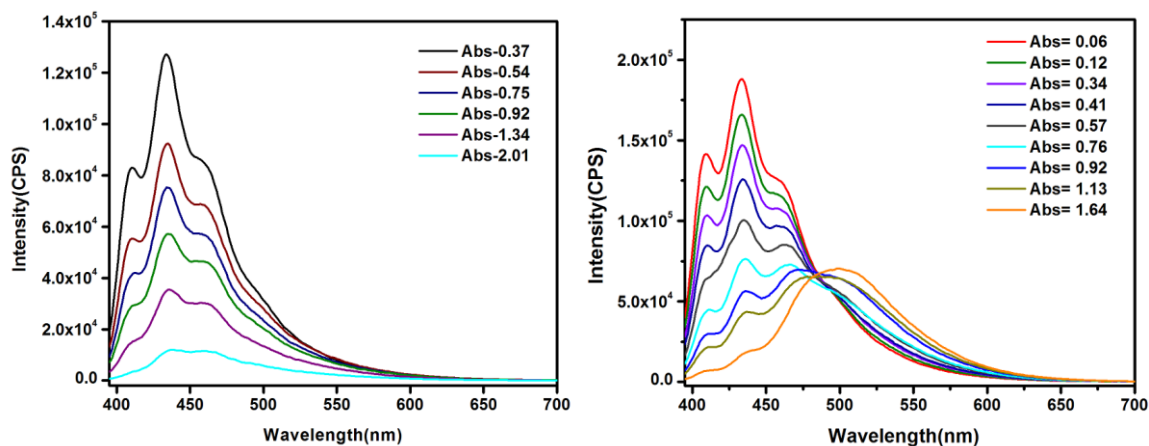
**Figure 5.18:** (a) HOMO-LUMO gap of the two isomers and (b) Tauc's plots showing the optical band gaps of the two isomers **5.1.1** and **5.1.2** {inset is the UV-visible spectra ( $10^{-6}$  M) of the two isomers in chloroform}.

The Z-isomer (**5.1.2**) in chloroform showed emissions at 411 nm, 436 nm, and 462 nm ( $\lambda_{\text{ex}} = 380$  nm). These three peaks were due to the anthracenyl group's transition from S1 to the S0 state ( $\pi^*$ -to- $\pi$  transition). The three peaks were due to vibronic contributions. Peaks at similar places were observed for such a transition earlier in metal complexes having anthracenyl-based ligands.<sup>39</sup> The position of the emissions of the Z-form **5.1.2** in chloroform was unchanged upon dilution, but the intensity of each peak was enhanced (Fig. 7a). This suggested that the isomer in a higher concentration in chloroform was in a fluorescence partial quenched state and upon dilution it got dis-assembled. A concentration-dependent emission study of the E-isomer (**5.1.1**) in chloroform showed an excimer-like emission at 500 nm ( $\lambda_{\text{ex}} = 380$  nm).

This emission was due to assembling, leading to eclipsing among the anthracenyl groups in the E-isomeric molecules. It may be noted that the anthracenyl group-containing complexes were reported earlier to have shown emission at 555 nm upon excitation at 365 nm, and this peak was assigned to excimer emission from  $\pi$ - $\pi$  interacting anthracene pairs.<sup>39-40</sup> Upon a decrease in the isomer concentration in chloroform, this emission (Figure 5.19b) diminished, and a new emission peak resembling the emission peaks of the Z-isomer was observed. The new peak was significantly enhanced upon further dilution. In the crystal structure of the Z-

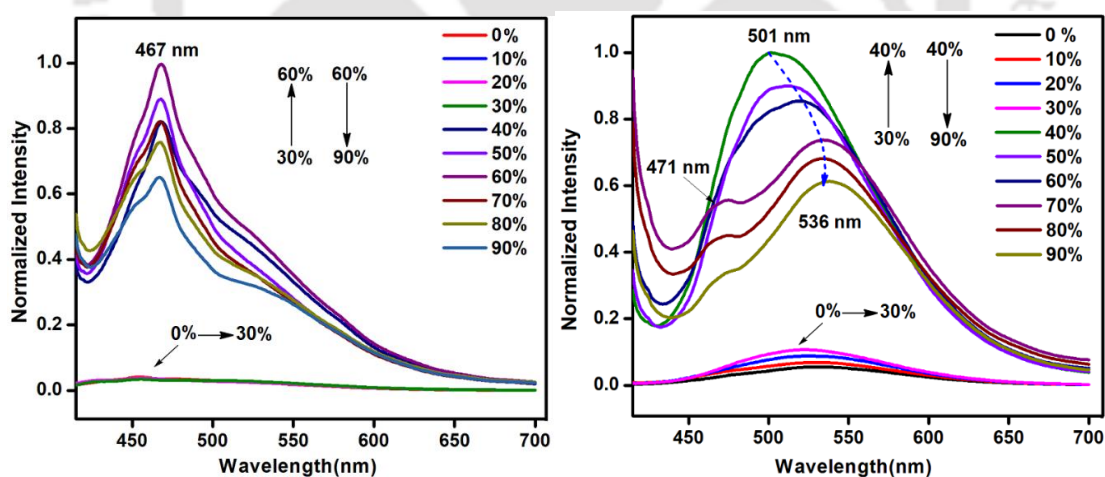
isomer, the anthracenyl groups were parallel but located at displaced positions. Upon dilution, the assembly was disassembled to show the property of discrete anthracenyl groups, and thereby, the emission intensities were increased.

In general, the  $\pi$ -stacking and  $Hg \cdots \pi$  interactions quench emission spectra of anthracene-based mercury complexes.<sup>29</sup> In the present case, the two isomers have either  $N-H \cdots \pi$  or  $C-H \cdots \pi$  interactions. These interactions contributed to the observed poor emissions from the isomers.



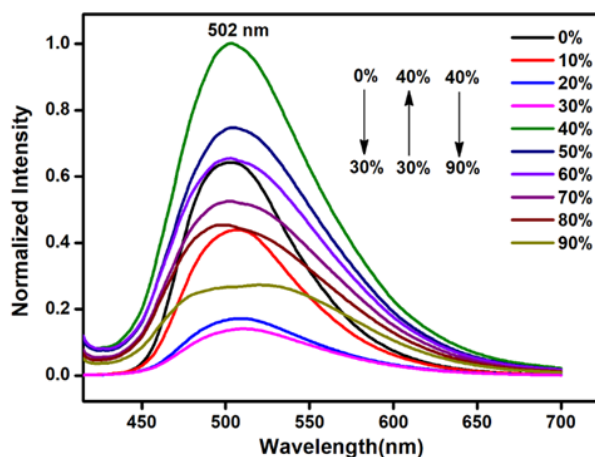
(a)

(b)



(c)

(d)



(e)

Figure 5.19: The changes in fluorescence emission of (a) Z-isomer **5.1.2**, (b) E-isomer **5.1.1** at different molar concentrations in chloroform ( $\lambda_{\text{ex}} = 380 \text{ nm}$ ,  $10^{-8}$  to  $5 \times 10^{-7} \text{ M}$ ) Changes in the fluorescence emission ( $\lambda_{\text{ex}} = 400 \text{ nm}$ ) of (c) E-isomer **5.1.2**, (d) Z-isomer **5.1.1** at different fractions of water in DMSO solution (e) E isomer **5.1.3**

It is a practice to probe aggregation-induced emission by adding different amounts of water in an organic solvent.<sup>41</sup> We have carried out an emission study by varying the fractions of water in the solution of the two isomers in the dimethyl sulfoxide (DMSO) solvent. A dimethyl sulfoxide solution of the Z-isomer (**5.1.2**) was also in a quenched state (Fig 5.19c), and there was no change in emission until 30 % water was added to the solution. But with an increasing amount of water from 30 % to 60 %, a peak developed at 467 nm. This peak resembles the E-isomer, attributing to the dilution effect and causing the disassembly of the isomer by water.

The shape change resulted from the differently aggregated form, where the vibrational contributions had changed. Beyond 60%, the emission decreased due to precipitation. The fluorescence emission of the E-isomer (**5.1.1**) in the DMSO solution was barely changed up to 30 % water (initially, the **5.1.1** was in a quenched state with a negligible emission at 503 nm; Fig. 5.19d). Upon increasing the fractions of water up to 40 %, there was a sudden increase in the fluorescence intensity of the E-isomer, showing aggregation-induced enhancement. Between 40 % and 90%, the fluorescence intensity was decreased due to precipitation. The different geometry of functional groups of a fluorophore influences the aggregation-induced emissions.<sup>42-43</sup> Conversely, chelation-induced emission contributes to the AIE of inorganic complexes.<sup>44</sup> The hydrogen bond plays a vital role in stabilizing the conformer of hydrazone derivatives.<sup>45</sup> In our case, the aggregated state of the E-form was different from the Z-form, showing the difference in emission changes in each case.

The long wavelength emissions in anthracenyl derivatives were usually attributed to aggregation-induced emission.<sup>28</sup> The complex **5.1.3** in chloroform showed a relatively strong emission at 506 nm ( $\lambda_{\text{ex}} = 380$  nm,  $\phi = 0.012$ ) (Fig. A5.6) due to excimer emission; this emission was associated with vibrational features. The **H5.1** and **5.1.3** showed a single exponential emission decay profile with a short lifetime of 0.151 ns and 0.152 ns, respectively, as shown in Fig. A5.10 and A5.9. The emission decay profiles monitored at 429 and 456 nm in the DMSO solvent of the Z-isomer showed bi-exponential behaviour of their respective decay profiles. The average lifetime of the emissions at those excitations was 6.84 ns and 4.45 ns, respectively, as shown in Fig. A5.28. The emission decay at 528 nm in DMSO of the E-isomer **5.1.1** was also bi-exponential; it had an average lifetime of 2.77 ns, as shown in Fig. A5.27. The solvent-dependent emission of palladium complexes having anthracenyl-derived ligands in dynamic equilibrium is known in the literature.<sup>46</sup> The observation of the biexponential features from our E-form of the complex suggests the involvement of two emission paths in the E-isomers, that is, conventional  $\pi^*$ -to- $\pi$  transition and exciplex emission. Both the isomers showed short lifetimes involving exciplex emission, and the effect of the mercury ion was not directly felt by anthracene; a similar observation was earlier made in related systems.<sup>20</sup>

The presence of a chloride ligand in an anthracene-based mercury complex can turn on the fluorescence emission of an anthracene unit.<sup>30</sup> The examinations on the emission spectra of the complexes in solution showed a significant difference from the observations made in solution. In **5.1.3**, there were no stacks among the anthracene rings, and the rings were oblique, and at translated positions to each other, as there were no  $\pi$ -stacks among anthracene rings, it showed emission at 552 nm (Fig. 5.20) in the solid state. In the solid state, the free ligand **H5.1** had extensive  $\pi$ -stacks (Fig. A5.4a) among the anthracene rings, with separation among the rings being 3.9 Å; hence, it was weakly emissive.

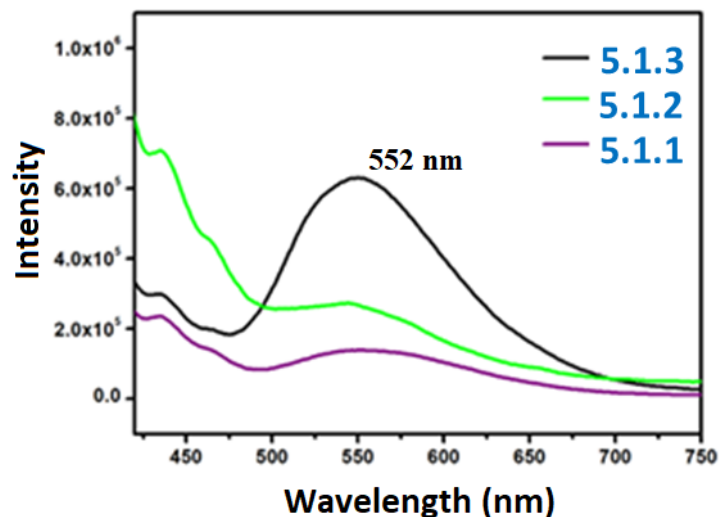


**Figure 5.20:** Solid-state fluorescence emissions of the mercury complexes (**5.1.1- 5.1.3**)

### 5.6: Conclusions

Due to the large activation barrier for the inter-conversion of E and Z geometry of the ligands across the conjugated C=N-N=C-N functional group unit, two stable isomers (**5.1.1** and **5.1.2**) of the bis-chelated mercury (II) were observed. Those stable isomers in pure form could be prepared. Energetically the inter-conversion of E to Z isomers of the parent ligand **H5.1** is not favorable, hence, the hydrogen bonding of solvent to the mercury complex influenced the conversion by providing partial double bond character to the C=N bond, allowing the change of the orientation of phenyl or anthracenyl group. Conventionally, E isomer does not easily transform to Z isomer, but in the present circumstance, this was facile. The characteristic and distinct features of the respective isomers were shown through the  $^1\text{H}$ NMR studies and the distinct emission features arising from different orientations of the isomers could be shown. These examples established the role of solvents in guiding the conversions of the complexes and the rationally showed that the concentration of the complexes and the solvent significantly affected their optical properties. The E-isomer showed exciplex emission, whereas the Z-isomer showed conventional  $S_1$ - $S_0$  emission.

### 5.7: References

1. Rohmer, M.-M.; Bénard, M. Bond-Stretch Isomerism in Strained Inorganic Molecules and in Transition Metal Complexes: A Revival? *Chem. Soc. Rev.* **2001**, *30* (6), 340–354.
2. Pantazis, D. A.; McGrady, J. E. A Three-State Model for the Polymorphism in Linear Tricobalt Compounds. *J. Am. Chem. Soc.* **2006**, *128* (12), 4128–4135.

3. Jensen, K. G.; Soling, H.; Thorup, N. The Crystal Structure of Two Conformational Isomers Of. *Acta Chem. Scand.* **1970**, *24* (3), 908-918.
4. Orthaber, A.; Karnahl, M.; Tschierlei, S.; Streich, D.; Stein, M.; Ott, S. Coordination and Conformational Isomers in Mononuclear Iron Complexes with Pertinence to the [FeFe] Hydrogenase Active Site. *Dalt. Trans.* **2014**, *43* (11), 4537–4549.
5. Chen, D.-S.; Sun, L.-B.; Liang, Z.-Q.; Shao, K.-Z.; Wang, C.-G.; Su, Z.-M.; Xing, H.-Z. Conformational Supramolecular Isomerism in Two-Dimensional Fluorescent Coordination Polymers Based on Flexible Tetracarboxylate Ligand. *Cryst. Growth Des.* **2013**, *13* (9), 4092–4099.
6. Zhang, C.; Feng, G.; Xu, S.; Zhu, Z.; Lu, X.; Wu, J.; Liu, B. Structure-Dependent Cis/Trans Isomerization of Tetraphenylethene Derivatives: Consequences for Aggregation-Induced Emission. *Angew. Chemie* **2016**, *128* (21), 6300–6304.
7. Wang, S.; Dormidontova, E. E. Tunable Supramolecular Networks via Cis-Trans Metal–Ligand Isomerization. *Soft Matter* **2010**, *6* (5), 1004–1014.
8. Brittain, H. G.; Desreux, J. F. Luminescence and NMR Studies of the Conformational Isomers of Lanthanide Complexes with an Optically Active Polyaza Polycarboxylic Macrocyclic. *Inorg. Chem.* **1984**, *23* (26), 4459–4466.
9. Nangia, A. Conformational Polymorphism in Organic Crystals. *Acc. Chem. Res.* **2008**, *41* (5), 595–604.
10. Cruz-Cabeza, A. J.; Bernstein, J. Conformational Polymorphism. *Chem. Rev.* **2014**, *114* (4), 2170–2191.
11. Karmakar, A.; Sarma, R. J.; Baruah, J. B. Polymorphism in an Aqua-Bridged, Dinuclear 2-Nitrobenzoate Complex of Cobalt (II). *Eur. J. Inorg. Chem.*, **2007**, 643 – 647.
12. Li, Z.-H.; Xue, L.-P.; Miao, S.-B.; Zhao, B.-T. Assembly of 4-, 6- and 8-Connected Cd (II) Pseudo-Polymorphic Coordination Polymers: Synthesis, Solvent-Dependent Structural Variation and Properties. *J. Solid State Chem.* **2016**, *240*, 9–15.
13. Han, L.-L.; Hu, T.-P.; Mei, K.; Guo, Z.-M.; Yin, C.; Wang, Y.-X.; Zheng, J.; Wang, X.-P.; Sun, D. Solvent-Controlled Three Families of Zn (II) Coordination Compounds: Synthesis, Crystal Structure, Solvent-Induced Structural Transformation, Supramolecular Isomerism and Photoluminescence. *Dalt. Trans.* **2015**, *44* (13), 6052–6061.

14. Melnik, M. Isomers in the Chemistry of Mercury Coordination Compounds. *Cent. Eur. J. Chem.* **2010**, *8*, 469–485.
15. Sanchez-Ferez, F.; Solans-Monfort, X.; Calvet, T.; Font-Bardia, M.; Pons, J. Controlling the Formation of Two Concomitant Polymorphs in Hg (II) Coordination Polymers. *Inorg. Chem.* **2022**, *61* (12), 4965–4979.
16. Samie, A.; Salimi, A. Conformational Variation of Ligands in Mercury Halide Complexes; High and Low *Z'* Structures. *CrystEngComm* **2019**, *21* (33), 4951–4960.
17. Arion, V. B. Coordination Chemistry of S-Substituted Isothiosemicarbazides and Isothiosemicarbazones. *Coord. Chem. Rev.* **2019**, *387*, 348–397.
18. Aguirre, A. R.; Parrilha, G. L.; Louro, S. R. W.; Alves, O. C.; Diniz, R.; Durval, F.; Rocha, W.; Beraldo, H. Structural and Theoretical Studies on Copper(II) and Zinc(II) Complexes with a 9-Anthraldehyde-Derived Thiosemicarbazone. *Polyhedron* **2022**, *217*, 115724.
19. Ding, S.-Y.; Dong, M.; Wang, Y.-W.; Chen, Y.-T.; Wang, H.-Z.; Su, C.-Y.; Wang, W. Thioether-Based Fluorescent Covalent Organic Framework for Selective Detection and Facile Removal of Mercury (II). *J. Am. Chem. Soc.* **2016**, *138* (9), 3031–3037.
20. Uritis, S.; Thummel, R. P.; Lee, H.-S.; Hancock, R. D. A Study of the Complexes of Hg (II) with Polypyridyl Ligands by Fluorescence, Absorbance Spectroscopy, and DFT Calculations. The Effect of Ligand Preorganization and Relativistic Effects on Complex Stability. *Inorganica Chim. Acta* **2022**, *530*, 120670.
21. Cho, M.; Shin, H. J.; Kusumahastuti, D. K. A.; Yeo, H.; Min, K. S. Monomeric and Tetrameric Mercury (II) Complexes with Iodo and N<sub>2</sub>O<sub>2</sub>/N<sub>3</sub>O Ligands: Structure and Blue Luminescence. *Inorganica Chim. Acta* **2020**, *511*, 119789.
22. Tekuri, V.; Sahoo, S. K.; Trivedi, D. R. Hg<sup>2+</sup> Induced Hydrolysis of Thiazole Amine Based Schiff Base: Colorimetric and Fluorogenic Chemodosimeter for Hg<sup>2+</sup> Ions in an Aqueous Medium. *Spectrochim. Acta Part A Mol. Biomol. Spectrosc.* **2019**, *218*, 19–26.
23. Bai, C.-B.; Qiao, R.; Liao, J.-X.; Xiong, W.-Z.; Zhang, J.; Chen, S.-S.; Yang, S. A Highly Selective and Reversible Fluorescence “OFF-ON-OFF” Chemosensor for Hg<sup>2+</sup> Based on Rhodamine-6G Dyes Derivative and Its Application as a Molecular Logic Gate. *Spectrochim. Acta Part A Mol. Biomol. Spectrosc.* **2018**, *202*, 252–259.

24. Ghosh, S.; Alghunaim, A. S.; Al-mashhadani, M. H.; Krompiec, M. P.; Hallett, M.; Perepichka, I. F. 4, 5-Diazafluorene Co-Oligomers as Electron-Deficient Light-Emitting Materials and Selective Fluorescence Sensors for Mercury (II) Cations. *J. Mater. Chem. C* **2018**, *6* (14), 3762–3773.
25. Vedamalai, M.; Kedaria, D.; Vasita, R.; Mori, S.; Gupta, I. Design and Synthesis of BODIPY-Clickate Based Hg<sup>2+</sup> Sensors: The Effect of Triazole Binding Mode with Hg<sup>2+</sup> on Signal Transduction. *Dalt. Trans.* **2016**, *45* (6), 2700–2708.
26. Saha, S.; Agarwalla, H.; Gupta, H.; Baidya, M.; Suresh, E.; Ghosh, S. K.; Das, A. New Chemodosimetric Probe for the Specific Detection of Hg<sup>2+</sup> in Physiological Condition and Its Utilisation for Cell Imaging Studies. *Dalt. Trans.* **2013**, *42* (42), 15097–15105.
27. Balasaravanan, R.; Siva, A. Synthesis, Characterization and Aggregation Induced Emission Properties of Anthracene Based Conjugated Molecules. *New J. Chem.* **2016**, *40* (6), 5099–5106.
28. Hu, J.; Lin, R.; Yip, J. H. K.; Wong, K.-Y.; Ma, D.-L.; Vittal, J. J. Synthesis and Electronic Spectroscopy of Luminescent Cyclometalated Platinum– Anthracenyl Complexes. *Organometallics* **2007**, *26* (26), 6533–6543.
29. Yoon, J.; Ohler, N. E.; Vance, D. H.; Aumiller, W. D.; Czarnik, A. W. A Fluorescent Chemosensor Signalling Only Hg (II) and Cu (II) in Water. *Tetrahedron Lett.* **1997**, *38* (22), 3845–3848.
30. Lee, H.; Lee, H.-S.; Reibenspies, J. H.; Hancock, R. D. Mechanism of “Turn-on” Fluorescent Sensors for Mercury (II) in Solution and Its Implications for Ligand Design. *Inorg. Chem.* **2012**, *51* (20), 10904–10915.
31. Udhayakumari, D.; Velmathi, S.; Venkatesan, P.; Wu, S.-P. Anthracene Coupled Thiourea as a Colorimetric Sensor for F<sup>-</sup>/Cu<sup>2+</sup> and Fluorescent Sensor for Hg<sup>2+</sup>/Picric Acid. *J. Lumin.* **2015**, *161*, 411–416.
32. Blackburn, J. R.; Nordberg, R.; Stevie, F.; Albridge, R. G.; Jones, M. M. Photoelectron Spectroscopy of Coordination Compounds. Triphenylphosphine and Its Complexes. *Inorg. Chem.* **1970**, *9* (10), 2374–2376
33. Louis, H.; Charlie, D. E.; Amodu, I. O.; Benjamin, I.; Gber, T. E.; Agwamba, E. C.; Adeyinka, A. S. Probing the Reactions of Thiourea (CH<sub>4</sub>N<sub>2</sub>S) with Metals (X= Au, Hf, Hg, Ir, Os, W, Pt, and Re) Anchored on Fullerene Surfaces (C<sub>59</sub>X). *ACS omega* **2022**, *7* (39), 35118–35135.

34. Drew, M. G. B.; McFall, S. G.; Nelson, S. M. Pentagonal-Pyramidal Cadmium (II) and Mercury (II) Complexes of the Quinquedentate Macrocyclic Ligand 2, 15-Dimethyl-3, 7, 10, 14, 20-Penta-Azabicyclo [14.3. 1] Eicosa-1 (20), 2, 14, 16, 18-Pentaene. *J. Chem. Soc. Dalt. Trans.* **1979**, No. 4, 575–581.
35. Yang, L.; Powell, D. R.; Houser, R. P. Structural Variation in Copper (I) Complexes with Pyridylmethanamide Ligands: Structural Analysis with a New Four-Coordinate Geometry Index,  $\tau$  4. *Dalt. Trans.* **2007**, No. 9, 955–964.
36. Tarai, A.; Baruah, J. B. Conformation and Visual Distinction between Urea and Thiourea Derivatives by an Acetate Ion and a Hexafluorosilicate Cocrystal of the Urea Derivative in the Detection of Water in Dimethylsulfoxide. *ACS Omega* **2017**, 2 (10), 6991–7001.
37. Tauc, J.; Grigorovici, R.; Vancu, A. Optical Properties and Electronic Structure of Amorphous Germanium. *Phys. status solidi* **1966**, 15 (2), 627–637.
38. Makuła, P.; Pacia, M.; Macyk, W. How to Correctly Determine the Band Gap Energy of Modified Semiconductor Photocatalysts Based on UV–Vis Spectra. *J. Phys. Chem. Lett.*, **2018**, 9, 6814 - 6817.
39. Ma, X.-F.; Huang, X.-D.; Zheng, L.-M. Tuning the Single-Molecule Magnet and Photoluminescence Properties of Binuclear Dysprosium Complexes by Light. *Cryst. Growth Des.* **2022**, 23 (2), 1095–1103.
40. Huang, X.-D.; Ma, X.-F.; Shang, T.; Zhang, Y.-Q.; Zheng, L.-M. Photocontrollable Magnetism and Photoluminescence in a Binuclear Dysprosium Anthracene Complex. *Inorg. Chem.* **2023**, 62 (5), 1864–1874.
41. Hong, Y.; Lam, J. W. Y.; Tang, B. Z. Aggregation-Induced Emission: Phenomenon, Mechanism and Applications. *Chem. Commun.* **2009**, No. 29, 4332–4353.
42. Yang, H.; Zheng, J.; Xie, M.; Luo, D.; Tang, W.-J.; Peng, S.-K.; Cheng, G.; Zhang, X.; Zhou, X.-P.; Che, C.-M. Aggregation-Enhanced Emission in a Red Cu (I) Emitter with Quantum Yield > 99%. *ACS Mater. Lett.* **2022**, 4 (10), 1921–1928.
43. Gayathri, P.; Karthikeyan, S.; Pannipara, M.; Al-Sehemi, A. G.; Moon, D.; Anthony, S. P. Aggregation-Enhanced Emissive Mechanofluorochromic Carbazole-Halogen Positional Isomers: Tunable Fluorescence via Conformational Polymorphism and Crystallization-Induced Fluorescence Switching. *CrystEngComm* **2019**, 21 (43), 6604–6612.

44. Alam, P.; Climent, C.; Alemany, P.; Laskar, I. R. "Aggregation-Induced Emission" of Transition Metal Compounds: Design, Mechanistic Insights, and Applications. *J. Photochem. Photobiol. C Photochem. Rev.* **2019**, *41*, 100317.
45. Shao, B.; Baroncini, M.; Qian, H.; Bussotti, L.; Di Donato, M.; Credi, A.; Aprahamian, I. Solution and Solid-State Emission Toggling of a Photochromic Hydrazone. *J. Am. Chem. Soc.* **2018**, *140* (39), 12323–12327.
46. Li, Y.; Rajasree, S. S.; Lee, G. Y.; Yu, J.; Tang, J.-H.; Ni, R.; Li, G.; Houk, K. N.; Deria, P.; Stang, P. J. Anthracene–Triphenylamine-Based Platinum (II) Metallacages as Synthetic Light-Harvesting Assembly. *J. Am. Chem. Soc.* **2021**, *143* (7), 2908–2919

## Appendix - Chapter 5

### 5A.1: Experimental section

**Caution:** Mercury compounds are potentially hazard. Hence, experiments with them should be done in a fume hood and with adequate precautions.

#### Synthesis and spectral data of the three mercury complexes 5.1.1, 5.1.2 and 5.1.3:

**(5.1.1):** A solution of ligand **H5.1** (355 mg, 1 mmol) and mercury chloride (136 mg, 0.5 mmol) in DMF (30 ml) was stirred at room temperature for 8 h. The resulting clear solution was filtered and kept undisturbed for slow evaporation. After 4-5 days, block type crystals of **5.1.1** were obtained. Yield, 70 %. IR (Neat,  $\text{cm}^{-1}$ ): 3385 (w), 3258 (w), 3049 (w), 1662 (s), 1595 (s), 1489 (s), 1430 (s), 1384 (w), 1308 (s), 1247 (s), 1178 (s), 1085 (s), 1062 (m), 1034 (w), 947 (m), 883 (s), 837(s), 807 (m), 780 (w), 750 (w), 727 (s), 689 (s), 659 (s), 600 (w), 583 (s), 524 (m), 498 (s), 428 (s).  $^1\text{H}$ NMR (600 MHz,  $\text{DMSO-d}_6$ , ppm): 9.19 (s, N-H), 8.57 (s, H-C=N-), 8.41 (s, N-H), 8.13 (d,  $J = 9$  Hz, 4H), 7.95 (s, 2H), 7.95 (d,  $J = 8.4$  Hz, 4H), 7.6 (t,  $J = 7.8$  Hz, 4H), 7.51 (t,  $J = 7.8$  Hz, 4H), 7.48 (d,  $J = 7.8$  Hz, 4H), 7.26 (t,  $J = 7.2$  Hz, 4H), 6.99 (t,  $J = 7.2$  Hz, 2H), 2.89 (s, 6H). 2.73 (s, 6H).  $^{13}\text{C}$  NMR (125 MHz,  $\text{DMSO-d}_6$ ): 162.39, 162.3, 151.27, 140.75, 130.86, 129.95, 129.16, 129.1, 128.05, 126.65, 126.09, 125.2, 124.63, 121.66, 120.59, 35.78, 30.77. Analysis calculated for  $[\text{C}_{44}\text{H}_{32}\text{HgN}_6\text{S}_2] \cdot 2\text{C}_3\text{H}_7\text{NO}$  (**5.1.1**): C, 56.89; H, 4.39; N, 10.61; S, 6.07; Analysis found: C, 56.81; H, 4.36; N, 10.67; S, 6.09. ESI-MS. Calculated  $m/z$ - 911.1836; found:  $m/z$ -911.2279  $[(\text{M} + \text{H})^+, 100\%]$ .

**(5.1.2):** A solution of ligand **H5.1** (355 mg, 1 mmol) and mercury chloride (271 mg, 1 mmol) in DMF solvent (20 ml) was stirred at room temperature for 24 hrs. A yellow precipitate was

obtained; which was dissolved in dichloromethane. The resulting solution was filtered and to it, 0.5 ml of DMF solvent was added and kept undisturbed for slow evaporation. After 2 days standing needle-type crystals of **5.1.2** were obtained. Yield, 60 %. IR (Neat,  $\text{cm}^{-1}$ ): 3254 (w), 3049 (w), 2919 (w), 2851 (w), 1664 (s), 1598 (s), 1532 (s), 1492 (s), 1432 (s), 1383 (m), 1310 (s), 1249 (s), 1184 (s), 1083 (s), 1064 (m), 1037 (m), 1014 (w), 953 (w), 938 (w), 887 (s), 840(s), 809 (s), 781 (s), 756 (s), 725 (s), 690 (s), 658 (s), 606 (s), 585 (s), 519 (m), 494 (s).  $^1\text{H}$ NMR (600 MHz,  $\text{DMSO-d}_6$ , ppm): 9.57 (s, 2H), 8.73 (s, 2H), 8.69 (s, 2H), 8.16 (d,  $J = 8.4$  Hz, 4H), 7.95 (s, 2H), 7.88 (d,  $J = 8.4$  Hz, 4H), 7.48 (t,  $J = 7.2$  Hz, 4H), 7.31 (t,  $J = 7.8$  Hz, 4H), 6.80 (d,  $J = 7.8$  Hz, 4H), 6.56 (t,  $J = 7.2$  Hz, 2H), 6.46 (t,  $J = 7.8$  Hz, 4H), 2.89 (s, 6H), 2.73 (s, 6H).  $^{13}\text{C}$  NMR (125 MHz,  $\text{DMSO-d}_6$ ): 164.35, 162.3, 150.72, 140.16, 130.69, 129.52, 128.66, 127.94, 127.48, 126.34, 125.55, 125.5, 121.43, 120.55, 119.53, 35.78, 30.77. Analysis calculated for  $[\text{C}_{44}\text{H}_{32}\text{HgN}_6\text{S}_2] \cdot 2\text{C}_3\text{H}_7\text{NO}$  (**5.1.2**): C, 56.89; H, 4.39; N, 10.61; S, 6.07; Analysis found: C, 56.49; H, 4.33; N, 10.66; S, 6.13. ESI-MS. Calculated  $m/z$ -911.1836; found:  $m/z$  911.2341  $[(\text{M} + \text{H})^+, 100\%]$ .

**(5.1.3):** A solution of ligand (355 mg, 1 mmol) and mercury chloride (136 mg, 0.5 mmol) in dichloromethane (30 ml) was stirred at room temperature for 8 h. The precipitate was obtained in the case of methanol solvent, and there was a clear solution in the case of dichloromethane solvent. The yellow precipitate was dissolved in dichloromethane and the solution was filtered and kept undisturbed for slow evaporation. After 1-2 days, the block crystal of **5.1.3** was obtained. Yield, 70 %. IR (Neat,  $\text{cm}^{-1}$ ): 3250 (w), 3153 (w), 3038 (w), 2991 (w), 1624 (m), 1589 (m), 1546 (s), 1510 (s), 1451 (s), 1412 (w), 1349 (m), 1270 (s), 1206 (s), 1053 (s), 1022 (w), 952 (s), 935 (s), 910(m), 888 (s), 841 (s), 783 (s), 759 (s), 723 (s), 695 (s), 637 (s), 591 (s), 557 (m), 497 (s), 485 (s), 454 (s), 420(m).  $^1\text{H}$ NMR (600 MHz,  $\text{DMSO-d}_6$ , ppm): 12.13 (s, 2H), 10.13 (s, 2H), 9.45 (s, 2H), 8.74 (s,  $\text{H-C=N}$ , 2H), 8.58 (d, 4H), 8.16 (d,  $J = 8.4$  Hz, 2H), 7.59- 7.65 (m, 12H), 7.36 (t,  $J = 7.8$  Hz, 4H), 7.19 (t, 2H), 5.75 (s, 2H).  $^{13}\text{C}$  NMR (125 MHz,  $\text{DMSO-d}_6$ ): 174.55, 144.08, 138.69, 130.84, 130.69, 129.76, 128.96, 128.69, 128.25, 127.90, 127.36, 126.45, 125.61, 124.81, 53.52. Analysis calculated for  $[\text{C}_{44}\text{H}_{34}\text{Cl}_2\text{HgN}_6\text{S}_2] \cdot \text{CH}_2\text{Cl}_2$  (**5.1.3**): C, 50.64; H, 3.40; N, 7.87; S, 6.01; Analysis found: C, 50.39; H, 3.33; N, 7.83; S, 6.05.

**Table A5.1:** Hydrogen bond parameters of ligand **H5.1.DMF** and the mercury complexes (**5.1.1-5.1.3**).

Ligand and complexes	D-H...A (Symmetry)	$d_{\text{D-H}}$ (Å)	$d_{\text{H...A}}$ (Å)	$d_{\text{D...A}}$ (Å)	$\angle \text{D-H...A}$ (°)
----------------------	--------------------	----------------------	------------------------	------------------------	-----------------------------

<b>H5.1.DMF</b>	N(2) -H(2N) ...S(1) [1-x, 2-y, -z]	0.85(3)	2.55(3)	3.388(2)	171(3)
	N(3) -H(3N) ...O(1) [1-x, 1-y, 1-z]	0.87(4)	2.03(3)	2.847(3)	156(3)
	C(7) -H(7) ...S(1) [-1+x, -1+y, z]	0.93	2.85	3.649(3)	145
<b>5.1.1</b>	N(3) -H(3N) ...O(2) [1-x, 1-y, -z]	0.86	2.03	2.8712(2)	165
	N(6) -H(6N) ...O(1) [1+x, y, z]	0.86	2.10	2.9156(2)	159
	C(22) -H(22) ...O(2) [1-x, 1-y, -z]	0.93	2.47	3.2359(2)	139
<b>5.1.2</b>	C(44) -H(44) ...O(1) [1+x, y, z]	0.93	2.33	3.1358(2)	145
	N(3) -H(3) ...O(2) [1+x, y, 1+z]	0.86	2.16	3.001(10)	164
<b>5.1.3</b>	N(6) -H(6) ...O(1) [x, y, z]	0.86	2.02	2.854(8)	163
	N(2) -H(2N) ...Cl(1) [x, y, z]	0.91(9)	2.36(9)	3.244(5)	163(8)
	N(3) -H(3N) ...Cl(1) [1/2+x, -y, z]	0.91(6)	2.66(5)	3.378(5)	137(5)

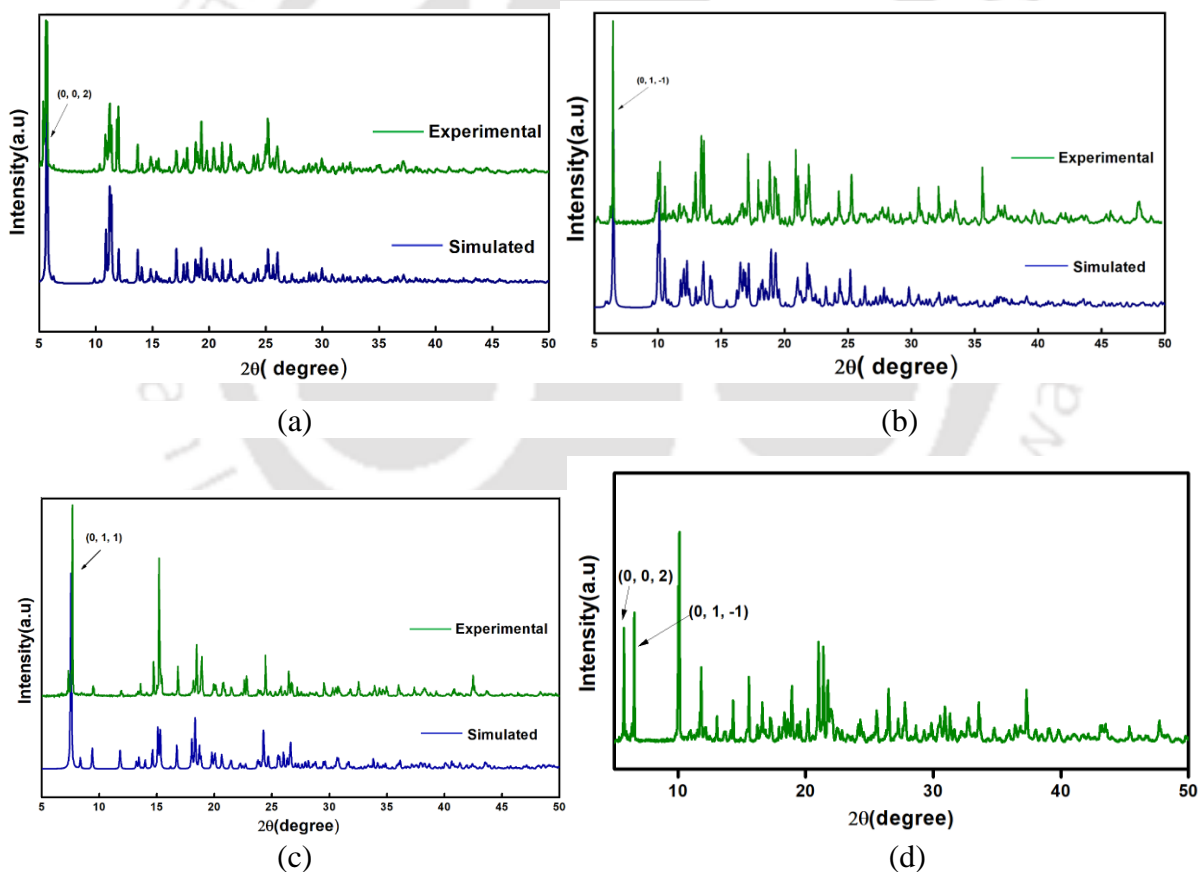
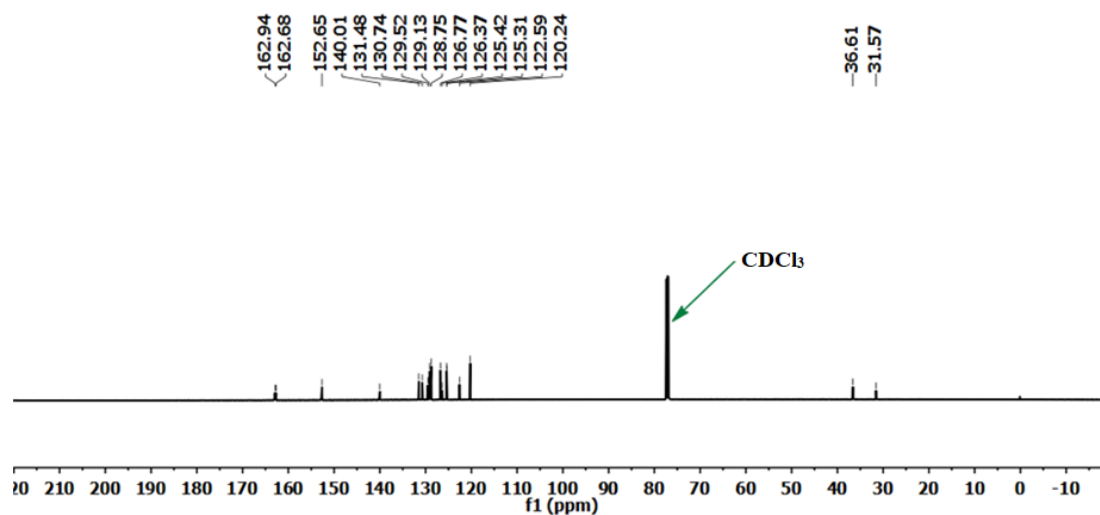
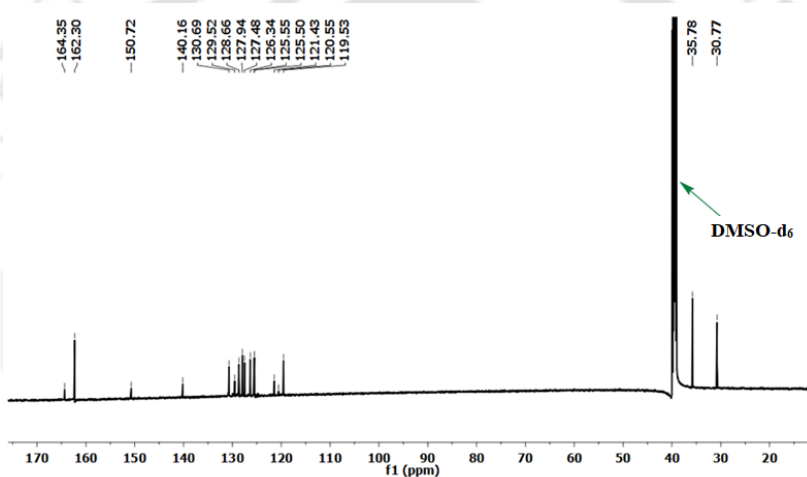


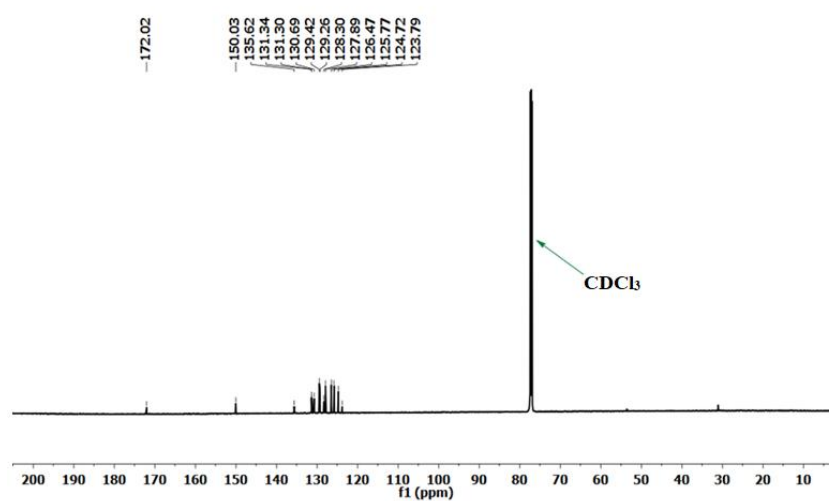
**Figure A5.1:** Powder X-ray diffraction patterns of (a) 5.1.1 (b) 5.1.2 (c) 5.1.3 and (d) mixture of both isomers.



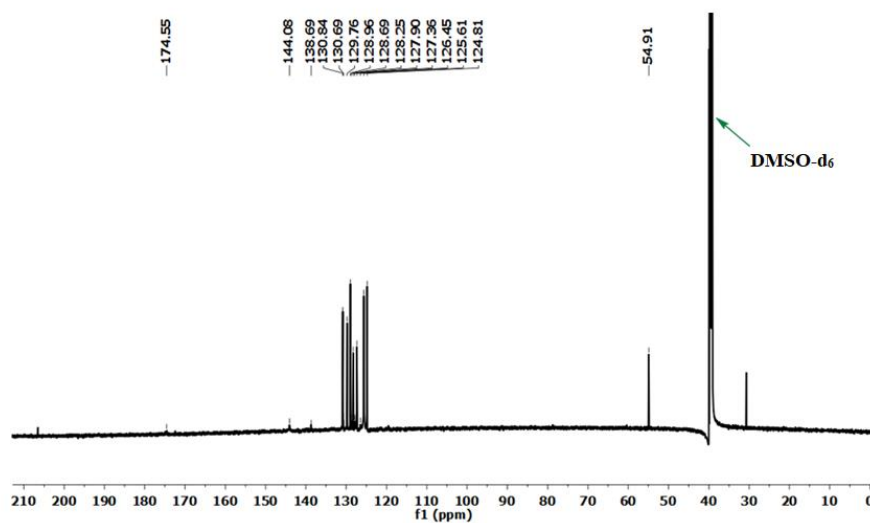
(a)



(b)

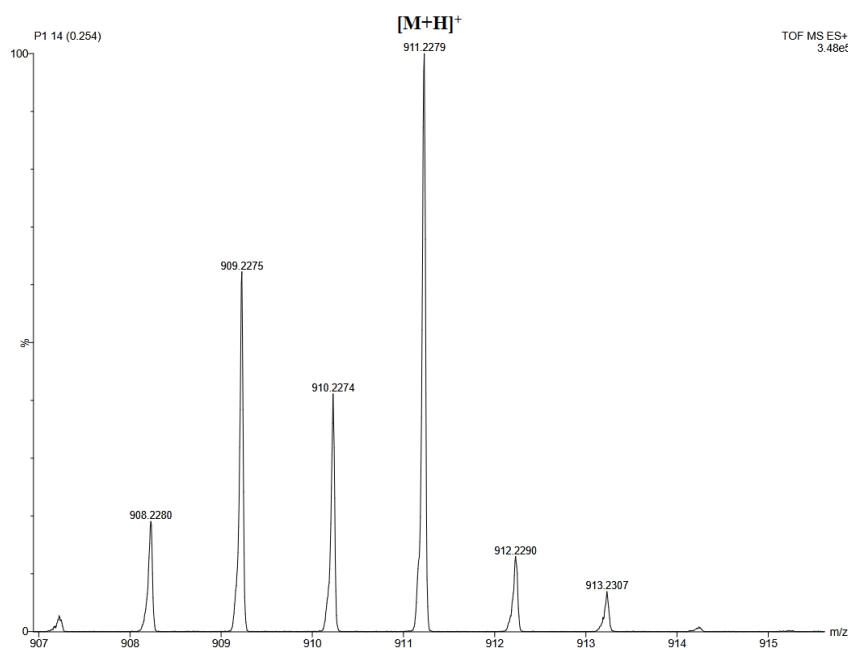


(c)

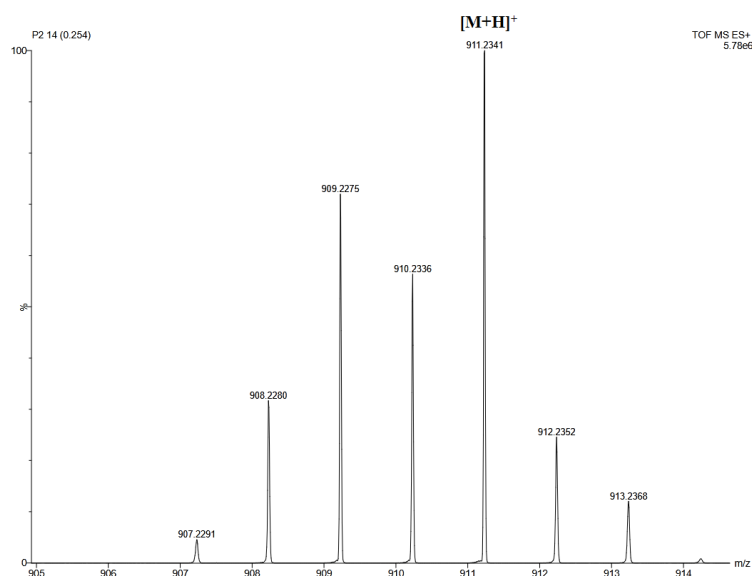


(d)

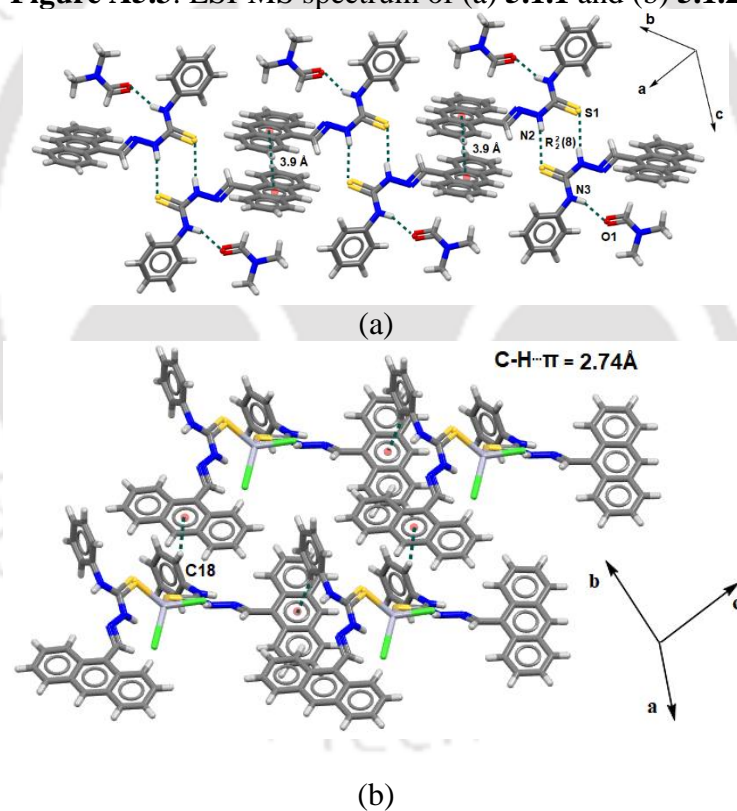
Figure A5.2: <sup>13</sup>CNMR (125 MHz, CDCl<sub>3</sub>) spectra of (a) 5.1.1, (b) 5.1.2 (c) 5.1.3 and (d) <sup>13</sup>CNMR (125 MHz, DMSO-d<sub>6</sub>) spectra of the 5.1.3



(a)



(b)  
Figure A5.3: ESI-MS spectrum of (a) 5.1.1 and (b) 5.1.2



(b)  
Figure A5.4: Packing diagram of (a) H5.1.DMF and (b) 5.1.3

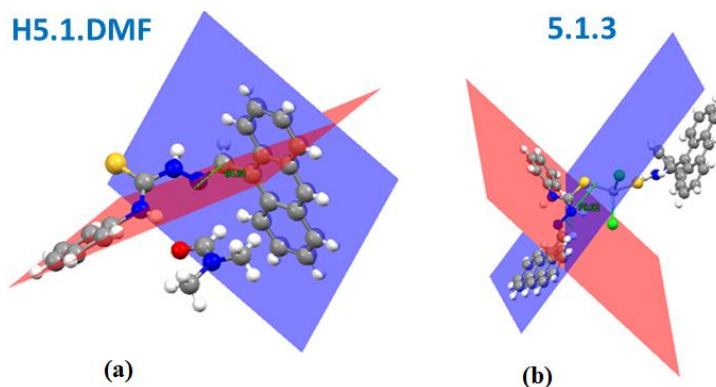


**Figure A5.5** : Angle between anthracene part and phenyl part of (a) **H5.1.DMF** and (b) **5.1.3**

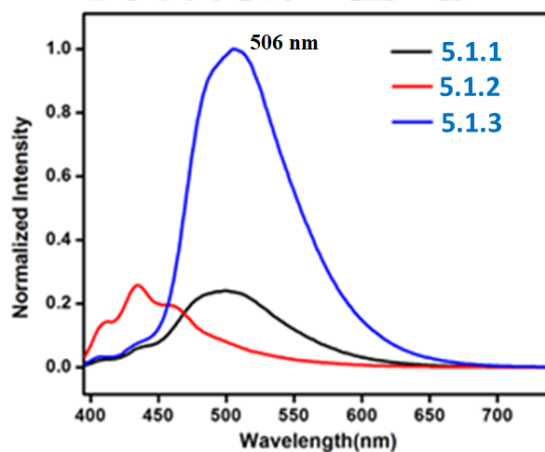
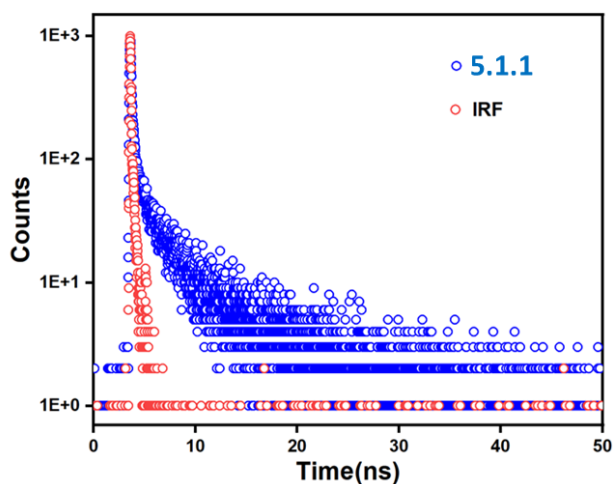


**Figure A5.6**: (a) Fluorescence spectra of three mercury complexes **5.1.1-5.1.3** ( $3 \times 10^{-6}$  M) in  $\text{CHCl}_3$  solvent ( $\lambda_{\text{ex}} = 380$  nm)

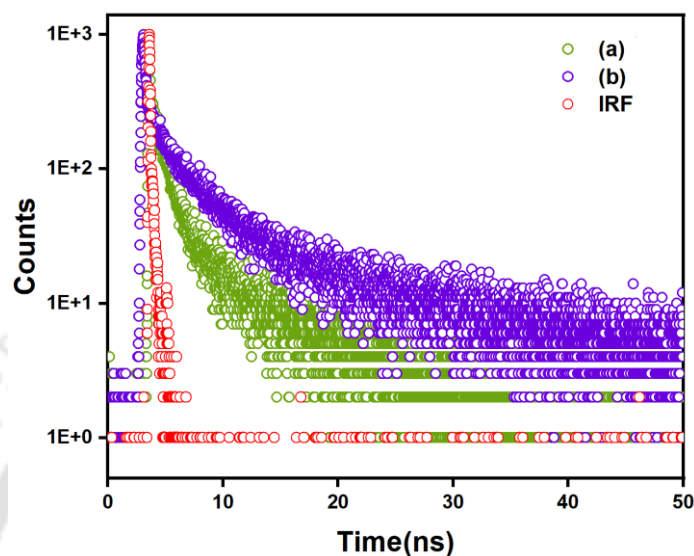


<b>5.1.1</b>	$B_i$	$\Delta B_i$	$f_i$ (%)	$\Delta f_i$ (%)	$\tau_i$ (ns)	$\Delta \tau_i$ (ns)
1	225.6458	3.9160	24.129	7.286	0.279	0.079
2	55.6298	0.8358	75.871	1.224	3.558	0.004

Average lifetime =  $0.24 \cdot 0.279 + 0.76 \cdot 3.558 = 2.77$  ns.

**Figure A5.7:** Fluorescence lifetime decay profile of **5.1.1** in dimethyl sulfoxide solvent ( $\lambda_{\text{ex}} = 400$  nm) monitored at 528 nm.

(IRF= Instrument Response Function)



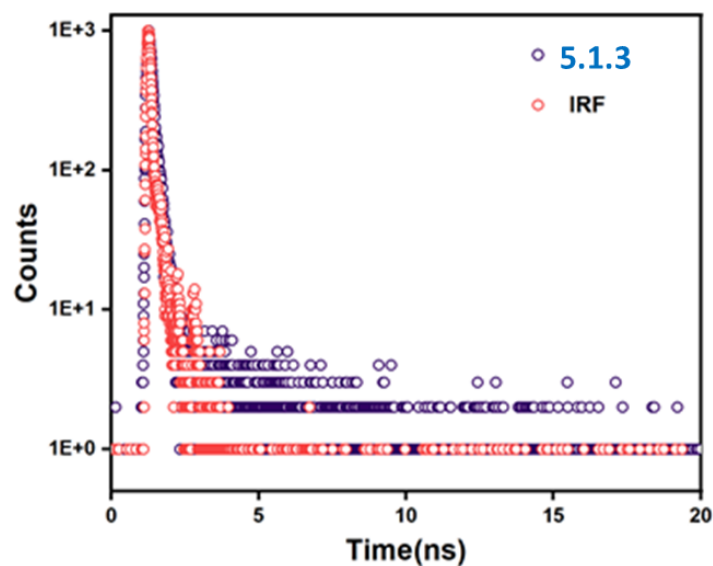
(a)	$B_i$	$\Delta B_i$	$f_i$ (%)	$\Delta f_i$ (%)	$\tau_i$ (ns)	$\Delta \tau_i$ (ns)
1	277.9727	1.7334	58.762	0.724	1.212	0.007
2	23.7217	0.6248	41.238	1.099	9.964	0.003

Average life time =  $0.59 \cdot 1.21 + 0.62 \cdot 9.9 = 6.84$  ns

(b)	$B_i$	$\Delta B_i$	$f_i$ (%)	$\Delta f_i$ (%)	$\tau_i$ (ns)	$\Delta \tau_i$ (ns)
1	232.8767	1.8332	48.717	0.848	1.138	0.011
2	36.4288	0.9129	51.283	1.304	7.661	0.003

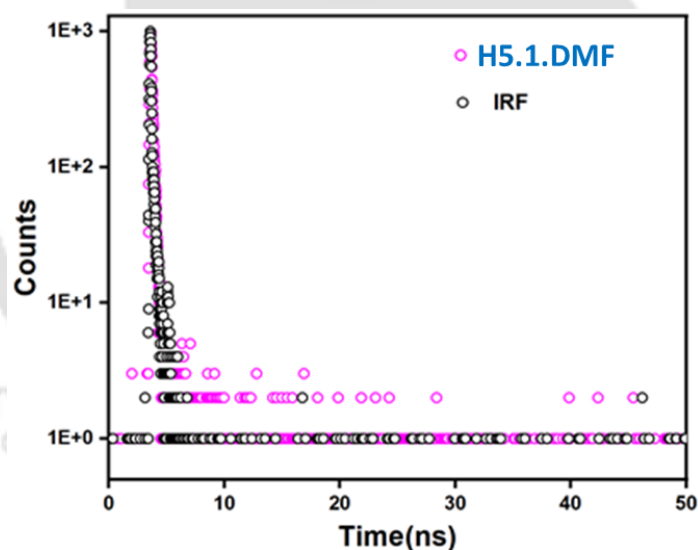
Average life time =  $0.49 \cdot 1.138 + 0.51 \cdot 7.66 = 4.45$  ns

**Figure A5.8:** Fluorescence lifetime decay profile of **5.1.2** in dimethyl sulfoxide solvent ( $\lambda_{\text{ex}} = 400$  nm) monitored at (a) 429 nm (b) 456 nm.



5.1.3	$B_i$	$\Delta B_i$	$f_i$ (%)	$\Delta f_i$ (%)	$\tau_i$ (ns)	$\Delta \tau_i$ (ns)
1	1016.8063	5.3923	100.000	18.632	0.152	0.028

**Figure A5.9:** Fluorescence lifetime decay profile of **5.1.3** in dimethyl sulfoxide solvent ( $\lambda_{\text{ex}} = 400$  nm) monitored at 505 nm.



H5.1.DMF	$B_i$	$\Delta B_i$	$f_i$ (%)	$\Delta f_i$ (%)	$\tau_i$ (ns)	$\Delta \tau_i$ (ns)
1	1230.1014	11.3906	100.000	32.054	0.151	0.047

**Figure A5.10:** Fluorescence lifetime decay profile of **H5.1.DMF** in dimethylsulfoxide solvent ( $\lambda_{\text{ex}} = 400$  nm) monitored at 505 nm.

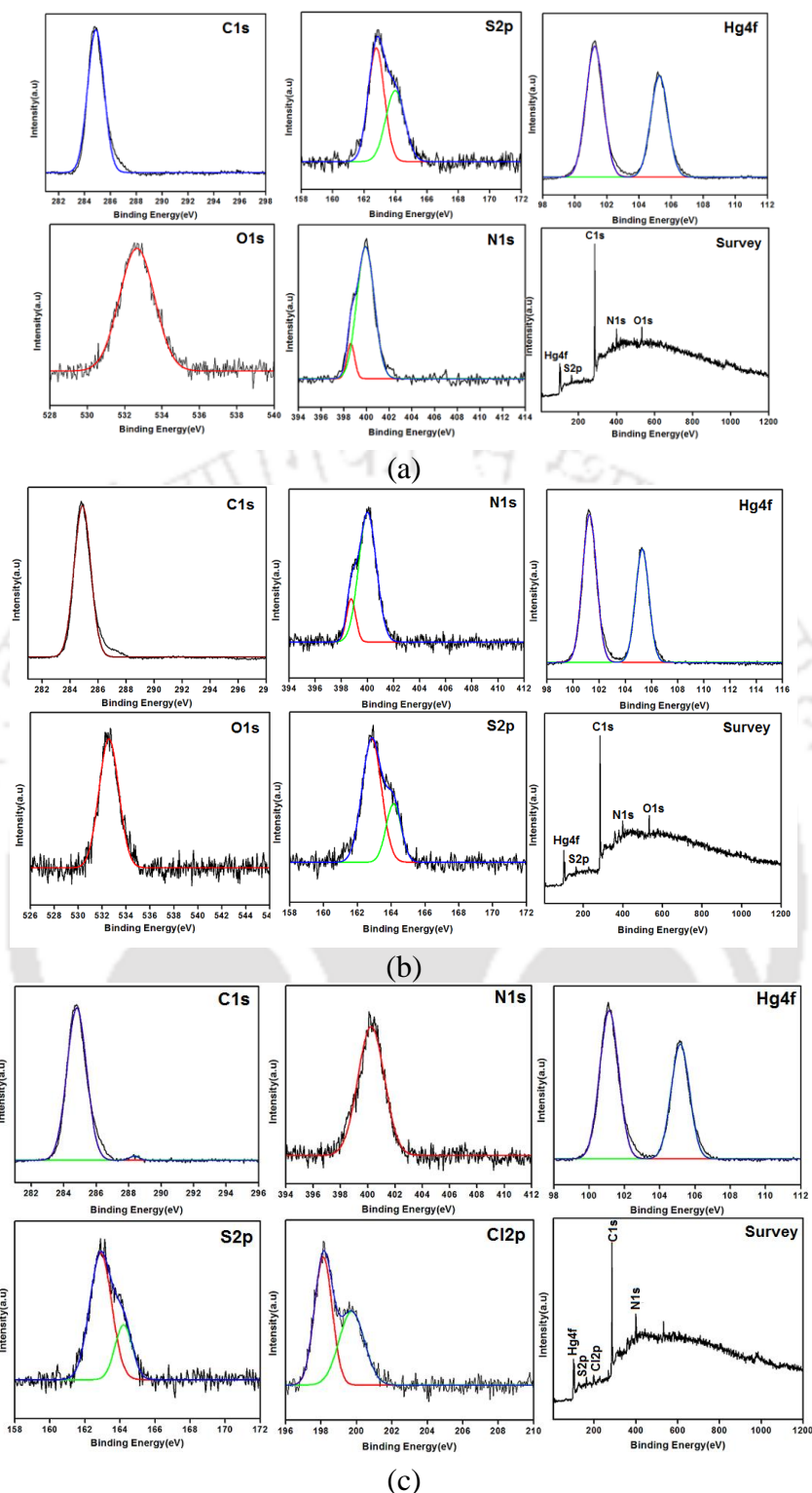


Figure A5.11: Survey and high-resolution XPS spectra of a) 5.1.1 (b) 5.1.2 and (c) 5.1.3.

## *Thesis Conclusion*

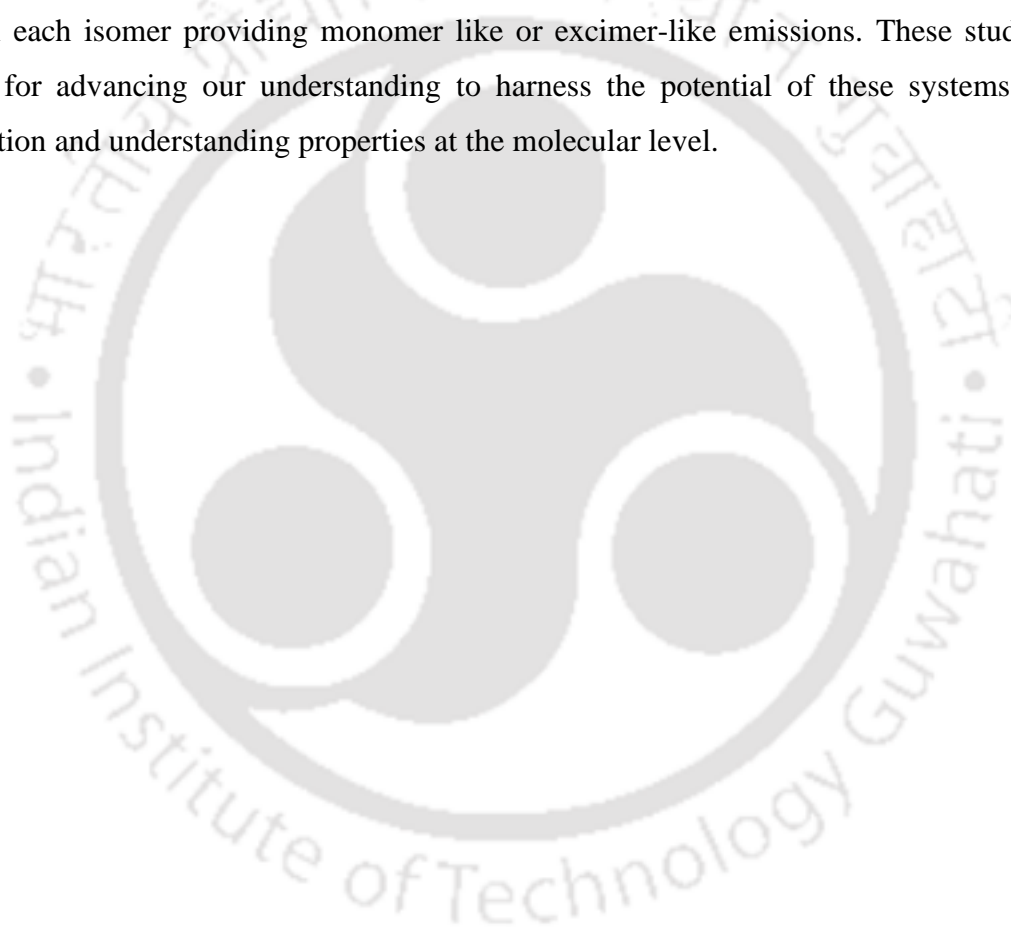
In the thesis, the self-assemblies of a series of urea and thiourea derived from sulfa-drug molecules, each having a sulphonamide unit, were comprehensively analyzed. The research was focused on the assemblies in the solid state to characterize and study the physical properties of the parent compounds, hydrates, solvates, polymorphs, and ionic co-crystals of the chosen host molecules. The research also included a study on the role of the mercury complex of a thiourea analogue linked to an anthracenyl unit to generate conformational isomers. In general, the research was performed through the lens of crystal engineering, aiming to understand various self-assembly properties of the crystal structures for desired properties and also to check the binding processes through solution studies by using various spectroscopic techniques. Selected energy optimization by DFT was carried out to decipher the structure-property relations.

From the studies on the urea derived sulfa-drugs, a notable observation was the identification of the homo-dimeric synthons within their assemblies and their roles in forming polymorphic solvates, two different solvates from the same solvent, and systematic formation of a series of inclusion of three tetrabutylammonium halide (halide = chloride, bromide iodide) with same host and C-N bond formation by tetrabutylammonium salt. The urea derivatives derived from the sulfadiazine drug molecule exhibited the ability to accommodate one or two dimethylformamide (DMF) molecules into their interstitial spaces depending on the crystallization conditions. The structural arrangement of a hydrogen-bonded dimer was present in the inclusion complex having two DMF was reflected in the inclusion complexes with the tetrabutylammonium halides with the host. Thus, the homodimer facilitated the inclusion of halide anions, including chloride, bromide, and iodide, resulting in the formation of three isostructural ionic co-crystals. On the contrary, the fluoride ion was engaged in the deprotonation of acidic N-H protons, thereby led to tetrabutylammonium salt of the host. This was attributed to smaller ionic radius and higher electronegativity of fluoride ions. This phenomenon underscores the distinct reactivity of the fluoride ion compared to other halide ions, with these unique interactions being explored both in solid and solution phases for fluoride ion detection. The urea derivative of sulfamethoxazole demonstrated a capability to form different polymorphic solvates. The polymorph of DMF solvates were having distinct hydrogen bonding signatures that were formed between the DMF molecules and the host. The polymorphs of solvate are particularly important in pharmaceutical sciences, which influence

the bioavailability, stability and dissolution rate of the drug molecules. Furthermore, the tetrabutylammonium salts of bromide and fluoride induce deprotonation of the acidic proton, resulting in salt formation in this particular example. On the other hand, the host reacted with tetrabutylammonium iodide salt to provide a new salt; it was formed through the formation of a C-N bond on the host to form a modified N-butylated host. The sulfathiazole-derived urea host had provided solvates with DMF and DMSO, and an ionic co-crystal with the tetrabutylammonium iodide.

Structural sites on a series of thiourea derived sulfa-drugs provided various self-assemblies, displaying versatile conformations (*syn-syn*, *syn-anti*, *anti-anti*, and *anti-syn*). The notable feature was the formation of conformational polymorphs of the phenylthiourea derived sulfathiazole. In these polymorphs, the thiourea moiety exhibited *anti-anti* in one form and the other form was having *syn-anti* conformation. Comparative stability analysis, confirmed the *syn-anti* conformation of the thiourea component is energetically more stable than the *anti-anti* conformation. The 4-nitrophenylthiourea derived sulfathiazole exhibited various solvates, providing diversity in solvent dependent conformations in the respective thiourea segment of solvates. The anhydrous form had *syn-anti* conformation, solvates having DMF, DMA, or DMSO exhibited *anti-anti* conformation of the host. In the self-assembly processes of positional isomers such as 2,3-, 2,4-, and 3,4-dichlorophenylthiourea derived sulfathiazole, there were different types of chlorine-chlorine interactions vary depending on the positions of the chlorine atoms on the phenyl ring. The orientations of the sulphonamide groups across the dimeric assemblies were dependent on the orientation of the urea units and had a major contribution to the respective hydrogen-bond scheme. The optimized energy of the homodimers within the self-assemblies could be used to describe the trends in melting points of the self-assemblies three positional isomers. Though the hydrogen-bonded homodimers were prominent in various forms of thiourea derived sulfathiazole, the 4-nitrophenylthiourea derived sulfamethazine did not engage in the formation of such hydrogen bonded homodimer. This was attributed to the steric effects of the methyl groups present in the parent sulfamethazine host. This derivative led to the formation of cyclic or chain-like hydrogen bond assemblies in assemblies of hosts in different crystalline forms. The hydrogen-bonded chain formation in the DMSO solvate was observed; it was attributed to participation of DMSO molecule in hydrogen bonding by disrupting the homodimers. Having the nitro-group as auxochrome in the 4-nitrophenylthiourea derivative enhanced its ability to detect fluoride ions at various concentrations. This showcased its potential utility in analytical applications.

Conformational isomers of an anthracenyl-derived thiosemicarbazone mercury complex were reported. This example was the first isolated mercury complex that had maintained clear distinctions in solution as well as in solid to show distinct properties. The isomers were established by NMR studies in solution, and in solid state those were characterized by X-ray crystal structures. In this case, the E or Z form across an extended conjugated structure was stabilized in independent isomers. The interactions of solvent molecules with the isomers helped to interconvert the isomers in solvent by varying solvent and reaction conditions. The two isomers had characteristic emission features in the solution. The independent types of emissions originated from the stacking patterns of the anthracenyl units in each isomer providing monomer like or excimer-like emissions. These studies are critical for advancing our understanding to harness the potential of these systems in ion recognition and understanding properties at the molecular level.



---

## Details of the analytical equipment

### **X-Ray Crystallography**

The X-ray crystallographic data were collected at 296 K with Mo K $\alpha$  radiation ( $\lambda = 0.71073$  Å) using a Bruker Nonius SMART CCD diffractometer or Oxford SuperNova diffractometer. CrysAlisPro software was used for analysis of data obtained by Oxford SuperNova diffractometer; whereas SAINT and XPREP softwares were used for Bruker Nonius SMART APEX CCD diffractometer. The structures were solved by direct methods and refined by full-matrix least-square calculations using SHELXTL-14 and SHELXTL-97 software.<sup>1</sup> All the non-H atoms were refined in the anisotropic approximation against  $F^2$  of all reflections. All the H atoms were refined in isotropic approximation and treated as ‘riding’ in calculated positions. The locations of the H atoms of the protonated organic molecules were justified by difference Fourier synthesis map. The H-atoms attached to water molecules were located in the difference Fourier synthesis maps, and refined with isotropic displacement coefficients. It was also necessary to apply restraints to optimize the distances of some hydrogen atoms of water molecules. The CIF of all the compounds characterized by single crystal X-ray structure are included in the soft copy.

Powder X-ray diffraction patterns were recorded by using a Rigaku X-ray diffractometer where copper K $\alpha$  ( $\lambda=1.54$ Å) was used as the source with 9 kW power equipped on a glass surface of air-dried sample using a secondary curved graphite monochromator. Diffraction patterns were collected over a  $2\theta$  range of 5–45° at a step scan rate of 0.02°. For molecular packing diagram we used mercury-3.7 software.<sup>3</sup>

### **FT-IR, UV-visible, Fluorescence, NMR, Mass spectroscopy, Quantum yields and Lifetime measurements**

The infra-red spectra of the solid samples were recorded with a Perkin Elmer Spectrum Two Fourier transform infrared (FT IR) spectrometer in the region of 4000–400  $\text{cm}^{-1}$  by using the ATR method. UV-visible absorption spectra were recorded using Perkin-Elmer Lambda 750 spectrophotometer equipped with double cell compartment. Fluorescence emissions were measured using Horiba Jobin Yvon Fluoromax-4 spectrofluorometer by taking definite amount of solutions and powder samples by exciting at required wavelengths.  $^1\text{H-NMR}$  was recorded on a Varian 400 MHz and BRUKER Ascend 600 MHz NMR spectrometer using TMS as internal standard.

The ESI-mass spectrum of all the compounds were recorded on an Agilent QTOF 6520 mass spectrometer. Quantum yields of solution compounds were measured by of by exciting at the stipulated wavelength in a Horiba Jobin Yvon Fluoromax-4 spectrofluorometer. Lifetime decay profiles were measured on an Eddinburg Instrument, Model: FSP920 (by using excitation source 336 nm). The X-ray photo electron spectroscopy (XPS) study was performed using a PHI5000 Versa Probe III XPS system using monochromatic K $\alpha$  radiation at a 1486.7 eV X-ray source. Elemental analyses were carried out on a 3000 series EuroEA elemental analyzer.

All the chemicals and solvents used were as obtained from the standard suppliers such as Sigma Aldrich, E. Merck, Ranbaxy etc. The solvents for spectroscopic were of HPLC grade (Aldrich or Merck) and used as such.

### **Thermal analyses (TGA and DSC), elemental analyses and FESEM**

Thermogravimetry were carried out by using a thermal analyser (STA449 F3 Jupiter and SDTQ600) under argon with a heating rate of 10 °C min<sup>-1</sup>. DSC-thermograms were recorded on a Mettler Toledo DSC-1 with a heating rate of 10 °C min<sup>-1</sup>. Elemental analyses were performed with a Perkin-Elmer PE 2400 II CHNS micro analytical analyzer. FESEM studies were performed on a Gemini 300 FESEM instrument (Carl Zeiss) with samples prepared by placing ~2  $\mu$ L of 1 mM in DMF solution by drop-cast method on a glass plate covered with aluminium foil.

### **References:**

1. (a) G. M. Sheldrick, *Acta Cryst.*, 2008, **A64**, 112-122; (b) G. M. Sheldrick, *Acta Cryst.*, 2015, **A71**, 3-8.
2. L. J. Farrugia, *J. Appl. Cryst.*, 1997, **30**, 565.
3. C. F. Macrae, P. R. Edgington, P. McCabe, E. Pidcock, G. P. Shields, R. Taylor, M. Towler, J. van de Streek, *J. Appl. Cryst.*, 2006, **39**, 453-457

### **Crystallographic data and refinement parameters for compounds**

Compound No.	2.1.1	2.1.2	2.1.3	2.1.4

Formulae	C <sub>17</sub> H <sub>14</sub> N <sub>6</sub> O <sub>5</sub> S	C <sub>23</sub> H <sub>28</sub> N <sub>8</sub> O <sub>7</sub> S	C <sub>33</sub> H <sub>50</sub> N <sub>7</sub> O <sub>5</sub> S <sub>1</sub> Cl <sub>1</sub>	C <sub>33</sub> H <sub>50</sub> N <sub>7</sub> O <sub>5</sub> S <sub>1</sub> Br <sub>1</sub>
CCDC No.	<b>1994468</b>	<b>2086584</b>	<b>1994471</b>	<b>1994470</b>
Mol. wt.	487.50	560.59	692.31	736.77
Space group	<i>P</i> $\bar{1}$	<i>P</i> $\bar{1}$	<i>P</i> 2 <sub>1</sub> / <i>n</i>	<i>P</i> 2 <sub>1</sub> / <i>n</i>
<i>a</i> /Å	5.9689(6)	8.4829(18)	9.050(2)	9.0438(6)
<i>b</i> /Å	8.1807(8)	9.972(2)	26.019(6)	25.8772(18)
<i>c</i> /Å	23.330(2)	17.103(4)	16.318(4)	16.5480(12)
$\alpha$ /°	83.186(8)	74.507(8)	90	90.00
$\beta$ /°	85.440(8)	81.154(8)	90.644(9)	90.654(2)
$\gamma$ /°	81.828(9)	85.623(8)	90	90.00
V/ Å <sup>3</sup>	1117.40(19)	1376.7(5)	3842.2(15)	3872.4(5)
Density/g.cm <sup>-3</sup>	1.449	1.352	1.197	1.264
Abs. Coeff. /mm <sup>-1</sup>	0.198	0.174	0.200	1.161
F(000)	508	588	1480	1552
Total No. of reflections	3944	4860	6808	6866
Reflections, <i>I</i> > 2σ( <i>I</i> )	1819	3417	3533	3911
Max. θ/°	25.049	25.049	25.050	25.049
Ranges (h, k, l)	-7 ≤ h ≤ 7 -7 ≤ k ≤ 9 -19 ≤ l ≤ 27	-10 ≤ h ≤ 10 -11 ≤ k ≤ 11 -20 ≤ l ≤ 20	-10 ≤ h ≤ 10 -31 ≤ k ≤ 31 -19 ≤ l ≤ 19	-10 ≤ h ≤ 10 -30 ≤ k ≤ 30 -19 ≤ l ≤ 19
Complete to 2θ (%)	99.9	99.9	100.0	100.0
Data/ Restraints/Parameters	3944/0/341	4860/0/368	6808/11/428	6866/19/432
Goof ( <i>F</i> <sup>2</sup> )	0.975	1.103	1.081	0.953
R indices [ <i>I</i> > 2σ ( <i>I</i> )]	0.0629	0.0549	0.1094	0.0662

wR <sub>2</sub> [ $I > 2\sigma(I)$ ]	0.1207	0.1269	0.1835	0.2206
R indices (all data)	0.1511	0.0822	0.1955	0.1199
wR <sub>2</sub> (all data)	0.1733	0.1401	0.2268	0.2856

Compound No.	2.1.5	2.1.6	3.1.1	3.1.2
Formulae	C <sub>33</sub> H <sub>50</sub> N <sub>7</sub> O <sub>5</sub> S <sub>1</sub> I <sub>1</sub>	C <sub>33</sub> H <sub>49</sub> N <sub>7</sub> O <sub>5</sub> S	C <sub>20</sub> H <sub>22</sub> N <sub>6</sub> O <sub>7</sub> S	C <sub>20</sub> H <sub>22</sub> N <sub>6</sub> O <sub>7</sub> S
CCDC No.	<b>1994472</b>	<b>1994469</b>	<b>2114796</b>	<b>2114797</b>
Mol. wt.	783.76	655.85	490.49	490.49
Space group	$P 2_1/n$	$P 2_1/c$	$P 2_1/n$	$P \bar{1}$
$a / \text{\AA}$	9.0973(16)	20.3850(17)	5.4023(8)	7.375(2)
$b / \text{\AA}$	25.648(5)	9.3503(7)	23.533(4)	12.029(3)
$c / \text{\AA}$	17.041(3)	20.0936(13)	18.032(3)	13.589(3)
$\alpha / ^\circ$	90	90	90	108.408(9)
$\beta / ^\circ$	90.385(5)	111.978(8)	93.805(6)	94.844(9)
$\gamma / ^\circ$	90	90	90	93.191(11)
$V / \text{\AA}^3$	3976.0(12)	3551.6(5)	2287.4(6)	1135.5(5)
Density/g.cm <sup>-3</sup>	1.308	1.227	1.424	1.435
Abs. Coeff. /mm <sup>-1</sup>	0.903	0.140	0.196	0.197
F(000)	1620	1408	1024	512
Total No. of reflections	7038	6277	4060	4014
Reflections, $I > 2\sigma(I)$	5546	2674	2826	3091
Max. $\theta / ^\circ$	25.047	25.048	25.049	25.047
Ranges (h, k, l)	-10 ≤ h ≤ 10 -30 ≤ k ≤ 30 -20 ≤ l ≤ 20	-24 ≤ h ≤ 20 -9 ≤ k ≤ 11 -23 ≤ l ≤ 23	-6 ≤ h ≤ 6 -28 ≤ k ≤ 28 -21 ≤ l ≤ 21	-8 ≤ h ≤ 8 -14 ≤ k ≤ 14 -16 ≤ l ≤ 16
Complete to 2 $\theta$ (%)	100.0	99.9	99.9	100.0

Data/ Restraints/Parameters	7038/3/432	6277/0/419	4060/0/321	4014/0/310
Goof ( $F^2$ )	1.242	1.000	1.111	1.038
R indices [ $I > 2\sigma(I)$ ]	0.0732	0.0690	0.0691	0.0468
wR <sub>2</sub> [ $I > 2\sigma(I)$ ]	0.2241	0.1531	0.1737	0.1263
R indices (all data)	0.0926	0.1614	0.0985	0.0641
wR <sub>2</sub> (all data)	0.2465	0.2120	0.1931	0.1378

Compound No.	3.1.3	3.1.4	3.2.1	3.2.2
Formulae	C <sub>33</sub> H <sub>50</sub> N <sub>6</sub> O <sub>6</sub> S	C <sub>37</sub> H <sub>59</sub> N <sub>6</sub> O <sub>6</sub> SI <sub>1</sub>	C <sub>19</sub> H <sub>20</sub> N <sub>6</sub> O <sub>6</sub> S <sub>2</sub>	C <sub>18</sub> H <sub>19</sub> N <sub>5</sub> O <sub>6</sub> S <sub>3</sub>
CCDC No.	<b>2114795</b>	<b>2126026</b>	<b>2114798</b>	<b>2114799</b>
Mol. wt.	658.85	842.86	492.53	497.56
Space group	$P \bar{1}$	$P \bar{1}$	$P 2_1/n$	$P 2_1/c$
$a/\text{\AA}$	8.756(2)	9.4076(13)	6.620(4)	25.35(5)
$b/\text{\AA}$	11.006(3)	9.9862(12)	17.561(11)	5.0173(8)
$c/\text{\AA}$	19.951(5)	24.181(3)	19.335(11)	17.801(8)
$\alpha/^\circ$	76.116(8)	101.513(4)	90	90
$\beta/^\circ$	84.901(9)	90.566(5)	98.96(2)	105.40(11)
$\gamma/^\circ$	69.801(8)	104.734(4)	90	90
$V/\text{\AA}^3$	1751.7(7)	2148.4(5)	2220.34	2183(4)
Density/g.cm <sup>-3</sup>	1.249	1.303	1.473	1.514
Abs. Coeff. /mm <sup>-1</sup>	0.143	0.841	0.290	0.386
F(000)	708	880	1024	1032
Total No. of reflections	6209	7609	3927	3834
Reflections, $I > 2\sigma(I)$	5010	4508	1722	1908
Max. $\theta/^\circ$	25.049	25.049	25.050	25.050
Ranges (h, k, l)	$-10 \leq h \leq 10$ $-13 \leq k \leq 13$	$-11 \leq h \leq 11$ $-11 \leq k \leq 11$	$-7 \leq h \leq 7$ $-20 \leq k \leq 20$	$-30 \leq h \leq 29$ $-5 \leq k \leq 5$

	$-23 \leq l \leq 23$	$-28 \leq l \leq 28$	$-22 \leq l \leq 23$	$-13 \leq l \leq 21$
Complete to $2\theta$ (%)	99.9	100.0	100	99.9
Data/ Restraints/Parameters	6209/0/420	7609/3/466	3927/0/312	3834/0/303
Goof ( $F^2$ )	1.068	1.026	1.081	1.015
R indices [ $I > 2\sigma(I)$ ]	0.0586	0.0528	0.0490	0.0721
wR <sub>2</sub> [ $I > 2\sigma(I)$ ]	0.1509	0.1446	0.1346	0.1516
R indices (all data)	0.0742	0.1033	0.0939	0.1484
wR <sub>2</sub> (all data)	0.1687	0.1807	0.1764	0.2107

Compound No.	<b>3.2.3</b>	<b>4.1.1</b>	<b>4.1.2</b>	<b>4.2</b>
Formulae	C <sub>32</sub> H <sub>49</sub> N <sub>6</sub> O <sub>5</sub> S <sub>2</sub> I <sub>1</sub>	C <sub>16</sub> H <sub>14</sub> N <sub>4</sub> O <sub>2</sub> S <sub>3</sub>	C <sub>16</sub> H <sub>14</sub> N <sub>4</sub> O <sub>2</sub> S <sub>3</sub>	C <sub>17</sub> H <sub>16</sub> N <sub>4</sub> O <sub>3</sub> S <sub>3</sub>
CCDC No.	<b>2114800</b>	<b>2291589</b>	<b>2291590</b>	<b>2291594</b>
Mol. wt.	788.79	390.49	390.49	420.52
Space group	$P \bar{1}$	$P 2_1/c$	$P \bar{1}$	$P 2_1/c$
$a / \text{\AA}$	9.2845(6)	21.496(3)	8.1247(19)	17.9282(11)
$b / \text{\AA}$	10.2816(5)	9.2005(6)	10.437(2)	8.8657(5)
$c / \text{\AA}$	21.5213(13)	19.4002(18)	11.019(3)	12.2141(8)
$\alpha / ^\circ$	95.205(5)	90	107.127(7)	90
$\beta / ^\circ$	90.068(5)	116.093(14)	96.722(8)	106.293(2)
$\gamma / ^\circ$	103.897(5)	90	95.613(8)	90
$V / \text{\AA}^3$	1985.5(2)	3445.9(7)	878.1(4)	1863.4(2)
Density/g.cm <sup>-3</sup>	1.319	1.505	1.477	1.499
Abs. Coeff. /mm <sup>-1</sup>	0.954	0.449	0.440	0.424
F(000)	816	1616	404	872
Total No. of reflections	7020	6071	3094	3297
Reflections, $I > 2\sigma(I)$	3929	4581	1528	2511
Max. $\theta / ^\circ$	25.050	25.048	24.992	25.048

Ranges (h, k, l)	$-11 \leq h \leq 10$ $-12 \leq k \leq 12$ $-24 \leq l \leq 25$	$-25 \leq h \leq 21$ $-10 \leq k \leq 10$ $-23 \leq l \leq 23$	$-9 \leq h \leq 9$ $-12 \leq k \leq 12$ $-13 \leq l \leq 13$	$-21 \leq h \leq 21$ $-10 \leq k \leq 10$ $-14 \leq l \leq 14$
Complete to $2\theta$ (%)	99.9	99.7	99.7	99.9
Data/ Restraints/Parameters	7020/4/431	6071/0/451	3094/0/226	3297/0/245
Goof ( $F^2$ )	1.093	1.070	1.031	1.063
R indices [ $I > 2\sigma(I)$ ]	0.0624	0.0865	0.0781	0.0437
wR <sub>2</sub> [ $I > 2\sigma(I)$ ]	0.1328	0.2028	0.1636	0.1101
R indices (all data)	0.1117	0.1115	0.1741	0.0608
wR <sub>2</sub> (all data)	0.1639	0.2154	0.1981	0.1165

Compound No.	4.3	4.4	4.5	4.6.1
Formulae	$C_{16}H_{12}Cl_2N_4O_2S_3$	$C_{16}H_{12}Cl_2N_4O_2S_3$	$C_{16}H_{12}Cl_2N_4O_2S_3$	$C_{16}H_{13}N_5O_4S_3$
CCDC No.	<b>2291591</b>	<b>2291592</b>	<b>2291593</b>	<b>2291596</b>
Mol. wt.	459.38	459.38	459.38	435.49
Space group	$P \bar{1}$	$P \bar{1}$	$P 2_1/n$	$P 2_1/n$
$a / \text{\AA}$	7.8370(8)	8.1394(10)	7.9736(4)	7.9685(14)
$b / \text{\AA}$	10.9199(11)	11.1797(13)	11.3191(6)	11.1444(19)
$c / \text{\AA}$	11.5898(12)	11.9324(15)	21.6791(12)	21.544(4)
$\alpha / ^\circ$	102.755(3)	108.212(4)	90	90
$\beta / ^\circ$	93.648(3)	98.078(4)	91.928(2)	90.805(6)
$\gamma / ^\circ$	95.688(3)	98.437(4)	90	90
$V / \text{\AA}^3$	958.86(17)	1000.0(2)	1955.52(18)	1913.0(6)
Density/ $\text{g.cm}^{-3}$	1.591	1.526	1.560	1.512
Abs. Coeff. / $\text{mm}^{-1}$	0.686	0.657	0.672	0.422
F(000)	468	468	936	896
Total No. of reflections	3392	3545	3480	3384
Reflections, $I > 2\sigma(I)$	2351	2262	2558	2633

Max. $\theta$ /°	25.040	25.050	25.046	25.042
Ranges (h, k, l)	$-9 \leq h \leq 9$ $-13 \leq k \leq 13$ $-13 \leq l \leq 13$	$-9 \leq h \leq 9$ $-13 \leq k \leq 13$ $-14 \leq l \leq 14$	$-9 \leq h \leq 9$ $-13 \leq k \leq 13$ $-25 \leq l \leq 25$	$-9 \leq h \leq 9$ $-13 \leq k \leq 13$ $-25 \leq l \leq 25$
Complete to $2\theta$ (%)	100.0	100.0	100.0	99.8
Data/ Restraints/Parameters	3392/0/244	3545/0/244	3480/0/244	3384/0/253
Goof ( $F^2$ )	1.052	1.030	1.065	1.046
R indices [ $I > 2\sigma(I)$ ]	0.0421	0.0609	0.0482	0.0712
wR <sub>2</sub> [ $I > 2\sigma(I)$ ]	0.0981	0.1699	0.1109	0.1877
R indices (all data)	0.0750	0.1039	0.0711	0.0868
wR <sub>2</sub> (all data)	0.1081	0.1916	0.1185	0.1936

Compound No.	<b>4.6.2</b>	<b>4.6.3</b>	<b>4.6.4</b>	<b>4.7.1</b>
Formulae	C <sub>19</sub> H <sub>20</sub> N <sub>6</sub> O <sub>5</sub> S <sub>3</sub>	C <sub>20</sub> H <sub>22</sub> N <sub>6</sub> O <sub>5</sub> S <sub>3</sub>	C <sub>20</sub> H <sub>25</sub> N <sub>5</sub> O <sub>6</sub> S <sub>5</sub>	C <sub>22</sub> H <sub>27</sub> N <sub>7</sub> O <sub>6</sub> S <sub>2</sub>
CCDC No.	<b>2291595</b>	<b>2291597</b>	<b>2291598</b>	<b>2291599</b>
Mol. wt.	508.59	522.61	591.75	549.62
Space group	$P \bar{1}$	$P \bar{1}$	$P 2_1/c$	$P \bar{1}$
$a/\text{Å}$	8.2989(7)	8.1560(4)	10.2992(18)	10.9925(7)
$b/\text{Å}$	9.4780(8)	9.4655(5)	8.3282(15)	11.1925(7)
$c/\text{Å}$	16.2747(12)	16.8599(8)	31.021(6)	12.0078(8)
$\alpha$ /°	83.841(6)	81.108(2)	90	76.210(2)
$\beta$ /°	81.363(7)	81.715(2)	95.378(6)	64.831(2)
$\gamma$ /°	69.635(8)	73.502(2)	90	73.899(2)
V/Å <sup>3</sup>	1184.40(18)	1226.09(11)	2649.1(8)	1272.27(14)
Density/g.cm <sup>-3</sup>	1.426	1.416	1.484	1.435
Abs. Coeff./mm <sup>-1</sup>	0.356	0.346	0.483	0.262
F(000)	528	544	1232	576
Total No. of reflections	4188	4342	4664	4500
Reflections, $I > 2\sigma(I)$	3118	3519	3228	4085
Max. $\theta$ /°	25.049	25.047	24.997	25.049

Ranges (h, k, l)	-9 ≤ h ≤ 9 -10 ≤ k ≤ 11 -17 ≤ l ≤ 19	-9 ≤ h ≤ 9 -11 ≤ k ≤ 11 -20 ≤ l ≤ 20	-12 ≤ h ≤ 12 -9 ≤ k ≤ 9 -36 ≤ l ≤ 36	-13 ≤ h ≤ 13 -13 ≤ k ≤ 13 -14 ≤ l ≤ 14
Complete to 2θ (%)	99.9	99.8	100.0	100.0
Data/ Restraints/Parameters	4118/4/308	4342/3/310	4664/0/329	4500/0/346
Goof ( $F^2$ )	1.022	1.062	1.049	1.092
R indices [ $I > 2\sigma(I)$ ]	0.0659	0.0677	0.0462	0.0534
wR <sub>2</sub> [ $I > 2\sigma(I)$ ]	0.1683	0.1889	0.1019	0.1326
R indices (all data)	0.0870	0.0798	0.0772	0.0565
wR <sub>2</sub> (all data)	0.1889	0.1999	0.1128	0.1353

Compound No.	<b>4.7.2</b>	<b>4.7.3</b>	<b>4.7.4</b>	<b>H5.1.DMF</b>
Formulae	C <sub>19</sub> H <sub>20</sub> N <sub>6</sub> O <sub>5</sub> S <sub>2</sub>	C <sub>23</sub> H <sub>27</sub> N <sub>7</sub> O <sub>5</sub> S <sub>2</sub>	C <sub>23</sub> H <sub>27</sub> N <sub>6</sub> O <sub>6</sub> S <sub>4</sub>	C <sub>25</sub> H <sub>24</sub> N <sub>4</sub> OS
CCDC No.	<b>2291600</b>	<b>2291601</b>	<b>2291602</b>	<b>2156292</b>
Mol. wt.	476.53	545.63	611.74	428.54
Space group	<i>P</i> 1	<i>P</i> 1	<i>P</i> 1	<i>P</i> 1
<i>a</i> /Å	8.1853(19)	9.0132(8)	8.318(3)	9.6205(15)
<i>b</i> /Å	8.962(2)	10.6922(10)	10.169(4)	10.1369(14)
<i>c</i> /Å	15.321(4)	14.7621(13)	18.184(7)	12.2575(16)
$\alpha$ /°	79.102(13)	83.183(3)	103.056(13)	101.035(6)
$\beta$ /°	83.990(10)	75.513(2)	98.471(14)	96.439(5)
$\gamma$ /°	78.336(8)	74.145(2)	94.230(14)	101.582(5)
<i>V</i> / Å <sup>3</sup>	1078.3(5)	1323.1(2)	1472.7(10)	1135.2(3)
Density/g.cm <sup>-3</sup>	1.468	1.370	1.379	1.254
Abs. Coeff. /mm <sup>-1</sup>	0.292	0.249	0.370	0.167
F(000)	496	572	638	452
Total No. of reflections	3804	4620	5168	3936
Reflections, $I > 2\sigma(I)$	2697	3795	3618	2879
Max. $\theta$ /°	25.046	25.969	24.995	25.045

Ranges (h, k, l)	-9 ≤ h ≤ 9 -10 ≤ k ≤ 10 -18 ≤ l ≤ 18	-10 ≤ h ≤ 10 -12 ≤ k ≤ 12 -17 ≤ l ≤ 17	-9 ≤ h ≤ 9 -12 ≤ k ≤ 12 -21 ≤ l ≤ 21	-11 ≤ h ≤ 11 -12 ≤ k ≤ 12 -14 ≤ l ≤ 14
Complete to 2θ (%)	99.3	99.2	99.9	97.6
Data/ Restraints/Parameters	3804/0/294	4620/0/339	5168/2/374	3936/0/290
Goof ( $F^2$ )	1.052	1.147	1.066	1.014
R indices [ $I > 2\sigma(I)$ ]	0.0922	0.0762	0.0498	0.0451
wR <sub>2</sub> [ $I > 2\sigma(I)$ ]	0.2273	0.1306	0.1317	0.1236
R indices (all data)	0.1191	0.0940	0.0762	0.0703
wR <sub>2</sub> (all data)	0.2436	0.1413	0.1432	0.1467

Compound No.	5.1.1	5.1.2	5.1.3
Formulae	C <sub>50</sub> H <sub>46</sub> N <sub>8</sub> O <sub>2</sub> S <sub>2</sub> Hg	C <sub>50</sub> H <sub>46</sub> N <sub>8</sub> O <sub>2</sub> S <sub>2</sub> Hg	C <sub>44</sub> H <sub>32</sub> N <sub>6</sub> Cl <sub>2</sub> S <sub>2</sub> Hg
CCDC No.	<b>2156295</b>	<b>2156296</b>	<b>2133994</b>
Mol. wt.	1055.66	1055.66	980.36
Space group	$P 2_1/n$	$P \bar{1}$	$I2/a$
$a/\text{Å}$	16.2442(9)	9.782(6)	15.1199(3)
$b/\text{Å}$	9.3243(6)	16.642(11)	15.0065(3)
$c/\text{Å}$	31.1240(17)	17.023(10)	19.0418(5)
$\alpha/^\circ$	90	107.900(19)	90
$\beta/^\circ$	93.077(2)	105.41(2)	98.545(2)
$\gamma/^\circ$	90	105.33(2)	90
$V/\text{Å}^3$	4707.4(5)	2354(3)	4272.56(17)
Density/g.cm <sup>-3</sup>	1.490	1.489	1.527
Abs. Coeff. /mm <sup>-1</sup>	3.406	3.406	3.863
F(000)	2120	1060	1944
Total No. of reflections	8337	8352	3752
Reflections, $I > 2\sigma(I)$	5822	6938	3302
Max. $\theta/^\circ$	25.049	25.048	24.997

Ranges (h, k, l)	$-19 \leq h \leq 19$ $-11 \leq k \leq 11$ $-37 \leq l \leq 37$	$-11 \leq h \leq 11$ $-19 \leq k \leq 19$ $-20 \leq l \leq 20$	$-10 \leq h \leq 17$ $-11 \leq k \leq 17$ $-22 \leq l \leq 19$
Complete to $2\theta$ (%)	99.9	100.0	99.9
Data/ Restraints/Parameters	8337/0/572	8352/0/572	3752/0/249
Goof ( $F^2$ )	1.005	1.111	1.101
R indices [ $I > 2\sigma(I)$ ]	0.0443	0.0356	0.0366
wR <sub>2</sub> [ $I > 2\sigma(I)$ ]	0.0955	0.0841	0.1034
R indices (all data)	0.0792	0.0497	0.0424
wR <sub>2</sub> (all data)	0.1114	0.101	0.1070



---

### List of Publications

1. **Nath, J.**; Tarai, A.; Baruah, J. B. Copper(II), Zinc(II), and Cadmium(II) Formylbenzoate Complexes: Reactivity and Emission Properties. *ACS Omega* **2019**, *4* (19), 18444–18455.
2. **Nath, J.**; Baruah, J. B. Self-Assemblies of Solvates, Ionic Cocrystals, and a Salt Based on 4-[[4-Nitrophenyl]Carbamoyl]Amino}- N-(Pyrimidin-2-Yl)Benzene-1-Sulfonamide: Study in the Solid and Solution States. *Cryst. Growth Des.* **2021**, *21* (9), 5325–5341.
3. **Nath, J.**; Baruah, J. B. Polymorphic Solvates, Ionic Cocrystals and C-N Bond Formation to Form Ionic Cocrystals in Sulfamethoxazole and Sulfathiazole-Derived Urea. *CrystEngComm* **2022**, 3394–3408.
4. **Nath, J.**; Baruah, J. B. E- or Z-Isomers Arising from the Geometries of Ligands in the Mercury Complex of 2-(Anthracen-9-Ylmethylene)-N-Phenylhydrazine Carbothioamide. *ACS Omega* **2023**, *8* (45), 42827–42839.
5. **Nath, J.**; Baruah, J. B. Assemblies of Sulfathiazole and Sulfamethazine Derived Thiourea: Polymorphs, Solvates and Fluoride Detection, *Cryst. Growth Des.* **2024**, *24*, 1910–1925.



# JITENDRA NATH

## RESEARCH SCHOLAR

## EDUCATION

**2024**

Doctor of Philosophy (Ph.D.) in Chemistry (Supramolecular Chemistry and Crystal engineering)

Indian Institute of Technology Guwahati

Thesis Title: *Self-assemblies of Sulphonamide Derived Urea, Thiourea and Conformational Isomers of a Mercury Complex*

Supervisor: Prof. Jubaraj Bikash Baruah

Status: Defended thesis

**2016**

Master of Science (M.Sc.) in Chemistry (69%)

Ravenshaw University, Odisha, India

**2013**

Bachelor of Science (B.Sc.) in Chemistry (72%)

Utkal University (Stewart Science College), Odisha, India

## WORK EXPERIENCE

SC-XRD Operator (July 2019 - Dec 2023) Expertise in Bruker and Rigaku Oxford Single Crystal Machines Proficient in XShell, OLEX, WinGX for crystal structure solving and have been acknowledged in seven research articles

## TEACHING EXPERIENCE

Teaching Assistantship (TA) at IIT Guwahati at the undergraduate lab in July-November 2019

Research interest:

❖ Supramolecular Chemistry, Coordination Chemistry, Coordination Polymer, Polymorphism and Ion Sensing

## PRESENT ADDRESS

C/O – Prof. Jubaraj Bikash Baruah

Department of Chemistry

IIT Guwahati

Guwahati, 781039

Assam, India

## PERMANENT ADDRESS

Vill.- Ichhanagar Patana

P.O.- Chhatia

P.S.- Byree

Dist.-Jajpur

Odisha, India – 754023

## CONTACT

### PHONE

+919658134468

+917008364218

### EMAIL:

[jitendra18@iitg.ac.in](mailto:jitendra18@iitg.ac.in)

[nathjitendra5@gmail.com](mailto:nathjitendra5@gmail.com)

## PERSONAL INFORMATION

**Sex:** Male

**Date of Birth:** 1<sup>st</sup> July, 1993

**Nationality:** Indian

**Languages:** Odia, English, and Hindi

## ORCID

 <https://orcid.org/0000-0003-2862-8708>

TH-3407\_186122013

## ACADEMIC ACHIEVEMENTS

---

- Qualified for the CSIR-Junior Research Fellowship (All India Rank = **51**) in the *National Eligibility Test (NET)*, [2017]
- Ranked AIR-491 in *Graduate Aptitude Test in Engineering (GATE)* [2017]

## CONFERENCE AND SEMINARS ATTENDED

---

- Participated in the poster presentation in “**Chemical Research Society of India (CRSI)-2020**”, Organized by Department of Chemistry, School of Advanced Science, VIT, Vellore, India. [Feb 2020]
- Participated in the poster presentation on “**International Conference on Modern Trends in Inorganic Chemistry**” Organized by Department of chemistry, Institute of Science, Banaras Hindu University. [Dec 2022]

## DECLARATION

---

I hereby declare that all the information given above are correct and true to best of my knowledge

Jitendra Nath

